Chiral, polymorphic and stoichiometric selectivity in the continuous production of multi-component targets

Cousen, Alexander

Award date:
2018

Awarding institution:
University of Bath

CMAC
FUTURE MANUFACTURING
RESEARCH HUB

Chiral, polymorphic and stoichiometric selectivity in the continuous production of multi-component targets

Alexander James Pearson Cousen

A thesis submitted for the degree of Doctor of Philosophy

University of Bath

Department of Chemistry

Supervisor: Professor Chick C. Wilson

September 2018

Abstract

The work outlined in this thesis explores the development of multi-component crystalline materials, in terms of the methods used for their preparation and how these materials can be applied so as to exploit their physicochemical properties. Focussing on co-crystals and salts, by combining two molecular entities within the same crystal lattice, the resultant multi-component system can present a different structure and, therefore, different physical attributes when compared to the starting materials. In many cases, these changes are beneficial, with implications for properties such as solubility, melting point and resolution processes. Like with many crystalline forms, multi-component materials can demonstrate structural variations. Here, these can manifest as either polymorphic, stoichiometric or enantiomeric variants, with the possibility of accessing each form depending upon the crystallisation conditions used. As such, each preparative method is reliant on the composition of material used and the kinetic parameters governing the process. These concepts, examples thereof and the methods of analysis used are detailed in Chapters 1-3.

The research discussed within this volume was conducted at the University of Bath as part of the EPSRC Future Manufacturing Hub in Continuous Manufacturing and Advanced Crystallisation (CMAC), a collaboration between academia and industry. The aim is to explore the future manufacturing needs of key commercial bodies, particularly the pharmaceutical industry, concentrating on unit operations such as crystallisation, with a drive to facilitate the adoption of continuous processing techniques.

Chapters 6-8 explore the potential of the chiral active pharmaceutical ingredient (API) naproxen (*NPX*) to form novel multi-component materials, with applications towards the preferential resolution of enantiomers *via* crystallisation. *NPX* preferentially forms a racemic crystalline phase at racemic compositions, rendering it unsuitable for direct resolution by crystallisation. Using a combined approach of mechanochemical and solution-based crystallisation methods, novel materials incorporating the API with a secondary molecule (co-former) were discovered, each displaying different chiral crystalline properties. These ranged from further racemic compounds, racemic solid solutions and that of metastable racemic conglomerates. Samples were phase characterised at enantiopure and racemic compositions using X-ray diffraction (Single Crystal X-ray Diffraction, SCXRD, and Powder X-ray Diffraction, PXRD), thermal methods (Differential Scanning Calorimetry, DSC, and Hot-Stage Microscopy, HSM) and Infrared (IR) spectroscopy.

Chapter 6 focusses particularly on the system of *NPX* with the co-former 2-aminopyridine (*2AP*), a metastable conglomerate. This was determined using crystallographic and binary (melting point) phase diagram analysis. Despite the existence of a racemic solid at the corresponding compositions and through the design of initial cooling crystallisations, based upon ternary (solubility) phase diagram analysis, the homochiral phase was shown to crystallise at compositions tending towards racemic. This demonstrated a system with direct applications towards a preferential crystallisation process.

Finally, in chapter 9, a variety of preparative methods were assessed in terms of their ability to selectively produce either of the stoichiometric co-crystals (1:2 or 1:1) of oxalic acid (*OA*) and urea (*U*). The methods used ranged from mechanochemical to slurrying to evaporation. Both phases could be accessed using these techniques depending upon the solvent or composition of material used. Furthermore, both co-crystals were shown to be selectively yielded from batch cooling crystallisations, with the (1:2) and (1:1) phases being accessed at room and higher temperatures, respectively. Selecting the more stable (1:2) phase and using the continuous crystallisation platforms based at the University of Bath, the Continuous Oscillatory Baffled Crystalliser (COBC) and the Kinetically Regulated Automated Input Crystalliser (KRAIC), it was further shown that this co-crystal could be consistently crystallised in continuous environments.

Acknowledgements

I must say that, without a shadow of a doubt, the last four years have been the best of my life. Not only have I been exposed to lots of amazing science and seen its application in industry, but I have met, worked, collaborated, socialised, lived and just generally had the best time with some of nicest, hardworking and inspiring people I have ever met. I would like to take this opportunity to thank some of them.

First and foremost, I would like to thank Prof. Chick Wilson for being a truly brilliant supervisor. He offered me this PhD and gave me the space to explore my own ideas and interests, not just in terms of my research, but also in allowing me to indulge in my passions for public engagement and teaching. With that I would like to extend my thanks to all the members of the Wilson Group, past and present, for helping me along during this journey, providing me with helpful advice and kindness whenever it was needed. Particularly, I would like to thank Dr. Piba Flandrin for all his help with the continuous crystallisation experiments, Dr. Lauren Hatcher for her crystallography knowledge, Dr. Lauren Agnew for all the hugs and (future Dr.) Polly Payne for being a great project student, assisting me with my experiments and keeping me company over the last few months.

This research was conducted as a collaborative effort, so I would like to thank the EPSRC for all the funding and CMAC for all the opportunities it has brought. I would like to give a special thanks to Prof. Joop ter Horst for all his advice on the chiral crystallisation work and Andy Dunn for working with me and helping me to characterise some of my multi-component materials.

I was also fortunate to go on a three month placement at Bayer Gmbh in Wuppertal, Germany. This was a fantastic experience, exposing me to the important work carried out in pharmaceutical industry, inspiring me to make the transition to industry after my PhD. I would like to thank my industrial supervisor Dr. Guillaume Levilain for the opportunity and for all the advice he gave, both during the placement and after. I would also like to extend my warmest gratitude to the Early Solid State and Polymorphism teams for being truly lovely and welcoming.

Submitting this thesis means an end to my time in the Department of Chemistry at the University of Bath, so with that I would like to say thank you to all the people who have been supported me over the years. Particularly, I would like to thank Dr. Matthew Jones and Prof. Gareth Price for all their assistance and guidance in helping me become an Associate Fellow of the Higher Education Academy (AFHEA).

I would like to thank all my friends and family for their love and support over the years. I would like to mention my Mum, Dad and sister, without whom, I would not be where I am today. I am reflection of them and I hope that I have done them proud. Throughout my time in Bath, I have made some great friends, people who I have been through a lot with. I hope that our friendship never wavers and I give them my deepest thanks. Finally, I would like to thank Vicky. The process of writing this thesis has been a long and frustrating experience, but she has been a ray of sunshine amongst the dark clouds. I would not have met her if it hadn’t been for my PhD, so for that, I am eternally thankful.

Table of Contents

List of Figures

List of Equations

List of Tables

1 Background and theory

Across many industries, particularly the pharmaceutical industry, the ability to manufacture materials in the solid-state is of great importance, with the vast majority of pharmaceutical products being administered as solid dosage forms, be it through tablets, powders or capsules.[1, 2] It is widely understood that the physicochemical properties of a material are directly related to its solid-state structure, with implications on properties such as solubility, stability and bioavailability.[3, 4] In the case of pharmaceuticals, many compounds do not reach the marketplace owing to deficiencies in properties that can affect manufacturing or efficacy upon reaching the end-patient.[5] As a result, the industry today is focussed on addressing these issues, through the manipulation of solid-state structures of active pharmaceutical ingredients (APIs), influencing properties, leading to materials that perform better throughout the pharmaceutical manufacturing and drug life cycles.[6, 7]

In this introduction, many of the principles underpinning solid-state chemistry, particularly in the context of the pharmaceutical industry, will be outlined. The concept of structural variations within small organic molecule crystalline materials, including polymorphic, multi-component and chiral variants, will be introduced, along with the underlying theory of crystallisation and crystallisation techniques, exploring how crystallisation is currently utilised in industry and how it is being developed for the future.

1.1 Solid-state materials – Crystalline and amorphous

Solid materials[7, 8] are divided into subcategories representing different degrees of order, either described as crystalline or amorphous. Amorphous materials[7, 9] have little or no long-range order, but do exhibit short-range order similar to that of liquids. This short-range order stems from atoms or molecules being assembled and connected through a range of localised intermolecular interactions, comparable to that observed in crystalline phases. However, these local arrangements do not extend in a periodic manner throughout the structure, hence, minimising the overall order observed. This disparity between long and short-range order generally leads to less efficient packing and larger overall volumes, when compared to crystalline materials.

In contrast, crystalline solids[10, 11] show both short and long-range order, being built up through the regular and repeating arrangement of structural units in three-dimensions. These structural units can consist of individual or groups of atoms, molecules or ions, each related to each other through symmetry. These units interact through various interactions, from distinct chemical bonds, such as covalent or ionic bonds, to intermolecular bonds, like hydrogen bonds. For a more detailed description of crystalline materials, see Chapter 2. The homogeneous arrangement of units within crystals leads to reproducible and consistent properties, including melting point and solubility.

The absence of long-range order in amorphous materials results in a higher free energy, with respect to crystalline materials, making amorphous solids comparatively less stable (Figure 1.1a).[8] A characteristic phenomenon observed for amorphous materials is that of the glass transition (T_g)[12], whereby, over a specific temperature range, the solid in question changes from a '*glass*' to a viscous liquid phase, known as a '*supercooled liquid*'.[12] With increasing temperature, the molar mobility continues to increase until the material reaches its melting point (T_m) and a liquid is formed. This is not observed in crystalline materials which possess only a characteristic melt at a given temperature.

Likewise, dissolution properties of crystalline and amorphous materials are also different. Due to the less favourable intermolecular interactions observed in amorphous phases, interactions with different solvent environments becomes increasingly favourable. Thus, amorphous materials are generally able

to dissolve more readily than crystalline solids. When an amorphous form of a material is present, dissolving it to excess of the equilibrium solubility exhibited by the crystalline phase results in so called '*supersatured*' solutions. With increasing supersaturation, the thermodynamic driving force for crystallisation increases and over time crystalline solid will begin to nucleate and grow (Figure 1.1b).[8, 9] Depending upon the discrepancy in dissolution rates between amorphous and crystalline solids, amorphous materials can also be used within the pharmaceutical industry as an attractive medium for drug delivery.

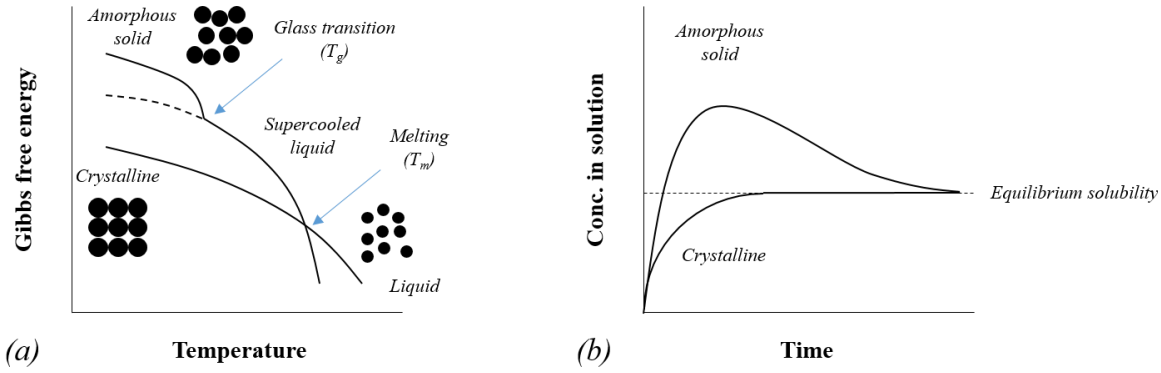

Figure 1. 1 - (a) Gibbs free energy-temperature and (b) Dissolution comparison of amorphous and crystalline materials

Whilst amorphous materials play an important role in many pharmaceutical formulations, given the inherent stability, order and applicability of crystalline materials as APIs, the rest of this introduction will focus on crystalline solid phases only.

1.2 Small-molecule crystalline materials

Crystals have a distinct advantage over other solid forms, due to their stability, reproducibility during manufacture and consistent physicochemical properties, arising from their inherent ordered structure.[1, 13] However, particularly with pharmaceutical products, many molecular materials have been shown to have structural variations that possess certain undesirable properties. Many common APIs, administered orally as tablets or powders, are made up of small molecular units that have the potential to form favourable interactions with receptors of choice to produce beneficial therapeutic effects. However, in many cases, these materials also exhibit unsuitable characteristics that can limit their performance, either for the patient or during manufacturing, and, for API materials in screening, hinder their progress to market. This can be seen through the '*Biopharmaceutics Classification System*' (BCS), where therapeutic materials are assessed based upon their aqueous solubility and permeability.[14] Although synthetic modification of APIs has shown promising results in addressing some of these issues, manipulation of the molecular structure itself can lead to undesirable changes in other factors, such as biological activity. Another route, therefore, to changing the physicochemical properties of a material is through the alteration of its intrinsic crystal structure. This can be achieved in a variety of ways, either through the discovery of new crystalline forms (polymorphism) or through the addition of secondary components in the crystal lattice to generate a multi-component system.

1.2.1 Single and multi-component materials

Upon crystallising an API as a single-component system, the molecules may occupy a variety of different crystalline assemblies, where the same molecular components are present, but the molecules themselves reside in different orientations in three-dimensional space. This phenomenon is known as

'*polymorphism*'[14], with each polymorph showing its own set of physical properties. This will be discussed in greater detail in Section 1.2.2.

An API molecule can also be combined with a secondary (or ternary) molecular entity, interacting through non-covalent interactions, to form a novel crystalline structure. Such multi-component complexes[13, 15] occur in a variety of forms, including salts, solvates, hydrates and, more recently, co-crystals. A schematic of the different single and multi-component complexes possible is shown in Figure 1.2.

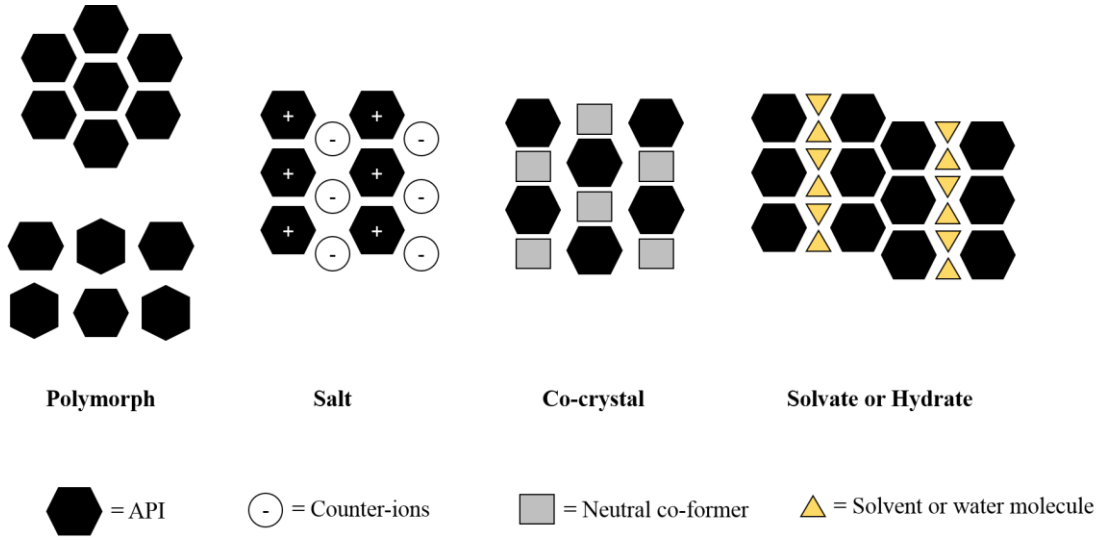

Figure 1. 2 - Schematic diagram of some of the possible single and multi-component complexes used for physicochemical property enhanced with APIs

Salt formation[16, 17] has been one of the primary methods for pharmaceutical material property enhancement for several decades. In the case of multi-molecular complexes, this involves the interaction between an acid and a base, forming a network of electrostatic and intermolecular interactions; this interaction often occurs due to proton transfer. The main limitation in salt formation is the necessity for the species involved to possess ionisable sites, with a sufficient pK_a difference to encourage proton transfer.

In comparison, the formation of co-crystals[18] does not require these ionisable sites, interacting primarily through neutral intermolecular interactions. Co-crystals can be described as *"multiple component crystals in which all components are solid under ambient conditions … and co-exist as a stoichiometric ratio of a target molecule with a neutral molecular co-former".*[19] For pharmaceutical co-crystals, the API is preferably combined with benign molecules from the GRAS (Generally Regarded As Safe) list.

Solvates and hydrates[1, 20], as for co-crystals, are made up from a combination of neutral molecular entities incorporated into a single crystal lattice. However, instead of existing as a solid under ambient conditions, the secondary component or guest molecule can be a liquid. As such, the formation of these materials arises from the amalgamation of a given API with the solvent used for the crystallisation, specifically water in the case of hydrates; these are also commonly known, inaccurately, as '*pseudopolymorphs*'.

By generating beneficial physicochemical properties through structure manipulation[21, 22], the development of multi-component API materials also offers opportunities for intellectual property.[23] In order for a material to be patented, the substance must demonstrate novelty, usefulness and non-

obviousness. The discovery of new multi-component materials between two (or more) molecular entities, defined by the unique arrangement of intermolecular contacts for the construction of a complete crystalline structure, is, by definition, novel, and the characteristic physicochemical properties arising from that structure also highlights the usefulness of these materials. The obviousness in the discovery and preparation of a given material can be related to its predictability. Despite continuing advances in this research area, the disparity between crystallisation and the resultant crystalline phase formed remains, showing that the ability to predict what solid state material will form still remains uncertain, hence, non-obviousness.

1.2.2 Polymorphism

Whilst molecular crystals are made up from an assembly of molecular entities held together by a network of intermolecular interactions, for a given system, the orientation and directionality of the molecules and their associated interactions can vary depending upon crystallisation conditions and relative stabilities of the structural variations.[4] '*Polymorphism*' in the solid state can be described as *"the ability of a compound to crystallise in two or more crystalline phases with different arrangements and/or conformations of molecules in the crystal lattice"*[24, 25], with each different arrangement, or '*polymorph*', having a different set of physical properties. Polymorphism can be classified into the categories of packing and conformational polymorphism. Packing polymorphism occurs through the varied packing of rigid conformations of molecules in three-dimensions, whilst conformational polymorphism relies on the flexibility of the molecular components within crystalline materials. In reality, most polymorphic forms are classified as both having variations in packing and conformation. Selective preparation of individual polymorphs is of great importance for the pharmaceutical industry as each solid form for a particular compound brings its own physical properties, with implications for processing, formulation and drug availability.[14] In addition, this can lead to regulatory concerns and can determine the development process used for a given material. As a result, polymorph screening[1] is now a routine part of solid state development for most APIs.

The relative stabilities of different polymorphic phases is dependent upon their relative free energies, with the most thermodynamically stable phase possessing the lower free energy.[24-26] Under a given set of crystallisation conditions, only one polymorph will have the minimum free energy, with other phases, deemed '*metastable*' polymorphs, having higher free energies and only being able to exist as solid forms as a result of slow transformation kinetics. The stability relationship and possible types of phase transitions between polymorphic forms are described thermodynamically using the terms '*enantiotropy*' and '*monotropy*'.[27] Enantiotropic polymorphs (Figure 1.3a)[24, 25] exhibit interconversion, with one phase transforming into another at a given transition temperature. Here, the form that possesses the lowest Gibbs free energy changes, resulting in a change in relative thermodynamic stability between polymorphs and thus interconversion. This transition is reversible, with the transition temperature being less than the melting point of either polymorphic phase. For monotropic systems (Figure 1.3b)[24, 25], the Gibbs free energy curve of the liquid phase intersects the curves of the polymorphs at a temperature lower than that of the transition point. Here, melting of the more stable phase occurs before the point of interconversion, meaning that under specified conditions, only one polymorphic form is observed.

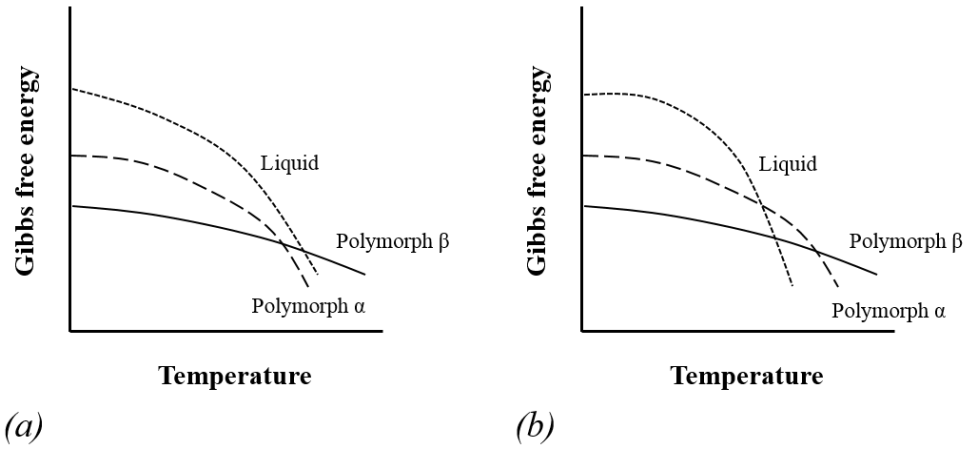

Figure 1. 3 - Gibbs free energy curves for two polymorphic forms (α and β) and a liquid phase for (a) enantiotropic and (b) monotropic systems

By relating the free energy of a polymorphic material to its solubility, it can be shown that the more thermodynamically stable form has a lower comparative solubility.[26] For enantiotropic systems (Figure 1.4a), the solubilities of the polymorphic forms are temperature dependent, highlighting that at a given temperature, the different forms can be interconverted, whilst for monotropic polymorphic materials (Figure 1.4b), the relative solubilities are temperature independent and no interconversion is allowed.

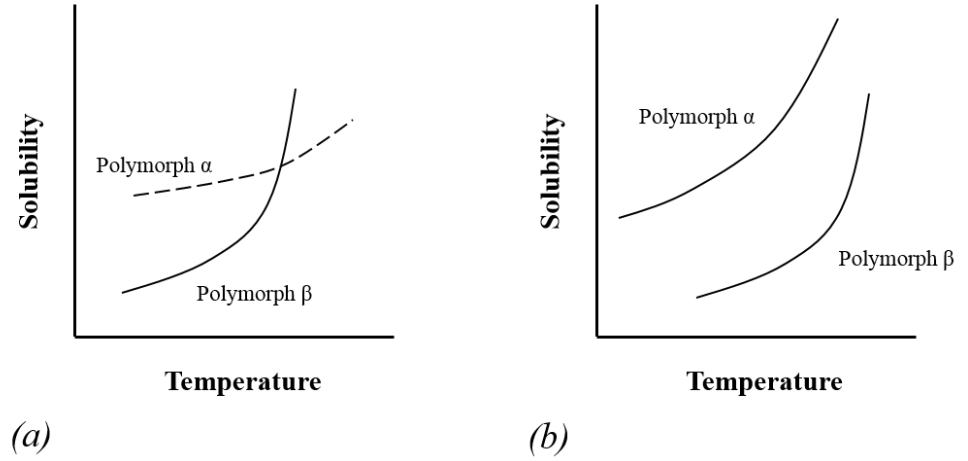

Figure 1. 4 - Relative solubility curves for two polymorphic forms (α and β) for (a) enantiotropic and (b) monotropic systems

Polymorphism is a constant issue within the pharmaceutical industry[1], where the majority of API materials used are small organic molecules, many of which show polymorphic traits. Whilst common in single-component systems, polymorphic variations in multi-component materials, until recently, have had little scrutiny.[3, 28] One intended advantage of co-crystals, salts, etc., is that by combining two or more molecular entities within the same crystal lattice, the variability in intermolecular interactions and, hence, polymorphism would be minimised. However, this hypothesis has, with increasing number of studies, been shown not to be true.[28-30]

1.2.3 Stoichiometric variants in multi-component materials

As well as showing polymorphic variability, whereby molecules pack together in a given stoichiometry within the same crystal lattice, multi-component materials can also show variation in structure by changing the ratio of the distinct molecular entities (Figure 1.5).[31, 32] Stoichiometric variations are classified in a subtly different manner to polymorphs of a different stoichiometry, but for each set ratio

of molecular units, polymorphs thereof are also possible, with each phase showing its own physicochemical properties.

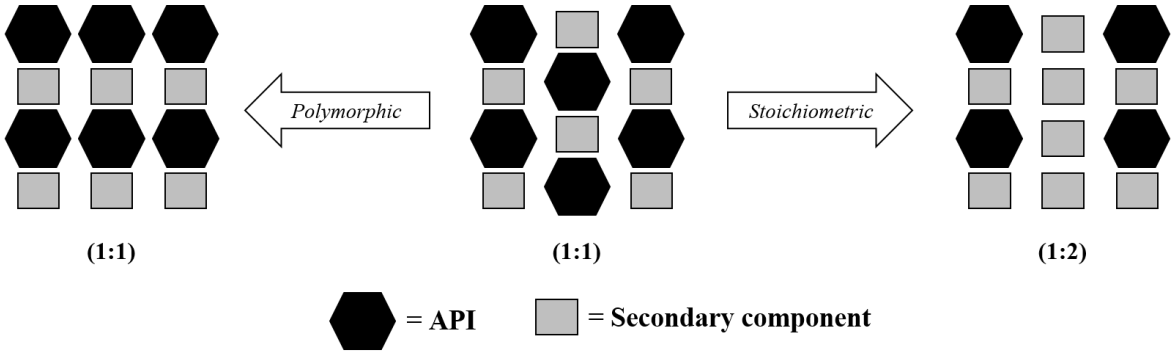

Figure 1. 5 - Schematic diagram comparing polymorphism and stoichiometric variations in multi-component materials

1.2.4 Chiral crystalline materials

Many molecules in nature, as well in the pharmaceutical industry, exhibit a particular form of isomerism called '*stereoisomerism*'.[27, 33] Stereoisomers differ only in the spatial arrangement of their constituent atoms and possess no plane or centre of symmetry. The asymmetry associated with these molecules is usually localised about a specific atom, known as a '*chiral*' centre (Figure 1.6).[34] Chirality leads to molecules having mirror image forms, which are non-superimposable when overlaid. Different chiral forms of the same molecules are called '*enantiomers*' and broadly possess the same properties, except, notably, their ability to rotate plane-polarised light, i.e. optical activity. Molecules of a specific chirality can rotate the light in a clockwise manner (*(+)-dextrorotatory*), whilst another form can rotate in an anti-clockwise direction (*(-)-levorotatory*). Classification of enantiomers, therefore, can be done in two ways; either based upon either their optical activity or their 'handedness'[33]. The method of assigning the handedness of molecules is laid out based upon nomenclature outlined in the Cahn-Ingold-Prelog Rules. By following these rules, each enantiomer can be labelled as either '*Rectus*' (*R*) or '*Sinister*' (*S*):

1. Assigning the atoms about the chiral centre in a ranked order based upon their atomic number
2. Arranging the molecule so that the lowest priority atom is facing backwards
3. Assessing the rotary direction of the larger substituents, labelling clockwise rotations as *R* and anti-clockwise rotations as *S*

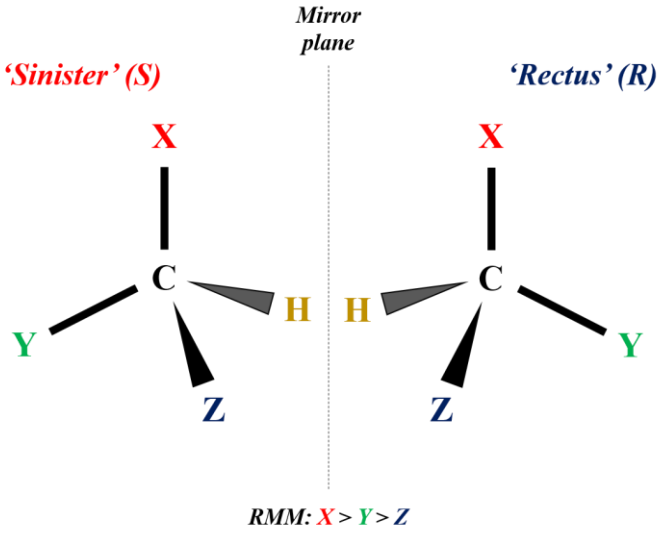

Figure 1. 6 - Opposite chiral molecules, classified as either R or S, as defined by the Cahn-Ingold-Prelog Rules

Whilst opposite enantiomers have the same overall physical properties, each chiral form does show significant differences in terms of their pharmacodynamics or pharmacokinetic activity, i.e. their ability to interact with different receptors within the body. This disparity can manifest itself to different degrees; from seeing little or no difference in the effects of enantiomeric molecules in biological systems, to catastrophic differences, as seen from the case of thalidomide.[35] For this reason, many common APIs are prescribed as enantiomerically pure formulations. However, many synthetic processes yield mixtures of enantiomers that need to be separated[36]. A mixture of enantiomers, made up of 50% *S* and 50% *R* is known as a '*racemic*' mixture and whilst a variety of methods are available for their complete resolution, crystallisation offers a convenient and cost effective way of separating out enantiomers. Broadly, there are two main chiral crystallisation separation techniques; '*preferential*'[37, 38] and '*diastereomeric*'.[39, 40] The research outlined in later Chapters will focus on preferential crystallisation, though both methods are explained here. It should be noted that the efficacy of this crystallisation process is dependent upon the classification of the chiral crystalline phase formed from a racemic solution.

Upon crystallisation of a single-component material (i.e. a chiral molecule at racemic compositions), three types of systems are possible; '*racemic compounds*, *racemic conglomerates* and *racemic solid solutions*' (Figure 1.7a).[35, 36, 41] Racemic compounds are by far the most common phase and consist of both enantiomers, related through symmetry, crystallising together within the same crystal lattice, to form a distinct phase from that of the homochiral. Racemic conglomerates and solid solutions are both comparatively rare. In the former case, both enantiomers crystallise individually, generating a physical mixture of enantiomerically pure crystals, whilst in solid solutions, both enantiomers crystallise together, but are distributed in a more random fashion throughout the structure. In order for individual enantiomers to be selectively crystallised from a racemic solution, a process otherwise known as '*preferential crystallisation*'[38, 42], the system in question must express specific properties, i.e. it must exhibit the characteristics of a racemic conglomerate forming system.

Likewise, these classifications can also be applied to multi-component materials (Figure 1.7b)[41, 43, 44]. By introducing a secondary component (typically achiral) to a target molecule, composed at racemic compositions, a material has the potential, depending upon the nature of the interactions present, of being transformed from a racemic compound to a racemic conglomerate. However, to date, few studies have been conducted exploring the potential of co-crystal or salt formation through which chiral crystalline material can form.

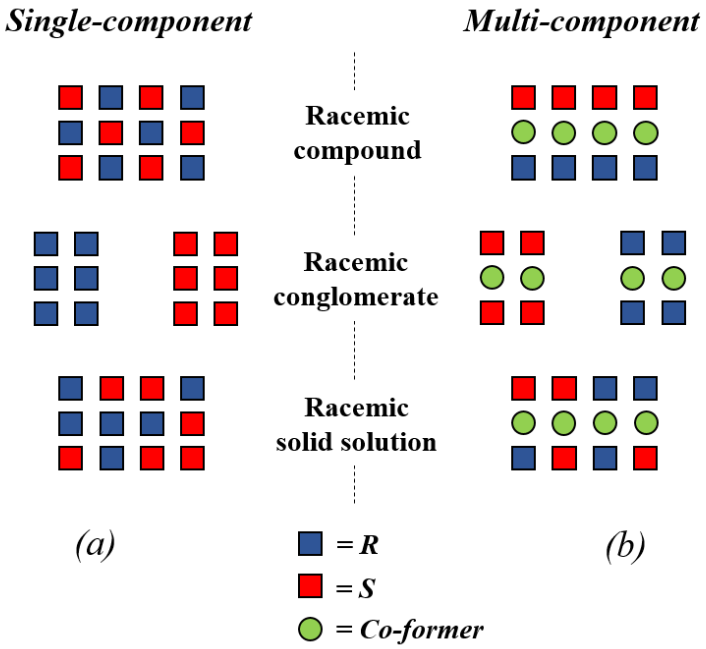

Figure 1. 7 - Schematic diagram comparing the structures of racemic compounds, racemic conglomerates and racemic solid solutions for (a) single-component and (b) multi-component chiral crystalline systems

The distinct advantage of preferential crystallisation is its simplicity; with a conglomerate forming system, opposite enantiomers can be directly resolved through a series of enrichments and seeding crystallisations. However, as previously stated, conglomerate systems are rare. The traditional method of chiral separation through crystallisation is from the preparation of '*diastereomeric salts*' (Figure 1.8).[39, 45] Enantiomerically pure chiral resolving agents are added to a racemic solution, generating two distinct multi-component materials, typically salts. Due to the diastereomeric chiral relationship between the individual enantiomers and the single enantiomer resolving agent (e.g. R, S and S, S), two different crystalline materials are made, each with their own crystalline structure and hence, their own set of physicochemical properties. As a result, these diastereomeric materials have a disparity in solubility, through which the different enantiomers can be separated. Upon optimisation, this method can be a powerful resolution tool, but can require extensive salt screening and a significant enough solubility difference between diastereomeric pairs.

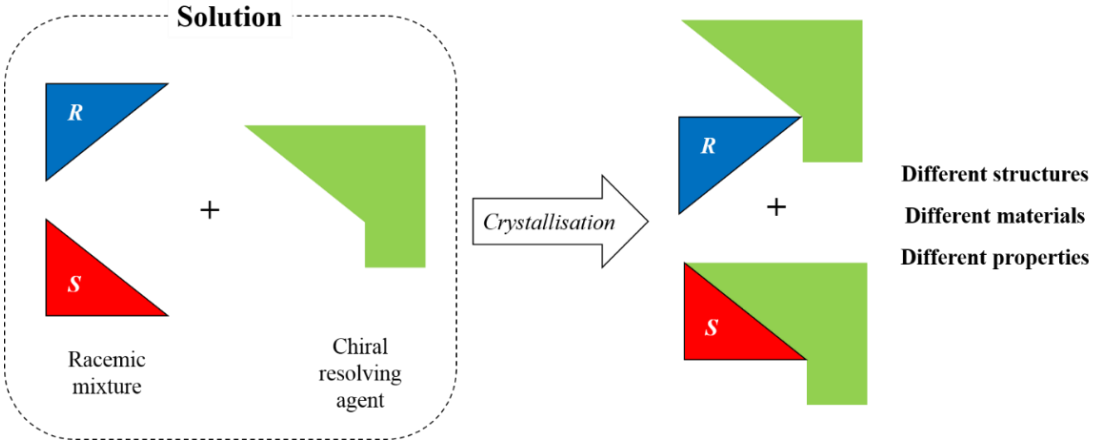

Figure 1. 8 - Classical resolution via the crystallisation of diastereomeric salts

1.3 Crystal engineering – Designing crystalline materials

Molecular crystals consist of the ordered arrangement of discrete units, connected by a network of intermolecular interactions, which collectively determine the stability of the solid.[3, 6, 19] Different polymorphic forms arise due to the multitude of possible interactions, individually giving rise to their own local free energy minimum assembly of molecules. As discussed previously, multi-component materials offer a route to physicochemical property manipulation by changing the intermolecular interactions through the addition of further components and, hence, altering the overall crystal structure for a material. These materials present a unique opportunity for the design of substances with desired attributes. However, predicting what structures will form remains an on-going issue.

In the last few decades, attempts to address this issue have come about through the use of '*crystal engineering*'. Crystal engineering is *"the understanding of intermolecular interactions in the context of crystal packing and the utilisation of such understanding in the design of new solids with desired physical and chemical properties"*[4]. The basis of the method is to rationalise the structure of crystalline materials through an appreciation of the atomic, molecular and ionic components and accounting for their possible interactions. Through these considerations, predictions can be made about the structure of crystalline materials, allowing for an element of design to be introduced for novel solid-state assemblies. Once structures have been rationalised and prediction is possible, physical properties associated with a given structure can also be predicted.

This process relies on an understanding of the functionalities within molecules and the interactions they can form. There are many possible intermolecular interactions, including hydrogen bonds[46], halogen bonds[47], π-π interactions[6] and van der Waals interactions[48], and once recognised, these can be categorised and applied in future crystal designs.

1.3.1 Intermolecular interactions – Hydrogen bonding, halogen bonding and π-π interactions

Crystalline solids can contain a variety of interactions, ranging from strongly bonded ionic[49] and covalent[33] networks to weaker interactions between molecules. As defined by Pauling, chemical bonds arise *"between two atoms or groups of atoms in the case that the forces acting between them are such as to lead to the formation of an aggregate with sufficient stability to make it convenient for the chemist to consider it as an independent molecular species"*[48, 50], where the aggregates themselves result from the interplay between attractive and repulsive interactions. In order for bonds of any type to form, the overall interaction must be attractive. Despite being fundamentally weaker interactions than that of chemical bonds, this principle can also be applied to the intermolecular interactions[6] between molecules.

The focus of modern crystal engineering relies on intermolecular forces to predict and design the structure of molecular-based crystals. '*Hydrogen bonds*' play a particularly important role and can be described as *"an attractive interaction between a hydrogen atom from a molecule or a molecular fragment, X-H, in which X is more electronegative than H, and an atom or a group of atoms in the same or a different molecule, in which there is evidence of bond formation"*.[46, 51, 52] Broadly, in order for a hydrogen bond to form, a proton donor group (X-H) must interact with a proton acceptor (Y), where the donor has a local dipole moment orientated towards electron density associated with the proton acceptor group. Hydrogen bonding interactions can have a wide range of geometries and coordinations, from dimeric pairs to catemeric chains to shared bifurcated interactions, as well as intramolecular hydrogen bonds, each with an inherent set of stabilities and energetics. As such, these interactions can be classified based upon their relative strengths; strong, moderate and weak (Table 1.1).[52]

Table 1. 1 - The key differences between strong, moderate and weak hydrogen bonds, in terms of interaction types, bond lengths, angles and energies

	Strong	**Moderate**	**Weak**
X-H···Y interaction	Mostly covalent	Mostly electrostatic	Electrostatic
Bond lengths	X-H ≈ H···Y	X-H < H···Y	X-H << H···Y
H···Y (Å)	~1.2 – 2.5	~1.5 – 2.2	2.2 – 3.2
X···Y (Å)	2.2 – 2.5	2.5 – 3.2	3.2 – 4.0
Bond angles (º)	175 – 180	130 – 180	90 – 150
Bond energy (kcal mol^{-1})	14 – 40	4 – 15	<4

In the case of strong hydrogen bonds, interaction formation is aided by either the hydrogen bond acceptor or donor groups having a greater electronegativity. Owing to the polarisation across the X-H bond, electron density is drawn away from the hydrogen atom, leaving a slight positive charge. This charge interacts with the electron density or distinct negative charge present on the acceptor atom, thus giving rise to the hydrogen bond. By increasing the electronegativity or electron deficiency of atom X or the electron density associated with atom Y, the polarisation of the X-H bond increases and the electrostatic interactions between the hydrogen atom and atom Y increases, thus giving a shorter and stronger bond. Whilst the increasing electrostatic nature of the interaction can strengthen the hydrogen bond, the position of the hydrogen atom itself becomes increasingly equidistant between the accepting and donating atoms, giving the stronger interactions more covalent characteristics. Typical strong to moderate hydrogen bonds include O-H···O, N-H···O and N-H···N interactions. Weaker hydrogen bonds span a wide energy range[51], with some evidence of weaker interactions having H···Y distances greater than the sum of the van der Waals radii. Such interactions include C-H···O, O-H···π and C-H···π bonds[53], where the electronegativities of either the X or Y atoms are comparatively low.

A more recent focus of intermolecular interactions has been on halogen bonds.[4, 47] Halogen bonds are denoted as R-X···Y-Z and *"occur when there is a net attractive interaction between an electrophilic region on a halogen atom (X) belonging to a molecule or molecular fragment (R-X), where R can be another atom, including X, or a group of atoms, and a nucleophilic region of a molecule, or molecular fragment (Y-Z)".*[54] In many cases, halogen and hydrogen bonds are analogous in terms of their directionality and geometry.

π-π stacking[6] is a common feature of many small-organic molecule crystalline materials, be it single or multi-component, in which aromatic rings are present. These interactions form a dominant network of stabilising contacts and arise from maximised interactions between electron rich and electron deficient regions of aromatic functionalities within the crystals. In terms of orientation, π-π stacking can occur either as an offset face-to-face or edge-to-face aromatic ring interaction.

1.3.2 Supramolecular synthons

When trying to rationalise crystalline structures, two main issues arise.[4, 51] Firstly, the probability of forming an intermolecular interaction depends upon, not only the individual functional groups, but also on their location and orientation with respect to all other functionalities in the immediate environment. Secondly, the process of crystallisation is, by definition, complex. In principle, in order for a crystal to develop, a molecule must come together with other molecules to form a cluster and then form nuclei. Once the size of the cluster is beyond a particular threshold, stable nuclei are able to form and crystal growth can take place. The regularity of this process is by no means definitive, affecting the predictability of crystalline materials from molecular units.

In order to simplify matters, each functional group present and their relative intermolecular interactions can be condensed into individual contact units called '*supramolecular synthons*'.[4, 50, 55] Supramolecular

synthons are structural units that can be used to build collective assemblies based upon the intermolecular interactions present. The main assumption is that the synthon is a reasonable approximation of the building blocks of the crystal structure, meaning that the method of piecing them together is evident.

The most robust synthons are those that utilise the most directional and strongest interactions; the strongest synthons are used first, followed by the next strongest and so on. Due to the varying strengths of the interactions that make up each synthon, there is a degree of competition, giving rise to some unpredictability. However, the notion that a crystal structure can be described through a series of interactions that decrease in strength is a useful tool. By using the molecules as synthon nodes and the interactions between functionalities as synthon node connections, the three dimensional assembly of a crystal can be rationalised. As in organic retrosynthesis[34], these structural units can be derived from a '*retroassembly*' analysis of previously studied structures and then applied to new systems with related molecular units.

Based upon this synthon rationale, a series of guidelines for determining which intermolecular interactions will form were laid down by *Etter et al.*.[56] For hydrogen bonding interactions, this means that all suitable proton acceptors and donors are to be utilised, with intramolecular hydrogen bonds forming in preference to intermolecular bonds. For all other possible interactions, intermolecular hydrogen bonds may form in order of strength, meaning the best acceptors and donors interact first. Though a useful guide, these rules are by no means universal and should be applied with caution.

Figure 1.9 outlines four common hydrogen bonding synthons; two homo and two heterosynthons, and can be characterised based upon their hydrogen bond donating and accepting abilities.[4, 47] In examples *(a)* and *(c)*, a homo and hetero-dimeric interaction is formed, respectively. In both cases, the two functional groups present consist of a proton acceptor and a donor. This is noted as a DA-AD interaction, where D denotes a proton donor and A a proton acceptor. In examples *(b)* and *(d)*, the hydroxyl component of the carboxylic acid group acts as the proton donor, with the carbonyl and pyridine functionalities playing the role of the acceptor for the homo and hetero-synthon, respectively. Hence, each can be illustrated with the D-A notation.

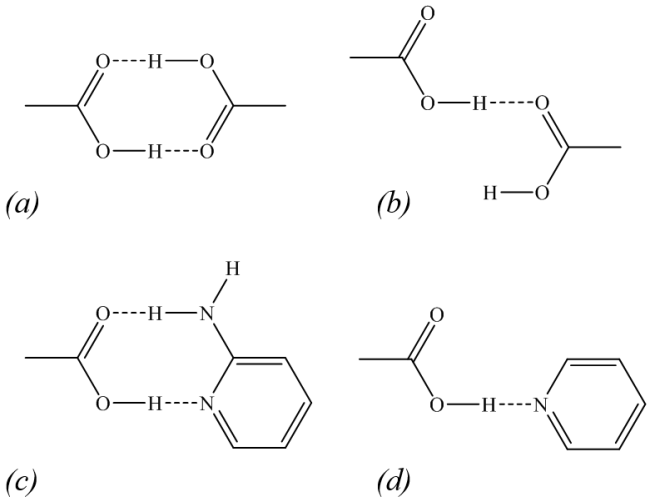

Figure 1. 9 - A set of common hydrogen bond based supramolecular synthons. (a) carboxylic acid dimer homo-synthon, (b) carboxylic acid catemer homo-synthon, (c) amine/aromatic nitrogen···acid dimer hetero-synthon, (d) acid···pyridine hetero-synthon

The hydrogen bonding pattern can be further described using the '*graph set*' notation, as established by *Etter et al.* (Equation 1.1).[4, 56] X represents the type of hydrogen bonding interaction present, of which there are four types: a ring (R), a chain (C), a non-cyclic dimer (D) and an intramolecular interaction (S). From the examples laid out in Figure 8, synthons *(a)* and *(c)* both have notations of $R_2^2(8)$, whilst examples *(b)* and *(d)* have the $C_1^1(4)$ and $D_1^1(3)$ notation, respectively.

$$X_D^A(n)$$

Equation 1. 1 - Graph set notation for hydrogen bonding interactions in supramolecular synthons, highlighting type of hydrogen bonded unit (X), the number of hydrogen bond acceptors (A) and donors (D), as well as the total number of atoms involved in the unit (n)

1.3.3 pK_a rule

In multi-component materials, co-crystal and salt formation is dependent upon the acid-base relationship of the two interacting components[1, 6]. Depending upon pK_a values, a proton can dissociate from an acidic species and transfer to a base, forming a conjugate acid and base, leading to the formation of a salt (Equation 1.2a). In order for a salt to form, the pK_a difference (ΔpK_a, Equation 1.2b) should be greater than 3, whereas co-crystals depend upon no proton transfer, thus require a minimum ΔpK_a. Between the ΔpK_a values 0 and 3, a region known as the '*salt-co-crystal continuum*', the occurrence of proton transfer is uncertain, highlighting ambiguity in the pK_a rule[1, 57].

$$(a)\ AH + B \rightarrow A^- + BH^-$$
$$(b)\ \Delta pK_a = pK_a(base) - pK_a(acid)$$

Equation 1. 2 - (a) Acid-base equilibrium and (b) ΔpKa, for determining salt or co-crystal formation

1.3.4 CCDC Cambridge Structural Database

Once possible synthons have been established for a given set of target materials, comparisons can be made with other crystal systems possessing similar synthons, giving an indication of the likelihood of the interactions.[58] For co-crystal and salt screening, knowledge of previous interactions can be invaluable in determining likely salt or co-formers. The Cambridge Structural Database (CSD) from the Cambridge Crystallographic Data Centre (CCDC) contains all published organic and metal-organic small-molecule crystal structures, as determined by X-ray and neutron diffraction methods, with over 800,000 structures as of 2015.[59, 60] Within the database, both single and multi-component structures are deposited, making it invaluable for statistical studies of molecular complementarity and potential intermolecular interactions.

1.4 Solid-state screening in the pharmaceutical industry

Research, development and design of a manufacturing procedure for a pharmaceutical product is a lengthy process, typically taking between eight to twelve years, sometimes even longer (Figure 1.10).[1, 14] The process of drug development takes a discovered molecule of sufficient biological activity to a formulated drug that can be introduced to the market and, generally, can be divided into two main stages; first, discovery and research, and secondly, development, regulation and manufacture. In the initial discovery stages, screenings are conducted for the selection of molecules with appropriate sensitivity towards specific disease targets. These molecules are selected directly from synthesis or from a library of compounds, and once proven to have a degree of potency, are subjected to further characterisation, in terms of their physicochemical and pharmokinetic properties. Molecules that show particular promise are taken forward to '*clinical*' trials, where the potential APIs are put through

toxicology and, for the first time, human testing, first with healthy volunteers and subsequently with larger patient populations. These steps are subject to a great deal of regulation and also provide an opportunity for the materials of interest to be put forward for drug registration. Assuming these stages yield promising results, synthesis and production methods are developed, scaled-up and refined, ready for complete registration and approval from the relevant regulatory body, such as the Food and Drugs Administration (FDA) in the USA or the European Medicines Agency (EMA) in Europe.

Most drug products are administered orally, either as tablets, capsules or powders. Even for drugs delivered *via* solutions, leaving the material as a solid up to the point of use where it can be dissolved in the appropriate medium, due to the enhanced stability of the solid phase, can often be a preferred option. As well as for API delivery, most drug substances will, at some stage, be handled as a solid during the manufacturing process. As a result, solid-state form and properties are of paramount importance within the pharmaceutical industry, with great lengths being taken in terms of material screening.

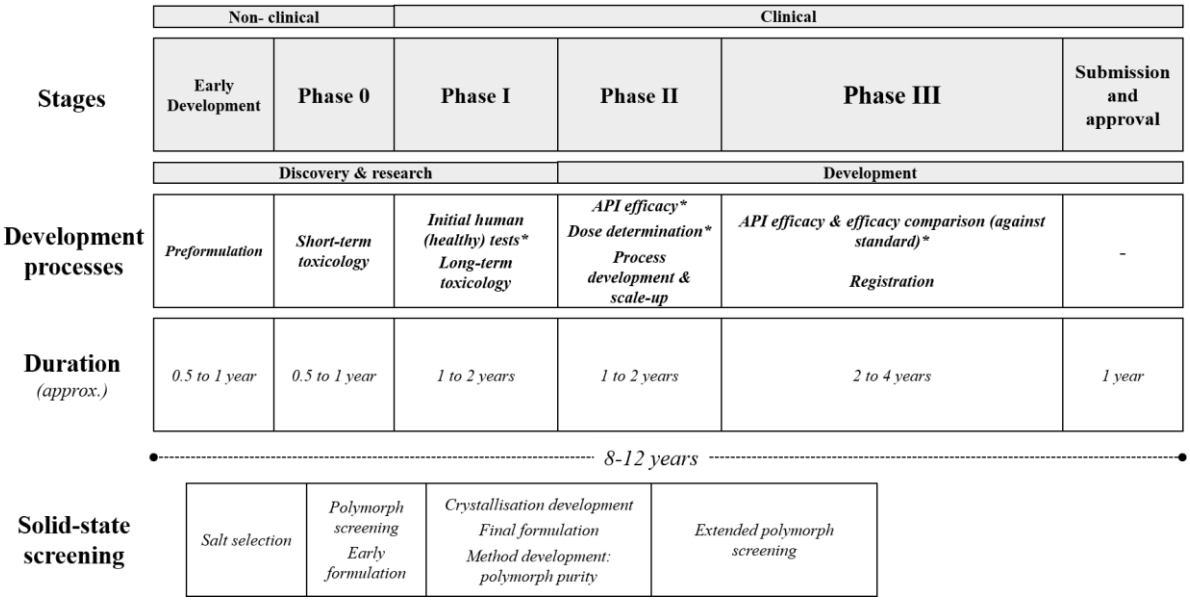

Figure 1. 10 - An overview of the overall drug development process, highlighting key development steps, timescales and a focus on solid-state screening procedures (* = Human clinical trials)

Typical solid screening[2, 3, 61] involves several steps, from initial salt screening, for solubility enhancement, to assessment of the polymorphic landscape to the development of crystallisation processes. More recent pharmaceutical screenings have also included the examination of co-crystalline materials for physicochemical property enhancement, with each new phase (be it polymorphic, salt or co-crystal) offering new opportunities for property or process improvement, as well as patentability. This section will examine, in brief, the aims and methods of three types of solid-state screening; polymorphic, salt and co-crystalline.

1.4.1 Polymorph screening

As previously outlined, many crystalline API materials have the potential to show different polymorphs, each with its own unique stabilities and properties. For many polymorphic materials, the thermodynamically stable polymorph is the favoured phase for drug product development, owing to its inability to interconvert to other polymorphic phases, under given conditions[14, 62]. However, being the most stable form intrinsically means that this phase has the lowest solubility, leading to implications for processing and bioavailability. In many cases, the most stable polymorph is favoured, but depending upon the disparity in solubility, dissolution rates or patentability, it might be the case that the metastable phase is taken forward for drug formulation.[1, 3, 24] In addition to polymorphs, the hydrate and solvate landscape[20] is also assessed as part of the screening process. This might be to try and expand the library of solid-state materials for a given material, so as to avoid their crystallisation, or for the discovery of a more stable '*pseudo-polymorphic*' phase.

Polymorphic screening is vital for the reliable preparation of pharmaceutical materials and owing to the need for consistency in drug substance when transferring to clinical trials, the implementation of screenings must be early in the discovery and research process. The development of formulated drugs, in most circumstances, relies on the preparation of the most stable phase, but due to changing crystallisation conditions and improving impurity profiles during the development and scale-up steps, it is possible that the most stable phase could have been missed during initial screenings. A famous case when an unexpected polymorph appeared in later manufacturing stages is that of Ritonavir.[14, 63] Hence, it is now common practice to conduction additional late-stage polymorph screenings.

During screening, different polymorphs can be prepared through various crystallisation methods under different conditions. Screening conducted within the pharmaceutical industry utilises a wide range of techniques, from solution-based methods, like cooling and evaporative crystallisation, to mechanochemical preparations and crystallisations from the melt, amongst others.[61, 64] Each method uses different pathways for cluster formation, nucleation and crystal growth, with every pathway potentially yielding different polymorphic forms. The principles underlining crystallisation and the various methods thereof are outlined in Sections 1.6 and 1.7. Preparation methods used for polymorph screening can also be translated to salt and co-crystal screening.

Once a polymorphic form has been isolated, its physical, chemical and crystallographic properties need to be assessed.[65-68] A variety of analytical techniques can be used for assessing the characteristics of individual polymorphs; structural information can be gained from single crystal X-ray diffraction (SCXRD), phase identification can be conducted through powder X-ray diffraction (PXRD), whilst thermal properties and temperature based phase transitions can be detected using differential scanning calorimetry (DSC) and hot-stage microscopy (HSM). Spectroscopic methods, particularly infrared spectroscopy (IR), can also be used for structural analysis, by probing the vibrational effects related to bonding and intermolecular interactions. These techniques are discussed in detail in Chapter 2 and can be used for the characterisation of any crystalline material, including salts and co-crystals.

1.4.2 Salt screening

If an API molecule forms a crystalline material that demonstrates unfavourable physicochemical properties, a traditional method of improving its characteristics is through the preparation of a salt.[57, 69] The reasons for salt selection can be due to a number of factors, in particular low aqueous solubility, low crystallinity, high hygroscopicity or low chemical stability.[17]

In general, the formation of salts is made possible by the molecule in question possessing acidic or basic groups[6, 70], a feature common to many APIs. Prepared predominantly through solution-based methods,

salt formation is dependent upon the pK_a of the two species interacting with each other (see Section 1.2). It should be noted that most pK_a values are calculated with water as the solvent, though this can be used as an initial starting point for other solvent systems.

If salt formation is deemed necessary, an appropriate salt selection strategy is required, with the chemical compatibility of the materials concerned being assessed.[69, 71, 72] Once the API in question has been deemed amenable to salt formation, a suitable counter-ion needs to be found. This must be able to undergo acid-base interactions and be classified as safe.

1.4.3 Co-crystal screening

The use of co-crystals within the pharmaceutical industry has grown in recent years, with co-crystals showing a range of advantages over other solid phases, specifically as ionisable functionalities are not a prerequisite and the principles of crystal engineering are particularly amenable[3]. The process through which pharmaceutical co-crystals can be prepared is a multi-stage, involving interaction assessment, co-former selection, material screening, characterisation and scale-up (Figure 1.11).[1, 3, 13, 70]

Having selected an API, the structure should be assessed for its possible intermolecular interactions, applying the rules and principles of crystal engineering[4], with reference also to previous structures utilising that same API or related compounds. The same process should be carried out for potential co-formers, assessing the prevalence of interactions that might be complementary to most of the API. Ideally, the co-former should be pharmaceutically acceptable i.e. using molecules that are '*generally regarded as safe*'.[1]

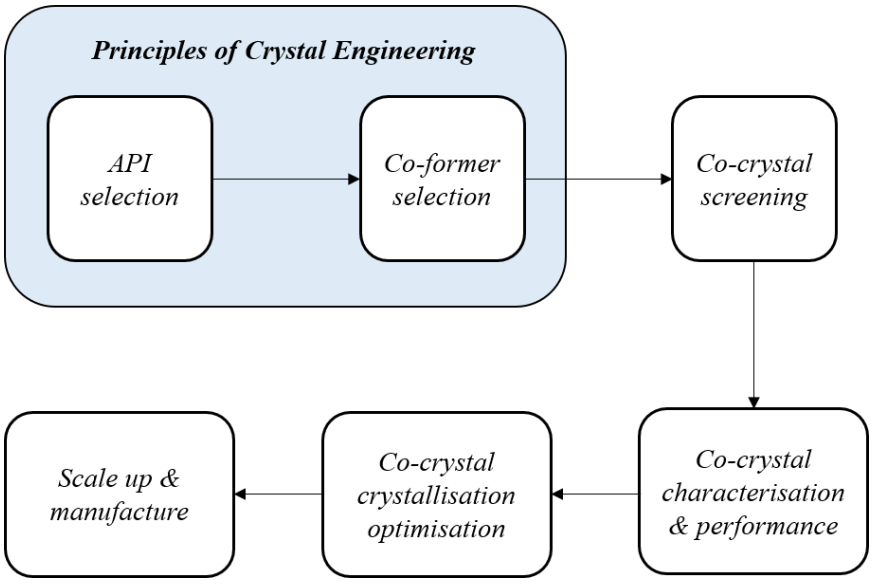

Figure 1. 11 - Multi-step process for designing and preparing co-crystals

Once a combination of API and co-former has been selected, small-scale co-crystallisation screenings can be conducted. These methods can be used to determine the propensity of whether or not a novel co-crystalline form can be produced.[18, 73] Common techniques used include solvent-based crystallisations, typically evaporative or cooling methods, or mechanochemical methods. If novel co-crystals are discovered, the material is characterised, as for polymorphs and salts, in terms of their physicochemical properties and structure, and, if deemed suitable, are taken forward for crystallisation optimisation and scale-up.

1.5 Phase equilibria

An understanding of the equilibria between liquids and solids is of great significance in rationalising the thermodynamic basis of all crystallisation processes, either from the melt or solution. Based upon equilibrium information, graphical representations of the crystalline phases present for a given system can be generated, i.e. phase diagrams. Though often not known, particularly for new materials, knowledge of the phase diagram under a given set of conditions (temperature, pressure, composition, etc.) can be vital in designing selective crystallisation methods. In order to appreciate all aspects contributing towards a phase diagram, firstly, the phase rule must be understood.

1.5.1 The Phase Rule and phase diagrams

A phase is an individual constituent of a system that does not show variation in terms of its chemical composition and physical state.[74, 75] Typical phases are either gaseous, liquid or solid and can exist purely in isolation from other phases (pure phase) or in combination with other phases (mixed phases). In this sense, any mixture of gases or miscible liquids can be classed as one phase. Similarly, an undersaturated solution of a solute in a solvent can also be a single phase, whilst a mixture of two immiscible liquids or a solid suspended in a solvent (solution crystallisation) are classed as having two phases.

A system is said to be at the thermodynamic equilibrium when, at a specific temperature, pressure and composition, the phases present remain constant. By changing the conditions, the position of equilibrium can be shifted, thus changing the possible phases present. These systems can be defined by the '*Phase Rule*' (Equation 1.3), which relates the number of components (*C*), phases (*P*) and degrees of freedom (*F*).[26, 74, 76] For solid-liquid equilibria, pressure is often ignored, thus reducing the overall degrees of freedom, denoted as F'.

$$P + F' = C + 2$$

Equation 1. 3 - The Phase Rule for solid-liquid equilibria, linking the number of distinct phases (P) with the number of degrees of freedom (F') and the relative number of chemical components (C) present

The number of components is related to the number of distinct chemical compounds needed to describe the overall composition of a particular phase. For example, a system consisting of two enantiomers dissolved in a solvent can be described as a ternary system. For every system, the number of degrees of freedom represents the number of variables (e.g. temperature, pressure, composition) that must be fixed in order to define the phases present at the point of equilibrium.

The phase rule can be used universally to understand phase behaviour exhibited at equilibrium, under a set of conditions. Phase diagrams depict, in two or three dimensions, the variation in phases at different equilibria, when temperature and composition or concentration are changed.[75, 77] For equilibria between liquids and solids, phase diagrams give information relating to the different solid phases occurring, such as polymorphs and multi-component materials (co-crystals, salts, solvates and hydrates). In these systems, pressure is usually assumed to be constant. A simple binary phase diagram, highlighting the melts of two components, (A) and (B), is shown in Figure 1.12. A similar phase diagram can also be constructed for the binary dissolution of a solute in a solvent.

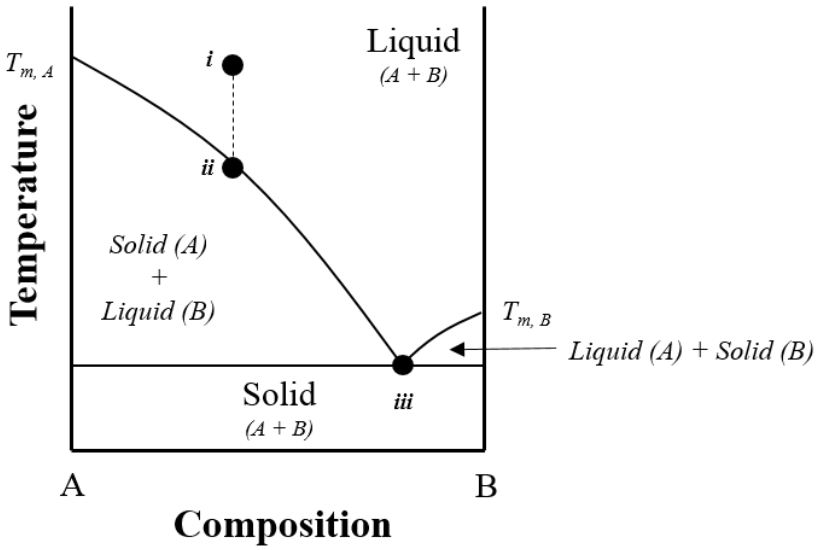

Figure 1. 12 - Simple melting point phase diagram for the binary mixture of components (A) and (B), where Tm,A and Tm, B represent the melting points of components A and B, respectively, highlighting the transition from liquid (point *i*) to the precipitation of the A (point *ii*) and then B (point *iii*) phases upon cooling

In this two component system (C = 2), when only one phase is present (P = 1), e.g. a liquid (point *i* in Figure 1.12), the degree of freedom is two (F = 2), meaning the temperature and composition can be varied, independently, without changing the phase exhibited. As the temperature is lowered and the number of phases in equilibrium changes to two (point *ii*), the degree of freedom becomes one, making temperature and composition no longer independent of each other. When the number of phases that can exist together at equilibrium is three (point *iii*), the system no longer has any degrees of freedom, i.e. all three phases (solid A, solid B and liquid) can only coexist at one specific temperature and composition. This point is called the eutectic point, at temperature T_e.

1.5.2 Applications of the phase rule for polymorphic, multi-component and chiral materials

The phase rule can be used to describe crystallisation phenomena, such as polymorphism, with each polymorph constituting different solid-state phases for a specific chemical entity (single component).[75, 77] For a system consisting of two polymorphic forms and given the phase rule at constant pressure, the equilibrium between the two phases would only have one degree of freedom. Figure 1.13a shows the binary phase diagram between the polymorphic material, A, and a given solvent, highlighting the transition temperature between forms (i.e. $T_{m,\,A-I}$ to $T_{m,\,A-II}$).

When combining two molecular species, A and B, within a single crystal lattice to make a multi-component material, i.e. a co-crystal, salt, solvate or hydrate (Figure 1.13b),[78, 79] there can be a change in the number of components. The formation of multi-component crystals occurs at mixed compositions of the pure starting material, giving rise to a distinct region in the phase diagram, characterised by the novel material melting point ($T_{m,\,CC}$). It should be noted here that the secondary component, B, can exist either as a solid at room temperature, resulting in a co-crystal or salt, or as a liquid, yielding a solvate.

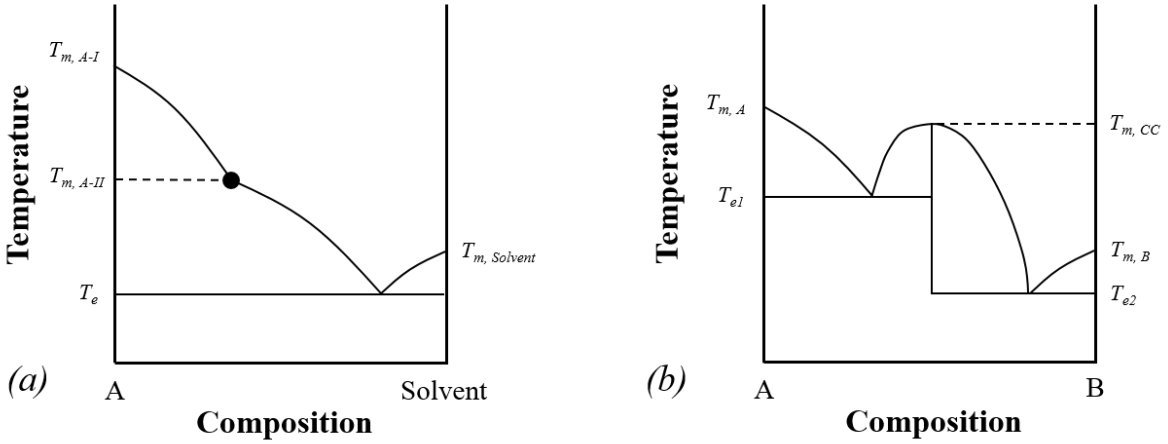

Figure 1. 13 - Binary phase diagrams for (a) polymorphic and (b) multi-component materials, highlighting polymorphic transition temperatures, melting and (T_m) eutectic points (T_e)

Analysis of solid-liquid equilibria through binary phase diagrams can also be applied to chiral crystalline materials. Upon crystallisation of chiral molecules from various enantiomeric compositions, from the melt or otherwise, three types of material are possible; racemic compounds, racemic conglomerates or racemic solid solutions.[35, 36, 41] Each class consists of two components, i.e. the two enantiomers, *R* and *S*, but, depending upon the composition, can vary in terms of the number of phases that are present (Figure 1.14).

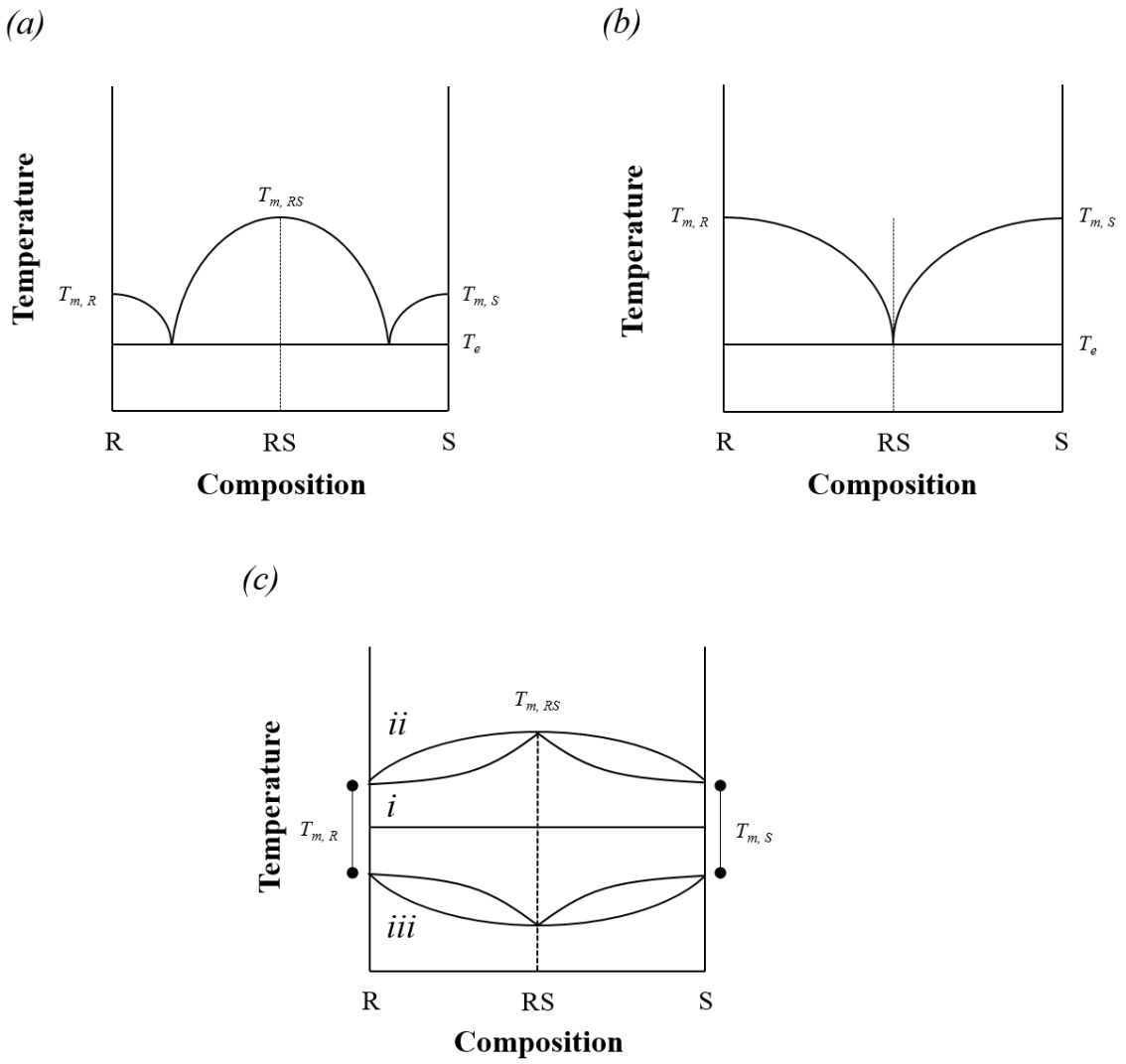

Figure 1. 14 - Binary phase diagrams for the three types of chiral crystalline material; (a) racemic compound, (b) racemic conglomerate and (c) racemic solid solution, which in turn can be subcategorised into (*i*) ideal, (*ii*) Roozeboom Type I and (*iii*) Roozeboom Type II solid solutions

Due to the identical properties of both enantiomers, particularly with respect to melting point, the binary phase diagrams for all types of chiral material demonstrate symmetry, from racemic to enantiomerically pure compositions. Overall, the racemic compound can form three distinct phases, i.e. the racemic and two enantiomerically pure forms, whilst the conglomerate can produce two and for solid solutions, only one continuous phase is possible. These solid solutions can be subcategorised into three other groups; '*Ideal*', Roozeboom Type I and Roozeboom Type II.[35, 41, 77] Each type differs in terms of their respective melting points when comparing the homochiral and heterochiral (50:50) phases. In ideal solid solutions, no matter the enantiomeric composition, there is no variation in the melting point, whilst the melting point of the racemic phase is higher and lower than that of the pure chiral phase for Roozeboom Type I and Type II materials, respectively. A key characteristic of solid solutions, when compared to racemic compound or conglomerate systems, is their lack of eutectic melting.

Binary phase diagrams can account for two component systems, which can cover the dissolution of individual solutes in particular solvents, highlighting polymorphic variations, or the melting phenomena when two materials are combined. However, in order for systems with three components to be assessed, i.e. two solutes dissolved in a solvent, a different type of phase diagram must be used. Ternary phase

diagrams are of key importance when assessing solution crystallisations, at a specified temperature, that either contain impurities, involve the formation of multi-component materials or that of chiral crystalline systems.[3, 36, 75, 80] Figure 1.15 shows several examples of ternary phase diagrams, for two simple multi-component material forming systems (a and b) and for the three types of chiral phases (c, d and e) possible.

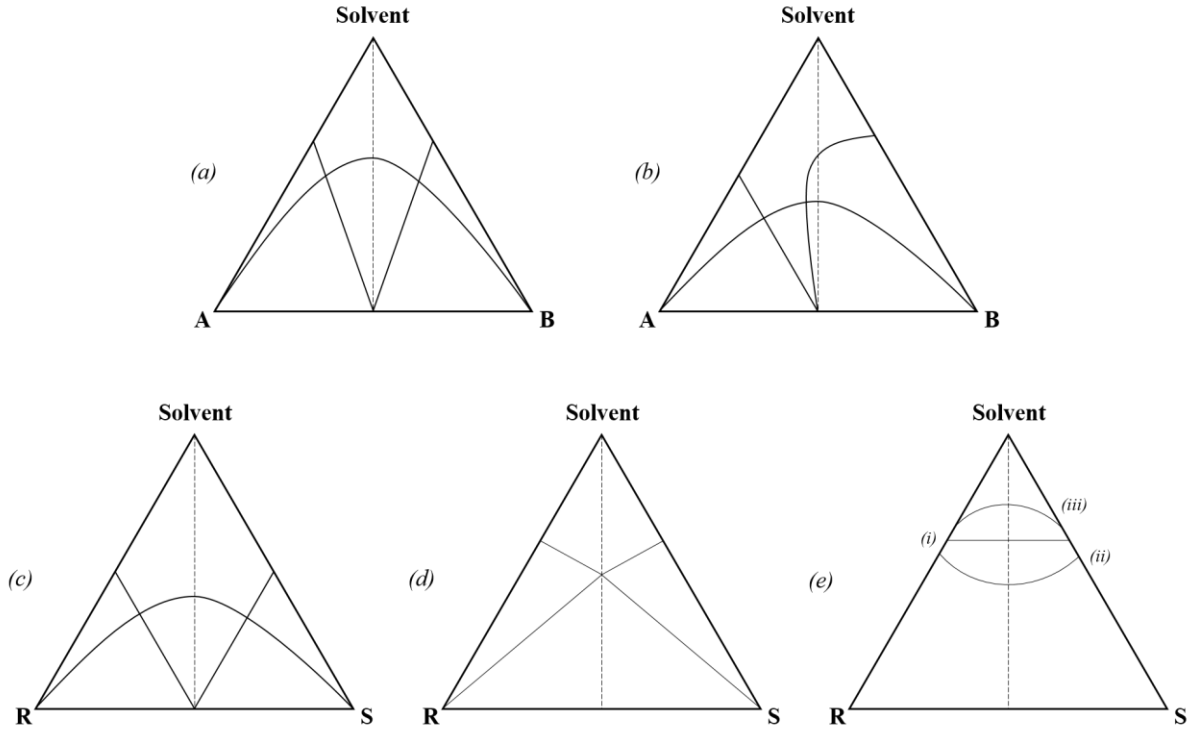

Figure 1. 15 - Isothermal ternary phase diagrams of two solutes and a solvent, highlighting multi-component material formation for (a) equally soluble and (b) unequally soluble solutes, A and B, as well as that for chiral crystalline systems; (c) racemic compounds, (d) racemic conglomerates and (e) racemic solid solutions, with its three types (I-*i*, II-*ii* and III-*iii*)

1.6 Crystallisation

'*Crystallisation*' is an important operation in many fine chemical industries, as both a separation and purification technique. However, it holds particular significance within the pharmaceutical industry as many APIs are delivered as solid dosage forms. The process of crystallisation from solution refers to *"the transfer of matter initially solvated to form crystallised particles"*.[77] Through crystallisation, critical properties such as crystal shape, size and form are determined, all of which have implications for the end product, as well as other manufacturing steps further downstream, such as filtration and milling. In order to control these properties, the principles of crystallisation must be understood.

1.6.1 Supersaturation

Whilst the equilibrium between a solid and liquid is determined by thermodynamics, crystallisation is a kinetic process[26] driven by the relative '*supersaturation*' of a solution.[11, 26, 77, 81] A solution, at a specified temperature, is considered supersaturated when the concentration of a solute in a particular solvent exceeds its thermodynamic solubility but can be sustained as a solution over a finite concentration range without crystallisation occurring. This concentration range is called the '*metastable zone*', existing between concentrations of solute above that of the solubility curve and an upper limit called the '*metastable limit*'.[82] As shown by Figure 1.16[81], the composition of a solution below the

solubility curve is considered '*undersaturated*', with equilibrium favouring the liquid or solution phase, whilst compositions above the metastable limit favour the formation of the solid phase. In this '*labile*' region, spontaneous nucleation is likely to occur. In a similar manner, supersaturation can be generated through the cooling of a saturated solution, at a given temperature. The time taken for nuclei to form, after supersaturation has been reached, is known as the '*induction time*'.

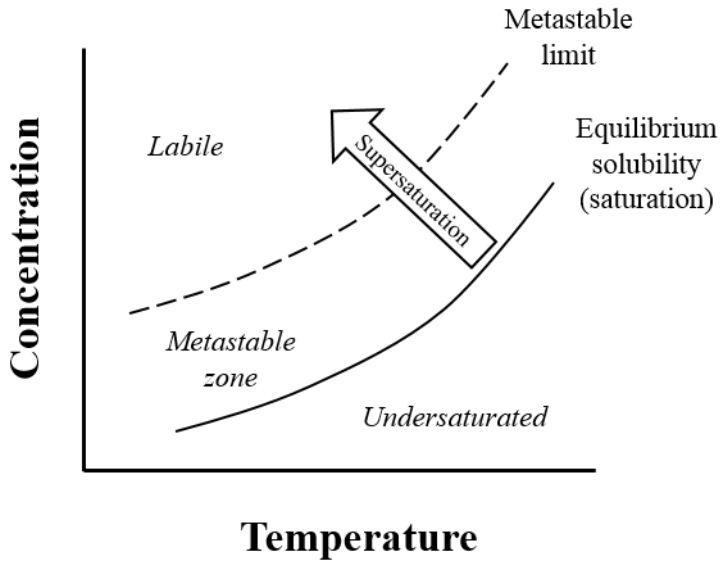

Figure 1. 16 - Solubility phase diagram, highlighting the equilibrium solubility, undersaturated, supersaturated and labile regions

Though the equilibrium solubility is a thermodynamic property, the nature of the metastable zone is governed through kinetics and can vary greatly depending on experimental conditions[11]. A key factor that can affect the width of the zone is the rate at which supersaturation is achieved. This is dependent on the method of crystallisation and the environments present. Key factors that can affect this rate include variations in temperature, solvent composition, impurities or additives and mixing.

Crystals can nucleate and grow only if the given solution is supersaturated. Supersaturation can be expressed in many ways (Equations 1.4a, b and c), each comparing supersaturation and equilibrium concentrations. These are absolute supersaturation (Δx), relative supersaturation (σ), and the supersaturation ratio (S)[26, 27].

$$\text{(a) } \Delta x = x_{ss} - x_{eq}$$

$$\text{(b) } \sigma = \frac{\Delta x}{x_{eq}}$$

$$\text{(c) } SS = \frac{x_{ss}}{x_{eq}}$$

Equation 1. 4 - Expressions for supersaturation, highlighting (a) absolute supersaturation, Δx, (b) relative supersaturation, σ, and (c) the supersaturation ratio, SS, with x_{ss} and x_{eq} representing the supersaturation concentration and equilibrium/solubility concentration

Whilst governed by the level of supersaturation, crystallisation itself can be broken down into two distinct kinetic processes; '*nucleation*' and '*growth*' (Figure 1.17).[26] Upon exceeding the saturation limit, the kinetics of growth are dominant, with any initial nuclei present being given the opportunity to

grow, resulting in larger particle sizes. But as supersaturation increases and goes beyond the metastable limit, the rate of nucleation begins to surpass that of growth. This results in the formation of smaller crystals. These considerations, the careful balance between the kinetics of nucleation and growth, form the basis for designing effective crystallisation processes with desired particle attributes.

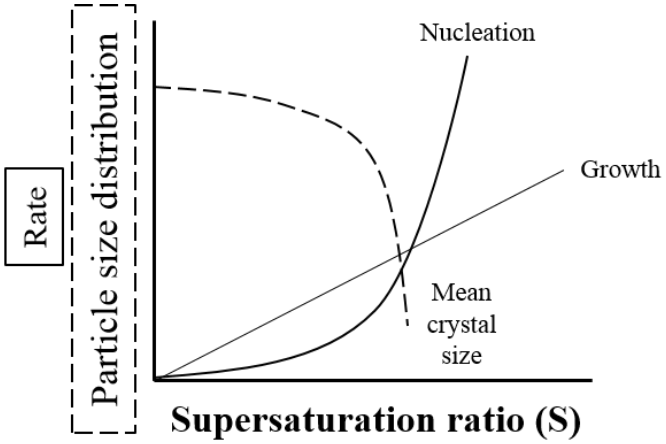

Figure 1. 17 - Effect of supersaturation on particle size, nucleation and growth

1.6.2 Nucleation

The first step in the formation of new crystalline solids from the solution or liquid phases is nucleation, a key phenomenon in the control of particle size and number.[2] Nucleation refers to initial particle formation and can occur *via* a number of routes, depending upon the presence of various growth interfaces (Figure 1.18).[11, 26, 81] Primary nucleation involves the spontaneous formation of nuclei from solution: particles can form without the prior existence of any solute particles. This can occur either homogeneously, the completely spontaneous formation of nuclei from solution, or heterogeneously, whereby the initial particles form on a heterogeneous surface. Secondary nucleation, in contrast, only occurs heterogeneously and includes the formation of nuclei on previously formed solute particles. The mechanism of secondary nucleation underpins the common practice of '*seeding*' a crystallisation process.

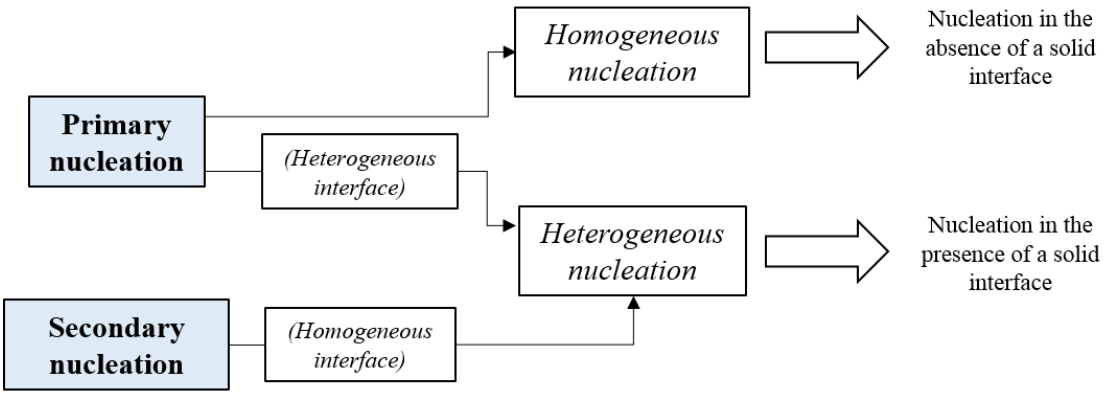

Figure 1. 18 - Diagram differentiating the homogeneous and heterogeneous primary nucleation and heterogeneous secondary nucleation

The study of homogeneous nucleation processes is difficult due to the inherent small size of the critical nucleus, with each nucleus being made up of only 10-1000 molecules, and short phenomena time scales,

though this varies from system to system.[2] Current understanding of nucleation is based upon two main theories of cluster formation; '*classical nucleation theory*' (CNT)[2, 11, 81] and the '*two-step*' approach.[2]

CNT is a widely used theory and assumes that molecules add together sequentially until a cluster of sufficient size is formed (Figure 1.19). When these clusters are small, the free energy of the cluster surface dominates with respect to that of the bulk, with the molecules at the surface forming a greater proportion of interactions with surrounding solvent molecules. This leads to smaller clusters redispersing back into the solution. However, as the clusters get bigger, the disparity in free energy between the surface and the bulk decreases until a critical size (r_C) is reached, whereby the free energy of the bulk stabilises the cluster. It should be noted that for spherical nuclei, the free energy of surface has a positive value, whilst that of the bulk takes a negative term.

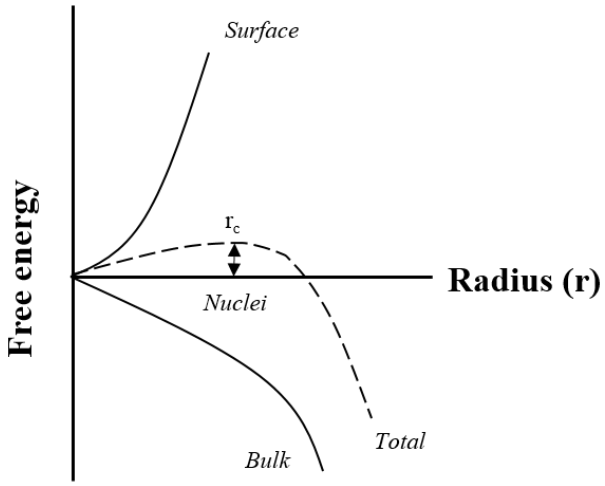

Figure 1. 19 - Free energy diagram of nucleation, highlighting the free energy of the surface, bulk and their sum, indicating the critical cluster size for stable nuclei

The relative stability of an individual cluster is dependent upon the supersaturation of the system (Figure 1.20). Systems are driven by the desire to lower their free energy. For smaller clusters, the free energy can only be minimised through dissolution, whilst for larger aggregations beyond a critical size, this is achieved through the growth of the cluster. With increasing supersaturation, this free energy barrier decreases, as well as the value of the critical cluster size leading to the eventual spontaneous nucleation of individual crystallites. An important consideration here is that of '*Ostwald ripening*'.[11, 27] For the smaller molecular clusters, where the free energy of the surface dominates, resulting in destabilisation and redissolution, the molecules from these clusters are deposited back into the solution, enabling them to be used for the growth of larger clusters. Through this continual ripening of larger clusters, the overall particle size for a crystallisation process can be controlled.

.

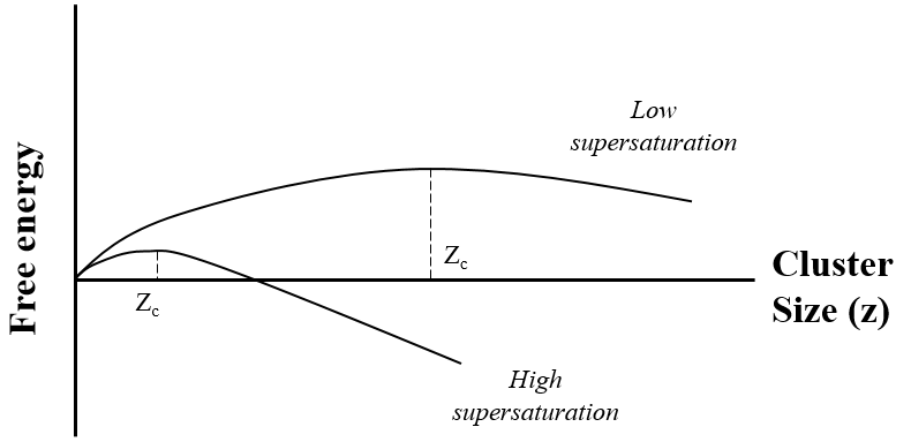

Figure 1. 20 - Free energy as a function of cluster size (z) and supersaturation

Though useful, CNT has several fundamental limitations.[2, 81] It assumes that classical thermodynamics can be applied to small nucleating clusters. These considerations are based on the averages of very large groups of molecules and these often cannot be directly transferred to smaller units. CNT also assumes that cluster growth occurs through the step-wise addition of molecules, with the end crystal structure being built-up directly through this. As a result, only size is used as the limiting criterion for nucleation, this with this often being insufficient for many solution based crystallisations.

An alternative is the two-step theory.[2] Here it is proposed that solute molecules rapidly aggregate into initial fractional clusters and then progressively condense into structures resembling that of the end crystalline form. This gives rise to the two-step notion where the initial density of the structure fluctuates and eventually settles to a higher density ordered state. A great deal of study has gone into the two-step process and it is widely favoured as a more useful theory.[83, 84] The differences between CNT and the two-step theory are shown in Figure 1.21.

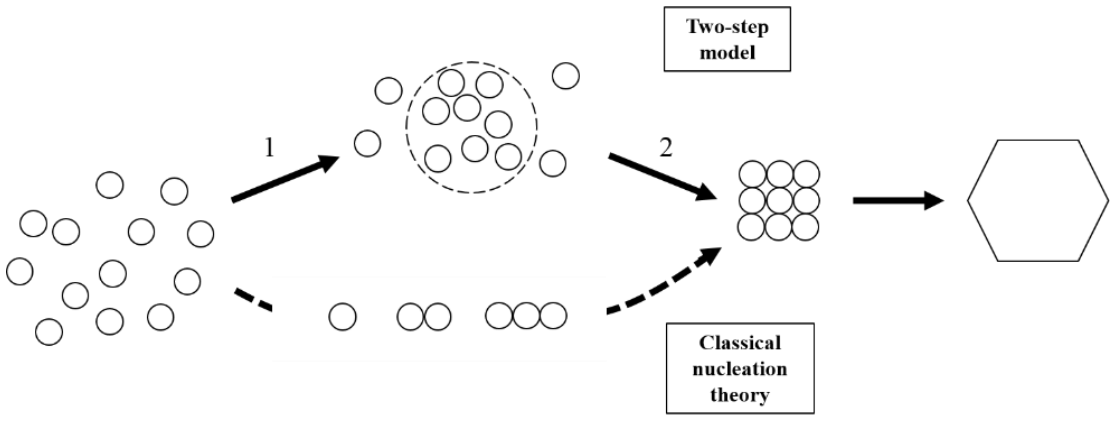

Figure 1. 21 - Diagram comparing classical nucleation theory and the two-step model

Whilst fundamental, homogeneous nucleation of a particular phase from a 'clean' solution is not always realistic. Heterogeneous nucleation occurs at the surfaces of pre-existing bodies, either as a primary or secondary process.[85] Through a primary heterogeneous nucleation mechanism, nuclei develop on the surface of a foreign entity, be it an impurity or templating material, whilst in secondary processes, cluster formation occurs on surfaces of previously established crystals of the phase of interest, acting as a '*seed*'. The presence of these surfaces, foreign or otherwise, allows for the adsorption of molecules from solution, lowering the free energy barrier, and encouraging nucleation at lower supersaturation levels. The favourability of heterogeneous processes is dependent upon the overall free energy of the

system. If, through the introduction of these additional interfaces, the overall free energy is lowered, then spontaneous homogeneous nucleation is no longer favoured and nuclei form on pre-existing surfaces.

Secondary heterogeneous nucleation is particularly significant in the control of many crystallisation processes. Here, a number of different mechanisms are possible, including initial seeding, needle breeding, fluid shear and contact nucleation. Initial seeding works through the addition of crystalline seeds to an already supersaturated solution. Here, micro-particles are shed from the surface of the seeds and become new centres for crystal growth. In these kinds of crystallisation, the shear forces generated from mixing can also have an impact on secondary nucleation. The flow of the surrounding solution in any crystallisation vessel can have an effect on what crystal faces can develop.

The crystallisation of different crystalline phases (polymorphic, multi-component and chiral materials) is inherently controlled by the process of nucleation. The occurrence of various forms, e.g. polymorphs, which are not the most thermodynamically stable can be explained in terms of nucleation, by the principles laid out in '*Ostwald's rule of stages*'.[81, 86, 87] This rule states that the initial nucleating structure need not be the final, most stable phase, but rather that it represents the smallest change in free energy possible, as the system shifts from a supersaturated state to equilibrium. As a result, stepwise formation of different phases would occur before crystals of the thermodynamic form eventually appear.

1.6.3 Growth

Once a cluster of critical size and order has formed (a nucleus), a crystal can then begin to grow. When a crystal surface is exposed to a supersaturated environment, the movement of material to the surface exceeds the movement away: the net effect is the growth of the crystal surface.[11, 26, 81] The ability of a surface to attract material and utilise this for growth is dependent upon the number of interactions possible, as well as their relative strengths. The classic picture of crystal growth involves the steady maturing of layers, where atoms, ions or molecules (or clusters thereof) arrive at a surface, shed themselves of their solvation layer, and bind to previously deposited material. The surface of a growing crystalline entity can be characterised in terms of three types of contact site; faces, steps and kinks (Figure 1.22).[26, 27] For faces, particles can form one attachment with a surface, whilst for steps and kinks, two and three points of contact are possible, respectively. It should be noted that with increasing points of contact, the favourability of interaction increases and the energetic barrier to binding decreases.

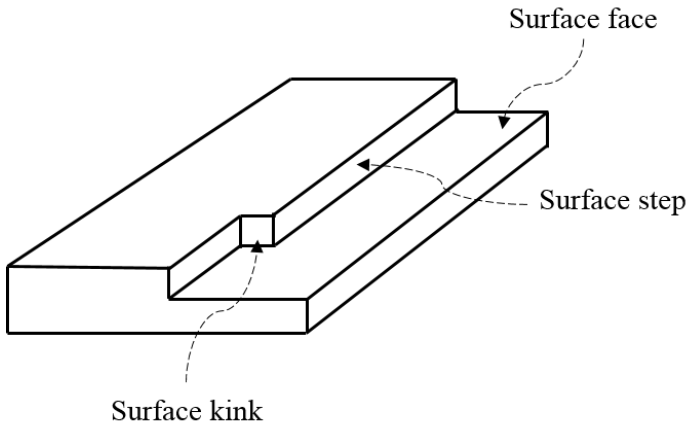

Figure 1. 22 - Surface structure, indicating surface kinks, steps and faces

The final crystal shape or '*morphology*'[88] will thus depend upon the growth from the slowest growing site: the faces[26]. However, in order for crystals to grow at an appreciable rate, effective growth sites must be created. These growth sites generally utilise sites with a higher number of interactions: kinks and steps. The formation of such sites depends upon the nature of the interactions at the surface and the surrounding supersaturated solution. In order to describe how these key growth sites form and, hence, determine the mechanism for crystal growth, the '*multi-layer*' model can be used (Figure 1.23).[26] Here, hypothetical blocks are used to define solid and liquid phases, the solid being formed from a number of layers. By roughening the interface between the phases, the model can be used to predict the energy change (ΔE) from the movement of one block to form a new layer.

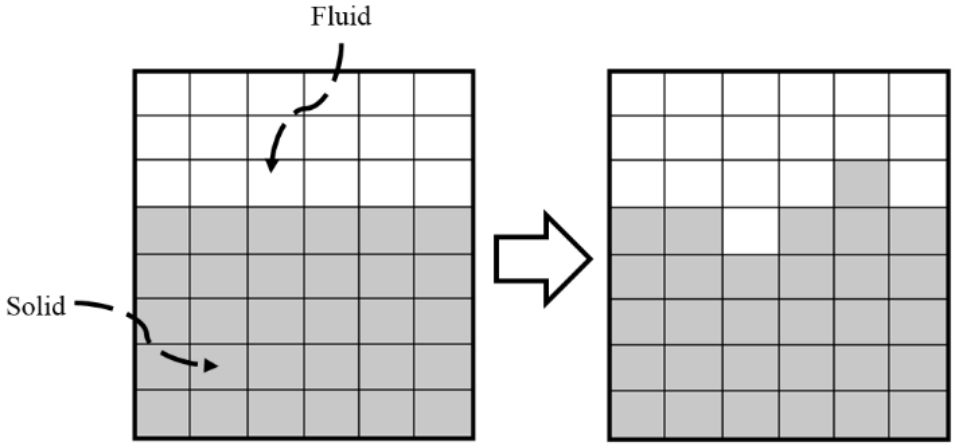

Figure 1. 23 - 'Multi-layer' model of the solid-fluid interface for surface roughening

This energy change can be further used to express the α-factor, which reflects how well a surface can develop sites of multiple interaction (Equation 1.5). This gives an indication as to the ease of surface growth and the growth mechanism followed.

$$\alpha = \frac{\Delta E}{kT}$$

Equation 1. 5 - α-factor, indicating the relative ease of surface growth (k = Boltzmann constant, T = temperature)

There are three common pathways, each of which exhibit an increasing tendency for multiple site formation; continuous growth method, surface nucleation and spiral growth.[26, 27, 81] In some crystalline systems, the formation of higher interaction binding sites (kinks and steps) is comparatively easy; these systems undergo 'continuous growth' characterised by a low α-factor (less than 3). This continuous growth mechanism indicates that as long as growth species keep moving to the surface, they will find binding sites and the surface will grow. Therefore, the growth rate is proportional only to the level of supersaturation of the surrounding solution.

Systems exhibiting continuous growth are rare, with the majority of materials not having sufficient roughness. In most cases, as the atoms, ions or molecules of interest approach the surface, they either bind directly to a pre-existing layer, are unable to bind and return to the surrounding fluid or adsorb to previously deposited species to form surface nuclei (Figure 1.24).[81] Here, the outer ridges of the nuclei act as new kink or step sites. In this manner, these nuclei can grow and spread across a surface, with growth species adding from either the surrounding fluid or from species diffusing over the surface. This process is called '*growth by surface nucleation*' and is characterised by an α-factor of between 3 and 5.[26] The growth rate for surface nucleation depends on the number of critical size nuclei formed at a given time, the flux of material to or across the surface and the resultant step sizes.

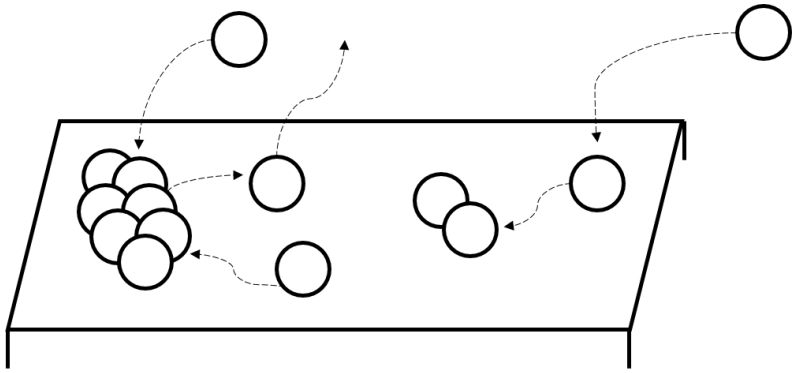

Figure 1. 24 - Formation of two-dimensional critical nuclei on a crystal surface

In systems where α has a value great than 5, the formation of sites with a higher number of surface interactions is extremely difficult. For growth to occur, steps and kinks must be generated through a different process that requires the minimum amount of energy. The mechanism of '*spiral growth*' utilises so-called '*dislocations*', defects that are derived from primary and secondary heterogeneous nucleation processes, as a route to growth. Dislocations occur through a misalignment of crystal faces and can be built up to form a series of sequential steps, winding up through a spiral, extruding from the crystal surface (Figure 1.25).[81]

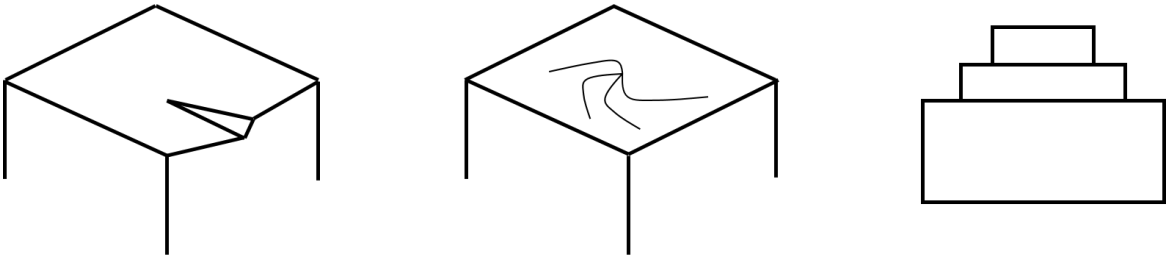

Figure 1. 25 - The development of spiral growth, showing a spiral dislocation build-up

The rate of spiral growth can be expressed in terms of the height, the flux of material to the step and step density, which represents the nature of the spirals formed. The winding of the spiral becomes tighter with increasing supersaturation, increasing the step density. The rate is system dependent, as each system will has its own unique structure of dislocations.

1.7 Crystalline material preparation

When preparing any solid-state material, there is a balance between the thermodynamics and kinetics of crystallisation. Both nucleation and growth depend upon the notion of supersaturation, but subject to the rate at which this is achieved and its extent, it is possible to access a variety of phases, stable and metastable (Figure 1.26).[1, 64] In order to control this, different crystallisation techniques can be used, each exploiting a different mechanism over various timescales.[61] These methods can be described as being either from solution or not and include methods such as evaporative and cooling crystallisation, slurrying and mechanochemical preparations. Whilst there are many other techniques, these shall be the focus here.

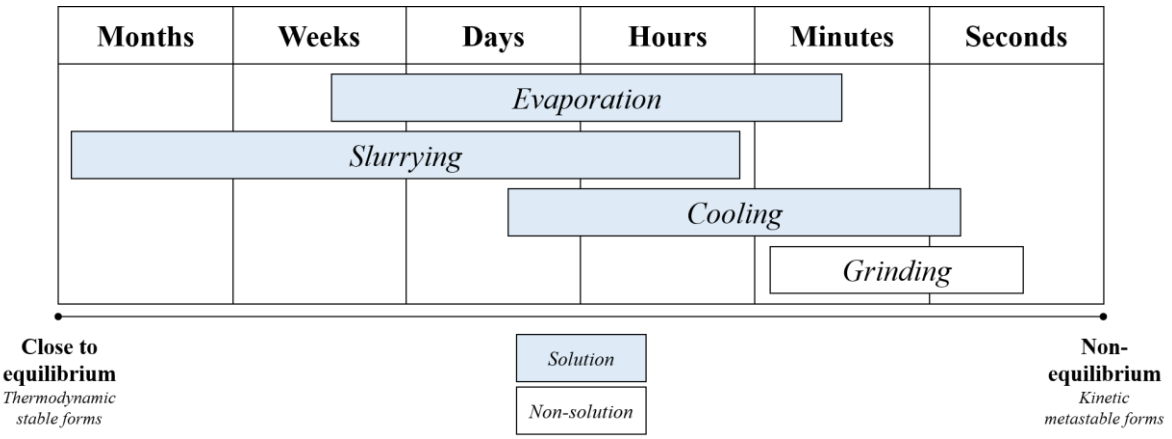

Figure 1. 26 - A selection of methods for producing different crystalline forms, highlighting timescales and material stabilities

1.7.1 Crystallisation from solution – Evaporation, cooling and slurrying

A method extensively used in solid-state screening is '*evaporative*' crystallisation (Figure 1.27a).[21, 64, 89, 90] Held at a particular temperature, supersaturation is achieved by allowing solvent to be evaporated from a solution, transitioning from undersaturation to supersaturation.[64, 77] Eventually enough solvent is driven off to reach the metastable limit, where nucleation occurs spontaneously. The rate at which supersaturation can be achieved can be varied depending upon the temperature of evaporation. This can have a direct impact on the solid-state forms that can be produced. Evaporation demonstrates several advantages, including ease of setup and its ability to be combined with additional crystallisation methods.[81] As well as this, there is no prerequisite of solubility knowledge. However, despite these advantages, issues arise in terms of nucleation control, with implications for particle size, shape and form.

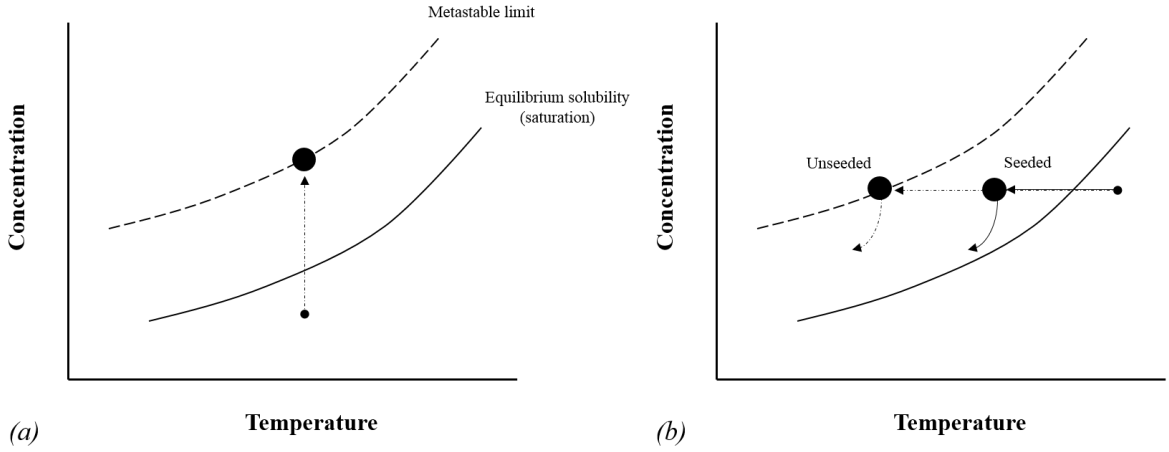

Figure 1. 27 - Solubility phase diagrams for (a) evaporative and (b) cooling crystallisation, seeded and unseeded

In the pharmaceutical industry, evaporation can also be combined with '*cooling*' crystallisation[81], often for improving product yields. Cooling crystallisation (Figure 1.27b) is conducted by taking an initially undersaturated solution at a starting temperature and cooling at a given rate.[64] Upon crossing the solubility line, the solution becomes supersaturated, with the metastable limit representing the point at which spontaneous nucleation can occur. This limit signifies the extent of supersaturation that can be

reached and can be varied depending upon the crystallisation conditions imposed, particularly with respect to the cooling rate and mixing profile. As a result of these different conditions, the crystallisation kinetics for a system can be altered, influencing the solid phase produced.[91]

In order to instigate a degree of control, many cooling crystallisations can be '*seeded*' so as to improve the crystal quality and allow for the formation of a particular crystalline phase.[64, 92, 93] Through the introduction of a small quantity of end-product crystals, secondary nucleation can be induced well below the metastable limit, at lower supersaturations. By forcing crystallisation to occur within the metastable zone, where the kinetics of crystal nucleation and growth are more balanced, uncontrolled nucleation can be avoided, allowing for the formation of fewer, larger crystals.[94] In addition, the end phase produced can also be controlled by seeding, as it allows for the nucleation of material akin to the seeds introduced.

Both evaporative and cooling crystallisation work, through different processes, to achieve supersaturation; by allowing undersaturated solutions to go beyond the point of saturation, eventually enabling nucleation to occur. Another common method for not only generating new crystalline phases, but also for encouraging the formation of the most stable forms, is that of '*slurrying*'.[64, 95, 96] Slurrying operates through the suspension of solid material in a quantity of solvent, insufficient to allow for complete dissolution, mitigating primary nucleation effects.[42] Depending upon the composition of the suspended solid and the solvent utilised, different solid-state forms can be accessed, with the least stable forms nucleating first and maturing to the more stable phases over time, as dictated by Ostwald's rule of stages. The key advantage of this method is its ability to access polymorphic forms of different stabilities over a period of time, simply by mixing a suspension.

For all crystallisations conducted in solution, consideration of the process parameters is important in terms of supersaturation control. Solvent selection is key, with a material expressing different solubilities in each solvent environment, but in addition, the rate at which supersaturation is achieved is also significant. Cooling rates and evaporation temperatures directly affect how quickly supersaturation is achieved and the relative size of the metastable zone.

1.7.2 Mechanochemical preparations

An alternative to solution-based crystallisations is that of '*mechanochemical*' methods. Mechanochemistry[97, 98] refers to the transformation of materials in the solid-state through the application of mechanical force and has several advantages over other crystallisation techniques, with its inherent sustainability and ability to mitigate the bulk effects of solubility. Traditionally, grinding experiments were carried out on materials or combination of materials without the assistance of solvent, but more recently, the use of so-called '*liquid-assisted*' grinding[99-101] has taken greater prominence. By adding the minimum amount of solvent to the samples being ground, the formation of different solid phases can be facilitated, many of which are inaccessible through alternative methods. Furthermore, studies have also been conducted whereby changing the volume of liquid added can also have an impact on polymorphism and multi-component material formation.[101]

Whilst mechanochemistry is not a fully understood process, on-going research in this area has proposed three possible mechanisms for its operation[102, 103]; through surface transportation[104], liquid eutectic intermediates[105] or *via* amorphous phase formation.[106] The first mechanism considers systems where the molecular building blocks are only held at the surface loosely, hence with mechanochemical stress, they can be relocated and reconstructed into various other forms. For compounds or, in the case of multi-component systems, eutectic mixtures that express a low melting point, localised melting can occur, aiding in molecular transportation and phase crystallisation. The final route exploits materials that have initially strong lattices. However, when these materials are ground, a phase transition to an

amorphous form can occur and through Ostwald's rule of stages, can allow for multiple crystalline structures to precipitate.

Whilst utilising different processing routes, each of these mechanisms have several features in common. Firstly, upon the application of mechanochemical pressure, the particles in question are broken down into smaller particulates, generating larger surface areas. Combined with this, phase transitions are also aided by the efficient mixing of material inherent to the grinding process. Coupled with the potential for defect introduction and the localised heat of friction generated from grinding or milling, these phenomena are able to enhance or accelerate the process of crystallisation *via* mechanochemistry. No matter the mechanism, it can be said that under the conditions imposed, systems are not necessarily at equilibrium, offering routes to preparation of metastable phases.[107]

Upon the addition of solvent in liquid-assisted grinding, many samples demonstrate higher crystallinity compared to those obtained from neat preparations. This can be rationalised through the enhanced molecular mobility and increased effect of solvation with the addition of solvent, though given that systems are always at high supersaturations, the crystallisation of metastable forms is still inherent.

Mechanochemistry can be an attractive option for exploring the preparation of co-crystalline materials[108], with a particular focus on variations in stoichiometry and polymorphic form. Often different stoichiometric co-crystals[96] of the same starting components can be generated simply by grinding different molar ratios of the starting materials together. In a similar manner, polymorphic co-crystals can also be accessed, depending upon conditions such as solvent type, quantity and grinding time.[97, 101]

1.8 Industrial crystallisation

As stated above, crystallisation processes are vital in the industrial production of many pharmaceuticals and fine chemicals.[81, 92] The following section will focus on the two main classifications of process operation, batch and continuous, highlighting their setups and context in industry.

1.8.1 Batch crystallisation

'*Batch*' processing is used in a range of chemical industries for a variety of purposes.[109] Due to its inherent simplicity and comparatively low start-up costs, batch operation can be applied to many unit operations (reaction, crystallisation, mixing, etc.) for the production of many different materials.

Simple batch crystallisations from solution typically utilise setups such as individual '*stirred tank reactors*', STRs (Figure 1.28).[26] Such setups consist of a main reactor vessel, a temperature controlled jacket, a mixing element and an inlet. The solution of a given system is held in the body of the reactor, in which, by changing various process parameters, supersaturation can be induced, either by cooling or evaporation. For these methods, the temperature of the process is controlled using heated jackets and mixing achieved through mixing units, such as impellers. Once supersaturation is eventually reached, nucleation can be prompted either spontaneously or through the addition of a seed.

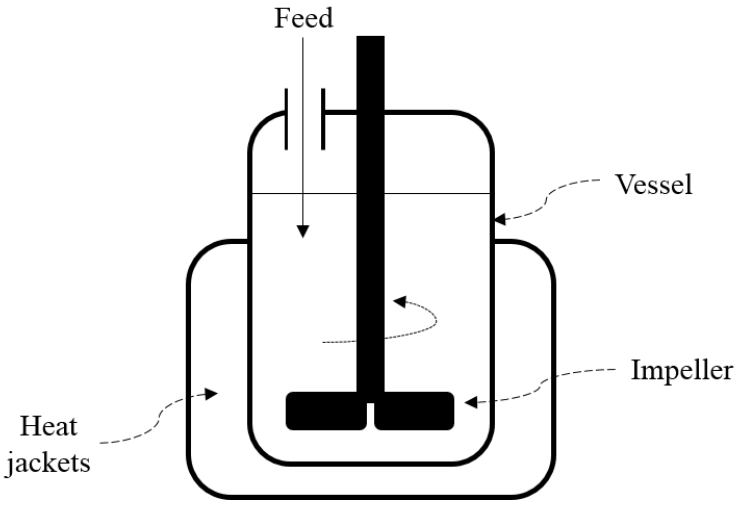

Figure 1. 28 - Basic stirred tank reactor setup

Despite its versatility, batch processing has inherent flaws, particularly in terms of poor heat and mass transfer with increasing scales[110], which can lead to issues in the consistency of the end-product. These batch-to-batch inconsistencies can manifest themselves through variations in particle size, crystal shape and solid form, with implications for downstream processing steps such as filtration, drying and formulation.[111]

1.8.2 Continuous crystallisation

In contrast, '*continuous*' operations offer a number of benefits, including shorter processing times, reduced energy costs and better mass-heat transfer, yielding more consistent product.[110, 112] Historically, research into continuous methods has been focussed on flow synthesis[113], but more recent work has applied these principles to other unit operations, including crystallisation, with motivation towards the development of fully integrated end-to-end production processes.[114]

Continuous operations are characterised by *"parameters which may be geographically distributed within the system but are unchanged with time"*[81]. This means that whilst process conditions can vary at different stages of a reactor or crystalliser, due to the characteristic setup of such continuous platforms, the individual process parameters have far greater consistency and, hence, can be managed more effectively.[115] The implications for materials moving through the system is that each molecule should experience the same conditions. As a result, continuous processes can be scaled-up and out more easily, by either increasing the throughput of material or running the process for longer.[111]

The ideal operation of a continuous platform would be to operate at '*plug flow*'.[110] Plug flow is defined as the regular movement of material through a reactor, whereby all the elements of the fluid flow in the same direction over the same time period, with perfect mixing. It is through this that process parameter consistency can be achieved. In reality, most reactors work at near-plug flow conditions, with the flow exhibiting '*laminar*' and '*turbulent*' contributions (Figure 1.29).[110]

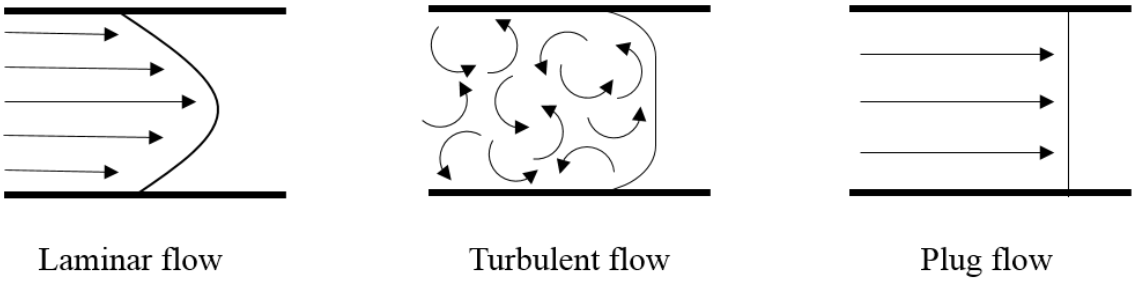

Figure 1. 29 - Types of flow; laminar flow, turbulent flow and plug flow

Two conventional methods of achieving near plug flow conditions use a cascade of stirred tank reactors (cSTR)[116] or a tubular reactor acting under turbulent flow.[111] For cSTRs or mixed suspension mixed product removal (MSMPR)[116-118] setups, a series of well-mixed batch STRs are connected in series, with plug flow achieved, in principle, when an infinite number of reactors are present. In practice, 5-10 reactors are used, meaning the system is far from plug flow conditions, but with every additional reactor leading to an increase in inventory and associated capital cost. To date, the MSMPR platform has been used for the effective crystallisation of many API materials, with examples including cyclosporine, paracetamol and aliskiren hemifumarate.[118]

In many tubular reactors, turbulent mixing is also introduced to try and improve mixing with a platform. The nature of turbulent flow only allows mixing through the net flow of material, resulting in tubular reactors being very long, even for short residence times. In practice, tubular reactors are altered[111, 119] to promote more homogeneous mixing of material. An example of such a system is the '*continuous oscillatory baffled crystalliser*' (COBC)[120, 121], a jacketed tubular cooling crystalliser with periodically spaced orifice baffles. Material is moved *via* a net flow rate through the system but gentle mixing is induced through a superimposed oscillatory motion by which the solution moves back and forth through the baffles, generating eddies. The advantage of such a method is that the mixing can be decoupled from the net flow that is driven by turbulent action. With baffles situated along the crystalliser, mixing can be considered uniform in each interbaffle zone, leaving cumulative plug flow conditions along the length of the platform. To date, continuous crystallisation processes, either cascade tanks or tubular, have been used for the precipitation of a number of systems. A case of particular note was the selective crystallisation of the metastable polymorph of Paracetamol, Form II.[120]

One of the newest directions for continuous crystallisation has been in the assessment and modification of the mixing parameters within the reactors themselves. Rather than using traditional mixing features, such as impellers and baffles, alternative methods have been explored for the efficient homogenisation of solution throughout the crystallisation process. One such method has been that of '*solution segmentation*'.[122, 123] By mixing a crystallisation medium with an immiscible liquid and feeding them through a channel, the separation of phases can result in discrete and uniform segments, also known as '*slugs*'. Once formed, these slugs can travel through a tubular reactor at a given rate, allowing for efficient mixing through the generation of internal vortices.

An example of the application of solution segmentation in flow was demonstrated through the use of the '*Kinetically Regulated Automated Input Crystalliser*', or KRAIC.[124] This tubular crystalliser operates as cooling crystallisation reactor, whereby a solution, initially heated to ensure complete dissolution, is mixed with an appropriate immiscible carrier fluid at a mixing piece, generating the necessary slugs. Through the application of a carrier fluid with suitable wetting properties, the solution slug can be coated so as to minimise contact with the surrounding tube walls, reducing the possibility of heterogeneous nucleation. In the case illustrated in Figure 1.30, air was also introduced, resulting in three segments, allowing for the maximisation of throughput through the crystalliser. As the slugs move

through consecutive coils, the solution is gradually cooled to room temperature, achieving supersaturation and primary nucleation. Figure 1.30a outlines the general setup of the KRAIC, with Figure 1.30b emphasising the formation of the different segments within the crystalliser. To date, this platform has been used for the efficient crystallisation of a range of molecular and organometallic materials[125], with examples including selective preparation of the polymorphs of succinic acid.

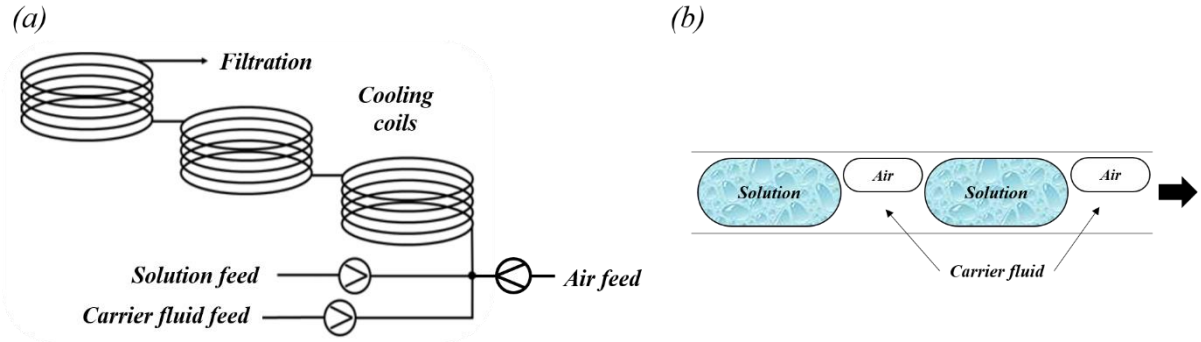

Figure 1. 30 - The Kinetically Regulated Automated Input Crystalliser (KRAIC), highlighting (a) the segment feeds and cooling coils, along with (b) the three segments of generator within the platform

2 Analytical techniques

Any product obtained from a crystallisation process should be characterised using a range of complementary analytical techniques, particularly in the case of novel materials. With particular emphasis on the crystalline phase, this section will cover the basic principles of some of the techniques used for solid-state characterisation, including microscopy, X-ray diffraction methods, thermal analysis, spectroscopic methods and solubility determination.

2.1 Microscopy

Optical microscopy[126, 127] allows the user to observe materials down to dimensions of a few micrometres, depending upon the magnification, and can be divided into two sub-types; polarising and reflectance microscopy.[128] Polarising microscopy is a transmission technique and can be used for the analysis of crystalline materials, fine powders or thin slices of material. It uses white or monochromatic light that is shone through a polariser which only transmits parallel components of the light with the same vibrational direction. The resultant '*plane polarised light*' passes through a lens and onto a sample. Light is then transmitted by the sample to an objective lens and through an analyser, where only light 90° in its vibrational direction to the polariser is transmitted and observed. When an analyser is present, a sample can be viewed between the cross polars of the polariser and the analyser, allowing the user to distinguish whether the same is '*isotropic*' (dark) or '*anisotropic*' (light or coloured). By varying the extinction direction, crystalline samples can be assessed for their quality depending upon their anisotropic nature. Reflectance light microscopes operate in a similar manner, except that the light source and objective lens are on the same side as the sample. By using optical microscopy, properties such as morphology, sample homogeneity, purity and crystal defects can be identified.

2.2 X-ray crystallography

X-ray diffraction methods are one of the most important family of techniques used in crystallisation science. Once a crystal has been prepared, it is necessary to characterise it in terms of its crystalline structure, assessing bond and interaction angles and lengths, which can be then related back to other physicochemical properties. The two techniques that utilise the diffraction of X-rays are '*Single Crystal X-ray Diffraction*' (SCXRD)[10, 129, 130] and '*Powder X-ray Diffraction*' (PXRD).[10, 131] Whilst broadly SCXRD is used for the determination of the 3-dimensional crystalline structure and PXRD is used as a method of phase identification, both rely on the same fundamentals for crystal analysis. This section will cover crystallographic definitions of crystalline structure and how it can be related to X-ray diffraction. From there, the unpinning principles of X-ray diffraction will be explored, assessing their application for structure determination and phase analysis, using SCXRD and PXRD respectively.

2.2.1 Crystal symmetry

Crystals are built up through the regular and repetitive arrangement of structural units in three-dimensions.[128, 132] These structural units can consist of individual atoms, a group of atoms, molecules or ions. The repetition of such species can be represented by a repeat unit called the '*unit cell*', the smallest repeating volume that shows the full symmetry of the crystal structure (Figure 2.1).[129, 133] The unit cell itself is made up from individual components that are related to each other through this fundamental symmetry. These components, also called '*asymmetric units*', represent the most basic structural motif, expressing no internal symmetry themselves, from which the entire crystal structure can be generated.

Crystal structures comprise of the periodic arrangement of identical environments in three-dimensions[134]. This repetition is defined in terms of an array of '*lattice points*', which, when repeated, can be used to create an infinite array, or a '*lattice*'.[10, 49] A lattice point can be used to denote an equivalent environment within an ordered material. Depending upon how these points are connected together, different unit cells can be made, the best of which are generally decided through a series of rules based upon the relative lengths and angles of the unit cell. The unit cell for a given system is defined by three axial lengths (*a*, *b* and *c*) and three intersecting angles (α, β and γ).[128]

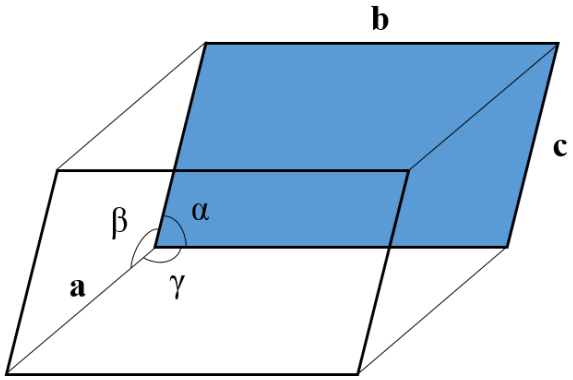

Figure 2. 1 - The unit cell, defined by the axis lengths (a, b and c) and the angles (α, β and γ)

A unit cell can be categorised into seven different crystal systems, based on its symmetry (Table 2.1), ranging from cubic, which is the most symmetrical, to triclinic, the least. There are four types of lattice[128] that can be built up from the arrangement of lattice points and used for the construction of the unit cell; primitive (P), face-centred (F), body-centred (I) and side-centred (A, B or C, depending upon the face in question). In terms of contributions to defining the unit cell, P-lattices possess one lattice point in total, F-lattices four lattice points, I-lattice two lattice points and the A/B/C-lattice two lattice points (Figure 2.2). By combining the lattice types and crystal systems, 14 Bravais lattices can be generated. Certain Bravais lattices are not possible due to symmetry violations or can be reduced to give one of the other 14 lattices.

Table 2. 1 - Seven crystal systems, unit cell parameters and Bravais lattices

Crystal system	Unit cell parameters	Bravais lattice
Cubic	$a = b = c, \alpha = \beta = \gamma = 90^o$	P, I, F
Hexagonal	$a = b \neq c, \alpha = \beta = 90^o, \gamma = 120^o$	P
Trigonal	$a = b = c, \alpha = \beta = \gamma \neq 90^o$	P
Tetragonal	$a = b \neq c, \alpha = \beta = \gamma = 90^o$	P, I
Orthorhombic	$a \neq b \neq c, \alpha = \beta = \gamma = 90^o$	P, C, I, F
Monoclinic	$a \neq b \neq c, \alpha = \gamma = 90^o, \beta \neq 90^o$	P, C
Triclinic	$a \neq b \neq c, \alpha \neq \beta \neq \gamma \neq 90^o$	P

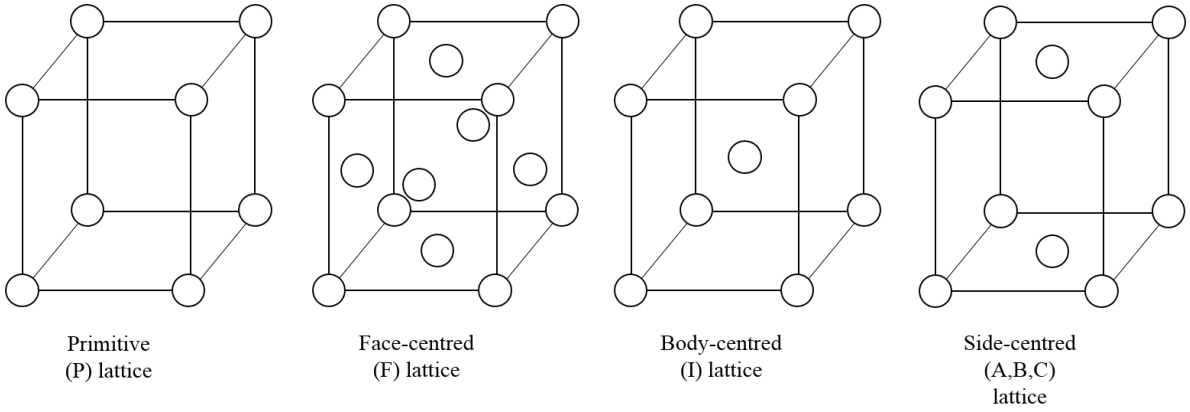

Figure 2. 2 - Lattice types; Primitive (P), Face-centred (F), Body-centred (I) and Side-centred (A, B or C)

Whilst unit cells can only be related to each other through translational symmetry, the individual atoms, ions, molecules or groups thereof that make up a unit cell can be related through combinations of *translational*, *rotational*, *inversion* or *reflection* symmetries.[129, 133] A '*symmetry operation*' is a symmetry movement that moves a component into a new configuration that is equivalent to its original position. A '*symmetry element*' defines the point, line or plane through which said symmetry operation can be performed. Through combinations of these symmetry elements, including '*glide planes*' and '*screw axes*' that include translational elements, unit cells can categorised into '*space groups*', of which 230 are possible.

2.2.2 X-ray diffraction – Bragg's Law and intensities

It has already been highlighted that crystalline structures can be described through lattice points and lattices. Due to the regularity of these points, it is also possible to define '*planes*' in a range of orientations throughout the lattice. A lattice can have a number of planes, each defined by '*Miller indices, hkl*'.[129, 131, 135] These indices represent a family of parallel planes that cut through arbitrary axes in reciprocal space. As well as these values, sets of planes can also be defined in terms of their interplanar distances, known as '*d-spacing*'.

Due to the periodic nature of the lattice points in a given crystal, X-rays are able to interact with the components that make up these points in a coherent manner, resulting in constructive interference at specific angles. These interactions are manifest in the form of diffraction, where the waves of the X-ray radiation can interact in or out-of-phase, respectively. A geometrical interpretation of how X-ray diffraction works was proposed by W. H. Bragg and W. L. Bragg and relates the diffraction and interference of X-rays to a reflective process when in contact with a crystal lattice (Figure 2.3).[10]

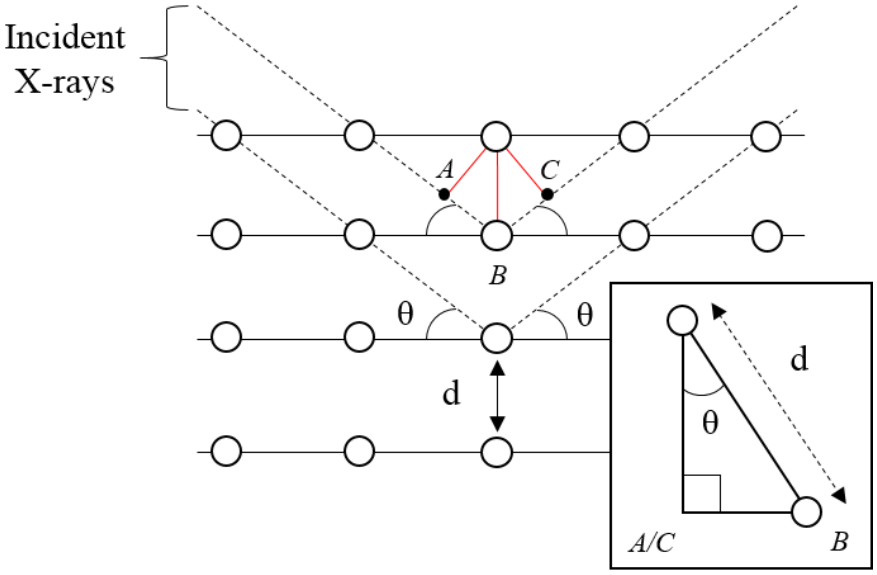

Figure 2. 3 - A representation of Bragg's Law, highlighting the reflection of X-ray radiation with lattice planes and the associated X-ray pathway difference

Here, two incident X-rays are reflected by two adjacent planes, each X-ray having a different path length, travelling the additional distance AB + BC. '*Bragg's law*'[129] is used to define the conditions through which X-ray waves will occur in phase and for a reflection to be observed. In order for this to be so, the path difference must equal to integer numbers of wavelengths, as defined in Equation 2.1.[68, 129, 130] From this equation, the interplanar distances for a family of planes can be determined and hence, the unit cell parameters for a crystal system.

$$n\lambda = 2d_{hkl}\sin\theta$$

Equation 2. 1 - The Bragg equation, highlighting the conditions necessary for in phase diffraction to occur (n = reflection order, λ = wavelength of X-ray radiation, d_{hkl} = interplanar distance for a given set of Lattice planes, θ = angle of incidence)

Routine crystallographic studies collect diffraction data from a range of angles and orientations of the crystal, sampling all the lattice planes that define a given material, generating a pattern of diffraction spots. The symmetry of a pattern is closely related to the symmetry and, therefore, structure within a crystalline sample. By rearranging the Bragg equation, it can be shown that the diffraction angle is related to the interplanar spacing in a reciprocal manner (i.e. $\sin\theta = (n\lambda/2).(1/d)$). As a result of this, the dimensions within a diffraction pattern is inversely related to that of the real structure. Therefore, the diffraction symmetry is defined through '*reciprocal space*'[135], with dimensions on 1/d and units of $Å^{-1}$. Analogous to crystal symmetry, the symmetry of the diffraction pattern in reciprocal space can be classified into different classes known as the 11 '*Laue classes*'. When looking at a diffraction pattern, it is sometimes observed that certain diffraction spots for a given crystal structure are missing. These are known as '*systematic absences*'[129] and arise when a lattice is centred or a symmetry element possesses translational symmetry. Hence, by considering the positions of the diffraction spots, the size and shape of the unit cell can be defined.

Whilst Bragg's law dictates the conditions through which diffraction can occur, providing information as to the size and shape of the unit cell, from this alone, there is no indication as to what the contents of the unit cell might be. This information is contained in the intensities of the diffracted X-ray beam. Diffraction intensities rely on the relative in or out-of-phase nature of X-ray waves interacting with a crystalline material, the value of which are related to the crystal symmetry, atomic positions and their respective electron densities.[129, 136]

The atoms of each element exhibit characteristic scattering of X-ray radiation over various diffraction angles. At scattering angle of zero ($2\theta = 0^{o}$), waves are scattered completely in-phase by the electron density associated with each atom, but as the angle of diffraction increases, destructive interference also increases, causing a drop off in the diffraction intensity. The relationship between intensity and the angle of diffraction for a specific element is shown in Figure 2.4 and is known as the '*atomic scattering factor'* (f_i).[129, 131]

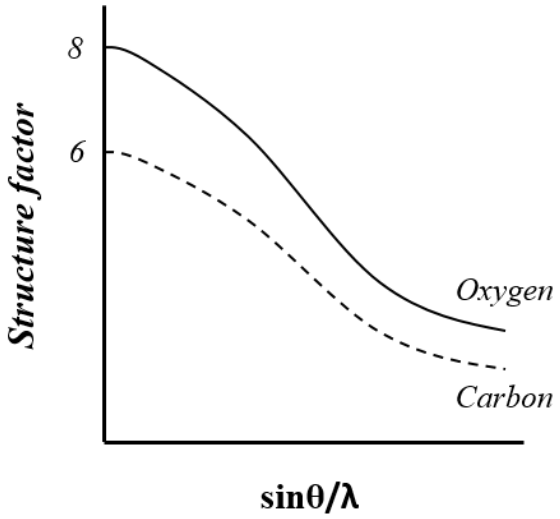

Figure 2. 4 - X-ray atomic scattering factors (f_i) for oxygen and carbon

By taking all these parameters into consideration and through Fourier transform manipulation, the amplitudes and phases for a given set of reflections can be related to the individual atoms within the unit cell. This relationship is expressed through the '*structure factor*' (Equation 2.2).

$$F(hkl) = \sum_{j=1}^{N} f_j . exp[2\pi i(hx_j + ky_j + lz_j)]$$

Equation 2. 2 - The forward Fourier transform, highlighting the structure factor (F(hkl)) for a particular crystal structure, as defined by the summation of all amplitudes and phases (i) for diffracting X-rays, taking into account the ability of individual atoms (j) to scatter X-rays (f_j)

By only considering its magnitude, the structure factor is shown to be proportionally related to the intensity of the scattered X-ray beam, as shown in Equation 2.3.[10] In turn, the magnitude can also be used to describe the relative amplitudes of a particular wave.

$$I(hkl) \propto |F(hkl)|^2$$

Equation 2. 3 - The relationship between diffraction intensity (I_{hkl}) and the amplitude of the diffracted wave ($|F_{hkl}|$), for a given set of lattice planes

Once determined, the structure factor can be linked to the electron density and relative positions of the associated atoms within the unit cell. By conducting a reverse Fourier transform, an electron density map can be obtained directly from the diffraction pattern (Equation 2.4).[129, 136] Here, the electron density is defined by taking all the diffracted X-ray waves together, taking into account their relative amplitudes and phases.

$$\rho(xyz) = \frac{1}{V}\sum_{hkl}|F(hkl)|.exp[i\varphi(hkl)].exp[-2\pi i(hx + ky + lz)]$$

Equation 2. 4 - The reverse Fourier transform, highlighting the relationship between the electron densities (ρ(hkl)) associated with a unit cell of a given volume (V), the structure factors, relating to the amplitudes, and the relative phases of the incoming waves

The mathematical description of the phases can be broken down into two components; the intrinsic phase, ϕ (hkl), of the waves themselves and their shift. Whilst the shift can be calculated based upon the different path lengths, intrinsic phasing cannot be determined directly from the diffraction experiment. In crystallographic terms, this is known as the '*phase problem*'.[10, 130, 136] As a result, diffraction intensities cannot be directly related to the structure factor, and hence the electron density, based solely on experimental data.

2.2.3 Structure solution

Once diffraction data have been collected, the relative positions of the atoms within the unit cell and, hence, the overall structure of a crystal can be determined. Structures are generated based upon the initial assignment of atoms to positions of electron density on the electron density map, which can be derived from the reverse Fourier transform.[136] Here, the amplitudes and phase shifts of the diffracting X-rays across all the lattice planes can be obtained directly from the experimental data. However, as highlighted above, knowledge of the intrinsic phasing must also be established. The phase problem cannot be resolved directly, so secondary methods need to be employed.

When it comes to solving crystal structures, many methods are available. Whilst structure determination using the '*Patterson synthesis*'[129] (identifying atoms with the highest electron density) is common for metal-organic and inorganic structure analysis, given that the focus here is on small molecular crystal systems, the structures in this project will be solved with either '*direct*'[129, 137] or '*dual space*'[138] methods.

Direct methods is a family of techniques that solve the phase problem by defining a probabilistic relationship between the experimentally known structure factor amplitudes and the unknown phases. By ranking diffraction intensities, the most significant are selected first and their probable relationship to the correct phase can be determined. This process is repeated through a number of iterations, assigning phases and building up the electron density map. In order to achieve this, several assumptions are made, whereby the electron density is defined as being positive across the structure and localised to distinct atomic locations.

Dual space or '*charge flipping*'[139] methods operate by constraining the phases through combined observations from reflection intensities in reciprocal space and properties of the electron density in real space. This means defining constraints that relate the amplitudes of the electron density derived from the Fourier transform with those of the experimentally observed amplitudes, as well as treating all observed electron density as positive.

2.2.4 Structure refinement

Solving a crystal structure reveals the relative positions of the atoms present based upon their electron density. In the early stages of structure solution, a partial structure is obtained, with only some of the atomic positions determined. This generates an initial model that needs to be refined.

Refinement involves the systematic adjustment of parameters governing the structure factor (atomic positions, thermal vibrational parameters, etc.) to give the best fit between the observed intensities (F^{obs})

and those calculated for the modelled structure (F^{calc}). The procedure through which this refinement is achieved is that of '*least squares*'.[140] Typically, diffraction experiments generate more observed data points when compared to the number of parameters. As a rule, the more data points, the more reliable the refinement parameters, with a data-to-parameter ratio of >10 considered acceptable for a high quality structure determination.[129, 141] To quantify this, each parameter has associated with it standard uncertainties (s.u.), which depend on the error related to the data, the agreement between the measured and calculated results and the overall quantity of the data. An initial reflection of the reliability of the data comes from the '*goodness of fit*' value.[129]

The relative disparity can be assessed in variety of ways, but most commonly through the residual '*R*' factor (Equation 2.5).[129, 142] As the phases cannot be taken directly from the experimental data, structure and refinement assessments must be based on amplitudes. This refinement indicator highlights the difference between the observed and calculated amplitudes, divided by that of the observed.

$$R = \frac{\sum \left| |F^{obs}| - |F^{calc}| \right|}{\sum |F^{obs}|}$$

Equation 2. 5 - Residual 'R' factor for assessing structure refinement

Whilst useful, the 'R' factor does not take into account the relative importance of some diffraction intensities with respect to others. By incorporating a weighting scheme, the different contributions to the observed and calculated structure factors can be accounted for. Hence, a better statistical evaluation can be yielded through the use of the '*wR2*' factor (Equation 2.6)[129, 142], where the squared structure factors can be related directly to intensities.

$$wR2 = \sqrt{\frac{\sum w(F^{obs^2} - F^{calc^2})^2}{\sum w(F^{obs^2})^2}}$$

Equation 2. 6 - 'wR2' weighted factor for assessing structure refinement, where 'w' is the weighting factor

For all structural refinements, the aim is to minimise the discrepancies between the observed and the calculated intensities. To achieve this, a range of parameters must be refined[141]. Amongst the most significant of these are those associated with the positioning and vibrations of atoms. Each atom has three positional coordinates (*x*, *y* and *z*) and a displacement parameter (*U*). The displacement of atoms can either be described '*isotropically*', whereby atoms are represented with isotropic spherical thermal motion, or more commonly '*anisotropically*'. Here, atoms are defined by their movement in six different directions. For the best results, diffraction data is collected at lower temperatures (e.g. 150 K) so as to minimise thermal vibrations. Typically, most non-hydrogen atoms are assigned anisotropic displacement variables, resulting in up to nine parameters that can be refined for each atom. Owing to their inherently low electron density, the assignment and refinement of hydrogen atoms is conducted at later stages of the process, usually by incorporating isotropic '*constraints*'.[143] Constraints are imposed refinement conditions, usually to fulfil symmetry requirements or to control refinement parameters that are poorly defined by the diffraction data.

Once completed, a final structure is generated, demonstrating the accurate positions of atoms in the unit cell, together with their individual anisotropic thermal vibrations, providing estimates of bond lengths and angles, as well as their relative errors.[76]

2.2.5 Considerations for single crystal X-ray diffraction (SCXRD)

The most common method used for structure determination is SCXRD. Utilising the principles of X-ray diffraction outlined above, the regular arrangement of atoms, ions and molecules can be determined from electron density maps, as derived from the diffraction pattern. The basic steps used in SCXRD are highlighted in Figure 2.5.[129]

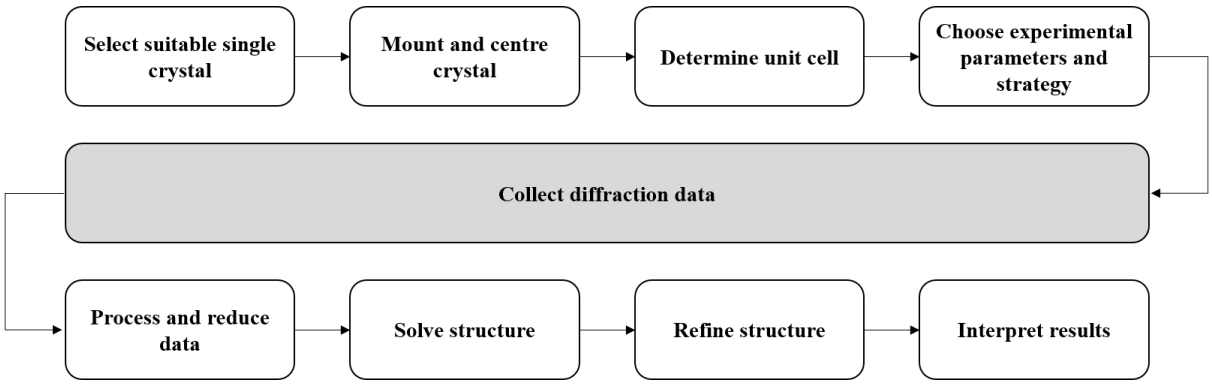

Figure 2. 5 - Schematic of the fundamental steps required for structure determination through SCXRD

Once a crystal of sufficient quality has been selected, it can be mounted onto a '*goniometer head*' and centred so as to be in the direct pathway of the X-ray beam. At this stage, an initial diffraction screen can be conducted. Whilst not always necessary, this initial assessment can provide important information as to the quality of the crystal being analysed. This can be in terms diffraction quality or for comparison with previously collected structures, *via* determination of the unit cell.

One of the key decisions when designing any diffraction experiment is the choice of X-ray wavelength[144]. Although a wide range X-ray sources are available, the most common sources used in laboratory diffractometers are copper (Cu-K_α 1.54178 Å) and molybdenum (Mo-K_α 0.71073 Å). Whilst the use of molybdenum radiation can mitigate excessive X-ray absorption effects and give data at higher diffraction angles, the longer wavelength inherent to copper sourced radiation is particularly useful in yielding more intense diffraction patterns. This is of particular significance when analysing weakly diffracting materials, such as small molecular structures.

As well as this, X-rays from copper sources are also widely used for determining the absolute structures of materials that possess chirality[144]. Single enantiomers are only able to crystallise within one of 65 chiral space groups, where no symmetry elements that allow for the incorporation of the opposite enantiomer are present. These systems are described as '*non-centrosymmetric*', whilst systems that do have mirror or inversion symmetry are known as '*centrosymmetric*'.

When X-rays are generated, a series of filters and optics are used to remove all other wavelengths, apart from the desired wavelength[135]. At the '*X-ray absorption edges*' that are key to this filtering, certain wavelengths are able to excite or eject electrons from atoms, resulting in a phase change in the X-rays scattered by specific atoms in the structure being analysed. This has implications for the intensity and, in non-centrosymmetric structures, can lead to the breakdown of '*Freidel's law*' and the observation of weak anomalous scattering.[130, 144] Freidel's law states that in the absence of anomalous scattering, diffraction in one direction will have the same intensities as those in the opposite, resulting in a centrosymmetric diffraction pattern. However, in the case of enantiomerically pure materials, this is not true. As a result, distinctions can be made between the diffraction patterns of the enantiomeric pairs and chirality can be resolved. This highlights the advantage of using copper radiation as it can allow for the anomalous scattering effects to be observed at a greater intensity.

Opposite chiral structures can be considered as inversions of each other. Upon structure solution and refinement, these inversion structures can be considered within the model and refined against each other. The '*Flack*' parameter[141, 145] is used to compare how close the model is to each of the inversion related structures and the correct chirality is assigned accordingly. Absolute structure determination[142] by X-ray diffraction is not always reliable, owing to the inherently weaker scattering effects used to observe the differences in phase between opposite diffractions. As a result, confirmation of the absolute configuration should be clarified by other means, either by referencing to the chirality of a known molecule used during crystallisation or through another analytical technique, such as chiral HPLC or circular dichroism spectroscopy (discussed below).

When analysing crystalline samples, an important consideration is its homogeneity. To achieve the best diffraction data, single crystals are required. However, a common problem when determining a crystal structure is that of '*twinning*'.[146] A crystal can be twinned when two or more orientations of the same structure reside together in a defined relationship. As a result, the overall diffraction pattern demonstrates the superposition of the different individual diffraction patterns of the constituent components. Common consequences of twinning include exaggerated intensities from overlapping diffraction spots and apparent alterations to the unit cell parameters. Although structures can be resolved from twinned materials, the process is by no means simple and has inherent complications with respect to conventional structure solutions.

2.2.6 Powder X-ray diffraction (PXRD)

Though useful in its own right, particularly for structure solution, one of the main drawbacks of SCXRD is the prerequisite of individual single crystals. In many cases, the growth of sufficiently homogeneous and large crystals is not always possible, with crystalline solids from synthesis or screening often being microcrystalline in nature. A common method for analysing bulk crystalline product is PXRD.

Like with SCXRD, PXRD works on the principle of X-ray diffraction upon interaction with a crystalline material.[10, 130] However, due to the nature of poly-crystalline samples, where many crystallites are arranged in a range of orientations, all lattice planes are exposed simultaneously. PXRD operates by sweeping through a range of diffraction angles. At any given position, a certain proportion of the crystallites present will have the necessary alignment to allow for X-ray waves to be diffracted, thus satisfying Bragg's law. Unlike in SCXRD, the resultant diffraction pattern is made up of a series of concentric rings, otherwise known as '*Debye rings*', rather than individual diffraction spots (Figure 2.6a).[10] These rings arise from the diffraction from individual lattice planes (defined by the Miller indices, *hkl*) common across the many crystallites present. The resultant pattern is recorded at characteristic 2θ values, corresponding the angle made between the diffracted and incident beams. This results in a range of peaks with given intensities, which can be indexed to the different planes present, their respective interplanar spacing and hence used to define the representative dimensions of the unit cell for that material .[131] A schematic of a standard PXRD diffractometer is shown in Figure 2.6b.[10]

An important consideration for PXRD analysis is that of '*preferred orientation*'.[130] Often, polycrystalline materials deviate from the ideal random distribution of crystallite orientations. When samples contain larger individual crystals and depending upon their morphology, certain lattice planes can be expressed to a greater degree with respect to all of the other planes present. This results in the dominance of the peaks that correspond to these lattice planes, sometimes swamping the other intensities present and creating misleading diffraction patterns.

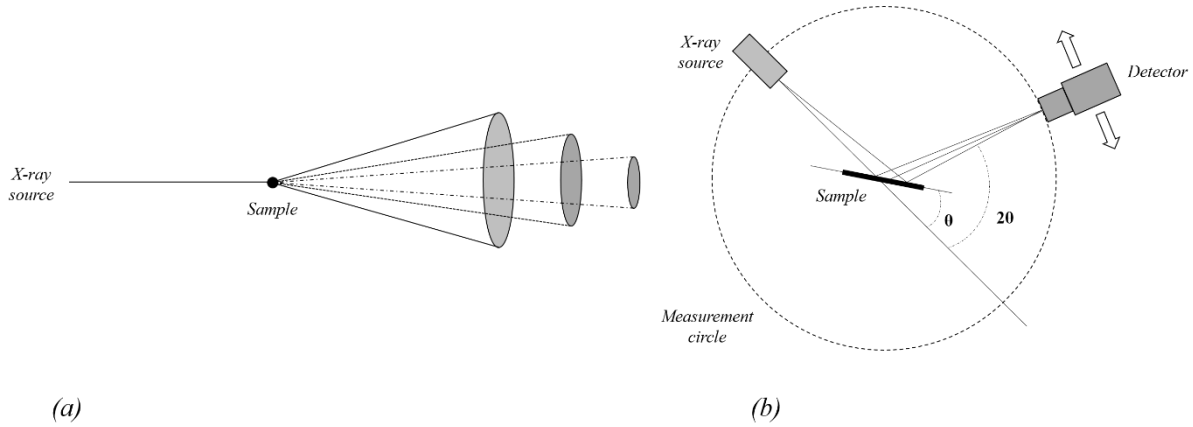

Figure 2. 6 - Diagrams highlighting (a) the ring arising from the diffraction of a poly-crystalline sample and (b) a typical setup of a PXRD diffractometer

One of the most important uses of PXRD is qualitative phase analysis, giving information as to which crystalline phases or combination of phases may be present.[100, 147-149] Each material expresses its own unique pattern that can be used as a fingerprint for identification purposes. In the pharmaceutical industry, in particular, PXRD is commonplace, owing to its ability to rapidly assess polymorphism in the solid-state. Figure 2.7 outlines an example two-dimensional diffraction pattern for the racemic form of the API, naproxen, highlighting the unique arrangement of intensities at different values of 2θ.

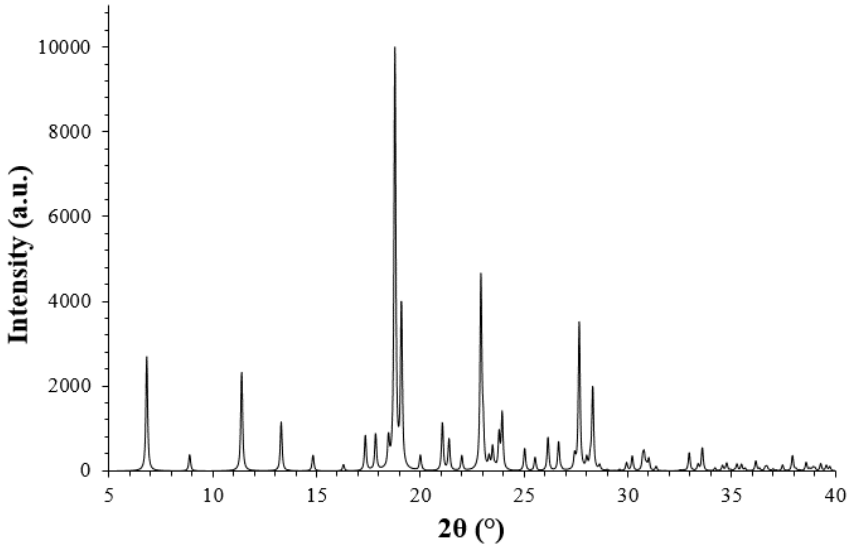

Figure 2. 7 - An example PXRD pattern for the racemic API, naproxen (PAPTUX)[150], highlighting intensities at respective values of 2θ

2.3 Thermal analysis

Thermal analytical techniques[65, 68] work on the basis of measuring the changes observed in a material as a function of heat flow. By varying the temperature, thermal events can be recorded and subsequently interpreted in relation to physical and chemical properties for a given system. These thermal events can be classified as exothermic or endothermic processes, which incorporate phenomena such decomposition, solvent loss and a range of phase transitions (melting, crystallisation and solid-to-solid). A variety of thermal techniques are available, but the focus here will be on '*differential scanning calorimetry*' and '*hot-stage microscopy*'.

2.3.1 Differential scanning calorimetry (DSC)

Differential scanning calorimetry (DSC)[65, 68] is one of the most widely used thermal techniques for the analysis of pharmaceutical materials. Upon analysis with DSC, a sample is subjected to a regime of temperatures, from which heat flows can be recorded, highlighting any thermal induced phase transitions. Most commercially available DSCs operate through one of two mechanism; '*power compensation*' or '*heat-flux*'. In power compensating devices, a sample and a reference are positioned on different heating elements, but the same temperatures are maintained for both. When a thermal event occurs, the energy taken in or given out by the sample is compensated for in the reference, therefore keeping the overall temperature between the two heating elements the same. This compensation is recorded in terms of heat flow and attributed to an observed thermal event. For heat-flux DSC instruments, the sample and reference are subjected to heating and cooling in two separate compartments in the same oven. Here, the temperature difference is measured as a function of temperature, from which the heat flow difference can then be calculated.

In DSC, a variety of heating and cooling rates can be employed, from which thermal data can be obtained, including melting points and key enthalpies. DSC analysis is particularly important for the assessment of crystalline materials as it can differentiate between the melting points of polymorphic forms, as well as yield information relating to transitions between various phases.[148, 151-153] Figure 2.8 highlights some of the key phenomena observed from a typical DSC trace.[68]

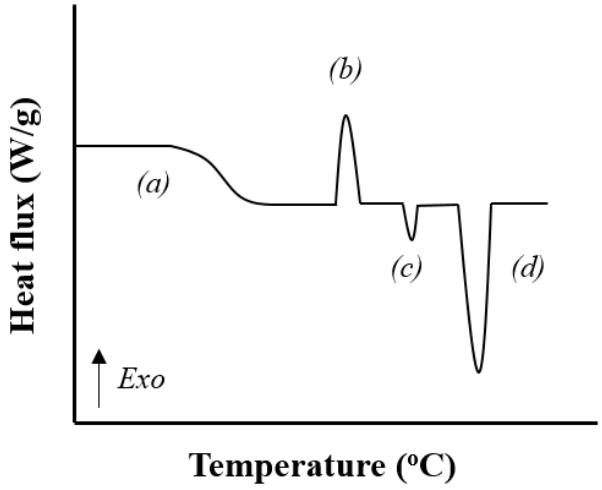

Figure 2. 8 - DSC trace showing common thermal phenomena, such as (a) a glass transition (baseline shift), (b) a recrystallisation from the melt (exothermic), (c) a phase transition (here, endothermic) and (d) a melting point (endothermic)

2.3.2 Hot-stage microscopy (HSM)

The ability to observe solids under a microscope often provides useful insight into the properties of a material. In hot-stage microscopy (HSM)[65], samples can be observed whilst being exposed to different temperature profiles, similar to those used in DSC. Through these observations, thermal phenomena can be visually assessed and related back to quantitative data obtained from DSC.[154]

2.4 Spectroscopy

Spectroscopy[76, 155] is a family of analytical methods that utilises either the absorption or transmission of specific energies of '*electromagnetic*' radiation. These correspond directly to quantised energies for

excitations within a given atom, ion or molecule. From analysis of the different energetic transitions exhibited upon interaction with the various wavelengths of radiation, information relating to atomic and molecular structural features can be obtained. In terms of the different types of electromagnetic radiation, γ-rays possess the shortest wavelength and the highest energy whilst radio waves have the longest wavelength and lowest energy.

Common laboratory spectrometers predominately operate by detecting absorption transitions, with that of ultraviolet visible (UV-vis) and infrared (IR) radiation being the most utilised, used to explore electronic, vibrational and rotational transitions, respectively. The techniques described here are '*infrared*' (IR) spectroscopy and the UV-vis based method of '*circular dichroism*' (CD) spectroscopy.

2.4.1 Infrared spectroscopy

Infrared spectroscopy[66, 155] refers to techniques that probe materials with wavelengths corresponding to the infrared region of the electromagnetic spectrum. Upon absorption of radiation, bonds within molecules are excited, demonstrating '*vibrational*' excitation. These types of excitation manifest themselves as either higher energy stretches or lower energy bends. As a result, the absorption of certain wavelengths can be correlated to the bending and stretching of specific bond types, common to a large number of molecular structures. Although key to identifying individual bonds, single vibrations should not be considered in isolation. Upon absorption of infrared radiation, bonds throughout a molecular structure begin to oscillate, affecting the whole molecule and giving rise to overtones and other harmonics.

Based upon these principles, infrared spectra can be used either quantitatively or, more commonly, qualitatively. By considering that bonds of greater strength will show greater vibrational frequencies, spectra can be analysed and judgements can be made as to the relative strengths of different bonds, the presence or absence of particular functionalities and the existence and directionality of intermolecular interactions, particularly hydrogen bonds. Broadly, infrared spectra can be categorised into three regions; 4000-2000 cm^{-1}, 2000-1500 cm^{-1} and 1500-600 cm^{-1}. The first two regions are synonymous with characteristic stretches for individual functional groups particularly those of the O-H, N-H and C-O bonds, with the lower energy range of wavelengths being used to describe bond bending. These can be used as a unique fingerprint for a given molecular entity. Figure 2.9 outlines the example IR spectra of the racemic API, naproxen, in the solid state.

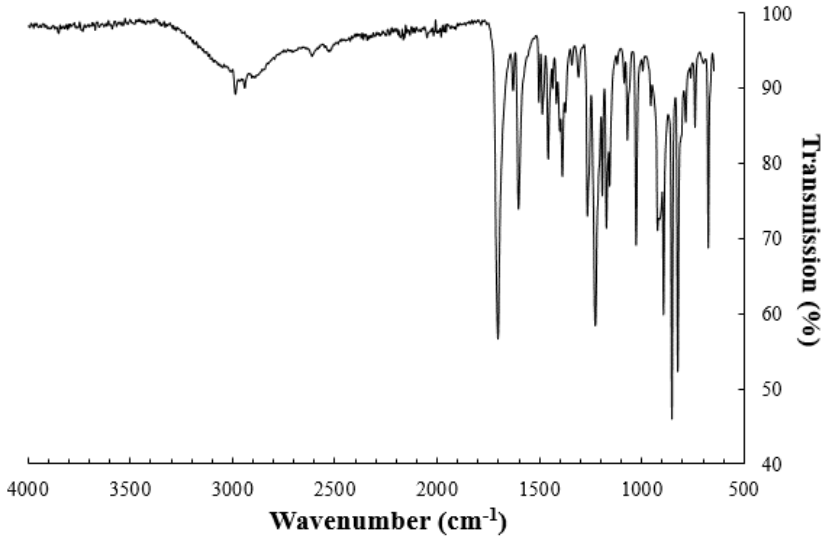

Figure 2. 9 - IR spectra for the racemic API, naproxen, in the solid state

2.4.2 Circular dichroism

Circular dichroism spectroscopy[156, 157] is a technique which measures the difference in absorption between left and right-handed '*circularly polarised light*', typically utilising wavelengths associated with the ultraviolet and visible regions of the electromagnetic spectrum (Figure 2.10). The main application of this method is for the analysis of molecules and structures (e.g. proteins) that exhibit chirality. These systems exhibit '*circular birefringence*', whereby a solution consisting of a chiral substance is able to propagate left and right circularly polarised light at different velocities. As a result, the waves rotate. It should be noted that this propagation effect does not result in strictly circular polarisation, but rather that of an ellipsoid. This phenomenon is common to both circular dichroism and '*polarimetry*', but whilst the latter deals exclusively with the degree of optical rotation, circular dichroism also incorporates the relative absorption of the different handed forms of polarised light. This absorption only occurs at wavelengths that can be absorbed by a chiral material.

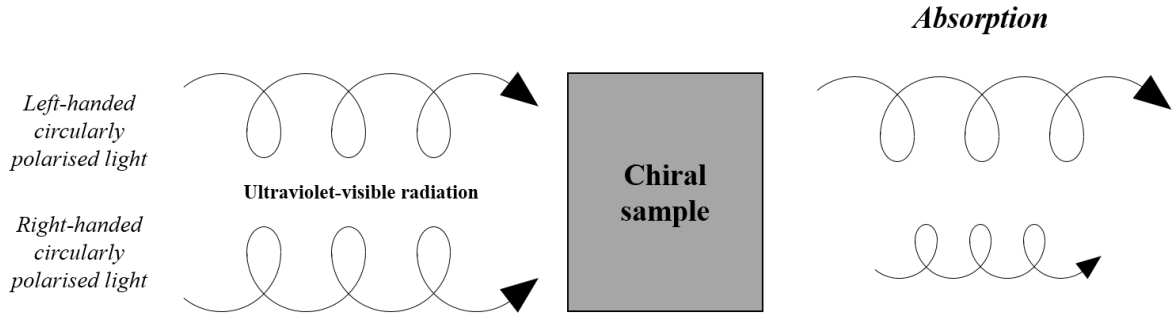

Figure 2. 10 - Schematic diagram demonstrating the different absorptions of circularly polarised light by a chiral substance

Polarised light can be represented as the combination of two linearly polarised states set at 90° to each other. At this point, both waves have the same amplitude and are in-phase. But by shifting the waves with respect to each other, they become out-of-phase resulting in non-linearly polarised light. Depending on the direction of this shift, the two waves of light now form a helix, spiralling in either a right or left-handed manner. This relationship is known as circular polarisation.

In order to gain meaningful data from this technique, the material of interest must fulfil certain criteria.[157] The substance should possess, not only chirality, but also a '*chromophore*'. These functionalities usually consist of conjugated (π) bonds and are responsible for the absorption of ultraviolet and visible light. Systems that exhibit strong circular dichroism typically have chromophores that are chiral.

The output from circular dichroism spectroscopic experiments is usually reported in terms of absorbance (ΔA) or '*ellipticity*' (millidegrees or m). Absorbance (Equation 2.7a) reflects the disparity in absorbance between the different handed forms of circularly polarised light, whilst ellipticity (Equation 2.7b) describes the degree to which the circularly polarised light forms an ellipsoid upon interaction with the chiral medium. Both of these units can be related to each other and using the '*Beer-Lambert law*', both can be corrected to be independent of solution concentration, in terms of '*molar absorbance and ellipticity'* (Equations 2.7c and d).

(a) $\Delta A = A(Left\ CPL) - A(Right\ CPL)$

(b) $\theta = \Delta A.(32.98)$

(c) $\Delta\varepsilon = \frac{\Delta A}{C.L}$

(d) $[\theta] = \Delta\varepsilon.(3298)$

Equation 2. 7 - (a) Absorbance circular dichroism, (b) ellipticity, (c) molar absorbance circular dichroism and (d) molar ellipticity (32.982 is a scale factor between absorbance and the ellipticity)

In practise, by measuring solutions of given concentration in terms of the molar ellipticity, the proportion of the enantiomers present can be measured. As shown in Figure 2.11, clear distinctions can be made between not only the individual two enantiomers, with each demonstrating a specific sign in terms of its molar ellipticity, but also the racemic composition, where the absorption associated with a particular chiral form is cancelled out by that of the opposing enantiomer.

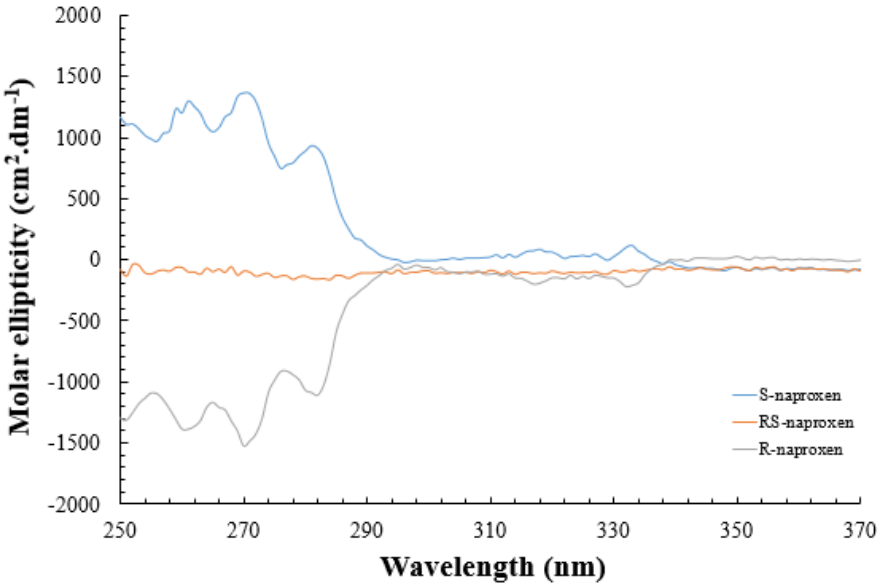

Figure 2. 11 - Molar ellipticity plot, comparing the absorptions of both enantiomeric forms of the API, naproxen, as well as its racemic form

2.5 Solubility determination

In order to design efficient crystallisation processes from solution, the solubility of materials in a given solvent or combinations thereof must be known. By understanding the equilibrium solubility at a given temperature, initial investigations into the supersaturated region can be conducted. A variety of methods can be used to determine the solubility, including '*gravimetric*'[158-160] and '*temperature variation*' techniques.[159, 161]

Gravimetric analysis is the most reliable method for determining the thermodynamic solubility, but is dependent upon the relative stability of particular phases (i.e. polymorphs) and can be experimentally time-consuming. Suspensions are prepared and mixed for an extended period of time, at a specified temperature, allowing the system to reach saturation. Here, the saturated solution is filtered and allowed

to evaporate, accounting for the mass of solvent and saturated solution (Figure 2.12a). From this, equilibrium concentrations can be determined.

Due to the time-consuming nature of gravimetric analysis, most commercial equipment derives the solubility for a system based upon variations in temperature. Solutions of a known concentration are prepared and exposed to a temperature cycling regime. Typically, measurements are taken based upon turbidity, from which both the solubility and metastable limit can be found for a given concentration. Turbidity is a measure of the cloudiness of a fluid caused by particles being suspended in the solution. Upon cooling, the point at which nucleation occurs can be used to determine the metastable limit, whilst upon heating, the point at which there is complete dissolution can be taken as the solubility (Figure 2.12b). Despite turbidity measurements having advantages in terms of being able to characterise various aspects of a solution undergoing dissolution and crystallisation, caution should be taken. In comparison to gravimetric methods, the system in question is not strictly allowed to equilibrate, meaning that in many cases, the solubility value being measured is not always reflective of the true thermodynamic solubility.

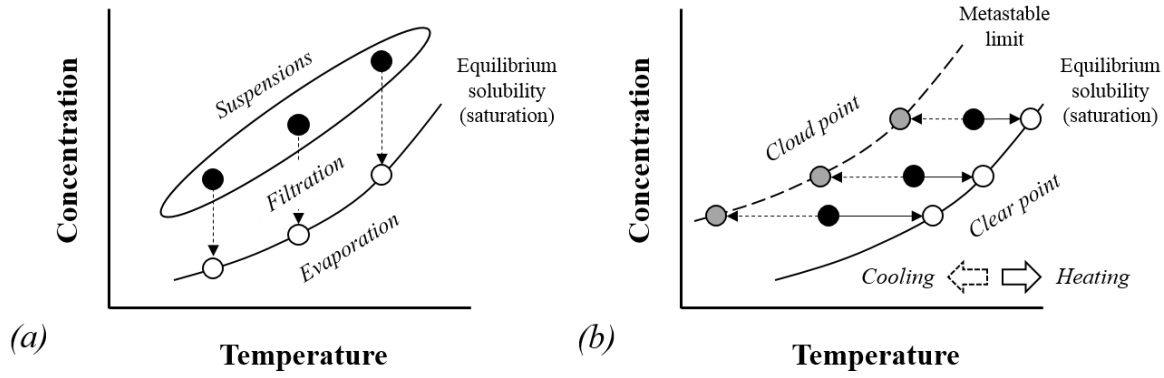

Figure 2. 12 - Methods for determining solubility, through (a) gravimetric and (b) temperature variation measurements

3 Material review

Thus far, the principles of pharmaceutical solid-state chemistry, crystallisation and the methods for the analysis of the resulting solid products have been described in detail. The purpose of this chapter is to put these principles into context, focussing on a set of materials which form the basis of the research outlined in later sections of this thesis. Firstly, the API, *naproxen*, will be discussed, exploring its structure and related physicochemical properties, highlighting previous reported multi-component materials and their application to enantiomeric separation. This pharmaceutical ingredient will form the basis for the multi-component material screenings and characterisations conducted in Chapters 6, 7 and 8. Secondly, the stoichiometrically diverse co-crystals of *oxalic acid* and *urea* will be introduced, emphasising the structural differences between the two forms and assessing previously studied methods for their respective preparation. These co-crystals are examined further in Chapter 9.

3.1 Chirality and multi-component materials of the API, naproxen

Naproxen (*NPX*), (*2-(6-methoxy-2-naphthyl) propionic acid*) is a non-steroidal anti-inflammatory drug (NSAID) used in the treatment of pathophysiological conditions, ranging from fevers and headaches, to degenerative diseases, such as osteo and rheumatoid arthritis.[162-165] Typically administered orally, *NPX* is one of the most common NSAIDs and has a proven record of effectiveness. However, despite this, *NPX* has a dosage limit owing to side effects resulting from irritation and ulceration of the gastro-intestinal tract. In addition, this API is categorised as a Class II drug[166] under the '*Biopharmaceutics Classification System*' (BCS), exhibiting high permeability across membranes but low aqueous solubility.

NPX is made up of three principal functionalities; methoxy, naphthyl and propionic acid groups (Figure 3.1). Key to its solid-state structure are the naphthyl and carboxylic acid groups, through which π-stacking and hydrogen bonding can take place, respectively. *NPX* also possesses chirality about the methyl substituent adjacent to the carboxylic acid and naphthyl groups. Despite both showing therapeutic benefits, the S-enantiomer (*sNPX*) has been shown to demonstrate significantly higher activity than the R form (*rNPX*), justifying the delivery of a homochiral API formulation.[150, 167]

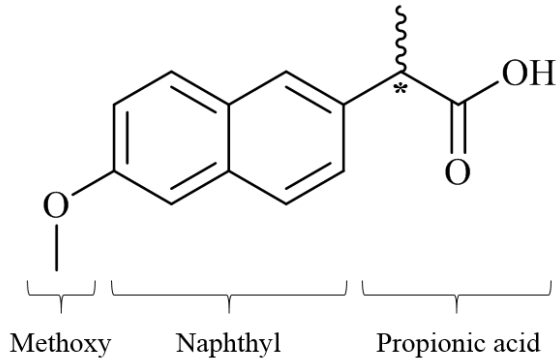

Figure 3. 1 - Schematic of the molecular structure of the API, naproxen (*NPX*), highlighting its chiral centre (*)

Currently, enantiomeric separation is conducted post-synthesis, *via* a variety of means including chiral high performance liquid chromatography (HPLC) and classical diastereomeric resolution.[168] The limiting factor for the application of *NPX* to a preferential crystallisation process is its inherent preference to form a racemic crystalline material at racemic compositions. As outlined in Chapter 1, preferential crystallisations can only be carried out when the material in question exhibits the properties of a racemic conglomerate at racemic compositions. Conglomerate systems arise when the like

enantiomers preferentially interact, resulting in a physical mixture of crystals precipitating, where each crystallite is composed of one single enantiomer. Figure 3.2 provides a structural comparison of the homochiral[169-171] and heterochiral[150] crystal structures of *NPX*, which crystallise in the $P2_1$ and *P*bca space groups respectively. For the enantiomerically pure structure, the *sNPX* molecules form channels held together by extended hydrogen bonded backbones, utilising individual $C_1^1(3)$ interactions between the hydroxyl donors and carbonyl acceptors, whilst the racemic structure utilises $R_2^2(8)$ dimers between opposite enantiomers (see Appendix for further crystallographic information).

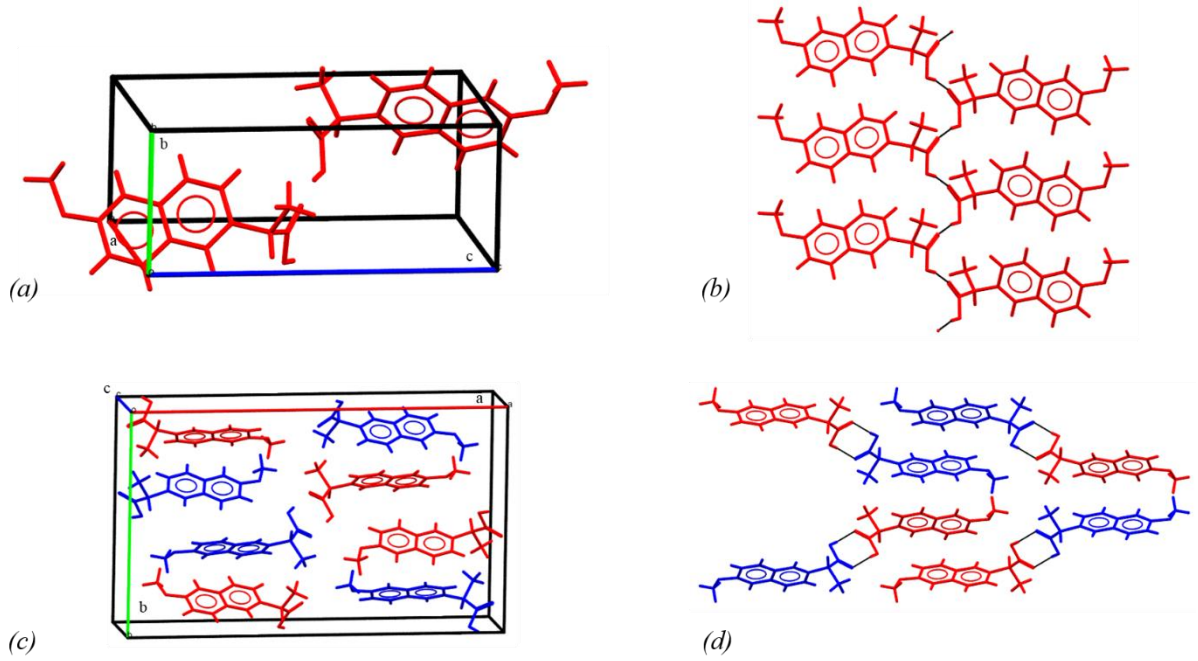

Figure 3. 2 - Crystal structures of *sNPX*[169-171] and *rsNPX*[150], highlighting their unit cells, (a) and (c), as well as the key hydrogen bonding motifs, (b) and (d), respectively (red = *sNPX*, blue = *rNPX*)

Whilst synthetic derivatisation of *NPX* has been shown to allow for conglomerate formation[172], in many cases, this can be an energy intensive process. Another technique for generating materials that are amenable to a preferential crystallisation (i.e. a racemic conglomerate) is through the preparation of multi-component materials. Previous studies have shown that through the addition of an achiral secondary component, novel co-crystal or salt forms can be made that demonstrate a change in the class of chiral crystalline material when compared to that of the starting materials. An example of this (Figure 3.3a) is the co-crystal system of ibuprofen, another NSAID, with 4,4'-bipyridine.[41] By co-crystallising different enantiomeric compositions of the API with the co-former in a 2:1 ratio, a solid solution is formed, whereby broadly the overall interaction motifs and packing remains the same, but the locations of R to S ibuprofen throughout the structure are continuous. This phenomenon is in contrast with ibuprofen, which forms a racemic compound. Likewise, upon combining 2,3-dichlorophenylacetic acid with (±)-trans-N,N'-dibenzyldiaminocyclohexane (Figure 3.4b)[44], the resultant 2:1 salt form has been shown to produce a conglomerate that can be applied to preferential crystallisation processes.

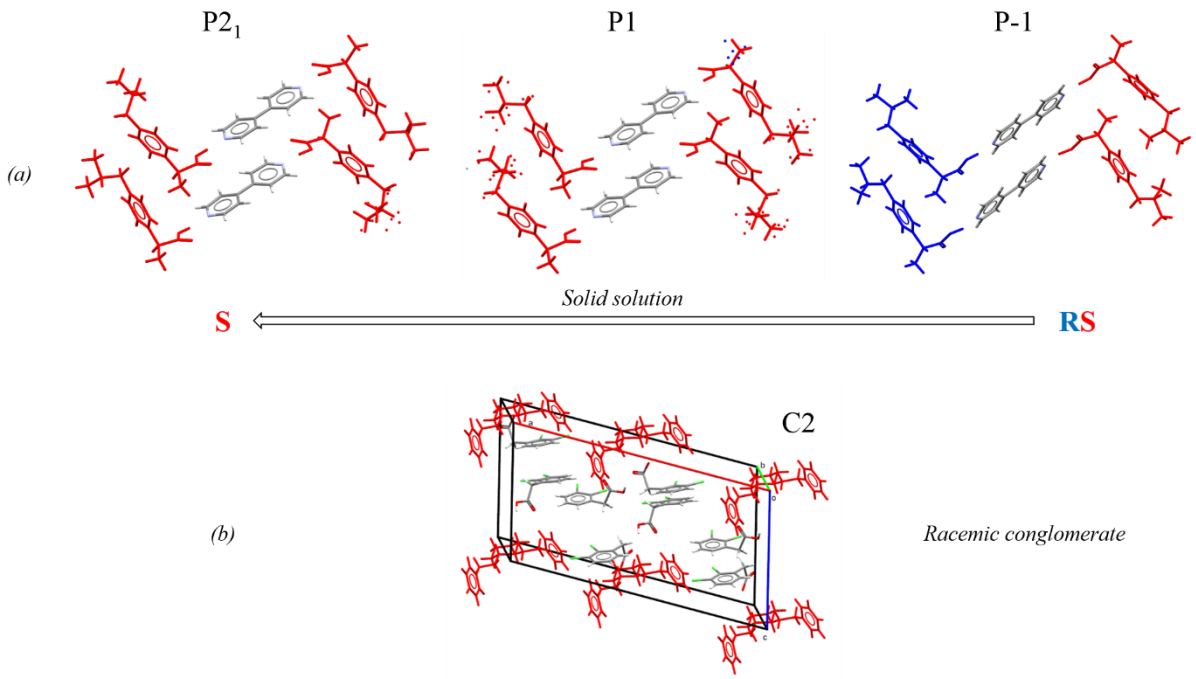

Figure 3. 3 - Crystal structures of the (a) 2:1 ibuprofen:4,4'-bipyridine co-crystal[41] and (b) 2:1 2,3-dichlorophenylacetic acid:(±)-trans-N,N'-dibenzyldiaminocyclohexane salt[44], highlighting solid solution and racemic conglomerate formation, respectively (red = S-enantiomer, blue = R-enantiomer)

To date, most multi-component material screening incorporating *NPX* has been conducted either to enhance its aqueous solubility[173] or for the preparation of diastereomeric materials.[168, 174] Based upon searches of the CSD (conducted June 2018), 48 structures could be found including *NPX* either in its protonated or de-protonated state, excluding organometallic materials. Once the single-component *sNPX* and *rsNPX* structures had been discounted, the remaining 41 multi-component structures can be classified in terms of their salt or co-crystal properties, as well as in terms of the chirality of the salt or co-former being used (Table 3.1). Further crystallographic details can be found in the Appendix.

Table 3. 1 - Classification of the previously report multi-component materials of *NPX*, based upon salt/co-former chirality and the ratio of salt to co-crystalline structures

Salt/co-former chirality	No. of salts	No. of co-crystals
Chiral (diastereomeric)	8	9
Achiral	11	13

It should be noted that the vast majority of the literature structures utilise enantiomerically pure *NPX* (R or S), with few studies exploring the chiral crystalline nature of the novel multi-component materials at racemic compositions. However, two studies that did explore this covered three sets of co-crystalline materials, where *sNPX* and *rsNPX*, respectively, were combined in 2:1 molar ratios with the co-formers nicotinamide[175], 4,4'-bipyridine[176] and piperazine[176] (Figure 3.4). In each case, the co-crystals exhibited racemic compound-like behaviour, rendering them unsuitable for direct preferential crystallisation. Nevertheless, the study exploiting the *NPX*:nicotinamide co-crystals, counterintuitively, showed that by manipulating the crystallisation conditions (in this case, anti-solvent crystallisation with compressed CO_2) to encourage rapid nucleation, a mixture of enantiopure and racemic co-crystal could be obtained at racemic compositions. In such scenarios, the homochiral phase is kinetically stabilised and, hence, can be described as a metastable conglomerate.

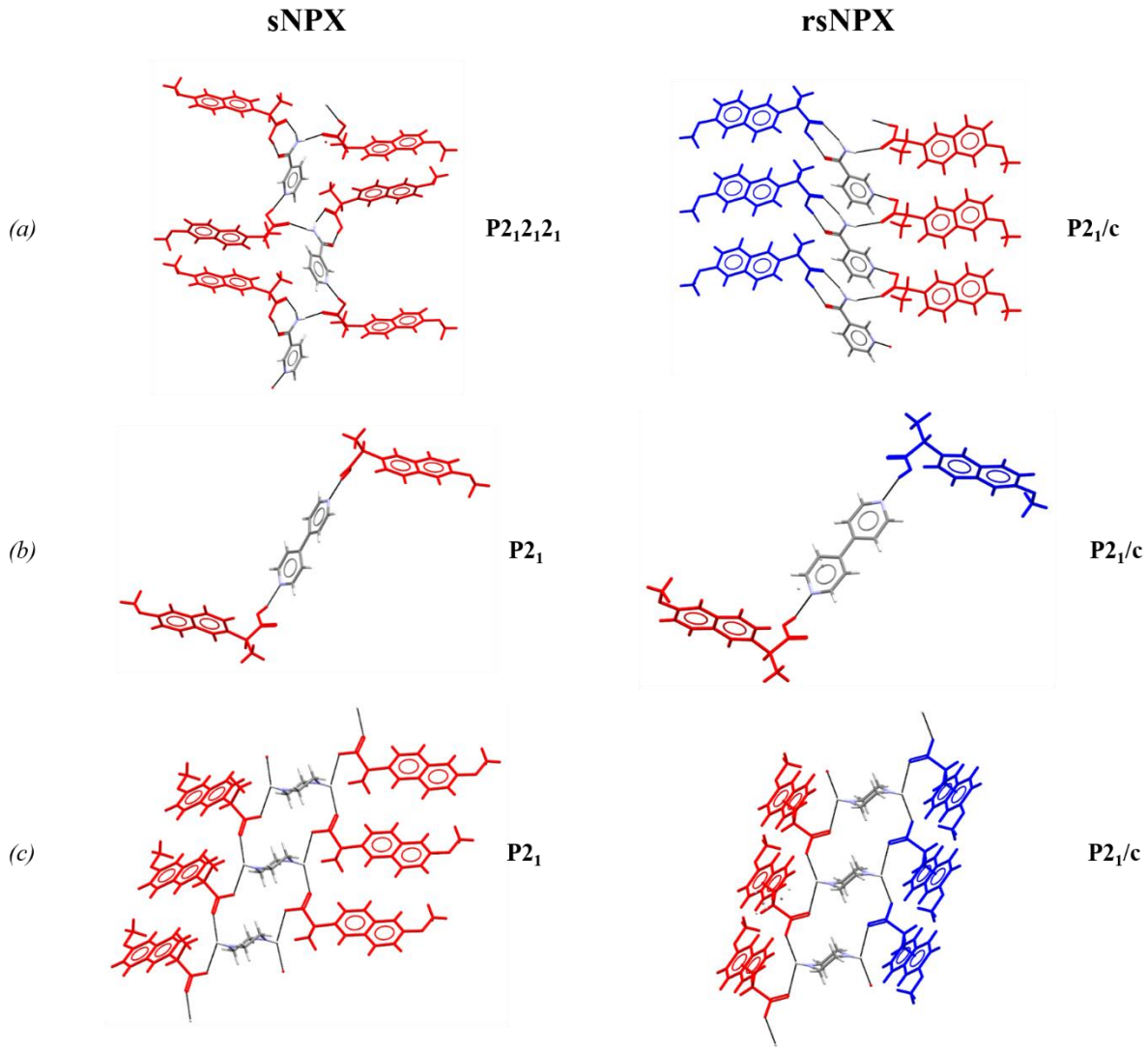

Figure 3. 4 - Crystal structures of the homochiral and racemic co-crystals of *NPX* with (a) nicotinamide[175], (b) 4,4'-bipyridine[176] and (c) piperazine[176], whereby the first forms a metastable racemic conglomerate and the latter two form racemic compounds (red = *sNPX*, blue = *rNPX*)

As such, the work discussed in Chapters 6, 7 and 8 explores the potential of *NPX* to form multi-component materials with a range of salt and co-formers. From comparison of the materials prepared at racemic and enantiopure compositions, the chiral crystalline nature is assessed. Upon finding a system that demonstrated characteristics akin to that of a conglomerate or metastable conglomerate, further solution analysis is conducted so as to provide information useful for the design of preferential crystallisations.

3.2 Stoichiometric co-crystals of oxalic acid and urea

As discussed in previous chapters, multi-component systems, particularly co-crystalline materials, exhibit structural variations, not only in polymorphic terms, but also with respect to the stoichiometry of the constituent molecules within the crystalline structure. An example of this can be seen in co-crystals of oxalic acid (*OA*) and urea (*U*). Both these simple molecules are readily available and have been applied in many co-crystal studies to date.[177-180] *OA* (Figure 3.5a) itself can crystallise as one of two polymorphs (*OA*-α or β)[181], but due to its high hygroscopicity (the ability to uptake water from the surroundings and incorporate it into the crystal lattice) it also readily forms a dihydrate (*OAD*)[182, 183]

under ambient conditions. In comparison, *U* (Figure 3.5b) forms only one polymorphic form (Form I) at room temperature and pressures[184-186], though studies conducted at higher temperatures and pressures have shown the existence of further structures; Forms II-IV.[187] The unit cell parameters for each of the associated structures of these materials can be found in Appendix A3.

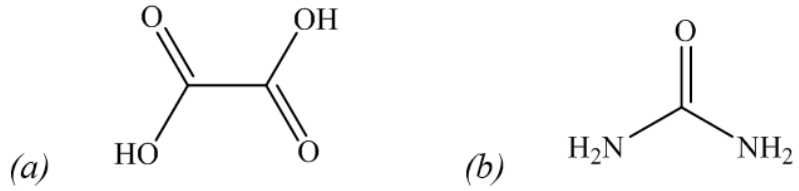

Figure 3. 5 - Schematic of the molecular structures of (a) oxalic acid (*OA*) and (b) urea (*U*)

Upon combining *OA* with *U*, under given crystallisation conditions, co-crystals have been shown to form. These co-crystals were first reported by Dalman[188] in 1934, but only in the 1970s were the crystal structures of the *OAU*-1:2[189] and *OAU*-1:1[190] cocrystals determined *via* X-ray diffraction. Figure 3.6 and Table 3.2 demonstrates the disparity between the stoichiometric co-crystals in terms of their crystal structures, hydrogen bonding and unit cell parameters. Both materials are made from two-dimensional hydrogen bonded networks built up into layers. In case of the *OAU*-1:1 co-crystal, the *OA* molecules in the plane are surrounded by alternating arrangements of equal number of *OA* and *U* molecules, whilst in the *OAU*-1:2 co-crystal, to account for the higher proportion of hydrogen bonding interactions, every *OA* molecular entity has two associated *U* molecules.

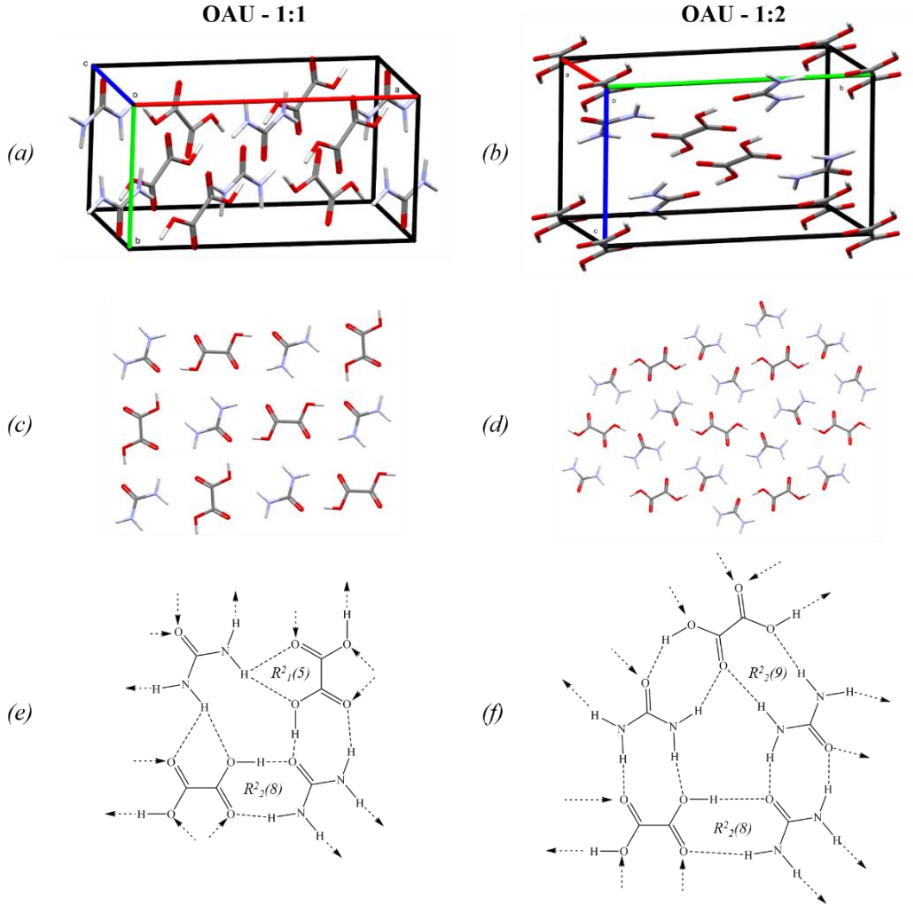

Figure 3. 6 - Crystal structures of the *OAU*-1:1[190] and *OAU*-1:2[189] co-crystals, highlighting their respective unit cells, (a) and (b), packing arrangements, (c) and (d), and the hydrogen bonding motifs, (e) and (f)

Table 3. 2 - Unit cell parameters of the *OAU*-1:1[190] and *OAU*-1:2[189] co-crystals

Co-crystal	Space group	a (Å)	b (Å)	c (Å)	α (º)	β (º)	γ (º)	Volume (Å^3)
***OAU* – 1:1**	Monoclinic *C*2/c	13.06	6.64	6.84	90	92.47	90	593.72
***OAU* – 1:2**	Monoclinic $P2_1/c$	5.048	12.374	6.876	90	96.4	90	426.83

To date, only three methods of preparation have been used for making either the 1:1 or 1:2 co-crystal of oxalic acid and urea; evaporative crystallisation[189, 190], slurrying[188, 191] and mechanochemistry[192]. The purpose of early studies was to obtain single crystals of sufficient quality for the determination of the crystal structures of each of the co-crystalline forms. For each diffraction study, evaporative crystallisation was preferred method used to yield suitable individual crystals. The focus of subsequent research shifted to the analysis of bulk properties (spectroscopic, thermal and thermodynamic data) of the respective co-crystals, thus slurry and mechanochemical methods were used. Table 3.3 highlights the key studies and the relevant preparation methods used to obtain each co-crystal.

Table 3. 3 - Previous studies into the *OAU*-1:1 and *OAU*-1:2 co-crystals, outlining the relevant preparation methods utilised

Author	*OAU* co-crystal	Preparation method
S. Harkema et al. (1972)[189]	1:2	1:2 molar ratio of *OA* to *U* dissolved in an aqueous solution and allowed to evaporate at room temperature
V. Chithambaram et al. (2013)[193]	1:2	1:2 molar ratio of *OA* to *U* dissolved in distilled water and evaporated at room temperature, recrystallisation using seeds from evaporation in aqueous saturated solution maintained at 30ºC
L. H. Dalman (1934)[188] & Y. Feng et al. (2012)[191]	1:2	1:1/1:2 molar ratios of *OA* to *U* slurried in water at 40ºC for 24 hours
S. Harkema et al. (1979)[190]	1:1	5:1 molar ratio of *OAD* to *U* dissolved in aqueous solution and allowed to evaporate at 40ºC
L. H. Dalman (1934)[188] & Y. Feng et al. (2012)[191]	1:1	4.5:1 molar ratio of *OA* to *U* slurried in water at 40ºC for 24 hours
O. Onija et al. (2012)[192]	1:1	1:1 molar ratio of *OA* to *U* ground in a mortar and pestle, with minimum distilled water added at room temperature

The studies conducted thus far have broadly focussed on the structural and physical properties of the two *OAU* co-crystals, but few have assessed, in depth, the methods for their preparation. From the work that led to the initial discovery of these materials, Figure 3.7 outlines the ternary phase diagram upon the combination of *OA* and *U* in water. A key feature is the comparative stability of the *OAU*-1:2 co-crystal over a large composition range, particularly when compared to that of the 1:1 system. It should be noted that this early research does not account for *OAD*, made readily under aqueous conditions.

In the research outlined in Chapter 9, the co-crystals of *OA* and *U* are used as a model system through which the methods utilised in early phase screening could be assessed; mechanochemical, slurrying and evaporative crystallisation. Routes to the selective preparation of each co-crystal are determined, accounting for the solvent environment and stoichiometry, in terms of both molar contribution of *OA* to *U* and that of solute to solvent. From here, cooling crystallisations, previously unexplored for these

multi-component materials, are developed, translating from the standard batch environment to the continuous crystallisation rigs available at the University of Bath.

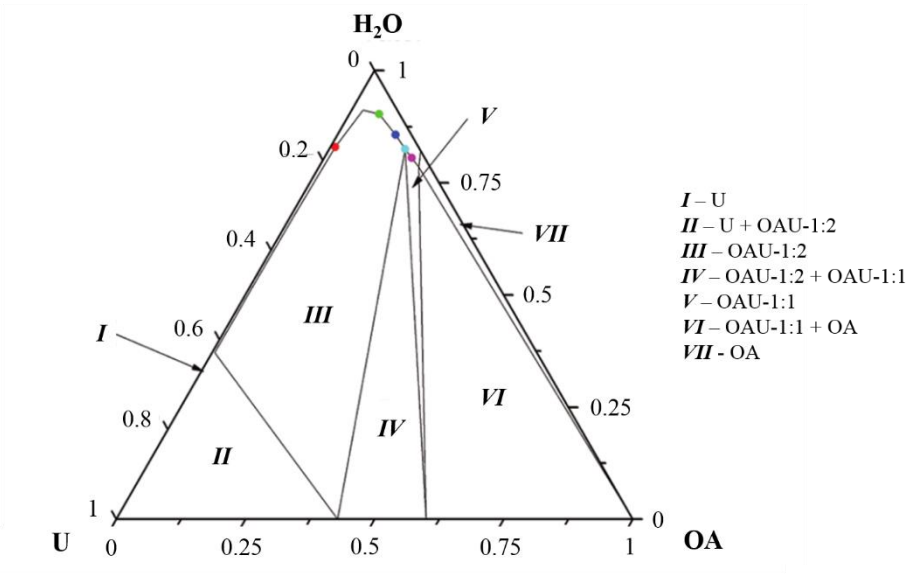

Figure 3. 7 - Ternary phase diagram for *OA* and *U* in water at 40ºC, obtained from the work conducted by L. H. Dalman[188, 191]

4 Research outline and aims

Various studies have shown that through the introduction of a secondary molecular component with complementary interactions, novel multi-component materials (co-crystals, salts, hydrates, and solvates) can be generated that exhibit different crystalline structures when compared to the constituent components and hence, altered physicochemical properties. This can have particular implications for pharmaceutical materials, offering a pathway to the tuning of material characteristics.

In the research described in subsequent chapters, the selective preparation of various multi-component materials are studied as part of two main projects; the *solid-state screening for novel multi-component materials of the API, naproxen, for application into a preferential crystallisation process*, and the *selective preparation and crystallisation of the stoichiometric co-crystals of oxalic acid and urea, driving towards continuous crystallisation*.

4.1 Solid-state screening for novel chiral multi-component materials of the API, naproxen, for application into a preferential crystallisation process

As highlighted from previous chapters, chiral molecules can be separated by a variety of techniques. Preferential crystallisation offers a simple, efficient and economically viable route through which individual enantiomers can be resolved from a racemic solution. However, an important prerequisite is that the chiral system of interest crystallises as a racemic conglomerate at racemic compositions. This significantly limits the application of preferential crystallisation owing to the relative scarcity of conglomerates found in the literature.

In the work outlined and discussed in Chapters 6, 7 and 8, the API naproxen (*NPX*), a racemic compound forming system, is subjected to extensive salt and co-crystal screenings, exploiting a range of potential achiral co-formers, so as to determine their chiral crystalline configuration. Chiral co-formers are not covered owing to the desire to focus on materials with the characteristic required for preferential crystallisation processes, as opposed to that of classical or diastereomeric resolution methods. The multi-component materials are prepared with racemic and enantiopure compositions of *NPX*, using a range of screening techniques, from mechanochemical to solution-based crystallisation methods, particularly evaporation and cooling. Each phase is characterised in terms of its crystalline structure, intermolecular interactions and thermal properties, from which they can be categorised in terms of their chiral crystalline nature. Systems that demonstrate interesting properties or that aid in development of a preferential crystallisation are explored further, developing initial crystallisation methods for preparation their respective phases at homo and hetero-chiral compositions. This work was carried out as part of an on-going collaboration between the Wilson group (University of Bath) and the ter Horst group (University of Strathclyde), looking towards the application of novel chiral multi-component materials into various preferential crystallisation setups. The work presented here is all that of the author.

Chapter 6 focusses on the characterisation of *NPX* itself, establishing methods for distinguishing between its homo and heterochiral forms. Based upon CSD searches, a series of likely co-formers are selected and from the initial selection of 2-aminopyridine (*2AP*), multi-component materials thereof are screened and characterised. Cooling crystallisation methods are then developed for the materials of *NPX* and *2AP*, exploring their applicability towards a preferential crystallisation. Further multi-component material screenings are discussed in Chapters 7 and 8, with the former focussing on direct 2-aminopyridine derivatives and the latter on co-formers that offer key aromatic nitrogen functionalities.

4.2 Selective preparation and crystallisation of stoichiometric co-crystals of oxalic acid and urea, driving towards continuous crystallisation

As with their single-component counterparts, multi-component materials can demonstrate structural variations, leading to distinctly different crystalline phases with their own set of physicochemical properties. Whist exhibiting classic polymorphism, these types of materials can also show variations in terms of constituent molecule stoichiometries. Producing a particular solid state phase is dependent upon the delicate interplay between the thermodynamics inherent to a given system and the kinetics governing a specific technique of crystallisation.

To exemplify this, the work detailed in Chapter 9 focusses on the model co-crystalline system of oxalic acid and urea, which, to date, exhibits two stoichiometrically varying forms, *OAU*-1:1 and *OAU*-1:2. Using various preparation methods, ranging from methods that use minimal solvent (mechanochemical), to solid suspensions in solution (slurrying) to the direct crystallisation from solution (evaporative), the propensity for the formation of the two co-crystals, respectively, is assessed, determining the optimal parameters for their preparation in each case.

From here, the focus is shifted to the more industrially scalable method of cooling crystallisation. Routes to the selective preparation of the respective co-crystals are initially carried out using batch methods, outlining the key conditions required for the transition into continuous crystallisation platforms. With particular emphasis on the 1:2 co-crystal, two continuous crystallisation setups, based at the University of Bath, are used; the continuous oscillatory baffled crystalliser (COBC) and the kinetically regulated automated input crystalliser (KRAIC). These initial studies are conducted in order to demonstrate the capabilities and efficiencies of the two individual platforms.

5 Experimental

5.1 Solid-state screening for novel chiral multi-component materials of the API, naproxen, for application into a preferential crystallisation process

5.1.1 Starting materials

Naproxen, *NPX*, was purchased, in both its racemic, *rsNPX* (>98%) and enantiopure S-naproxen, *sNPX* (>99%) form, purchased from Tokyo Chemical Industry Ltd (TCI). The co-formers 2-aminopyridine, *2AP* (>99%), 2-amino-4,6-dimethylpyrimidine, *2ADMP* (95%), acridine, *A* (97%), imidazole, *I* (99.5%) and benzimidazole, *BI* (98%) were obtained from Sigma-Aldrich Chemie GmbH, whilst 2-aminopyrimidine, *2AMP* (97%), 2-amino-3-chloropyridine, *2A3CP* (98%), 2-amino-4-chloropyridine, *2A4CP* (99%), 2-amino-5-chloropyridine, *2A5CP* (98%) and 2-amino-6-chloropyridine, *2A6CP* (98%) were purchased from Fluorochem Ltd, UK. Laboratory grade (>99.8%)) solvents, including acetone, acetonitrile, chloroform, diethyl ether, ethanol, hexane, isopropanol, methanol and toluene were provided by VWR Ltd. Deionised water was obtained from an on-site water purification source.

5.1.2 Co-former selection

Co-formers were selected based upon on an initial assessment of key interactions derived from previously studied multi-component materials incorporating either homo or heterochiral *NPX*. Searches of the CCDC Cambridge Structural Database (CSD), using ConQuest version 1.22 © 2018 CCDC software[194], were conducted for both protonated and deprotonated forms of *NPX*, to account for both co-crystal and salt forms. Single crystal diffraction data was selected only, with the *NPX* derivatives and organometallic structures being excluded from the search.

For comparison purposes, the PXRD patterns for both the racemic and enantiopure API, as well as for each of the different co-formers, were taken from literature, accessed through the CSD. These patterns were generated based on published single crystal structures.

5.1.3 Multi-component material screening

5.1.3.1 Mechanochemical screening

Initial multi-component material screenings were conducted through mechanochemical means, either neat or with application of minimum solvent, typically ethanol. *sNPX* or *rsNPX*, (25 mg, 0.11 mmol) were combined in either 2:1, 1:1 or 1:2 molar quantities with the given co-former and ground using a mortar and pestle for up to 10 minutes. Liquid-assisted grindings were carried out using the same procedure, but upon combining the materials, 3-4 drops of the desired solvent were added and the sample was ground until the solvent was deemed to have completely evaporated. Each sample was typically analysed using PXRD and DSC.

5.1.3.2 Combined evaporative and (crash) cooling crystallisation screening

Small-scale cooling crystallisations were setup to encourage single crystal growth for SCXRD analysis, as well as for comparison against the samples prepared through mechanochemical means. As determined from turbidity measurements, solutions of *sNPX* (0.09g, 0.39 mmol) or *rsNPX* (0.057g, 0.25 mmol) in ethanol (1 g, 21.7 mmol), or *sNPX* (0.059g, 0.26 mmol) or *rsNPX* (0.039g, 0.17mmol) in isopropanol (1 g, 16.6 mmol) were prepared such that the solutions were saturated at 30ºC with respect to their given enantiomeric composition and solvent. Quantities of each co-former, respectively, were

then added to give solutions, so as to yield either 2:1, 1:1 or 1:2 molar compositions of API to co-former. The vials were then sealed and placed in a temperature controlled water bath, set at 45°C. Dissolution was encouraged through sonication and upon completion, the sealed vials were placed in a temperature controlled environment set at 4°C and allowed to cool. To aid in the growth of individual crystals, the solutions were not mixed. Each vial was monitored over the course of a few days to see whether crystallisation had occurred.

If no crystallisation was observed after one week for a given sample, the lid of the vial was punctured several times so as to allow for slow evaporation of the solvent and encourage crystallisation. Several samples were also prepared using acetonitrile as the solvent. The same procedure was used as above, but owing to the unquantified solubility of *rsNPX* or *sNPX* in this solvent, the same quantities of homo and heterochiral API were used as for ethanol. In specific cases where phases prepared via mechanochemistry could not be directly reproduced through solution crystallisation, saturated solutions, cooled to 4°C, were seeded with minimal quantities of mechanochemically prepared material.

Upon crystallisation, images were taken under a microscope and individual crystals were picked out of solution and mounted onto a goniometer head for SCXRD screening and complete structure analysis.

5.1.3.3 Binary phase diagrams

Using either *NPX* starting material or *NPX* in combination with a co-former, so as to yield a multi-component material with a given stoichiometry, further mechanochemical samples were prepared with varying enantiomeric compositions of *NPX*. Combinations of *sNPX* and *rsNPX* (total *NPX* mass: 25 mg, 0.11 mmol) were combined, with or without co-former, so as to yield samples that represented 0.5, 0.6, 0.7, 0.8, 0.9 and 1.0 mole fractions of *sNPX* to *rNPX*. Excess of only one enantiomeric form of *NPX* was used due to the excessive cost of the *rNPX* and the assumption that one side of the binary phase diagram would mirror the other. Samples were then ground for up to 10 minutes, either neat or with the addition of 3-4 drops of a selected solvent, typically ethanol. Each sample was subsequently analysed using PXRD, to confirm the different composition of phases, and DSC, taking onset and peak temperatures for each enantiomeric composition, so as to construct a binary (melting point) phase diagram. For each diagram, lines are added as a guide.

5.1.4 Further crystallisation studies

5.1.4.1 Bulk solvent-mediated (slurrying) preparation

In order to collect solubility measurements, build a ternary phase diagram and conduct further cooling crystallisation experiments on the racemic and enantiopure salt form of *NPX* with *2AP*, bulk preparations of sample were made. Solvent-mediated preparation, or slurrying, was used as a quick and efficient way of achieving this.

Prior to bulk preparations, the necessary solvent environment for slurrying was screened. *sNPX* and *rsNPX* (0.15 g, 0.65 mmol) were weighed into vials, respectively, along with *2AP* in a 1:1 molar ratio, to which minimum quantities of solvent were added, so as to generate a suspension of solid and avoid complete dissolution. The solvents used were ethanol, isopropanol and hexane. The suspensions were sealed and then mixed using a magnetic stirrer bar for 1 hour at 200 rpm.

Subsequent bulk preparations of both the homo and heterochiral salt were prepared exclusively with hexane. *sNPX* and *rsNPX* (2 g, 8.69 mmol) were weighed into a 25 mL round bottomed flask (RBF), respectively, along with *2AP* in a 1:1 molar ratio. Suspensions were generated with the addition of hexane (20 g, 0.23 mol) and mixed using a magnetic stirrer bar for 1 hour at 200 rpm.

All preparations were done at room temperature (approximately 20°C) on a standard benchtop mixer-heater plate in a laboratory fume cupboard. After mixing, the suspensions were filtered using a Buchner funnel and filter paper under vacuum, and allowed to dry for up to 12 hours. The solids yielded were analysed using PXRD and DSC to confirm their phase.

5.1.4.2 Ternary phase diagrams

Ternary (solution) phase diagrams were constructed to assess the impact of varying enantiomeric compositions on material solubility. Solubility measurements were taken based on gravimetric analysis. Initial sample preparations of single component *NPX* were made by combining *sNPX* and *rsNPX* (total *NPX* mass: 0.6 g, 2.61 mmol) starting material, so as to generate samples of mole fractions 0.5, 0.6, 0.7, 0.75, 0.8, 0.85, 0.9, 0.95 and 1.0, corresponding to an excess of *sNPX*. These materials were suspended in ethanol (5 g, 1 mol) at either 20°C or 30°C for up to 3 days, mixed at 200 rpm using a magnetic stirrer bar. Using 1 mL syringes fitted with a suitable filter, to avoid excess solid being taken up, aliquots of liquor were taken from each suspension and deposited into individual pre-weighed vials. The combined mass of the vial and liquor was recorded and the solutions were allowed to evaporate to dryness at the same temperature at which they were slurried. The solubility for a given enantiomeric composition of *NPX* was determined upon comparison of the mass of dried solid and that of solvent evaporated.

The same gravimetric procedure was also used for establishing the solubility of material at given compositions of the racemic and enantiopure salt of *NPX* and *2AP*. Here, material was taken from bulk slurrying (see Section 5.1.4.1) and different combinations of homo and heterochiral salt were combined to generate mixtures with mole fractions corresponding to 0.5, 0.6, 0.7, 0.75, 0.8, 0.85, 0.9, 0.95 and 1.0, with respect to excess *sNPX*. For suspensions to be conducted at 20°C, the total mass of salt used exceeded 0.7 g (2.15 mmol) in 6 g (0.13 mol) of ethanol, whereas for preparations at 30°C, up to 1.3 g (4 mmol) of salt was suspended in 5 g (1 mol) of ethanol. In addition, the solid of the salt materials was also subjected to PXRD analysis.

All slurrying was conducted on the Polar Bear Plus platform from Cambridge Reactor Design™ (Figure 5.1). The platform operates through a thermoelectric Peltier with a working temperature range of -40°C to 150°C, allowing for the controlled heating and cooling of samples at a desired rate, from sample volumes of 1.5mL to 250mL. Samples can be also stirred through magnetic stirring capabilities. In order to build the above ternary diagrams, the Polar Bear Plus was used to maintain constant temperatures at 20°C and 30°C.

Figure 5. 1 - The Polar Bear Plus crystallisation platform from Cambridge Reactor Design™ (CRD)

5.1.4.3 Cooling crystallisations

Cooling crystallisations were carried out to, first, demonstrate the reproducible formation of the racemic and enantiomerically pure *NPX* and *2AP* salt forms from solutions of ethanol and, secondly, to probe different areas of the ternary phase diagrams, highlighting any interesting properties found.

All crystallisation experiments were based upon solubilities derived from turbidity measurements. Initial cooling crystallisations were conducted at enantiomerically pure and racemic compositions, utilising bulk material made via slurrying (see Section 5.1.4.1). So as to saturate solutions at 30ºC quantities of homochiral (0.13 g, 0.4 mmol) and heterochiral (0.12 g, 0.37 mmol) salt were weighed out into vials, respectively, to which ethanol (1 g, 0.022 mol) was then added. These initial suspensions were then heated to 45ºC and held for 30 minutes, whilst being mixed using magnetic stirrer bars at 150 rpm. Once all the solid was deemed to have completely dissolved, the solutions were then cooled to 5ºC, at a rate of either 1ºC/minute or 0.1ºC/minute. Upon reaching the end temperature, the samples were quickly taken off and filtered using a standard Buchner setup.

Further cooling crystallisations were also conducted at given enantiomeric compositions to gauge the initial thermodynamic and kinetic stability of the homo and heterochiral phases. Using the saturation of the enantiopure salt form at 30ºC (0.13 g, 0.4 mmol) in ethanol (1 g, 0.022 mol) as a guide, bulk preparations of the two *NPX* and *2AP* phases were combined to yield solid mixtures that represented 0.7, 0.75 and 0.8 mole fractions, with respect to *sNPX*. These mixtures were then dissolved in the appropriate amount of solvent and heated to 45ºC at a given mixing rate (200 rpm). Upon complete dissolution, the samples were subjected to linear cooling regimes, at rates of either 1ºC/minute or 0.1ºC/minute, ending at either 10ºC, 5ºC or 0ºC. Samples were immediately filtered upon reaching their end cooling temperature.

All crystallisations were performed on the Polar Bear Plus platform (detailed in Section 5.1.4.2), with every sample being assessed in terms of the solid phases present, using PXRD.

5.2 Selective preparation and crystallisation of stoichiometric co-crystals of oxalic acid and urea, driving towards continuous crystallisation

5.2.1 Starting materials

Oxalic acid, *OA* (98%) and urea, *U* (Bioreagent) were both purchased from Sigma-Aldrich Chemie GmbH. Oxalic acid dihydrate, *OAD*, was prepared by slurrying *OA* in deionised water for an hour. *OA* was stored under with a desiccant in order to minimise the conversion to *OAD* under atmospheric conditions. Laboratory grade (>99.8%)) solvents, including ethanol, isopropanol and methanol were provided by VWR Ltd. Deionised water was obtained from an on-site water purification source.

For comparison purposes, the PXRD patterns for the starting materials (*OA* (α)[181], *OA* (β)[181], *OAD*[183] and *U* Form I[185]), as well as that of the co-crystals of oxalic acid and urea[189, 190], were taken from literature, accessed through the CSD. These patterns were generated based on published single crystal structures.

5.2.2 Mechanochemical preparations

Mechanochemistry was used as a minimal solvent or solvent free method of producing the two co-crystals of *OA* and *U*. For all mechanochemical experiments conducted, the two starting materials were mixed in either 2:1, 1:1 or 1:2 molar stoichiometries. *OA* (25 mg, 0.27 mmol) was combined with U in each of these ratios and ground, initially, for 10 minutes using a mortar and pestle, either without solvent (neat) or with the assistance of a 3-4 drops of a given solvent (water, methanol, ethanol or isopropanol). If the solvent was not deemed to have evaporated fully, grinding was allowed to continue.

Subsequent neat grindings, utilising the same stoichiometries, were carried out over a series of time periods (2, 5, 10, 20 and 30 minutes), with either anhydrous OA or OAD (25 mg, 0.02 mmol), so as to gauge the effects of water and extended grinding on the co-crystallisation process. In addition, further liquid-assisted grindings were carried out with varying quantities of water (0, 20, 40, 60, 80, 100, 120 and 140 μL), with samples being ground until all the solvent appeared to have evaporated.

Mechanochemistry was also used as a means of assessing the interconversion between the two co-crystal forms of *OA* and *U*. Initial preparations with the two starting materials were prepared, using the same molar masses as above, so as to reflect the stoichiometry exhibited within the crystalline structures, i.e. either a 1:1 or 1:2 ratio. These samples were then ground either neat or with the same solvents as before (water, methanol, ethanol or isopropanol) for 10 minutes. After this, the stoichiometry of the samples was changed through the introduction of excess starting material, with additional *U* being added to the 1:1 combination and *OA* to the 1:2 preparation. Once added, the samples were ground for a further 10 minutes using the same solvent environments, respectively.

For each sample prepared via mechanochemical means, phase analysis was conducted using PXRD.

5.2.3 Solvent-mediated (slurrying) preparations

Initial suspensions of *OA* and *U* were prepared by combining the starting materials in given stoichiometries in different solvent environments. *OA* (0.5 g, 5.55 mmol) was mixed with U in the corresponding 2:1, 1:1 and 1:2 molar quantities, and subsequently suspended in up to 7mL of solvent, either water, methanol, ethanol or isopropanol. The solvent-mediated preparations were then mixed using the Polar Bear Plus platform at 20°C at 200 rpm for 24 hours. The solid material was then filtered off using the standard Buchner funnel setup and analysed using PXRD.

Using the same setup, bulk preparations of the oxalic acid:urea (1:2) co-crystal (*OAU*-1:2) were subsequently prepared via slurrying. *OA* (1 g, 11.11 mmol) was mixed with *U* in a 1:2 stoichiometry and suspended in up to 10 mL of water for up to 1 hour, mixing at 200 rpm at 20°C. After filtration, the material yielded from this preparation was used to determine the solubility of this co-crystalline phase using the turbidity method.

Slurrying was also used to explore the different regions of the ternary phase diagram at 20°C, assessing its potential for the precipitation of the co-crystalline phases. Based upon the solubility of the *OAU*-1:2 co-crystal at 30°C in water (0.063 g/g, 5.4 mmol/mol), suspensions were prepared at different stoichiometries of *OA* and *U* (5:1, 4:1, 3:1, 2:1, 1:1 & 1:2), utilising the same overall mass as for the 1:2 case. The solid mass for 30°C was utilised as a reference so as to ensure the consistent establishment of a stable slurry. Furthermore, this reference mass was also used as a means to explore the effect of solid loading for the different stoichiometric compositions. As such, various solid loadings, corresponding to x2, x3, x4 and x5 that of the original masses, were prepared. The masses of *OA* utilised for the given molar ratios of starting materials, at the different solid loadings, are expressed in Table 5.1. Upon combining the given amounts of *OA* and *U*, water (10 g, 0.56 mol) was added and the suspensions were mixed at 200 rpm for either 1, 4, 16 or 64 hours, after which the samples were filtered and analysed using PXRD.

Table 5. 1 - Masses of *OA* (g) used in slurrying experiments with different stoichiometric (5:1, 4:1, 3:1, 2:1, 1:1 and 1:2) solutions of *OA* and *U* in water (10 g), highlighting increasing solid loading levels (x2, x3, x4 & x5 the saturation of the oxalic acid:urea (1:2) co-crystal at 30°C)

Suspension stoichiometry (*OA* to *U*)	**Solid loading** ***w.r.t. the solid mass of the oxalic acid:urea (1:2) co-crystal at 30°C*** **(*OA* g)**				
	x1	**x2**	**x3**	**x4**	**x5**
1:2	0.2699	0.5398	0.8097	1.0796	1.2145
1:1	0.3779	0.7558	1.1337	1.5116	1.7005
2:1	0.4724	0.9448	1.4173	1.8897	2.1259
3:1	0.5154	1.0308	1.5462	2.0616	2.3193
4:1	0.5399	1.0799	1.6198	2.1598	2.4298
5:1	0.5558	1.1117	1.6675	2.2234	2.7792

5.2.4 Evaporative crystallisations

Initial evaporative crystallisations were conducted either from aqueous solutions or from those of alcohols, specifically methanol, ethanol and isopropanol. *OA* (0.03 g, 0.33 mmol) was weighed out with the appropriate quantity of *U*, so as to generate solid mixtures that represented the 2:1, 1:1 and 1:2 molar stoichiometries required. The individual solvents were added dropwise, so as to allow for dissolution with the minimum amount, with the samples then being sealed. The vials were then sonicated at 40°C to ensure that all solid had dissolved and were then placed in temperature controlled environments to reflect evaporation at either 20°C or 40°C. The lids of the vials were partially exposed to the surroundings and allowed to evaporate to dryness.

Further evaporative samples were prepared at given stoichiometries of *OA* to *U* and evaporated at a variety of different temperatures. Fixed quantities of *OA* (0.03 g, 0.33 mmol) were weighed out and combined with *U* in molar masses equating to the necessary 7:1, 6:1, 5:1, 4:1, 3:1, 2:1, 1:1 and 1:2 stoichiometries. These compositions were then dissolved in a minimum quantity of water (typically 1

g, 1 mL), sealed and sonicated at 40ºC to allow for complete dissolution. Each sample was then placed in a temperature controlled environment, at either 4ºC (fridge), room temperature (approximately 18ºC) or 40ºC (benchtop hot-plate), with the lid of each vial having been perforated in order to allow for evaporation. Subsequent samples were prepared through the same procedure, utilising only the 1:1 *OA* to *U* stoichiometry. Here, higher evaporation temperatures were used, including 60ºC, 80ºC, 100ºC, 120ºC and 140ºC. For each sample yielded from evaporation, images of the crystals were taken under the microscope and analysed for the solid phases present using PXRD.

5.2.5 Batch cooling crystallisations

Cooling crystallisations were initially carried out in a batch setup, where each experiment was conducted using the Polar Bear Plus platform from Cambridge Reactor Design™. The capabilities of this setup are detailed in Section 5.1.4.2. All crystalline materials yielded were analysed using PXRD.

5.2.5.1 Cooling crystallisations from isopropanol

Prior to conducting cooling crystallisations, the saturation of *OA* starting material in isopropanol at 20ºC was established by gravimetric means. Suspensions of *OA* were prepared by mixing excess material in isopropanol at 20ºC for 24 hours. From here, approximately 1g of the solution liquor was extracted, weighed and allowed to evaporate. The mass of the resultant solid was compared against that of the solvent dissipated off, providing a value for the quantity of solute dissolved in this solvent environment. This process was repeated three times, providing an average solubility of *OA* in isopropanol, that of 0.22 g/g (0.15 mol/mol).

Given this value, cooling crystallisations were conducted using a range of *OA* to *U* solution stoichiometries. Initial solutions of *OA* were prepared by mixing this starting component (2.2 g, 0.024 mol) in isopropanol (10 g, 0.16 mol) with molar quantities of *U*, so as to create solution stoichiometries reflecting 4:1, 3:1, 2:1, 1:1 and 1:2 of *OA* to *U*. The subsequent mixtures were then heated to 65ºC, to ensure complete dissolution, and cooled to 20ºC. Each preparation was cooled and mixed at rates of 0.1ºC/minute and 200 rpm, respectively. Further crystallisations were then conducted using the same stoichiometries and crystallisation parameters, but with different degrees of saturation. These saturations represented x0.5, x0.25, x0.125 and x0.0625 the amount of *OA* used originally. The solid generated were filtered under a vacuum and allowed to dry.

5.2.5.2 Cooling crystallisation of the oxalic acid:urea (1:2) co-crystal from water

Based upon the solubility of the *OAU*-1:2 co-crystal in water at 30ºC (0.063 g/g, 5.4 mmol/mol), initial cooling crystallisations were prepared, whereby *OA* (0.053 g, 0.59 mmol) was combined with *U* in a 1:2 molar ratio with water (2 g, 0.11 mol). Four preparations were made, with each being heated to 45ºC and mixed at 200 rpm, using a magnetic stirrer bar, for 30 minutes to ensure complete dissolution. The samples were then cooled to either 25ºC or 20ºC, using cooling rates of 0.1ºC/minute or 1ºC/minute, respectively.

Subsequent crystallisations were also established at various scales. Utilising the same saturation levels as before, further solutions were setup using 10 g, 30 g or 100 g of solvent (water), from which the samples were heated to 45ºC and held for 1 hour, mixed at 200 rpm. The solutions were then cooled to 20ºC at a rate of 1ºC/minute, maintaining the same degree of mixing. For each of the cooling crystallisation processes described, the solid material yielded was filtered using standard Buchner filtration apparatus and subsequently allowed to dry.

5.2.5.3 Cooling crystallisation of the oxalic acid:urea (1:1) co-crystal from water

Further cooling crystallisations were conducted so as to devise a route to the selective preparation of the *OAU*-1:1 co-crystal. As for the exploratory suspension experiments in water, the total mass of solid required to saturate aqueous solutions with respect to the (1:2) co-crystal at 30ºC was exploited as a reference from which preparations of increasing saturation (x2.5, x3 and x3.5) for a given stoichiometry could be established. As dictated by the masses outlined in Table 5.2, *OA* was weighed out and combined with molar ratios of *U*, establishing the 5:1, 4:1, 3:1 or 2:1 stoichiometries. Water (10 g, 0.56 mol) was added and the suspensions were heated to 75ºC and held for 30 minutes to ensure complete dissolution. The solutions were then cooled at either 0.1ºC/minute or 1ºC/minute to 20ºC, with the resultant solid material being filtered off, dried and analysed.

Table 5. 2 - Masses of *OA* (g) used in cooling experiments with different stoichiometric (5:1, 4:1, 3:1 and 2:1) solutions of *OA* and *U* in water (10 g), highlighting increasing saturation levels (x2.5, x3 & x3.5 the saturation of the oxalic acid:urea (1:2) co-crystal at 30ºC)

Solution stoichiometry (*OA* to *U*)	**Saturation level *w.r.t. the saturation of the oxalic acid:urea (1:2) co-crystal at 30ºC* (*OA* g)**			
	x1	**x2.5**	**x3**	**x3.5**
2:1	0.4724	1.1811	1.4173	1.6535
3:1	0.5154	1.2885	1.5462	1.8039
4:1	0.5399	1.3499	1.6198	1.8898
5:1	0.5558	1.3896	1.6675	1.9454

Using the same procedure, additional cooling crystallisations were set up, cooling from 75ºC to 30ºC at a rate of 0.1ºC/minute. The solid yielded was immediately filtered, dried and analysed. This procedure was conducted through five iterations. For each experiment, a constant mixing rate of 200 rpm was used.

5.2.6 Continuous cooling crystallisations

Following on from its reliable precipitation from batch cooling environments, the OAU-1:2 co-crystal was selected to assess the capabilities of the continuous cooling crystallisation platforms based at the University of Bath. These included the Continuous Oscillatory Baffled Crystalliser (COBC) and the Kinetically Regulated Automated Input Crystalliser (KRAIC), exploiting baffled and segmented flow mixing, respectively. The principles for the operation of both these setups can be found in Chapter 1.

5.2.6.1 Continuous oscillatory baffled crystalliser (COBC)

Initial continuous crystallisation experiments were conducted using the COBC. The setup consisted of 12 individual jacketed tubes and five non-jacketed bends, each with an internal orifice diameter of 15 mm. These units were constructed into six straights (numbered 1-6), orientated in a vertical geometry, and were fed from a feed vessel using a PTFE tube. The jacket temperature were controlled through four Grant R3 TX150 heater/chillers, setting the temperatures for straights 1, 2/3, 4/5 and 6 respectively, with water used as the heating medium. Thermocouples were used to monitor the temperature of each straight during each crystallisation run.

For all experiments, the movement of solution throughout the system was modulated through combined pumping via a Watson Marlow peristaltic pump and an oscillating set of bellows. The pump was set at a standard rate of 4.1 rpm, whilst a frequency and amplitude of 2 Hz and 25 mm for oscillation were

employed, respectively, resulting in an overall flow rate of approximately 50 mL/minute. The residence time of solution within the crystalliser, including that of the feed pipe, was estimated to be 35 minutes. The pressure for the system was maintained at 1.5 bar, with any deviations away from this forcing a stop to any on-going experiment.

Prior to each run, the platform was filled with water so as to maintain a homogenous environment and to ensure no air bubbles were present, thus minimising heterogeneous nucleation with surfaces other than that of the crystalliser internal walls. Feed solutions were prepared at the 5 L scale, whereby the solutions were saturated at either 30°C (0.063 g/g, 5.4 mmol/mol) or 35°C (0.078 g/g, 6.7 mmol/mol) with respect to the *OAU*-1:2 co-crystal in water. The solutions were prepared in a round bottomed flask of appropriate volume and heated to 60°C. The suspension was mixed at 200 rpm with a magnetic stirrer bar, with the solid being allowed to completely dissolve. Once ready, the solution was then fed into the body of the crystalliser, using the peristatic pump, through a feed tube. From there, the solution was pumped through the straights, gradually being cooled depending upon the cooling regime used, and mixed via oscillation through the baffles. A total of five runs were carried out, each using a different stepped cooling profile of the straights and different solution saturations. These parameters are highlighted in Table 5.3.

Table 5. 3 - Solution saturations, with respect to the solubility of the oxalic acid:urea (1:2) co-crystal at 30°C in water, and straight temperatures used for the five COBC runs for the crystallisation of the oxalic acid:urea (1:2) co-crystal

Run	**OAU-1:2 saturation temperature (°C)**	**Straight temperature (°C)**					
		1	**2**	**3**	**4**	**5**	**6**
1	*30*	50	40	40	30	30	20
2	*30*	50	40	40	25	25	20
3	*30*	50	30	30	25	25	20
4	*30*	50	20	20	20	20	20
5	*35*	50	20	20	20	20	20

The resultant crystalline materials were collected through an end piece of PTFE tubing and filtered from solution via a standard Buchner funnel setup. For each residence time or for any solid yielded, phase analysis was conducted using PXRD. Further to this, each run was monitored, observing the location of nucleation within the crystalliser, as well as that of any encrustation on its internal surface.

5.2.6.2 Kinetically regulated automated input crystalliser (KRAIC)

Based upon the outcomes from the COBC experiments, a further continuous crystallisation run was carried out using the KRAIC. This platform operated through the mixing of three distinct components through a purpose designed cross piece, so as to generate the necessary segmentation in flow; a heated feed solution, an immiscible carrier fluid and air. For the experiment conducted here, the carrier fluid used was that of the liquid polymer, perfluoropolyether Galden SV110.

The feed solution was prepared by saturating a given volume of water (1 L, 55.5 mol) with OA and U in a 1:2 combination, reflecting a solution saturation at 35°C with respect to the (1:2) co-crystalline form. After being heated to 40°C and mixed at 200 rpm to allow for complete dissolution, the hot feed solution was fed through a heated PTFE tube (40°C) to the mixing piece at a rate of 3 mL/minute. Air and carrier fluid were also fed to the cross piece, at rates of 4.2 mL/minute and 2.1 mL/minute, respectively. The characteristic segmentation for this system was generated upon the mixing of these three immiscible phases, which were subsequently fed into the body of the crystalliser at a collective rate of 9.3 mL/minute. The individual slugs were able to flow through 15 m of FEP tubing, with an

internal diameter of 3.2 mm, allowing for the solution to cool from 40°C to room temperature (approximately 20°C) over a residence time of 17 minutes. Upon reaching the end of the tubing, the individual segment components were separated and any solid yielded was analysed using PXRD.

5.3 Material and solution analysis

5.3.1 Microscopy

Micro-crystalline material, single crystals or otherwise were visualised using an optical microscope from Brunel Microscopes Ltd, complete with a camera accessory for capturing observations.

5.3.2 Single crystal X-ray diffraction (SCXRD)

Upon the growth of suitable individual crystals, SCXRD analysis was conducted to determine the crystal structure for a given sample. All analysis of this nature was conducted either using the Rigaku Oxford Diffraction SuperNova™ or Xcalibur™ diffractometers. Each instrument consists of an X-ray radiation source, area detector, Cryostream, goniometer and head, and an observation camera (Figure 5.2). Whilst the SuperNova possesses a dual X-ray radiation source, for both Copper (Cu-K_α 1.54056 Å) and Molybdenum (Mo-K_α 0.71073 Å) radiation, with micro-focussed beam for higher intensity X-ray radiation, the Xcalibur only utilises Molybdenum sourced radiation. Both setups are equipped with a graphite monochromator and an Eos S2 Smart Sensitivity area detector, as well as a four-circle kappa goniometer. This allows for movement through four different rotation circles (φ, ω, χ, 2θ), allowing for all diffraction angles to be captured, generating a complete data set. Temperature regulation is achieved by Oxford Cryosystems 700 series Cryostreams, allowing for low and high temperature data collections. All samples were placed under the nitrogen Cryostream, cooled to 150K and maintained for data collection.

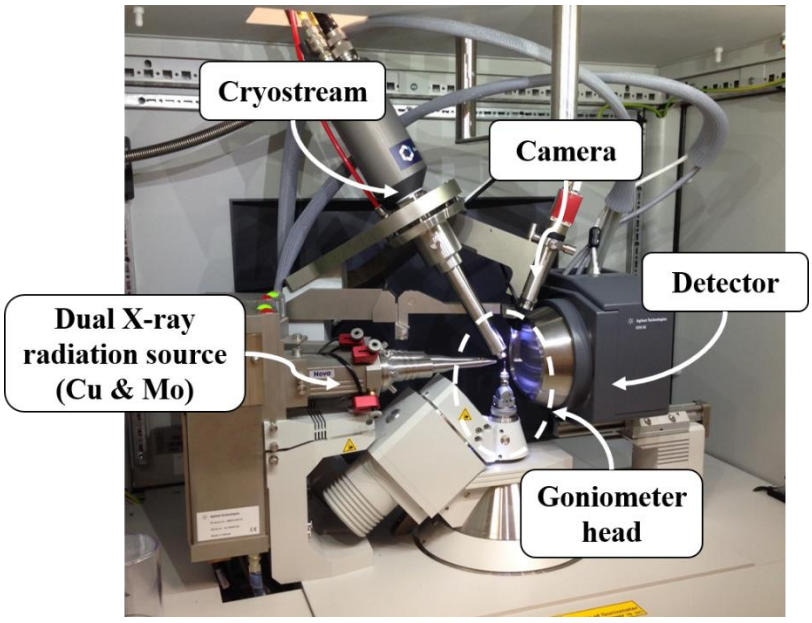

Figure 5. 2 - The Rigaku Oxford Diffraction SuperNova, highlighting X-ray sources, Cryostream, camera, area detector and goniometer head

Individual crystals were mounted on the goniometer. Data were collected and processed using CrysAlisPro version 171.38.43 © 2014 Rigaku Oxford Diffraction software, allowing for data reduction and verification of the space group. Olex2 version 1.2 © 2004-2018 OlexSys Ltd software[195] was used

to solve and refine each structure, utilising either Direct Methods in ShelXS[196] or Dual Space in ShelXT[138] for structure solution and Least Squares minimisation in ShelXL[197] for structure refinement. All non-hydrogen atoms were located and refined with anisotropic thermal parameters. Hydrogen atoms were placed in either calculated positions or located and refined with isotropic thermal parameters, depending upon their contribution to hydrogen bonding. The resultant structures were visualised and assessed using Mercury CSD version 3.10.2 © 2001-2018 CCDC software[194]. The CIF files for each of the materials discovered can be found on the accompanying CD-ROM, with the file titles detailed in Appendix 5.

Due to the importance of chirality to this research and the inherently weak diffraction properties of the materials in question, the Flack parameter[145] could not be solely relied upon for absolute configuration confirmation. Hence, chirality was ultimately confirmed with reference to the starting materials used in the preparation to the given materials.

5.3.3 Powder X-ray diffraction (PXRD)

All PXRD data was collected using the Bruker D8 Advance laboratory diffractometer (Figure 5.3) at the University of Bath. The instrument was equipped with monochromatic Cu-K_α radiation source (λ = 1.54056 Å) and a Vantec-1 detector, set-up for material analysis in the reflection geometry.

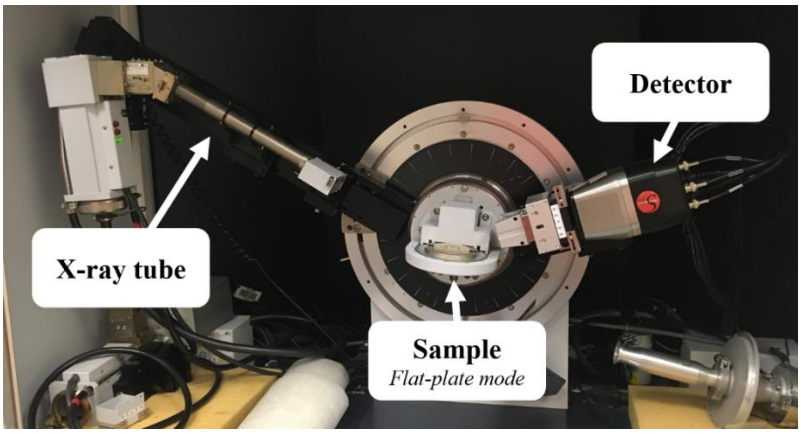

Figure 5. 3 - The Bruker D8 Advance diffractometer, highlighting the X-ray source, sample holder (in flat-plate mode) and the area detector

Typically, small quantities of the ground solid were placed onto a glass slide and pressed so as to produce an even surface. The slide was then mounted onto a flat-plate sample holder using a non-diffracting adhesive material and exposed to X-ray radiation. Samples were scanned through 2θ angles ranging from 5^o to 40^o in 0.01^o step sizes, with an exposure time of 0.3 seconds per step. The sample holder itself was rotated at 15 rpm to minimise the effects of preferred orientation. Experimental parameters were applied using the Bruker DIFFRACplus XRD Commander Version 2.6.1 © 2000 Bruker-AXS GmbH software. All analyses were conducted at room temperature. Patterns were plotted in terms of intensity, in arbitrary units (a.u.), and 2θ (^{o}). In each case, patterns are plotted with reference to those collected from the CSD or simulated from SCXRD for the relevant starting or comparative materials.

All mechanochemically prepared samples were analysed using PXRD, along with all materials obtained from the controlled cooling crystallisation experiments. In addition, selected samples obtained from the combined evaporative/cooling crystallisation screening method were also assessed using this technique.

Where necessary, the materials were ground using a mortar and pestle in order to achieve homogeneous crystalline samples.

5.3.4 Differential scanning calorimetry (DSC)

DSC analysis was carried out using a Thermal Advantage Q20 instrument from TA Instruments, set up with the Thermal Advantage Cooling System 90, operating under a dry nitrogen purge at a flow rate of 18 mL/min (Figure 5.4). Samples were weighed (2-4 mg) into Tzero aluminium pans, sealed and placed on a heating plinth, alongside an empty reference pan, after which, the materials in question were exposed to a heating/cooling regime. Typically, samples were heated at a rate of 10°C/minute, sweeping from 20°C up to 200-250°C, unless otherwise stated. Temperatures and ramp rates were calibrated against an Indium standard (melting point 156.6°C). Thermal traces were processed and analysed using the TA Advantage version 5.5.22 © 2001-2011 and TA Universal Analysis 2000 version 4.5A © 1998-2007 software (TA Instruments-Waters LLC), respectively, from which thermal onsets, end points and enthalpies were taken. For all DSC plots, downward and upward phenomena are taken as endothermic and exothermic events, respectively.

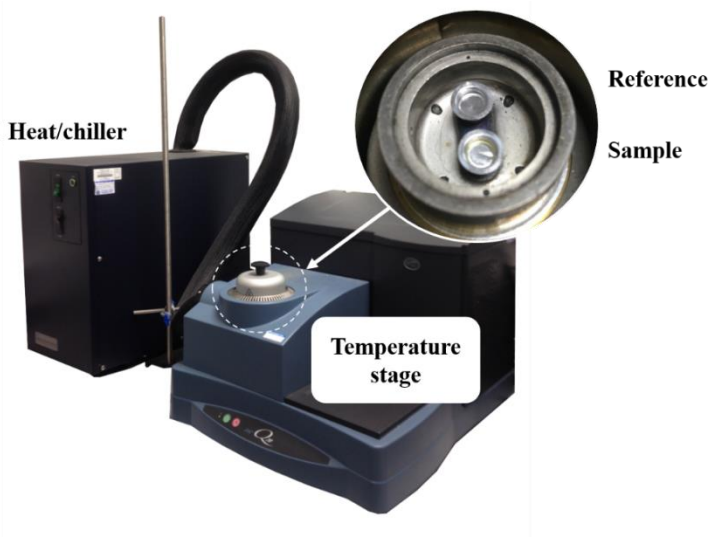

Figure 5. 4 - The Thermal Advantage Q20 DSC from TA, highlighting heating/cooling unit, temperature stage, sample and reference pan positions

All samples prepared via mechanochemical means, i.e. samples from screening or for binary phase diagram analysis, were analysed using DSC. Single crystals derived from crash cooling were also assessed so as to confirm the melting point for a given crystalline material. Samples taken from slurrying and controlled cooling crystallisation processes were also analysed by DSC.

5.3.5 Hot-stage microscopy (HSM)

HSM was used to corroborate and visualise thermal phenomena initially observed in DSC. HSM was carried out with the Mettler Toledo FP82 hot-stage equipped a Leica DM1000 microscope. Crystalline samples, individual crystals or polycrystalline, were mounted onto glass slides, subjected to similar temperature regimes used during DSC analysis, as controlled by the FP90 Central Processor and filmed using a Lumenera Infinity 2 microscopy camera. Media data was processed using Studio Capture software version 4.0.1. © 2001-2010 Studio86Designs.

Typically, individual crystals taken from the samples prepared by the combined evaporative and cooling method were analysed using HSM and, where possible, compared to the DSC traces taken for comparable mechanochemical samples.

5.3.6 Infrared spectroscopy (IR)

The assessment of key bonds and intermolecular interactions was conducted through infrared spectroscopy. Fourier transform infrared (FTIR) spectra of the mechanochemically prepared samples were collected using a Perkin Elmer FTIR Spectrometer at room temperature with an attenuated total reflectance (ATR) sampling accessory, scanning through a range from 4000 to 800 cm^{-1}. Spectroscopic data was collected and processed through Spectrum version 10.400.0190 © 2013 PerkinElmer Inc. software. This technique was used for the analysis of materials in the solid-state only, both polycrystalline and single crystal samples.

5.3.7 Circular dichroism (CD)

Ethanol solutions of *NPX* with given enantiomeric mole fractions, with respect to *sNPX* (0.5, 0.6, 0.7, 0.8, 0.9 and 1.0), and concentration (0.00075M, 0.0005M and 0.0001M) were analysed for their circular dichroism (CD) using the Chirascan™ Circular Dichroism Spectrometer from Applied Photophysics. The instrument utilises of a nitrogen-cooled 150 watt Xenon arc lamp coupled with a dual polarising, dual dispersing monochromator, as well as a photomultiplier detector. Samples were syringed into 1 cm path-length Quartz curvettes and placed into a single cell, Peltier controlled sample holder within the spectrometer. For each experiment, the samples were held at 20°C and scanned over a 250 to 380 nm wavelength range, with a step size of 1 nm and a bandwidth of 2 nm. The CD and UV-visible absorption was collected for each sample, from which the molar ellipticity could be calculated. Using these data, calibration plots could be generated so as to ascertain solution enantiomeric composition.

5.3.8 Turbidity measurements (Crystal16)

Dissolution and turbidity measurements were conducted for the starting materials and related multi-component materials in either water, ethanol or isopropanol using the Technobis Crystal16, based at the University of Strathclyde. The instrument consists of 16 parallel wells, each capable of holding 1 mL vials, and uses the percentage transmissivity of a laser beam through a solution to determine to clear (solubility) and cloud point (metastable limit) of a given solvent-solute system. Suspensions with given concentrations were prepared and were initially allowed to equilibrate at 0°C for 30 minutes. From here, each sample was subjected to three iterations of temperature cycling, noting the points of dissolution and crystallisation; heated from 0°C to 50°C, held for 30 minutes, cooled back to 0°C and held for another 30 minutes, each ramp conducted at 0.2°C/minute (Figure 5.5). Data were collected and analysed using Crystallization Systems version 1.8.1 © Technobis (formerly Avantium) software.

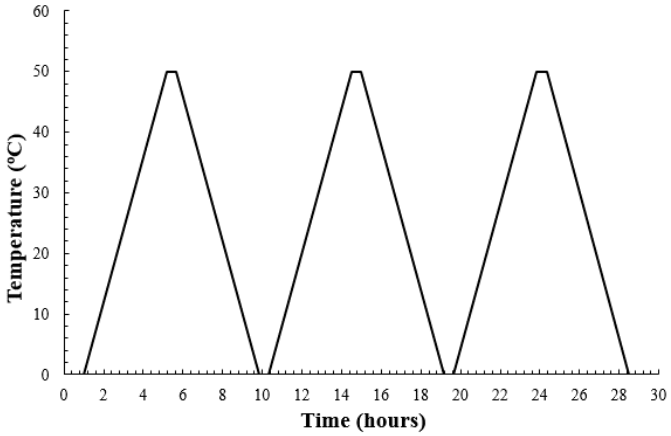

Figure 5. 5 - Temperature-time plot, highlighting the three temperature cycles conducted during Crystal16 turbidity measurements

6 Chiral multi-component materials of naproxen with 2-aminopyridine (*2AP*)

As discussed in Chapter 3, the non-steroidal anti-inflammatory drug naproxen (*NPX*) exhibits not only poor permeability properties, but solid state structures at racemic compositions that demonstrate little applicability to the direct resolution of the two chiral forms of the API from solution. In this chapter, the properties of *NPX* were assessed, in both the solid state and in solution. From here, the techniques used in multi-component material screening were used in the development of novel molecular complexes incorporating the achiral co-former, 2-aminopyridine (*2AP*). Furthermore, based upon the results of solution analysis, initial cooling crystallisations were designed, highlighting the formation of a metastable conglomerate material with direct implications for the separation of the different enantiomeric forms.

6.1 Characterisation of racemic and enantiopure naproxen (*NPX*)

In this section, the physical properties of *NPX*, both as a solid and when allowed to dissolve in a solvent (ethanol or isopropanol), were assessed. The information detailed below was used to make comparisons and to inform subsequent multi-component material experiments.

6.1.1 Solid state characterisation

As previously highlighted from the material literature review (Chapter 3), *NPX* can precipitate as different crystalline phases depending upon the composition of enantiomers present. Figure 6.1 highlights the crystal structures of homo (COYRUD[169]) and heterochiral (PAPTUX[150]) *NPX*, with the key unit cell parameters of each of these materials highlighted in Table 6.1.

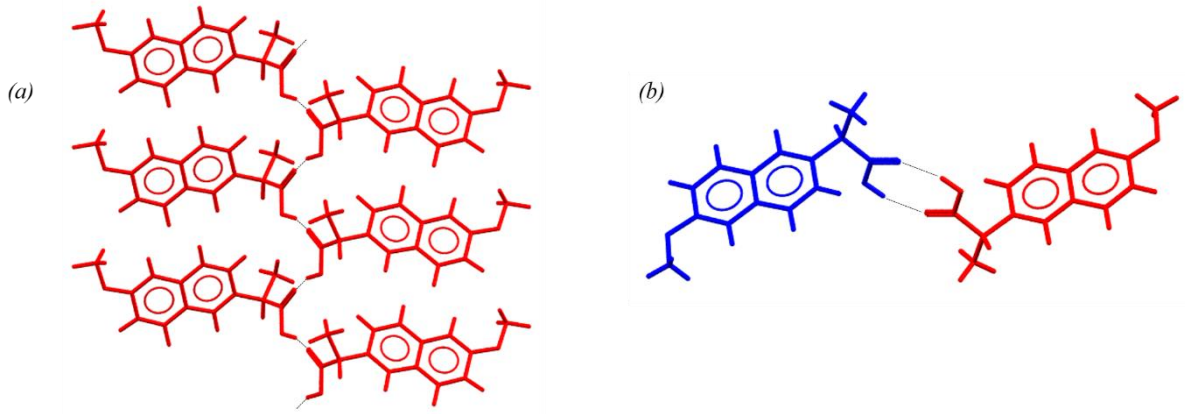

Figure 6. 1 - Crystal structures and key hydrogen bonding interactions of (a) *sNPX* and (b) *rsNPX* (*sNPX* in red, *rNPX* in blue)

Table 6. 1 - Unit cell and crystallographic parameters for *sNPX* and *rsNPX*

Material	a (Å)	b (Å)	c (Å)	α (º)	β (º)	γ (º)	Volume (Å^3)	Space group	Formula
S-naproxen[169]	7.7354(11)	5.7181(8)	13.3641(18)	90	93.737(2)	90	589.861	$P2_1$	$C_{14}H_{14}O_3$
RS-naproxen[150]	25.8301(13)	15.4939(4)	5.9465(2)	90	90	90	2379.84	*P*bca	$C_{14}H_{14}O_3$

Due to the fact that two distinct structures are generated upon transitioning from racemic to enantiopure contributions, the system of *NPX* can be described as that of a racemic compound. This means that two

discrete phases are yielded at racemic and enantiopure ratios, respectively, with the heterochiral form expressing a greater degree of stability in the solid state, shown from DSC analysis of the respective starting materials, as outlined in Table 6.2. The individual thermal traces are depicted in Appendix A6.1. The melting point of the racemic phase was shown to be higher, though only marginally, than that of the single enantiomeric case. This suggested that the interactions utilised, a combination of hydrogen bonding and π stacking contacts, were collectively stronger.

Table 6. 2 - Onset and peak temperatures for the melting of *sNPX* and *rsNPX*

Material	Melting onset (ºC)	Melting peak (ºC)
S-naproxen	155.1	156.6
RS-naproxen	156.2	157.6

Using this information and by exploiting mechanochemical preparation techniques, a binary (melting point) phase diagram was generated (Figure 6.2). Grinding was used as a simple method of preparing mixtures of the required enantiomeric composition (0.5, 0.6, 0.7, 0.8, 0.9 and 1.0 mole fractions with respect to *sNPX*), where minimal quantities of solvent were added to aid in homogenisation. Upon grinding for up to 10 minutes, the samples were analysed for their thermal properties, highlighting the presence of significant melting or eutectic phenomena. This phase diagram showed which of the two structures were stable, with respect to melting, when the composition of the enantiomers changed. As shown, the trajectory of the points at the liquid-solid equilibrium outlined distinct regions, highlighting that at compositions greater than the *sNPX* mole fraction 0.8 the homochiral material was the more stable phase, and from 0.5 to 0.8, the racemic phase was the most stable. Due to the inherent likeness of enantiomers, the melting point of the *rNPX* crystalline phase was assumed to be the same as that of *sNPX*, accounting for the symmetry observed within the phase diagram.

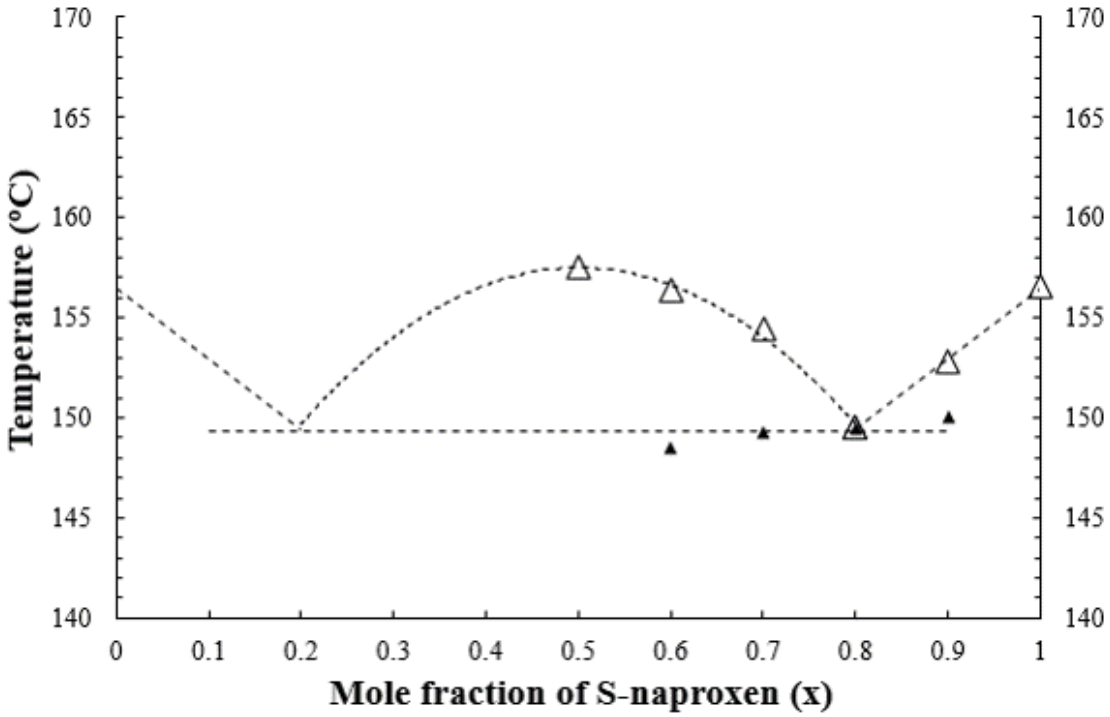

Figure 6. 2 - Binary (melting) point phase diagram, with changing enantiomeric composition of *rNPX* and *sNPX*, highlighting the liquidus (Δ) and the eutectic (▲) points

In addition to the liquidus line, the other key observation was that of the eutectic melt. Shown to take place between 147-150ºC, the eutectic point represents the point at which a number of phases (the

racemic solid, enantiopure solid and liquid) were in equilibrium. In this case, it was shown to reside at a *sNPX* mole fraction of 0.8. The location of this thermal event, in terms of enantiomeric contribution, could be used for comparison purposes when contrasting against the multi-component materials prepared in this Chapter and Chapters 7 and 8. By confirming the presence of the distinct regions of stability for the respective homo and heterochiral phases, and noting the presence of the eutectic point, the existence of a stable racemic compound forming system was confirmed for this API. The corresponding DSC and PXRD data for the different compositions can be found in Appendix A6.1.

6.1.2 Solution characterisation

As outlined above, in the solid state, this API was shown to form a racemic crystalline material at the corresponding composition of enantiomers. This phase had greater stability to that of the homochiral phase, which can be emphasised by their comparative melting points, but also from their individual solubilities in a given solvent environment. Figure 6.3 demonstrates the trends of the solubility of the two respective crystal forms in ethanol and isopropanol, with Table 6.3 showing the concentrations of materials dissolved at 20ºC and 30ºC for the given solvent systems. These initial measurements were collected using turbidity analysis, assessing the point of complete dissolution at concentrations of material ranging from 3-30 mmol/mol. Using the Technobis™ Crystal 16, samples with the pre-specified solid loadings were heated from 0ºC to 50ºC and monitored in terms of their transmissivity of a beam of light passing through the solution. At a given temperature, the solid was deemed to have completely dissolved when the transmission of light had reached 100%.

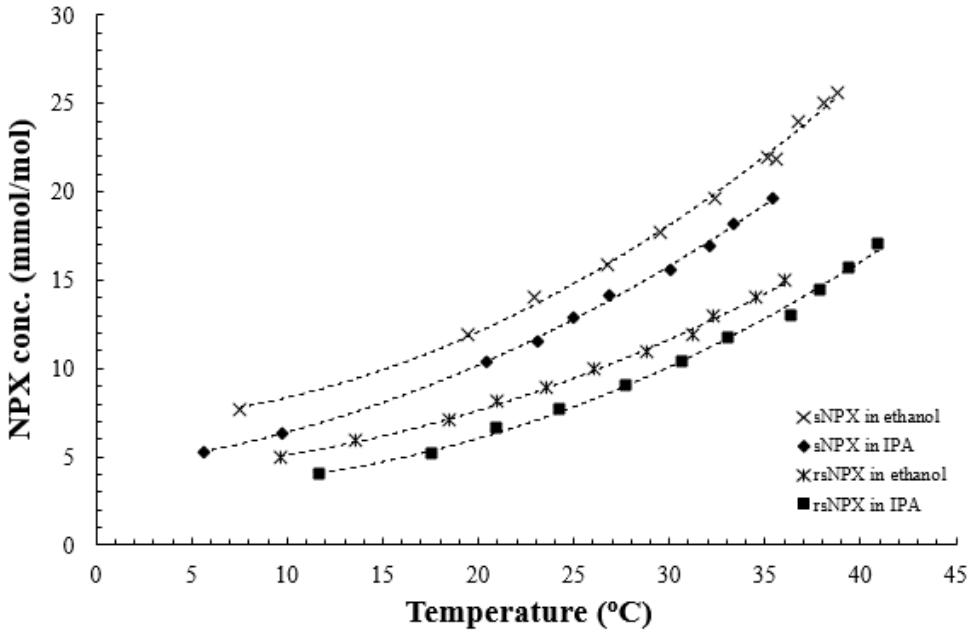

Figure 6. 3 - Solubility data of *sNPX* and *rsNPX* in ethanol and isopropanol, as determined from turbidity measurements (% standard error no greater than 1.5% across the range)

Table 6. 3 - Saturation points of *sNPX* and *rsNPX* in ethanol and isopropanol, respectively, at 20ºC and 30ºC

Material	Solvent	Saturation at 20ºC (*NPX* mmol/mol)	Saturation at 30ºC (*NPX* mmol/mol)
S-naproxen *(sNPX)*	Ethanol	12.1	18.1
	Isopropanol	10.2	15.8
RS-naproxen (*rsNPX*)	Ethanol	7.6	11.6
	Isopropanol	6.0	10.1

As is common in many small organic systems, the solubilities for the different materials of *NPX* were shown to increase with temperature. In each case, the solubility was shown to increase in excess of 1.5 times upon raising the temperature from 20ºC to 30ºC. Furthermore, as expected, the solubility of the racemic solid was shown to be consistently lower than that of the homochiral across the different solvent environments. This highlighted that there was an enhanced stabilisation effect of the enantiopure phase by solvation, corresponding to comparative stability of these phases in the solid state. Knowledge of the solubilities at these temperatures were later used as a guide from which to plan solution based crystallisations for the screening of novel multi-component materials.

Selecting ethanol as the solvent, the relative solubilities for different enantiomeric compositions at 20ºC and 30ºC could be determined. Based upon gravimetric analysis, the ternary (solubility) phase diagram, shown in Figure 6.4, was constructed. This two-axis representation of the ternary phase diagram could be directly related to that of the three-axis plot, with the contribution of solvent made relative to the respective enantiomers present. The individual saturation points for these two temperatures can be found in Appendix A6.1.

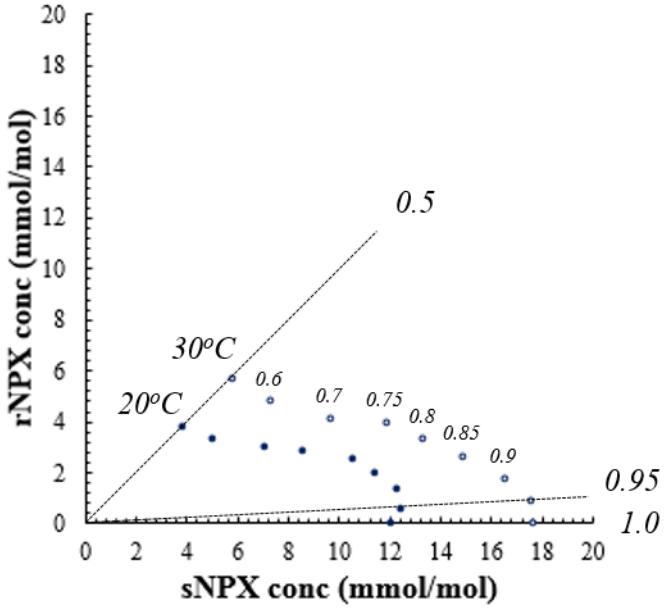

Figure 6. 4 - Ternary (solubility) phase diagram, corresponding to the saturation of different enantiomeric combinations of *NPX* (mole fractions of *sNPX* highlighted) in ethanol at 20ºC and 30ºC, respectively

The observations made from this analysis support the findings from that of the solid state, highlighting a clear change in solubility from racemic to enantiopure, with an inflection point, i.e. the eutectic point, discernible at *sNPX* mole fractions of 0.9-0.95 and 0.95 for the lower and higher temperature preparations, respectively. This emphasised the degree to which the racemic phase remained stable in solution with changing contributions of enantiomers. Given the large solubility difference between the racemic and enantiopure states, as well as the distinctive trend in solubility exhibited upon changing the chiral composition of the solutions, resolution of the two enantiomers was not deemed possible *via* crystallisation in its current crystalline form.

In addition to assessing the characteristics of *NPX*, various methods were explored that could account for the different contribution of enantiomers in solution. The method selected, with potential future applications into preferential crystallisation processes, was that of Circular Dichroism Spectroscopy. Prepared solutions of given compositions of the different chiralities of *NPX* (*sNPX* mole fractions of

1.0, 0.9, 0.8, 0.7, 0.6, 0.5 and 0.0) were analysed for their absorption behaviour with circularly polarised light. Samples of varying solution concentrations were assessed over a given wavelength range, from which the molar ellipticity could be calculated and correlated to the different enantiomeric compositions. The result was a calibration plot, as shown in Figure 6.5. The specific molar ellipticity versus wavelength spectra can be found in Appendix A6.1.

Given the correct dilution, this plot could be used confirm the combination of the two chiral forms of the API in solution. Circular dichroism was thus used to check the findings from the ternary phase diagram and formed the basis of an on-going collaboration for the use of CD in monitoring the crystallisation of chiral multi-component materials, between the Universities of Bath (Wilson group) and Strathclyde (ter Horst group).

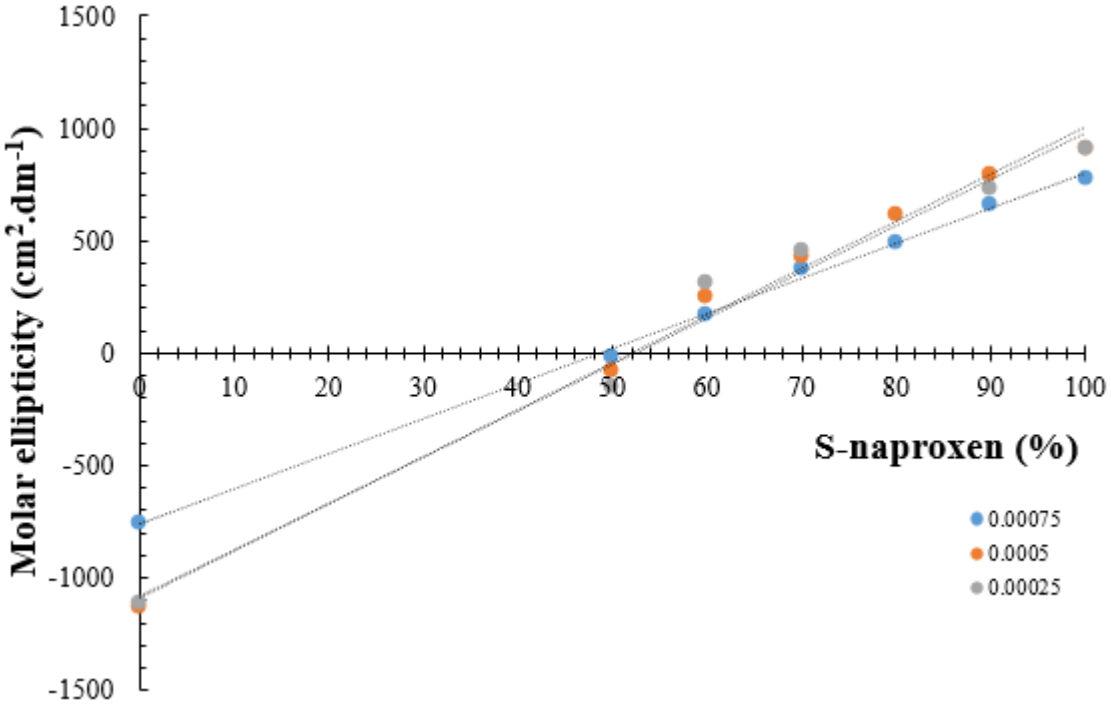

Figure 6. 5 - Calibration plot of molar ellipticity with changing enantiomeric composition of *NPX* in ethanol, at three different solution concentrations (0.75mM, 0.5mM and 0.25mM)

6.2 Material screening with racemic and enantiopure naproxen with 2-aminopyridine (*2AP*)

As emphasised above, *NPX* forms two distinct crystalline phases at the corresponding enantiopure and racemic compositions, resulting in a material unsuited to chiral resolution processes. To mitigate this, the API was combined with molar quantities of a variety of secondary molecular entities so as to screen for novel multi-component materials, i.e. co-crystals and salts. Screening was conducted using mechanochemical and solution crystallisation, assessing and comparing materials derived from homo and heterochiral preparations so as to determine the racemic crystalline nature of the material being studied.

6.2.1 Co-former selection

Prior to screening, the molecular structure of *NPX* was evaluated for the functional groups capable of forming key intermolecular interactions, such as hydrogen bonding. Whilst the methoxy group could act as a weak hydrogen bond acceptor, the most important supramolecular synthon was shown to be that of the carboxylic acid (COOH). This group has the capability of performing the role of an acceptor and a donor, through the C=O and O-H groups, respectively. Both of these were exploited differently in the homochiral and racemic crystal structure, with the former utilising individual $D_1^1(3)$ O-H···O contacts, forming extended chains, and the latter consisting of both the enantiomers dimerising together through a $R_2^2(8)$ interaction.

As shown from the literature review conducted in Chapter 3, a number of multi-component materials, salts and co-crystals, containing this API had been researched previously. From an assessment of these structures, the most common interactions formed between *NPX* and the co-formers were that of the carboxylic acid functionality interacting with a pyridine, amine or related salt forms. A summary of this initial CSD search can be found in Appendix A3. The interaction synthons most commonly shared exploiting neutral non-electrostatically enhanced contacts are shown in Figure 6.6.

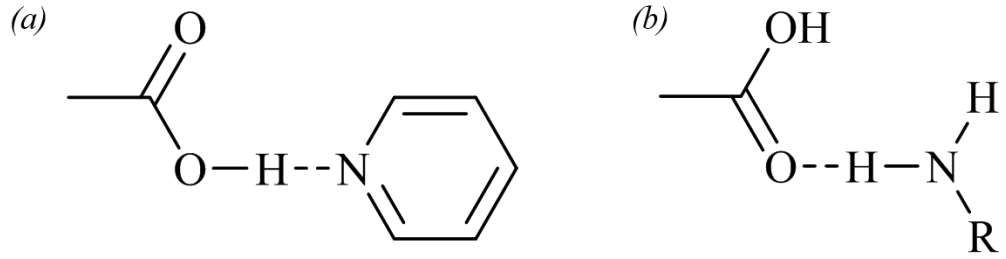

Figure 6. 6 - Key interaction synthons common with multi-component materials of *NPX*, highlighting (a) the O-H···N and (b) N-H···O interactions

One structure found from the previous screening[198] studies was that of the homochiral API interacting with the secondary molecular component 2-aminopyridine (*2AP*). This co-former, the molecular structure of which is outlined in Figure 6.7, consisted of a heterogeneous nitrogen and an amine bound at the two or ortho position. As such, this molecule expressed both the common functionalities from which many of the previous multi-component systems had been established. Furthermore, this material had only one known crystalline form (CSD reference: AMPYRD[199]), exhibiting a melting point at 57-59ºC. Given the pK_a values of the API and co-former were given as 4.2[162, 198] and 6.68[198], respectively, salt-co-crystal formation prediction could not be reliably ascertained. However, noted from the previous study, the combination of *sNPX* and *2AP* was shown to form a salt.

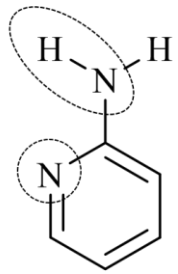

2-aminopyridine
(*2AP*)

Figure 6. 7 - The molecular structure of the co-former 2-aminopyridine (*2AP*), highlighting potential hydrogen bond donors and acceptors

Hence, it was clear that *2AP* possessed the necessary qualities required to form further novel multi-component materials with *NPX*. As such, this combination of materials, at racemic and enantiopure compositions of the API, formed the basis of the initial mechanochemical and solution crystallisation screenings. The aim of the screening was to confirm the preparation of the homochiral material *via* these methods, whilst also exploring the materials that could be made at racemic proportions. This process formed the basis of subsequent screenings carried out on different types of co-formers, as well as that with various *2AP* derivatives. These are discussed in Chapters 7 and 8.

6.2.2 Material screening

6.2.2.1 Mechanochemical screening

Screening was initially conducted through the application of mechanochemistry, whereby the API and co-former were ground together, neat, in different stoichiometries (2:1, 1:1 and 1:2) using a mortar and pestle. These stoichiometries were selected given the most likely ratio of molecular units possible within crystalline structures, allowing for different areas of the phase landscape to be probed. After being ground for 10 minutes, the samples were then analysed using PXRD and DSC so as to ascertain whether or not a new phase had formed.

The PXRD patterns for the enantiopure combination of *NPX* with *2AP* are shown in Figures 6.8. For each molar ratio preparation, uncomplexed starting material was noted for each sample, but in addition, diffraction peaks were detected that did not correlate to those of the starting materials. With a particular focus on the 2θ region between 10° and 14°, three distinct intensities were observed, indicating diffraction from three discrete planes of a crystal lattice attributed to a new material of long-range order. Furthermore, these peaks were consistent across the patterns of the three preparations, with each showing direct correlation to structure obtained from subsequent SCXRD analysis of the crystals grown from solution.

These samples were also assessed using thermal analysis, depicted in Figure 6.9. In each case, an initial melt/recrystallisation event was observed between 50-52°C, corresponding to the melt of the *2AP* starting component and the formation of a different phase. The 1:1 preparation showed a further endothermic event at 102-104°C, which was taken as the melt of the novel multi-component phase. The 2:1 preparation expressed two sequential phenomena, at 88-91°C and 92-95°C respectively, most likely relating to the melt of the complex and excess *NPX*, whilst the 1:2 phase showed a broad thermal process between 78-93°C. This latter observation could, again, could be related to the gradual melt of an impure sample of the novel complex.

Subsequent neat grindings at the 1:1 composition, ground for 30 minutes, yielded a PXRD pattern clear of additional starting material and a DSC with a single endothermic event, occurring between 104-105ºC. Collectively, the unique diffraction pattern and melting demonstrated the formation of a new phase. Furthermore, mechanochemical samples prepared with the aid of minimum quantities of solvent, including ethanol, were all shown to allow for the formation of this novel complex of *sNPX* and *2AP*. The relevant PXRD and DSC plots can be found in Appendix A6.2.

Mechanochemical processing was also used for the preparation of materials with racemic *NPX*. The same stoichiometries were utilised as before, with the combinations being ground neat. All attempts to yield material suitable for analysis from liquid-assisted samples failed, with the resultant materials displaying amorphous character, i.e. sticky or oily.

The PXRD patterns for the three stoichiometric samples of *rsNPX* and *2AP* are shown in Figure 6.10. The patterns produced for the preparations made in non-equimolar quantities showed diffraction peaks that could be directly related to those of the raw starting components, with the addition of some further peaks. The 1:1 sample showed a distinctive pattern, matching not only to that of the additional intensities observed in the other preparations, but that simulated from SCXRD data of the crystals obtained from parallel solution crystallisations (discussed below).

Common to all the DSC traces for these samples (Figure 6.11), an initial melt/recrystallisation process occurring between 50-52ºC was observed, with only the 1:1 sample exhibiting an additional single endothermic process. This was taken to occur from 97-100ºC. The additional thermal events noted in the other preparations could be attributed to the melting of either excess starting material or a depressed melt of the new racemic material. Subsequent grindings conducted for 30 minutes with the 1:1 combination produced a pure preparation of this new phase, with the melting point taken at 98-101ºC.

In both cases, mechanochemistry was shown to be able to yield novel materials, at the given enantiomeric compositions, particularly without the need for solvent. The fact that no solvent was required highlighted the relative favourability of complex formation in each case. However, the formation of sticky, amorphous materials from the further mechanochemical preparations at racemic quantities gave an initial indication as to the difficulty of the formation of this particular phase.

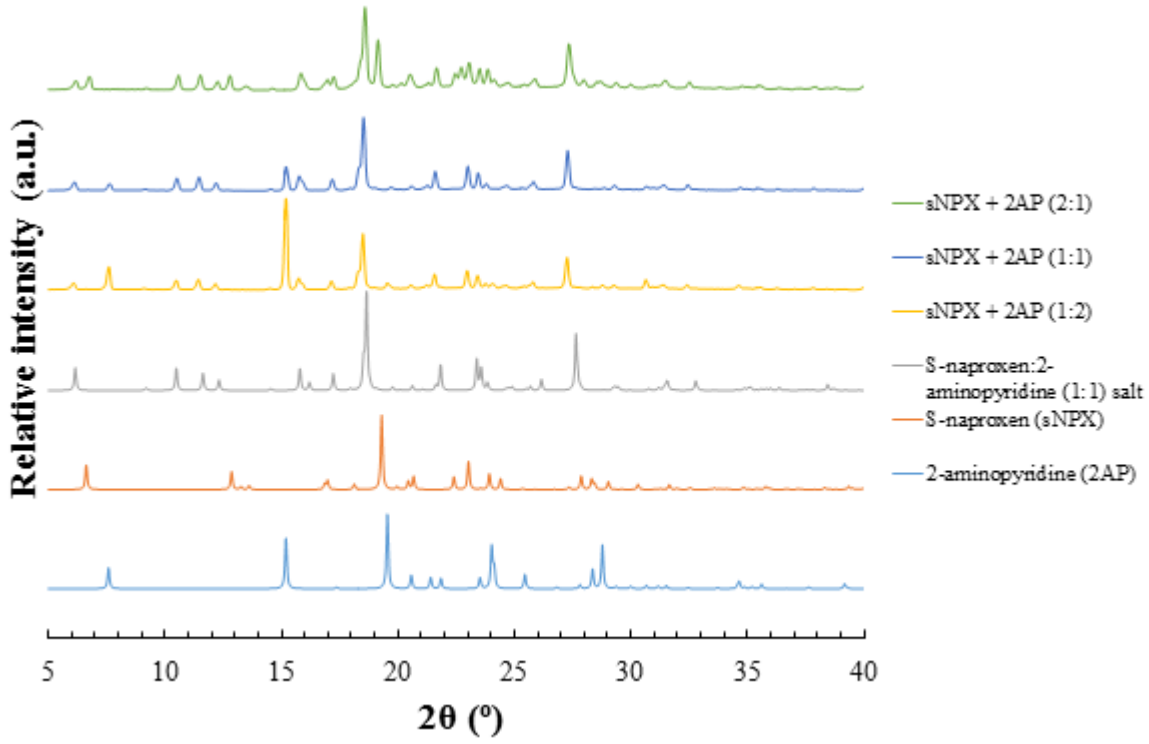

Figure 6. 8 - PXRD patterns from mechanochemically prepared samples of *sNPX* and *2AP*, ground neat in either 2:1, 1:1 or 1:2 molar ratios (top three patterns)

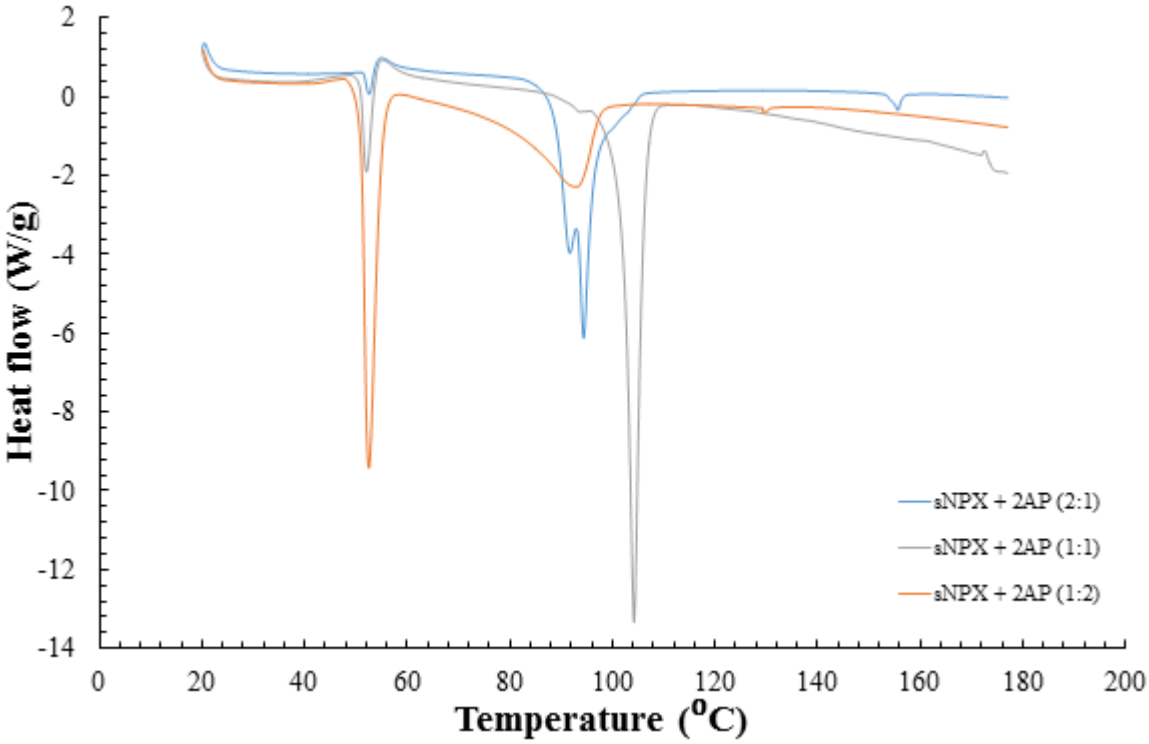

Figure 6. 9 - DSC traces from mechanochemically prepared samples of *sNPX* and *2AP*, ground neat in either 2:1, 1:1 or 1:2 molar ratios

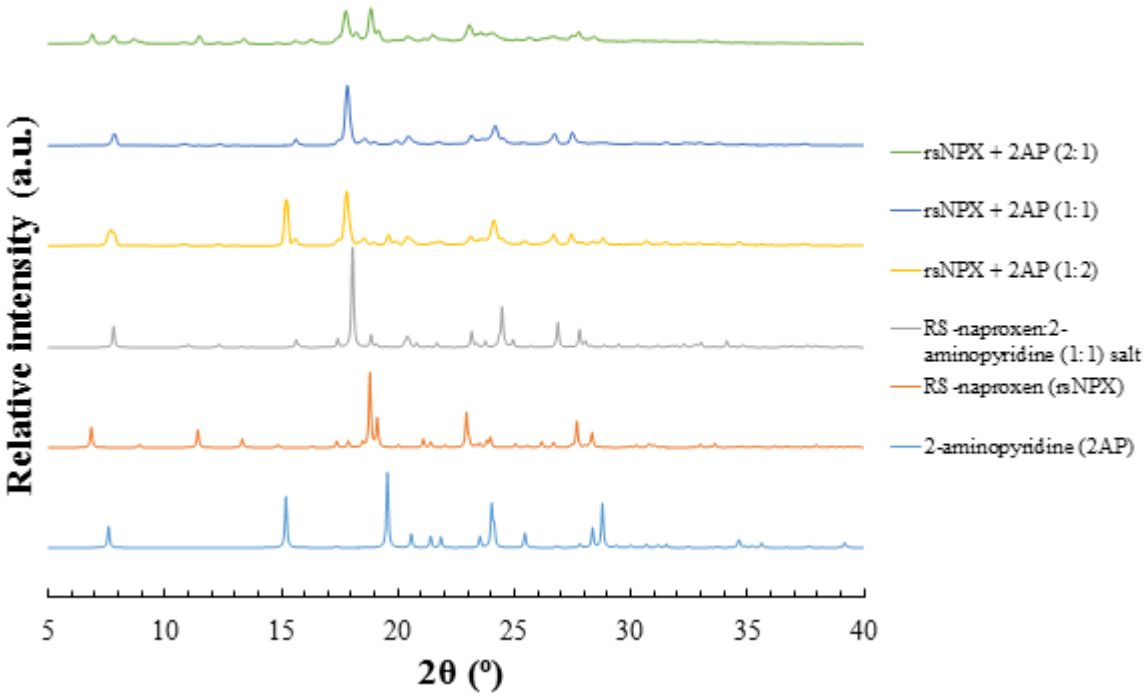

Figure 6. 10 - PXRD patterns from mechanochemically prepared samples of *rsNPX* and *2AP*, ground neat in either 2:1, 1:1 or 1:2 molar ratios (top three patterns)

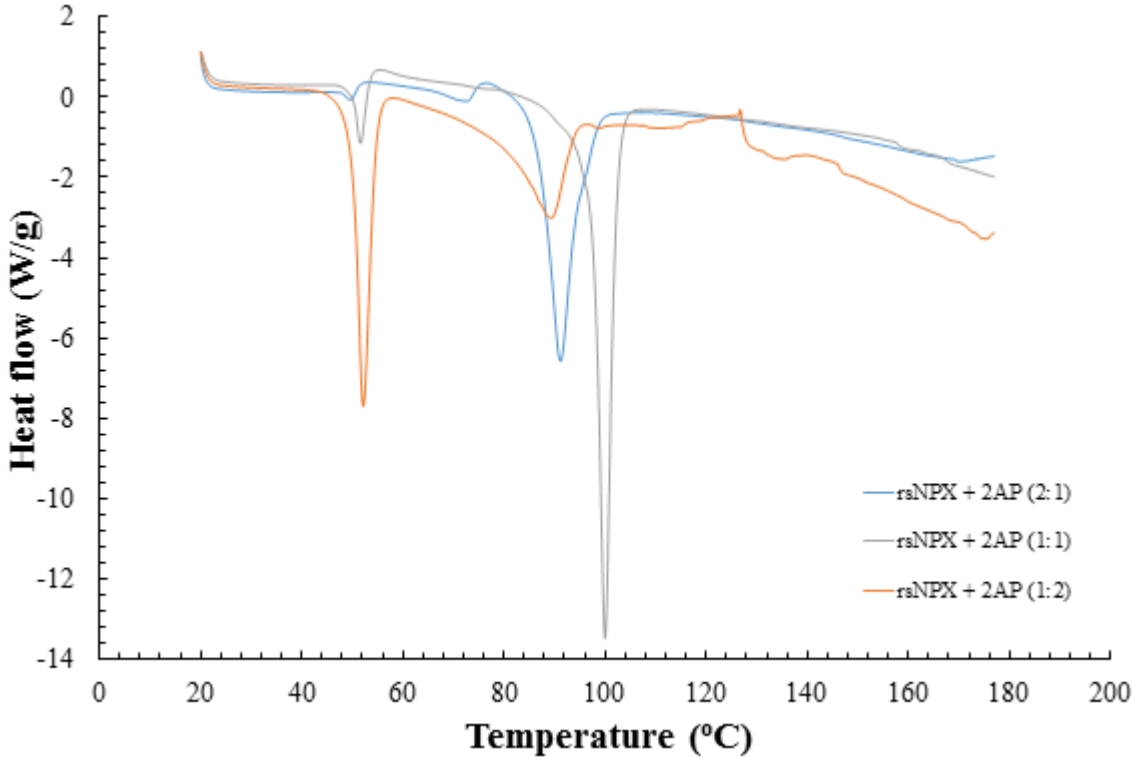

Figure 6. 11 - DSC traces from mechanochemically prepared samples of *rsNPX* and *2AP*, ground neat in either 2:1, 1:1 or 1:2 molar ratios

6.2.2.2 Combined evaporation & cooling crystallisation screening

Parallel to the materials made *via* mechanochemistry, individual crystals were grown from solution, to generate crystals suitable for SCXRD studies. Solutions were prepared by dissolving the necessary quantities of *sNPX* and *rsNPX*, respectively, into ethanol or isopropanol, so that they may be saturated at 30°C, and combining them in 2:1, 1:1 and 1:2 stoichiometric amounts with *2AP*. After allowing for complete dissolution, the solutions were placed in a temperature controlled environment, set at 4°C, and allowed to cool. If crystals were not observed after a period of time, the samples were exposed to the atmosphere, encouraging evaporation, increasing the supersaturation and, eventually, letting nucleation and growth occur.

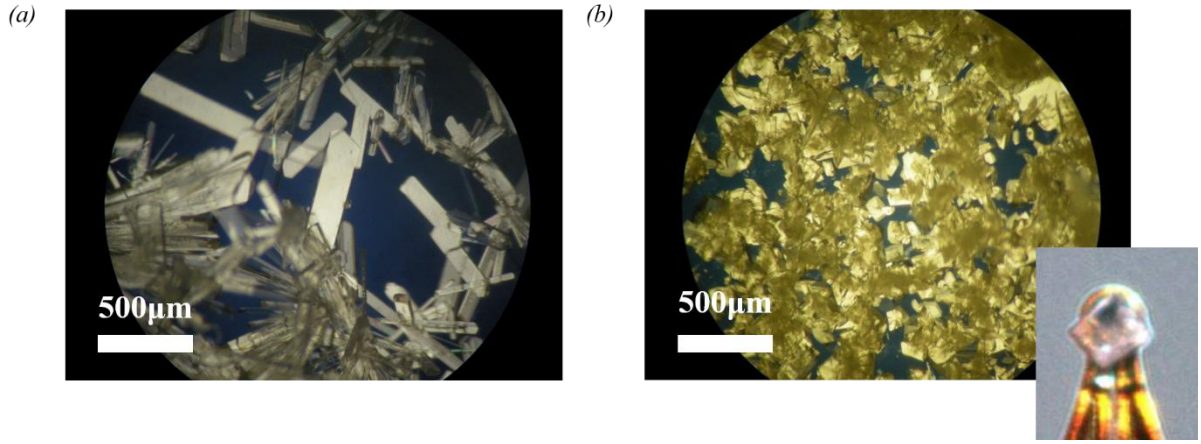

Figure 6. 12 - Microscope and mounted images of crystals yielded from 1:1 ethanol solutions of (a) *sNPX* and (b) *rsNPX* with *2AP*

The crystals grown from 1:1 ethanol solutions for both the enantiomerically pure and racemic complexes with *2AP* are shown in Figure 6.12. In the homochiral case, long flat blocks with distinctive edges were shown to precipitate, with the colour of the bulk material shown to be off-white. Despite agglomeration being evident, individual crystals of suitable quality for analysis could be selected. By contrast, the crystals grown from the corresponding racemic solution were shown to agglomerate, with only small crystallites being generated. The morphology resembled that of a block shape, though were by no means uniform, with the bulk colour of this material observed to be pale yellow. It was also noted that the time required for the racemic phase to precipitate was substantially greater than that for the enantiopure phase.

Highlighted in the previous section, the crystals obtained from these crystallisations were shown to correlate directly to those materials made from the corresponding mechanochemical experiments. This was gauged based upon the comparison of the collected PXRD patterns and that simulated from the SCXRD structure. Further confirmation was obtained *via* HSM. Individual crystals were selected from their respective solutions, placed on a slide and heated, whilst being observed under a microscope. Figures 6.13 and 6.14 show the thermal transitions expressed by the respective homo and heterochiral crystals. It was shown that the crystals melted between 100-106°C and 101-104°C, respectively. Accounting for the discrepancies between DSC analysis of bulk powder and HSM measurements of individual crystals, the melting point of the homochiral phase was taken to be higher than that of the racemic, concurring with those observations made for the mechanochemical samples.

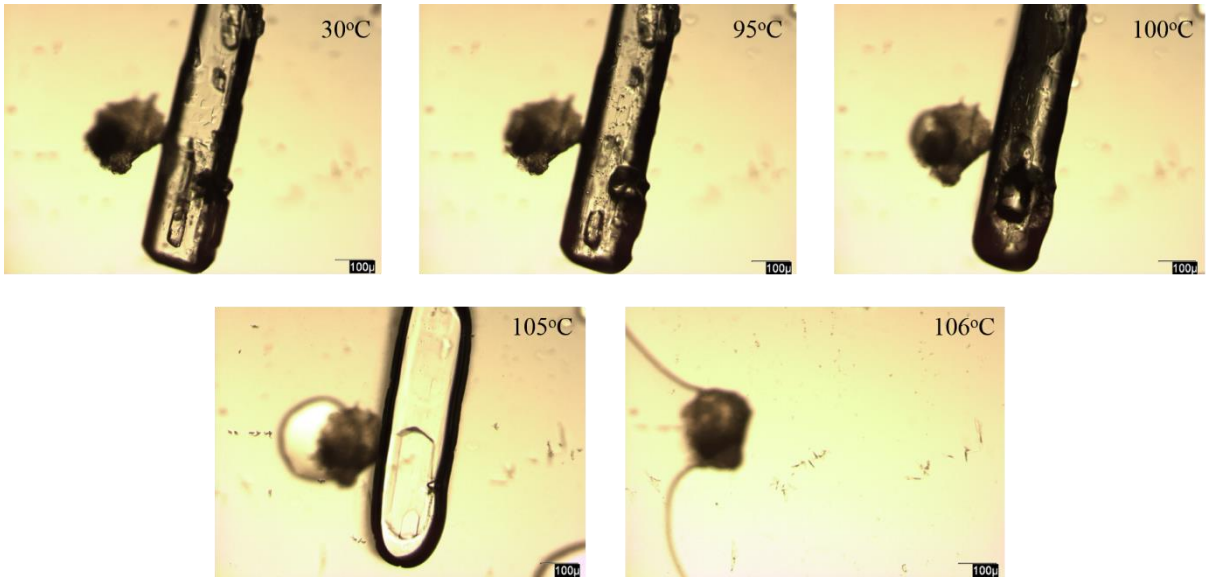

Figure 6. 13 - HSM images corresponding to the thermal phenomena exhibited by crystals selected from the 1:1 ethanol solution of *sNPX* and *2AP* (10ºC/min & 100µm scale)

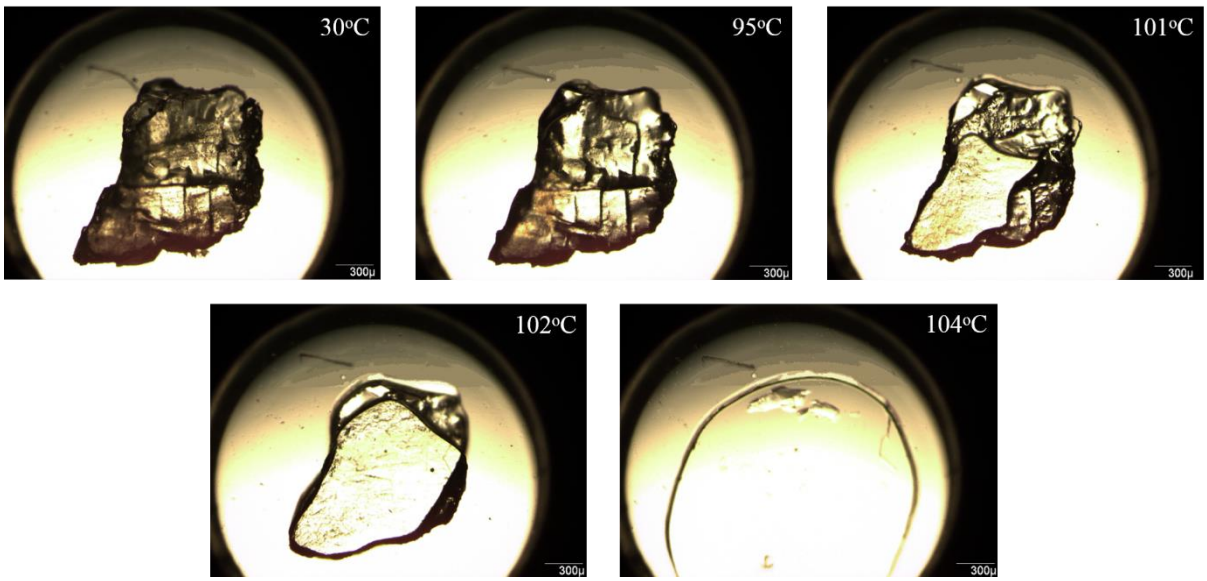

Figure 6. 14 - HSM images corresponding to the thermal phenomena exhibited by crystals selected from the 1:1 ethanol solution of *rsNPX* and *2AP* (10ºC/min & 300µm scale)

6.2.3 Material characterisation

The combination of mechanochemical and solution cooling crystallisation screening demonstrated the reproducible preparation of novel materials by combining *NPX* and *2AP* at racemic and enantiopure quantities. The next step was to characterise the complexes generated, in terms of their solid state structure and chiral crystalline nature.

6.2.3.1 Phase, thermal and spectroscopic analysis

As shown below (Figure 6.15), the simulated PXRD patterns derived from diffraction analysis of the individual crystals of the complexes formed are compared and contrasted to those of the starting materials. The diffraction data for the multi-component materials showed distinct peaks from those of the initial components, emphasising that unique complexes had been generated. Further to this, the patterns yielded at racemic and enantiopure compositions were also shown to be substantially different to each other. This showed that two discrete phases were produced and presented the first indication that upon multi-molecular structure formation between *NPX* and *2AP* at racemic quantities, a racemic compound forming system was produced.

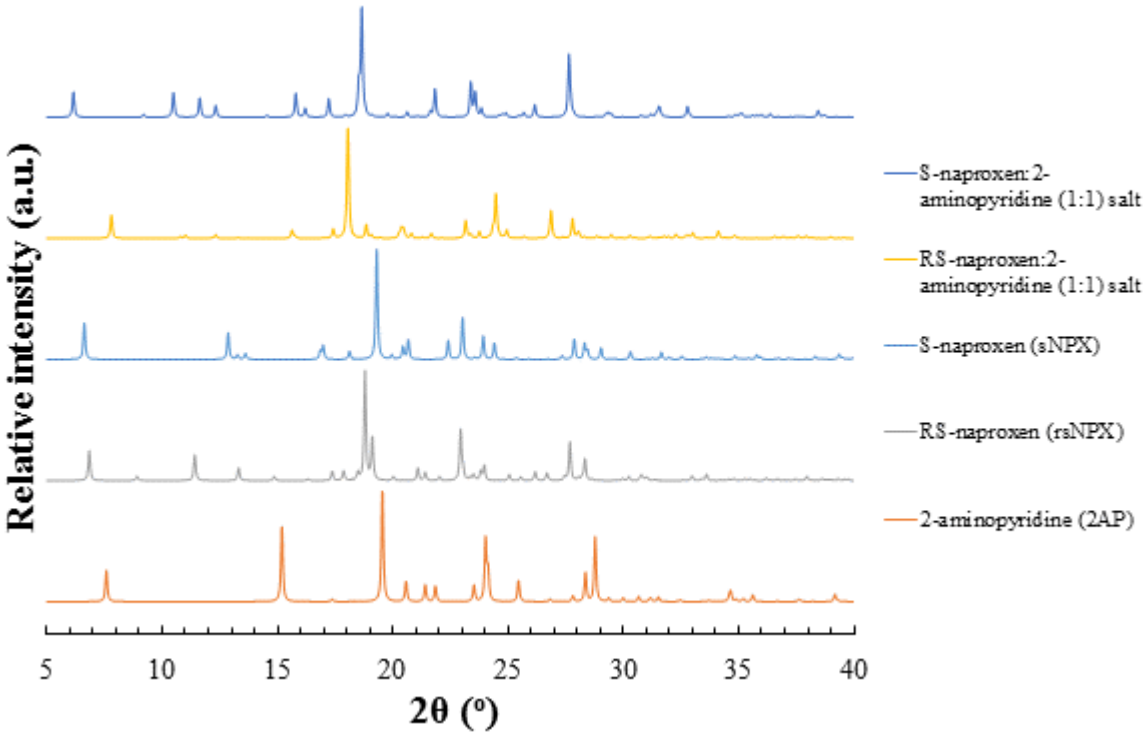

Figure 6. 15 - PXRD patterns of the S-naproxen:2-aminopyridine & RS-naproxen:2-aminopyridine (1:1) salts, as derived from SCXRD data, compared to that of the starting materials

The disparate nature of the materials yielded from the two enantiomeric combinations was also shown from their individual thermal phenomena. The DSC traces, depicted in Figure 6.16, show the major thermal events taken for the starting materials, as well as those of the novel complexes. The melting points of the multi-component samples were taken from the excessive neat grindings of *sNPX* and *rsNPX*, respectively, with the co-former in a 1:1 molar ratio. As shown, the endothermic events of the complexes resided between that of *2AP* and the *NPX* materials, indicating that upon interaction, there was a stabilisation with respect to the co-former and a destabilisation when compared to the API. It was also confirmed that the melting point of the enantiopure was greater (104-105°C) than that of the

heterochiral phase (98-101°C). Whilst only slight, this indicated that in the solid state, the interactions associated between like enantiomers were of greater strength than those found in the racemic case. Given that it had already been established that a different phase could be yielded at racemic compositions when compared to that at homochiral, this observation suggested that the enantiopure multi-component material presented metastability towards racemic compositions.

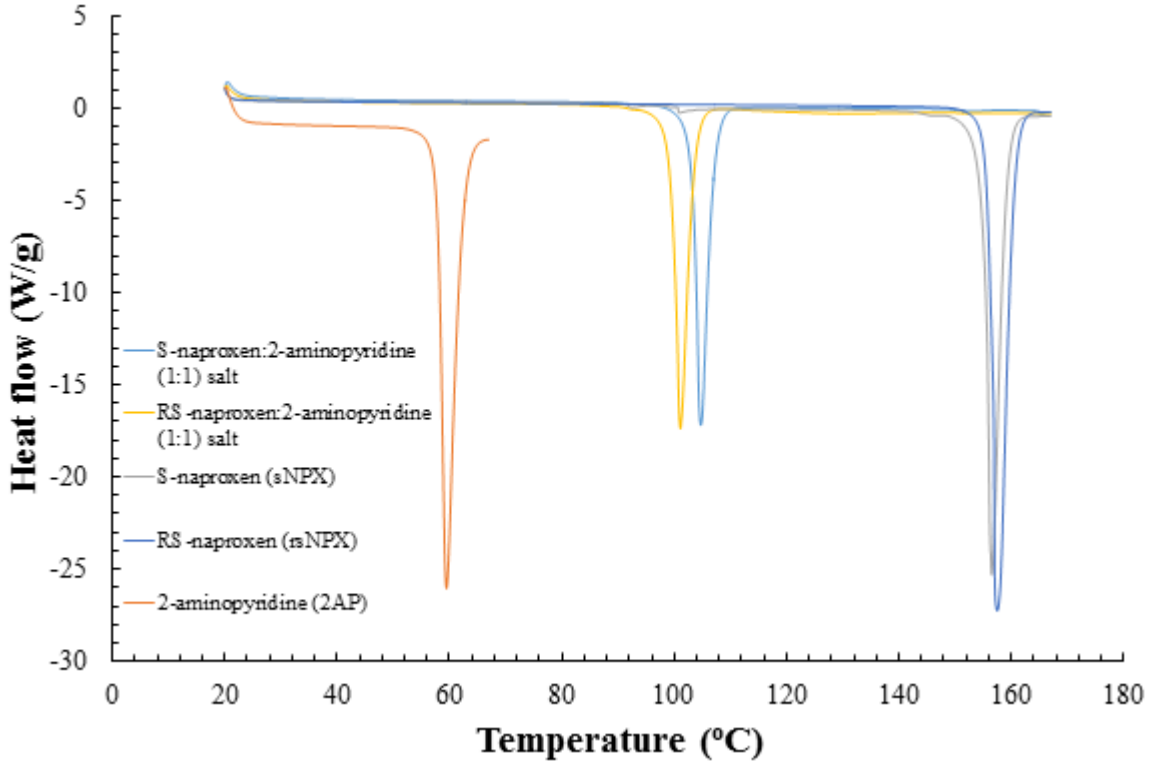

Figure 6. 16 - Traces of the S-naproxen:2-aminopyridine & RS-naproxen:2-aminopyridine (1:1) salts, prepared *via* mechanochemistry, compared to that of the starting materials

Before complete structural analysis could be conducted *via* SCXRD, an initial assessment of the structural features of the two novel multi-component materials of *NPX* and *2AP* was undertaken using infrared (IR) spectroscopy. The diagram shown in Figure 6.17 highlights the spectra of each of the starting components, as well as that of the individual complexes, prepared mechanochemically. The spectrum of *2AP* presented a variety of features, with the absorptions at 3444 cm^{-1} and 3285 cm^{-1} indicating the vibrational modes for the N-H bonds. The two spectra of *sNPX* and *rsNPX* both presented broadly similar characteristics, with a broad absorption occurring at 3104 cm^{-1} and 2987 cm^{-1}, respectively, indicating the O-H group forming hydrogen bonding interactions. A key functionality was that of the C=O stretch, with the racemic *NPX* phase showing a single peak at 1705 cm^{-1} and the enantiopure demonstrating two peaks at 1725 cm^{-1} and 1681 cm^{-1}. This indicated that the carbonyl group associated with the homochiral form possessed a greater degree of freedom than in the racemic case. Furthermore, it was also noted that the racemic phase exhibited two small peaks from 2700-2500 cm^{-1}, highlighting the dimeric nature of the interactions exhibited within its crystalline structure.

In contrast, the spectra of the complexes presented distinct differences to those of the starting materials. Focussing on the carbonyl functionality, the main peaks for the enantiopure and racemic cases were taken as 1655 cm^{-1} and 1632 cm^{-1}, respectively. In comparison to the *NPX* materials, both of these systems expressed red shifting, suggesting that the interactions formed between *NPX* and *2AP* in each case were weaker.

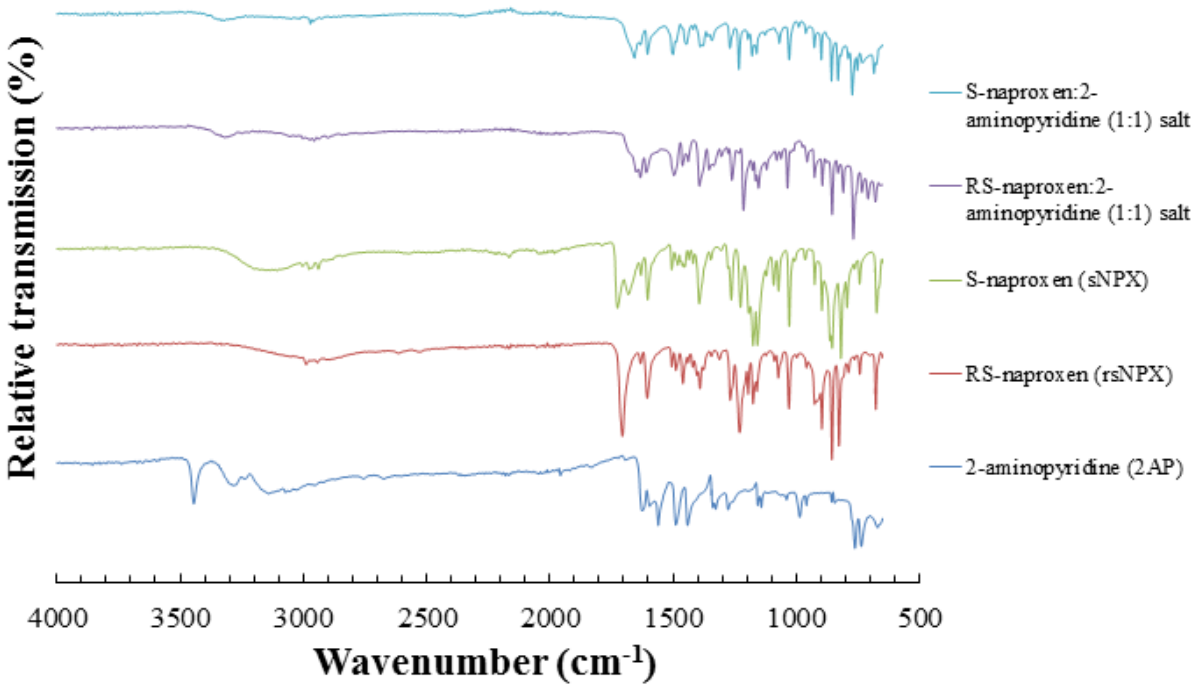

Figure 6. 17 - IR spectra for the mechanochemically prepared samples of S-naproxen:2-aminopyridine (1:1) and RS-naproxen:2-aminopyridine (1:1) salts, compared to that of the starting materials

6.2.3.2 Binary (melting point) phase diagram analysis – Classification of chiral crystalline materials

To clarify the chiral crystalline nature of this system when changing the composition from equal quantities of *rNPX* and *sNPX* to that of entirely enantiopure, binary (melting point) phase diagrams were prepared. Using mechanochemical means, two different types of sample preparation were carried out. Each preparation utilised a constant 1:1 stoichiometry of API to co-former, with the first set of samples using combinations of *rsNPX* with excess *sNPX*, and the second using the individual enantiomers, whereby *rNPX* was combined with extra *sNPX* to facilitate the change in the chiral composition. Samples were ground neat and analysed using DSC (Appendix A6.2). The thermal events were assessed and used to construct the different aspects of the phase diagrams shown in Figure 6.18.

Focussing initially on the ground combinations of *rsNPX*, *sNPX* and *2AP*, a clear trend was shown, highlighting distinct regions towards racemic and enantiopure compositions. Peaking at the melting points of the respective phases, as shown above, the trajectory from that of the *sNPX* and *rsNPX* complexes converged to exhibit a single thermal event at the *sNPX* molar fraction of 0.7. This was taken as the eutectic point and was consistent across several of the compositions, occurring between 94-97^{o}C. The presence of the distinct regions, corresponding to the racemic and enantiopure multi-component phases, along with the eutectic point, confirmed that this system could be classified as a racemic compound.

However, upon grinding the two individual enantiomers together with *2AP*, rather than producing the thermal phenomena observed as in the above case, a contrasting phase diagram was generated. Here, the path of the liquidus line, representing the thermodynamic boundary between the liquid and solid states, demonstrated that the regions present upon transitioning from hetero to homochiral compositions, corresponded to that of a single phase. This type of phase diagram is common for conglomerate systems, suggesting that upon combination with *2AP*, the two uncoupled enantiomers could form opposing enantiopure complexes, which could remain stable with increasing temperatures.

For this preparation, it was demonstrated that the homochiral phase could be accessed at compositions approaching racemic, giving credence to the notion of a metastable racemic conglomerate system.

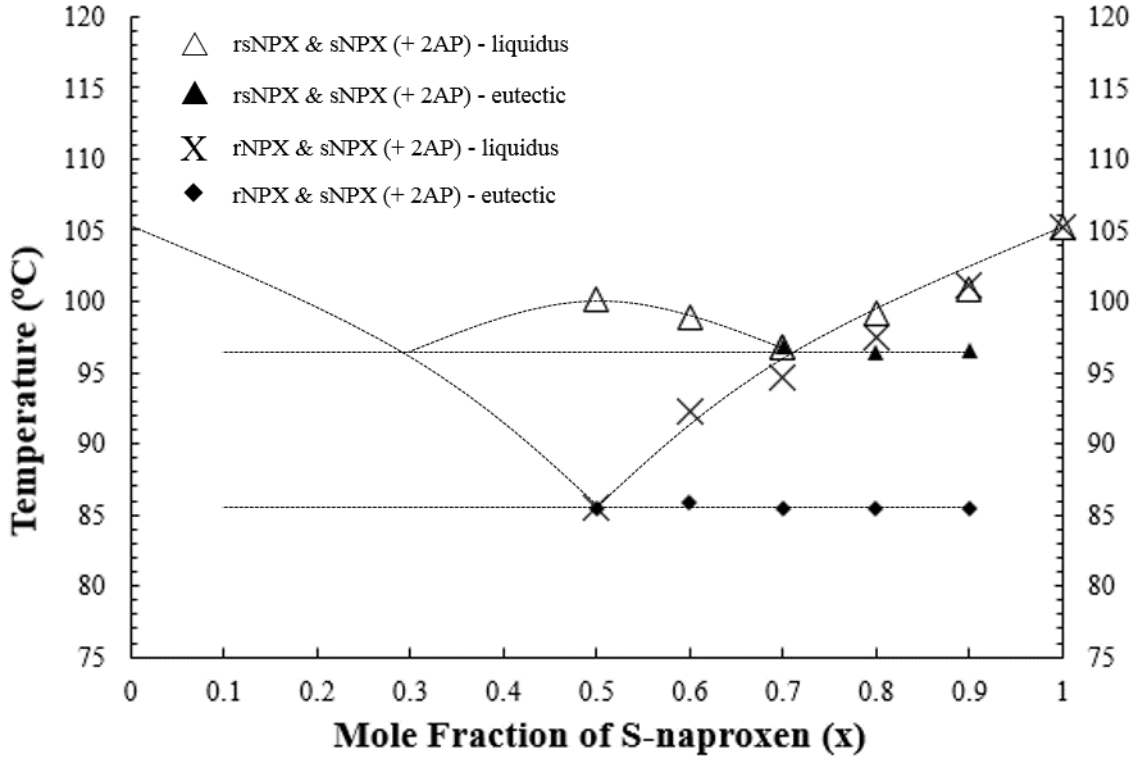

Figure 6. 18 - Binary (melting point) phase diagram, highlighting the melting and eutectic phenomena associated with mechanochemically prepared samples constituting either *sNPX* & *rNPX* (X, ♦) or *sNPX* & *rsNPX* (▲, Δ), with *NPX* in a 1:1 stoichiometry with *2AP*

6.2.3.3 Crystallography – Crystal structure analysis

Having established the existence of two discrete forms at racemic and homochiral compositions, respectively, and their metastable relationship in the solid state, the next step was to determine the crystalline structures of these materials. Individual crystals were selected from the previously prepared crash cooling crystallisations and analysed using SCXRD. The corresponding CIF files (1, 2) can be found on the accompanying CD-ROM.

The arrangement of molecules from the complex of *sNPX* and *2AP*, in terms of its unit cell, hydrogen bonding motifs and long range molecular assembly, is shown in Figure 6.19. The unit cell dimensions can be found in Table 6.4, along with further information describing the refinement of the diffraction data. Each of the asymmetric units consisted of one molecule of the enantiopure API and that of the co-former. These compounds were found to crystallise in the non-centrosymmetric monoclinic space group $P2_1$.

Hydrogen bonds were shown to be the key intermolecular interactions, forming between the relative accepting and donating groups of *sNPX* and *2AP*, respectively. The key atoms utilised in these interactions, as well as the defining lengths and angles, can be found in Appendix A6.2. The API and co-former were shown to form a heterodimeric interaction unit, consisting of two $D_1^1(3)$ hydrogen bonds, collectively making a $R_2^2(8)$ ring. Given the pK_a difference between the molecules, salt formation was deemed to be possible and as such, for this complex, proton transfer was observed from the Fourier electron density difference map. As a result, the two hydrogen bonding contacts of the

heterodimer consisted of a charge assisted interaction from the donating pyridinium moiety of the co-former to the accepting carboxylate functionality of the API, as well as that between the neutral amine and carboxyl groups. The formation of a salt allowed for this system to be described as a S-naproxen:2-aminopyridine (1:1) salt.

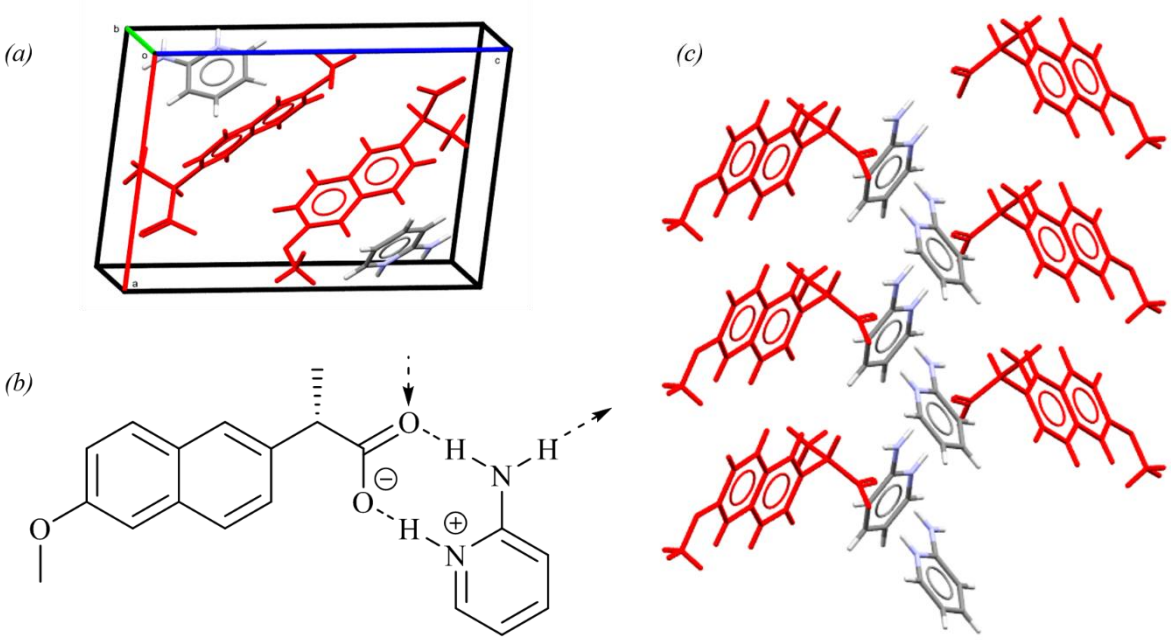

Figure 6. 19 - Crystal structure of the S-naproxen:2-aminopyridine (1:1) salt, highlighting (a) the unit cell, (b) hydrogen bonding synthon and (c) packing arrangement (*sNPX* in red)

Table 6. 4 - SCXRD data for the S-naproxen:2-aminopyridine (1:1) salt

Material	**S-naproxen:2-aminopyridine (1:1) salt**
Empirical formula	$C_{19}H_{20}N_2O_3$
Formula weight	324.37
Temperature (K)	150.01(10)
Crystal system	monoclinic
Space group	$P2_1$
***a* (Å)**	9.6568(5)
***b* (Å)**	6.0822(4)
***c* (Å)**	14.4228(8)
***α* (°)**	90
***β* (°)**	96.340(5)
***γ* (°)**	90
Volume (Å^3)	841.94(8)
Z*, *Z'	2, 1
ρ_{calc} (g/cm^3)	1.279
μ (mm^{-1})	0.087
F(000)	344.0
Crystal size (mm^3)	0.166 × 0.121 × 0.082
Radiation	MoKα (λ = 0.71073)
2Θ range for data collection (°)	6.708 to 51.356
Index ranges	$-7 \leq h \leq 11$, $-7 \leq k \leq 7$, $-17 \leq l \leq 17$
Reflections collected	5562
Independent reflections	3167 [R_{int} = 0.0355, R_{sigma} = 0.0633]
Data/restraints/parameters	3167/1/219
Goodness-of-fit on F^2	1.063
Final R indexes [I>=2σ (I)]	R_1 = 0.0467, wR_2 = 0.0941
Final R indexes [all data]	R_1 = 0.0620, wR_2 = 0.1024
Largest diff. peak/hole (e Å^{-3})	0.14/-0.23
Flack parameter	-1.2(10)

Taking the key interaction unit described above, the extended structure of this salt form can be built up. Exploiting the additional N-H bond not already utilised in the dimerised motif, an additional $D^1_1(3)$ N-H···O was able to form, connecting neighbouring interaction moieties and allowing for a chain to be generated. This chain takes on a three-dimensional spiral arrangement. Overall, the crystalline structure can hence be built up through a series of these chains, all interlocking and running parallel to each other.

For the material prepared from the racemic mixture of API with *2AP* in a 1:1 ratio, the crystal structure was solved and assessed as before. The important aspects, including the unit cell, hydrogen bonding synthon and the overall packing arrangement, are shown in Figure 6.20. As for the homochiral case, the unit cell consisted of two asymmetric units, each consisting of a single enantiomer and co-former molecule. The dimensions of the unit cell and refinement parameters are shown in Table 6.5. Upon combing the starting components and given the crystallisation conditions, the asymmetric units were shown to precipitate as part of a triclinic $P\bar{1}$ lattice.

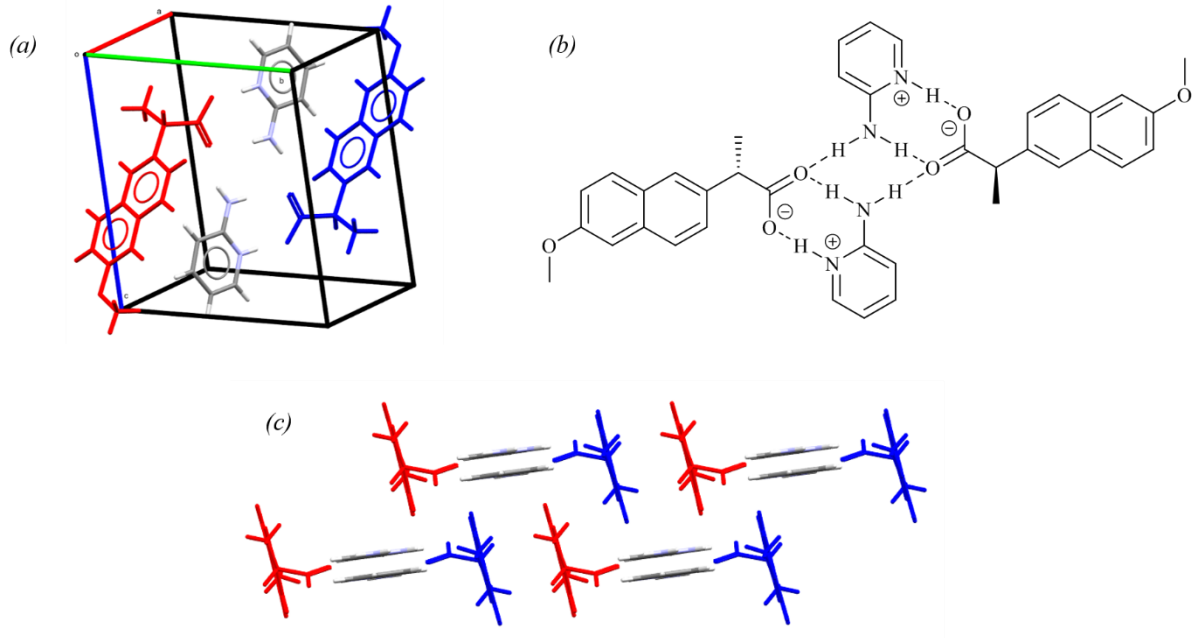

Figure 6. 20 - Crystal structure of the RS-naproxen:2-aminopyridine (1:1) salt, highlighting (a) the unit cell, (b) hydrogen bonding synthon and (c) packing arrangement (*sNPX* in red, *rNPX* in blue)

Once again mirroring that of the enantiopure complex, the key hydrogen bond motif noted was that of the heterodimer between the deprotonated carboxylic acid functionality of *NPX* and that of the protonated pyridine and amine groups of *2AP*. Given proton exchange and the stoichiometry observed, this system could be classified as a RS-naproxen:2-aminopyridine (1:1) salt. However, despite utilising the same initial dimer, the extended structure of the racemic phase was different to that of the homochiral complex. The further N-H hydrogen bond donor of *2AP*, rather than being used to form a chain, was used to bind two of the key interaction units together, each exploiting a different chiral form of *NPX*. Each heterodimeric unit formed bridging $D^1_1(3)$) contacts with its opposing unit, forming a dimer of dimers, characterised as a $R^2_4(8)$ ring.

These structural motifs can, hence, be used to describe the overall packing arrangement of the racemic salt form. Given the kinked plane existing through the co-former molecules of the interaction unit, the body of the different enantiomers (i.e. naphthyl and methoxy groups) were shown to protrude from opposite sides of this plane, allowing for the motif to express a three-dimensional herring-bone

structure. Utilising this, the overall long range assembly of the material was shown to consist of interlocked interaction units, forming distinct layers, each offset from the other.

Table 6. 5 - SCXRD data for the RS-naproxen:2-aminopyridine (1:1) salt

Material	**RS-naproxen:2-aminopyridine (1:1) salt**
Empirical formula	$C_{19}H_{20}N_2O_3$
Formula weight	324.37
Temperature (K)	292.63(10)
Crystal system	triclinic
Space group	$P\bar{1}$
***a* (Å)**	8.6586(4)
***b* (Å)**	8.9635(3)
***c* (Å)**	11.5676(6)
***α* (°)**	78.553(4)
***β* (°)**	83.951(4)
***γ* (°)**	68.062(4)
Volume (Å^3)	815.72(7)
Z*, *Z'	2, 1
ρ_{calc} (g/cm^3)	1.321
μ (mm^{-1})	0.730
F(000)	344.0
Crystal size (mm^3)	0.098 × 0.08 × 0.062
Radiation	CuKα (λ = 1.54184)
2Θ range for data collection (°)	7.802 to 146.716
Index ranges	$-10 \leq h \leq 10$, $-11 \leq k \leq 11$, $-14 \leq l \leq 14$
Reflections collected	26157
Independent reflections	3229 [R_{int} = 0.0383, R_{sigma} = 0.0194]
Data/restraints/parameters	3229/0/219
Goodness-of-fit on F^2	1.044
Final R indexes [I>=2σ (I)]	R_1 = 0.0458, wR_2 = 0.1250
Final R indexes [all data]	R_1 = 0.0540, wR_2 = 0.1321
Largest diff. peak/hole (e Å^{-3})	0.25/-0.21
Flack parameter	N/A

Given the crystal structures of these two salt forms, the previous finding of a racemic compound forming system upon the combination of *NPX* with *2AP* at different enantiomeric compositions was confirmed. Both were shown to exploit different hydrogen bonding interactions, from which different crystalline structures could be generated. In the case with *2AP*, the respective structures of the homochiral and racemic salts were shown to form interactions akin to that of single-component *NPX*, though with the comparative structures showing different stabilities.

6.3 Multi-component material cooling crystallisation

Having established that at enantiopure and racemic combinations, novel complexes corresponding to these compositions could be obtained, and given that the homochiral phase demonstrated a certain metastability under certain conditions, with respect to the racemic form, bulk methods were established for the reproducible preparation of each of the respective materials. From here, the different salts were characterised for their behaviour in solution, from which initial cooling crystallisations were derived so as to confirm the metastability of the single enantiomeric phase towards racemic compositions.

6.3.1 Bulk material preparation – Slurrying

It was shown from the initial screening experiments, detailed in Section 6.2, that the salts of *sNPX* and *rsNPX* with *2AP*, respectively, could be prepared *via* both mechanochemical and cooling crystallisation means. These experiments were carried out on relatively small scales, requiring excessive mechanical stress in the case of grinding or generating larger crystallites, when grown from an unmixed solution, which were deemed unsuitable for conducting further solution characterisation. Therefore, before more refined cooling crystallisation practices could be developed, '*solvent-mediated*' or slurrying techniques were utilised for the bulk preparation of the respective complexes.

Slurrying entailed the suspension of excess solid in a given solvent, at a specific temperature, with the material being continually mixed for a set amount of time. As such, three solvent systems were selected to ascertain their applicability for the bulk preparation of the two salts; ethanol, isopropanol and hexane. The alcohols were chosen to mimic the initial cooling crystallisations conducted in screening, whilst hexane was used as a contrast, being a non-polar solvent and showing minimal dissolution compatibility with the API. Suspensions were prepared and mixed for up to one hour at room temperature.

The PXRD patterns depicted in Figures 6.21 and 6.22 demonstrate the phases made in the three solvent environments for the individual enantiopure and racemic combinations of *NPX* with *2AP*, in comparison with the starting materials. For the homochiral preparations, the corresponding salt was shown to form in each case, with particular purity in the isopropanol and hexane systems. In the ethanol case, excess starting material was also shown to precipitate. For the racemic preparations, the heterochiral salt was shown to form consistently in each of the different solvent environments. However, the amorphous content of the material generated from hexane was shown to be slightly greater than that observed in either of the alcohol solutions. This concurred with previous observations made for this system from mechanochemical experiments

These slurrying experiments were conducted with low quantities of solvent and solid, but to provide a route to the bulk scale preparation of the two salts, larger volumes of solvent were required. Therefore, hexane was selected as a suitable solvent medium, owing to its ability to yield the necessary phases, with sufficient crystallinity. Furthermore, the solubility of the given materials in hexane was significantly lower than that of the other solvents, allowing for a greater quantity of solid to be suspended and, subsequently, collected. Hence, samples of each of the salt forms were prepared *via* slurrying in hexane, with the quantity of solvent and solid used substantially increased. The diffraction patterns and DSC traces were collected for three iterations of both the homo and heterochiral materials. These can be found in Appendix A6.3. Both forms were shown to be consistently prepared, with the materials yielded exhibiting bulk melting points at 103-105^{o}C and 99-101^{o}C for the enantiopure and racemic complexes, respectively, corresponding to those found from screening.

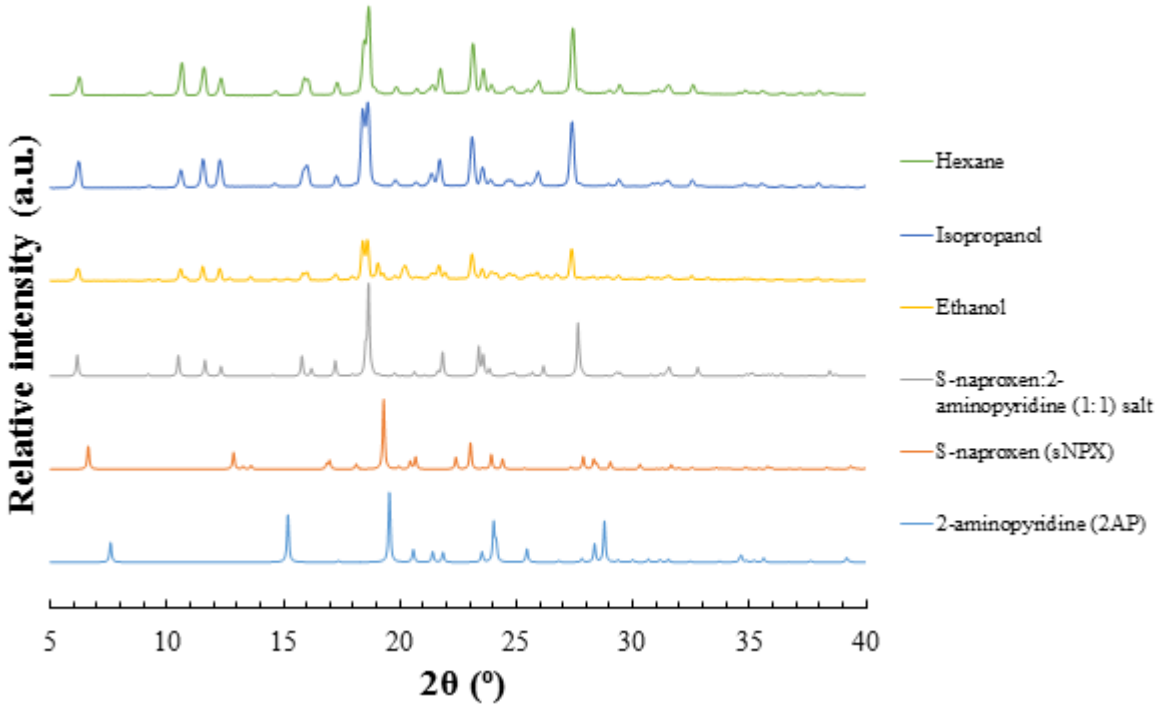

Figure 6. 21 - PXRD patterns for the bulk preparation of the S-naproxen:2-aminopyridine (1:1) salt, slurried in either ethanol, isopropanol or hexane (top three patterns)

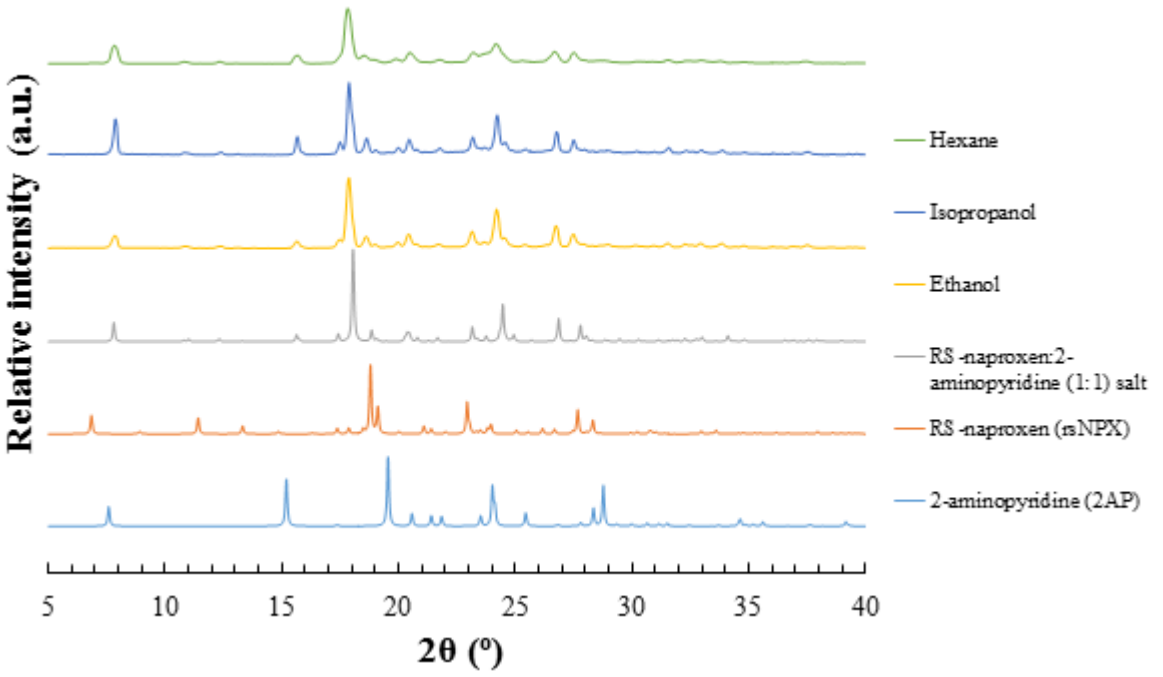

Figure 6. 22 - PXRD patterns for the bulk preparation of the RS-naproxen:2-aminopyridine (1:1) salt, slurried in either ethanol, isopropanol or hexane (top three patterns)

6.3.2 Material solubility

As highlighted in the previous section, slurrying could be used to reliably produce bulk quantities of the two salt forms of *NPX* and *2AP* at racemic and enantiopure contributions. This allowed for solubility analysis to be carried out. As before, these measurements were conducted based upon turbidity measurements, taking the clear point as the point of dissolution with increasing temperature, for a given concentration of material. Figure 6.23 shows the solubility curves taken for the respective salt forms in ethanol, with Table 6.6 demonstrating key solubilities determined for 20ºC and 30ºC. For information on the solubilities in isopropanol, see Appendix A6.3.

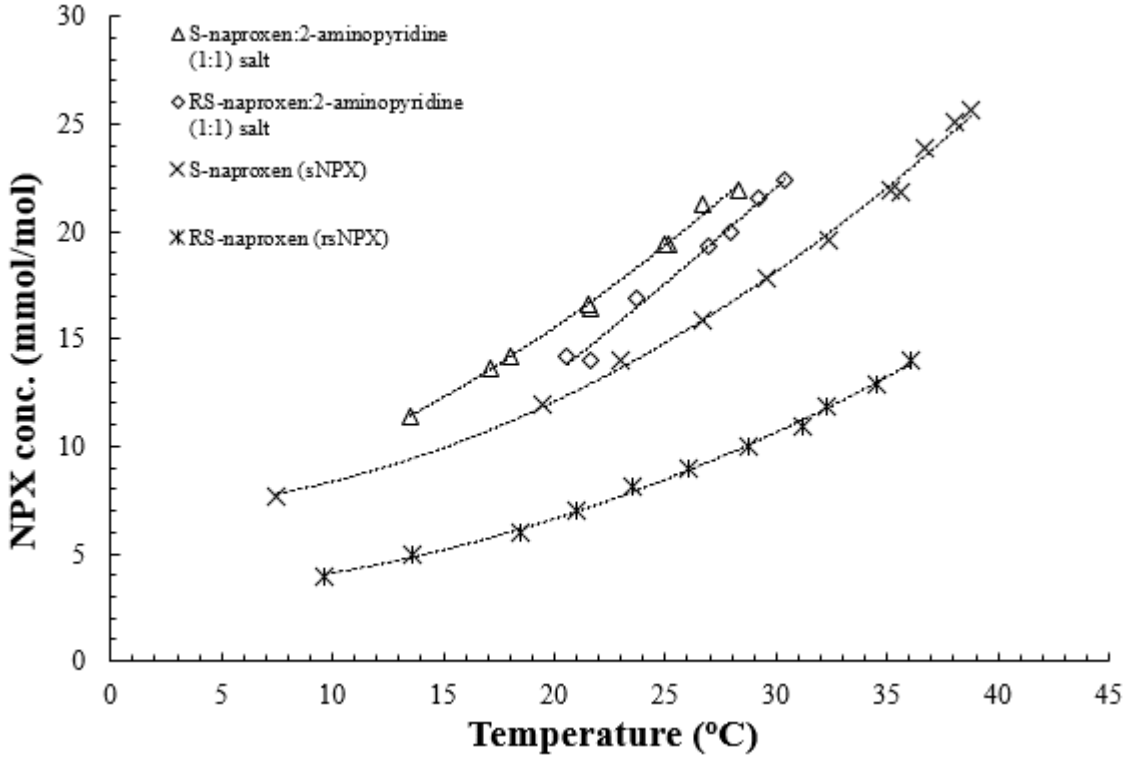

Figure 6. 23 - Solubility data of the S-naproxen:2-aminopyridine (1:1) and RS-naproxen:2-aminopyridine (1:1) salts in ethanol, as determined from turbidity measurements (concentration taken with respect to *NPX*) (% error no greater than 2.5%)

Table 6. 6 - Saturation points of the S-naproxen:2-aminopyridine (1:1) and RS-naproxen:2-aminopyridine (1:1) salts in ethanol, at 20ºC and 30ºC (concentration taken with respect to *NPX*)

Material	Saturation at 20ºC (*NPX* mmol/mol)	Saturation at 30ºC (*NPX* mmol/mol)
S-naproxen:2-aminopyridine (1:1) salt	15.5	23.7
RS-naproxen:2-aminopyridine (1:1) salt	13.3	22.1

In comparison with the single-component forms of *NPX*, whether at racemic or enantiopure compositions, the solubility of both the multi-component forms was shown to be consistently higher over the temperature range explored. For the homochiral materials, the salt form was shown to be around 1.28 and 1.31 times higher at 20ºC and 30ºC, whilst the racemic salt exhibited solubilities 1.75 and 1.9 times higher for the same temperatures. This emphasised the advantages of using multi-

component materials, in this case salts, for developing systems with enhanced physicochemical properties with respect to their starting components.

Further to this, both of the complexes displayed higher solubilities than that of single component *sNPX*, the enantiomeric composition of the API with the greater solubility. This observation was deemed to be key when considering developing future cooling crystallisation experiments as it demonstrated distinct regions where only the multi-component phase could be crystallised. This was in contrast to the solubility measurements taken for isopropanol. Here, the solubility of the multi-component materials was shown to coincide with that of *sNPX* and *rsNPX*, rendering this solvent system inappropiate for the selective crystallisation of the different *NPX* phases over the temperature range explored.

Finally, the solubility disparity between the two salt forms was shown to be smaller than that observed for *NPX* on its own, emphasising a smaller stability difference between the novel materials. Though by no means definitive, the trends of the solubility curves suggested that with increasing temperature the solubility gap between the homo and heterochiral multi-component materials decreased, providing an indication that the enantiopure salt had potential stability upon crystallisations at higher temperatures.

6.3.3 Ternary (solution) phase diagram analysis

To further explore the solubility relationship between the *sNPX* and *rsNPX* salts, providing further information for the design of cooling crystallisations, a ternary phase diagram was developed for the ethanol solvent system. Figure 6.24 shows the phase diagram, derived from gravimetric analysis, for different enantiomeric compositions of the API, combined in a 1:1 ratio with *2AP*, at 20ºC and 30ºC. The PXRD patterns of each of the slurried preparations, as well as the individual solubility points taken for each composition can be found in Appendix A6.3.

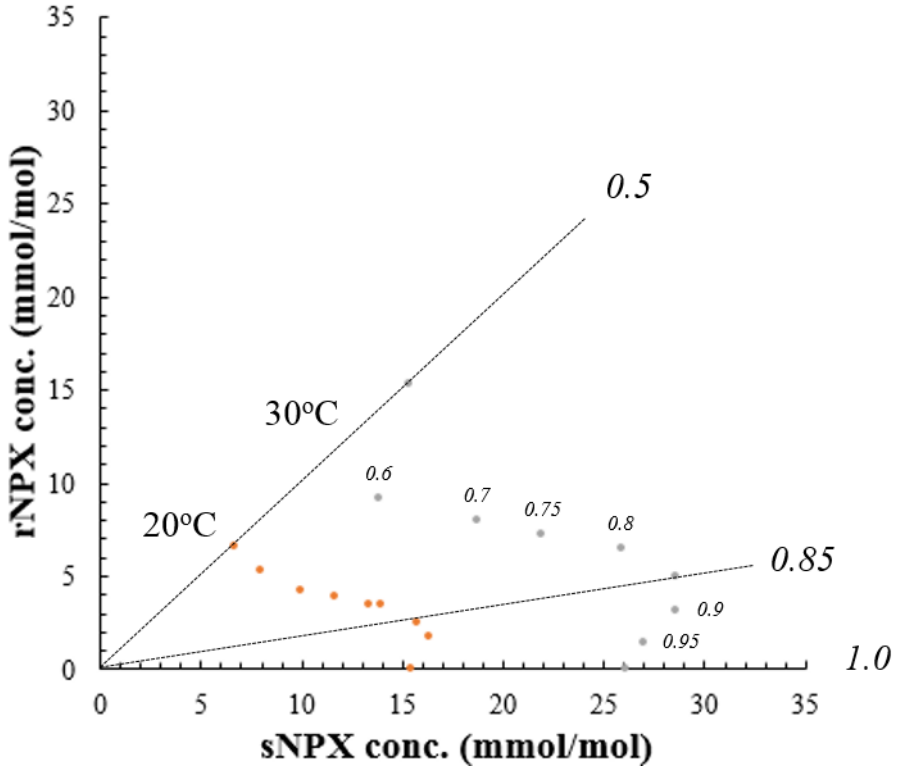

Figure 6. 24 - Ternary (solubility) phase diagram, corresponding to the solubility of different enantiomeric combinations of *NPX* in ethanol at 20ºC and 30ºC, respectively, whilst in a 1:1 combination with *2AP*

As shown, with particular evidence at 30ºC, the trend of the solubility points represented that of a racemic compound system, demonstrating specific regions that could be attributed to the either the S-naproxen:2-aminopyridine (1:1) or RS-naproxen:2-aminopyridine (1:1) salt. These regions were separated by a distinctive inflection point, the eutectic point, shown to occur at a *sNPX* mole fraction of 0.85. In order to test the hypothesis that this system truly represented a metastable conglomerate, it was established that cooling crystallisations should be developed that probed enantiomeric compositions from racemic to those below that indicated by the eutectic point.

The preparation of this diagram also highlighted some further interesting features of this system. The gravimetric samples were prepared *via* slurrying, for which diffraction analysis was conducted on the left over solid residue. For the solid yielded from lower temperature slurrying, the PXRD patterns demonstrated consistent preparation of the two distinct multi-component crystalline phases, either pure or as a mixture. However, for the higher temperature preparations, the complexes were also shown to crystallise along with excess starting material, predominately *NPX*. This could be attributed to either difficulties in salt formation at higher temperature or the evaporation of additional mother liquor from the solid sample, with a high concentration of *NPX*.

A further observation was that relating to the higher than expected solubility of the sample generated at purely racemic compositions at 30ºC. After slurrying, the mother liquor was extracted and allowed to evaporate at the given solvent-mediation temperature. This allowed for solid to crystallise and the solubility could be determined. In the racemic case at the higher temperature, the initial material generated post-evaporation was amorphous in nature, given its sticky and oily texture. Cooling crystallisation experiments for preparations at racemic compositions were thus deemed unnecessary.

6.3.4 Initial cooling crystallisations

Thus far, it has been demonstrated that both the racemic and enantiopure multi-component salts of *NPX* and *2AP* could be prepared through mechanochemical, slurrying or static cooling crystallisation means. For the most part, these were conducted at either purely homochiral or racemic compositions, with varying combinations of the different enantiomeric forms only being used in the development of the ternary phase diagram. In this final section, designed cooling crystallisation experiments were explored, establishing a definitive route to the preparation of the two complexed phases *via* cooling and exploring the potential of crystallising the enantiomerically pure salt at compositions tending towards racemic.

The first controlled cooling crystallisations were designed to reliably prepare the respective novel phases. Saturated solutions at 30ºC with respect to racemic and enantiopure contributions of the API, with the corresponding amount of co-former, were setup and heated to 45ºC so as to allow for complete dissolution. Mixed at a given rate, the solutions were then cooled at either 0.1ºC/minute (slow) or 1ºC/minute (fast) to 5ºC. Upon reaching the end temperature, the solid material yielded was analysed by PXRD. The diffraction patterns for these samples are shown in Figures 6.25 and 6.26.

For each of the respective preparations, the individual multi-component materials of the different corresponding enantiomeric composition were produced. This emphasised that both forms could be prepared *via* cooling crystallisation.

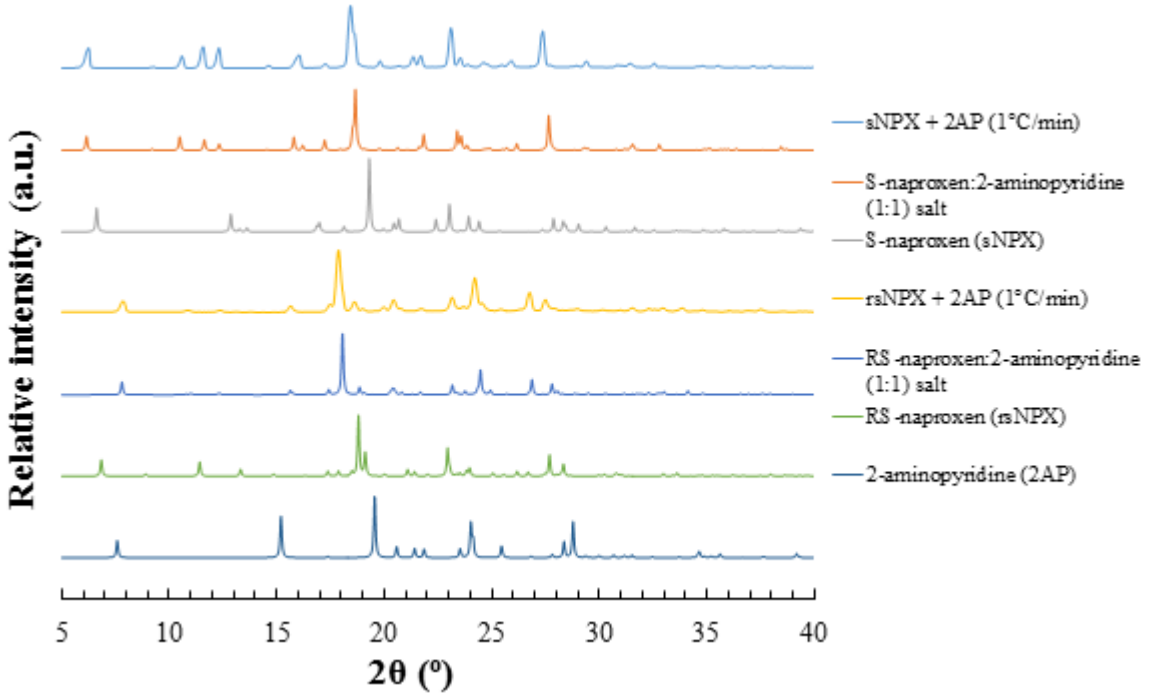

Figure 6. 25 - PXRD patterns for initial cooling crystallisation experiments for the preparation of the S-naproxen:2-aminopyridine (1:1) and RS-naproxen:2-aminopyridine (1:1) salts at enantiopure and racemic compositions, saturating the solution at 30ºC with respect to the salts, cooling from 45ºC to 5ºC at 1ºC/min, mixing at 150 rpm (*sNPX/rsNPX + 2AP*)

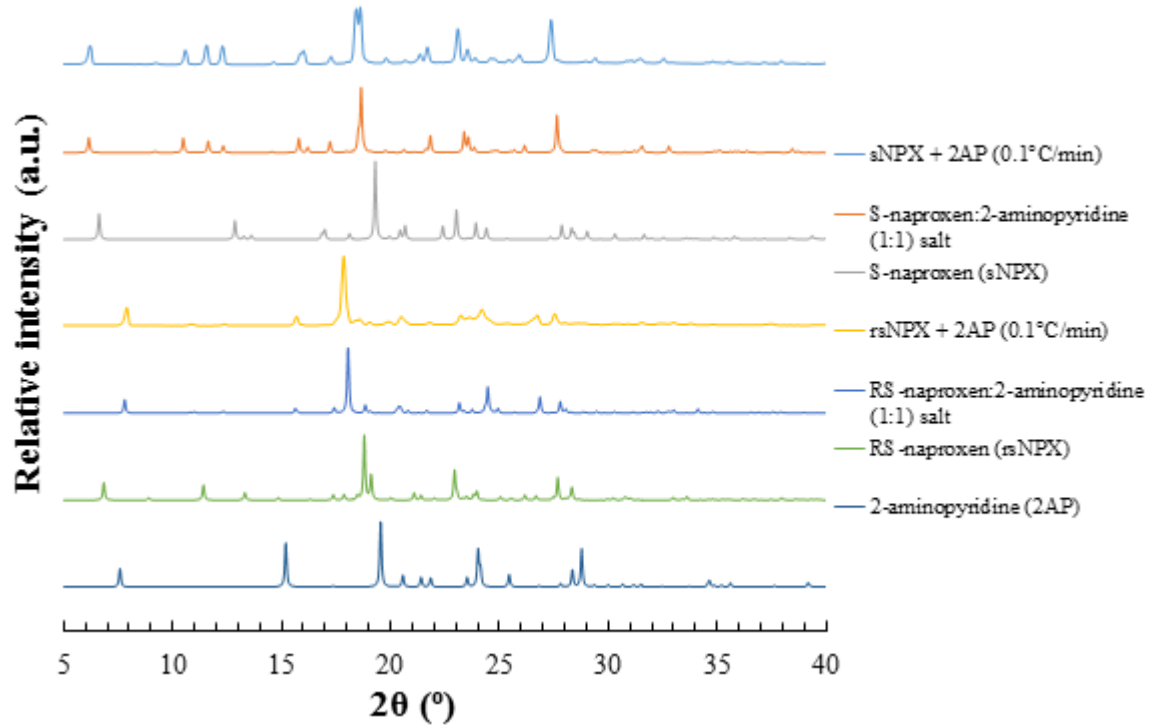

Figure 6. 26 - PXRD patterns for initial cooling crystallisation experiments for the preparation of the S-naproxen:2-aminopyridine (1:1) and RS-naproxen:2-aminopyridine (1:1) salts at enantiopure and racemic compositions, saturating the solution at 30ºC with respect to the salts, cooling from 45ºC to 5ºC at 0.1ºC/min, mixing at 150 rpm (*sNPX/rsNPX + 2AP*)

Having established that cooling could be used for the reproducible preparation of both multi-component phases, further crystallisations were carried out utilising different enantiomeric compositions. Based upon the findings from the ternary phase diagram analysis, cooling crystallisations were conducted at compositions below *sNPX* mole fractions of 0.85. Hence, mole fractions of 0.8, 0.75 and 0.7 were selected. The same cooling rates were utilised as previously, with mixing rate and end temperature being varied, either at 150 (slow) or 600 (fast) rpm and 10ºC, 5ºC and 0ºC, respectively. Upon reaching the temperature, each sample was filtered immediately. The solid phases produced were analysed again using PXRD, the data for which can be found in Appendix A6.3.

Upon analysing the materials generated at the slow cooling rate, it was noted that no matter the composition or the mixing rate, both crystalline salt forms were shown to precipitate to different extents. In the specific set of crystallisations where the samples were cooled to 10ºC, mixed at 600 rpm, no crystallisation was observed. In contrast, by cooling the solutions at the faster rate, mixing slowly at 150 rpm and only cooling to 10ºC, the enantiopure salt could be exclusively accessed at all the compositions used. The solids were collected immediately after precipitation and analysed, as highlighted in Figure 6.27. These observations could be rationalised by considering the mechanism of crystallisation taking place. By mixing at the slower rate at the given enantiomeric compositions, the collective metastable zone width for the two salts was deemed to be sufficiently wide so as to allow for the distinct nucleation of both of the multi-component phases. In addition, by cooling at the faster rate and given the kinetic stability of the homochiral form towards racemic contributions, the corresponding enantiopure salt was able to crystallise preferentially with respect to its racemic counterpart.

It was also shown that with the related coolings to 5ºC and 0ºC, the composition at which the homochiral complex could be obtained exclusively shifted towards compositions with higher contributions of *sNPX*. Furthermore, by increasing the mixing rate, the racemic phase was once again shown to crystallise with the enantiomerically pure multi-component material.

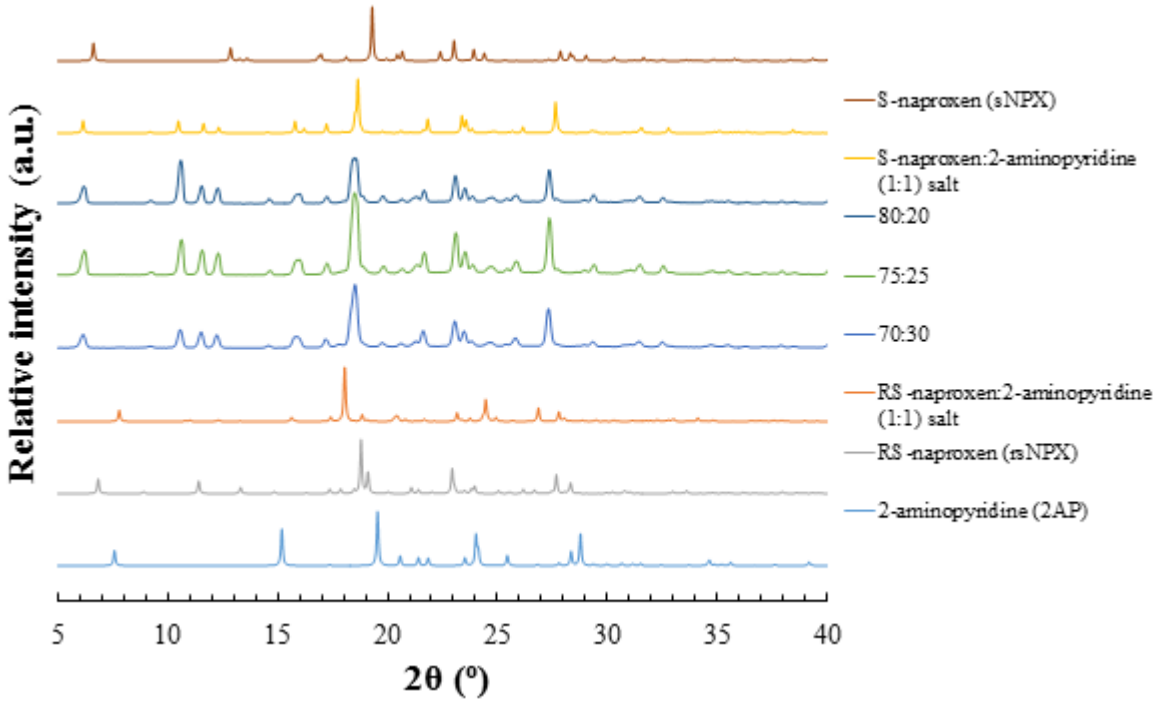

Figure 6. 27 - PXRD patterns of the solid yielded from cooling crystallisations, utilising 1:1 ethanol solutions of *NPX* to *2AP*, with varying enantiomeric compositions (80:20, 75:25 and 70:30, excess *sNPX*), cooled at 1ºC/min from 45ºC to 10ºC, mixing at 150 rpm

The solubility line, as dictated through the ternary phase diagram, represents the thermodynamic equilibrium between not only the solution and solid phases, but also that of the different *NPX*-*2AP* salt forms. Highlighted from the above cooling crystallisations, it has been shown that given the correct kinetics, the homochiral complex could be accessed at compositions closer to that of racemic. This confirmed the metastability of this phase and existence of a metastable conglomerate, with potential applications towards preferential crystallisation.

6.4 Summary, conclusions and future work

In this chapter, the API naproxen (*NPX*) has been re-evaluated in terms of its crystalline structure and melting point, at either enantiopure or racemic compositions. Based upon this, its binary (melting point) phase diagram was constructed and rationalised, emphasising the existence of a racemic compound system. This was supported by the solubility data for the different phases, showing a significant disparity in their respective solubilities, thus highlighting the relative stability of *NPX* at the two enantiomeric contributions. Furthermore, by assessing the solubility of the various heterochiral combinations at given temperatures, the characteristic trend of a racemic compound system was shown through the preparation of ternary (solubility) phase diagram. Together, these observations reiterated the impracticality of using this API, in its current form, in preferential crystallisation processes.

The chiral composition of the solutions of *NPX* was analysed using Circular Dichroism (CD) spectroscopy, a method that could account for not only solution concentration through the measurement of UV-vis light, but also enantiomeric mole fraction by accounting for the absorption of different circularly polarised light. Calibration plots were established and used to quantify future crystallisation outcomes. However, a limitation to CD spectroscopy was that it can be limited by concentration effects. This could be attributed to a detection limit associated with the detector. Hence, an effective dilution was necessary for each sample prior to analysis. However, the use of this analytical method formed the basis of a collaboration with the University of Strathclyde (ter Horst group), exploring its potential for in-line monitoring of chiral crystallisation processes, as well as establishing modifications to the technique to allow for its use with multi-component systems.

Given the impracticality of using *NPX* for the separation of its chiral forms, it was decided that by manipulating the crystalline lattice of the API through the introduction of a second, complementary molecular entity, a system could be generated that could be applied to preferential crystallisation processes. Based upon an assessment of the relative interactions exploited by *NPX* with other molecules, as determined from CSD searches, specific co-formers could be selected. One particularly promising co-former was that of 2-aminopyridine (*2AP*). This molecule exhibited the pyridine and amine functionalities deemed most likely to form a multi-component complex with *NPX*.

Various screening methods were used in the preparation of materials of *NPX* with *2AP* at both enantiopure and racemic compositions, including mechanochemical and preliminary crash cooling crystallisation methods. Mechanochemistry offers a quick and easy route to the development of novel multi-component complexes, be they co-crystals or salts. This technique allows for the direct assessment of stoichiometry, providing early indications of the ratio of molecular components in the structure. The role of solvent can also be evaluated, with minimum quantities being used in the preparations. Whether solvent is used or not, also provides an understanding of the propensity of the molecular entities to interact and hence form novel structures. However, the crystalline structure of a given material could not be directly obtained from the samples derived from mechanochemistry, due to their microcrystalline nature. Using the initial solubility data of one of the starting materials, saturated solutions can be set up and rapidly cooled with a specific stoichiometry of starting components. In this way, single crystals were able to be grown that were suitable for SCXRD analysis. In many cases, the

materials generated through mechanochemical means could also be correlated to the crystals grown from solution, potentially highlighting the stability of a given crystalline phase.

In the specific case of *NPX* and *2AP*, both preparation methods were shown to reproducibly yield distinct materials at homo and heterochiral compositions with characteristic diffraction patterns distinct from each other, as well as those of the starting materials. Thermal analysis indicated melting points at 103-105^{o}C and 99-101^{o}C for the enantiopure and racemic complexes, respectively. Utilising mechanochemical means, binary phase diagram analysis confirmed the existence of two discrete phases, providing an initial indication of that this combination yielded a racemic compound chiral crystalline system. Subsequent structural analysis highlighted that the two forms corresponded to that of a S-naproxen:2-aminopyridine (1:1) salt and a RS-naproxen:2-aminopyridine (1:1) salt.

Upon grinding racemic contributions of the API with the co-former, the amorphous content of the samples prepared were shown to be greater than that observed for the enantiomerically pure case. The melting point of the racemic phase was thus taken to be lower, an atypical phenomenon for many racemic compounds. This provided the first indication as to the potential metastability of the homochiral salt. The narrowing in the relative stabilities of the two forms was also emphasised from solubility analysis of the two materials, with the difference between them being substantially smaller than that observed for the enantiomeric compositions of just *NPX*. Whilst the ternary phase diagram of this system, again, demonstrated the existence of a racemic compound system, it was noted that at higher temperatures, the racemic salt tended towards the amorphous phase, highlighting its comparative instability and presenting an opportunity to crystallise the homochiral salt form at compositions closer to racemic.

Finally, the possibility of crystallising both phases using controlled cooling crystallisations was explored, with the aim to manipulate the enantiomeric composition and determine the conditions required for the precipitation of the homochiral salt at more even quantities of the two chiral forms. Having demonstrated that slurrying could be used to generate both of the novel phases, initial cooling crystallisations were carried out at fast and slow cooling rates to emphasise that both the enantiopure and racemic salts could be crystallised *via* this method. With this established, it was then shown that with immediate filtration, the enantiomerically pure complex could be obtained at compositions up to and including the *sNPX* mole fraction of 0.7. This represented a point beyond the thermodynamic eutectic boundary in solutions of ethanol, showing that the homochiral salt could be kinetically stabilised at compositions that tended towards racemic. As such, the complexes of *NPX* and *2AP* can be described a metastable conglomerate material, presenting opportunities for future preferential crystallisation processes.

Several aspects of the system of *NPX* and *2AP* should be explored further. Firstly, the stability of the racemic multi-component phase at higher temperatures should be established, assessing potential opportunities for the crystallisation of the homochiral material under these conditions. Additional cooling crystallisations should also be conducted, exploiting enantiomeric contributions even closer to racemic quantities, i.e. *sNPX* mole fractions of 0.65 and 0.6. Initial seeding experiments should also be carried out to ensure the crystallisation of the correct form at these compositions and to maximise yield.

As part of an on-going collaboration between the Wilson (University of Bath) and ter Horst (University of Strathclyde) groups, the development and application of multi-component materials for separation of chiral molecular forms from racemic solutions *via* crystallisation has been explored further. With the enantiopure combination of *NPX* and *2AP* expressing the characteristics of a metastable conglomerate, initial plans have been established for its application into a preferential crystallisation process, using the setup depicted in Figure 6.28. Here, a feed tank containing a racemic solution of *NPX* with *2AP* can be fed into a temperature controlled secondary vessel, where cooling crystallisation is allowed to take

place. In the crystallisation unit, the racemic solution is initially enriched through an enantiopure feed, so as to favour the crystallisation of only one of the enantiomeric forms of the API and to minimise the chance of the racemic phase precipitating. From this point, the system is cooled fairly rapidly at a given mixing rate until spontaneous nucleation occurs and the solid material is filtered and analysed. The solution dynamics, in terms of its enantiomeric composition and the crystallisation activity, can be monitored by in-line polarimetry and '*Focus Beam Reflectance Measurements*' (FBRM), respectively. Polarimetry establishes the composition of enantiomers within solution based upon the relative degree of optical rotation of light, whilst FBRM monitors the scattering of a beam of laser light so as to determine the point of nucleation. The point to which the system should be enriched is dependent upon the desired area of operation, as dictated by the ternary phase diagram for a given system, and the crystallisation conditions used. Together, these can both determine the degree of kinetic stabilisation awarded to the homochiral salt phase as the system is composited towards racemic contributions. As well as these experiments, seeded crystallisation should also be conducted, so as to further control the crystallisation of only the enantiopure complex, as well as that of the point of nucleation and growth.

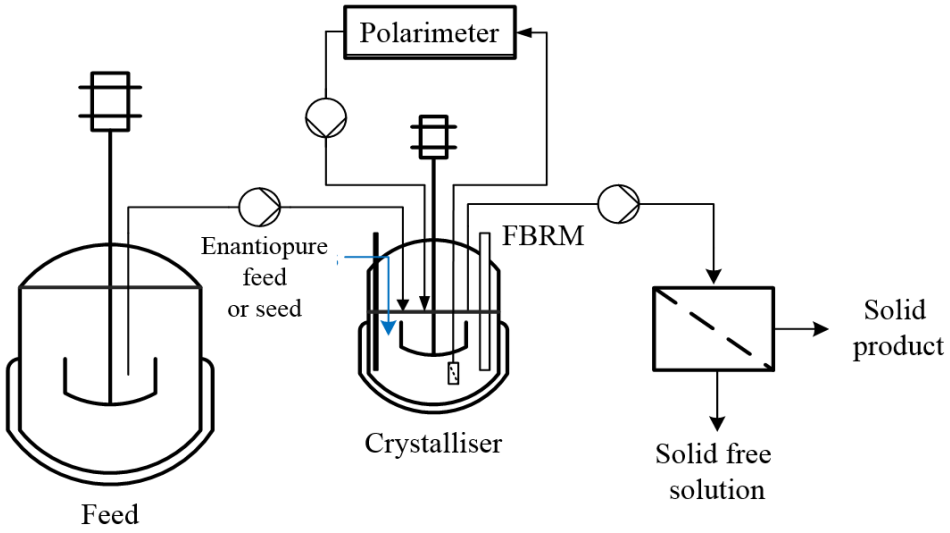

Figure 6. 28 - A schematic of the preferential crystallisation setup used by the ter Horst group (University of Strathclyde), highlighting the feed and crystallisation vessels, in-line polarimetry and FBRM, as well as the filtration units

In addition, this collaboration is exploring various aspects of chiral crystallisation, including exploring methods for the in-line determination the enantiomeric composition of solutions. Currently, polarimetry has been used to monitor the solution composition of the two enantiomers, but through the use of CD spectroscopy, both the composition and concentration can be monitored. Further studies are currently underway so as to assess the capability of this form of analysis in the characterisation of multi-component systems, as well as that for in-line analysis.

7 Chiral multi-component materials of naproxen with derivatives of 2-aminopyridine

Based upon the initial assessment and robust cooling crystallisations for the racemic and homochiral multi-component materials of *NPX* and *2AP*, further co-crystal and salt screenings were conducted using appropriate derivatives of the co-former. As discussed from the initial CSD search described in the previous chapter, it was determined that the key hydrogen bonding interactions, common to many systems incorporating *NPX*, were that of the carboxylic acid-pyridine, carboxylate-pyridinium and carboxylic acid-amine interactions. Given the propensity for *2AP* to form a heterodimeric interaction unit with *NPX*, the initial molecules selected were chosen to mimic these types of contacts. Hence, as shown in Figure 7.1, the molecules selected included 2-aminopyrimidine (*2APM*), 2-amino-4,6-dimethylpyrimdine (*2ADMP*), 2-amino-3-chloropyridine (*2A3CP*), 2-amino-4-chloropyridine (*2A4CP*), 2-amino-5-chloropyridine (*2A5CP*) and 2-amino-6-chloropyridine (*2A6CP*). For the unit cells and other crystallographic details relating to these co-former starting materials, see Appendix A7.

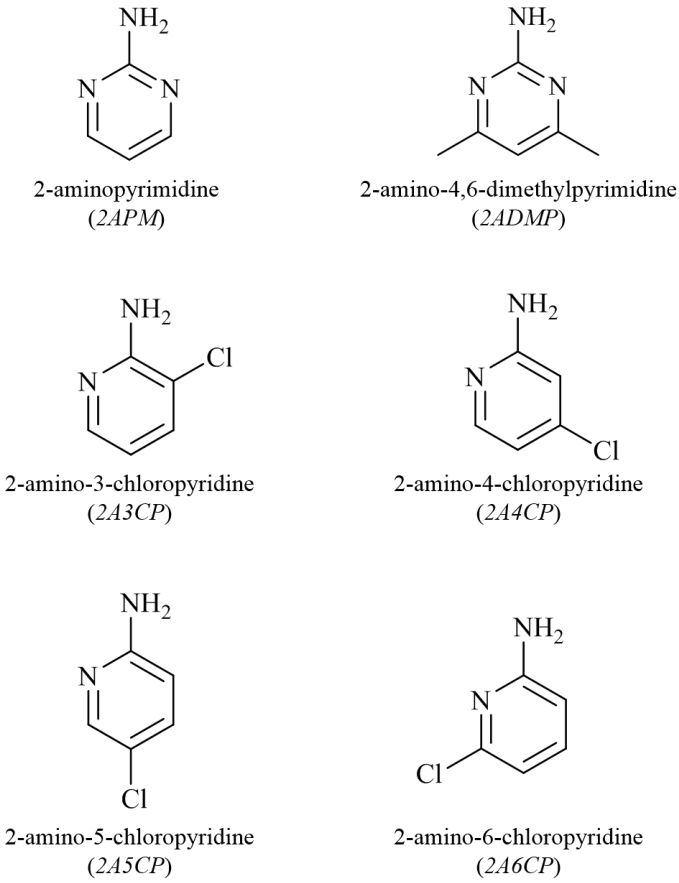

Figure 7. 1 - Molecular structures for the derivatives of *2AP* selected for the co-crystal and salt screening with *NPX*, highlighting 2-aminopyrimidine (*2APM*), 2-amino-4,6-dimethylpyrimdine (*2ADMP*), 2-amino-3-chloropyridine (*2A3CP*), 2-amino-4-chloropyridine (*2A4CP*), 2-amino-5-chloropyridine (*2A5CP*) and 2-amino-6-chloropyridine (*2A6CP*)

This chapter will outline the screening carried out with each of these co-formers with both racemic and enantiopure *NPX*, utilising mechanochemical and solution crystallisation methods, assessing their efficacy and compatibility in the preparation of particular phases. The relationship between the homo and heterochiral phases will be explored, establishing the relationship between the solid state structures at these enantiomeric compositions. This was done primarily through binary phase diagram analysis and exploration of crystalline structures of each of the respective materials.

7.1 Materials of racemic and enantiopure naproxen with 2-aminopyrimidine (*2APM*)

7.1.1 Material screening

Co-crystal and salt screening was conducted by combining both racemic and enantiopure *NPX*, respectively, with the co-former 2-aminopyrimidine (*2APM*). This co-former, obtained as an off-white powder, has only one known polymorphic form (CSD reference: AMPYRM10[200]), with a melting point between 124-126ºC. *2APM*, a symmetrical molecule, has similar functionalities to *2AP*, with both the amine and pyridine groups providing options for hydrogen bond donation and acceptance. However, unlike *2AP*, *2APM* possesses heterocyclic nitrogen atoms, one either side of the amine moiety (ortho), offering additional opportunities to accept hydrogen bonds. This co-former has weak basic properties[201], with a pK_a of 3.81, limiting the likelihood of proton transfer and salt formation with *NPX*.

7.1.1.1 Mechanochemical screening

The initial screening for novel multi-components of *NPX* and *2APM* was carried out through liquid-assisted grinding, where a few drops of ethanol were added to the material in the mortar and pestle. The co-former was ground in either 2:1, 1:1 or 1:2 stoichiometries with either *sNPX* or *rsNPX*. Phase and thermal analysis was then conducted on each of the preparations.

Assessment of the PXRD patterns for the enantiopure samples, shown in Figure 7.2, indicated the formation of a novel phase with respect to that of the starting materials, with particular evidence in the 1:1 and 1:2 mechanochemically combined samples. Whilst the presence of excess starting material was also noted, distinct peaks could be matched to the subsequent simulated pattern generated from SCXRD data of the 1:1 multi-component phase, as crystallised from solution (see Section 7.1.2).

Analysis of the DSC traces (Figure 7.3) highlighted that for the 1:1 preparation an initial melt/recrystallisation occurred approaching 80ºC, after which a minor endothermic event (101-103ºC) was followed by a major endotherm (109-112ºC). This indicated that complexation could be achieved not only through grinding, but with the aid of heating. The subsequent series of endothermic peaks highlighted solid-to-solid transitions for the various multi-component forms of *sNPX* and *2APM*, be that polymorphic or stoichiometric.

The PXRD patterns for the materials derived from the grinding of *rsNPX* and *2APM*, as shown in Figure 7.4, again highlighted the formation of a new phase, consistent across all three stoichiometric combinations. Preparation from the 1:1 stoichiometry, in particular, demonstrated the formation of this novel form free from excess starting material, again matching that taken from SCXRD (see below).

Traces taken from DSC analysis (Figure 7.5) validated that a novel multi-component phase was produced at racemic compositions. The thermal plot for the 1:1 stoichiometric preparation exhibited a small broad thermal event, peaking at 68ºC, followed by a minor endotherm (93-97ºC) and then a major endotherm (110-112ºC). The event occurring at the lower temperature could be attributed to the evaporation of excess solvent, followed immediately by either the melt of an additional impurity, related phase or that of a solid-to-solid transition. The final major endotherm was related to the melting of the novel multi-component racemic form.

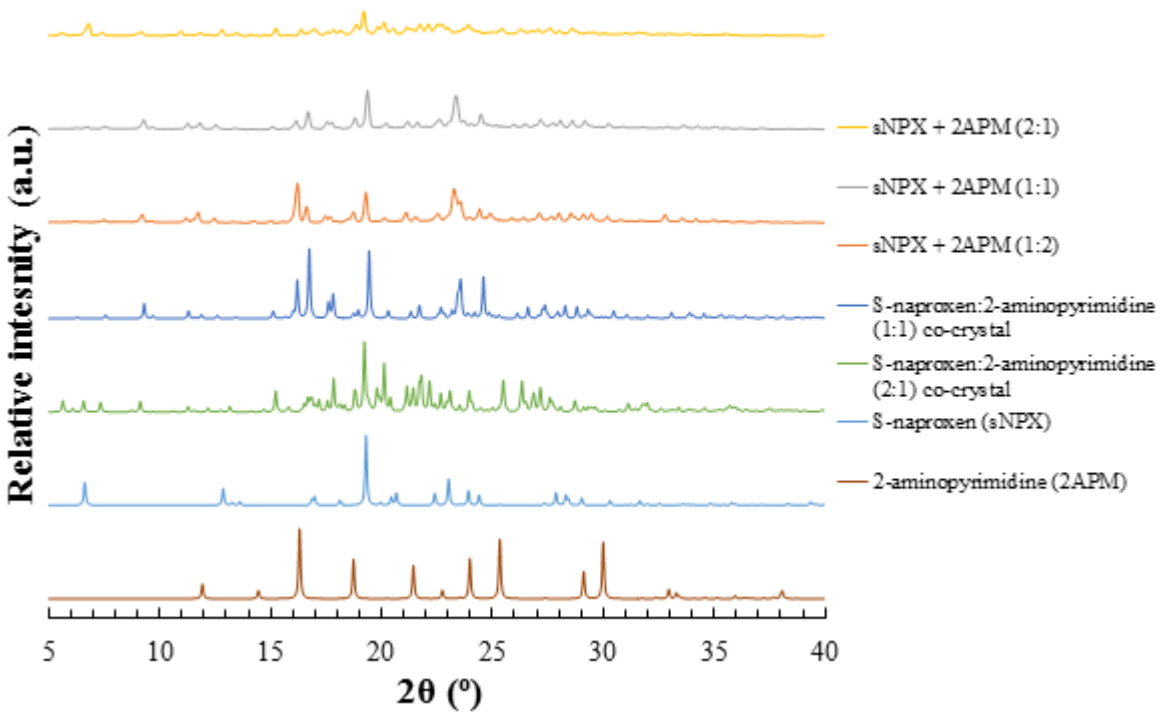

Figure 7. 2 - PXRD patterns from mechanochemically prepared samples of *sNPX* and *2APM* with ethanol, ground in either 2:1, 1:1 or 1:2 molar ratios (top three patterns)

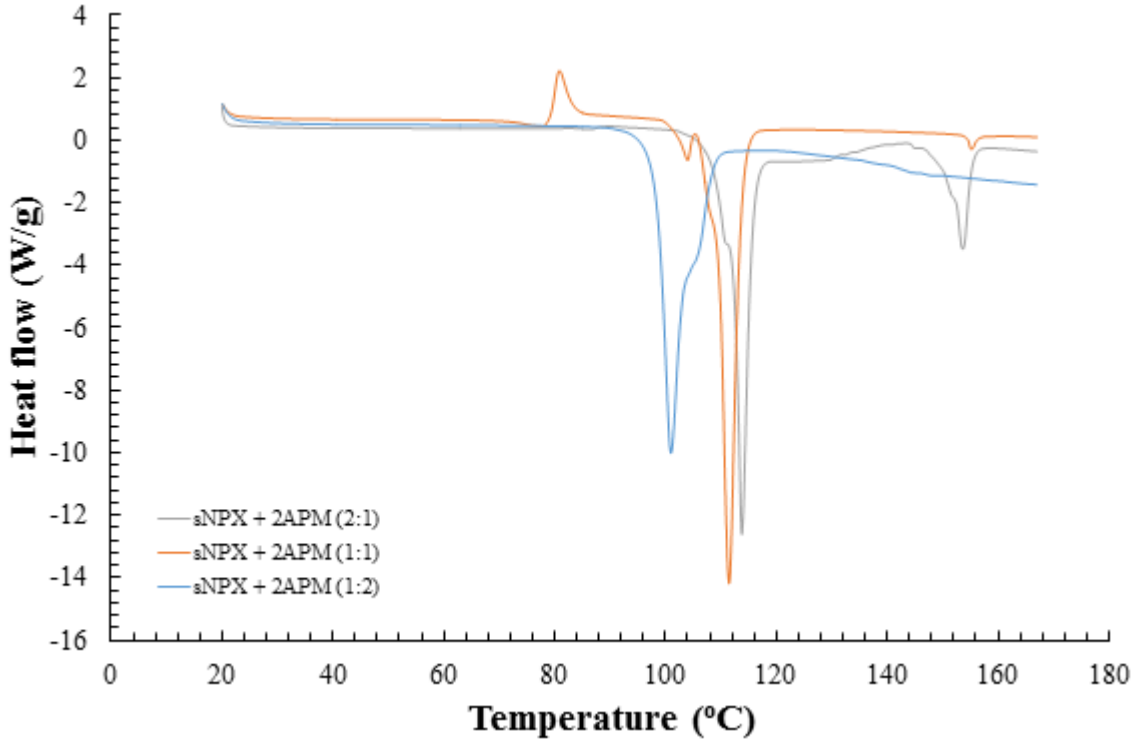

Figure 7. 3 - DSC traces from mechanochemically prepared samples of *sNPX* and *2APM* in ethanol, ground in either 2:1, 1:1 or 1:2 molar ratios

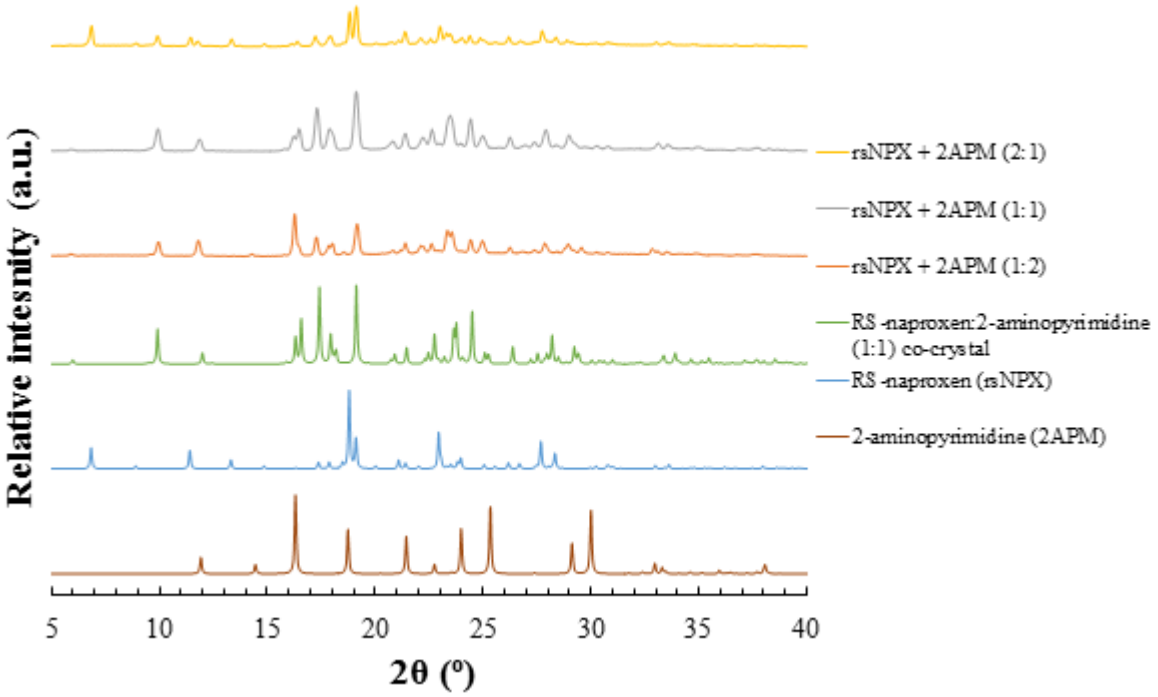

Figure 7. 4 - PXRD patterns from mechanochemically prepared samples of *rsNPX* and *2APM* in ethanol, ground in either 2:1, 1:1 or 1:2 molar ratios (top three patterns)

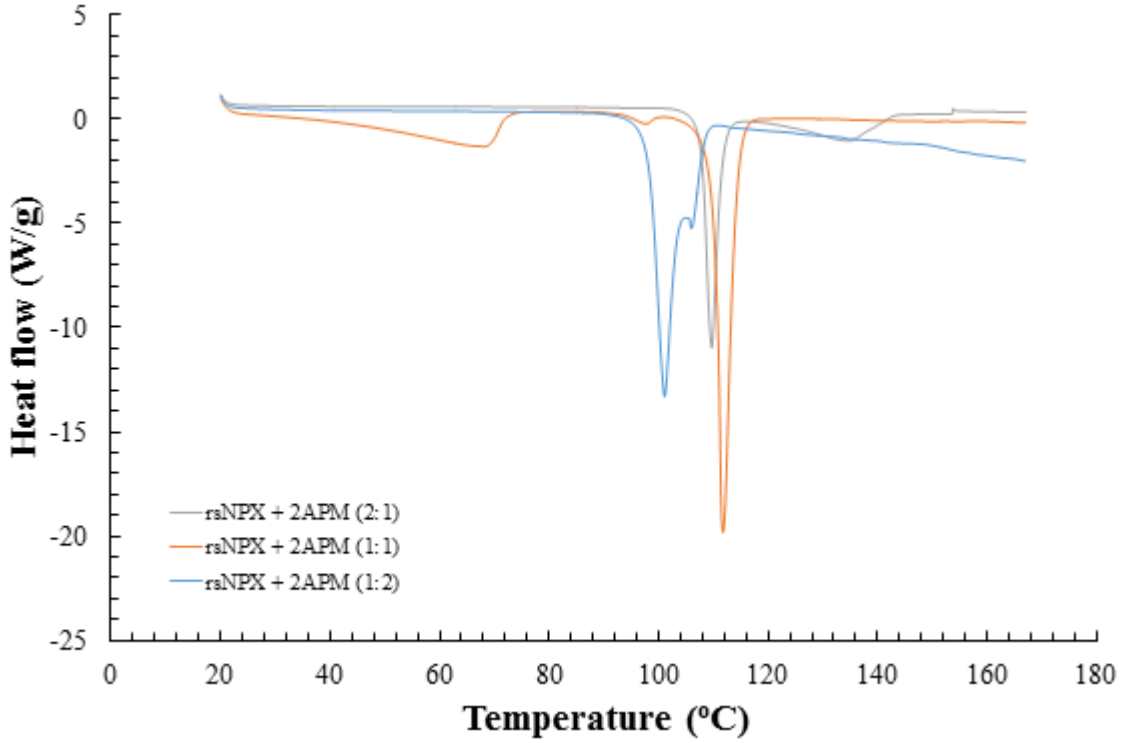

Figure 7. 5 - DSC traces from mechanochemically prepared samples of *rsNPX* and *2APM* in ethanol, ground in either 2:1, 1:1 or 1:2 molar ratios

7.1.1.2 Combined evaporation & cooling crystallisation screening

Initial cooling crystallisations, aided by slow evaporation, were conducted in ethanol, whereby 2:1, 1:1 and 1:2 solutions of *sNPX* and *rsNPX* with *2APM*, respectively, were prepared and placed in a temperature controlled environment, set at 4°C. Figure 7.6 shows the crystals produced from three 1:1 preparations of *NPX* and *2APM*, highlighting those from seeded and non-seeded homochiral solutions, and from heterochiral solutions. For each sample, the resultant crystals were elongated blocks, bordering on needle-like morphologies, with the bulk material of each showing an off-white colour.

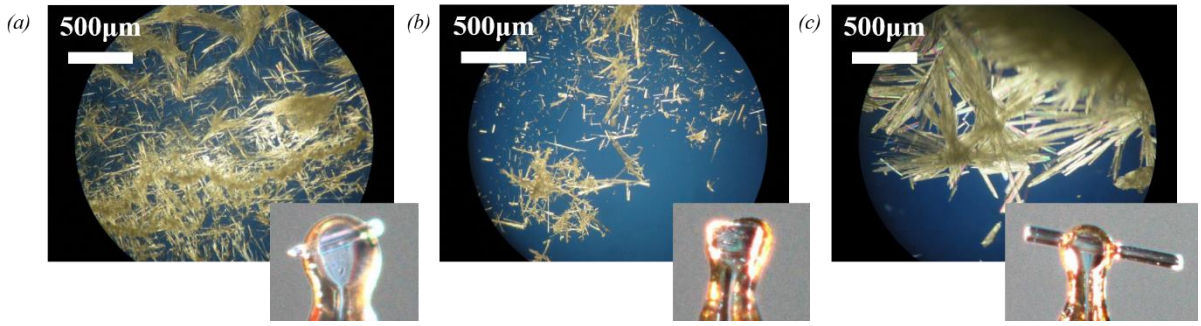

Figure 7. 6 - Microscope and mounted SCXRD images of crystals yielded from (a) 1:1 and (b) seeded 1:1 solutions of *sNPX* and *2APM*, as well as (c) 1:1 solutions with *rsNPX*

HSM thermal analysis was conducted on the crystallites taken from each crystallisation. The images taken for those prepared solely from racemic solutions, as well as those from seeded enantiomerically pure solutions are shown in Appendix A7.1. For these samples, the thermal events observed could be related back to those demonstrated from DSC analysis.

Figure 7.7 shows the crystals taken directly from the unseeded 1:1 combination of *sNPX* and *2APM*. Initial melting occurred prior to 108°C continuing to 115°C, followed by the subsequent melt of further crystallites between 115°C and 119°C. Recrystallisation and crystal growth was then noted, with the crystals being sustained until 150°C, after which further melting was observed. These observations indicated the presence of several novel forms, melting consecutively, followed by the recrystallisation of *sNPX* starting materials.

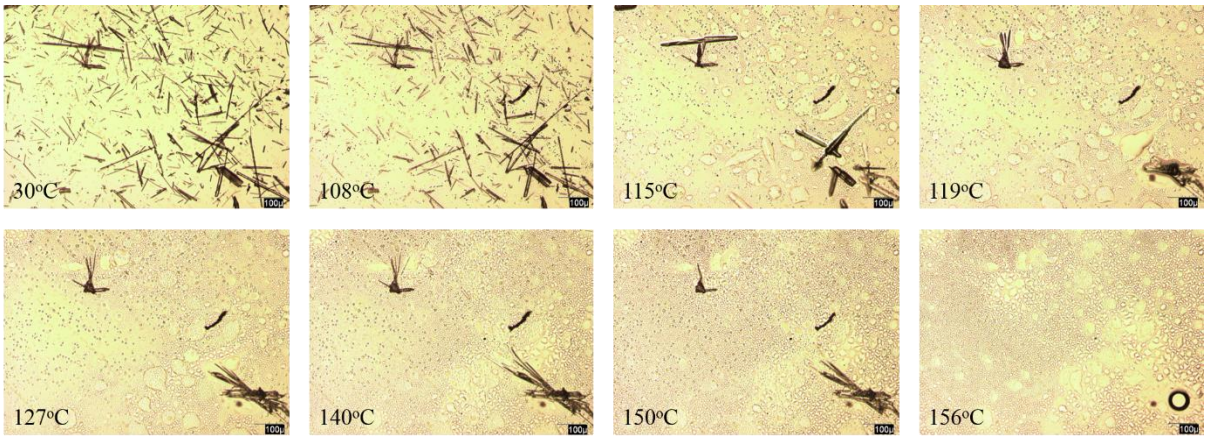

Figure 7. 7 - HSM images of the thermal events attributed to crystals taken from the straight crash cooling of *sNPX* and *2APM* in a 1:1 solution molar ratio (10°C/min & 100µm scale)

Subsequent diffraction experiments with the crystals yielded from the direct cooling of the 1:1 ethanol solution with *sNPX* and *2APM* showed that a new phase was generated when compared to that produced

mechanochemically. This phase was shown to have the API and co-former in a 2:1 stoichiometry, showing that the crystals observed for the corresponding HSM analysis represented a mixture of different crystalline phases. In order to obtain single crystals corresponding to that derived from grinding, a small quantity of mechanochemically prepared seed was added to solutions of the same composition at 4°C. This yielded the necessary crystals required for assessing the structure of the material generated using the mortar and pestle.

7.1.2 Material characterisation

After establishing routes for the initial preparation of the respective racemic and enantiopure phases by both mechanochemical and solution crystallisation, further solid state analysis was conducted to define the phases present in terms of their thermal and structural properties. The analysis used included that of PXRD, DSC and SCXRD. Additional IR analysis was also carried out, the spectra of which can be found in Appendix A7.1.

7.1.2.1 Phase, thermal and spectroscopic analysis

The screening using both mechanochemical and solution crystallisation methods produced three distinct forms; two homochiral multi-component materials and one at racemic compositions. The *sNPX* form obtained from spontaneous nucleation, based upon HSM, exhibited a marginally higher melting point (115-119°C) to that prepared *via* mechanochemistry or seeded crystallisations, indicating slightly stronger interactions within the crystalline structure. Figure 7.8 shows the PXRD patterns of the two stoichiometric co-crystals of *sNPX* and *2APM*, the racemic co-crystal and the individual starting materials (taken from the CSD[150, 171, 200]), whilst thermal data, obtained using DSC, for the two 1:1 co-crystals are highlighted in Figure 7.9. No clear traces could be obtained for the crystals of the initial enantiopure multi-component material derived from the unseeded solution.

Comparison of the two mechanochemically prepared substances at the disparate enantiomeric ratios highlighted distinctly similar melting phenomena, whilst still displaying different diffraction patterns. Further HSM studies using single crystals (see Appendix A7.1) confirmed the melting point of the homochiral co-crystal, but indicated that the racemic had a slightly higher melting point, between 112-116°C. This highlighted the benefits of conducting analysis on single crystal samples and crosschecking against the results obtained from mechanochemically acquired samples. Despite this, the discrete patterns of the two phases indicated the formation of a racemic compound chiral crystalline system, with the interactions in the forms of similar energy.

The IR spectra obtained for the solid-state materials made either *via* mechanochemistry or crash cooling showed similarities in their stretching and vibrational frequencies, indicating the presence of the same functionalities as in the starting materials. However, differences were noted between the carbonyl stretches associated with each of the novel multi-component forms. Whilst the homochiral material collected directly from solution exhibited a major peak with an associated shoulder at 1694 cm^{-1}, that of the mechanochemically obtained materials demonstrated a single and double peak, respectively for the homochiral and racemic phases, occurring at 1685 cm^{-1} and 1645 cm^{-1}. This suggested that upon building the overall structures of the materials, different intermolecular interactions were utilised, involving the carbonyl group.

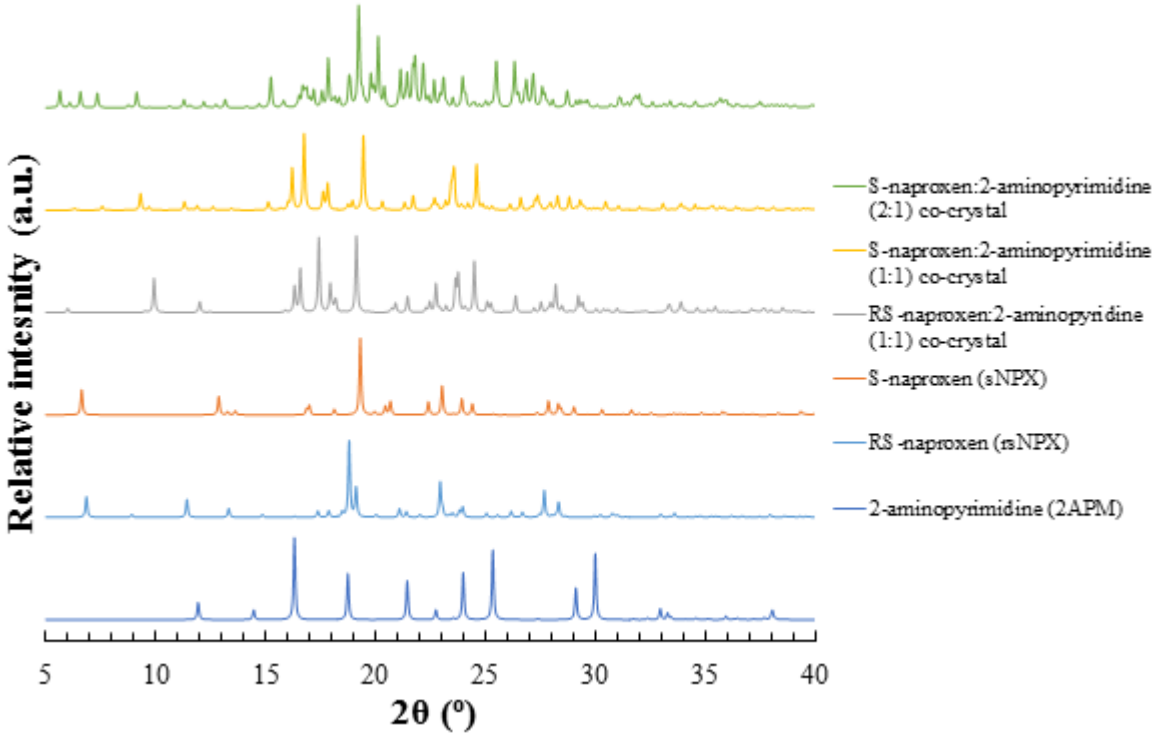

Figure 7. 8 - PXRD patterns of the S-naproxen:2-aminopyrimidine (2:1) & (1:1) co-crystals, the RS-naproxen:2-aminopyrimidine (1:1) co-crystal, as derived from SCXRD data, compared to that of the starting materials

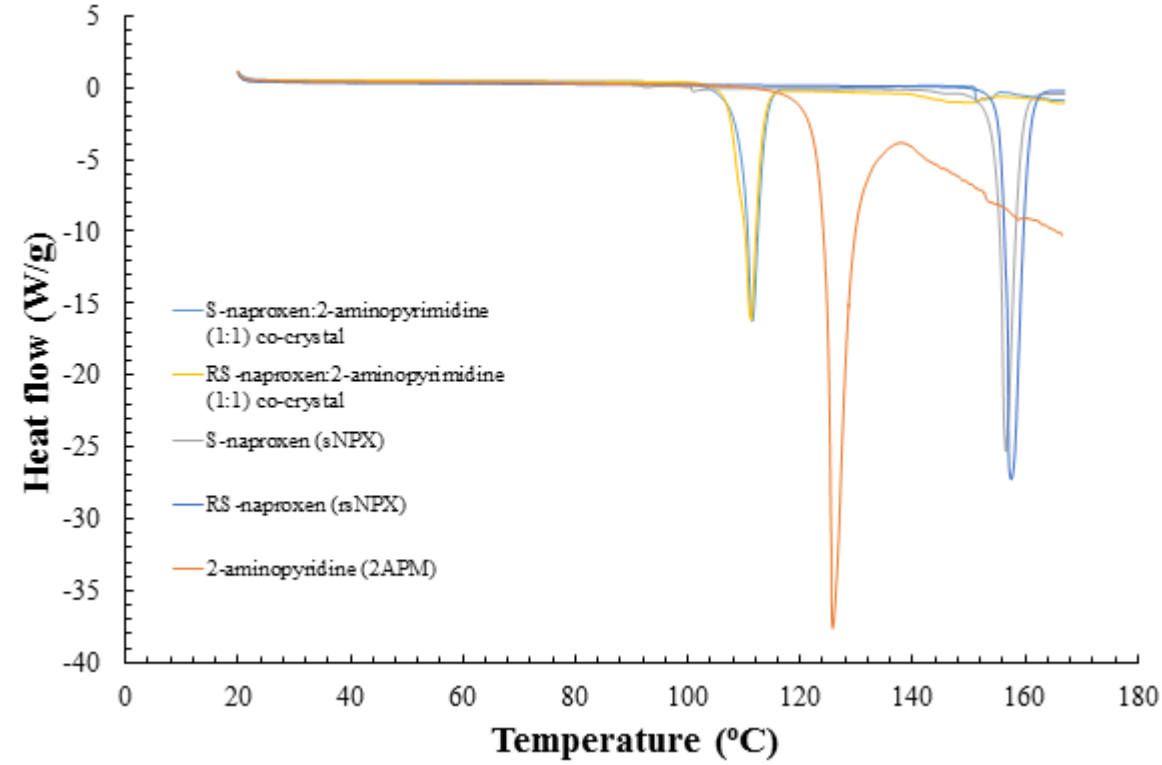

Figure 7. 9 - DSC traces of the S-naproxen:2-aminopyrimidine (1:1) and the RS-naproxen:2-aminopyrimidine (1:1) co-crystals, mechanochemically prepared, compared to that of the starting materials

7.1.2.2 Binary (melting point) phase diagram analysis – Classification of chiral crystalline materials

As highlighted above, the PXRD patterns of the ground samples and those generated from SCXRD for individual single crystals showed sufficient differences to indicate the existence of two discrete co-crystalline phases at racemic and enantiopure compositions of *NPX*, when combined with *2APM*. Using DSC, the thermal events of different mechanochemically prepared samples of the API and co-former were recorded with the enantiomeric mole fraction of *rNPX* to *sNPX* increased from racemic to enantiopure, with respect to the S-enantiomer. From these, a binary phase diagram was made, as shown in Figure 7.10. The supporting DSC traces and PXRD patterns for each of the individual compositions can be found in Appendix A7.1.

The phases form defined regions, highlighting the temperature and composition ranges at which only either the racemic or homochiral phases remained solid upon heating. The *rsNPX-2APM* phase was shown to be solely stable between the molar compositions of 0.3 to 0.7, whilst the *sNPX-2APM* was stable at higher molar compositions of *sNPX*, at fractions greater than 0.7. In addition, a eutectic melt was also observed over the enantiomeric range, between 106-107°C, with the single eutectic phenomenon being most pronounced at the 0.7 mole fraction. Due to the presence of the eutectic event and the evidence of the two clear regions of stability for the two phases, the relationship between the mechanochemically prepared materials of *NPX* and *2APM* can be definitively described as a racemic compound forming system, similar to that of single-component *NPX*. Therefore, this multi-component phase could not be utilised for preferential crystallisation.

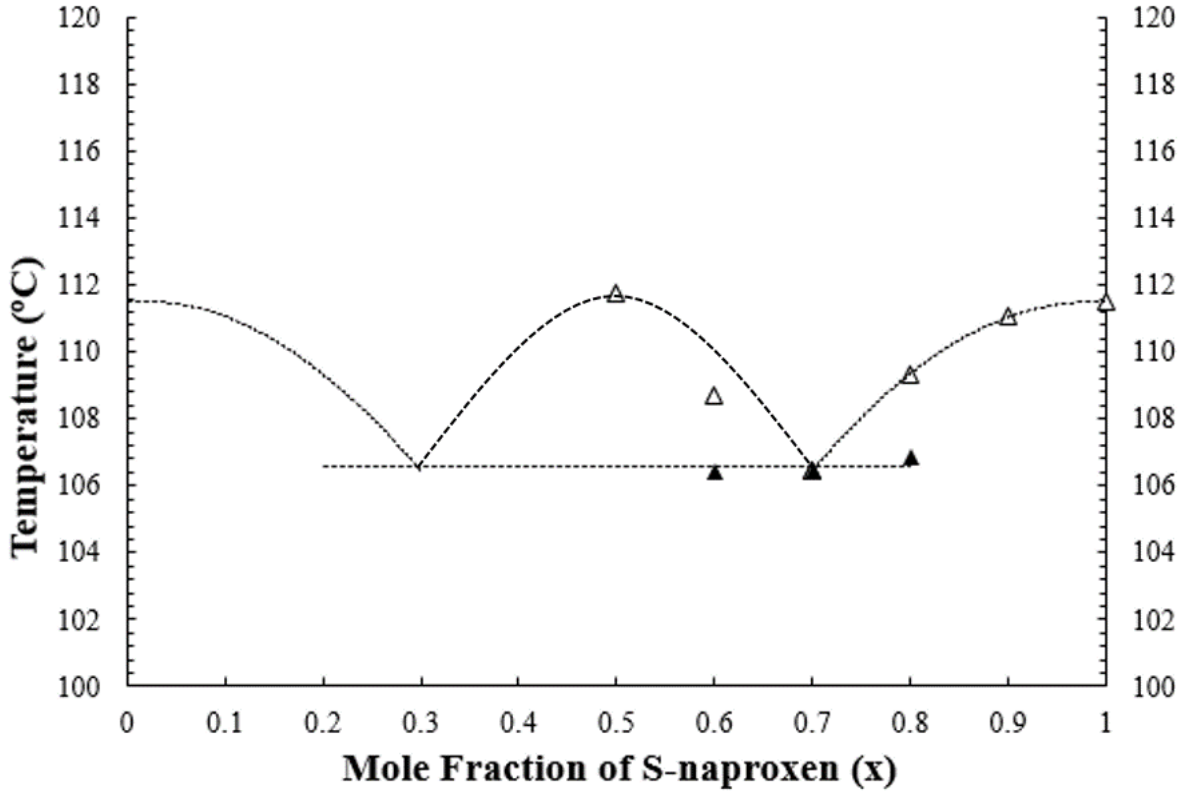

Figure 7. 10 - Binary (melting) point phase diagram, with changing enantiomeric composition of *rNPX* and *sNPX*, for the 1:1 co-crystals incorporating the co-former *2APM*, highlighting the liquidus (Δ) and the eutectic (▲) points

However, upon forming their respective multi-component forms, the stability range over which the racemic solid is prevalent, was reduced when compared to that of single component *NPX*. This

emphasises the ability of multi-component materials to manipulate properties, with the potential of working towards a racemic conglomerate.

7.1.2.3 Crystallography – Crystal structure analysis

Once crystallised *via* cooling crystallisation, crystals of sufficient quality were selected, mounted and assessed in terms of their crystalline structure using SCXRD. For all hydrogen bonding information for the three co-crystalline forms, see Appendix A7.1. The corresponding CIF files (3-5) can be found on the accompanying CD-ROM.

Shown in Figure 7.11, the crystal structure of the crystal derived from the combined crash cooling and evaporative crystallisation of *sNPX* and *2APM* in a 1:1 molar ratio in ethanol confirmed the formation of novel phase between the two starting materials. However, rather than crystallising in a 1:1 ratio within the crystal lattice, the resultant co-crystal was shown to form in a 2:1 stoichiometry between the API and co-former. Whilst through X-ray diffraction data the ability to definitively define the location of hydrogen atoms is limited, this structure showed no evidence of proton transfer, suggesting the formation of a co-crystal, as opposed to a salt. This material can, hence, be denoted as a S-naproxen:2-aminopyrimidine (2:1) co-crystal.

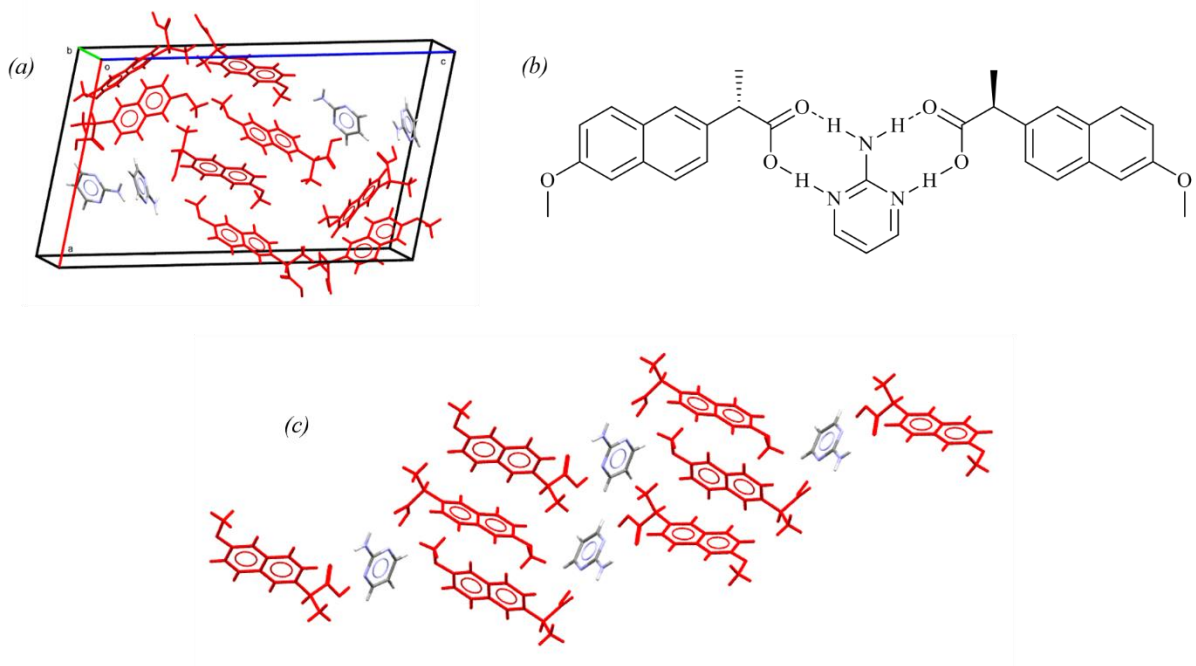

Figure 7. 11 - Crystal structure of the S-naproxen:2-aminopyrimidine (2:1) co-crystal, highlighting (a) the unit cell, (b) hydrogen bonding synthon and (c) packing arrangement (*sNPX* in red)

The molecules of *sNPX* and *2APM* crystallised in the non-centrosymmetric monoclinic $P2_1$ space group, with each unit cell (parameters outlined in Table 7.1) consisting of four sets of *sNPX* and *2APM* (2:1) units. As such, each asymmetric unit could be made up from two of these units, giving rise to *Z*' value of 2. The key interaction unit was held together through hydrogen bonding, whereby the *2APM* molecule bridges between the two *sNPX* entities, forming a *sNPX:2APM:sNPX* motif. Each of the individual API molecules forms a $R_2^2(8)$ synthon with the central co-former, with the amine and hydroxyl groups of *2APM* and *sNPX* acting as hydrogen bonding donors to the accepting carboxyl and pyridine groups, respectively. These units then interlock and stack in order to build up the whole crystalline assembly, giving rise to channels of oppositely orientated *sNPX* molecules.

Table 7. 1 - Unit cell and crystallographic parameters for the S-naproxen:2-aminopyrimidine (2:1) co-crystal

Material	**S-naproxen:2-aminopyrimidine (2:1) co-crystal**
Empirical formula	$C_{32}H_{33}N_3O_6$
Formula weight	555.61
Temperature (K)	150.01(10)
Crystal system	monoclinic
Space group	$P2_1$
***a* (Å)**	16.9054(4)
***b* (Å)**	5.70540(10)
***c* (Å)**	29.5031(7)
***α* (°)**	90
***β* (°)**	100.160(2)
***γ* (°)**	90
Volume (Å^3)	2801.01(11)
Z*, *Z'	4, 2
ρ_{calc} (g/cm^3)	1.318
μ (mm^{-1})	0.749
F(000)	1176.0
Crystal size (mm^3)	0.261 × 0.057 × 0.033
Radiation	CuKα (λ = 1.54184)
2Θ range for data collection (°)	6.086 to 140.114
Index ranges	$-19 \leq h \leq 20$, $-6 \leq k \leq 6$, $-29 \leq l \leq 35$
Reflections collected	19107
Independent reflections	10548 [R_{int} = 0.0329, R_{sigma} = 0.0475]
Data/restraints/parameters	10548/9/768
Goodness-of-fit on F^2	1.061
Final R indexes [I>=2σ (I)]	R_1 = 0.0428, wR_2 = 0.0964
Final R indexes [all data]	R_1 = 0.0514, wR_2 = 0.1015
Largest diff. peak/hole (e Å^{-3})	0.21/-0.19
Flack parameter	0.02(10)

In contrast, the crystals prepared *via* the seeding of 1:1 ethanol solutions with mechanochemically prepared preparations of *sNPX* and *2APM* yielded a different crystalline form. Structural analysis demonstrated the formation of another new phase, but in this case, the homochiral form of the API forms interactions with the co-former in a 1:1 relationship (Figure 7.12). The two molecular moieties crystallised in an orthorhombic $P2_12_12_1$ space group, with the unit cell possessing eight molecular units of *sNPX* and *2APM* in a 1:1 molar ratio. Thus, the asymmetric unit was deemed to consist of sets of two interaction motifs ($Z' = 2$). Similarly to the 2:1 co-crystal, the key interaction motifs formed from the hetero-dimerised $R_2^2(8)$ interaction between the amine and pyridine groups of the co-former molecule and the carboxylic acid group of the homochiral API. However, unlike for the stoichiometric variant, the symmetrical nature of the *2APM* molecules was not exploited, leaving a pyridine functionality devoid of hydrogen bonding. Instead, two dimerised interaction units were connected together through a further ring, where the second N-H amine constituted a hydrogen bond donor, forming a contact with carboxyl group associated with the other dimer. Taking into account all the interactions, this connecting ring can be described as a $R_4^2(8)$ hydrogen bonding synthon, generating an overall dimer of dimers. The zig-zagged configuration of these units allowed for stacking, forming distinct channels of homochiral API.

Upon assessment of the crystals obtained from racemic solutions, crystallographic analysis demonstrated the formation of a further multi-component material, where both enantiomeric forms of the API were shown to crystallise within the same monoclinic $P2_1/c$ lattice, as shown and detailed in Figure 7.13 and Table 7.3. Here, each asymmetric unit was made up of the *NPX* and *2AP* molecules in a 1:1 ratio, with the unit cell reflecting both chiral forms. As for the related homochiral phase, the racemic form was shown to allow for the API and co-former to crystallise in a 1:1 relationship, with no proton transfer being exhibited. As a result, this phase can be described as a RS-naproxen:2-aminopyrimidine (1:1) co-crystal.

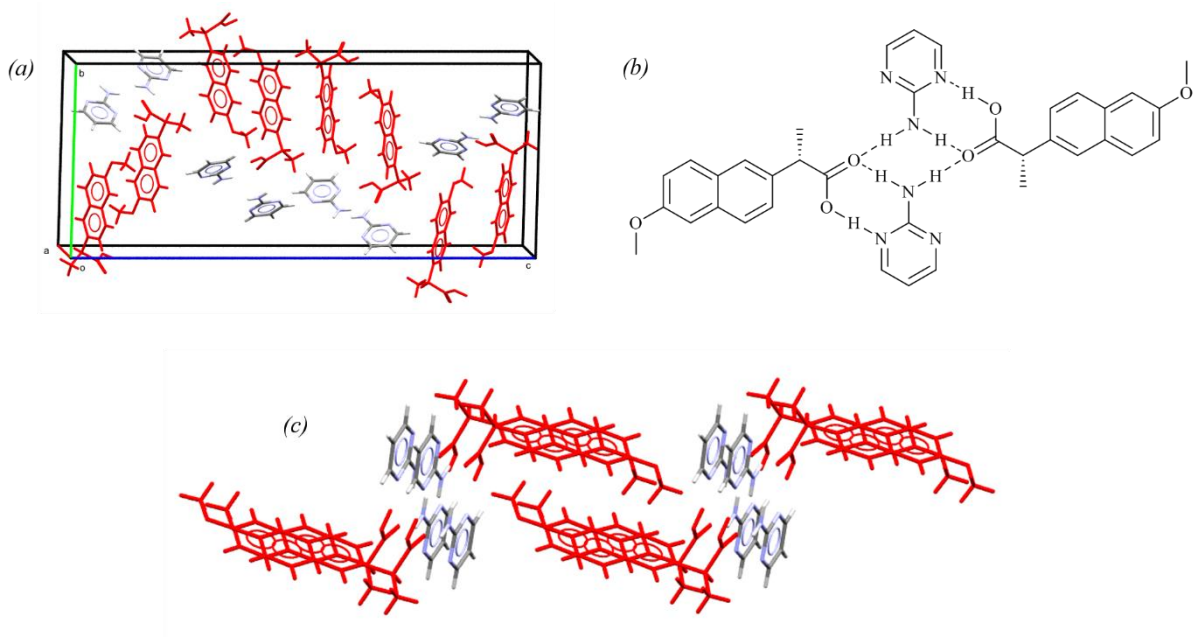

Figure 7. 12 - Crystal structure of the S-naproxen:2-aminopyrimidine (1:1) co-crystal, highlighting (a) the unit cell, (b) hydrogen bonding synthon and (c) packing arrangement (*sNPX* in red)

Table 7. 2 - Unit cell and crystallographic parameters for the S-naproxen:2-aminopyrimidine (1:1) co-crystal

Material	**S-naproxen:2-aminopyrimidine (1:1) co-crystal**
Empirical formula	$C_{18}H_{19}N_3O_3$
Formula weight	325.36
Temperature (K)	149.9(4)
Crystal system	orthorhombic
Space group	$P2_12_12_1$
***a* (Å)**	5.93398(16)
***b* (Å)**	15.2065(5)
***c* (Å)**	36.4930(7)
***α* (°)**	90
***β* (°)**	90
***γ* (°)**	90
Volume (Å^3)	3292.96(15)
Z, Z'	8, 2
ρ_{calc} (g/cm^3)	1.313
μ (mm^{-1})	0.744
F(000)	1376.0
Crystal size (mm^3)	0.472 × 0.083 × 0.06
Radiation	CuKα (λ = 1.54184)
2Θ range for data collection (°)	6.296 to 140.104
Index ranges	$-7 \leq h \leq 6$, $-15 \leq k \leq 18$, $-31 \leq l \leq 44$
Reflections collected	12767
Independent reflections	6232 [R_{int} = 0.0364, R_{sigma} = 0.0522]
Data/restraints/parameters	6232/2/442
Goodness-of-fit on F^2	1.050
Final R indexes [I>=2σ (I)]	R_1 = 0.0477, wR_2 = 0.1098
Final R indexes [all data]	R_1 = 0.0604, wR_2 = 0.1191
Largest diff. peak/hole (e Å^{-3})	0.19/-0.21
Flack parameter	-0.1(2)

This racemic co-crystal showed structural similarities to that of the 1:1 enantiopure phase, with both forms exploiting the same dimer of dimers interaction motif. In the racemic case, the respective API molecules in the motif possessed opposing chirality. This likeness in intermolecular interaction goes

some way to explaining the minor differences observed in their respective melting temperatures. The relative stability of these phases can also be highlighted through the similarities in their calculated packing densities. The homochiral and racemic co-crystals expressing densities of 1.313 g/cm^3 and 1.311 g/cm^3, respectively.

Despite this, as shown in Figure 7.14, the overall packing arrangement of these units was distinctly different. Whilst the homochiral structure showed alternating periods of API and co-former, the racemic form demonstrates continuous channels of *NPX* and *2APM*, with the repeated alternations between chiral forms. This difference in the overall packing assembly of the two 1:1 co-crystals, emphasised the formation of two discrete phases at the different enantiomeric compositions and therefore the formation of a racemic compound system.

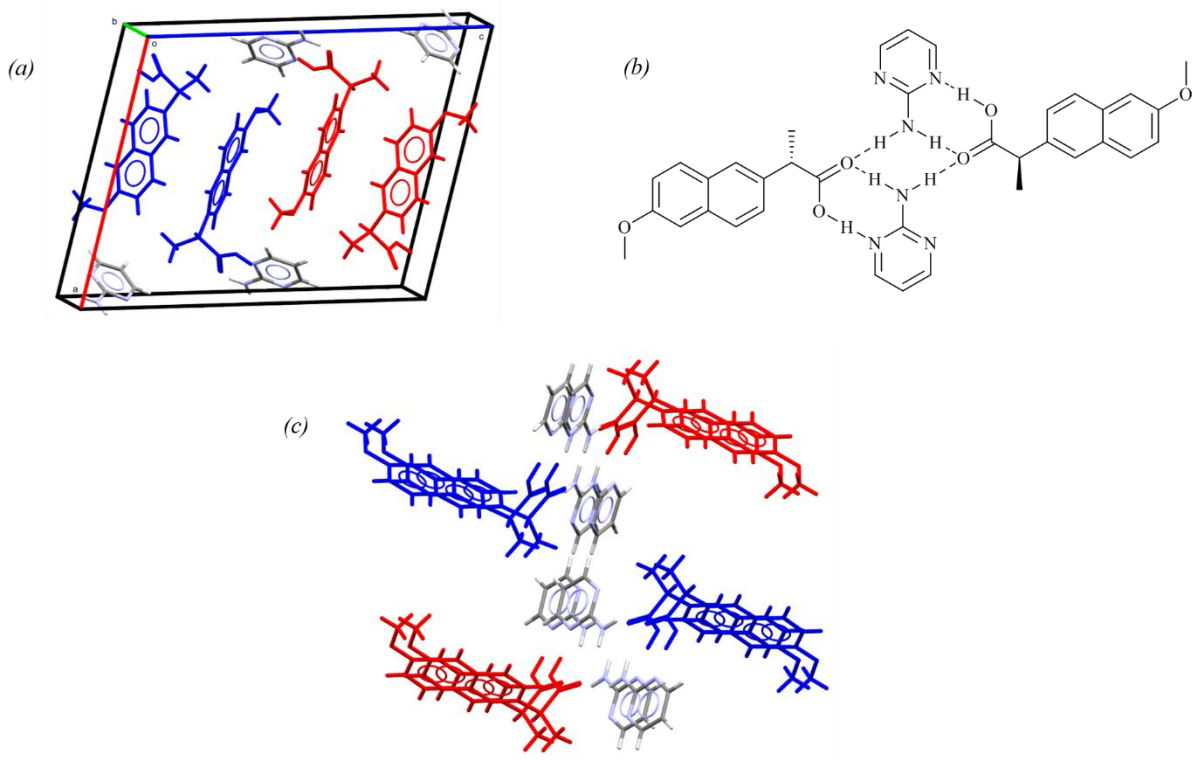

Figure 7. 13 - Crystal structure of the RS-naproxen:2-aminopyrimidine (1:1) co-crystal, highlighting (a) the unit cell, (b) hydrogen bonding synthon and (c) packing arrangement (*sNPX* in red, *rNPX* in blue)

Table 7. 3 - Unit cell and crystallographic parameters for the RS-naproxen:2-aminopyrimidine (1:1) co-crystal

Material	**RS-naproxen:2-aminopyrimidine (1:1) co-crystal**
Empirical formula	$C_{18}H_{19}N_3O_3$
Formula weight	325.36
Temperature (K)	149.9(4)
Crystal system	monoclinic
Space group	$P2_1/c$
***a* (Å)**	15.2222(4)
***b* (Å)**	5.84020(10)
***c* (Å)**	19.1479(5)
***α* (°)**	90
***β* (°)**	104.399(2)
***γ* (°)**	90
Volume (Å^3)	1648.79(7)
Z, Z'	4, 1
ρ_{calc} (g/cm^3)	1.311
μ (mm^{-1})	0.743
F(000)	688.0
Crystal size (mm^3)	0.134 × 0.087 × 0.049
Radiation	CuKα (λ = 1.54184)
2Θ range for data collection (°)	5.994 to 140.14
Index ranges	$-15 \leq h \leq 18$, $-7 \leq k \leq 6$, $-23 \leq l \leq 19$
Reflections collected	9917
Independent reflections	3127 [R_{int} = 0.0198, R_{sigma} = 0.0205]
Data/restraints/parameters	3127/1/223
Goodness-of-fit on F^2	1.041
Final R indexes [I>=2σ (I)]	R_1 = 0.0394, wR_2 = 0.1007
Final R indexes [all data]	R_1 = 0.0470, wR_2 = 0.1061
Largest diff. peak/hole (e Å^{-3})	0.29/-0.22
Flack parameter	N/A

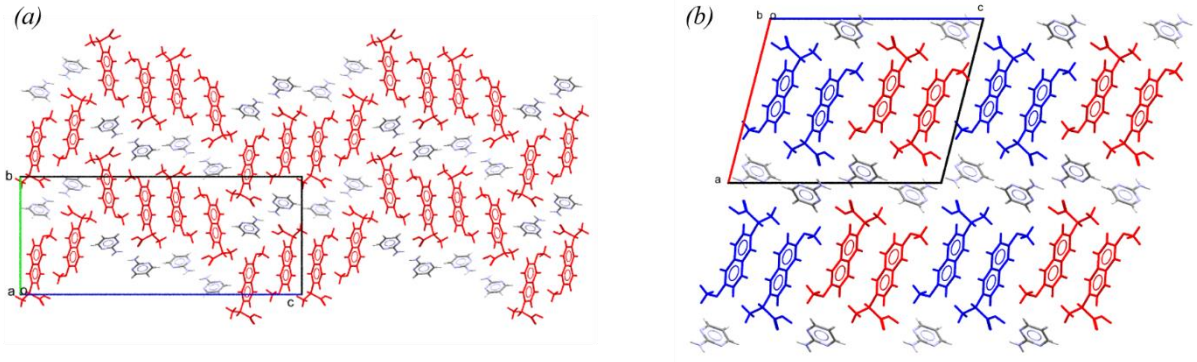

Figure 7. 14 - A comparison of the extended packing arrangements of the (a) S-naproxen and (b) RS-naproxen:2-aminopyrimidine (1:1) co-crystals

7.2 Materials of racemic and enantiopure naproxen with 2-amino-4,6-dimethylpyrimidine (*2ADMP*)

7.2.1 Material screening

The next co-former used in salt and co-crystal screening was 2-amino-4,6-dimethylpyrimidine (*2ADMP*). Related to *2APM*, *2ADMP* is a derivative of *2AP*, exhibiting two pyridine groups either side of the amine functionality. In addition, the co-former possesses methyl groups about the aromatic ring, adding to the steric bulk of the molecule. *2ADMP* has only one known polymorphic form (CSD reference: NEQLOM[202]), exhibiting a melting point between 151-153ºC, and was obtained as an off-white powder. As derived from literature[203], the pK_a for this material was taken as 4.4. Due to the minimal acidity difference, it was deemed unlikely that, upon combination, *NPX* and *2APM* would undergo salt formation.

7.2.1.1 Mechanochemical screening

Initial grinding experiments were conducted using *sNPX* and *2ADMP* in 2:1, 1:1 or 1:2 molar ratios with the aid of a mortar and pestle. These were initially carried out using no solvent (Appendix A7.2), but with no novel materials shown to be evident, minimal amounts of ethanol were subsequently added to the grinding mix. The PXRD patterns and DSC traces of those samples prepared with the assistance of solvent can be found in Figures 7.15 and 7.16, respectively.

Upon combining the two starting components in equal quantities, phase analysis conducted by PXRD highlighted the formation of a new phase, distinct from the patterns of the starting material. Little or no excess starting material was noted, suggesting the formation of a 1:1 multi-component form in high purity. By comparing with the diffraction pattern simulated from SCXRD data (see Section 7.2.2), there was significant likeness to confirm that liquid-assisted mechanochemistry was a reliable method of generating the homochiral multi-component phase. Thermal analysis of the 1:1 preparation showed only one exothermic event between 139ºC and 141ºC, confirming the direct formation of a single novel phase through liquid-assisted grinding.

Likewise, mechanochemical preparations of *rsNPX* with *2ADMP* were also made in the same molar ratios, either neat (Appendix A7.2) or with ethanol. When the two starting components were ground in equimolar quantities with a few drops of ethanol, phase analysis (Figure 7.17) again highlighted a PXRD pattern of sufficient difference to that of the raw starting materials, so as to suggest the formation of another novel multi-component phase. Evidence taken from DSC analysis (Figure 7.18) supported this finding, with the 1:1 preparation showing a minor endotherm (124-130ºC) followed by a significant thermal phenomenon between 153ºC and 155ºC. These were taken as a eutectic event between the *NPX* and *2ADMP*, and the melting point of a novel phase, respectively.

From this initial mechanochemical screening, novel multi-component crystalline materials were shown to have been made consistently with a high degree of purity *via* this technique. In contrast, the neat grinding with the two different enantiomeric compositions was shown to have little or no success in the preparation of such complexes, with only the starting materials evident from the initial phase analysis. Preparation of the novel phases could be achieved, in each case, upon heating, with the DSC traces for each enantiomeric composition showing the expected melting features. To date, no further evidence has been produced to prove the existence any further crystalline forms.

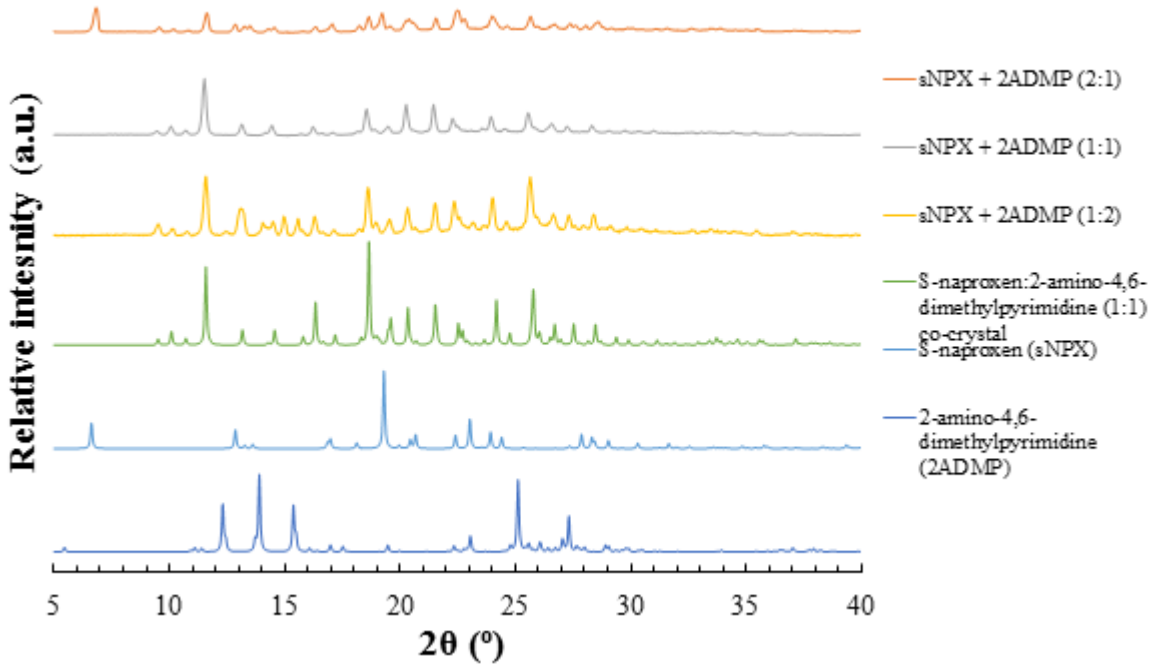

Figure 7. 15 - PXRD patterns from mechanochemically prepared samples of *sNPX* and *2ADMP* in ethanol, ground in either 2:1, 1:1 or 1:2 molar ratios (top three patterns)

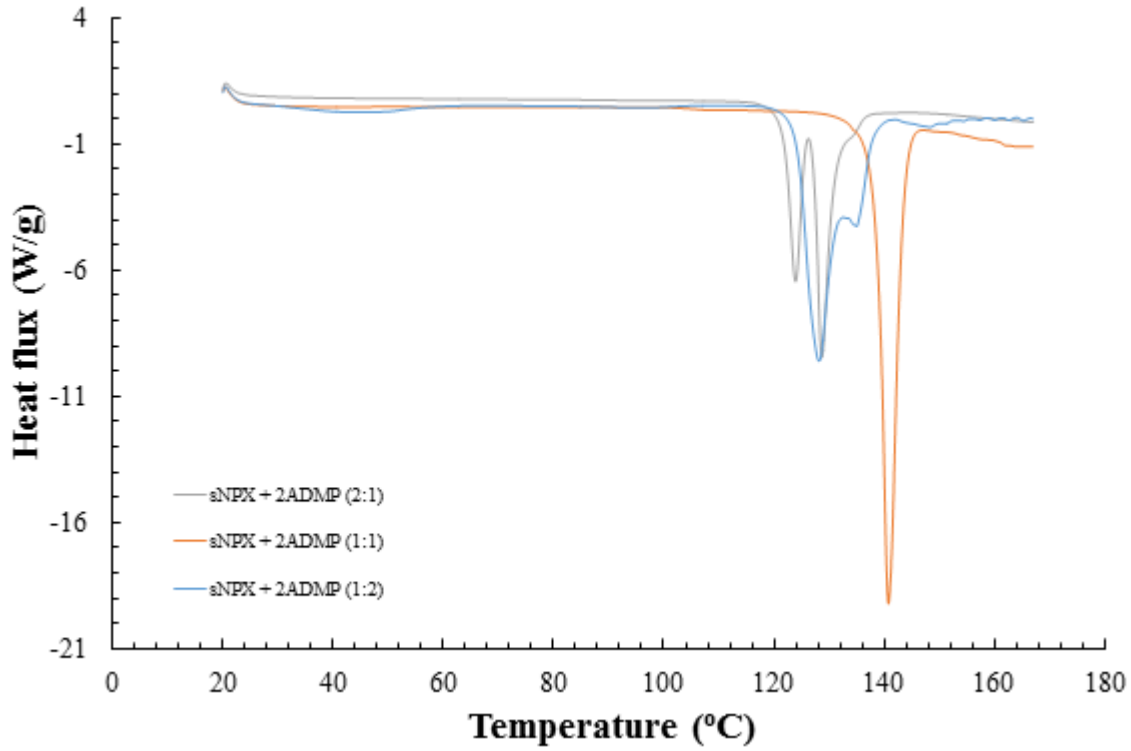

Figure 7. 16 - DSC traces from mechanochemically prepared samples of *sNPX* and *2ADMP* in ethanol, ground in either 2:1, 1:1 or 1:2 molar ratios

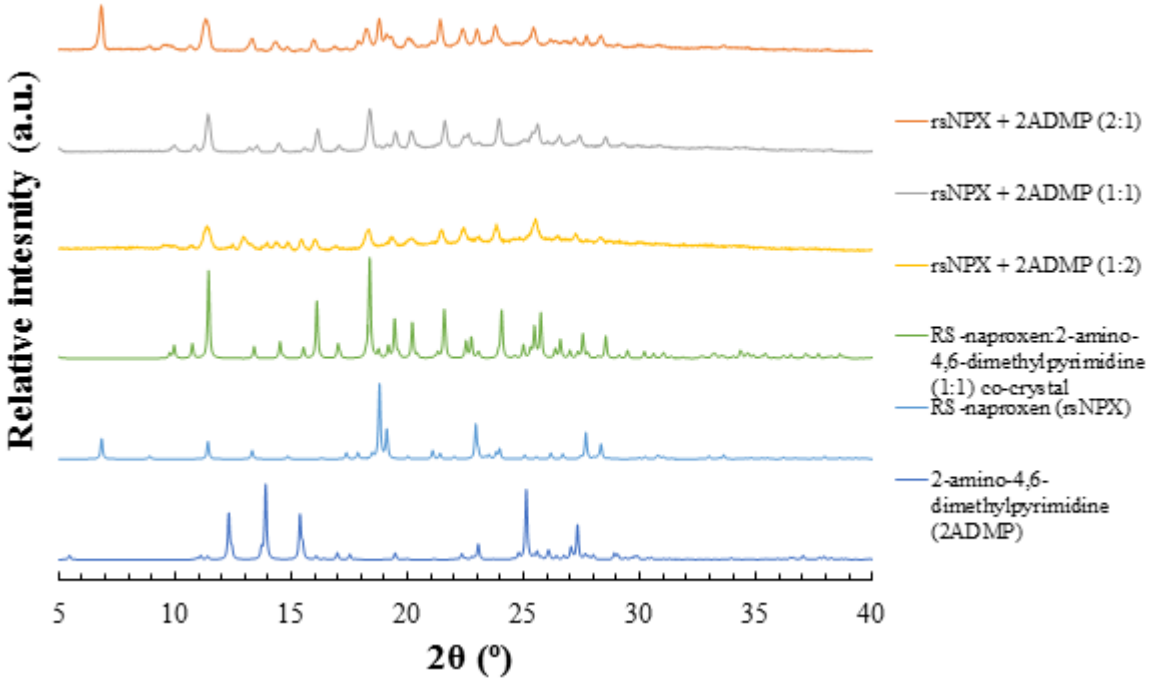

Figure 7. 17 - PXRD patterns from mechanochemically prepared samples of *rsNPX* and *2ADMP* in ethanol, ground in either 2:1, 1:1 or 1:2 molar ratios (top three patterns)

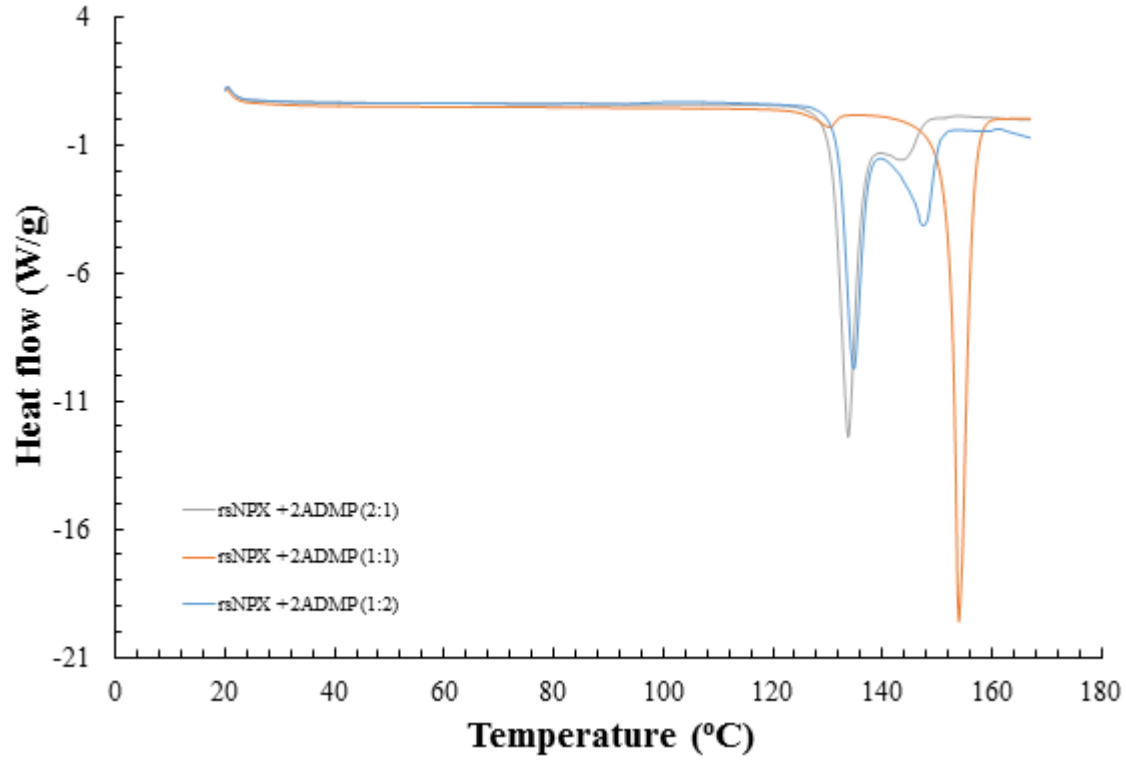

Figure 7. 18 - DSC traces from mechanochemically prepared samples of *rsNPX* and *2ADMP* in ethanol, ground in either 2:1, 1:1 or 1:2 molar ratios

7.2.1.2 Combined evaporation & cooling crystallisation screening

Single crystals were grown from 1:1 API to co-former saturated solutions of ethanol, for racemic and enantiopure *NPX*, respectively, through the combined crash cooling and evaporative crystallisation technique outlined previously. Both multi-component forms showed individual off-white crystals with needle morphologies (Figure 7.19). Individual crystals were selected for structural analysis and for each enantiomeric composition were shown to be the same phase as those obtained from mechanochemical means.

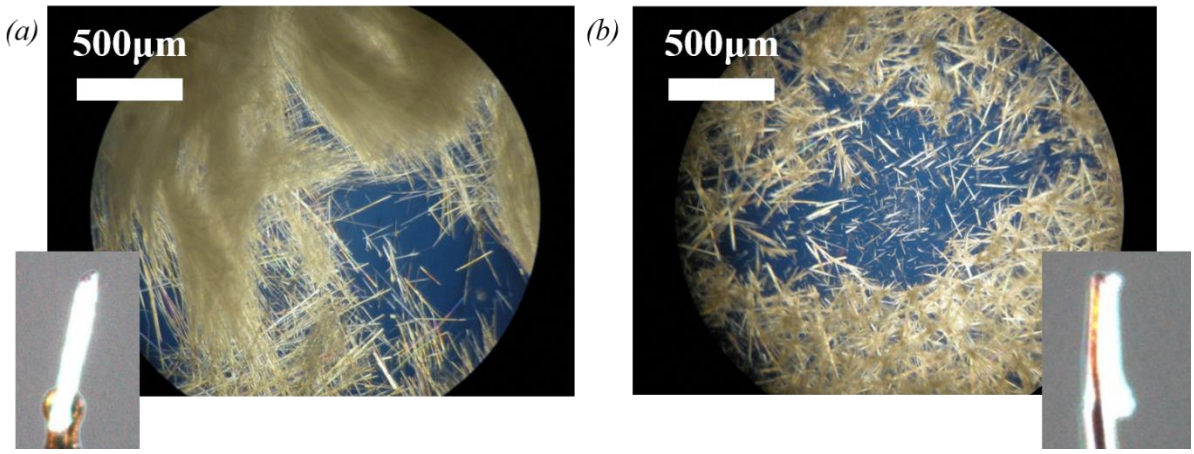

Figure 7. 19 - Microscope and mounted SCXRD images of crystals yielded from 1:1 ethanol solutions of (a) *sNPX* and (b) *rsNPX* with *2ADMP*, respectively

Crystals were also selected, from each enantiomeric solution, for HSM analysis (see Appendix A7.2) as a comparison to the thermal phenomena found for the mechanochemical samples from DSC. Whilst overall the same melting characteristics were found for both chiral multi-component crystals, the actual melting range was found to be over a broader range when compared to DSC, particularly for the racemic crystals. An initial darkening of the crystal was noted as the temperature approaches 115ºC, with the final melting occurring from 145ºC to 154ºC. These observations can be accounted for through an appreciation of how the samples were prepared for HSM when compared to DSC, with particular focus on the use of individual single crystals being placed in an unsealed environment.

7.2.2 Material characterisation

The results of the initial mechanochemical and solution crystallisation screenings demonstrated the reproducibility in preparation of both the homochiral and racemic multi-component phases. The nature of these materials were compared and contrasted with further characterisation using PXRD, DSC, SCXRD and phase analysis. IR spectra were also collected for the two materials, highlighting a number of similarities (Appendix A7.2).

7.2.2.1 Phase, thermal and spectroscopic analysis

PXRD patterns were simulated from the SCXRD structures (150 K) for the racemic and enantiopure multi-component were compared against the respective starting materials, as shown in Figure 7.20. This showed that *2ADMP* formed novel complexes with both *sNPX* and *rsNPX*. The patterns of both materials showed striking similarities to each other, possessing many of the same peaks. Despite certain shifts (e.g. the peak corresponding to the $11\bar{1}$ plane moving from 18.3° to 18.7° with increasing enantiopurity), it could be said that two phases appeared to be very similar and were intrinsically related.

Despite this, thermal analysis highlighted certain disparities between these crystalline forms. As shown in Figure 7.21, the melting point of the homochiral multi-component form (139°C-141°C) was more than 13°C lower than that of the material consisting of *rsNPX* and the co-former (153°C-155°C). In isolation, this difference could suggest the formation of another racemic compound, but owing to the observations made from X-ray diffraction, racemic solid solution was also possible, with the materials towards racemic compositions expressing greater stability to melting in the solid state.

The nature of the bonding and intermolecular interactions in the two multi-component phases was also assessed using the IR spectroscopy. As highlighted from their respective spectra, the vibrational and stretching modes associated with the homo and heterochiral forms were similar, indicating similarities between crystalline forms. This was particularly evident upon assessing the peaks associated with carbonyl functionality, where, in both cases, two peaks were observed from 1700-1660 cm^{-1}. This supports the notion of a racemic solid solution.

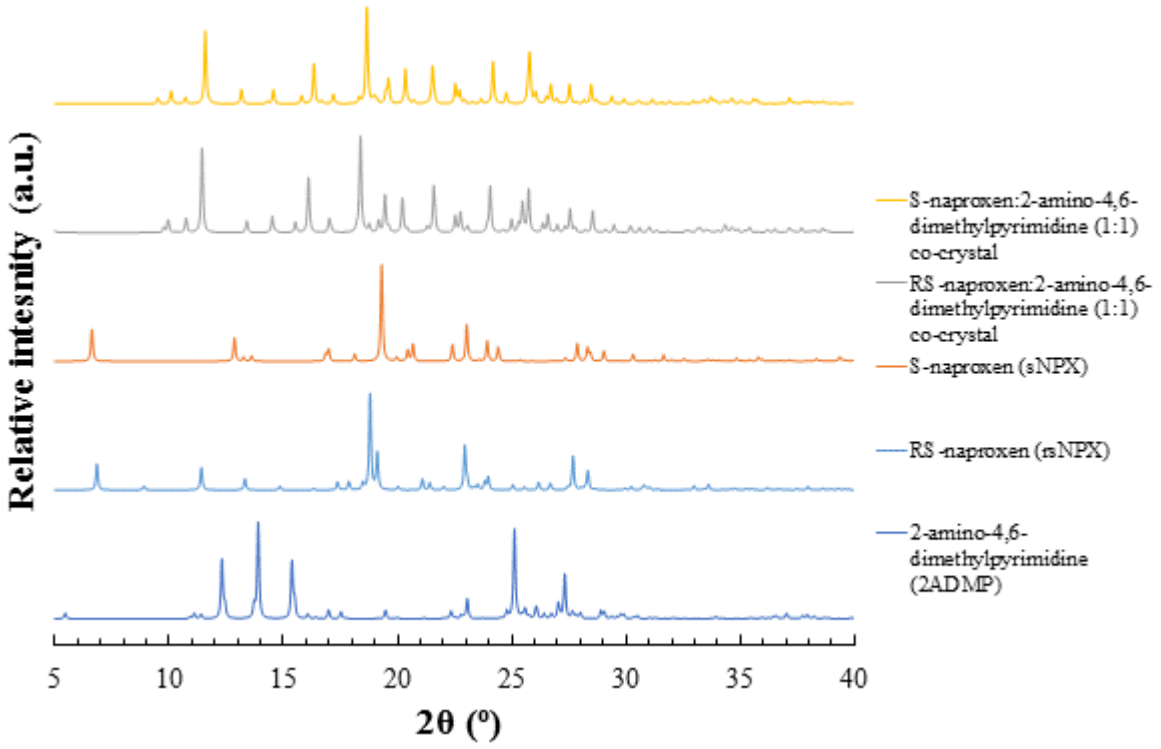

Figure 7. 20 - PXRD patterns of the S-naproxen:2-amino-4,6-dimethylpyrimidine (1:1) and RS-naproxen:2-amino-4,6-dimethylpyrimidine (1:1) co-crystals, as derived from SCXRD, compared to that of the starting materials

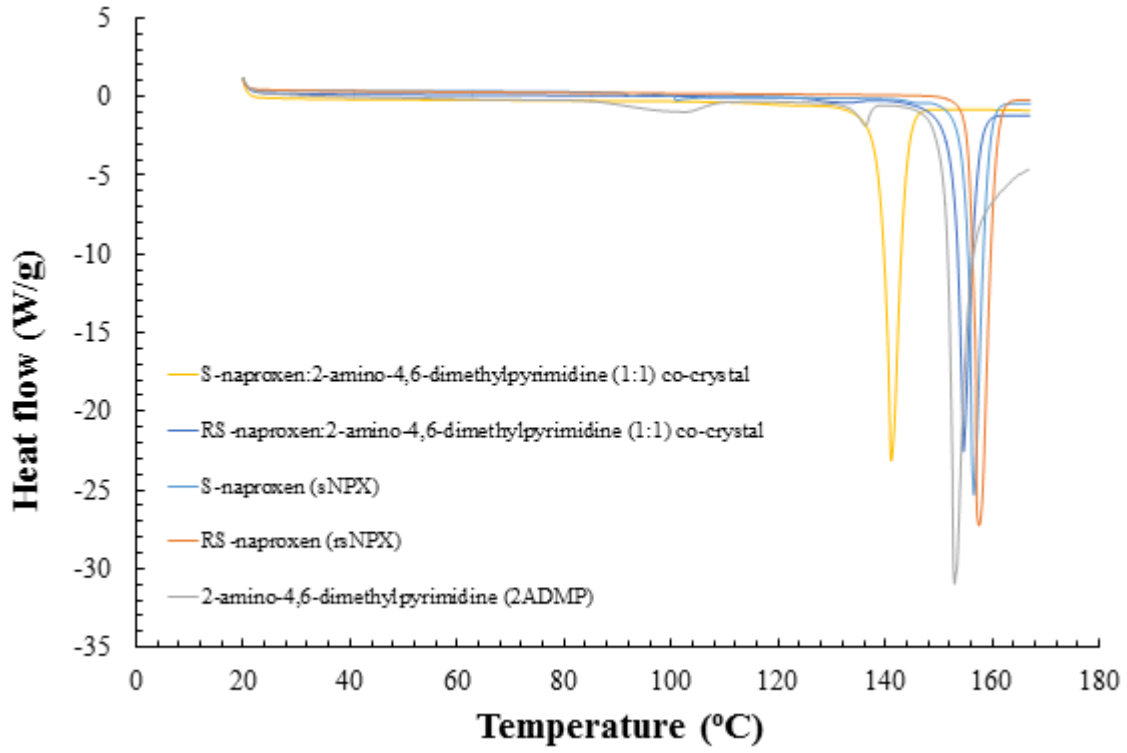

Figure 7. 21 - DSC traces of the S-naproxen:2-amino-4,6-dimethylpyrimidine (1:1) and RS-naproxen:2-amino-4,6-dimethylpyrimidine (1:1) co-crystals, compared to that of the starting materials

7.2.2.2 Binary (melting point) phase diagram analysis – Classification of chiral crystalline materials

Owing to the reproducibility of the phases observed through single crystal growth using mechanochemical preparation, a binary phase diagram assessing the melting point of the naproxen:2-amino-4,6-dimethylpyrimidine (1:1) complexes with varying compositions of enantiomer was prepared, as shown in Figure 7.22. The corresponding PXRD patterns and DSC traces can be found in Appendix A7.2.

As shown, with increasing contribution of *sNPX* from racemic compositions, the melting points of the ground samples gradually decreased. In addition, inspection of the DSC data showed no evidence of any eutectic phenomena, with the PXRD patterns showing only subtle changes in the peaks observed. Given these observations, rather than being a racemic compound, it could be said that the multi-component material of *NPX* and *2ADMP* better expressed the characteristics of a racemic solid solution, particularly that of a Roozeboom Type II. Whilst interesting in its own right, this type of system has no direct application towards preferential crystallisations.

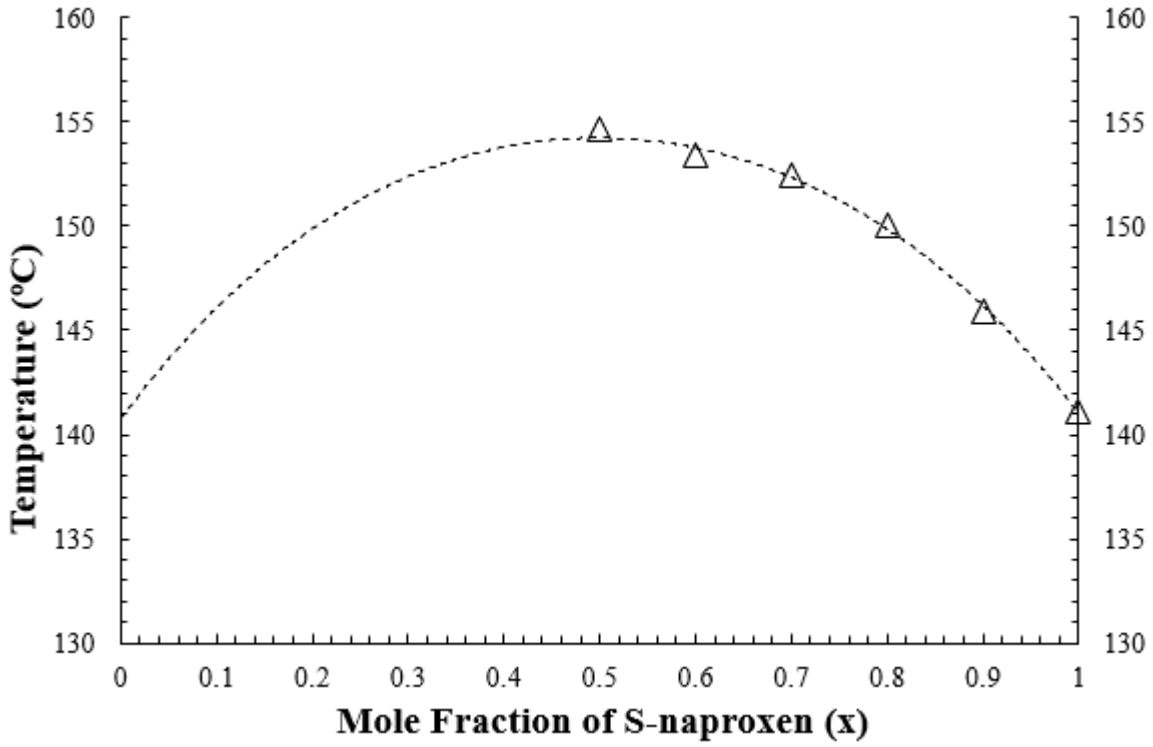

Figure 7. 22 - Binary (melting) point phase diagram, with changing enantiomeric composition of *rNPX* and *sNPX*, for the 1:1 co-crystals incorporating the co-former *2ADMP*, highlighting the liquidus (Δ) point

7.2.2.3 Crystallography – Crystal structure analysis

The unit cell parameters and refinement information for both the homochiral and racemic structures of *NPX* and *2ADMP* can be found in Table 7.4, with further details as to the hydrogen bond dimensions and disorder detailed in Appendix A7.2. The corresponding CIF files (6, 7) can be found on the accompanying CD-ROM.

In the case of the enantiomerically pure multi-component material, *sNPX* was shown to crystallise with the co-former molecule in a 1:1 ratio, with the unit cell being made up from four of these motifs. Therefore, each asymmetric unit was deemed to consist of four molecules ($Z = 4$, $Z' = 2$). The molecular components crystallised in a monoclinic $P2_1$ lattice, highlighted in Figure 7.23, and in accordance with

the minimal pK_a difference between the API and co-former, no proton transfer was not observed. As such, the S-naproxen:2-amino-4,6-dimethylpyrimidine (1:1) co-crystal was shown to form.

Table 7. 4 - SCXRD data for the two 1:1 co-crystals of *NPX* and *2ADMP*; the homochiral and racemic phases

Material	**S-naproxen:2-amino-4,6-dimethylpyrimidine (1:1) co-crystal**	**RS-naproxen:2-amino-4,6-dimethylpyrimidine (1:1) co-crystal**
Empirical formula	$C_{20}H_{23}N_3O_3$	$C_{20}H_{23}N_3O_3$
Formula weight	353.41	353.41
Temperature (K)	150.01(10)	150.01(10)
Crystal system	monoclinic	monoclinic
Space group	$P2_1$	$P2_1/c$
***a* (Å)**	8.8020(3)	8.8993(5)
***b* (Å)**	5.65999(14)	5.7686(4)
***c* (Å)**	37.2977(10)	36.301(2)
***α* (°)**	90	90
***β* (°)**	95.650(2)	94.554(5)
***γ* (°)**	90	90
Volume (Å^3)	1849.11(9)	1857.65(19)
Z*, *Z'	4, 2	4, 1
ρ_{calc} (g/cm^3)	1.269	1.264
μ (mm^{-1})	0.087	0.699
F(000)	752.0	752.0
Crystal size (mm^3)	0.204 × 0.051 × 0.039	0.373 × 0.095 × 0.052
Radiation	MoKα (λ = 0.71073)	CuKα (λ = 1.54184)
2Θ range for data collection (°)	5.488 to 51.36	9.778 to 140.148
Index ranges	$-10 \le h \le 10$, $-6 \le k \le 6$, $-45 \le l \le 32$	$-7 \le h \le 10$, $-6 \le k \le 6$, $-44 \le l \le 44$
Reflections collected	11996	13562
Independent reflections	6993 [R_{int} = 0.0293, R_{sigma} = 0.0590]	3485 [R_{int} = 0.0406, R_{sigma} = 0.0382]
Data/restraints/parameters	6993/5/479	3485/7/251
Goodness-of-fit on F^2	1.063	1.134
Final R indexes [I>=2σ (I)]	R_1 = 0.0509, wR_2 = 0.0993	R_1 = 0.0681, wR_2 = 0.1549
Final R indexes [all data]	R_1 = 0.0719, wR_2 = 0.1109	R_1 = 0.0856, wR_2 = 0.1634
Largest diff. peak/hole (e Å^{-3})	0.14/-0.19	0.24/-0.25
Flack parameter	0.2(9)	N/A

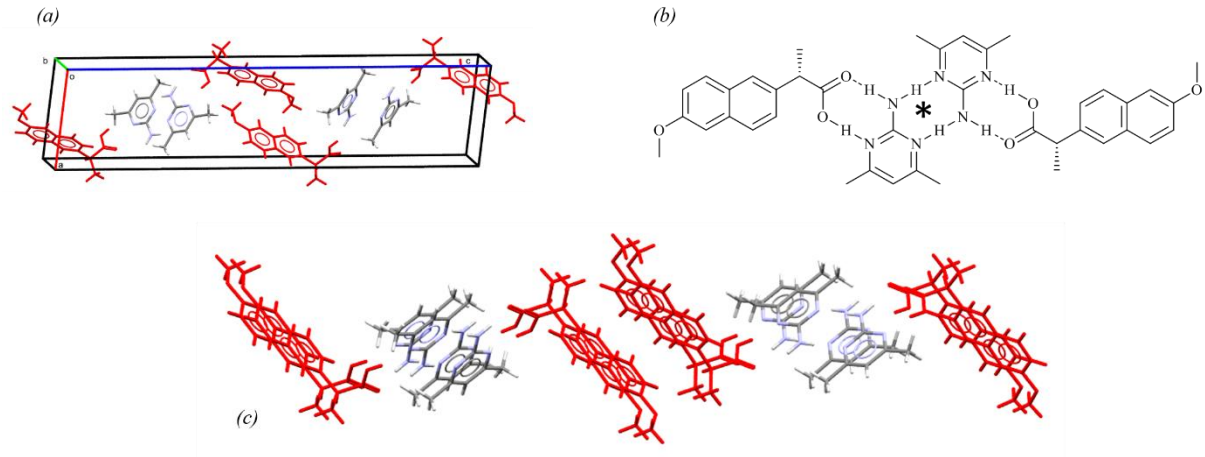

Figure 7. 23 - Crystal structure of the S-naproxen:2-amino-4,6-dimethylpyrimidine (1:1) co-crystal, highlighting (a) the unit cell, (b) hydrogen bonding synthon (* referring to a pseudo-inversion point) and (c) packing arrangement (*sNPX* in red)

As with many of the *2AP* derivatives, the key interaction unit between *sNPX* and *2ADMP* consisted of the hydrogen bonded dimer between the API carboxylic acid and the co-former pyridine-amine groups, yielding the $R_2^2(8)$ synthon. However, the opposite amine and pyridine functionalities of the symmetrical *2ADMP* molecule formed an additional ring hydrogen bond dimer, bridging between the two main heterosynthons. This homosynthon could also be classed as a $R_2^2(8)$interaction, with the

overall interaction unit consisting of a *sNPX:2ADMP:2ADMP:sNPX* moiety. Whilst inversion symmetry was not present, the main body of the interaction unit could be described through a point of pseudo-inversion, with the only discrepancies arising from the atoms located about the chiral centres. Using these units, the macro-crystalline assembly can be constructed, whereby the zig-zagged interaction motifs can be stacked and connected using side-on C-H···π contacts.

With changing enantiomeric contribution so as to reflect a racemic composition, no significant change in the co-crystalline structure was noted. As in the enantiopure form, the unit cell contained four molecular entities ($Z = 4$, $Z' = 1$) consisting of *NPX* and *2ADMP* in a 1:1 molar ratio. Each of these represented an asymmetric unit, whereby both enantiomers were evenly represented. As such, these units crystallised in a monoclinic $P2_1/c$ crystalline space group.

With no evidence of proton transfer, the RS-naproxen:2-amino-4,6-dimethylpyrimidine (1:1) co-crystal (Figure 7.24) was shown to utilise the same combination of hydrogen bonding interactions as exploited in the homochiral form, with two heterodimers, each specifying opposite enantiomers, being bridged by a homosynthonic interaction. The interaction unit could hence be described as a *sNPX:2ADMP:2ADMP:rNPX* unit, whereby the enantiomers were related through inversion symmetry. However, detailed in Appendix A7.2, disorder was noted, localised about the chiral centres, suggesting a fluidity of the enantiomeric composition throughout the structure. The structural similarities of these interaction units is highlighted in Figure 7.25. Further to this, the packing of the racemic interaction units was shown to express a great deal of similarity to that of the *sNPX* co-crystal, with the discrete four molecule motifs interlocking and stacking.

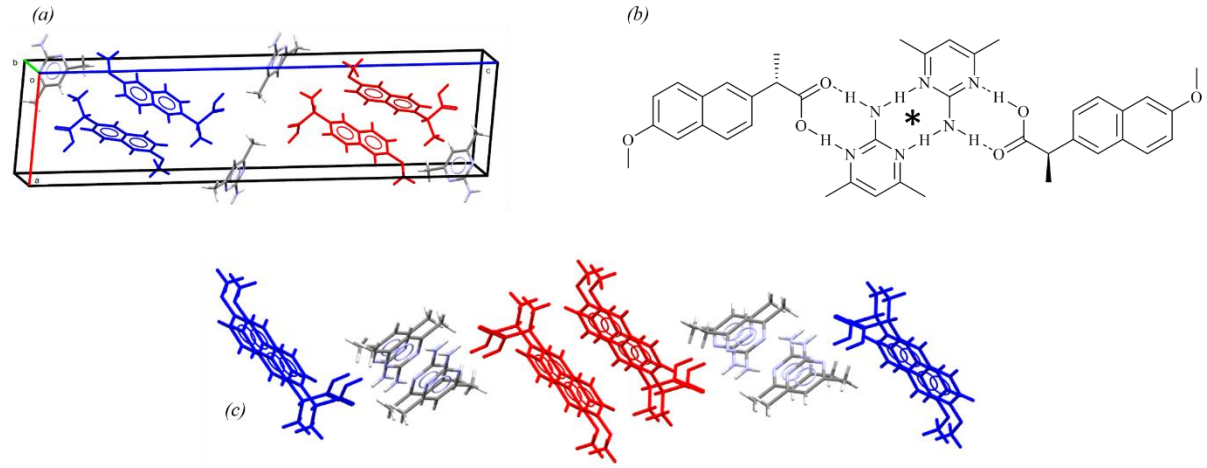

Figure 7. 24 - Crystal structure of the RS-naproxen:2-amino-4,6-dimethylpyrimidine (1:1) co-crystal, highlighting (a) the unit cell, (b) hydrogen bonding synthon (* referring to an inversion point) and (c) packing arrangement (*sNPX* in red, *rNPX* in blue)

The similarity between the RS-naproxen and S-naproxen:2-amino-4,6-dimethylpyrimidine (1:1) co-crystals was attributed to the favourability of the key hydrogen bonded unit responsible for holding the molecular entities together and allowing for limited flexibility for the overall configuration. The exception to this was that about the chiral centres. The interchangeability of *NPX* enantiomers highlighted the continuous nature of the chiral composition throughout the structure, confirming the presence of a solid solution.

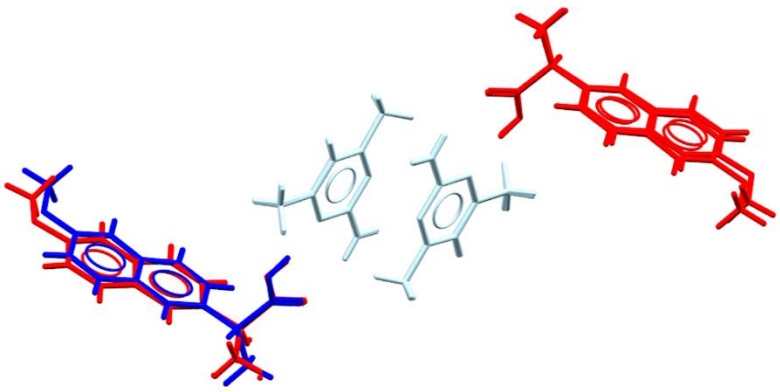

Figure 7. 25 - An overlap of the two interaction units for both the racemic and enantiopure co-crystalline form of *NPX* and *2ADMP*, highlighting their structural similarity (*sNPX* in red, *rNPX* in blue)

7.3 Materials of racemic and enantiopure naproxen with 2-amino-3-chloropyridine (*2A3CP*)

7.3.1 Material screening

2-aminochloropyridines (*2ACP*s) were also utilised as co-formers, where chlorine atoms were substituted at each of the available positions on the aromatic pyridine ring, respectively. With the aim to introduce a functionality that was able to contribute addition electron density and steric bulk, to explore their effects on the hydrogen bonding capabilities, as well as for the formation of different chiral crystalline materials.

The molecule of 2-amino-3-chloropyridine (*2A3CP*) presents opportunities to influence the hydrogen bonding expressed from the secondary N-H bond, pointing away from the heterodimeric interaction. To date, only one structural form of *2A3CP* (CSD reference: URAXER[204]) has been found, with a low melting point between 59-62ºC. The basicity of the co-former, pK_a, was shown to be 4.8 in water/ethanol systems at 25ºC[205], giving an initial indication that proton transfer with *NPX* was not likely.

7.3.1.1 Mechanochemical screening

Mechanochemical screening was conducted in 2:1, 1:1 and 1:2 molar stoichiometries, with minimum quantities of ethanol. As shown from the initial phase analysis conducted with *sNPX* and *2A3CP* (Figure 7.26), equimolar ground samples and that with increased amounts of the co-former both highlighted the formation of a novel crystalline form with respect to that of the starting materials. Given that little to no excess starting material was evident from these patterns, preliminary interpretations suggested the formation of a new homochiral multi-component phase. Subsequent comparison with the PXRD patterns generated using SCXRD data (see Section 7.3.2) highlighted that the same novel complex of *sNPX* and *2A3CP* could be made consistently by either method.

Thermal analysis confirmed the presence of a discrete phase, particularly for the sample prepared from a 1:1 combination. As shown in Figure 7.27, a single endothermic event was noted for this composition, with a melt evident between 107ºC and 109ºC.

Likewise, the ability to prepare materials of *rsNPX* and *2A3CP via* grinding was also shown to be possible, with particular emphasis on the samples made in equal molar quantities. PXRD analysis (Figure 7.28) indicated that a form distinct from that of the starting components could be made, with its DSC trace (Figure 7.29), again, emphasising the formation of a pure novel material, with only a single thermal phenomenon being noted. This represented a melting point at 123-125ºC. As with the homochiral case, phase comparison between the mechanochemical sample and that of individual crystals again showed the reproducibility of this material *via* a variety of methods.

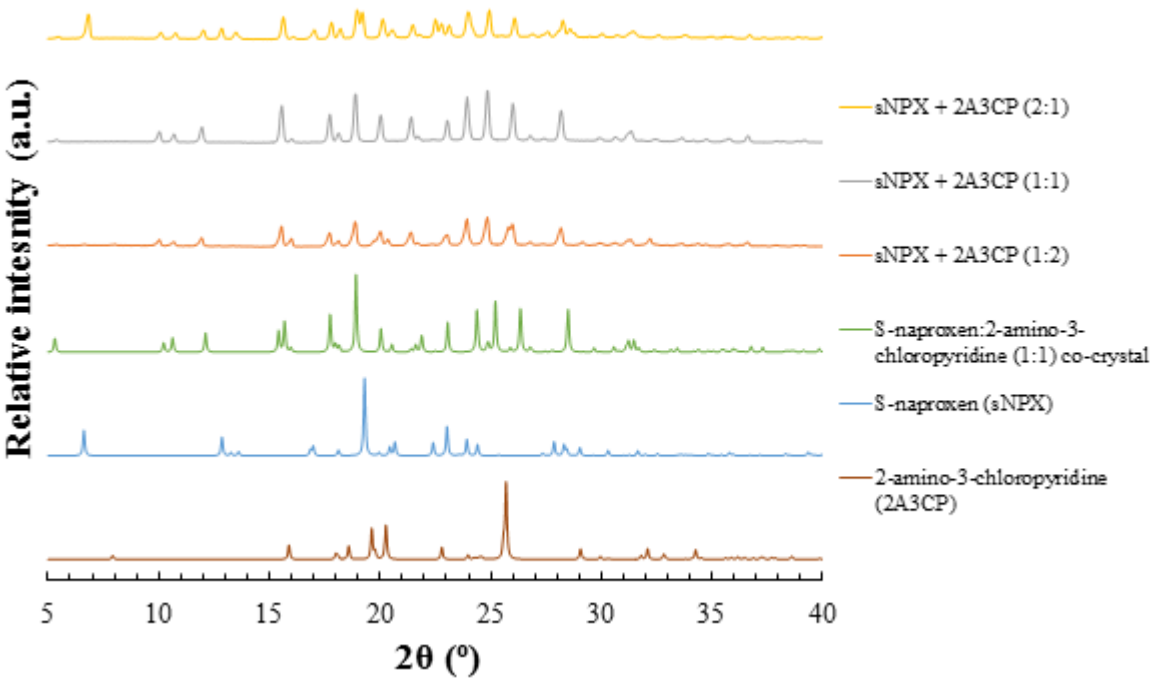

Figure 7. 26 - PXRD patterns from mechanochemically prepared samples of *sNPX* and *2A3CP*, ground, with ethanol, in either 2:1, 1:1 or 1:2 molar ratios (top three patterns)

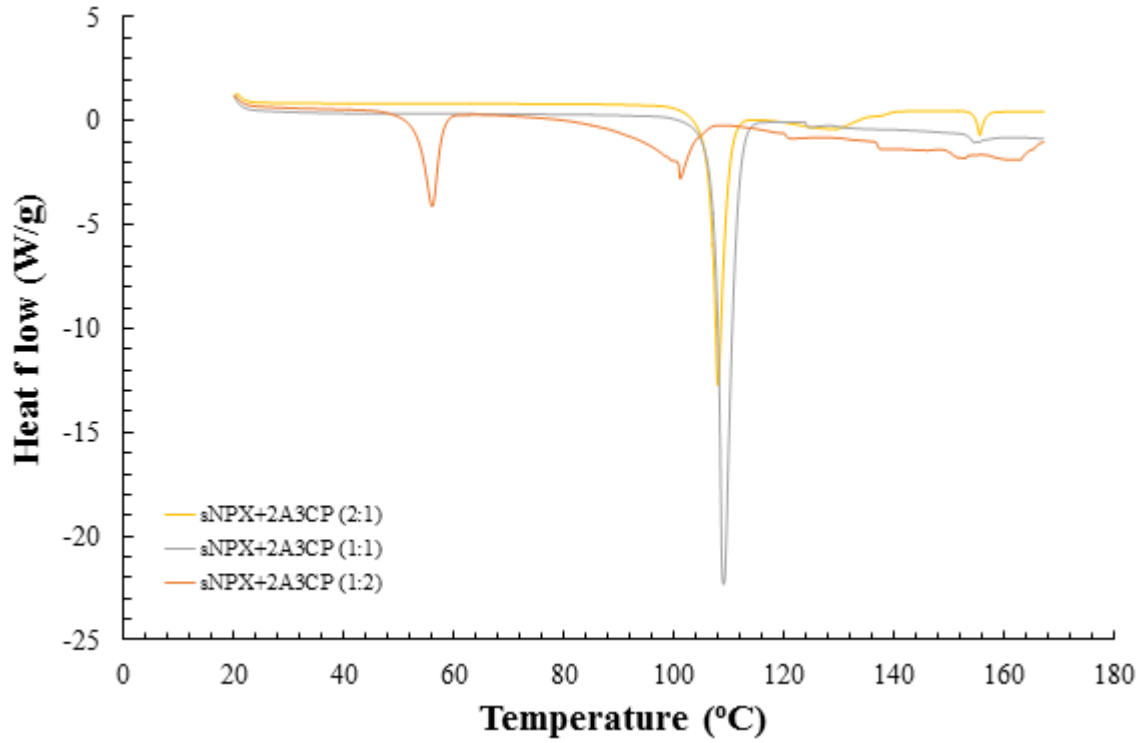

Figure 7. 27 - DSC traces from mechanochemically prepared samples of *sNPX* and *2A3CP*, ground, with ethanol, in either 2:1, 1:1 or 1:2 molar ratios

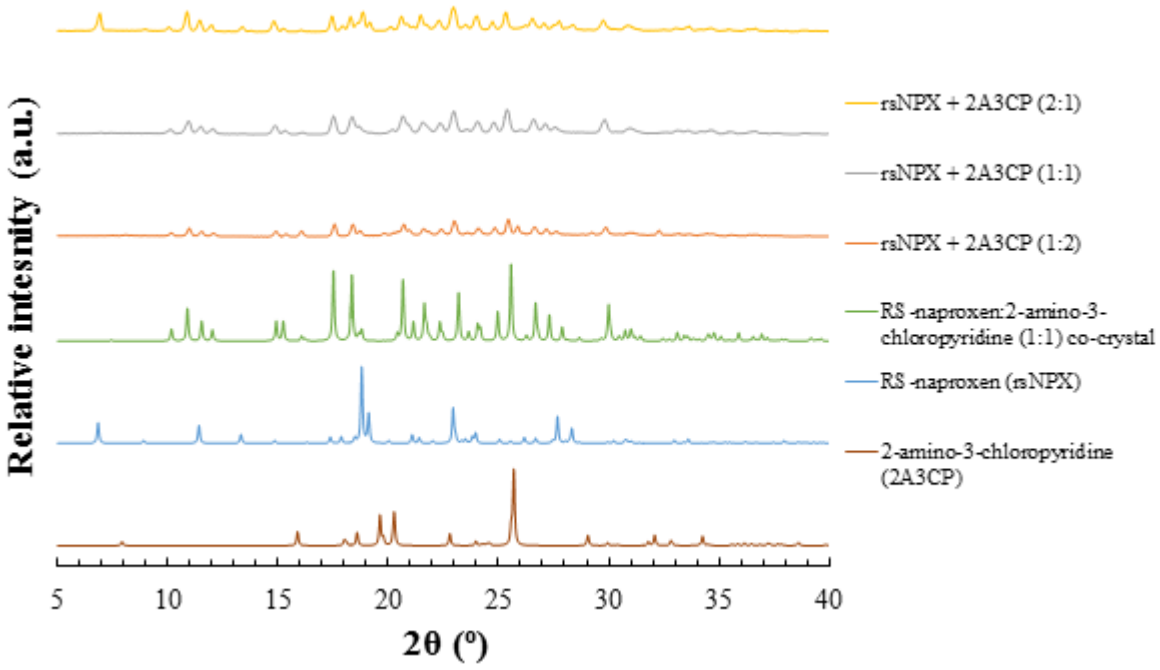

Figure 7. 28 - PXRD patterns from mechanochemically prepared samples of *rsNPX* and *2A3CP*, ground, with ethanol, in either 2:1, 1:1 or 1:2 molar ratios (top three patterns)

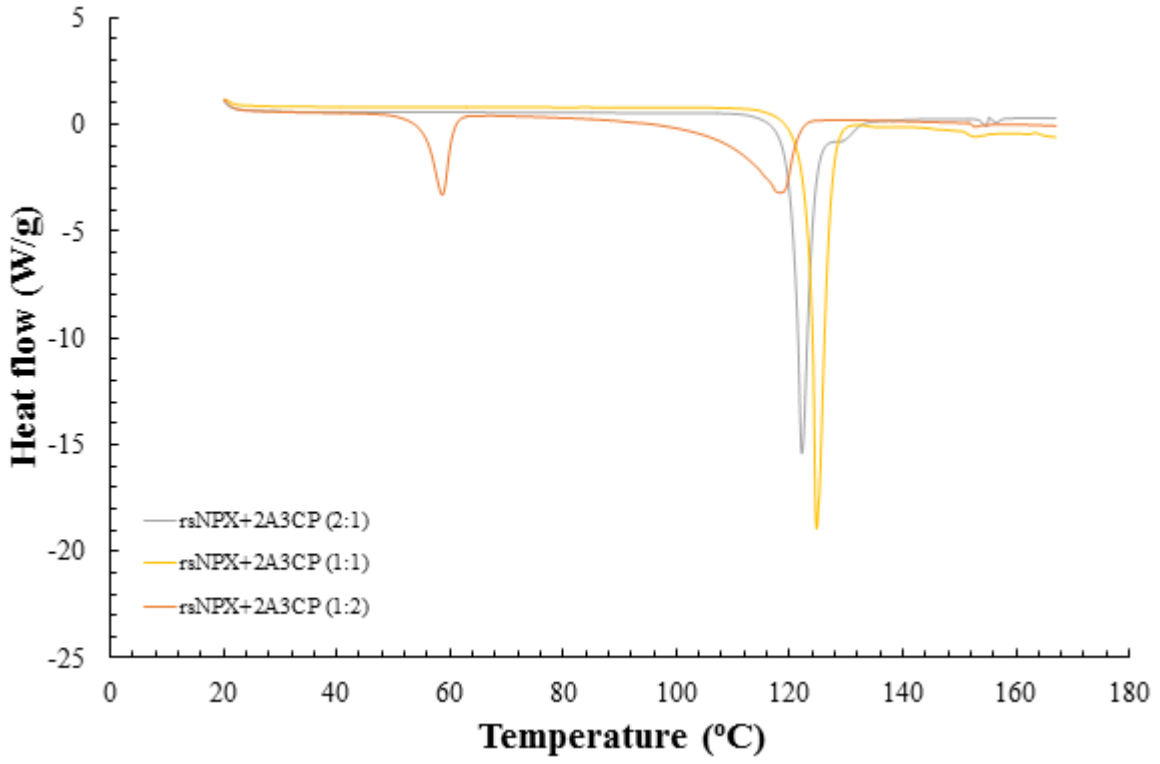

Figure 7. 29 - DSC traces from mechanochemically prepared samples of *rsNPX* and *2A3CP*, ground, with ethanol, in either 2:1, 1:1 or 1:2 molar ratios

7.3.1.2 Combined evaporation & cooling crystallisation screening

In parallel to the above mentioned liquid-assisted grinding experiments, single crystals were grown from equimolar solutions of ethanol using the previously described evaporative and cooling method. For both the homochiral and racemic cases, blocky needle crystals were prepared, each showing an off-white colour when in the bulk (Figure 7.30). Upon selecting suitable individual crystals, SCXRD analysis was conducted, showing the unique crystalline structure of each chiral form and confirming the translation of material preparation from mechanochemical to solution environments.

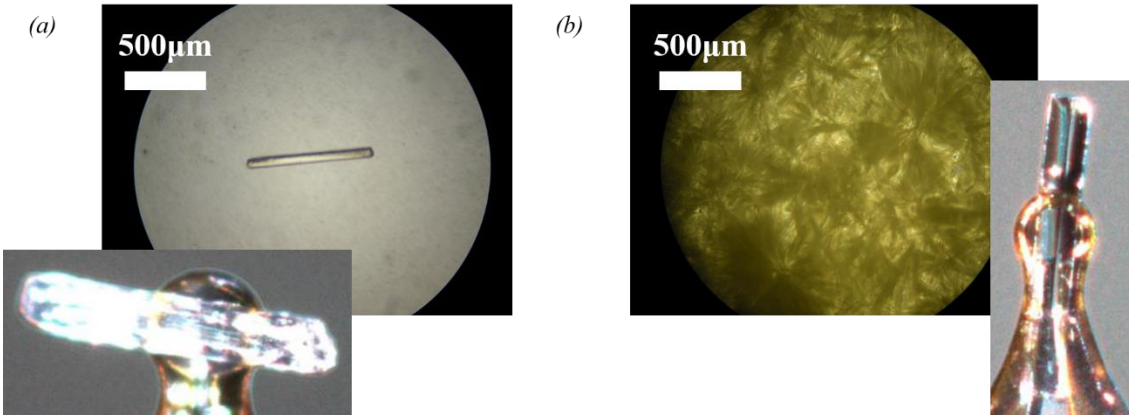

Figure 7. 30 - Microscope and mounted SCXRD images of crystals yielded from 1:1 ethanol solutions of (a) *sNPX* and (b) *rsNPX* with *2A3CP*, respectively

7.3.2 Material characterisation

The results of the initial mechanochemical and solution crystallisation screenings demonstrated the reproducibility in preparation of both the homochiral and racemic multi-component phases. The nature of these materials were compared and contrasted with further characterisation using PXRD, DSC, SCXRD and phase analysis. IR spectra were also collected for the two materials, highlighting a number of similarities (Appendix A7.3).

7.3.2.1 Phase, thermal and spectroscopic analysis

As highlighted in Figure 7.31, the novel multi-component phases showed different diffraction patterns to that presented by the starting materials, confirming the formation of new crystalline entities. However, distinct differences were noted between the patterns of the enantiopure and racemic complexes, indicating that upon varying the enantiomeric composition, a transition is made from one crystal phase to another. These observations suggested that upon combining the two respective starting components at racemic quantities of API, like with single-component *NPX*, a racemic compound was formed.

DSC traces were taken and compared for the single and multi-component phases. As shown from Figure 7.32, both the racemic and enantiopure complexes expressed lower melting points than those of the enantiomeric materials of *NPX*, but higher than that of *2A3CP*. This suggested that whilst the interactions between *NPX* and the co-former were favourable, they were not necessarily preferential when compared to single-component API, in the solid state. Upon comparing the melting points of the homo and heterochiral multi-component forms, the phase yielded from racemic composition demonstrated a higher melting point (123-125^{o}C) when compared to the phase containing a single enantiomer (107-109^{o}C). This observations supported the findings made from phase analysis, emphasising the formation of a racemic compound forming system.

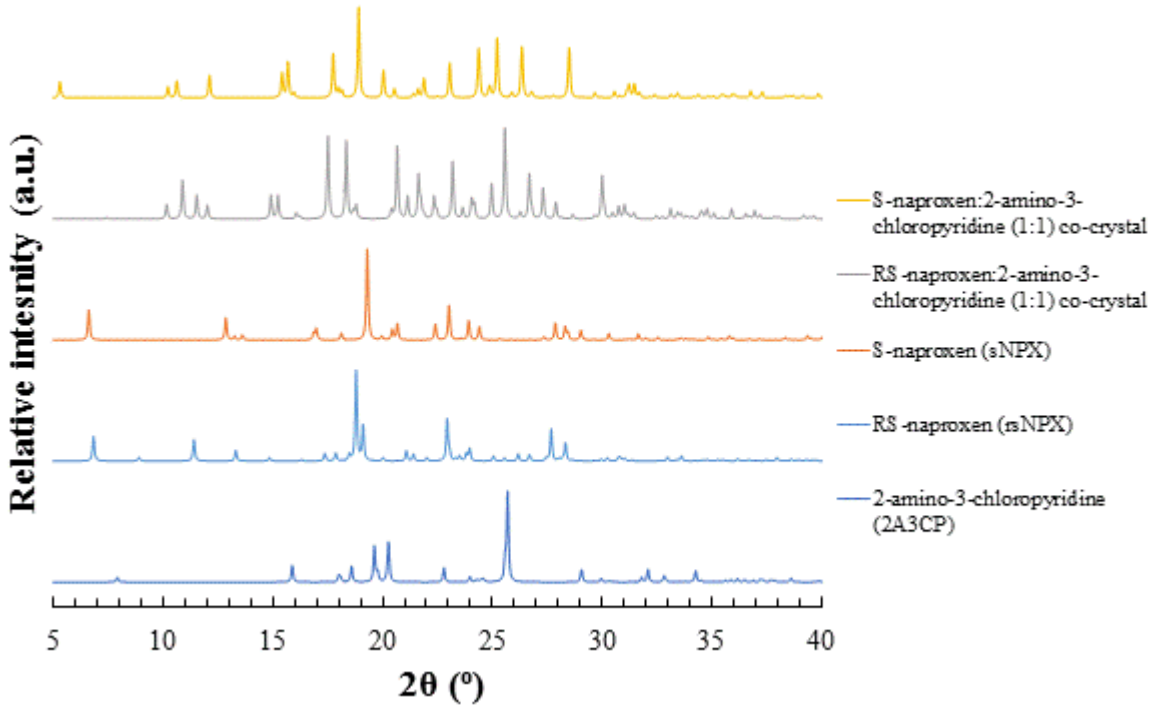

Figure 7. 31 - PXRD patterns of the S-naproxen:2-amino-3-chloropyridine (1:1) and RS-naproxen:2-amino-3-chloropyridine (1:1) co-crystals, as derived from SCXRD, compared to that of the starting materials

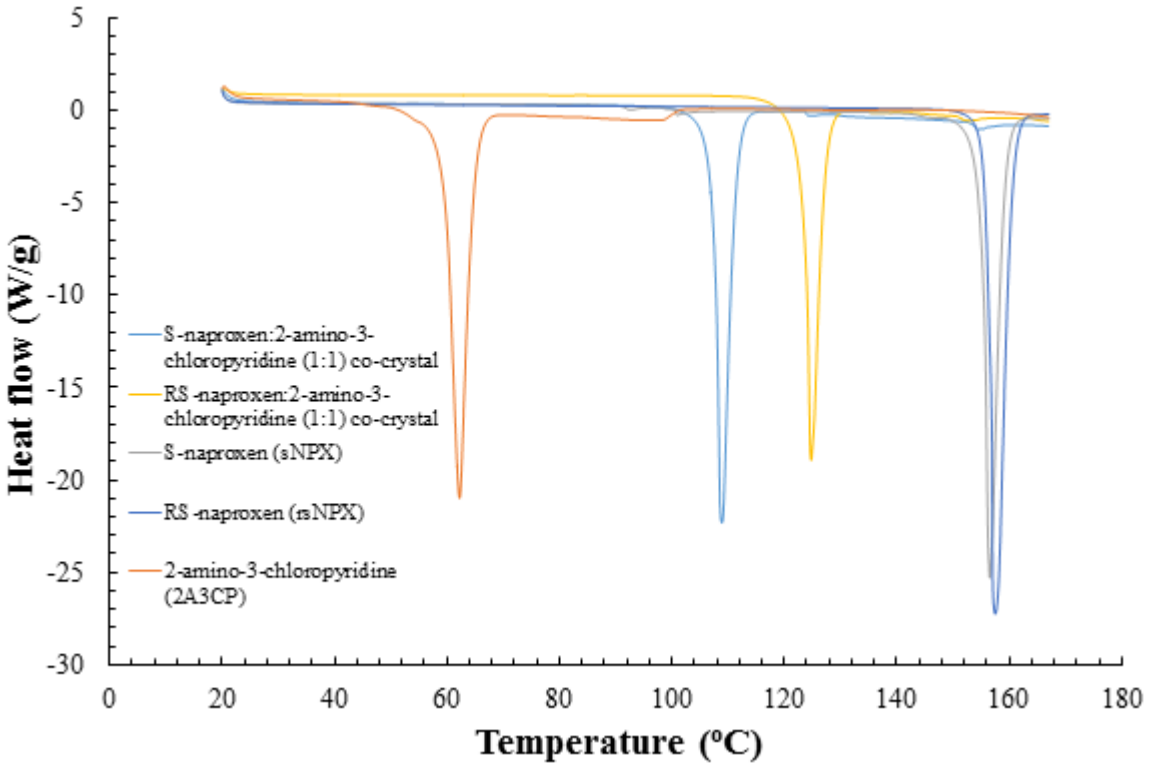

Figure 7. 32 - DSC traces of the S-naproxen:2-amino-3-chloropyridine (1:1) and RS-naproxen:2-amino-3-chloropyridine (1:1) co-crystals, compared to that of the starting materials

Infrared spectroscopy was also carried out on mechanochemical preparations of the novel multi-component complexes and compared to that of the starting materials (see Appendix A7.3). The spectra for the freshly prepared samples showed obvious differences to those of the initial components, again indicating the formation of novel materials with a diverse variety of interactions. However, it was also evident that the racemic and enantiopure complexes possessed striking similarities, suggesting that both solid phases have similar molecular conformations and interactions. Of particular note was that of the split vibrational modes of the carbonyl functional group of the API molecules, indicating the involvement of that moiety in several intermolecular interactions.

7.3.2.2 Binary (melting point) phase diagram analysis – Classification of chiral crystalline materials

Confirmation of the existence of a racemic compound upon combining *NPX* and *2A3CP* at racemic quantities was obtained through the construction of a binary phase diagram. The melting points of 1:1 mechanochemical combinations of API to co-former, where the enantiomeric composition was varied from racemic to enantiopure (*sNPX*), were taken and plotted, noting the presence of any eutectic phenomena. The PXRD patterns and DSC traces for each composition can be found in Appendix A7.3. As shown from Figure 7.33, discernible regions are observed, corresponding to regions of stability to melting for both the homochiral and racemic complexes, respectively. The enantiopure phase was shown to remain the stable solid phase only at high enantiomeric excesses (mole fraction of *sNPX* greater than 0.9), whilst the stability range of the racemic material was far greater, with this phase being stable to heating from racemic compositions to a 0.9 mole fraction of *sNPX*. In addition, consistent eutectic melting was also observed between 105ºC and 107ºC, with the key eutectic composition being evident at 0.9 contributions of *sNPX*. This culmination of phase and thermal analysis confirmed the presence of a racemic compound, making this system unsuitable for preferential crystallisation processes.

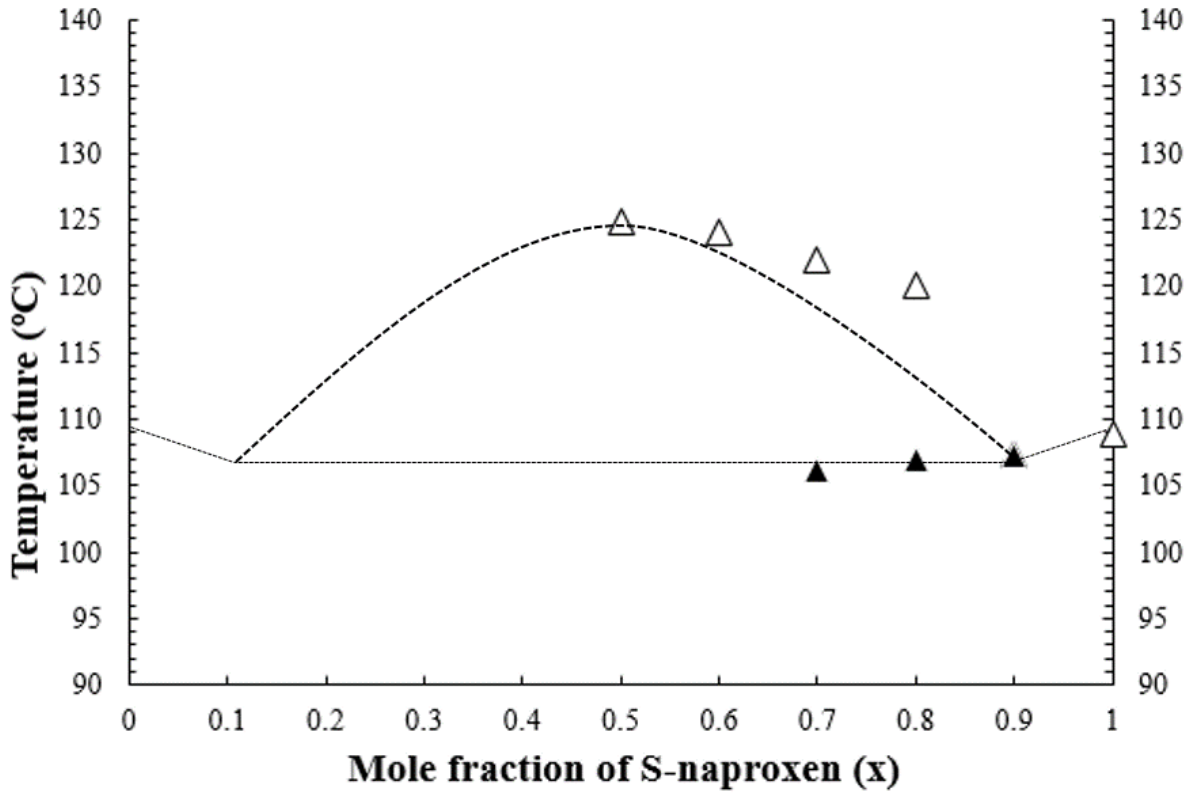

Figure 7. 33 - Binary (melting) point phase diagram, with changing enantiomeric composition of *rNPX* and *sNPX*, for the 1:1 co-crystals incorporating the co-former *2A3CP*, highlighting the liquidus (Δ) and the eutectic (▲) points

7.3.2.3 Crystallography – Crystal structure analysis

Individual crystals of both novel crystalline phases were taken from solution crystallisations and analysed by using SCXRD. Details of the hydrogen bonding dimensions and, where necessary, atomic occupancies, can be found in the Appendix A7.3. The corresponding CIF files (8, 9) can be found on the accompanying CD-ROM.

The homochiral multi-component crystal was found to consist of *sNPX* and *2A3CP* interacting through hydrogen bonding interactions in a 1:1 molar relationship. The unit cell was shown to contain two asymmetric units, each consisting of one API and one co-former molecule (Z = 2, Z' = 1). As such, these units crystallised in a monoclinic $P2_1$ space group, a non-centrosymmetric system.

As highlighted by Figure 7.34, proton transfer was not evident, showing that the combination of these molecular entities allowed for the formation of the S-naproxen:2-amino-3-chloropyridine (1:1) co-crystal. The presence of the substituent chlorine atom at the three-position demonstrated no hindrance in hydrogen bond formation, with the API and co-former forming the $R_2^2(8)$ heterosynthon common to many *2AP* derivatives. Further contacts, utilising a $D_1^1(3)$ interaction motif, connect these dimers, forming extended hydrogen bonded chains, similar to that seen in the structure of the S-naproxen:2-aminopyridine (1:1) salt. The overall crystal structure can then be described through an arrangement of these expansive chains.

Table 7. 5 - Unit cell and crystallographic parameters for the S-naproxen:2-amino-3-chloropyridine (1:1) co-crystal

Material	**S-naproxen:2-amino-3-chloropyridine (1:1) co-crystal**
Empirical formula	$C_{19}H_{19}N_2O_3Cl$
Formula weight	358.81
Temperature (K)	150.01(10)
Crystal system	monoclinic
Space group	$P2_1$
***a* (Å)**	8.71920(10)
***b* (Å)**	6.12300(10)
***c* (Å)**	16.7639(2)
***α* (°)**	90
***β* (°)**	97.3880(10)
***γ* (°)**	90
Volume (Å^3)	887.56(2)
Z*, *Z'	2, 1
ρ_{calc} (g/cm^3)	1.343
μ (mm^{-1})	2.077
F(000)	376.0
Crystal size (mm^3)	0.4 × 0.1 × 0.02
Radiation	CuKα (λ = 1.54184)
2Θ range for data collection (°)	10.23 to 140.128
Index ranges	$-10 \leq h \leq 10$, $-7 \leq k \leq 7$, $-14 \leq l \leq 20$
Reflections collected	6200
Independent reflections	3372 [R_{int} = 0.0116, R_{sigma} = 0.0139]
Data/restraints/parameters	3372/2/229
Goodness-of-fit on F^2	1.073
Final R indexes [I>=2σ (I)]	R_1 = 0.0246, wR_2 = 0.0675
Final R indexes [all data]	R_1 = 0.0249, wR_2 = 0.0678
Largest diff. peak/hole (e Å^{-3})	0.14/-0.21
Flack parameter	-0.006(6)

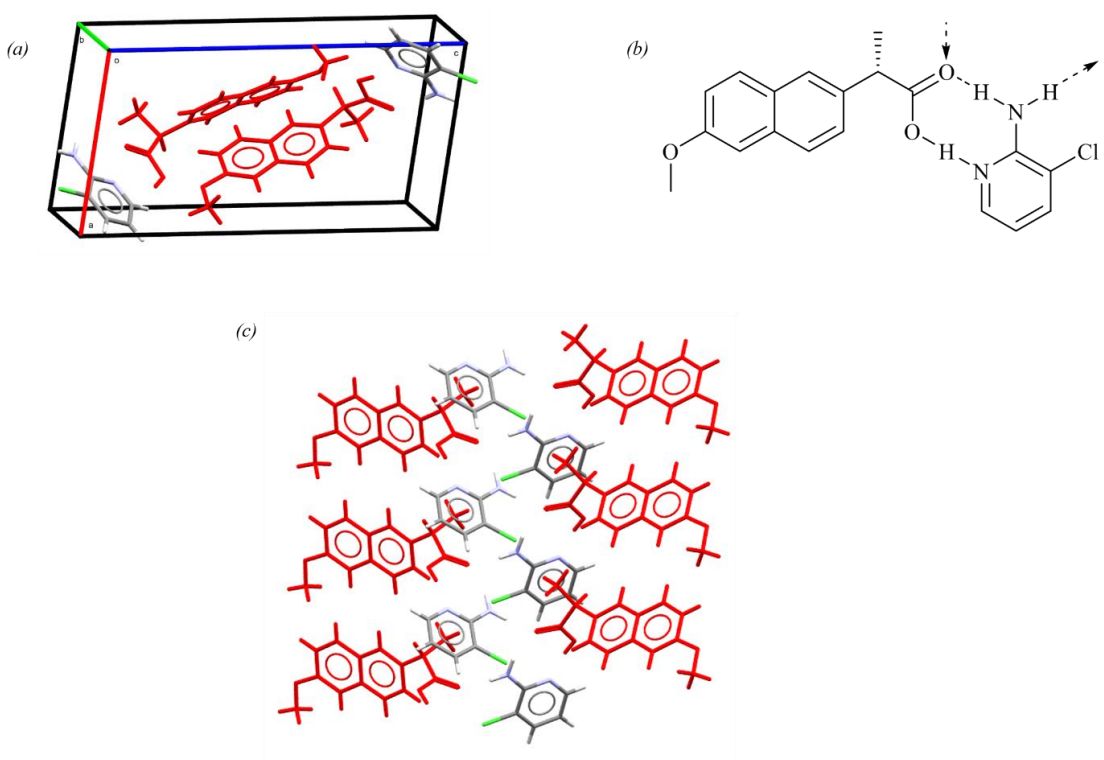

Figure 7. 34 - Crystal structure of the S-naproxen:2-amino-3-chloropyridine (1:1) co-crystal, highlighting (a) the unit cell, (b) hydrogen bonding synthon and (c) packing arrangement (*sNPX* in red)

In the racemic case, *NPX* was shown to crystallise with the *2A3CP* co-former in 1:1 stoichiometry, as part of an orthorhombic *P*na2$_1$ space group. The unit cell contained four asymmetric units (Z = 4, Z' = 1), each consisting of one API molecule and one co-former molecule, with both enantiomeric forms being reflected equally. The defining parameters of unit cell and crystallographic refinement are highlighted in Table 7.7. Despite this system being non-centrosymmetric (like in the homochiral material), the presence of mirror symmetry still allows for the presence of both enantiomers within the structure, making it non-enantiomorphic.

No proton transfer was observed, confirming the formation of a RS-naproxen:2-amino-3-chloropyridine (1:1) co-crystal. Here, the key interaction units utilised (Figure 7.35) the same hydrogen bonding interactions as seen in that of the homochiral co-crystal, i.e. the $R_2^2(8)$ dimer and $D_1^1(3)$connecting chain. This was in contrast to structure observed for the racemic salt of *NPX* and *2AP*, where a dimer of dimers was able to form. The structure, comparable to that of the homochiral co-crystal, indicated that with the introduction of the chlorine atom at the meta position, the closed hydrogen bonded interaction unit, allowing for symmetrical interaction of both enantiomeric moieties, was no longer favoured.

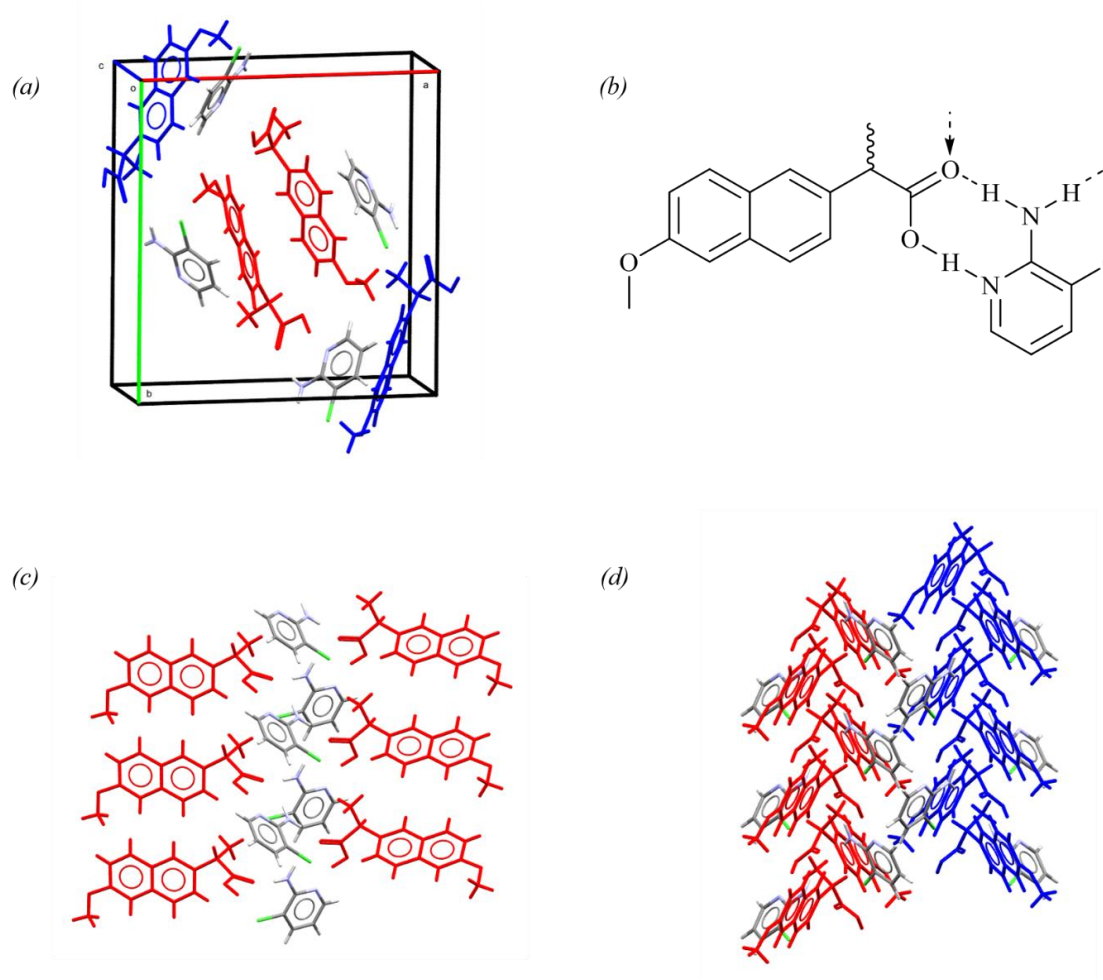

Figure 7. 35 - Crystal structure of the RS-naproxen:2-amino-3-chloropyridine (1:1) co-crystal, highlighting (a) the unit cell, (b) hydrogen bonding synthon and (c) & (d) packing arrangements (*sNPX* in red, *rsNPX* in blue)

By extending the hydrogen bonding interactions, chains selective to one chiral type were observed. These chains made up the main structure of the racemic co-crystal, with the enantiomeric homogeneity of these channels changing in an alternating fashion. As shown in Appendix A7.3, the racemic co-crystal was modelled with disorder about the chiral centre of every *NPX* molecule, with relative occupancies of approximately 0.81:0.19, in terms of the S and R enantiomers. Given the non-enantiomorphic nature of this system, this disorder was most likely averaged across the structure. With this disorder being consistent across all the API molecules, the chiral consistency of the individual hydrogen bonded chains was deemed constant, emphasising the defined enantiopurity of these alternating channels.

The complementary intermolecular interactions exhibited by both the homo and heterochiral co-crystalline materials supported the initial interpretation of the IR spectra. The main discrepancy between the two structures could be attributed to the enantiomeric composition of the individual hydrogen bonded channels. It can be said that due to the alternating chiral make-up of these chains in the RS-naproxen:2-amino-3-chloropyridine (1:1) co-crystal, they can pack together with greater efficiency than that observed in the enantiopure co-crystal. This was reflected by the higher structure density calculated from SCXRD for the racemic multi-component form, i.e. 1.343 g/cm^3 and 1.360 g/cm^3. As such, this can be used to explain the higher melting point of the racemic phase.

Table 7. 6 - Unit cell and crystallographic parameters for the RS-naproxen:2-amino-3-chloropyridine (1:1) co-crystal

Material	**RS-naproxen:2-amino-3-chloropyridine (1:1) co-crystal**
Empirical formula	$C_{19}H_{19}ClN_2O_3$
Formula weight	358.81
Temperature (K)	149.9(4)
Crystal system	orthorhombic
Space group	*P*na2_1
***a* (Å)**	16.2100(5)
***b* (Å)**	17.3936(5)
***c* (Å)**	6.2135(2)
***α* (°)**	90
***β* (°)**	90
***γ* (°)**	90
Volume (Å^3)	1751.91(9)
Z, Z'	4, 1
ρ_{calc} (g/cm^3)	1.360
μ (mm^{-1})	2.105
F(000)	752.0
Crystal size (mm^3)	0.58 × 0.076 × 0.032
Radiation	CuKα (λ = 1.54184)
2Θ range for data collection (°)	7.454 to 177.238
Index ranges	$-21 \leq h \leq 21$, $-19 \leq k \leq 19$, $-5 \leq l \leq 7$
Reflections collected	9587
Independent reflections	2673 [R_{int} = 0.0405, R_{sigma} = 0.0332]
Data/restraints/parameters	2673/8/240
Goodness-of-fit on F^2	1.132
Final R indexes [I>=2σ (I)]	R_1 = 0.0563, wR_2 = 0.1415
Final R indexes [all data]	R_1 = 0.0581, wR_2 = 0.1427
Largest diff. peak/hole (e Å^{-3})	0.22/-0.24
Flack parameter	N/A

7.4 Materials of racemic and enantiopure naproxen with 2-amino-4-chloropyridine (*2A4CP*)

7.4.1 Material screening

Different enantiomeric compositions of *NPX* were also screened with the co-former 2-amino-4-chloropyridine (*2A4CP*), an isomer of *2A3CP*. To date, no crystalline structures of *2A4CP* have been submitted to the CSD, so the number of polymorphic forms is currently unknown. As such, the reference PXRD pattern for *2A4CP* was taken directly from that of the starting material, as well as the melting point, taken as 129-131ºC. In addition, no pK_a data could be found from the literature, but owing to the combined electron donating ability of the chlorine atom combined with its positioning with respect to aromatic nitrogen, it can be anticipated that this co-former expresses increased basicity with respect to that of its *2A3CP* relative. Therefore, salt formation may be possible.

7.4.1.1 Mechanochemical screening

Figure 7.36 shows the PXRD patterns taken from mechanochemically prepared samples of *sNPX* with *2A4CP*. Whilst it was event that novel phases were prepared *via* this method, with respect to the starting materials, the phases formed from the 1:1 and 1:2 combinations do not reflect the findings from the subsequent solution-based crystallisations (see Section 2.4.2). Further liquid-assisted grindings were conducted using a range of different solvents (shown in Appendix A7.4) to explore the potential of mechanochemistry to produce the phases seen from cooling. It was highlighted that whilst neat grinding yielded a physical mixture, preparations utilising either methanol, isopropanol, acetonitrile or ethyl acetate demonstrated the reproducible formation of the original phase found from the initial screening experiments with ethanol. Samples made with toluene and hexane showed a physical mixture of both the forms produced, thus far, exclusively through mechanochemical means and that of the phase produced from solution. This emphasised that for certain systems, solvent could play a significant role in the mechanochemical processing.

DSC analysis (Figure 7.37) of the initial samples confirmed the formation of a unique material at the 1:1 stoichiometry, with its thermal trace highlighting only one endothermic event, occurring between 92ºC and 96ºC. Thermal analysis of further mechanochemical preparations with methanol, ethanol, isopropanol, acetonitrile and ethyl acetate showed consistency in this melting, whilst the case with toluene showed two consecutive melts, one at 89-92ºC and another 95-96ºC. These can be attributed to heating-assisted complexation and subsequent melting of a distinct phase.

In contrast, ground preparations of racemic API with the co-former were shown to produce a novel phase at 1:1 compositions. In addition, consistency was shown to be possible between the materials made through mechanochemical methods to that made by solution cooling crystallisation (Figure 7.38). As well as this, the DSC trace, shown in Figure 7.39, showed a clear single endothermic event, occurring between 102ºC and 104ºC.

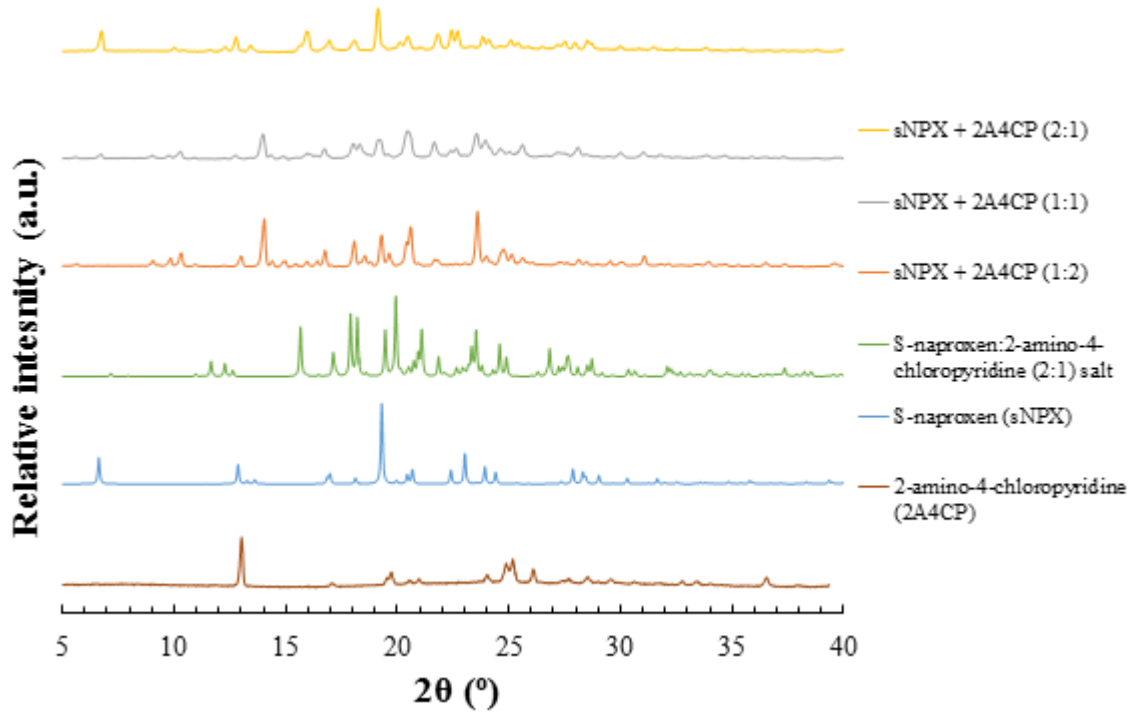

Figure 7. 36 - PXRD patterns from mechanochemically prepared samples of *sNPX* and *2A4CP*, ground, with ethanol, in either 2:1, 1:1 or 1:2 molar ratios (top three patterns)

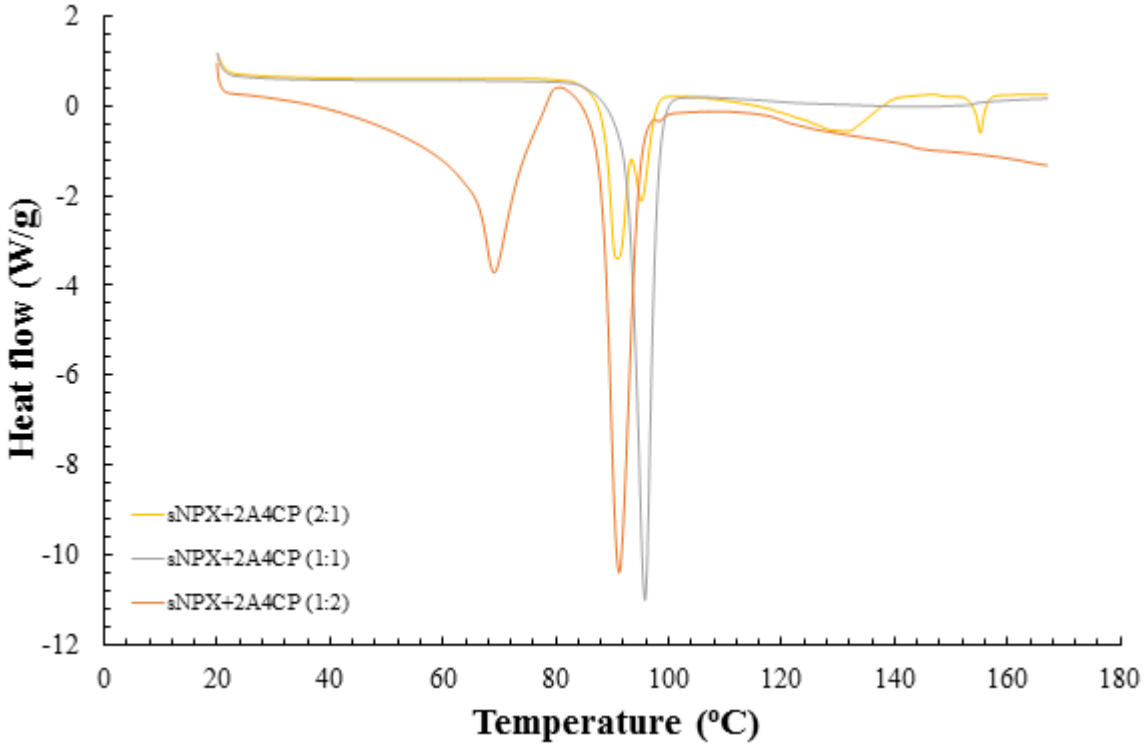

Figure 7. 37 - DSC traces from mechanochemically prepared samples of *sNPX* and *2A4CP*, ground, with ethanol, in either 2:1, 1:1 or 1:2 molar ratios

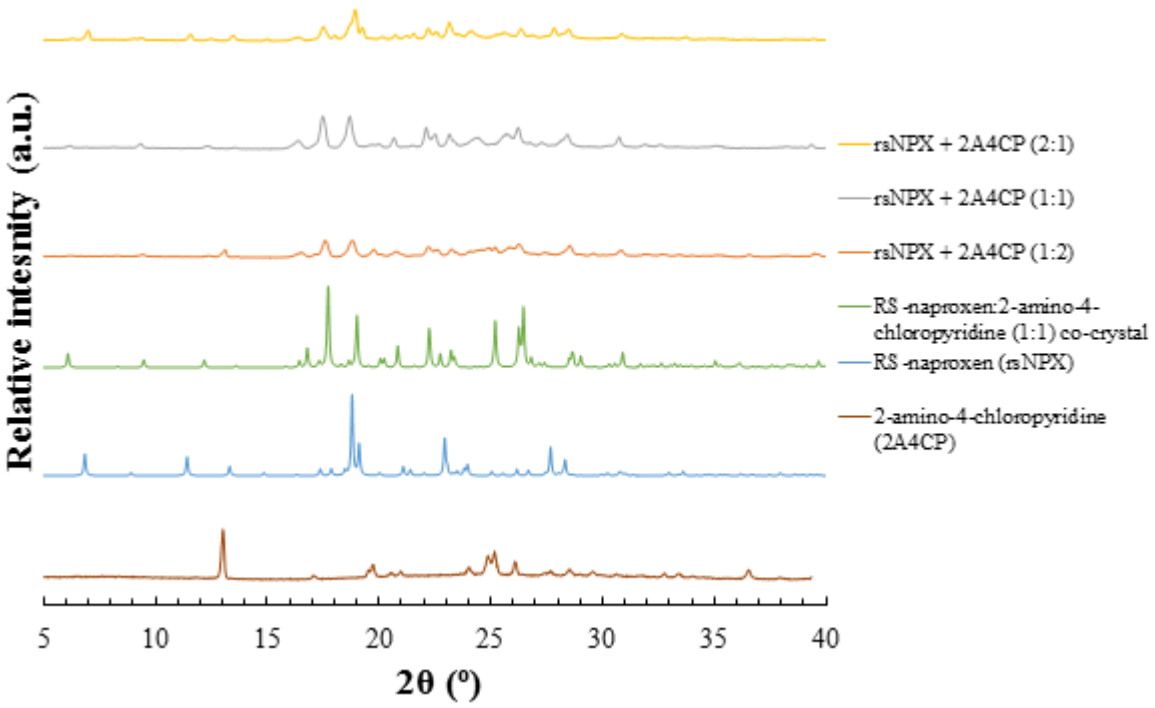

Figure 7. 38 - PXRD patterns from mechanochemically prepared samples of *rsNPX* and *2A4CP*, ground, with ethanol, in either 2:1, 1:1 or 1:2 molar ratios (top three patterns)

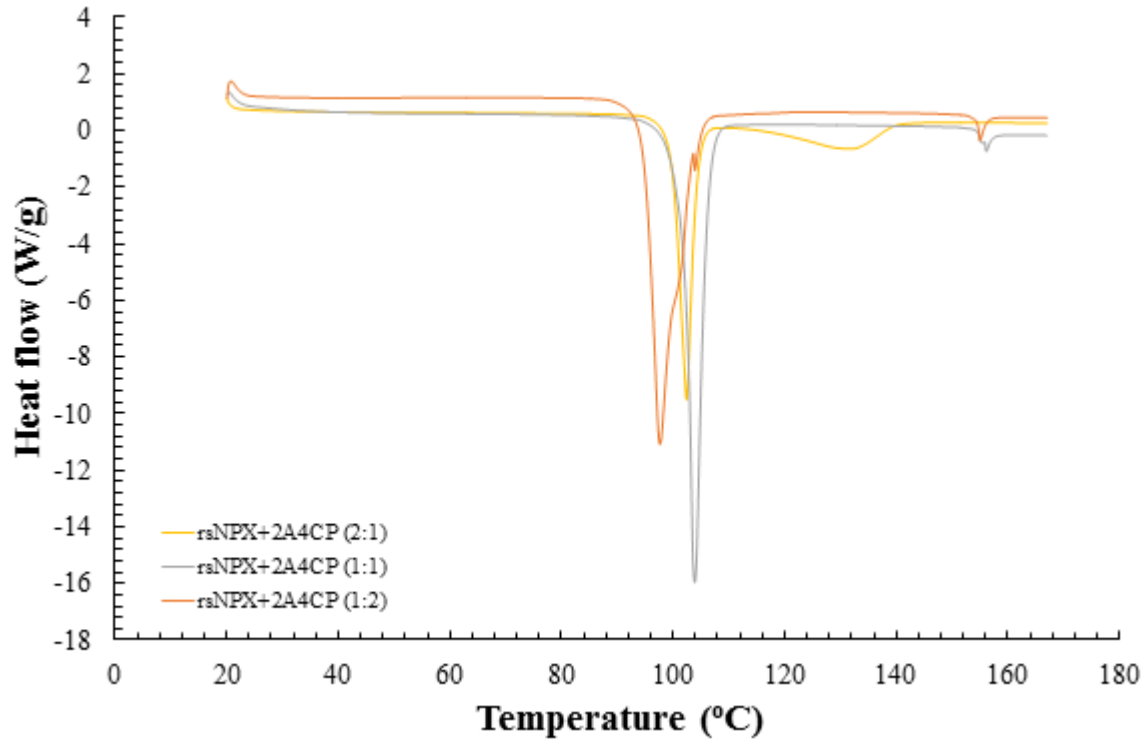

Figure 7. 39 - DSC traces from mechanochemically prepared samples of *rsNPX* and *2A4CP*, ground, with ethanol, in either 2:1, 1:1 or 1:2 molar ratios

7.4.1.2 Combined evaporation & cooling crystallisation screening

Single crystals were prepared from ethanol solutions, with varying stoichiometries and enantiomeric compositions, and were viewed under a microscope (Figure 7.40). Long thin needle agglomerates were shown to form for 1:1 solutions of *sNPX* and *2A4CP*, whilst non-uniform elongated planks were yielded from racemic preparations. As determined from SCXRD characterisation, the crystals from the homochiral sample generated a material that was different to that made *via* grinding. Despite using small amounts of mechanochemical sample as a seed to force the nucleation and growth of the desired form, the crystals selected and assessed were shown to only be that of the initial material made without seeding. This was later shown to correspond to a (1:1) homochiral salt. To date, efforts are continuing to grow single crystals of the form found from mechanochemistry.

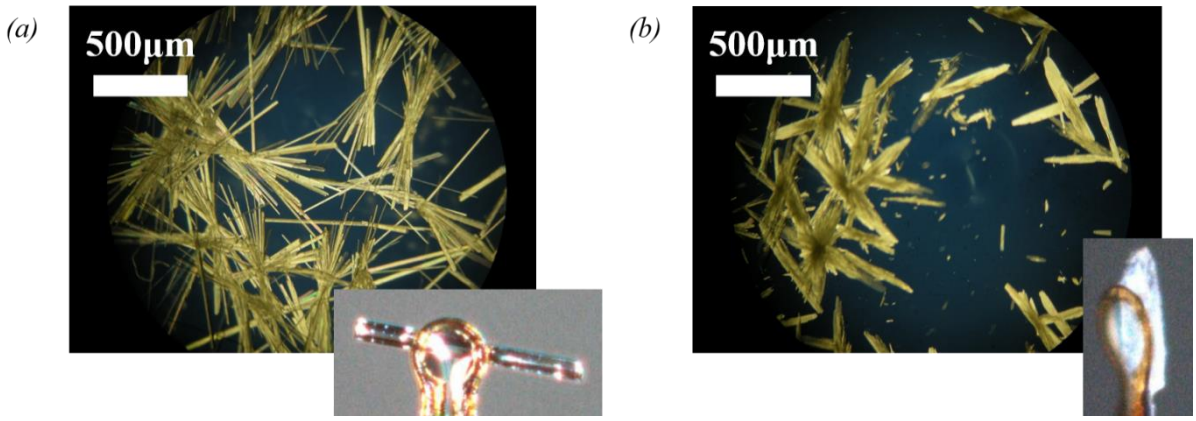

Figure 7. 40 - Microscope and mounted SCXRD images of crystals yielded from 1:1 ethanol solutions of (a) *sNPX* and (b) *rsNPX* with *2A4CP*, respectively

7.4.2 Material characterisation

7.4.2.1 Phase, thermal and spectroscopic analysis

By using mechanochemical and solution crystallisation techniques, novel materials of either *sNPX* or *rsNPX* with *2A4CP* were prepared. Figure 7.41 shows the PXRD patterns taken either from subsequent simulations produced *via* structure determination or directly from analysis of mechanochemically prepared samples. The patterns of the newly discovered phases emphasise the production of different crystalline forms and, with particular significance when assessing the racemic and homochiral materials prepared *via* grinding, this provided the first indication that with multi-component material formation, a racemic compound was produced.

This was supported by comparing the melting points of the mechanochemically prepared samples at the racemic and enantiopure combinations (Figure 7.42). The transition from a solid to the molten state for the homochiral phase (92-96^{o}C) was lower than that for the racemic (102-104^{o}C), suggesting that the interactions exhibited when both chiral forms of *NPX* were present was greater than when only one form was present, again highlighting the formation of a racemic compound.

IR spectroscopic analysis of the ground samples (Appendix A7.4) showed different carbonyl vibrational modes, respectively, suggesting that the interactions exploited between these two materials utilise a different combination of hydrogen bonding interactions with the C=O functionality of the API.

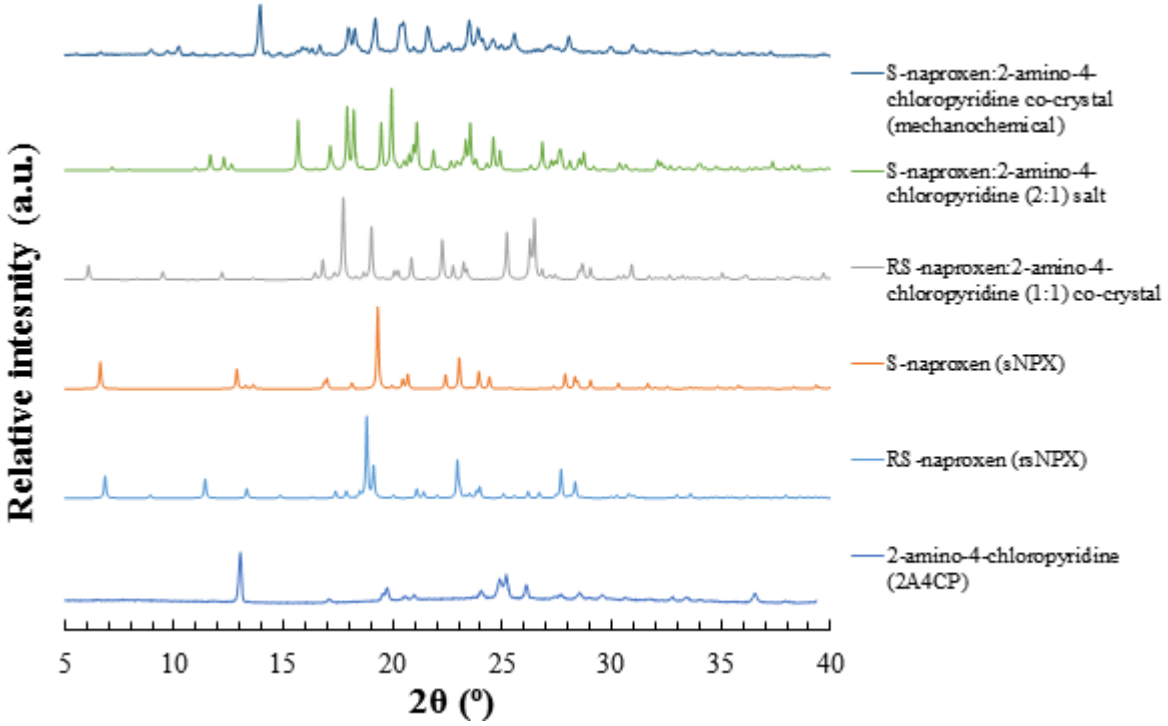

Figure 7. 41 - PXRD patterns of the S-naproxen:2-amino-4-chloropyridine co-crystal (prepared mechanochemically), as well as its stoichiometric (2:1) salt, and RS-naproxen:2-amino-4-chloropyridine (1:1) co-crystal, as derived from SCXRD, compared to that of the starting materials

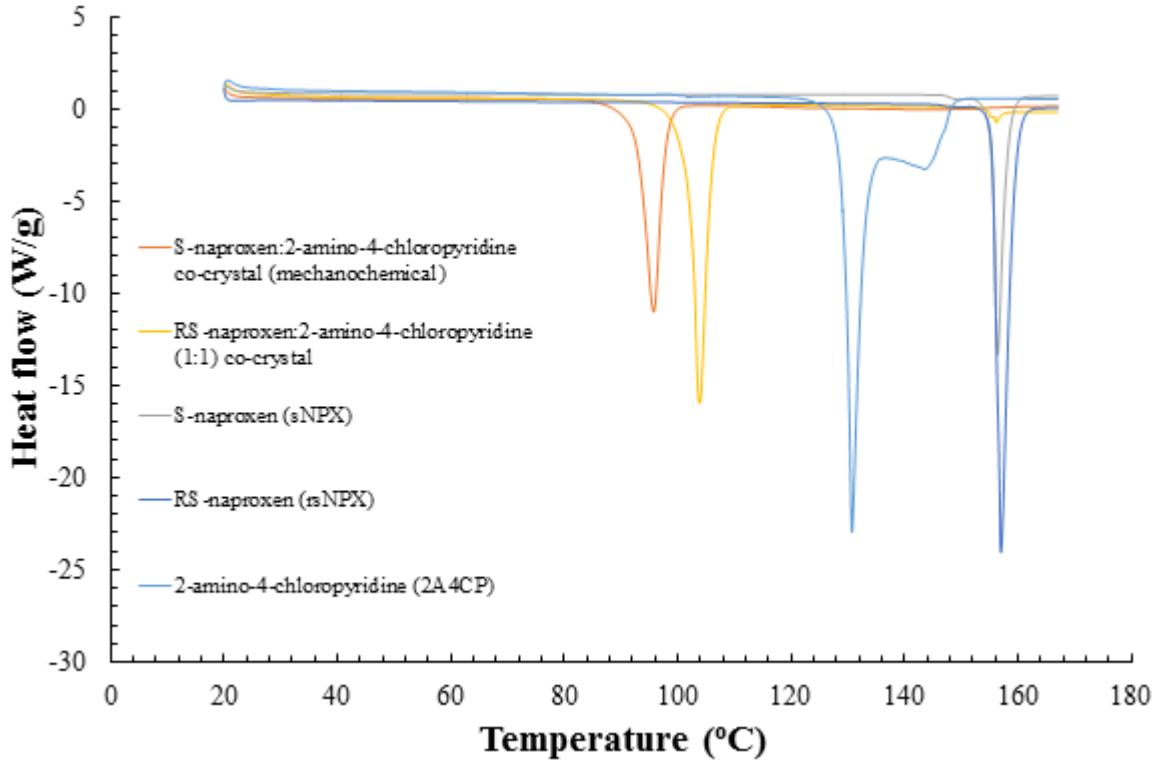

Figure 7. 42 - DSC traces of the S-naproxen:2-amino-4-chloropyridine (prepared mechanochemically) and RS-naproxen:2-amino-3-chloropyridine (1:1) co-crystals, compared to that of the starting materials

7.4.2.2 Binary (melting point) phase diagram analysis – Classification of chiral crystalline materials

Further phase analysis was carried out so as to confirm the relationship between homo and heterochiral phases generated *via* mechanochemical means. Data collected from DSC and PXRD analysis (see Appendix A7.4) was used to construct the diagram shown in Figure 7.43. As shown, towards racemic compositions a different solid-state material showed thermal stability compared to that towards enantiopure. Recognition of the characteristic racemic region, coupled with the presence of eutectic events, clarified the existence of a racemic compound chiral crystalline system.

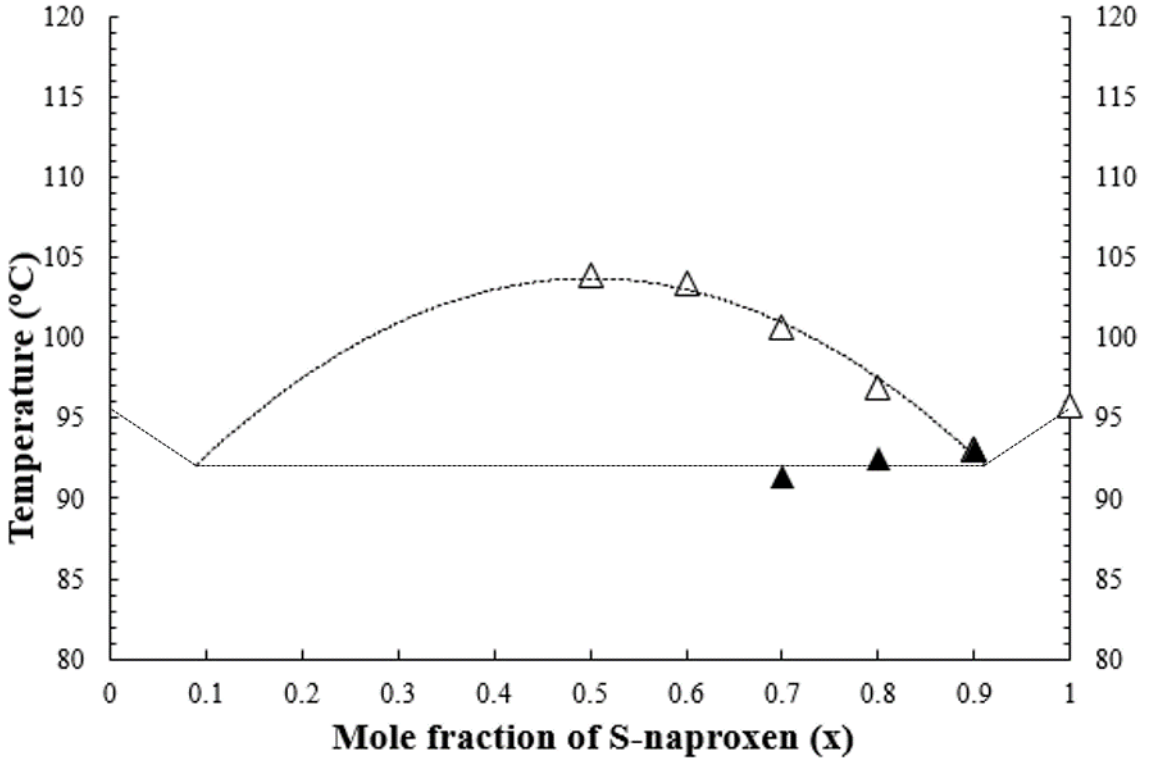

Figure 7. 43 - Binary (melting) point phase diagram, with changing enantiomeric composition of *rNPX* and *sNPX*, for the 1:1 co-crystals incorporating the co-former *2A4CP*, highlighting the liquidus (Δ) and the eutectic (▲) points

7.4.2.3 Crystallography – Crystal structure analysis

For detailed crystallographic data for the structures containing *2A4CP*, see Appendix A7.4. The corresponding CIF files (10, 11) can be found on the accompanying CD-ROM.

Despite not representing the material made through direct grinding of *sNPX* and *2A4CP*, crystals obtained from initial crash cooling crystallisations were investigated so as to confirm their crystalline structure. As shown in Figure 7.44, two molecular units of *sNPX* were able to interact with the co-former in a 2:1 molar ratio, with these motifs making up the asymmetric units of the unit cell ($Z = 2$, $Z' = 1$). The details of the unit cell, as well as further refinement parameters, can be found in Table 7.8. Hence, the molecules were shown to crystallise in a monoclinic $P2_1$ space group, a non-centrosymmetric system.

The key interaction unit consisted of the classic $R_2^2(8)$dimer motif, between one API molecule and a co-former molecule. It was noted that proton transfer had occurred, resulting in charge assisted hydrogen bonding interactions. Further contacts were utilised, connecting individual dimers through a $D_1^1(3)$ motif, forming an extended chain, similar to that seen in the homochiral structure with *2A3CP*.

However, a secondary *sNPX* molecule was shown to coordinate to the deprotonated oxygen atom of the original *sNPX* moiety, forming another $D_1^1(3)$ interaction. For this contact, no further proton transition took place. The overall assembly of the S-naproxen:2-amino-4-chloropyridine (2:1) salt was generated through a collection of these extended enantiopure chains. The presence of the chlorine atom at the para position presented no steric hindrance to hydrogen bond formation, but in this case, aided in the creation of a crystalline salt.

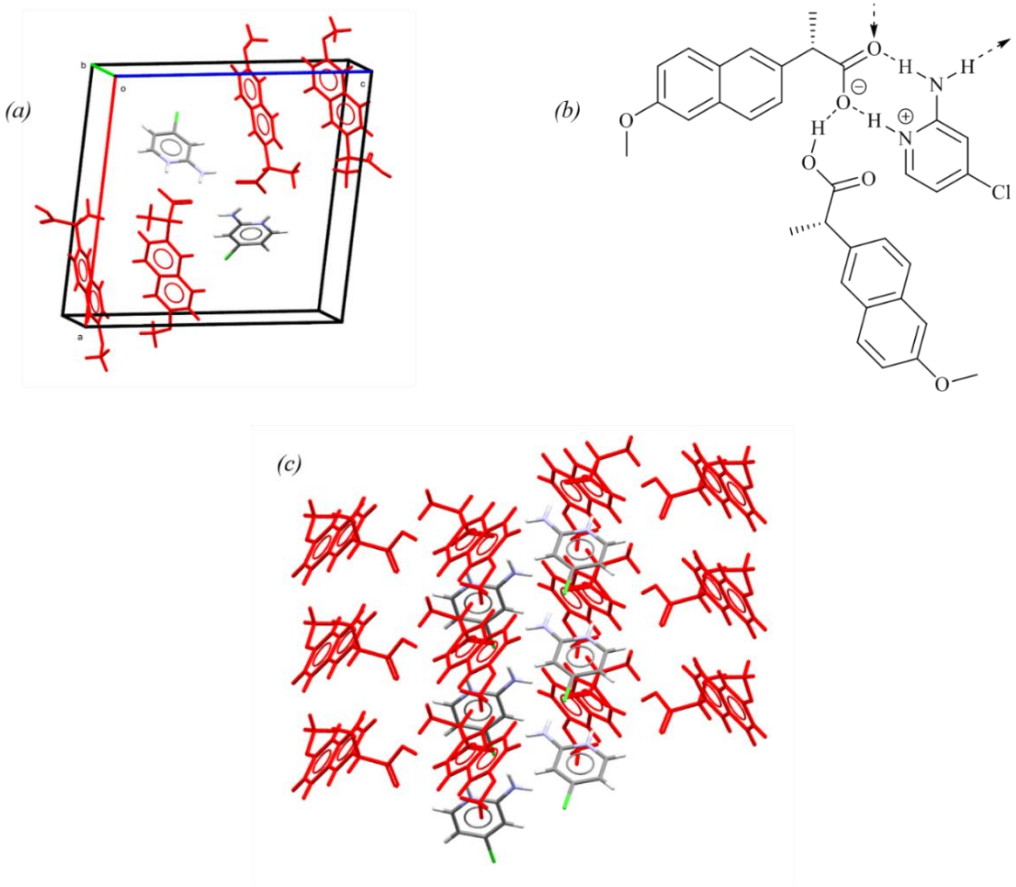

Figure 7. 44 - Crystal structure of the S-naproxen:2-amino-4-chloropyridine (2:1) salt, highlighting (a) the unit cell, (b) hydrogen bonding synthon and (c) packing arrangement (*sNPX* in red)

Table 7. 7 - Unit cell and crystallographic parameters for the S-naproxen:2-amino-4-chloropyridine (2:1) salt

Material	**S-naproxen:2-amino-4-chloropyridine (2:1) salt**
Empirical formula	$C_{33}H_{33}ClN_2O_6$
Formula weight	589.06
Temperature (K)	150.01(10)
Crystal system	monoclinic
Space group	$P2_1$
***a* (Å)**	16.2086(15)
***b* (Å)**	5.4036(5)
***c* (Å)**	17.029(2)
***α* (°)**	90
***β* (°)**	95.882(10)
***γ* (°)**	90
Volume (Å^3)	1483.6(3)
Z*, *Z'	2, 1
ρ_{calc} (g/cm^3)	1.319
μ (mm^{-1})	0.177
F(000)	620.0
Crystal size (mm^3)	0.221 × 0.098 × 0.042
Radiation	MoKα (λ = 0.71073)
2Θ range for data collection (°)	5.37 to 51.362
Index ranges	$-19 \leq h \leq 18$, $-6 \leq k \leq 6$, $-20 \leq l \leq 17$
Reflections collected	10522
Independent reflections	5608 [R_{int} = 0.0388, R_{sigma} = 0.0714]
Data/restraints/parameters	5608/314/387
Goodness-of-fit on F^2	1.030
Final R indexes [I>=2σ (I)]	R_1 = 0.0755, wR_2 = 0.1821
Final R indexes [all data]	R_1 = 0.0978, wR_2 = 0.2021
Largest diff. peak/hole (e Å^{-3})	0.99/-0.31
Flack parameter	0.04(5)

For the material prepared both mechanochemically and from solution crystallisation at racemic quantities, *NPX* was shown to crystallise in a 1:1 stoichiometry with *2A4CP* in a centrosymmetric $P\bar{1}$ triclinic space group. The asymmetric units within the unit cell ($Z = 2$, $Z' = 1$) consisted of one molecule of the API and one molecule of the co-former, with both enantiomers being accounted for. The arrangement of the molecules within this system are shown in Figure 7.45., with the parameters defining the unit cell and crystallographic refinements detailed in Table 7.8.

In this case, no proton transfer was exhibited, meaning that a RS-naproxen:2-amino-4-chloropyridine (1:1) co-crystal had formed. As with the racemic structure exhibited between *NPX* and *2AP*, the key interaction unit consisted of the dimerisation ($R_4^2(8)$) of the main heterodimer ($R_2^2(8)$), incorporating an inversion operation to account for both enantiomers. These zig-zagged units can be stacked in order to build up the whole crystal lattice, forming channels of a given enantiomeric form.

To date, no single crystals have been grown that represent that of the enantiopure multi-component phase first prepared *via* grinding. Despite this, upon comparison with racemic phase and the observations made from spectroscopic techniques, it could be suggested that this unknown phase is co-crystalline in nature, exhibiting a different set of interaction motifs to that exhibited by the racemic (1:1) co-crystal.

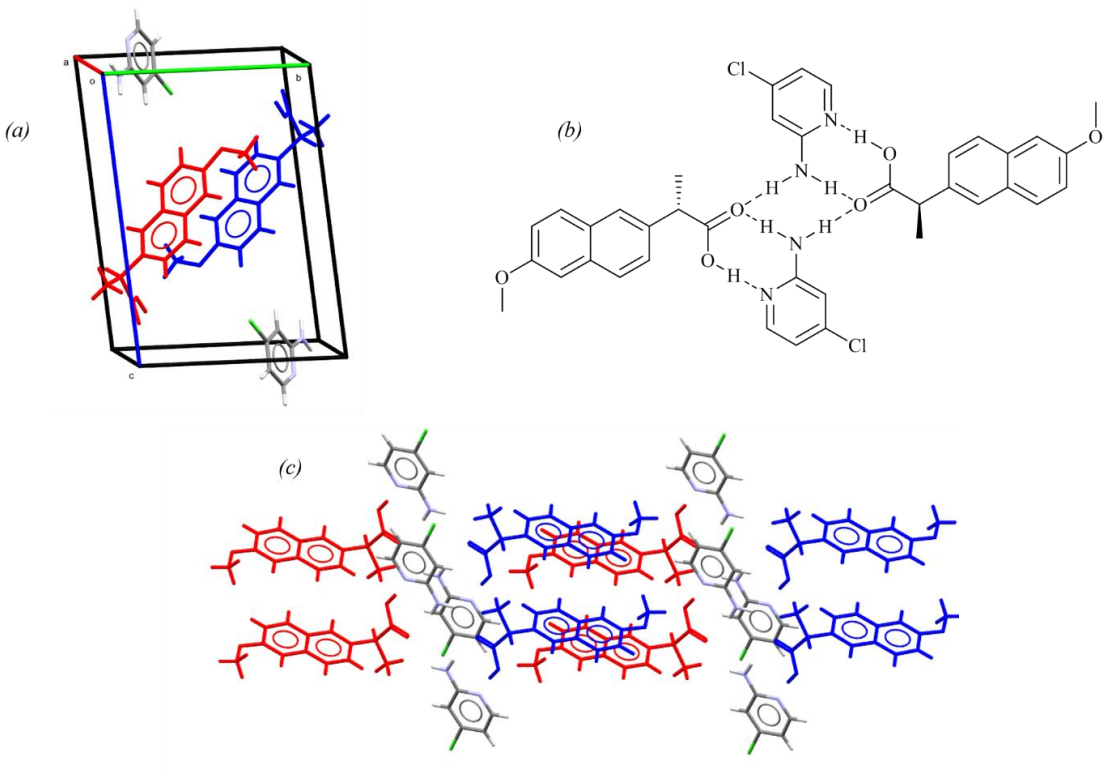

Figure 7. 45 - Crystal structure of the RS-naproxen:2-amino-4-chloropyridine (1:1) co-crystal, highlighting (a) the unit cell, (b) hydrogen bonding synthon and (c) packing arrangement (*sNPX* in red, *rNPX* in blue)

Table 7. 8 - Unit cell and crystallographic parameters for the RS-naproxen:2-amino-4-chloropyridine (1:1) co-crystal

Material	**RS-naproxen:2-amino-3-chloropyridine (1:1) co-crystal**
Empirical formula	$C_{19}H_{19}ClN_2O_3$
Formula weight	358.81
Temperature (K)	150.0(4)
Crystal system	triclinic
Space group	$P\bar{1}$
***a* (Å)**	5.4593(4)
***b* (Å)**	10.9119(9)
***c* (Å)**	14.7360(7)
***α* (°)**	80.310(5)
***β* (°)**	86.609(5)
***γ* (°)**	80.965(6)
Volume (Å^3)	854.10(10)
Z*, *Z'	2, 1
ρ_{calc} (g/cm^3)	1.395
μ (mm^{-1})	0.245
F(000)	376.0
Crystal size (mm^3)	0.287 × 0.104 × 0.068
Radiation	MoKα (λ = 0.71073)
2Θ range for data collection (°)	7.29 to 50.7
Index ranges	$-6 \leq h \leq 6$, $-13 \leq k \leq 10$, $-17 \leq l \leq 17$
Reflections collected	5589
Independent reflections	3121 [R_{int} = 0.0263, R_{sigma} = 0.0556]
Data/restraints/parameters	3121/1/232
Goodness-of-fit on F^2	1.049
Final R indexes [I>=2σ (I)]	R_1 = 0.0476, wR_2 = 0.1002
Final R indexes [all data]	R_1 = 0.0739, wR_2 = 0.1123
Largest diff. peak/hole (e Å^{-3})	0.25/-0.23
Flack parameter	N/A

7.5 Materials of racemic and enantiopure naproxen with 2-amino-5-chloropyridine (*2A5CP*)

7.5.1 Material screening

The co-former 2-amino-5-chloropyridine (*2A5CP*) exhibits its chlorine atom meta to the pyridine functionality, making its electron donating contributions similar to that of *2A3CP*. Searches of the CSD have highlighted only one polymorph (CSD reference: AMCLPY12[206]), an off-white solid, with a melting point between 135ºC and 136ºC. Further to this, its pK_a has been estimated to be approximately 4.7, highlighting weak basicity and the likelihood of co-crystal formation with *NPX*.

7.5.1.1 Mechanochemical screening

Enantiopure samples of *NPX* and *2A5CP*, prepared mechanochemically with minimum quantities of ethanol, were assessed using PXRD, the patterns of which are shown in Figure 7.46. With particular emphasis on the patterns generated from analysis of the 1:1 and 1:2 API to co-former preparations, the diffraction data demonstrated the formation of a novel crystalline phase, distinct from that of the starting materials. Comparison with the simulated PXRD pattern generated from subsequent SCXRD analysis of crystals obtained from solution crystallisation (see section 7.5.2) demonstrated the reproducibility of the enantiopure multi-component phase over the different methods. The DSC trace for this combination, shown in Figure 7.47, stressed the formation of a new phase, highlighting the presence of a single endothermic peak at 89-91ºC.

As with the homochiral case, samples were also made *via* grinding consisting of the racemic combination of API and the co-former. Depicted in Figure 7.48, PXRD analysis showed the formation of a distinct crystalline phase across all three stoichiometric combinations. For the 2:1 and 1:2 preparations, the unknown phase was found to be in a physical mixture with excess starting material. The consistency in preparation of this racemic multi-component phase across the preparation techniques was highlighted by the concurrency of diffraction patterns generated for the mechanochemical and cooling crystallisation samples. Thermal analysis, shown in Figure 7.49, confirmed the existence of a discrete racemic phase by noting a single endothermic feature for the 1:1 sample, at 103-105ºC.

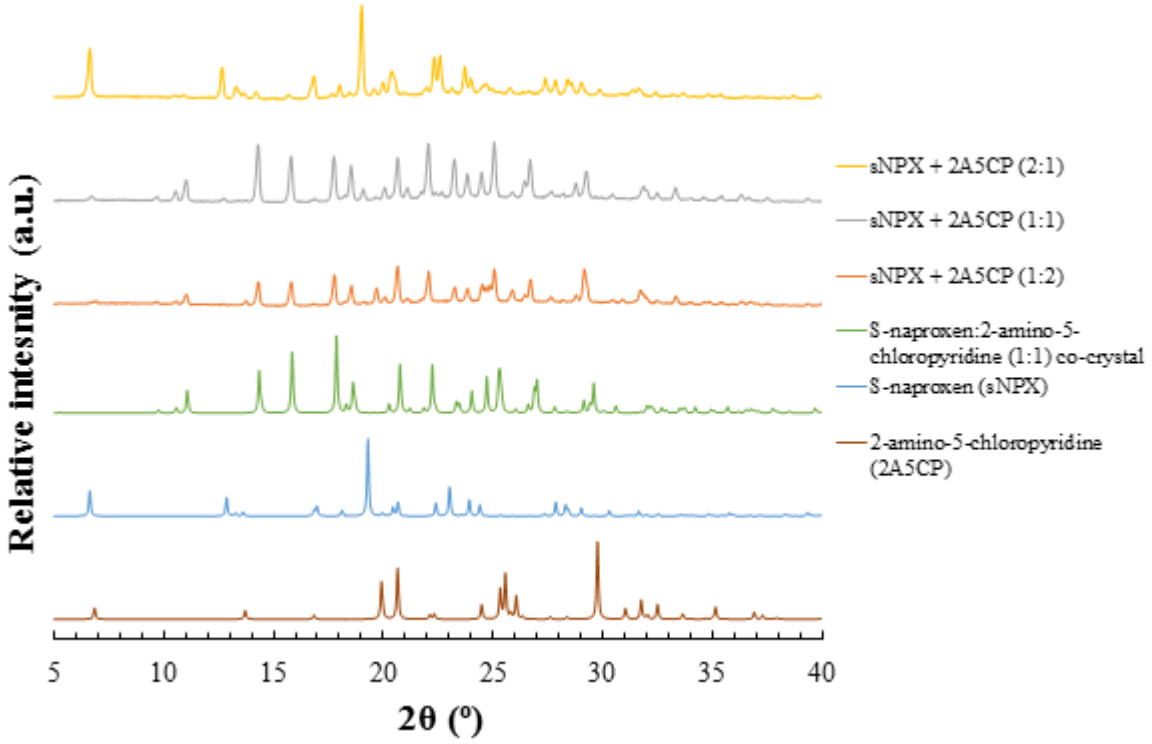

Figure 7. 46 - PXRD patterns from mechanochemically prepared samples of *sNPX* and *2A5CP*, ground, with ethanol, in either 2:1, 1:1 or 1:2 molar ratios (top three patterns)

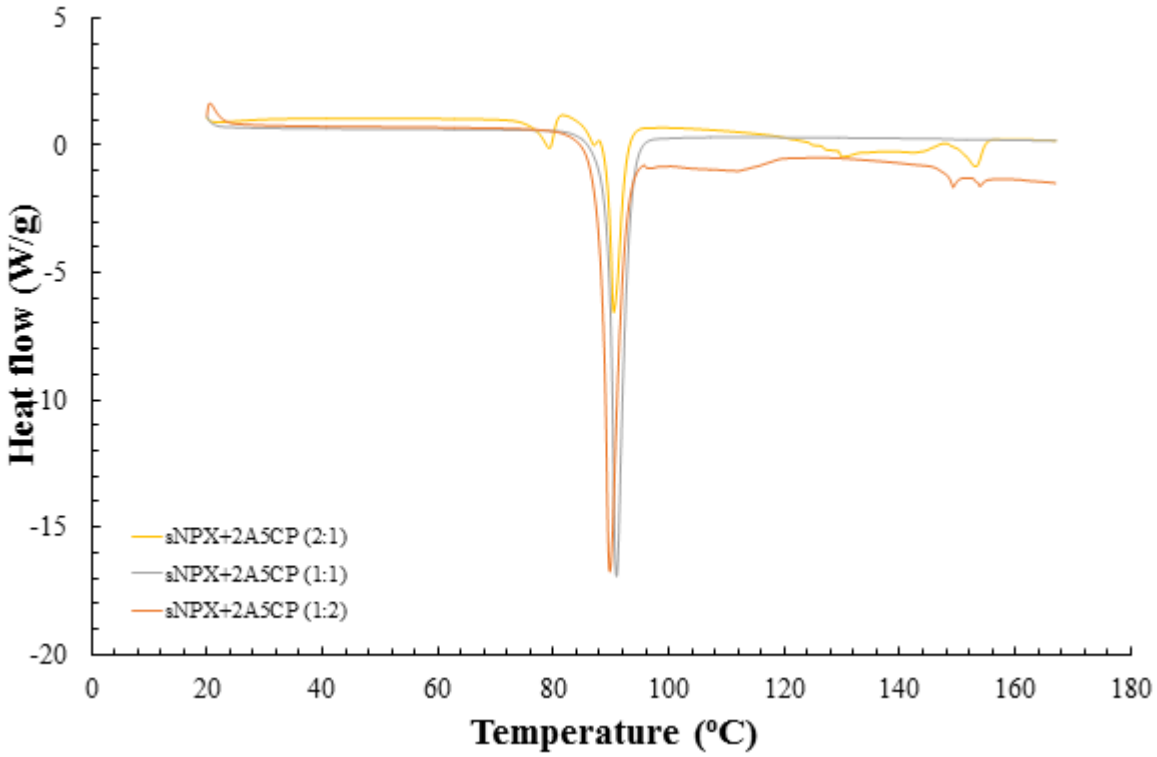

Figure 7. 47 - DSC traces from mechanochemically prepared samples of *sNPX* and *2A5CP*, ground, with ethanol, in either 2:1, 1:1 or 1:2 molar ratios

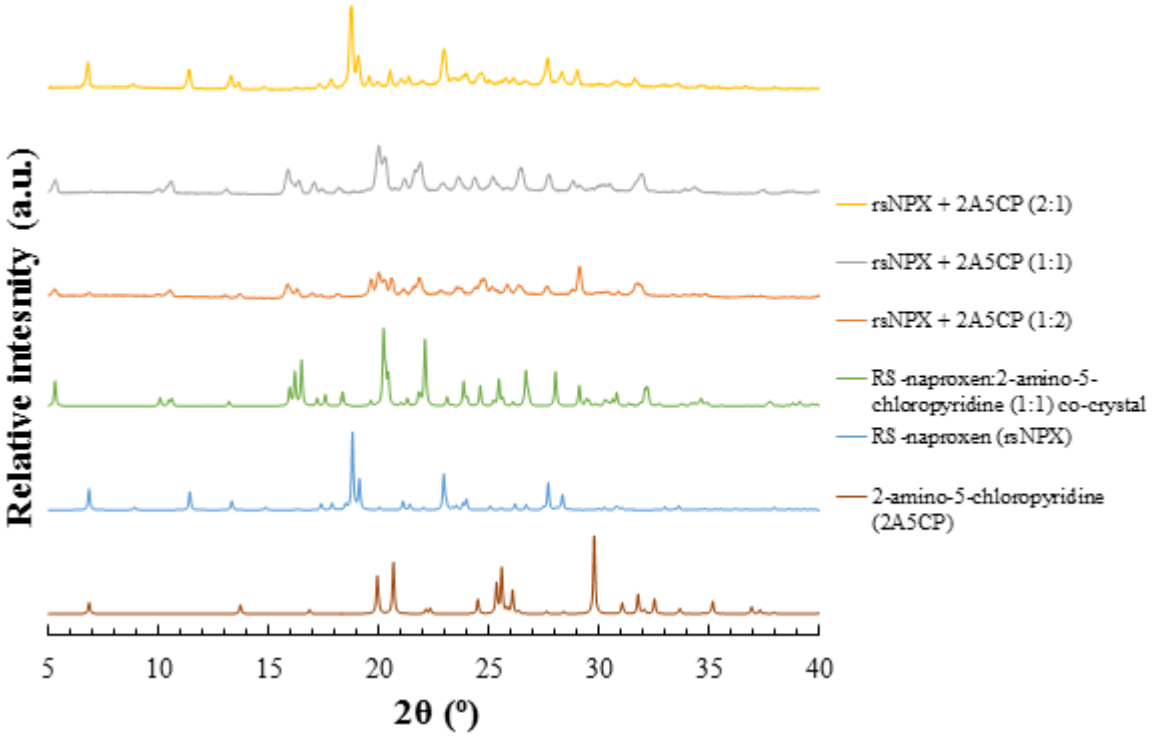

Figure 7. 48 - PXRD patterns from mechanochemically prepared samples of *rsNPX* and *2A5CP*, ground, with ethanol, in either 2:1, 1:1 or 1:2 molar ratios (top three patterns)

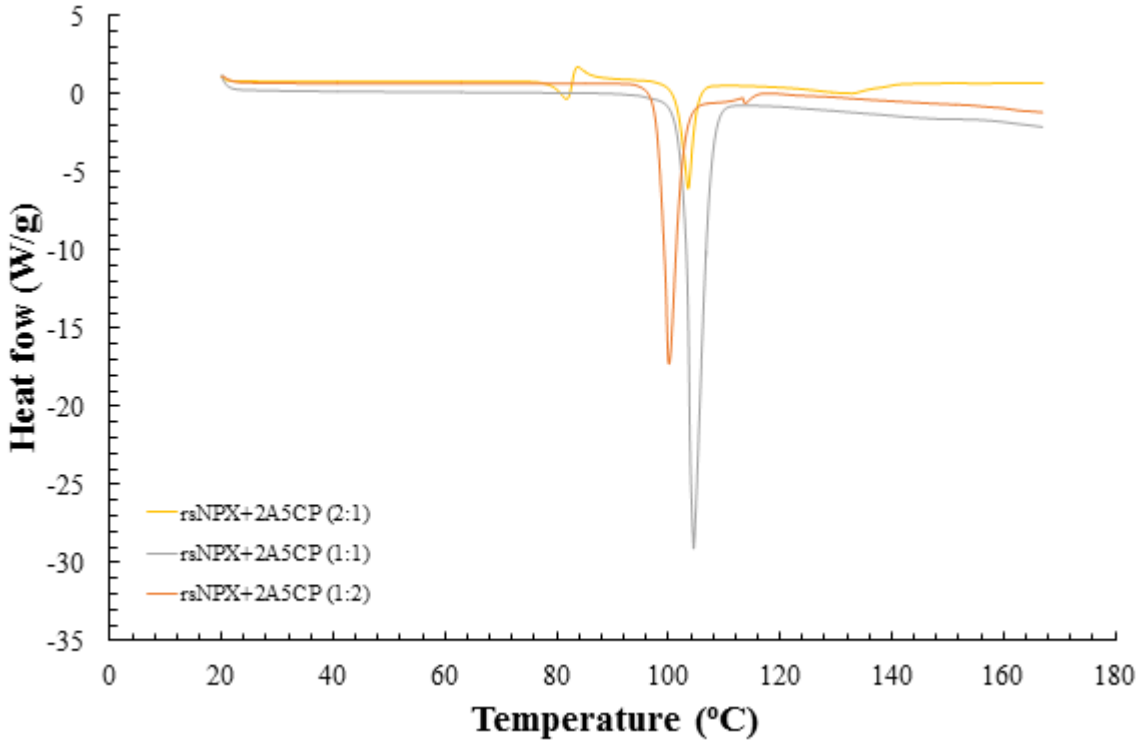

Figure 7. 49 - DSC traces from mechanochemically prepared samples of *sNPX* and *2A5CP*, ground, with ethanol, in either 2:1, 1:1 or 1:2 molar ratios

7.5.1.2 Combined evaporation & cooling crystallisation screening

Individual crystals were grown *via* the combined evaporative and crash cooling method, from solutions of ethanol, with the three defined stoichiometries of *NPX* to co-former (2:1, 1:1 and 1:2), for both racemic and enantiopure compositions of the API. Figure 7.50 shows the crystals formed from 1:2 solutions of *sNPX* and *rsNPX* with *2A5CP*, respectively. The crystals in both cases were shown to be off-white in colour and displayed long thin plate-like morphologies. It should be noted that for both crystallisations, the individual crystallites formed agglomerates. In addition, the shapes of the racemic multi-component crystals were far less uniform compared to its enantiopure counterpart. Single crystals were selected from each preparation and mounted for a diffractometer so as to ascertain their crystalline structure. As such, the crystals grown *via* cooling were found to be the same as the bulk material made with grinding.

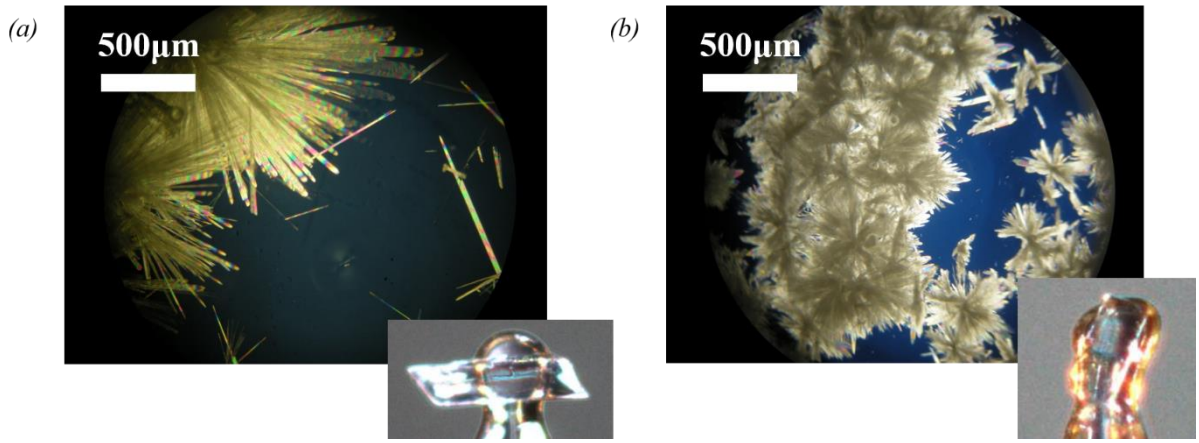

Figure 7. 50 - Microscope and mounted SCXRD images of crystals yielded from 1:2 ethanol solutions of (a) *sNPX* and (b) *rsNPX* with *2A5CP*, respectively

7.5.2 Material characterisation

7.5.2.1 Phase, thermal and spectroscopic analysis

Upon combining either *rsNPX* or *sNPX* with the co-former, *2A5CP*, mechanochemically or *via* solution crystallisation, novel crystalline phases were prepared. Figure 7.51 shows the simulated PXRD patterns of these multi-component phases, also showing that these phases differ from each other, demonstrating that by varying the enantiomeric composition from racemic to enantiopure, maintaining the required stoichiometry of API to co-former, a transition occurs. The presence of a unique phase at racemic compositions indicates that upon complexation with this given co-former, a racemic compound chiral crystalline system can be formed.

Comparison of the thermal traces of these materials suggested the existence of a racemic compound. Outlined in Figure 7.52, the melting points of both the homo and heterochiral materials were shown to be lower than that of the respective starting components, with the racemic form displaying a higher melting point (103-105^{o}C) than the homochiral phase (89-91^{o}C). For the structure using both enantiomeric forms of *NPX*, along with *2A5CP*, greater stability can be achieved when compared to that of the enantiopure phase.

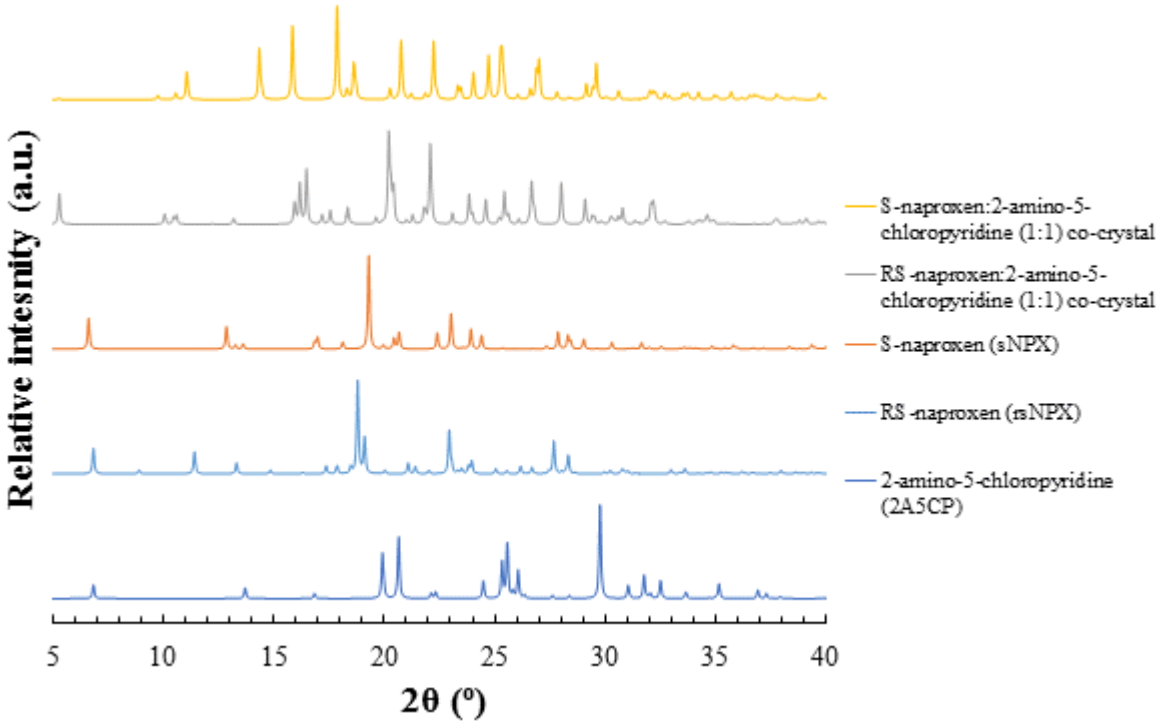

Figure 7. 51 - PXRD patterns of the S-naproxen and RS-naproxen:2-amino-5-chloropyridine (1:1) co-crystals, as derived from SCXRD, compared to that of the starting materials

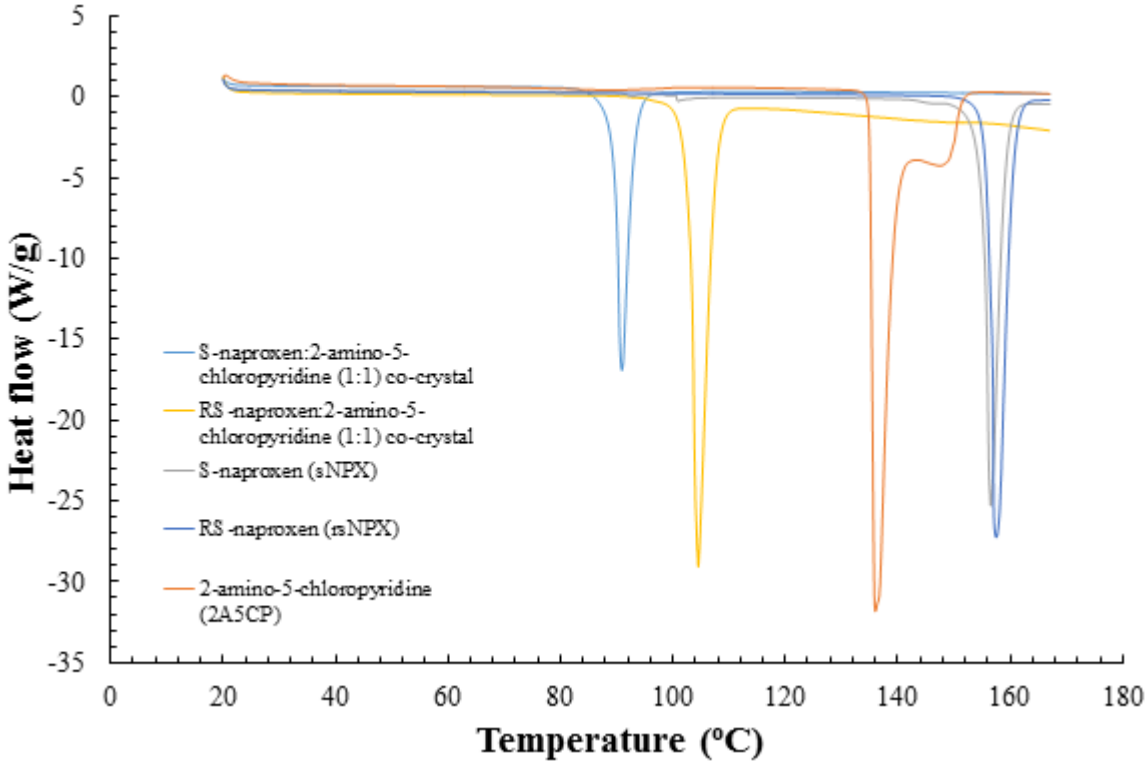

Figure 7. 52 - DSC traces of the S-naproxen and RS-naproxen:2-amino-5-chloropyridine (1:1) co-crystals, compared to that of the starting materials

Based upon data obtained from IR spectroscopy (for the spectra, see Appendix A7.5), it was shown that each of the novel chiral materials utilised similar intermolecular interactions, but with some subtle differences. With a focus on the carbonyl functionality, both phases exhibited a main vibrational mode at 1737 cm^{-1} with a shoulder at a slightly lower wavenumber. This would suggest that the carbonyl group formed a constituent part of two different hydrogen bonding interactions for both multi-component forms. Upon closer examination of the spectra for the homochiral material, the broad peak unique to this phase at 2430 cm^{-1} was noted and attributed to the amine group undergoing hydrogen bonding interactions in the solid state. The presence of this phenomenon exclusively for the enantiopure form suggested that one of the amine N-H bonds forms a more flexible contact than when compared to that of the racemic material. These observations provided further evidence that two distinct phases exist, collectively resulting in a racemic compound system.

7.5.2.2 Binary (melting point) phase diagram analysis – Classification of chiral crystalline materials

A culmination of the phase and thermal analysis for the system incorporating both *NPX* and *2A5CP* can be described using the binary (melting point) phase diagram shown in Figure 7.53. The corresponding DSC and PXRD data can be found in Appendix A7.5. Upon transitioning from racemic to enantiopure compositions, clear regions were evident, emphasising the stability of the homo and heterochiral phases, respectively. In addition, eutectic melting was also observed at 87-89ºC. The combined evidence of the distinct phases, higher racemic material melting and the existence of eutectic events upon changes in enantiomeric composition changes exemplify the formation of a racemic compound system.

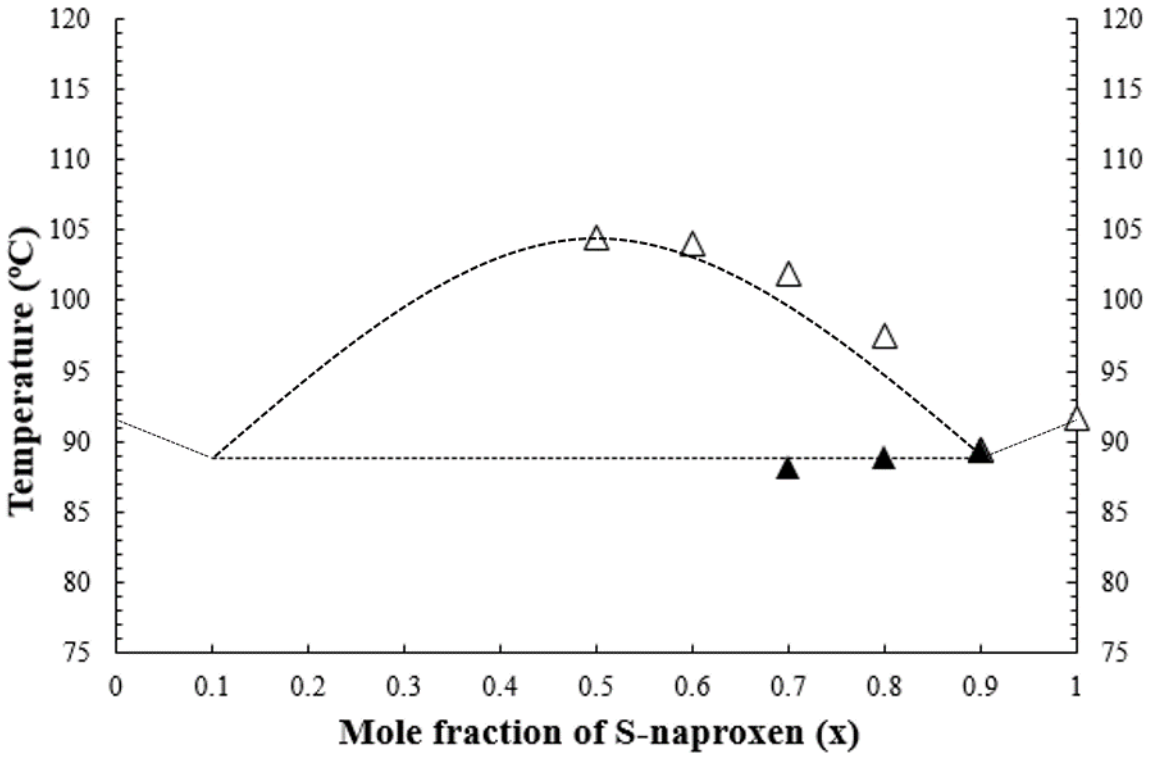

Figure 7. 53 - Binary (melting) point phase diagram, with changing enantiomeric composition of *rNPX* and *sNPX*, for the 1:1 co-crystals incorporating the co-former *2A5CP*, highlighting the liquidus (Δ) and the eutectic (▲) points

7.5.2.3 Crystallography – Crystal structure analysis

The crystal structures for the multi-component materials were determined from the X-ray diffraction patterns of single crystals taken from the respective racemic and enantiopure solutions. Visual representations of the key structural and interaction units for the materials utilising either *sNPX* or *rsNPX* with the co-former, can be found in Figures 7.54 and 7.55, respectively. The unit cell and refinement parameters in each case are outlined in Tables 7.10 and 7.11. Further information, including details of the hydrogen bond dimensions, can be found in Appendix A7.5. The corresponding CIF files (12, 13) can be found on the accompanying CD-ROM.

Crystals prepared from enantiopure solutions showed a 1:1 arrangement of *sNPX* to *2A5CP* molecules, with this unit constituting the asymmetric unit (Z = 2, Z' = 1). From this, the molecular entities were shown to crystallise in the non-centrosymmetric monoclinic $P2_1$ space group. No proton transfer was evident, demonstrating the formation of a S-naproxen:2-amino-5-chloropyridine (1:1) co-crystal.

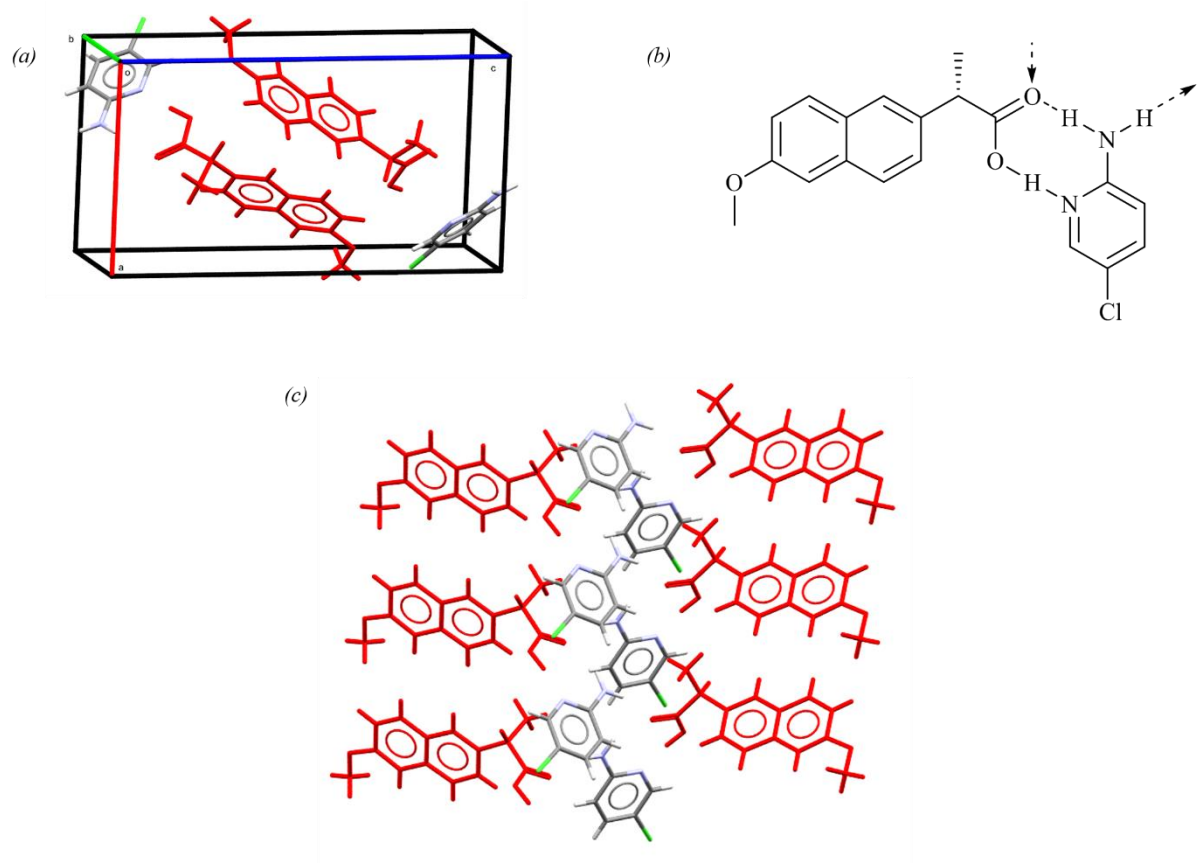

Figure 7. 54 - Crystal structure of the S-naproxen:2-amino-5-chloropyridine (1:1) co-crystal, highlighting (a) the unit cell, (b) hydrogen bonding synthon and (c) packing arrangement (*sNPX* in red)

The key interaction motif between the *sNPX* and *2A5CP* molecules was the hydrogen bonded heterodimer, whereby the hydrogen bond donors were represented by the amine and hydroxyl functionalities, and the acceptors by the carbonyl and pyridine groups. Collectively, this dimer could be defined as a $R_2^2(8)$ synthon. These dimerised units were further connected to other dimers through an additional single hydrogen bond interaction between the secondary amine donor and the carbonyl group on an adjacent API molecule. This synthon can be described in terms of a $D_1^1(3)$ contact. Resultant chains were built up in parallel so as to generate the overall crystalline assembly of this S-

naproxen:2-amino-5-chloropyridine (1:1) co-crystal. This material was structurally akin to that of the homochiral multi-component phases incorporating the co-formers *2AP* and *2A3CP*.

Table 7. 9 - Unit cell and crystallographic parameters for the S-naproxen:2-amino-5-chloropyridine (1:1) co-crystal

Material	**S-naproxen:2-amino-5-chloropyridine (1:1) co-crystal**
Empirical formula	$C_{19}H_{19}ClN_2O_3$
Formula weight	358.81
Temperature (K)	150.00(10)
Crystal system	monoclinic
Space group	$P2_1$
***a* (Å)**	9.05850(10)
***b* (Å)**	5.92910(10)
***c* (Å)**	16.7511(2)
***α* (°)**	90
***β* (°)**	90.4220(10)
***γ* (°)**	90
Volume (Å^3)	899.66(2)
Z*, *Z'	2, 1
ρ_{calc} (g/cm^3)	1.325
μ (mm^{-1})	2.049
F(000)	376.0
Crystal size (mm^3)	0.476 × 0.115 × 0.062
Radiation	CuKα (λ = 1.54184)
2Θ range for data collection (°)	5.276 to 144.242
Index ranges	$-6 \leq h \leq 11$, $-7 \leq k \leq 7$, $-20 \leq l \leq 20$
Reflections collected	10457
Independent reflections	3563 [R_{int} = 0.0243, R_{sigma} = 0.0187]
Data/restraints/parameters	3563/2/232
Goodness-of-fit on F^2	1.037
Final R indexes [I>=2σ (I)]	R_1 = 0.0318, wR_2 = 0.0861
Final R indexes [all data]	R_1 = 0.0319, wR_2 = 0.0863
Largest diff. peak/hole (e Å^{-3})	0.15/-0.23
Flack parameter	0.002(12)

Upon changing crystallisation medium to reflect that of a racemic composition, individual molecules of the API, of both chiralities respectively, were shown to precipitate with the *2A5CP* co-former in a 1:1 molar ratio in monoclinic $P2_1/c$ space group, a centrosymmetric system. With each asymmetric unit consisting of one molecule of the respective component materials, four units could be packed into the unit cell ($Z = 4$, $Z' = 1$) with the individual chiral forms being accounted for. As with the enantiopure form, no proton transfer was noted, allowing for this phase to be described as a RS-naproxen:2-amino-5-chloropyridine (1:1) co-crystal.

The racemic phase was shown to form a key interaction unit that utilised a combination of two $R_2^2(8)$ heterodimers between the *NPX* and *2A5CP* molecules, each exploiting a different enantiomer. These units were held together through subsequent $D_1^1(3)$ contacts, allowing for the formation of a $R_4^2(8)$ ring, resulting in dimer of dimers common to several racemic forms with *2AP* derivatives. This supports the findings of the IR spectroscopic analysis. The overall structure can then be constructed through the stacking of these core interaction units. This assembly is fundamentally related to that exhibited for the racemic salt form of *NPX* and *2AP*, but differs from that observed for *2A3CP*.

As confirmed by the crystallographic structures outlined above, two distinct phases can be generated at racemic and enantiopure compositions of *NPX* with the co-former *2A5CP*, respectively. The structures exhibited are structurally alike to those found upon combining the API with *2AP*, indicating that the positioning of the chlorine atom, meta to the pyridine group and para to that of the amine group does not hinder hydrogen bond formation, allowing for these specific interactions to form. However, as demonstrated from DSC analysis, the melting point of the racemic phase was higher than that of the

homochiral co-crystal. This was in contrast to the observations made for the *2AP* salts. By adding the halogen atom to the co-former molecule at this given position, the packing efficiency of the racemic material is enhanced (calculated packing density of the homochiral co-crystal, 1.325 g/cm^3, and that of the racemic co-crystal, 1.376 g/cm^3), aiding in its stabilisation relative to the S-naproxen:2-amino-5-chloropyridine (1:1) co-crystal and resulting in a stable racemate.

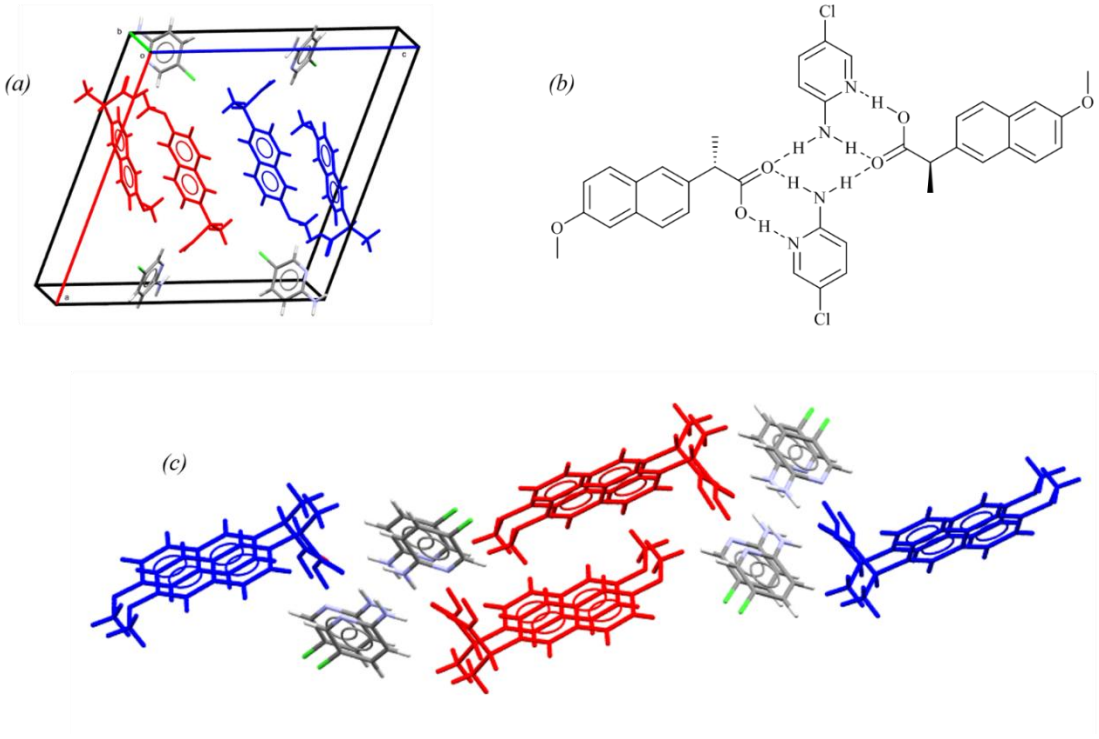

Figure 7. 55 - Crystal structure of the RS-naproxen:2-amino-5-chloropyridine (1:1) co-crystal, highlighting (a) the unit cell, (b) hydrogen bonding synthon and (c) packing arrangement (*sNPX* in red, *rNPX* in blue)

Table 7. 10 - Unit cell and crystallographic parameters for the RS-naproxen:2-amino-5-chloropyridine (1:1) co-crystal

Material	**RS-naproxen:2-amino-5-chloropyridine (1:1) co-crystal**
Empirical formula	$C_{19}H_{19}ClN_2O_3$
Formula weight	358.81
Temperature (K)	149.9(4)
Crystal system	monoclinic
Space group	$P2_1/c$
***a* (Å)**	17.6584(8)
***b* (Å)**	5.7923(2)
***c* (Å)**	17.9151(7)
***α* (°)**	90
***β* (°)**	109.095(5)
***γ* (°)**	90
Volume (Å^3)	1731.58(13)
Z*, *Z'	4, 1
ρ_{calc} (g/cm^3)	1.376
μ (mm^{-1})	2.130
F(000)	752.0
Crystal size (mm^3)	0.191 × 0.095 × 0.037
Radiation	CuKα (λ = 1.54184)
2Θ range for data collection (°)	10.052 to 144.214
Index ranges	$-17 \leq h \leq 21$, $-7 \leq k \leq 6$, $-19 \leq l \leq 22$
Reflections collected	10109
Independent reflections	3395 [R_{int} = 0.0343, R_{sigma} = 0.0360]
Data/restraints/parameters	3395/0/232
Goodness-of-fit on F^2	1.123
Final R indexes [I>=2σ (I)]	R_1 = 0.0560, wR_2 = 0.1482
Final R indexes [all data]	R_1 = 0.0676, wR_2 = 0.1576
Largest diff. peak/hole (e Å^{-3})	0.61/-0.49
Flack parameter	N/A

7.6 Materials of racemic and enantiopure naproxen with 2-amino-6-chloropyridine (*2A6CP*)

7.6.1 Material screening

The final chlorine derivative of *2AP* to be used in the screening for novel multi-component materials with *NPX* was that of 2-amino-6-chloropyridine (*2A6CP*). Searches of the CSD highlighted only one known structure of this co-former (CSD reference: XONQAU[207]), exhibiting a melting point between 69ºC and 71ºC. pK_a data could not be found, but salt formation was deemed unlikely.

7.6.1.1 Mechanochemical screening

Upon grinding enantiopure compositions of the API with the co-former, in a variety of different stoichiometries, incorporating minimum quantities of ethanol as a mediating solvent, it was shown that a novel phase could be prepared. As shown from the PXRD patterns in Figure 7.56, each preparation demonstrated diffraction intensities unique from those of the starting materials, with particular emphasis on the sample made from equimolar contributions of *sNPX* and *2A6CP*. In each case, excess starting material was noted, with this being the least evident for the 1:1 sample. Comparison of the material made mechanochemically with that crystallised from solution highlighted distinctly similar patterns, emphasising the transferability of the preparation of this homochiral complex.

Thermal analysis, conducted *via* DSC and shown in Figure 7.57, showed an initial melt and recrystallisation (exhibited through an endothermic and subsequent exothermic process), followed by a major endotherm observed at 100-103ºC. This phenomenon was particularly evident for the 1:1 preparation, again showing the ability of mechanochemistry to allow for the screening of novel materials.

In contrast, mechanochemistry with ethanol was shown to not yield any new phases with respect to the raw starting components. Figure 7.58 shows the PXRD patterns for the ground samples of racemic *NPX* with the co-former, *2A6CP*. Across the three stoichiometries used, no new peaks were accounted for that did not correspond to either of the starting components. The thermal traces taken for these preparations, depicted in Figure 7.59, each showed an initial endothermic event between 47ºC and 55ºC, followed by a series of minor thermal phenomena. First interpretations could attribute these to an initial melt of the co-former, followed by melting of excess *NPX*. In the case of the 1:2 preparation, an additional small endotherm was noted at 82-87ºC.

Further 1:1 mechanochemical preparations of *rsNPX* and *2A6CP* were made using not only ethanol, but also isopropanol and acetonitrile. The PXRD and DSC traces for these samples can be found in Appendix A7.6. As for the original ground materials, the samples made showed a great deal of similarity to that of the starting materials. However, assessment of the PXRD pattern of that utilising isopropanol demonstrated extra peaks, with a significantly intense peak at 19.5º. The thermal traces of the samples made with the assistance of isopropanol and acetonitrile both showed a more significant recrystallisation phenomenon, followed by a minor then a major event, between 74-79ºC and 84-89ºC respectively. This gave an indication that with the aid of heating, a new phase had the potential to precipitate from the melt.

Overall for the mechanochemical screenings utilising racemic compositions of *NPX*, no direct evidence of the formation of a novel multi-component materials was evident, though this could have dependence upon the solvent environment used. This could indicate that at racemic combinations, complexation was not possible.

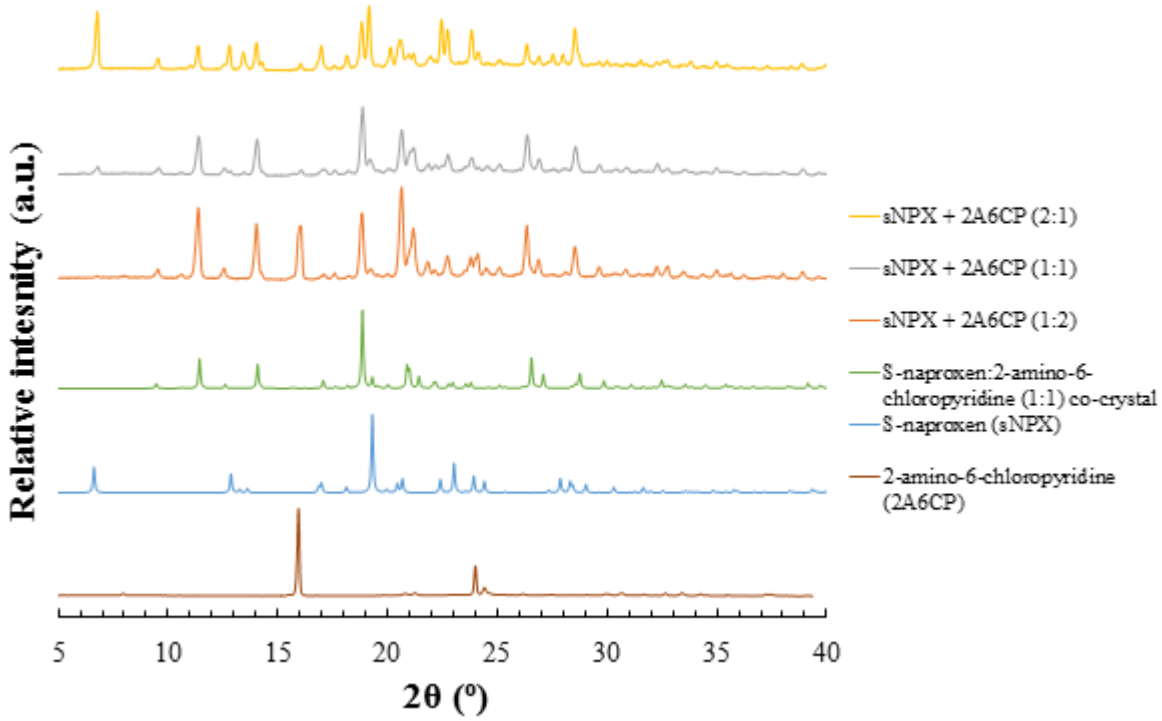

Figure 7. 56 - PXRD patterns from mechanochemically prepared samples of *sNPX* and *2A6CP*, ground, with ethanol, in either 2:1, 1:1 or 1:2 molar ratios (top three patterns)

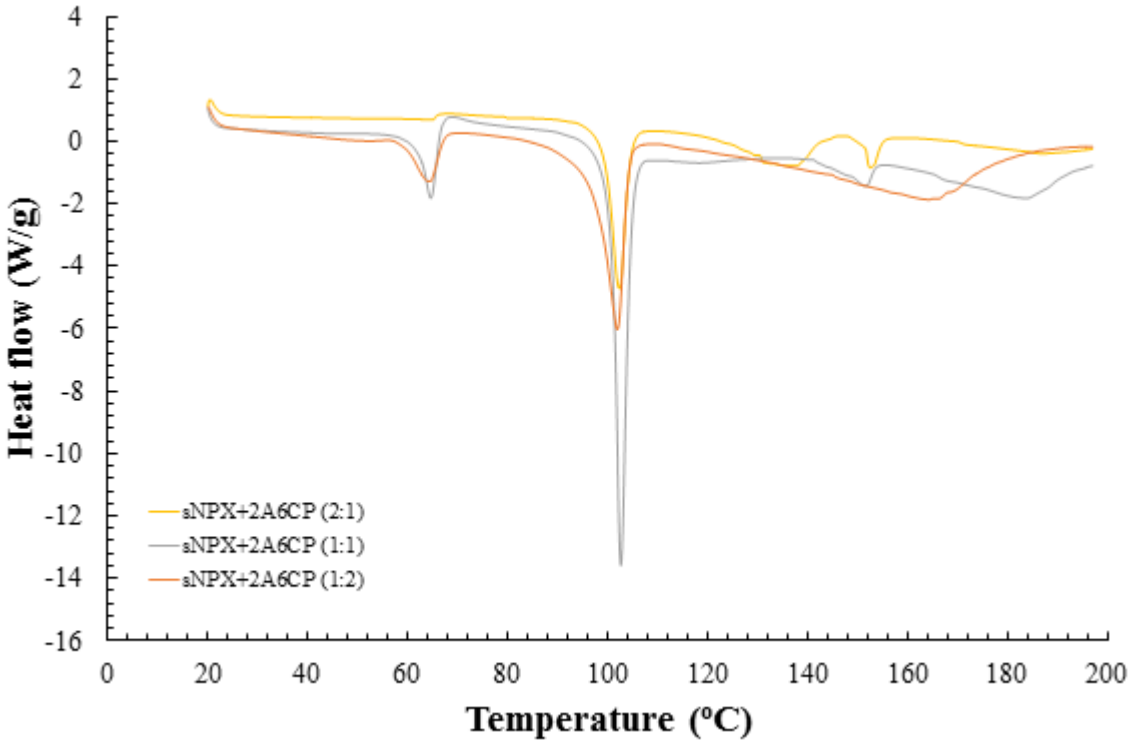

Figure 7. 57 - DSC traces from mechanochemically prepared samples of *sNPX* and *2A6CP*, ground, with ethanol, in either 2:1, 1:1 or 1:2 molar ratios

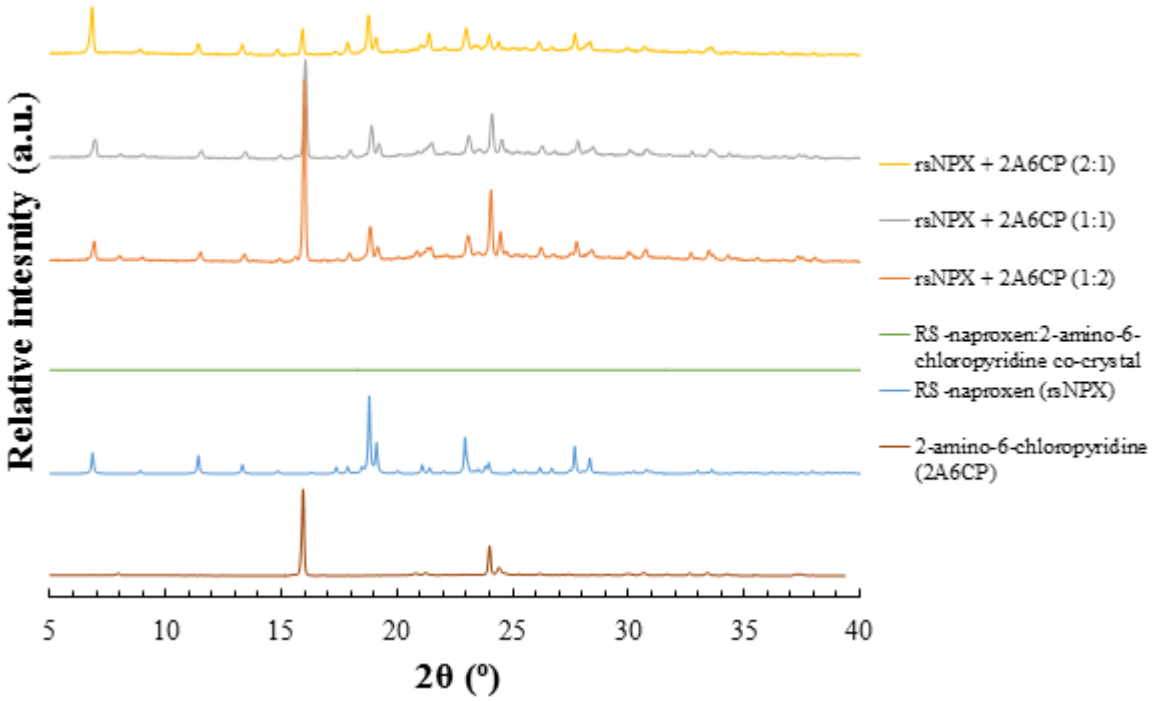

Figure 7. 58 - PXRD patterns from mechanochemically prepared samples of *rsNPX* and *2A6CP*, ground, with ethanol, in either 2:1, 1:1 or 1:2 molar ratios (top three patterns)

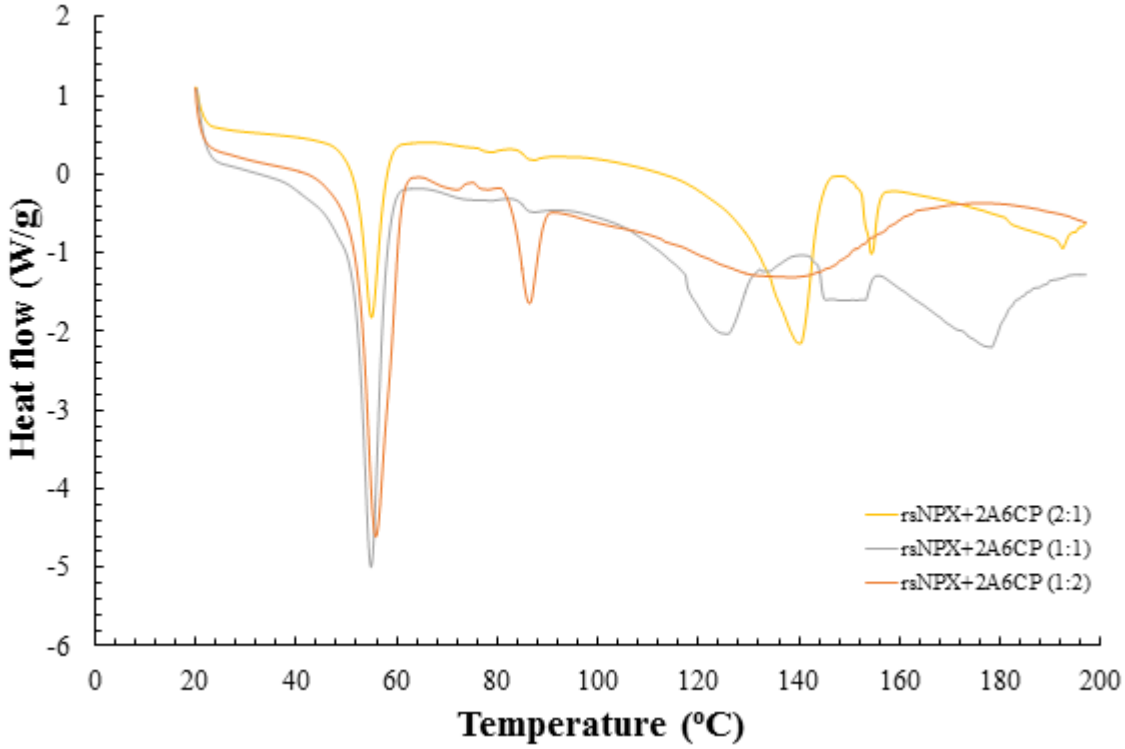

Figure 7. 59 - DSC traces from mechanochemically prepared samples of *rsNPX* and *2A5CP*, ground, with ethanol, in either 2:1, 1:1 or 1:2 molar ratios

7.6.1.2 Combined evaporation & cooling crystallisation screening

Single crystals were grown from homochiral solutions of *sNPX* and *2A6CP*, in a range of stoichiometries and solvent environments. The crystals used for diffraction studies of the enantiopure multi-component phase were taken from ethanol solutions, with a 1:1 molar ratio of API to co-former, and were shown to correspond to the same material generated *via* mechanochemistry. The individual crystals of exhibited an elongated plate morphology, with the bulk material showing an off-white colour.

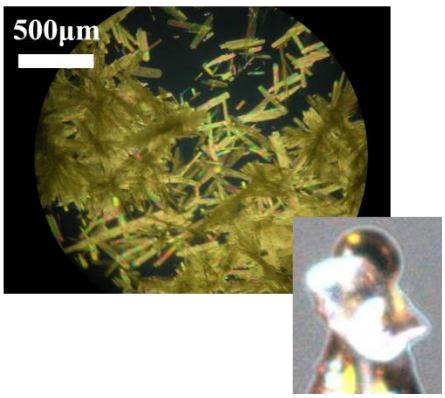

Figure 7. 60 - Microscope and mounted SCXRD images of crystals yielded from 1:1 ethanol solutions of *sNPX* with *2A6CP*

Whilst a multitude of cooling crystallisation samples were prepared in the racemic case, utilising ethanol, isopropanol and acetonitrile, again varying a number of stoichiometric and environmental parameters, to date all crystals screened *via* SCXRD were shown to be products from the recrystallisation of starting material.

7.6.2 Material characterisation

7.6.2.1 Phase, thermal and spectroscopic analysis

As highlighted from the mechanochemical and solution crystallisation screening, a novel multi-component phase could be prepared *via* both methods when the chiral composition tends towards enantiopure. This was not the case at racemic quantities. The simulated PXRD and thermal analysis of the homochiral phase along with those of the starting materials are shown in Appendix A7.6. The combined phase of *sNPX* and *2A6CP* demonstrated a discrete crystalline phase from that of the starting materials, whereby the transition from solid to liquid could be made at 84-89^{o}C. This was midway between the corresponding melting points of the two starting materials, suggesting a stabilisation of the intermolecular interactions in the solid state with respect the co-former and a destabilisation compared to the *NPX*.

Whilst no direct evidence of complexation between racemic contributions of the API with the co-former were observed, there were some indications that it was possible. Undefined thermal phenomena from the DSC traces taken from the mechanochemical preparations made with isopropanol and acetonitrile highlighted this.

7.6.2.2 Binary (melting point) phase diagram analysis – Classification of chiral crystalline materials

Due to the lack of distinction between the potential novel multi-component materials using the grinding preparation technique, a binary phase diagram could not be directly made for this system. However, as shown from the DSC traces in Figure 7.61, as the enantiomeric contributions shift toward racemic, the position of the melting endotherms shift gradually towards lower temperatures, though this trails off at compositions of *sNPX* below 70%. This could give an indication of the formation of a racemic conglomerate system.

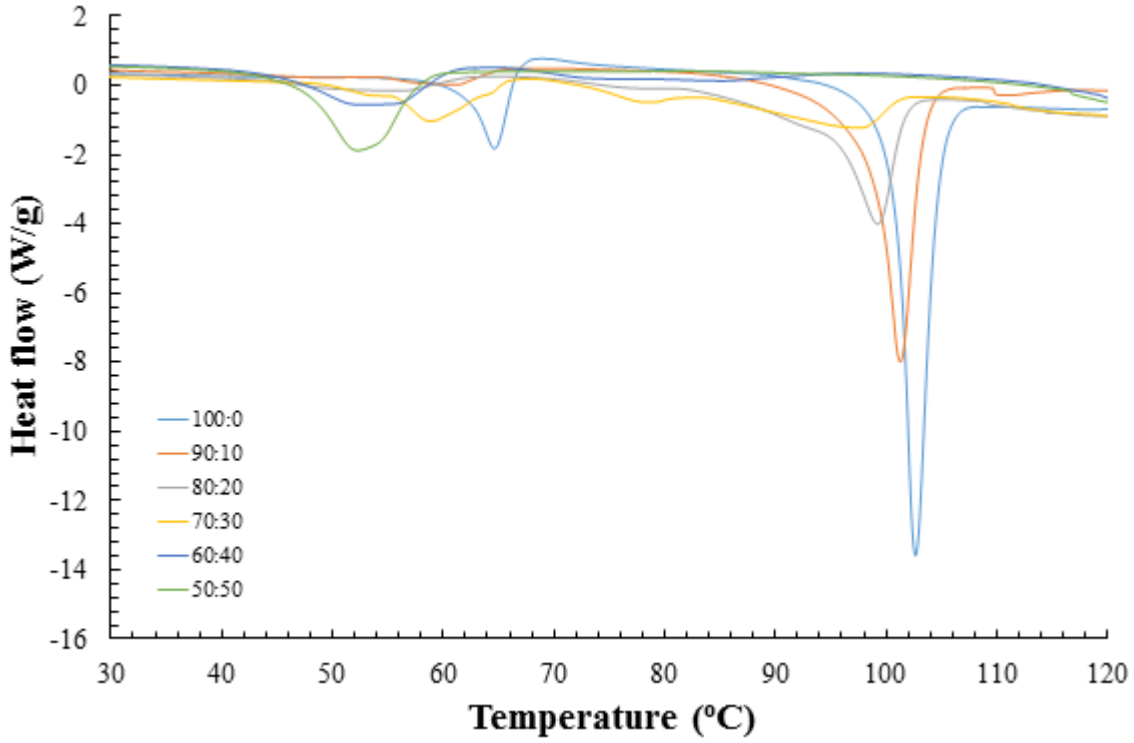

Figure 7. 61 - DSC traces, highlighting the change in phase from the racemic to the enantiopure (1:1) co-crystal of *NPX* and *2A6CP*, with increasing molar contributions of *sNPX*, prepared mechanochemically with ethanol

7.6.2.3 Crystallography – Crystal structure analysis

Individual crystals were taken from the 1:1 enantiopure solutions of *NPX* and *2A6CP* and the crystalline structure for the co-crystalline material was determined *via* SCXRD. The corresponding CIF file (14) can be found on the accompanying CD-ROM. The structure of this homochiral phase, along with the key hydrogen bonding interactions, are shown in Figure 7.62, with the defining interaction dimensions found in Appendix A7.6. The unit cell parameters are shown in Figure 7.12.

The molecules of *sNPX* were shown to crystallise with the co-former in a 1:1 relationship in an orthorhombic $P2_12_12_1$ space group. The asymmetric unit was shown to be made up from the respective molecules, with four units occupying the unit cell (Z = 4, Z' = 1). Having demonstrated no proton transfer, this system could be described as a S-naproxen:2-amino-6-chloropyridine (1:1) co-crystal.

The co-crystal exhibited the same key interaction unit common to many of the *NPX-2AP* derivative homochiral multi-component materials, that of the $R_2^2(8)$ heterodimer. The synthon acted through the carboxylic acid group of the API and the combined amine and pyridine functionalities of the co-former. These dimers were then used to form the backbone of an extended chain, whereby each co-former was connected through a further $D_1^1(3)$ hydrogen bond, acting between the carboxyl acceptor and the second

amine interaction, from *sNPX* and *2A6CP*, respectively. These chains extend to form elongated channels that can be packed together to form the overall crystalline lattice. This configuration again shows distinct similarity to that shown for the homochiral phases between *2AP*, *2A3CP* and *2A5CP*.

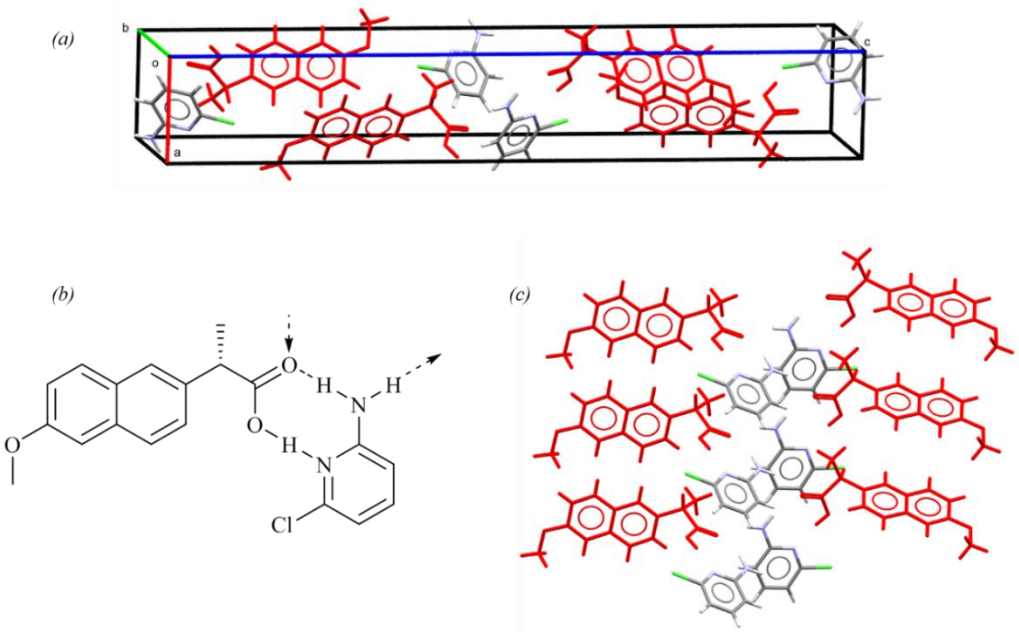

Figure 7. 62 - Crystal structure of the S-naproxen:2-amino-6-chloropyridine (1:1) co-crystal, highlighting (a) the unit cell, (b) hydrogen bonding synthon and (c) packing arrangement (*sNPX* in red)

Table 7. 11 - Unit cell and crystallographic parameters for the S-naproxen:2-amino-6-chloropyridine (1:1) co-crystal

Material	**S-naproxen:2-amino-6-chloropyridine (1:1) co-crystal**
Empirical formula	$C_{19}H_{19}ClN_2O_3$
Formula weight	358.81
Temperature (K)	150.00(10)
Crystal system	orthorhombic
Space group	$P2_12_12_1$
a (Å)	5.71330(10)
b (Å)	8.4990(2)
c (Å)	37.3574(8)
α (°)	90
β (°)	90
γ (°)	90
Volume (Å^3)	1813.98(7)
Z	4, 1
ρ_{calc} (g/cm^3)	1.314
μ (mm^{-1})	2.033
F(000)	752.0
Crystal size (mm^3)	0.211 × 0.121 × 0.069
Radiation	CuKα (λ = 1.54184)
2Θ range for data collection (°)	9.47 to 140.098
Index ranges	$-5 \leq h \leq 6$, $-9 \leq k \leq 10$, $-39 \leq l \leq 45$
Reflections collected	6628
Independent reflections	3435 [R_{int} = 0.0199, R_{sigma} = 0.0266]
Data/restraints/parameters	3435/0/232
Goodness-of-fit on F^2	1.191
Final R indexes [I>=2σ (I)]	R_1 = 0.0377, wR_2 = 0.0917
Final R indexes [all data]	R_1 = 0.0399, wR_2 = 0.0926
Largest diff. peak/hole (e Å^{-3})	0.23/-0.23
Flack parameter	0.012(8)

To date and despite extensive screening, no crystalline structures have been found for an equivalent racemic phase. These initial findings suggested an agreement with those found from mechanochemical screenings. As shown above, the location of the chlorine atom at the six-position did not hinder formation of the conventional elongated channels observed in many of the enantiopure forms of *NPX* with a *2AP* derivative. The methyl group, key to defining the chirality for a given API molecule, faced away from the halogen atom of the interacting co-former, indicating that steric hindrances were minimised when a single enantiomeric form was present. Whilst no racemic structures were found, the most likely form was thought to resemble that of the racemic form with *2A3CP*, with the overall structure forming from concurrent channels of these chains, each channel alternating in terms of its chirality.

Upon changing the composition to that of racemic, no structure correlating to the expected double dimer was observed. This could again be explained through the positioning of the chlorine atom relative to other functional groups and neighbouring atoms within the structure. The dimerised dimer synthon, seen in many racemic structures with *2AP* derivatives (*2AP*, *2A4CP* and *2A5CP*), was used as a main building block, through which the collective crystalline assembly could be constructed. As such, these units can be offset to each other and stacked. By introducing the chlorine atom at the ortho position to the pyridine functionality, steric stress between the halogen atom and a neighbouring *NPX* molecule would be introduced. This is depicted in Figure 7.63. Thus, this structure was deemed unlikely.

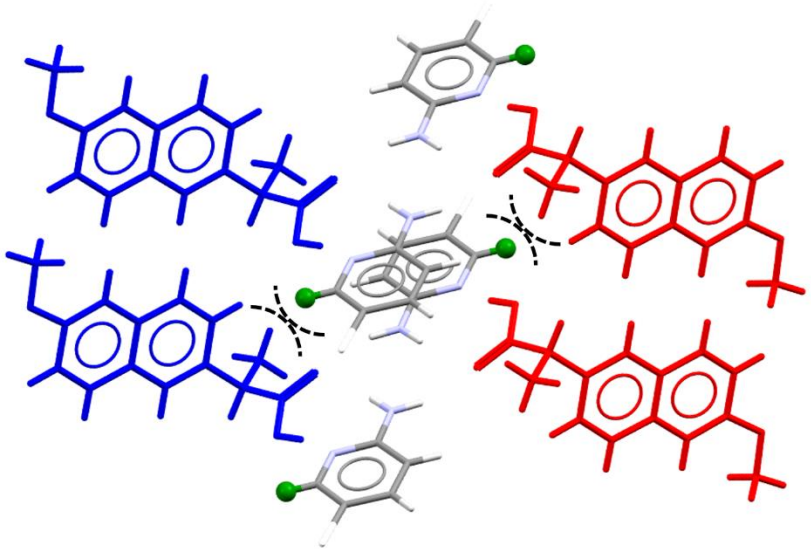

Figure 7. 63 - Visual representation of the hypothetical dimer of dimer structure formed between racemic *NPX* and *2A6CP*, highlighting the possible steric hindrance between the key interaction motifs

7.7 Summary, conclusions and future work

Throughout this chapter, the API naproxen (*NPX*) has been screened with a range of potential co-formers using a combined preparation approach of mortar and pestle grinding and crash cooled solution crystallisation. The aim was to conduct an initial assessment of the combination of materials, over a range of different stoichiometries and solvent environments, using mechanochemical means, seeing whether any novel phases were prepared and translating the process towards the growth of individual crystals. This combined approach attempted to provide a relatively quick method of screening, accounting for the existence of any novel phases, their melting points, their chiral crystalline nature and their individual crystal structures. To date, this method has allowed for the discovery of 12 novel multi-component forms of *NPX* with the six *2AP* derivatives discussed here, at both racemic and enantiopure compositions, highlighting the formation of several racemic compounds, racemic solid solution and an interesting system with the potential of being a racemic conglomerate. It should be noted that even through the development of multi-component materials, no conglomerate systems could be directly found, emphasising the rarity of their formation and occurrence.

In the case of the pyrimidine based co-formers, i.e. 2-aminopyrimidine (*2APM*) and 2-amino-4,6-dimethylpyrimidine (*2ADMP*), both were shown to form novel co-crystalline forms with the API. In the case of the former, three distinct species were found, an enantiopure and racemic (1:1) pair, as well as that of a (2:1) homochiral stoichiometric variant. The equimolar co-crystals were both shown to utilise the same dimer of dimer interaction motif as in the racemic salt of *NPX* with *2AP*, but with each system expressing a different packing arrangement, therefore forming a conventional racemic compound. For the *2ADMP* co-former, further (1:1) co-crystals were found, with both the racemic and enantiomerically pure phases expressing broadly the same interactions and packing arrangements, with the only variation occurring about the chiral centre of the API. Given the fluidity of chirality throughout the structure and the improved packing density at racemic compositions, it was shown that this combination of molecules represented a Roozeboom Type II racemic solid solution.

Additional screenings were conducted using further *2AP* derivatives, this time incorporating additional chlorine atoms as substituents. Broadly, it was shown that no matter the position of the halogen atom about the pyridine ring, particularly for the meta and para positioned species, racemic compound co-crystalline systems were produced. For each of the (1:1) homochiral co-crystals discovered, it was shown that the same hydrogen bonding motifs were exploited as in the *sNPX-2AP* salt, that of the heterodimer between the carboxylic acid and pyridine-amine groups, with the second N-H bond forming a contact with a neighbouring unit, establishing the elongated spiralled chain arrangement. Whilst the (1:1) co-crystal of the API with the 2-amino-4-chloropyridine (*2A4CP*) co-former has yet to have its structure fully resolved, it was thought that the enantiopure and racemic materials obtained via grinding were structurally related so as to generate a racemic compound forming system. For this para substituent, an additional stoichiometric salt form was also found, the only structural variant found for these types of derivatives. In contrast, the intermolecular interactions used for racemic (1:1) co-crystals was shown to vary depending upon the relative positioning of the chlorine atom around the pyridine ring. Transitioning from the three site to four and five sites, respectively, the interactions utilised changed from that mimicking the chain arrangement seen for the homochiral species, to that resembling the dimer of dimer motif exploited by the *rsNPX-2AP* salt.

In each of the above cases, the location of the chlorine atom was deemed inconsequential as to the formation of either the enantiopure or racemic multi-component phase with *NPX*, except in the case of the 2-amino-6-chloropyridine (*2A6CP*) co-former. Here, the chlorine atom was placed adjacent to the pyridine nitrogen atom and whilst a homochiral structure similar to those observed for the other derivatives was found, to date no evidence has been found of a racemic multi-component material incorporating this co-former. Though there could still be a racemic material, an initial suggestion is that

these initial observations could be due to the fact that the chlorine atom, a bulky substituent, at the ortho position has the potential to block the interactions required to allow for the efficient packing of both enantiomers of *NPX* within the same crystal lattice. As such, this particular co-former could have potential applications towards the development of a racemic conglomerate material capable of being applied into a preferential crystallisation setup.

For the systems detailed above, further screening should be carried out utilising a greater range of crystallisation conditions so as to find and characterise any polymorphic or stoichiometric multi-component variations. The crystallographic structure of the homochiral (1:1) phase of *NPX* with *2A4CP* should also be collected in order to confirm the spiralled chain arrangement, as hypothesised. Moreover, a detailed assessment of the system with *2A6CP* should be carried out, checking for the existence of a racemic (1:1) co-crystalline material and if it is absent (i.e. a conglomerate system), developing early stage crystallisations for the development of the direct enantiomeric resolution methods.

To extend the scope of this research, further derivatives of *2AP* could also be explored. Common to every structure discussed in this chapter was that of the heterodimer hydrogen bond motif between the carboxylic acid and pyridine-amine groups. By shifting the position of the amine group about the pyridine ring, different interactions can be accessed. Two potential co-formers that could be used are 3-aminopyridine (*3AP*) and 4-aminopyridine (*4AP*), as shown in Figure 7.64a. Alternatively, rather than changing the fundamental heterodimer, the substituents about the ring could also be changed. Different halogen substituents could be used, be it fluorine, bromine or iodine (Figure 7.64b). This could allow the effects of the varying electronegativities or steric bulks of each of the halogen atoms to be assessed.

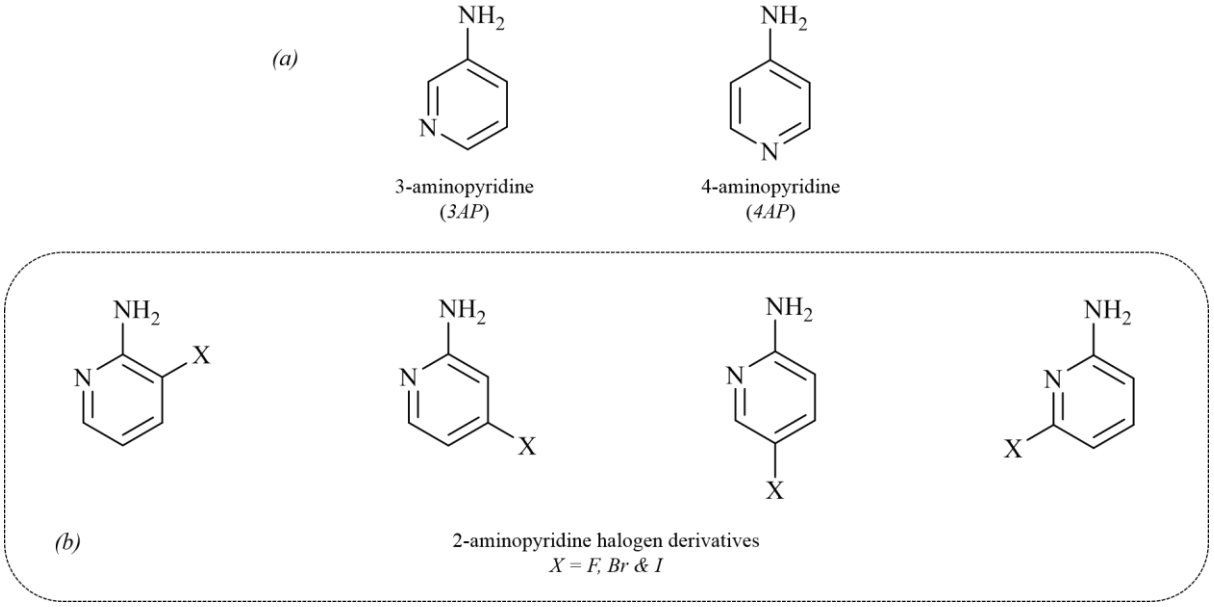

Figure 7. 64 - Molecular structures of (a) aminopyridine derivatives and (b) halogen derivatives of 2-aminopyridine (*2AP*)

8 Chiral multi-component materials of naproxen and polymorphic co-formers

When screening for novel multi-component materials, co-former selection is of particular importance. Based upon intermolecular interactions, crystalline materials can be constructed, with each form exhibiting their own set of defined characteristics. A key consideration when selecting which complementary molecules to use is that of their polymorphic nature. Polymorphism arises when a material possesses a number of different functionalities, each capable of forming intermolecular interactions. These interactions are in competition with each other and all, respectively, lead to different crystal forms. Therefore, the crystallisation of each form is dependent upon the flexibility of the given molecule and the crystallisation conditions used.

In multi-component systems, polymorphism or stoichiometric variance in this case is reliant on the interactions that form, their number and the orientations of the different molecular entities relative to each other. Whilst a given co-former may exhibit a range of polymorphic variants, upon crystallisation with a secondary molecule, this phenomenon does not necessarily translate to being demonstrated in multi-component materials. As in previous chapters, screenings for such materials were conducted with the API naproxen (*NPX*), using a range of co-formers. However, in the systems outlined here, the co-formers selected each demonstrate their own set of structural variations. These co-formers include imidazole (*I*), benzimidazole (*BI*) and acridine (*A*), which demonstrate two (CSD reference: IMAZOL21/22), three (CSD reference: BZDMAZ02/03/05) and five (CSD reference: ACRDIN) polymorphic forms, respectively. The molecular structures are shown in Figure 8.1 and further crystallographic information can be found in Appendix A8.

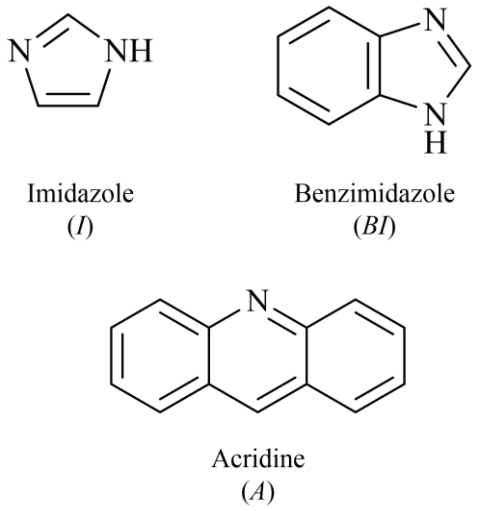

Figure 8. 1 - Molecular structures for the co-formers selected for the co-crystal and salt screening with *NPX*, highlighting imidazole (*I*), benzimidazole (*BI*) and acridine (*A*)

Using both mechanochemical and solution crystallisation methods, different enantiomeric compositions of *NPX*, enantiopure and racemic, were screened in combination with these three co-formers. As before, the aim was to gauge whether or not novel multi-component materials could be generated, assessing their structural and thermal properties, so as to ascertain the classification of chiral crystalline material generated. These materials were also explored in terms of their polymorphic behaviour, with a characterisation of each form.

8.1 Materials of racemic and enantiopure naproxen with imidazole (*I*)

8.1.1 Material screening

The first co-former to be selected in this context was imidazole (*I*). A diazine five-membered ring, *I* demonstrates two main functional groups; that of an amine and an aromatic nitrogen. In its neutral form, these functionalities act as a hydrogen bond donor and acceptor, respectively, the interactions from which form the basis of the two polymorphic phases of *I*[208]; the α and β forms. The α polymorph (CSD reference: IMAZOL21) is the most common form under standard atmospheric conditions, with a melting point of 89-91°C, whilst, to date, the β polymorph (CSD reference: IMAZOL22) has only been prepared from the melt under high pressure. The pK_a of *I* has been shown to be 6.9[209], so whilst this is an increase from some of the derivatives of *2AP*, the acidity difference between the co-former and API is such that the predicted co-crystal-salt nature of any multi-component materials is uncertain.

8.1.1.1 Mechanochemical screening

Initial mechanochemical screenings of *I* with homochiral compositions of *NPX* were prepared using a mortar and pestle, where the API and co-former were ground in either 2:1, 1:1 or 1:2 molar ratios with a few drops of ethanol. It should be noted that for the 1:1 and 1:2 combinations, the resultant materials were sticky and amorphous in nature. These samples did not crystallise when left and were deemed too difficult to handle for PXRD and DSC analysis. However, the combination of the components in a 2:1 did generate a material suitable for analysis, the diffraction pattern and thermal trace of which are shown in Figures 8.2 and 8.3, respectively.

As shown from the PXRD pattern of the 2:1 mechanochemically prepared sample, a distinct crystalline phase was prepared, exhibiting a different set of diffraction peaks to that of the starting materials. Upon comparison with that obtained subsequently from SCXRD, accounting for temperature dependent shifts, the phase made at this composition mechanochemically could be matched to those crystals grown from solution, emphasising the reproducibility of this phase. Thermal analysis highlighted two endothermic events; the first, a minor phenomenon, occurring at 84-89°C and the second, a major event, taking place at 124-127°C. These represented melting of excess *I* starting material and that of a novel multi-component phase, respectively.

Neat mechanochemical samples were also prepared and analysed, the PXRD patterns and DSC traces of which can be found in Appendix A8.1. Preparations made in the 2:1 ratio again showed the evidence of the formation of the same multi-component material made with the assistance of solvent, highlighted by the similarity between their diffraction and thermal characteristics. Further to this, the material obtained from the 1:1 mechanochemical preparation was taken to consist of a mixture of the 2:1 phase and an additional novel phase. This second phase corresponded directly to the peaks observed in the 1:2 neat sample. For the 1:1 sample, the thermal trace demonstrated a sharp endotherm (90-93°C) followed by a broad one (101-110°C), whilst that of the 1:2 phase presented an initial melt/recrystallisation phenomenon (69-72°C) with a further major endotherm at 92-94°C. The peak at 92°C suggested the formation of a different form to that observed from the 2:1 preparation, supporting the findings from PXRD.

When combining *I* with racemic compositions of *NPX* and grinding them together, as with the homochiral case, only the 2:1 sample was shown to form a crystalline form suitable for analysis. This was also seen for the neat combinations of the starting materials (see Appendix A8.1 for PXRD and DSC data). The PXRD patterns in Figure 8.4 indicated that a novel crystalline material was prepared, distinct from the individual starting materials and again matching the pattern simulated from SCXRD.

The melting point of this phase was taken as 113-117ºC, based upon the single endothermic event exhibited.

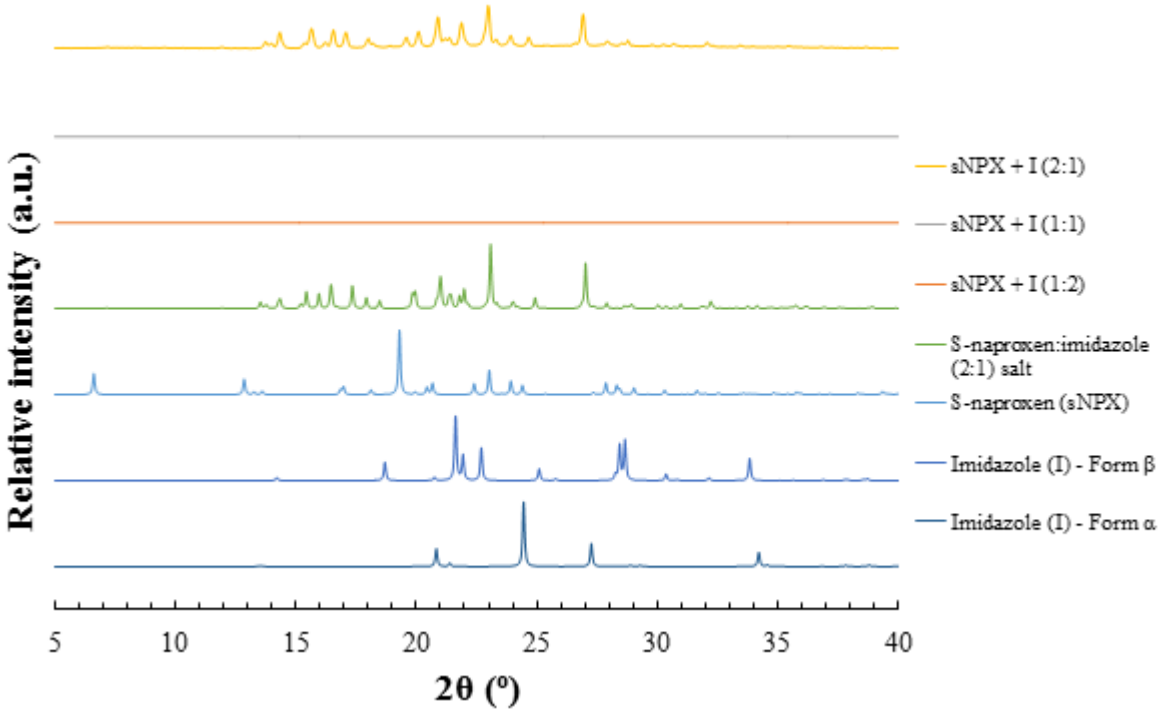

Figure 8. 2 - PXRD patterns from mechanochemically prepared samples of *sNPX* and *I* with ethanol, ground in either 2:1, 1:1 or 1:2 molar ratios (top three patterns)

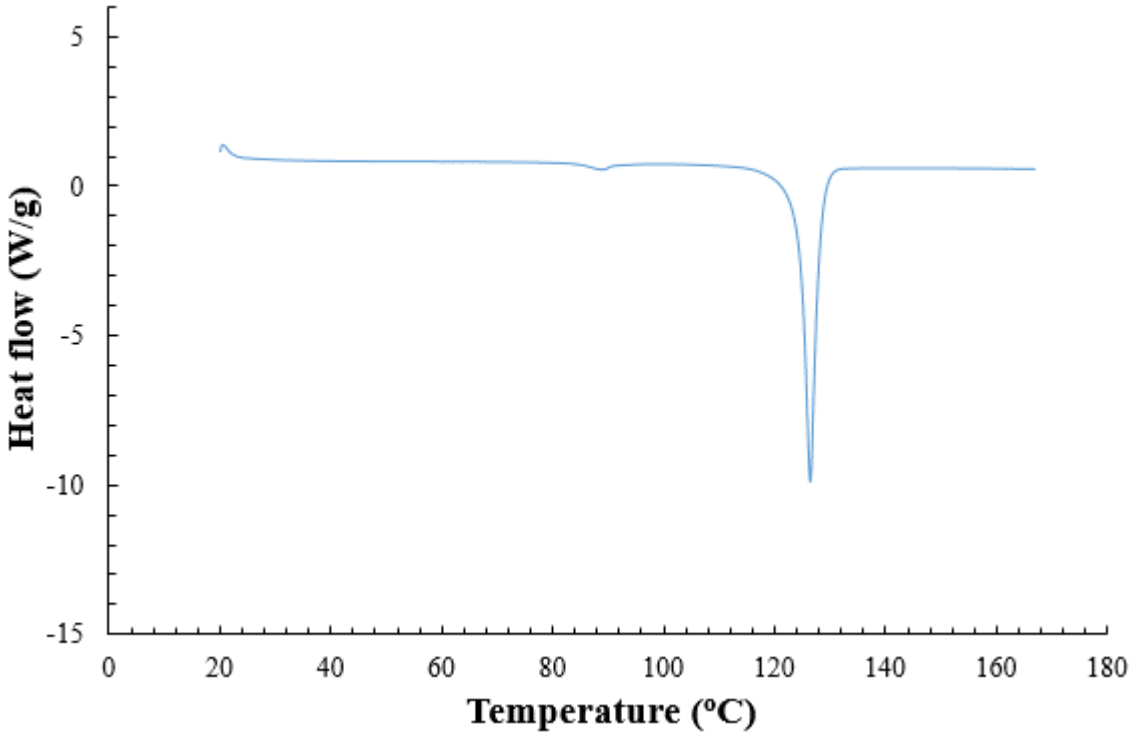

Figure 8. 3 - DSC traces from mechanochemically prepared samples of *sNPX* and *I* in ethanol, ground in a 2:1 molar ratio

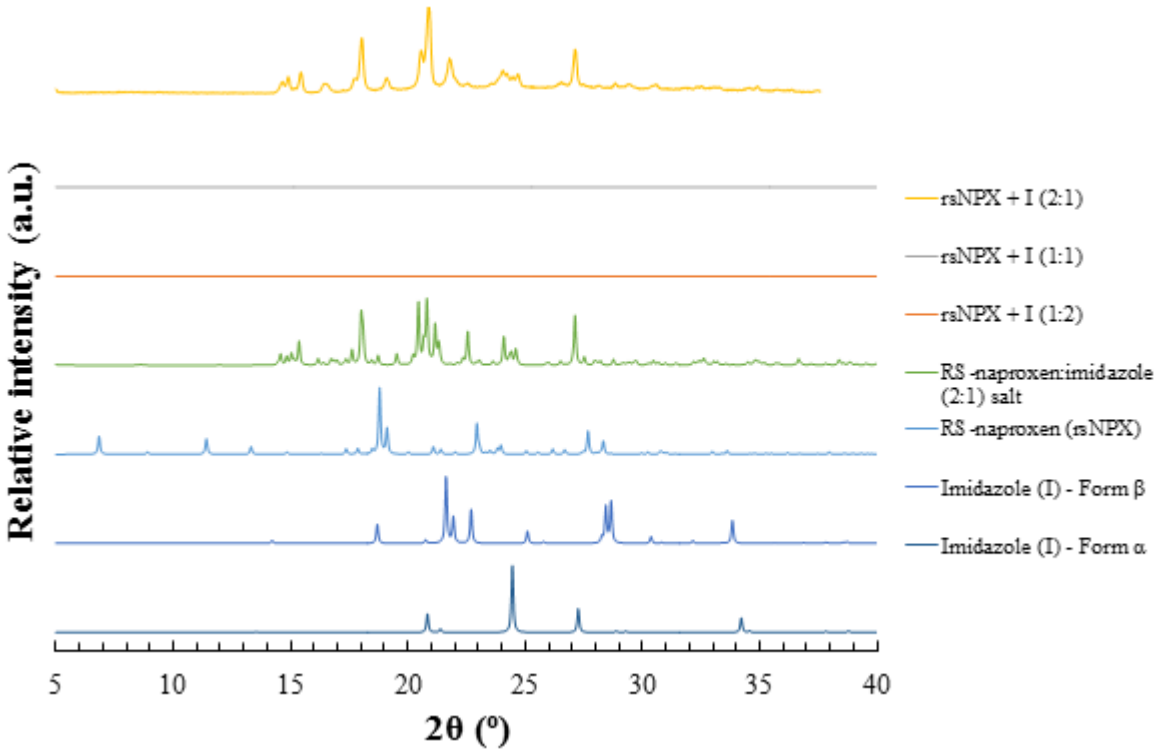

Figure 8. 4 - PXRD patterns from mechanochemically prepared samples of *rsNPX* and *I* with ethanol, ground in either 2:1, 1:1 or 1:2 molar ratios (top three patterns)

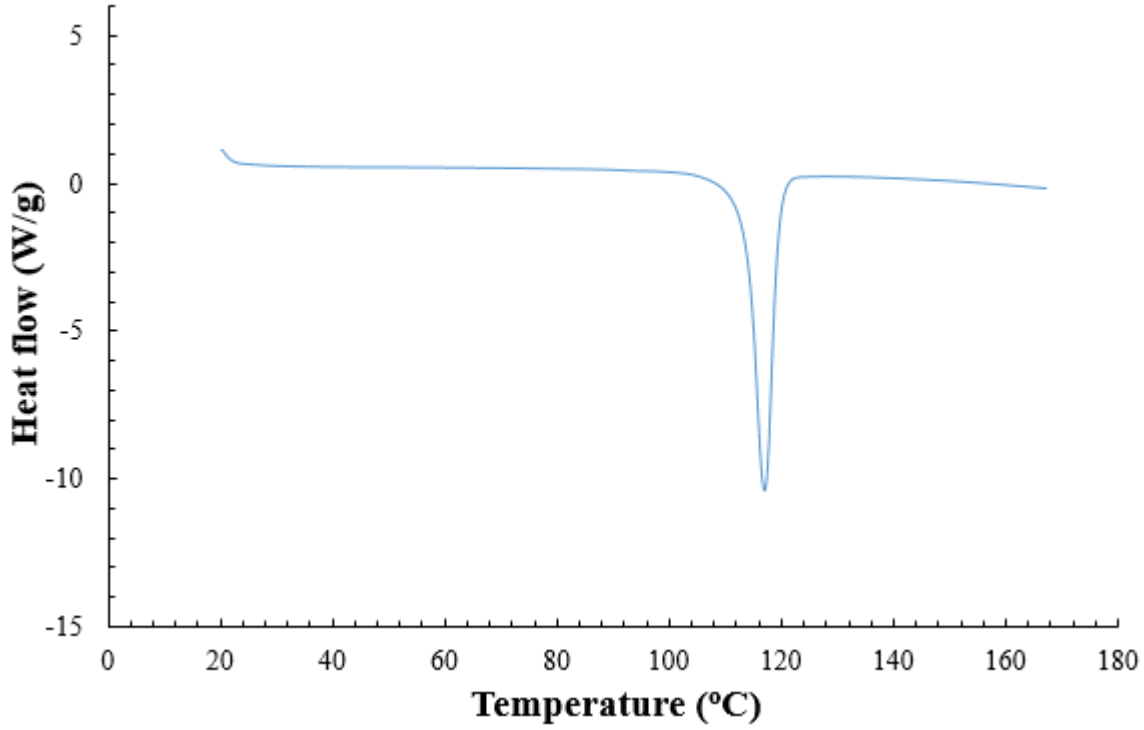

Figure 8. 5 - DSC traces from mechanochemically prepared samples of *rsNPX* and *I* in ethanol, ground in a 2:1 molar ratio

8.1.1.2 Combined evaporation & cooling crystallisation screening

Saturated solutions of *NPX*, racemic and enantiopure, were prepared with either ethanol or isopropanol in a range of API to co-former stoichiometries. These were then cooled, allowing for crystal growth. Where necessary evaporation was introduced to aid in this process. Figure 8.6 shows the crystals obtained from the homochiral and racemic crystallisations. In the enantiopure case, crystals were obtained from a 1:1 solution of API to co-former, whilst for the racemic, the same ratio of materials was used but in isopropanol. For both scenarios, flat elongated blocks were yielded, with the bulk material showing a white colour. SCXRD analysis was conducted to obtain the crystal structures for these novel materials, from which it was confirmed that the crystalline phases grown from solution corresponded to those yielded from mechanochemical means.

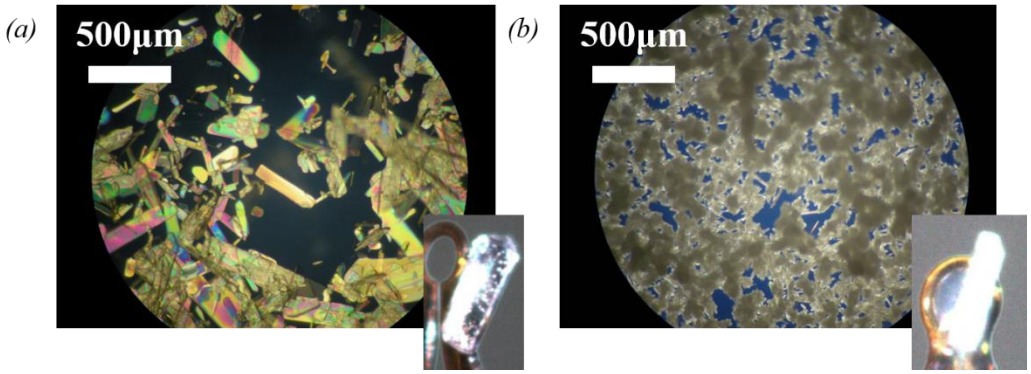

Figure 8. 6 - Microscope and mounted SCXRD images of crystals yielded from (a) a 1:1 *sNPX-I* ethanol solution and (b) a 1:1 *rsNPX-I* isopropanol solution

8.1.2 Material characterisation

Having established routes to the reproducible preparation of both the enantiopure and racemic multi-component forms via mechanochemical and solution crystallisation means, further solid state analysis was conducted to ascertain the chiral crystalline relationship of the species. This included PXRD, DSC and SCXRD analysis, culminating in the construction of a binary (melting point) phase diagram. IR spectroscopy was also carried out on the ground samples, to determine the key interactions acting in these given structures. These IR spectra can be found in Appendix A8.1.

8.1.2.1 Phase, thermal and spectroscopic analysis

A comparison of the X-ray diffraction patterns (simulated from SCXRD data) and the thermal traces of both the 2:1 phases of *NPX* and *I* at homo and heterochiral compositions, as well as those of the starting materials, are shown in Figures 8.7 and 8.8. As shown from the diffraction data, both forms express discrete patterns with respect to not only the starting materials, but also to each other. Their melting points reside between that of the *I* and the different enantiomeric combinations of *NPX*, with the homochiral material expressing a higher melt (124-127^{o}C) than that of the racemic (113-117^{o}C). This would suggest that the interactions between the API and co-former are stronger in the solid state at enantiopure compositions. These collective observations indicated that whilst a different phase forms at racemic quantities than that observed for just *sNPX*, the melting points demonstrated the possible existence of a metastable racemic conglomerate system. For these types of materials, the homochiral phase can be accessed towards racemic compositions, despite the existence of a racemic phase.

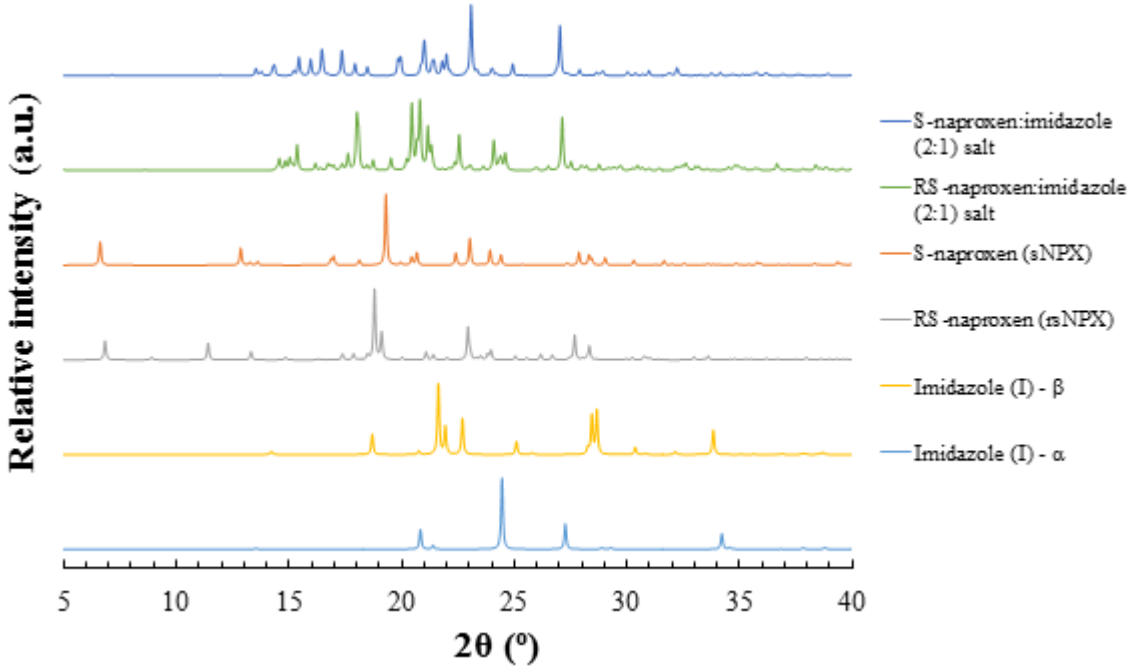

Figure 8. 7 - PXRD patterns of the S-naproxen:imidazole & RS-naproxen:imidazole (2:1) salts, as derived from SCXRD data, compared to that of the starting materials

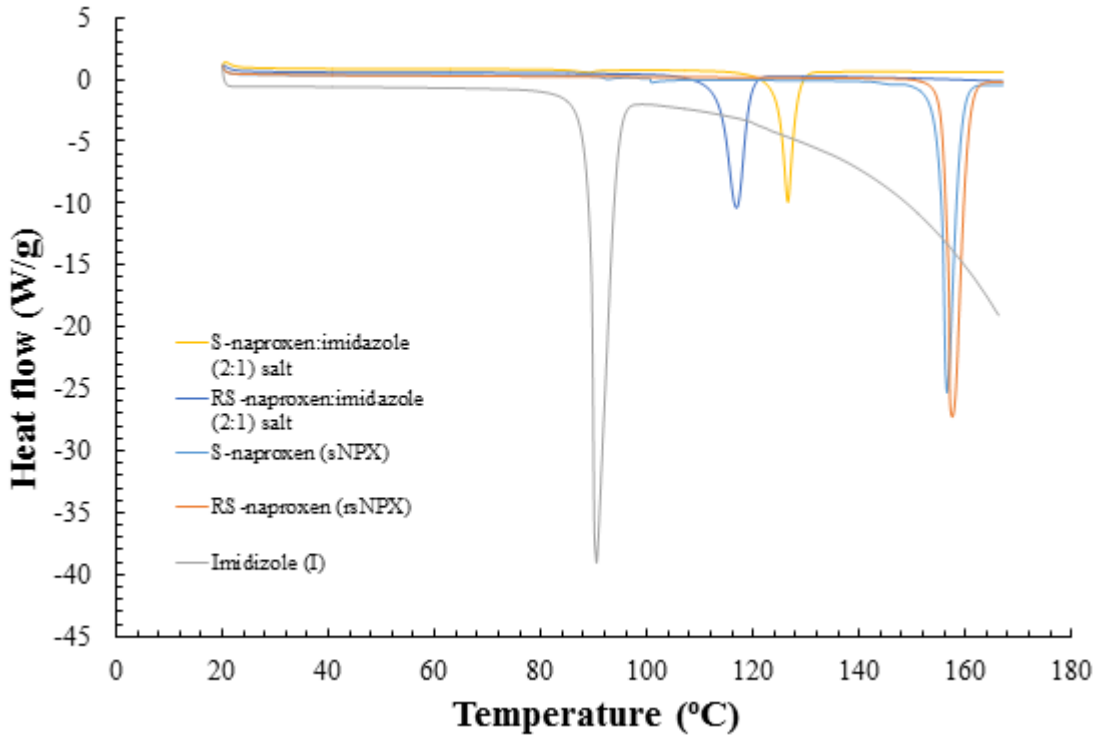

Figure 8. 8 - DSC traces of the S-naproxen:imidazole & RS-naproxen:imidazole (2:1) salts, prepared via mechanochemistry, compared to that of the starting materials

The IR spectra of the novel multi-component materials showed similar vibrational and stretching characteristics. This would indicate that both phases showed a similar range of intermolecular interactions and, therefore, structures. With a particular focus on the carbonyl stretch expressed for both

systems, a broad mode could be seen at 1703-1705 cm^{-1}. This ill-defined peak suggested that the carbonyl group was involved in a number of interactions.

8.1.2.2 Binary (melting point) phase diagram analysis – Classification of chiral crystalline materials

Due to the reliability of the mechanochemical methods to yield both of the novel crystalline forms, further samples were prepared via grinding, maintaining the same stoichiometry of *NPX* to *I*, but with variations in the enantiomeric composition. PXRD and DSC analysis were conducted (Appendix A8.1), from which the necessary data was taken so as to construct the binary phase diagram, shown in Figure 8.9. As highlighted from the phase diagram, distinct regions were noted, defined by the existence of both racemic and enantiopure multi-component materials, respectively. The melting points taken from racemic and homochiral compositions were shown to converge towards a common point, that of a eutectic point between 108°C and 112°C. This cumulative evidence supports the notion of a racemic compound system, with the lower melting point of the racemic phase suggesting the possibility of stabilising the homochiral form towards racemic compositions.

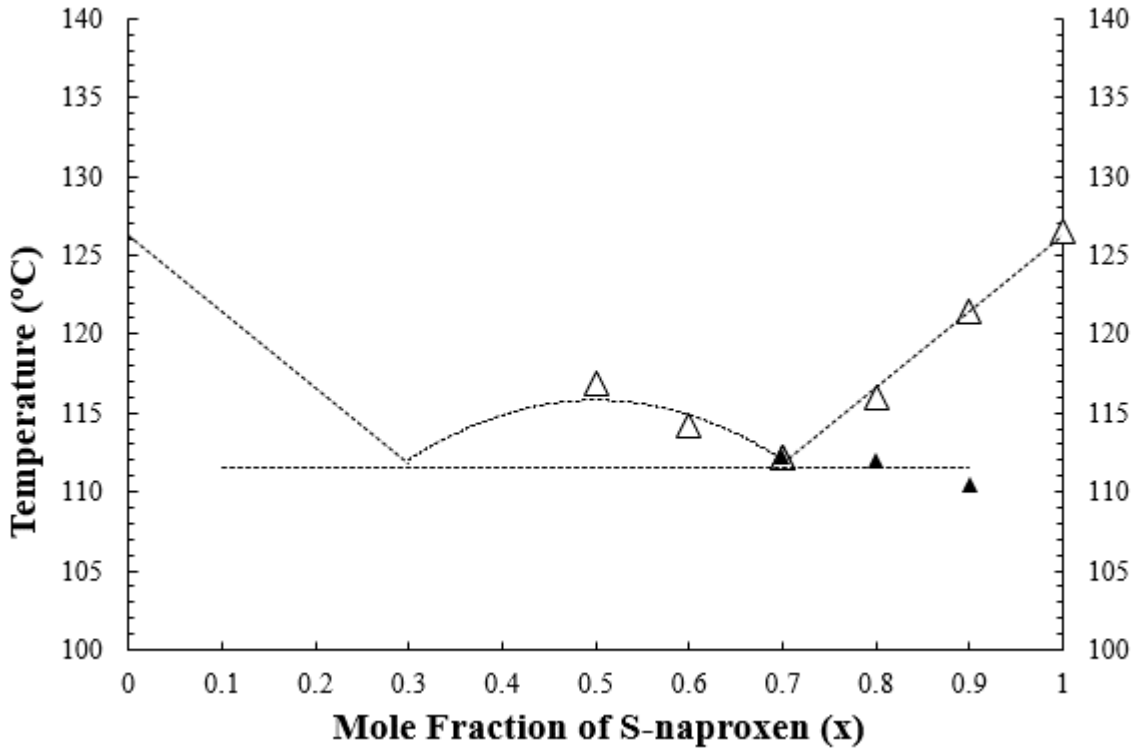

Figure 8. 9 - Binary (melting) point phase diagram, with changing enantiomeric composition of *rNPX* and *sNPX*, for the 2:1 salts incorporating the co-former *I*, highlighting the liquidus (Δ) and the eutectic (▲) points

8.1.2.3 Crystallography – Crystal structure analysis

SCXRD data was collected from individual crystals so as to determine the crystal structures of both the homo and heterochiral multi-component materials. For further crystallographic information, including details of the key lengths and distances for hydrogen bonding interactions, as well as that for any disordered atoms present, see Appendix A8.1. The corresponding CIF files (15, 16) can be found on the accompanying CD-ROM.

For the homochiral case, the API and co-former molecules were shown to crystallise in a 2:1 ratio, with two molecules of *sNPX* forming contacts with one molecule of *I*. Collectively these molecular entities crystallised in a non-centrosymmetric monoclinic $P2_1$ space group. This 2:1 combination formed the

basis of the asymmetric unit, of which two were used to construct the unit cell ($Z = 2$, $Z' = 1$). Figure 8.10 highlights the unit cell and the key interactions that were used to build up the whole crystal assembly. Table 8.1 shows the unit cell parameters for this homochiral multi-component system.

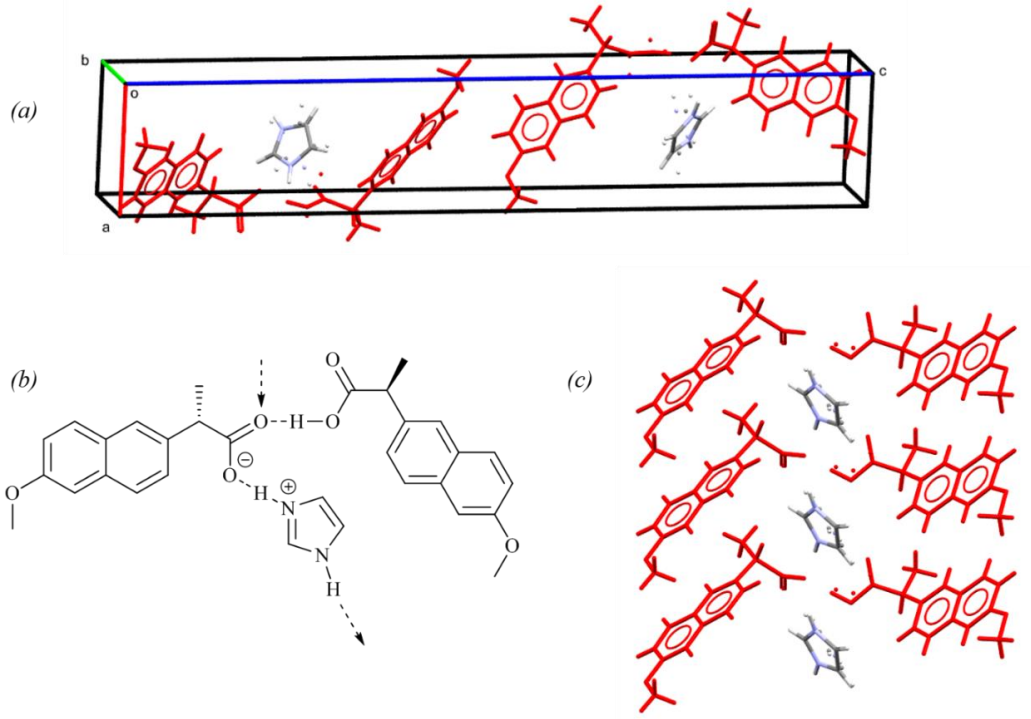

Figure 8. 10 - Crystal structure of the S-naproxen:imidazole (2:1) salt, highlighting (a) the unit cell, (b) hydrogen bonding synthon and (c) packing arrangement (*sNPX* in red)

Table 8. 1 - Unit cell and crystallographic parameters for the S-naproxen:imidazole (2:1) salt

Material	**S-naproxen:imidazole (2:1) salt**
Empirical formula	$C_{31}H_{32}N_2O_6$
Formula weight	528.58
Temperature (K)	150.00(10)
Crystal system	monoclinic
Space group	$P2_1$
***a* (Å)**	6.5408(2)
***b* (Å)**	5.6125(2)
***c* (Å)**	37.0129(13)
***α* (°)**	90
***β* (°)**	91.009(3)
***γ* (°)**	90
Volume (Å^3)	1358.54(8)
Z, Z'	2, 1
ρ_{calc} (g/cm^3)	1.292
μ (mm^{-1})	0.090
F(000)	560.0
Crystal size (mm^3)	0.341 × 0.151 × 0.067
Radiation	MoKα (λ = 0.71073)
2Θ range for data collection (°)	6.23 to 52.044
Index ranges	$-8 \leq h \leq 8$, $-6 \leq k \leq 6$, $-45 \leq l \leq 45$
Reflections collected	15487
Independent reflections	5303 [R_{int} = 0.0382, R_{sigma} = 0.0382]
Data/restraints/parameters	5303/26/386
Goodness-of-fit on F^2	1.083
Final R indexes [I>=2σ (I)]	R_1 = 0.0452, wR_2 = 0.1030
Final R indexes [all data]	R_1 = 0.0504, wR_2 = 0.1067
Largest diff. peak/hole (e Å^{-3})	0.43/-0.34
Flack parameter	0.0(6)

The key interaction unit was shown to consist of three $D_1^1(3)$ hydrogen bonding interactions, with contacts forming between the two API entities, one of the API and co-former molecules, as well as between neighbouring interaction units. The API-to-co-former contact arose through a hydrogen bond between the hydroxyl group of the first *NPX* molecule and the *I* aromatic nitrogen. Here, the intermolecular interaction was enhanced through proton transfer, forming a salt. Hence, this system can be defined as S-naproxen:imidazole (2:1) salt. In addition to this charge-assisted interaction, a further hydrogen bond was shown to form between the amine group of *I* and the carboxyl group of a *sNPX* molecule in an adjacent interaction unit. This chain of alternating API and co-former molecules forms the core backbone from which the main structure was built. The final interaction formed between the deprotonated API moiety and that of a second, neutral API molecule, from a hydrogen bond across the hydroxyl group of the neutral species and the carbonyl component of the charged entity. Collectively, these interactions formed a branched chain, built up into channels, from which the whole crystal structure could be constructed.

This structure was modelled with disorder, with the charged *sNPX* entity being anchored, additional flexibility was observed about the carboxylic acid group of the neutral API molecule and the whole co-former species. Enough space was observed within the structure to allow for these groups to rock about an axis. This disorder highlighted the dynamic nature of the structure, with a variations expected upon changes in temperature. Although disorder was noted about some of the key functionalities, not occupancy disparities were noted around the chiral centres of the API molecules, emphasising the enantiopure nature of the structure.

As in the homochiral system, the complex prepared with *rsNPX* and *I* was shown to utilise a 2:1 stoichiometry. The relationship was represented within the asymmetric unit, two of which formed the unit cell (Z = 2, Z' = 1). As such, these units were shown to crystallise in a centrosymmetric triclinic $P\bar{1}$ space group, accounting for both enantiomeric forms of the API to be accounted for. Proton transfer was noted, demonstrating the formation of a RS-naproxen:imidazole (2:1) salt. Figure 8.11 highlights the key structures and interactions for this material, with Table 8.1 outlining the unit cell and refinement parameters.

In a similar manner to that observed in its enantiopure counterpart, the predominant interactions with this complex were that of three $D_1^1(3)$ hydrogen bonds, linking the charged and neutral API species with that of the co-former. Two of these interactions were the same as observed for the other structure, with a charge-assisted contact forming between one of the *NPX* molecules and the co-former, as well as that forming between the *NPX* themselves. In contrast, however, the hydrogen bond connecting individual interaction units was shown to take place not between the co-former and the deprotonated species, but from the amine functionality of the co-former to the accepting carbonyl group on the neutral API molecule present in the interaction unit. As such, the combination of these interactions resulted in a zig-zagged continuous chain, with the *I* molecules residing down the centre of the chain, alternating between orientations between units. The chains were then packed together in order to generate the whole crystal structure.

These chains consisted of both enantiomeric forms, with the one form consistently undertaking proton transfer and the other remaining neutral. The composition of enantiomers either side of the co-former spine alternated moving along the chain, with the charged and uncharged forms remaining the same. For a given crystal, the overall construct maintains this relationship, but due to the disorder about the chiral centre of respective forms of *NPX*, alternation between enantiomers, in terms of the charged and uncharged nature, can be anticipated.

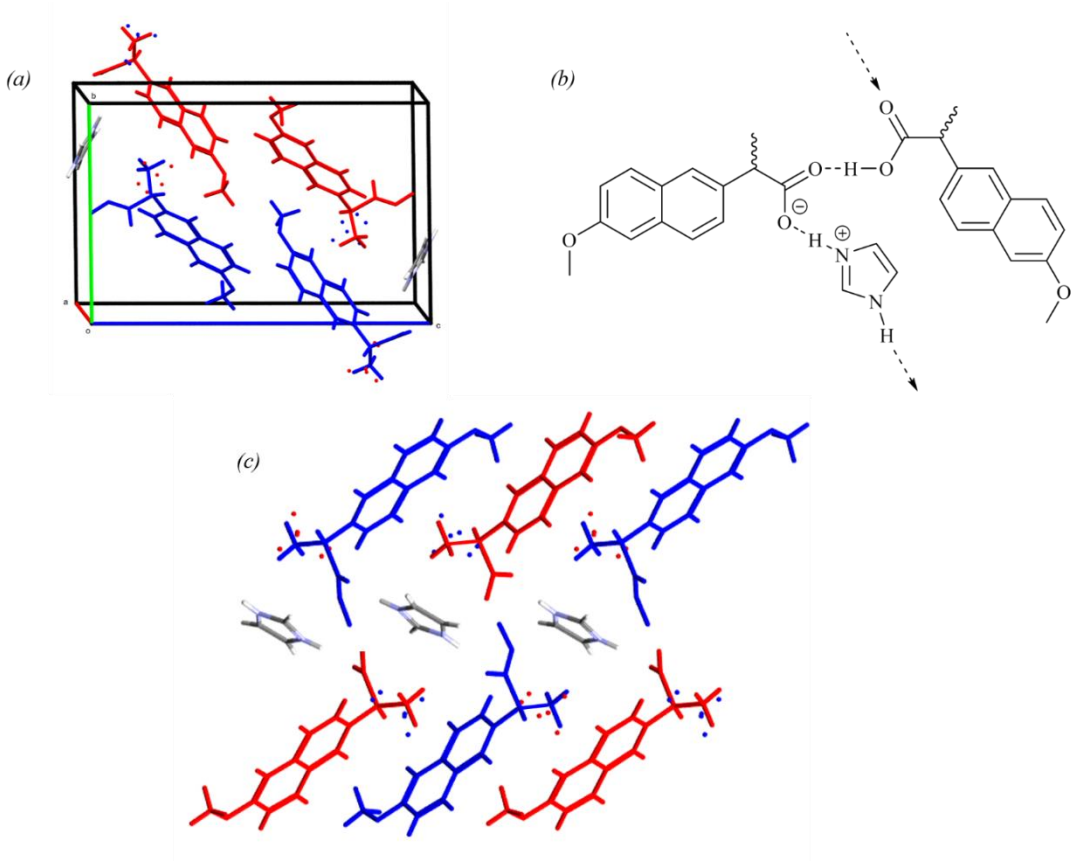

Figure 8. 11 - Crystal structure of the RS-naproxen:imidazole (2:1) salt, highlighting (a) the unit cell, (b) hydrogen bonding synthon and (c) packing arrangement (*sNPX* in red, *rNPX* in blue)

Table 8. 2 - Unit cell and crystallographic parameters for the RS-naproxen:imidazole (2:1) salt

Material	**RS-naproxen:imidazole (2:1) salt**
Empirical formula	$C_{31}H_{32}N_2O_6$
Formula weight	528.58
Temperature (K)	150.01(10)
Crystal system	triclinic
Space group	$P\bar{1}$
***a* (Å)**	6.01873(16)
***b* (Å)**	12.2567(4)
***c* (Å)**	18.3581(5)
***α* (°)**	90.876(2)
***β* (°)**	96.959(2)
***γ* (°)**	92.853(3)
Volume (Å^3)	1342.32(7)
Z*, *Z'	2, 1
ρ_{calc} (g/cm^3)	1.308
μ (mm^{-1})	0.742
F(000)	560.0
Crystal size (mm^3)	0.305 × 0.091 × 0.058
Radiation	CuKα (λ = 1.54184)
2Θ range for data collection (°)	7.222 to 136.498
Index ranges	$-7 \leq h \leq 5$, $-14 \leq k \leq 14$, $-22 \leq l \leq 22$
Reflections collected	14853
Independent reflections	4923 [R_{int} = 0.0187, R_{sigma} = 0.0172]
Data/restraints/parameters	4923/14/379
Goodness-of-fit on F^2	1.039
Final R indexes [I>=2σ (I)]	R_1 = 0.0568, wR_2 = 0.1534
Final R indexes [all data]	R_1 = 0.0657, wR_2 = 0.1615
Largest diff. peak/hole (e Å^{-3})	0.47/-0.37
Flack parameter	N/A

8.2 Materials of racemic and enantiopure naproxen with benzimidazole (*BI*)

8.2.1 Material screening

Further to the screening with *I*, its benzene derivative, benzimidazole (*BI*), was also utilised as a potential co-former for combinations with the *NPX*. Exhibiting the same aromatic nitrogen and N-H functionalities, *BI* has three polymorphic forms[210]; α, β and γ. The first two phases can be prepared under ambient conditions from aqueous or ethanol solutions, with β polymorph (CSD reference: BZDMAZ03) a metastable relationship to that of the α form (CSD reference: BZDMAZ02). The γ polymorph (CSD reference: BZDMAZ05), to date, can only be accessed under higher pressures. Raw material of *BI* can be purchased as an off-white powder as the α phase, with a melting point of 168-171ºC. The pK_a value of the co-former was taken from literature as 5.5[209] and making proton transfer unlikely.

8.2.1.1 Mechanochemical screening

Samples combining *sNPX* and *BI* were prepared using mechanochemical means, where 2:1, 1:1 and 1:2 stoichiometries were ground together with minimum quantities of solvent. Phase and thermal analyses were conducted using PXRD and DSC, highlighted in Figure 8.12 and 8.13, respectively.

The diffraction patterns of these homochiral combinations showed the presence of a novel crystalline form common across all stoichiometries. Though minimum starting material was also noted, the 1:1 pattern demonstrated the clearest signs of the formation of a distinct multi-component phase. DSC analysis of the 1:1 preparation highlighted two endothermic events, the first at 120-123ºC and the second at 128-130ºC. For the other stoichiometries, a single thermal phenomenon was observed, at 121-124ºC and 118-122ºC for the 2:1 and 1:2 samples, respectively. For the equimolar combination, the initial thermal event could be attributed to a possible phase transition from a low temperature form to that of high temperature form, followed by a melt.

Parallel neat grindings showed no direct complexation from any of the stoichiometries used (PXRD and DSC data in Appendix A8.2), with novel material formation only being derived from heating. After an initial phase transition between 77-85ºC, the two further thermal events were witnessed, at 119-123ºC and 128-130ºC, respectively, correlating to that observed from the liquid-assisted preparations.

Upon grinding racemic proportions of *NPX* with *BI* in a variety of molar ratios with ethanol, as with the enantiopure case, a novel multi-component phase was shown to form. The diffraction patterns for these combinations can be found in Figure 8.14. The formation of such a material was consistent over all stoichiometries used, omitting excesses in the starting material, with particular evidence in the 1:1 sample. DSC traces were also taken, shown in Figure 8.15. These mirrored the observations made for the homochiral 1:1 sample, with two distinct thermal events, occurring at 120-126ºC and 128-131ºC, respectively. The trends in thermal behaviour for the 2:1 and 1:2 samples also closely followed that of the enantiopure samples, exhibiting broader melting phenomena at 124-127ºC and 119-123ºC, respectively.

Neat grinding once showed little capability of preparing the novel material demonstrated in the liquid-assisted case, with heating the only route possible to allow for complexation. For the complete PXRD patterns and DSC traces for the neat preparations with homochiral and racemic *NPX*, see Appendix A8.2.

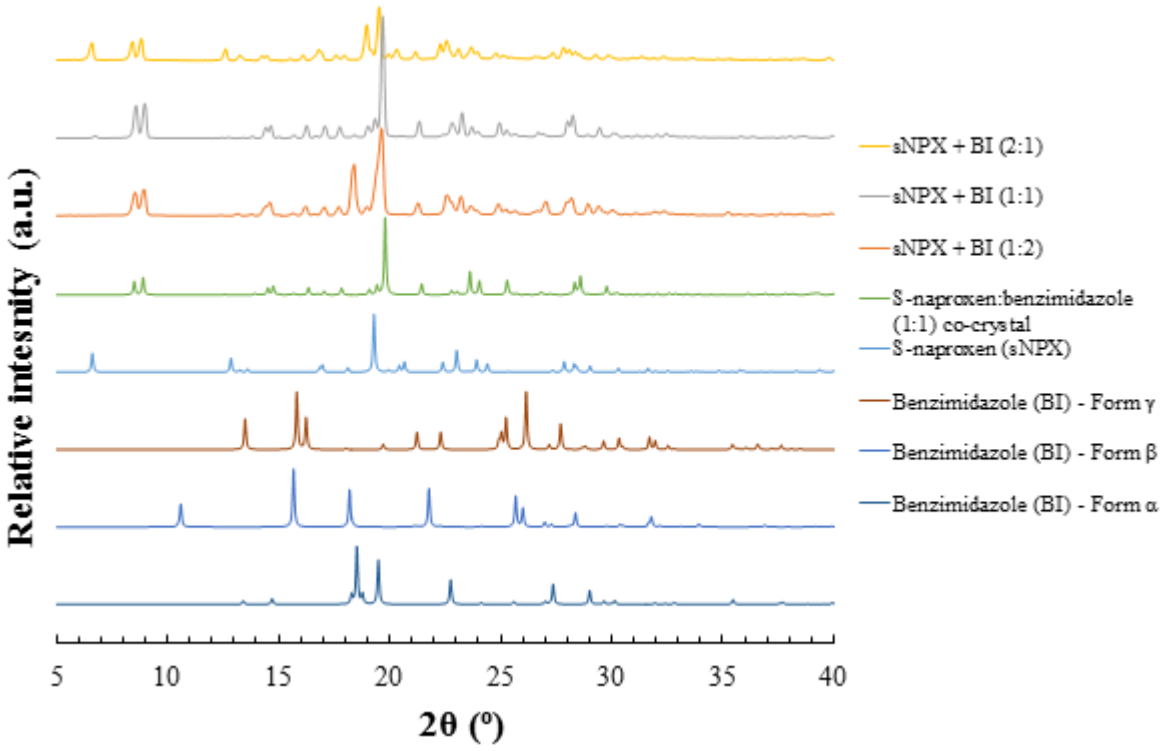

Figure 8. 12 - PXRD patterns from mechanochemically prepared samples of *sNPX* and BI with ethanol, ground in either 2:1, 1:1 or 1:2 molar ratios (top three patterns)

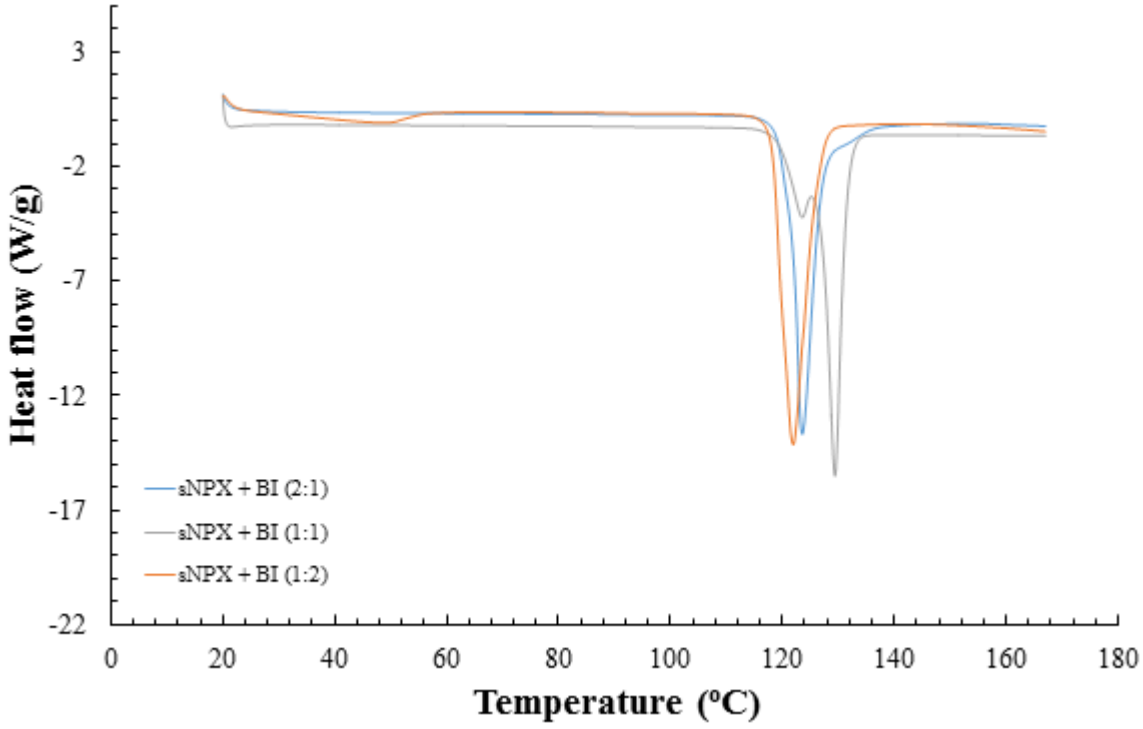

Figure 8. 13 - DSC traces from mechanochemically prepared samples of *sNPX* and *BI* in ethanol, ground in either 2:1, 1:1 or 1:2 molar ratios

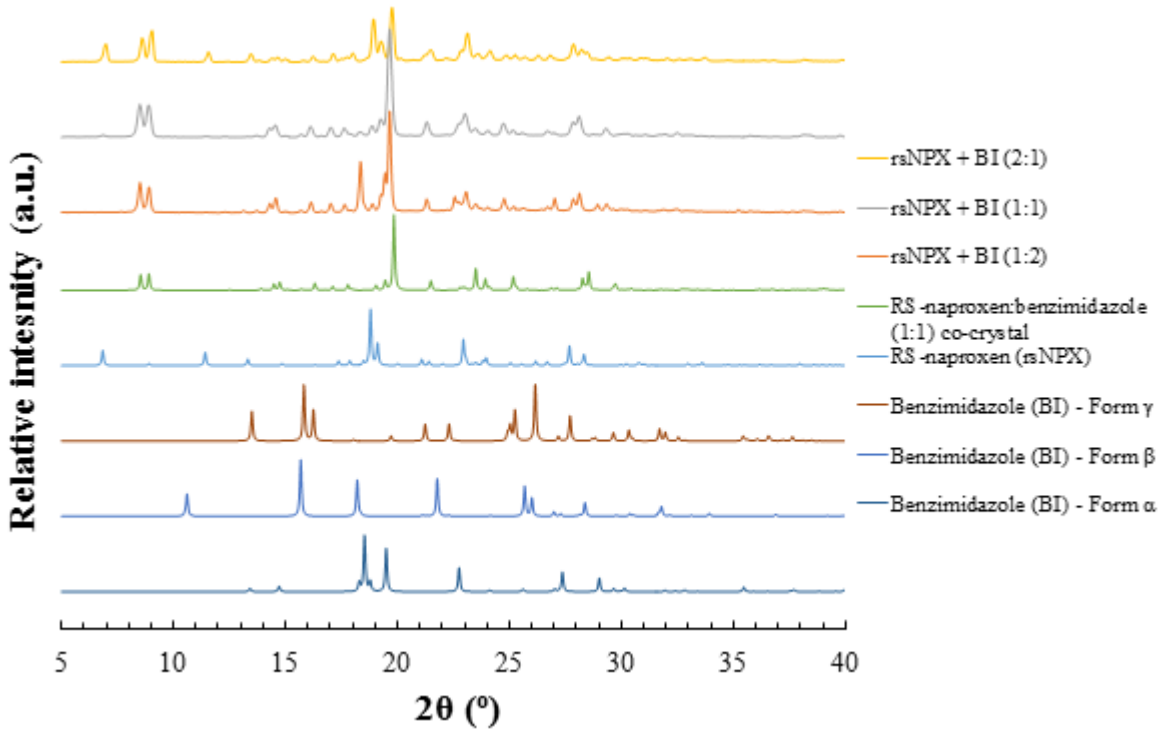

Figure 8. 14 - PXRD patterns from mechanochemically prepared samples of *rsNPX* and *BI* with ethanol, ground in either 2:1, 1:1 or 1:2 molar ratios (top three patterns)

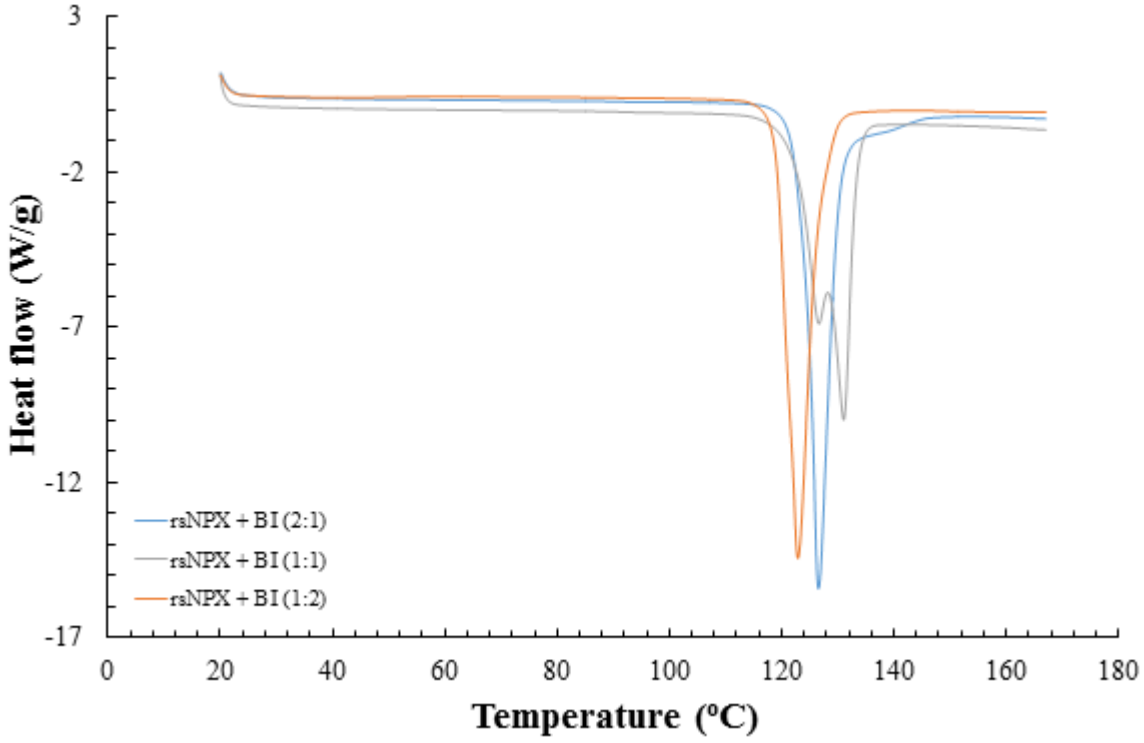

Figure 8. 15 - DSC traces from mechanochemically prepared samples of *rsNPX* and *BI* in ethanol, ground in either 2:1, 1:1 or 1:2 molar ratios

8.2.1.2 Combined evaporation & cooling crystallisation screening

Individual crystals were grown using crash cooling crystallisation for racemic and enantiopure solutions of *NPX*, where the API and co-former were combined in either 2:1, 1:1 or 1:2 molar ratios, in ethanol or isopropanol. Figure 8.16 depicts the single crystals made and analysed, through SCXRD, for both enantiomeric compositions. Crystallites taken from 1:1 solutions were shown to only be that of the starting components, whilst most crystals selected from the 1:2 racemic solutions with ethanol were deemed to be unsuitable for structural analysis. The crystals chosen were shown to directly correlate with the material made via mechanochemistry, with both entities exhibiting the same bulk white colour and elongated block morphology. For the racemic entity, it was noted that the crystals were shown to significantly agglomerate together upon crystallisation and grow.

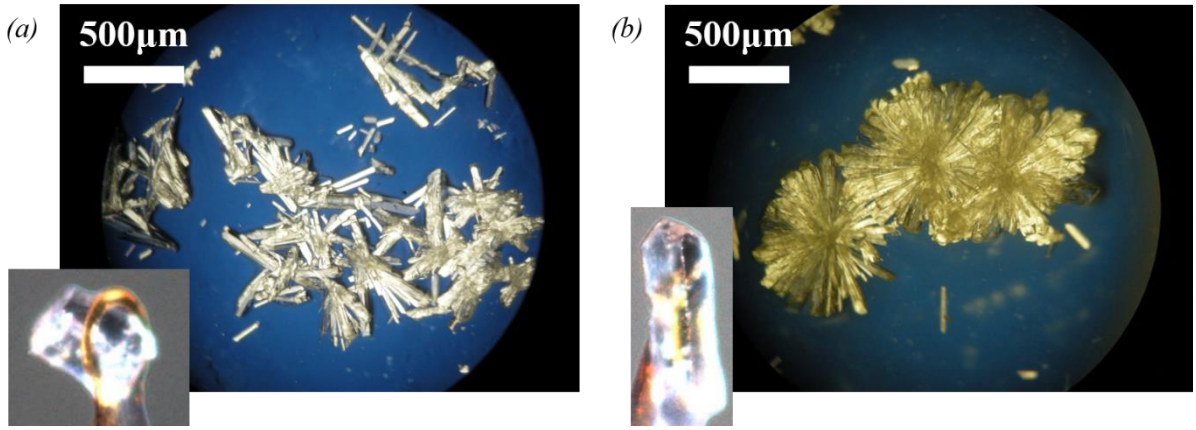

Figure 8. 16 - Microscope and mounted SCXRD images of crystals yielded from (a) a 1:2 *sNPX-BI* ethanol solution and (b) a 1:2 *rsNPX-BI* isopropanol solution

To explore the thermal events indicated in the mechanochemical preparations, crystals of suitable quality were selected and monitored using HSM, whilst the temperature was ramped. Figures 8.17 and 8.18 show images of crystals taken from the multi-component preparations with homochiral and racemic *NPX*, respectively. For both cases, no physical transformations were observed until beyond 117ºC. Upon reaching this point, the crystals of the different chiral compositions were shown to subtly darkening and become speckled between 117ºC and 123ºC. Prior to complete melting at temperatures beyond 131ºC, the crystals seemed to lighten. These observations corresponded to that seen from DSC analysis for the mechanochemically prepared samples, highlighting a solid-to-solid phase transition.

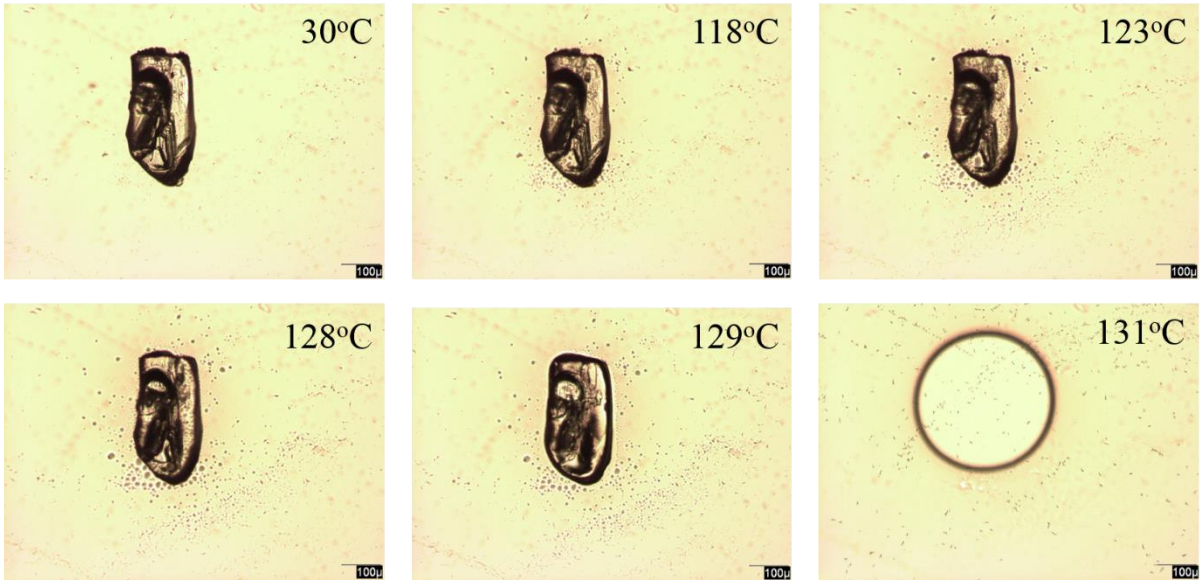

Figure 8. 17 - HSM images of individual crystals obtained from homochiral ethanol solutions, with 1:2 molar ratio of *NPX* to *BI*, taken at a variety of temperatures (10°C/min& 100µm scale)

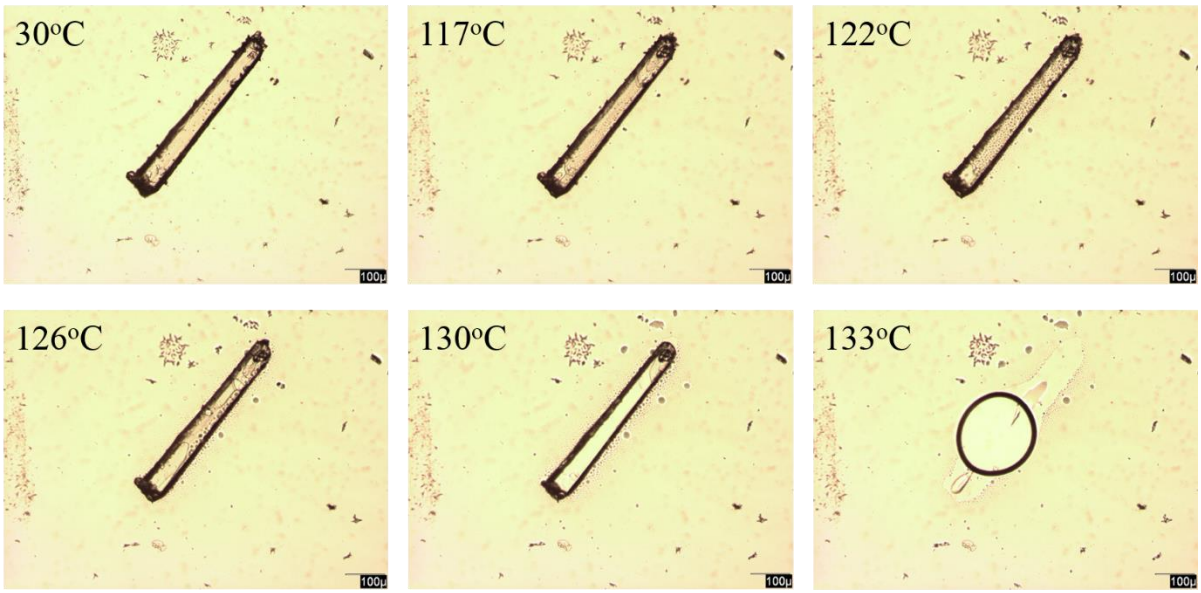

Figure 8. 18 - HSM images of individual crystals obtained from racemic isopropanol solutions, with 1:2 molar ratio of *NPX* to *BI*, taken at a variety of temperatures (10°C/min& 100µm scale)

8.2.2 Material characterisation

To determine the chiral crystalline relationship between the materials generated upon combining different enantiomeric contributions of *NPX* with *BI*, further analysis was conducted. This included comparisons of the relevant PXRD and DSC data, brought together to yield a binary phase diagram, as well as that of the relevant crystal structures, derived from SCXRD data.

8.2.2.1 Phase, thermal and spectroscopic analysis

Based upon the findings from mechanochemical screening and initial single crystal growth, it was shown that both the homo and heterochiral multi-component forms of *NPX* and BI could be reproducibly generated via the above mentioned techniques. Figure 8.19 allows for the comparison of the simulated PXRD patterns of each of the novel materials, as well as that of the different crystalline forms for the starting materials. As shown, the combinations of the API and the co-former produced distinctly different patterns to that of the single-component entities, emphasising the formation of new multi-component crystalline phases. However, it was noted that the diffraction arrays for both preparations expressed the exact same patterns, suggesting that both materials exhibited the same crystalline structure. This provided the first indication of either a racemic conglomerate or racemic solid solution.

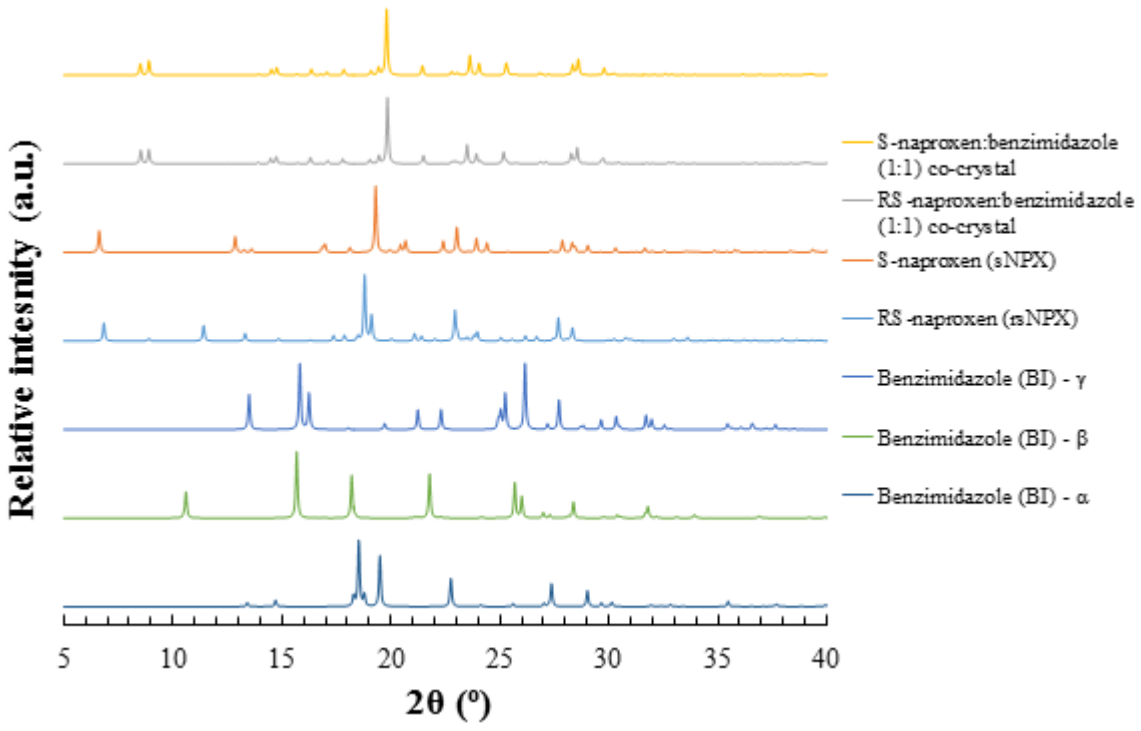

Figure 8. 19 - PXRD patterns of the S-naproxen:benzimidazole & RS-naproxen:benzimidazole (1:1) co-crystals, as derived from SCXRD data, compared to that of the starting materials

As previously explored, the mechanochemical preparations of the racemic and enantiopure multi-component combinations both expressed thermal traces with two clear subsequent endothermic events. Whilst it was most likely that these phenomena represented a phase transition of some kind, as highlighted in Figure 8.20, the similarity in the thermal properties of these two systems suggested that the interactions exploited were alike. This likeness in melting resembled the characteristics of a racemic solid solution.

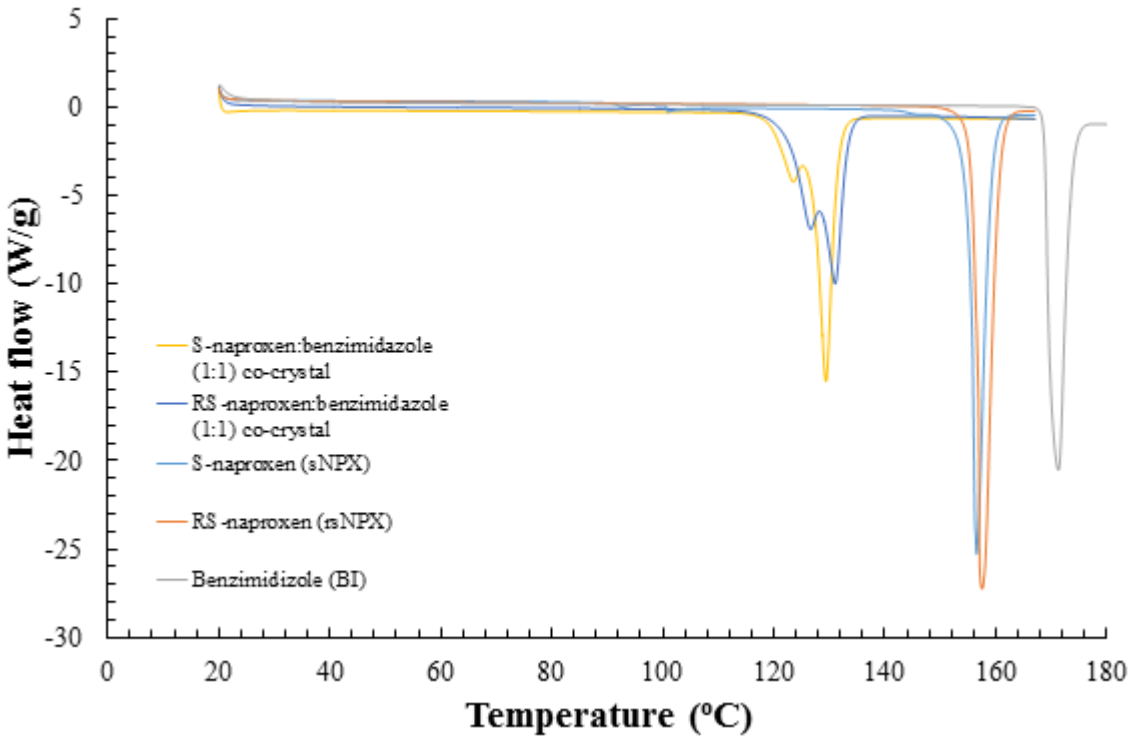

Figure 8. 20 - DSC traces of the S-naproxen:benzimidazole & RS-naproxen:benzimidazole (1:1) co-crystals, prepared via mechanochemistry, compared to that of the starting materials

IR spectroscopy was used to provide a first indication as to the intermolecular interactions and vibrational modes exhibited by for a given structure. Comparison of the *rsNPX-BI* and *sNPX-BI* materials using this technique (Appendix A8.2) demonstrated the same set of vibration and stretching modes, supporting the findings from DSC and PXRD analysis.

8.2.2.2 Binary (melting point) phase diagram analysis – Classification of chiral crystalline materials

Taking advantage of the capabilities of mechanochemistry to reliably produce the enantiomerically varying multi-component forms, different compositions of *sNPX* and *rNPX* were ground together with the co-former, *BI*, in a set molar ratio of 1:1. Minimum quantities of ethanol were used. The PXRD and DSC data for each sample can be found in Appendix A8.2. By taking the final melting point observed, the binary (melting point) phase diagram, shown in Figure 8.21, was constructed.

Despite changing the relative ratio of enantiomers for each preparation, little variation was noted in melting points from sample to sample. This indicated that the interactions holding the structure together did not change significantly with changing enantiomeric composition. The phase diagram reinforced the idea of a solid solution, demonstrating an example of a Type I Roozeboom or 'ideal' system.

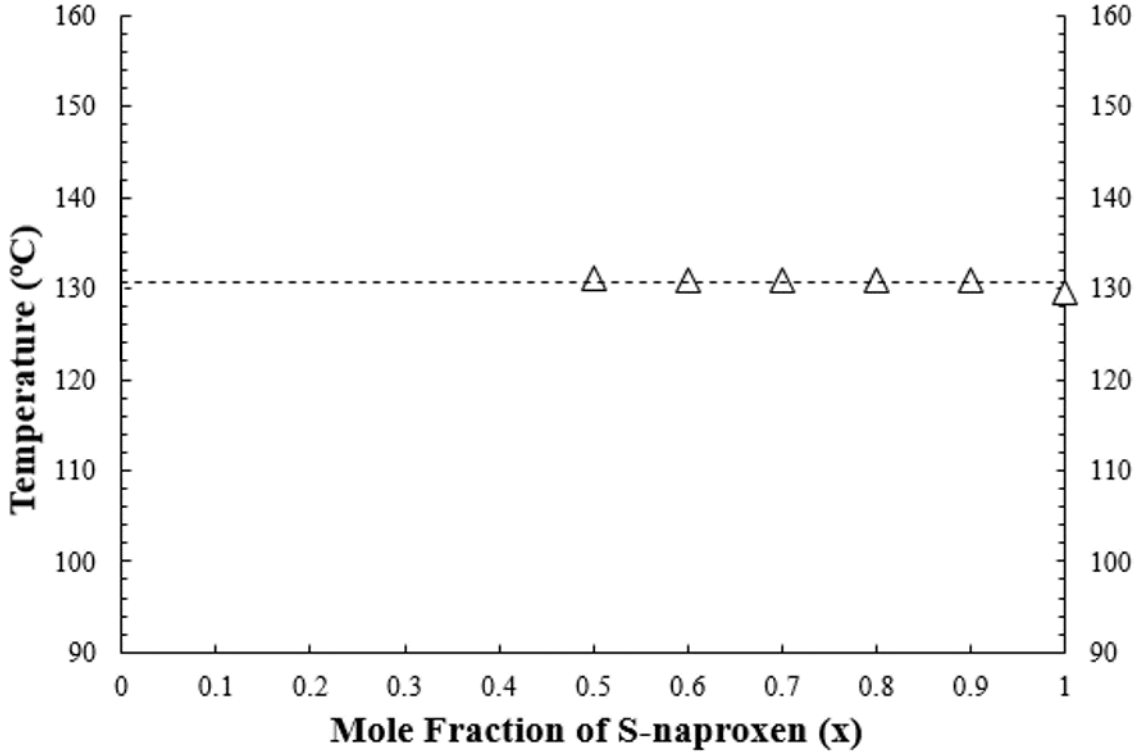

Figure 8. 21 - Binary (melting) point phase diagram, with changing enantiomeric composition of *rNPX* and *sNPX*, for the 1:1 co-crystals incorporating the co-former *BI*, highlighting the liquidus (Δ) point

8.2.2.3 Crystallography – Crystal structure analysis

Single crystals were grown from solution (as previous discussed) and analysed to ascertain their crystalline structure using SCXRD. The arrangement of the molecular entities within the assemblies, as well as the key interaction units, for the homo and heterochiral multi-component forms are shown in Figure 8.22 and 8.23, respectively. The unit cell parameters for these materials are detailed in Table 8.3. For further crystallographic information with particular emphasis on the hydrogen bonding and disorder exhibited, see Appendix A8.2. The corresponding CIF files (17, 18) can be found on the accompanying CD-ROM.

In the case of the enantiopure material, the S-enantiomer of *NPX* was shown to crystallise with *BI* in a 1:1 stoichiometry in a non-centrosymmetric monoclinic $P2_1$ space group. No proton transfer was noted, allowing for this system to be described as a S-naproxen:benzimidazole (1:1) co-crystal. The

asymmetric unit was constructed using two sets of the original 1:1 molecular combination (Z = 4, Z' = 2), collectively reflecting the individual contributions to key interaction unit. This unit was held together by four $D_1^1(3)$ hydrogen bonds, collectively set as a $R_4^4(16)$ ring. These contacts were classified into two distinct types; N-H···O and O-H···N interactions. With both enantiomeric forms contributing to this unit, the relationship between the molecules could not be defined using mirror or inversion symmetry, but could be described using a pseudo point of inversion, with the main body the molecular entities being related in this manner and remaining rigid. The only variation in structure that was noted was that about the chiral centre. Disorder was used to model the methyl group, emphasising the distinct mobility of this group within the crystalline structure, allowing for different chiral forms to be present. Here, the disorder was only such that a single enantiomer was present. Using these interaction units, the overall crystalline structure could be constructed, whereby the methyl functionalities line up, demonstrating a region within the assembly of potential chiral fluidity.

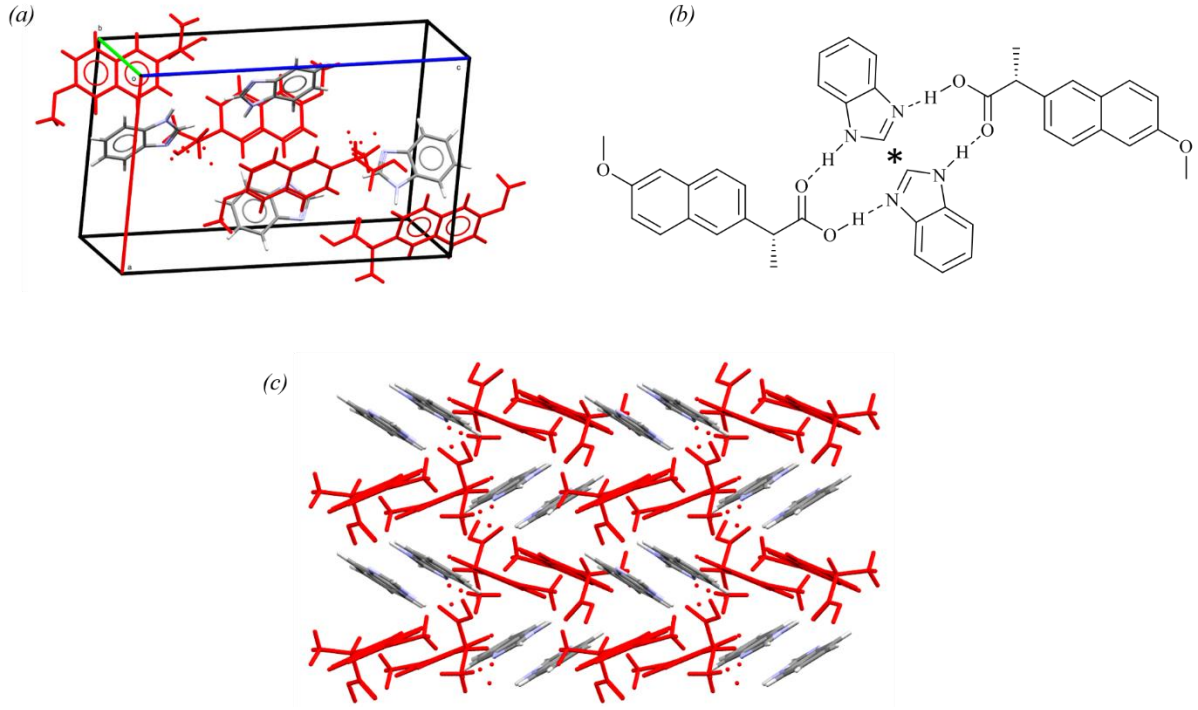

Figure 8. 22 - Crystal structure of the S-naproxen:benzimidazole (1:1) co-crystal, highlighting (a) the unit cell, (b) hydrogen bonding synthon (* = pseudo-inversion symmetry) and (c) packing arrangement (*sNPX* in red)

Upon introducing the opposite enantiomer of the API, it was shown that, as for the homochiral material, *NPX* was able to crystallise with the co-former in a 1:1 molar relationship. In the centrosymmetric monoclinic $P2_1/n$ space group, each of the asymmetric units within the unit cell reflected the 1:1 stoichiometry of API to co-former, though here both enantiomers were accounted for (Z = 4, Z' = 1).

Like that seen in the enantiomerically pure phase, no proton transfer was noted, allowing for this material to be described as a RS-naproxen:benzimidazole (1:1) co-crystal. A similar interaction unit was utilised, exploiting the same hydrogen bond interactions, with near identical orientations, but both enantiomers present within the motif, now related by inversion symmetry. Whilst the main body of the *BI* and *NPX* molecules were set to defined positions, the presence of disorder indicated variations about the chiral centres, demonstrating that there was enough space about each of the asymmetric carbon atoms to allow for variation in the enantiomeric composition. The units are then packed as before, showing distinct channels of interlocking motifs, central to which were the chiral centres, highlighting the regions of continuous enantiomeric composition.

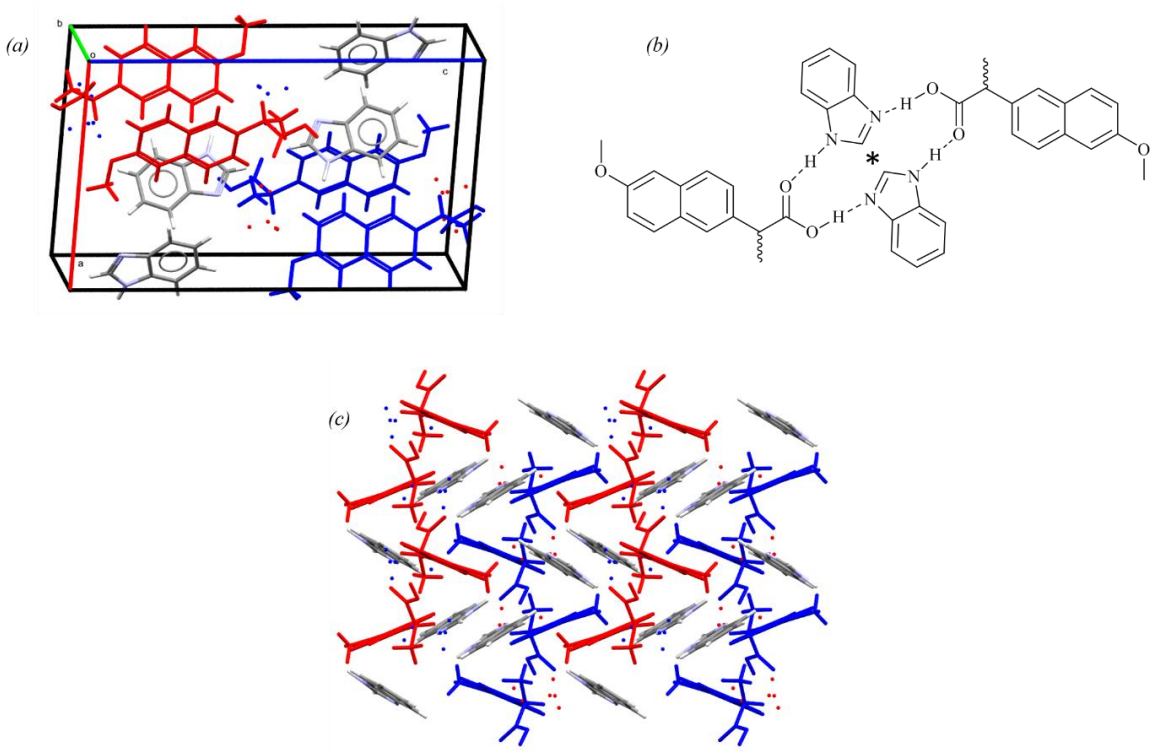

Figure 8. 23 - Crystal structure of the RS-naproxen:benzimidazole (1:1) co-crystal, highlighting (a) the unit cell, (b) hydrogen bonding synthon (* = inversion symmetry) and (c) packing arrangement (*sNPX* in red, *rNPX* in blue)

Table 8. 3 - Unit cell and crystallographic parameters for the S-naproxen:benzimidazole (1:1) and RS-naproxen:benzimidazole (1:1) co-crystal

Material	**S-naproxen:benzimidazole (1:1) co-crystal**	**RS-naproxen:benzimidazole (1:1) co-crystal**
Empirical formula	$C_{21}H_{20}N_2O_3$	$C_{21}H_{20}N_2O_3$
Formula weight	348.39	348.39
Temperature (K)	150.01(10)	150.00(10)
Crystal system	monoclinic	monoclinic
Space group	$P2_1$	$P2_1/n$
***a* (Å)**	11.8180(2)	11.7490(2)
***b* (Å)**	7.52380(10)	7.56745(17)
***c* (Å)**	19.8809(3)	19.8873(4)
***α* (°)**	90	90
***β* (°)**	93.0030(10)	93.2125(15)
***γ* (°)**	90	90
Volume (Å^3)	1765.31(5)	1765.41(6)
Z*, *Z'	4, 2	4, 1
ρ_{calc} (g/cm^3)	1.311	1.311
μ (mm^{-1})	0.716	0.716
F(000)	736.0	736.0
Crystal size (mm^3)	0.229 × 0.15 × 0.127	0.524 × 0.187 × 0.113
Radiation	CuKα (λ = 1.54184)	CuKα (λ = 1.54184)
2Θ range for data collection (°)	7.49 to 140.096	8.538 to 140.142
Index ranges	$-13 \leq h \leq 14$, $-9 \leq k \leq 9$, $-24 \leq l \leq 21$	$-14 \leq h \leq 14$, $-9 \leq k \leq 8$, $-24 \leq l \leq 22$
Reflections collected	13257	17819
Independent reflections	6670 [R_{int} = 0.0311, R_{sigma} = 0.0368]	3348 [R_{int} = 0.0228, R_{sigma} = 0.0149]
Data/restraints/parameters	6670/11/497	3348/8/253
Goodness-of-fit on F^2	1.038	1.042
Final R indexes [I>=2σ (I)]	R_1 = 0.0380, wR_2 = 0.1014	R_1 = 0.0502, wR_2 = 0.1243
Final R indexes [all data]	R_1 = 0.0402, wR_2 = 0.1048	R_1 = 0.0521, wR_2 = 0.1259
Largest diff. peak/hole (e Å^{-3})	0.20/-0.17	0.64/-0.45
Flack parameter	-0.06(14)	N/A

Further to the similarity in the unit cell dimensions, by overlaying the interaction units of both the homo and heterochiral co-crystals, as depicted in Figure 8.24, the distinct similarities between the crystalline materials could be emphasised, with the only region of difference that about the chiral centres, confirming the existence of a racemic solid-solution. In this case, despite changes in the enantiomeric composition of the co-crystal, the packing efficiency was shown not to change, highlighted by the same calculated packing density for each structure (1.311 g/cm^3). This emphasised the ideal nature of this solid solution system.

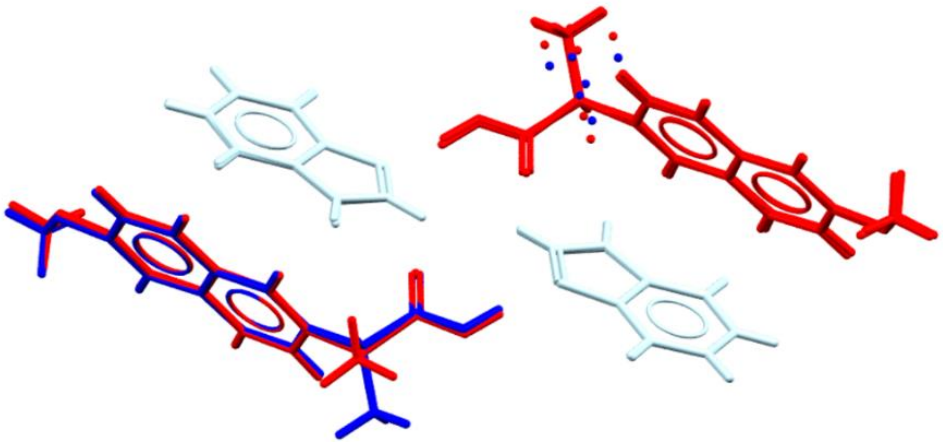

Figure 8. 24 - The overlapped key interaction units of the enantiopure and racemic (1:1) co-crystals of *NPX* and *BI*, highlighting their structural similarities

8.3 Materials of racemic and enantiopure naproxen with acridine (*A*)

8.3.1 Material screening

Acridine (*A*) was also used in combination with *NPX*, as part of the search for a racemic conglomerate. *A* exhibits a single hydrogen bond acceptor functionality, that of the aromatic nitrogen atom. Due to its extensively conjugated structure, the main intermolecular interaction possible is that of π-π stacking or C-H···π contacts. As such, this co-former expresses seven known structural variations; one hydrate[211] and six single-component polymorphs[212, 213] (II-VII). Despite the most stable form being reported as Form II (CSD reference: ACRDIN01), the raw material purchased for the purposes of screening was that of Form III (CSD reference: ACRDIN). This form is yellow in colour, with a melting point between 109-111ºC. The pK_a value of *A* was taken from the literature as 5.3 and, upon comparison with that of *NPX*, suspected to not undergo salt formation.

8.3.1.1 Mechanochemical screening

As for the previous co-formers, mechanochemical screening was conducted with *sNPX* and *A*, to gauge their potential for multi-component material formation. This was conducted using minimum quantities of solvent, in this case ethanol, as well as neat. The PXRD patterns and DSC traces for the liquid-assisted grindings are shown in Figures 8.25 and 8.26, respectively, with that of the neat preparations in Appendix A8.3.

Having combined the materials in given quantities (2:1, 1:1 and 1:2), phase analysis showed that for the equimolar sample ground with ethanol, a unique diffraction pattern was yielded when compared to the starting components. This demonstrated that a novel crystalline material could be prepared mechanochemically at a 1:1 stoichiometry. This was classified later as the (1:1) co-crystal, Form I. In the samples constituting excess of the co-former, the same novel peaks were also noted, along with those corresponding to *A* (Form III), whilst that with more API expressed a combination of peaks related to *sNPX* and that of a different phase generated from the equimolar preparation. This evidence of different distinct diffraction patterns at the varying stoichiometries of *sNPX* and *A* provided the first signs that structural variations with this combiantion of materials were possible.

The DSC traces showed major endothermic events at 88-91ºC, 90-94ºC and 87-89ºC for each of the stoichiometric samples, in descending quantities of *sNPX*, respectively. The 2:1 preparation also exhibited a broad phenonenon between 114ºC and 125ºC that could be attributed to the melting of the excess API, whereas the 1:2 showed a small endotherm at 75-80ºC that represented a possible phase transition to one of the newly discovered multi-component materials. Due to the relative impurities highlighted in the PXRD data, these melts, particularly for the 2:1 and 1:1 preparations, could not be directly taken as those of the actual novel complexed materials. However, the materials being analysed clearly showed significantly different melts to that of the starting material, indicating they are new crystalline forms consisting of *sNPX* and *A*.

For the corresponding neat preparations, the PXRD patterns for each sample was shown to only be a physical mixture of the starting materials, with the only evidence of complexation coming after heating. The DSC traces for each stoichiometry demonstrated the same thermal phenonema, to different extents, with an initial event occurring at 80-83ºC, followed by a second at 86-88ºC with a subsequent recrystallisation and major endothermic melt occuring from 93ºC to 96ºC. These observations could attributed to an initial complexation, followed by solid-to-solid transitions and a melt of the stable phase.

Again, this highlighted that with this combination of materials, polymorphic or stoichiometrically variant multi-component forms were possible.

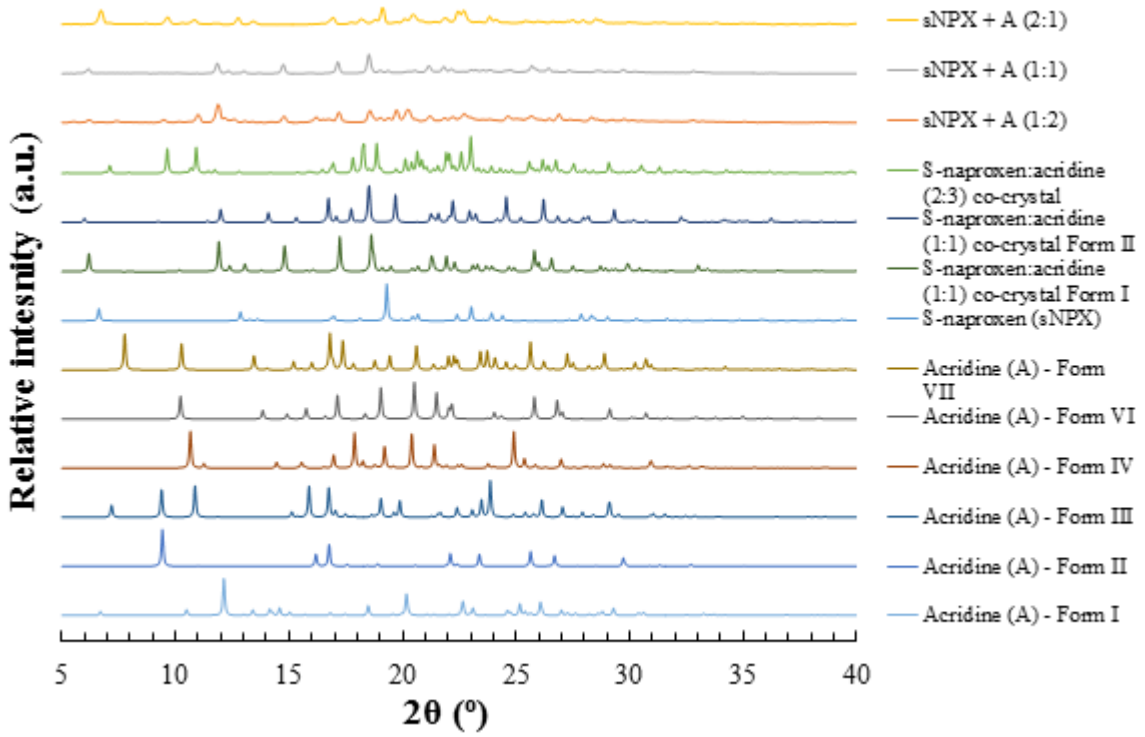

Figure 8. 25 - PXRD patterns from mechanochemically prepared samples of *sNPX* and *A* with ethanol, ground in either 2:1, 1:1 or 1:2 molar ratios (top three patterns)

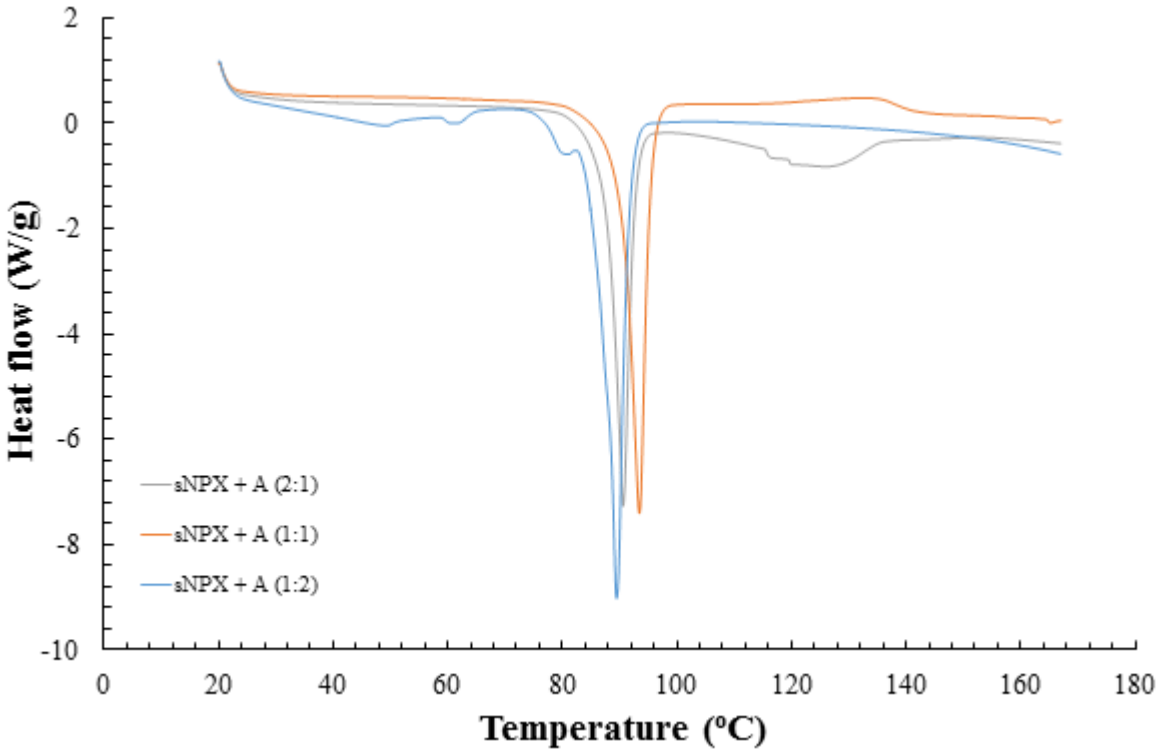

Figure 8. 26 - DSC traces from mechanochemically prepared samples of *sNPX* and *A* with ethanol, ground in either 2:1, 1:1 or 1:2 molar ratios

Racemic combinations of *NPX* and A were also ground in the same combinations as in the homochiral case. These grindings were conducted either neat (see Appendix A8.3 for analysis) or with minimum amounts of ethanol. Figures 8.27 and 8.28 show the PXRD and DSC data for the samples prepared via liquid-assisted mechanochemistry.

Phase analysis of these samples showed that upon combining the two consistent starting materials, a unique pattern could be generated, particularly for the 1:1 stoichiometry. The 2:1 and 1:2 sample showed the same diffraction patterns as for the equimolar preparation, but also with excess starting material noted. It should be noted that in terms of the excess contributions of the co-former present, distinction could not be made between that of Forms II and III.

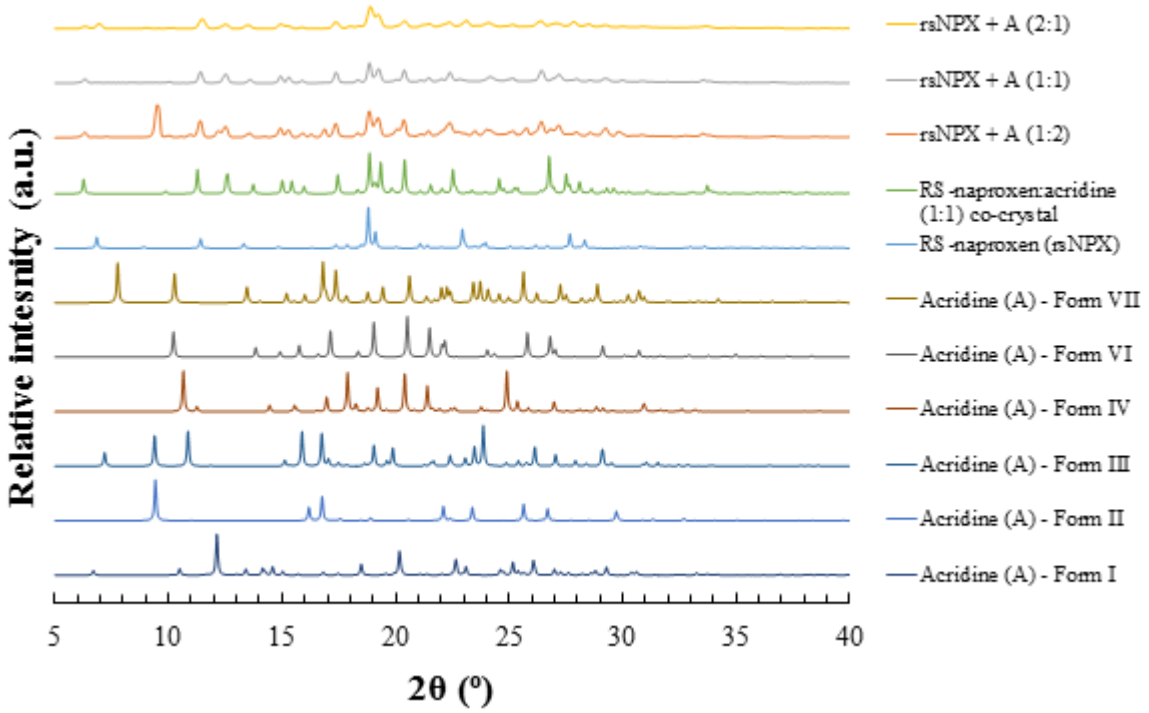

Figure 8. 27 - PXRD patterns from mechanochemically prepared samples of *rsNPX* and *A* with ethanol, ground in either 2:1, 1:1 or 1:2 molar ratios (top three patterns)

The DSC traces taken for these materials highlighted significantly different thermal events than compared to that of the starting materials, again, emphasising the formation of a novel crystalline phase. For the 2:1 and 1:1 samples, both showed a major melting phenomenon between 107-110°C, with the preparation consisting of uneven contributions of the starting components showing an additional broad endotherm at 125-131°C. This secondary event was attributed to that of excess *NPX*. The 1:2 sample demonstrated several endothermic processes. After excess solvent was driven off, two concurrent endothermic events were shown to occur at 86-88°C and 87-90°C, respectively, followed by a further broad endotherm, from 96-103°C. Collectively, these events could be related to the melt of the novel multi-component material and of excess A.

Neat grinding was shown to only partially allow for complexation to occur, the 1:1 combination showing the strongest signs of a novel form being made. As with the enantiopure grindings, the racemic combinations showed similar thermal properties across the stoichiometries, with an initial melt/recrystallisation occurring between 89°C and 91°C, followed by the melt at 108-110°C. Together, these findings showed that the same novel multi-component material could be prepared either with solvent or neat (with the assistance of heating).

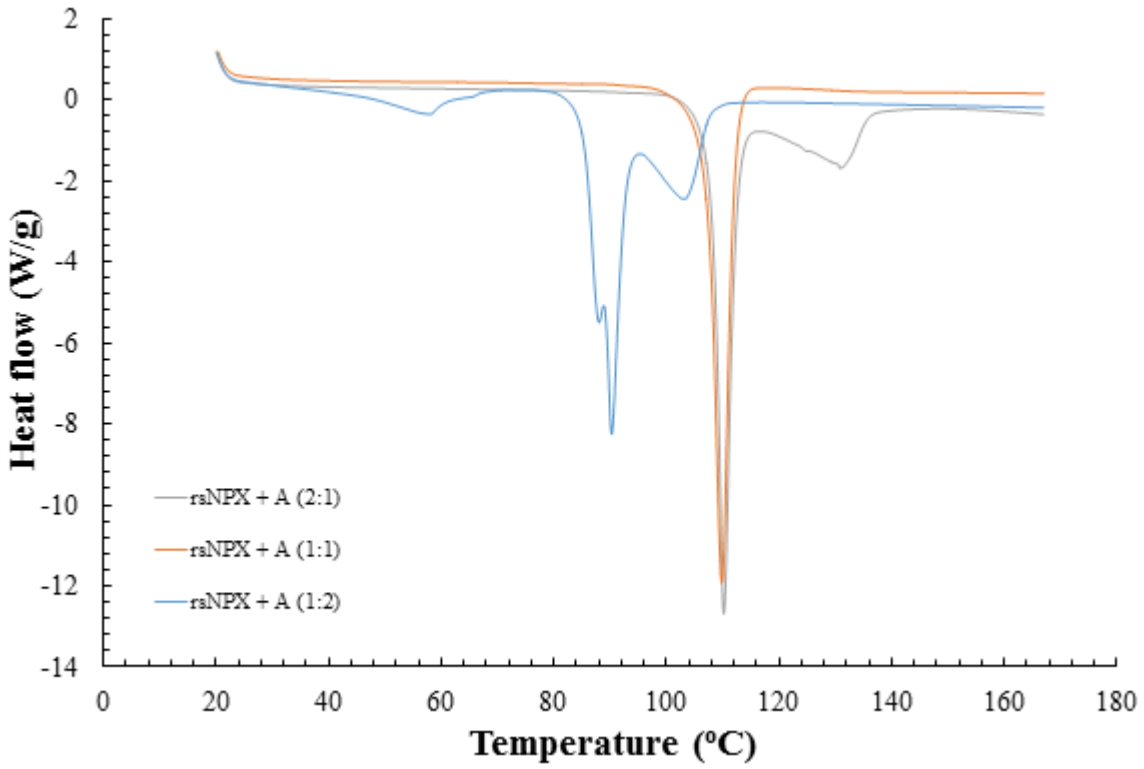

Figure 8. 28 - DSC traces from mechanochemically prepared samples of *rsNPX* and A with ethanol, ground in either 2:1, 1:1 or 1:2 molar ratios

To explore the possibility of preparing different polymorphic forms, homochiral and racemic compositions of *NPX* were ground with A in a 1:1 stoichiometry, in a variety of different laboratory solvents, including water, methanol, ethanol, isopropanol, acetonitrile, ethyl acetate, toluene and hexane. The respective PXRD and DSC data can be found in Appendix A8.3.

For the enantiopure preparations, the (1:1) multi-component phase, yielded initially from grindings with ethanol, was shown to be consistently made with the assistance of water, methanol, acetonitrile, ethyl acetate, toluene and hexane, each exhibiting a consistent melt between 93-96ºC. Samples prepared with water, toluene and hexane were also shown to have excess starting material, which gave rise to additional endothermic events. The PXRD pattern of the material produced with isopropanol highlighted the presence of a number of crystalline entities, both single and multi-component. It was noted that not only was the (1:1) Form I phase present, but also that corresponding to those observations made from the initial 2:1 ethanol preparation. This suggested that solvent environment had the potential to influence polymorphic or stoichiometric character for the system of *sNPX* and A. Furthermore, the thermal trace here demonstrated two consecutive endothermic events; at 86-90ºC and 93-95ºC, respectively, emphasising the presence of two multi-component forms.

In the racemic case, for all the solvent environments used, each demonstrated precipitation of the same distinct phase seen from the initial preparations. The DSC plots for each of these, exclude those events corresponding to that of excess solvent being released, demonstrated a single endothermic phenomenon between 109-112ºC. Together, this reinforced the notion that at racemic compositions, no structural variations were possible under the conditions used.

8.3.1.2 Combined evaporation & cooling crystallisation screening

Parallel to that from mechanochemistry, individual crystals were grown from solution, so as to ascertain their crystalline structure. Figure 8.29 depicts the crystals grown for each of the novel multi-component materials found. In conjunction with the SCXRD analysis, individual crystals were taken and assessed for their thermal properties using HSM, the images of which can be found in Appendix A8.3.

By first considering those grown from enantiopure solutions, where the API and co-former molecules were dissolved in a 1:1 molar ratio in ethanol, crystals with a long thin block, almost needle-like, morphologies were shown to form, collectively exhibiting bulk yellow colour. This material had a melting point between 101-104ºC, higher than that of the novel material prepared via mechanochemistry. The SCXRD data showed that these crystals were of a different multi-component form, subsequently described as the (1:1) co-crystal, Form II.

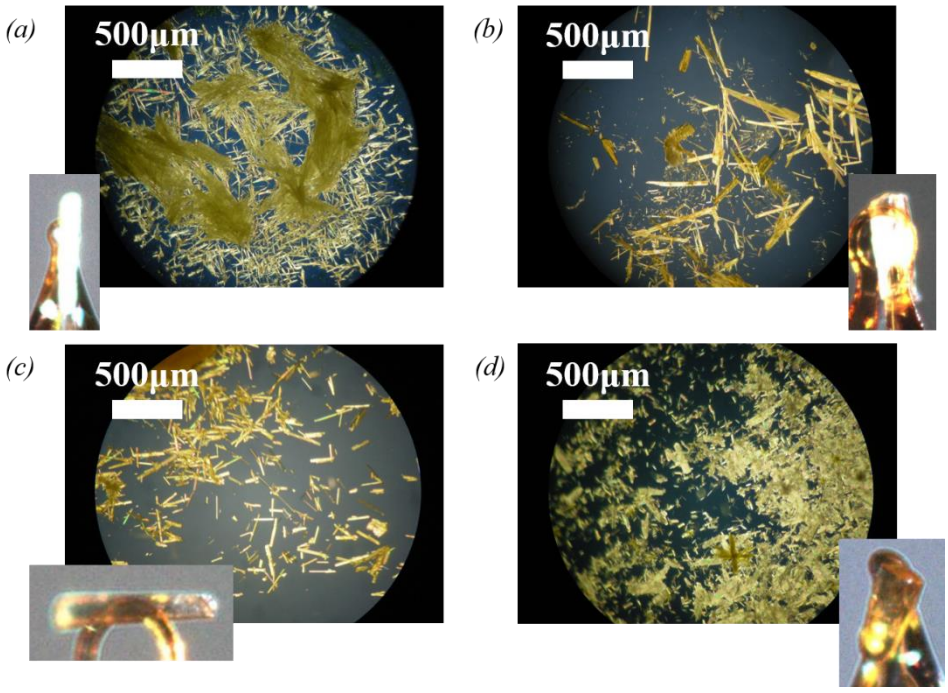

Figure 8. 29 - Microscope and mounted SCXRD images of crystals yielded from (a) 1:1 ethanol, (b) 1:1 acetonitrile and (c) seeded 1:1 ethanol enantiopure solutions, as well as that of (d) a racemic 1:1 solution in ethanol

In an effort to generate the mechanochemically yielded material with ethanol, further crystallisations were established; those relying on spontaneous nucleation and growth from acetonitrile solutions, and those acting through secondary nucleation and growth from ethanol solutions. The second set of crystallisations were conducted with the aid of seeds obtained from the previous mechanochemical preparations. For both processes, the crystals produced showed elongated block morphologies and were yellow in colour. HSM showed that those formed from acetonitrile and via seeding each showed melting phenomena between 88-96ºC and 93-98ºC, broadly relating to those observed from the 1:1 DSC traces of *sNPX* and *A* ground with ethanol and isopropanol, respectively. As such, SCXRD investigations demonstrated that the crystals from the acetonitrile and seeded ethanol solutions correspond to that of the (1:1), Form I, and (2:3) co-crystals (see Section 8.3.2.3).

The crystals grown from the racemic solutions of ethanol were shown to directly correspond to the material prepared from the 1:1 grinding of *rsNPX* and A. Based upon SCXRD, the structure of this material could be attributed to that of a (1:1) co-crystal of racemic *NPX* and the co-former. The images

produced over a range of temperatures using HSM highlighted a melting point from 110-112°C, corresponding to the findings from mechanochemistry.

8.3.2 Material characterisation

Thus far, the combination of mechanochemical and solution-based screening demonstrated that under given solvent environments, the API and co-former can interact to form a variety of different materials. From here, further analysis was conducted, emphasising any relationships towards that of a particular classification of chiral crystalline system.

8.3.2.1 Phase, thermal and spectroscopic analysis

As highlighted from the PXRD patterns highlighted in Figure 8.30, the three forms discovered for *sNPX* with *A* showed distinct diffraction peaks so as to make them discernible from each other, as well as that of the starting materials. To date, the three forms of enantiopure API and this given co-former demonstrated two (1:1) polymorphic phases and one (2:3) stoichiometric variation. In contrast, when both enantiomers were incorporated into the preparations, only one (1:1) co-crystal was shown to be prepared, consistent across all the methods used.

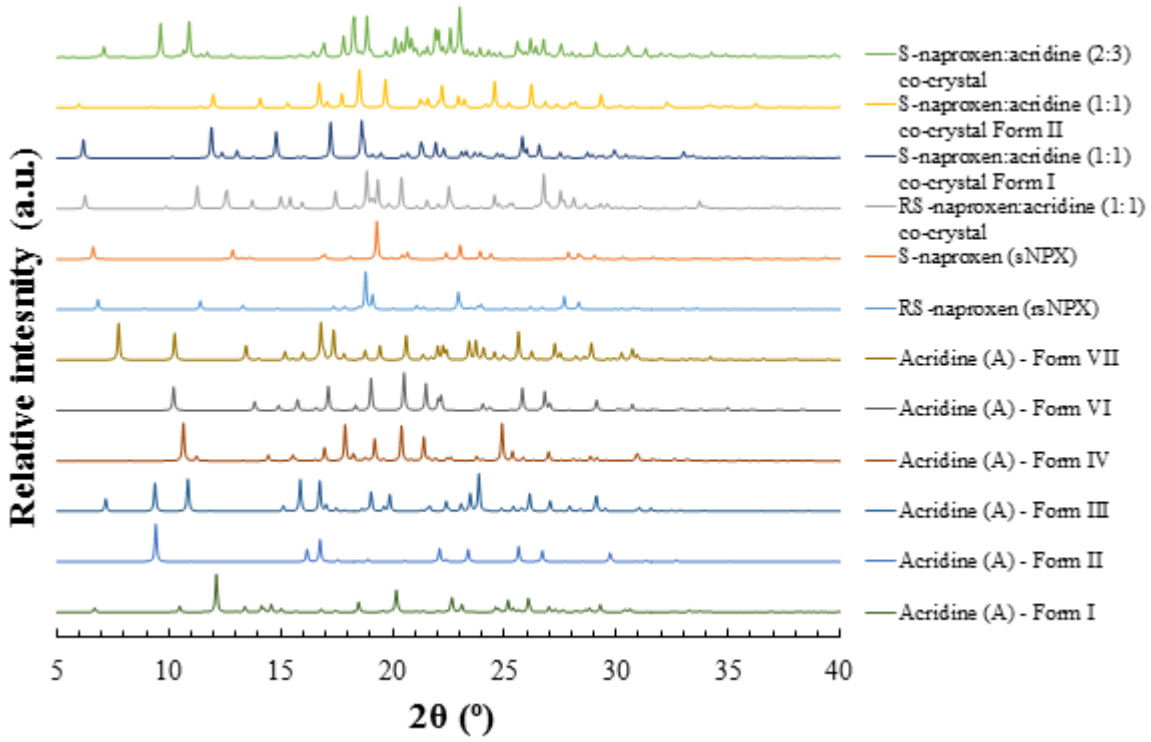

Figure 8. 30 - PXRD patterns of the S-naproxen:acridine (1:1), Forms I & II, and (2:3) co-crystals, as well as that of the RS-naproxen:acridine (1:1) co-crystal, as derived from SCXRD data, compared to that of the starting materials

Thus far, the melting points of these novel multi-component materials were taken based upon thermal analysis of their respective individual crystals and, where possible, from their mechanochemical preparations. A comparison of the collected melting events from DSC and HSM studies are tabulated in Table 8.5. Based on this data, it was shown that the thermal stability of the respective multi-component forms could be ranked as follows; (2:3) Form < (1:1) Form I < (1:1) Form II < (1:1) racemic co-crystal. With an initial focus on those phases made via mechanochemistry, the homochiral form was shown to have a lower melting point to that of the racemic, a sign of the enhanced stability of the solid-state at racemic compositions. The discrepancy between the values taken from DSC compared to that

observed for HSM could be credited to the potential for mechanochemical techniques to also possess excess starting material as part of the bulk, altering the particle-particle interactions present.

Table 8. 4 - Melting points for the four observed multi-component forms, incorporating either *sNPX* or *rsNPX* with *A*, as determined by DSC or HSM

Co-crystal Form	**Melting Point (ºC)**	
	DSC	***HSM***
S-naproxen:acridine (1:1) co-crystal, Form I	90-94	93-98
S-naproxen:acridine (1:1) co-crystal, Form II	N/A	101-104
S-naproxen:acridine (2:3) co-crystal	N/A	88-96
RS-naproxen:acridine (1:1) co-crystal	107-110	110-112

An initial assessment of the intermolecular interactions were made using IR spectroscopy, using ground up samples of the individual crystals prepared directly from solution. The spectra of each material can be found in Appendix A8.3. Broadly, all of the phases showed similar vibration and stretching modes, suggesting overall, similar set interactions were being used in the structure of each phase. The exception noted was that of the C=O stretch in the (1:1) Form I enantiopure co-crystal. In comparison to the other systems, where only one transmission peak was noted, here, two were observed, suggesting that this functionality displays some degree of variation in this structure.

8.3.2.2 Binary (melting point) phase diagram analysis – Classification of chiral crystalline materials

Focussing on the multi-component materials made via grinding, with varying enantiomeric composition, the melting points for the resultant samples could be taken and used for the construction of a binary phase diagram. Figure 8.31 depicts the change in the thermal phenomena as a function of enantiomeric composition. The corresponding PXRD patterns and DSC traces can be found in Appendix A8.3.

With the changing contribution of *sNPX* to *rNPX* from racemic to enantiopure, it was shown that the (1:1) racemic co-crystal gradually morphed into that of the corresponding homochiral phase, with the melting point of the bulk steadily decreasing. For each sample, no eutectic phenomena were observed, suggesting that despite the significant changes in the diffraction, the mechanochemically prepared combination of *NPX* and A represented a racemic solid solution. With the racemic phase possessing the higher melting point, this system could be classified as a Roozeboom Type II solid solution. What was clear from this system was that a crystalline material that incorporated both enantiomers could precipitate towards racemic compositions, a phase with great thermal stability to that of any of the polymorphic or stoichiometry forms of the homochiral co-crystal. As such, the co-former, A, was shown to not generate materials with the required characteristics for preferential crystallisation.

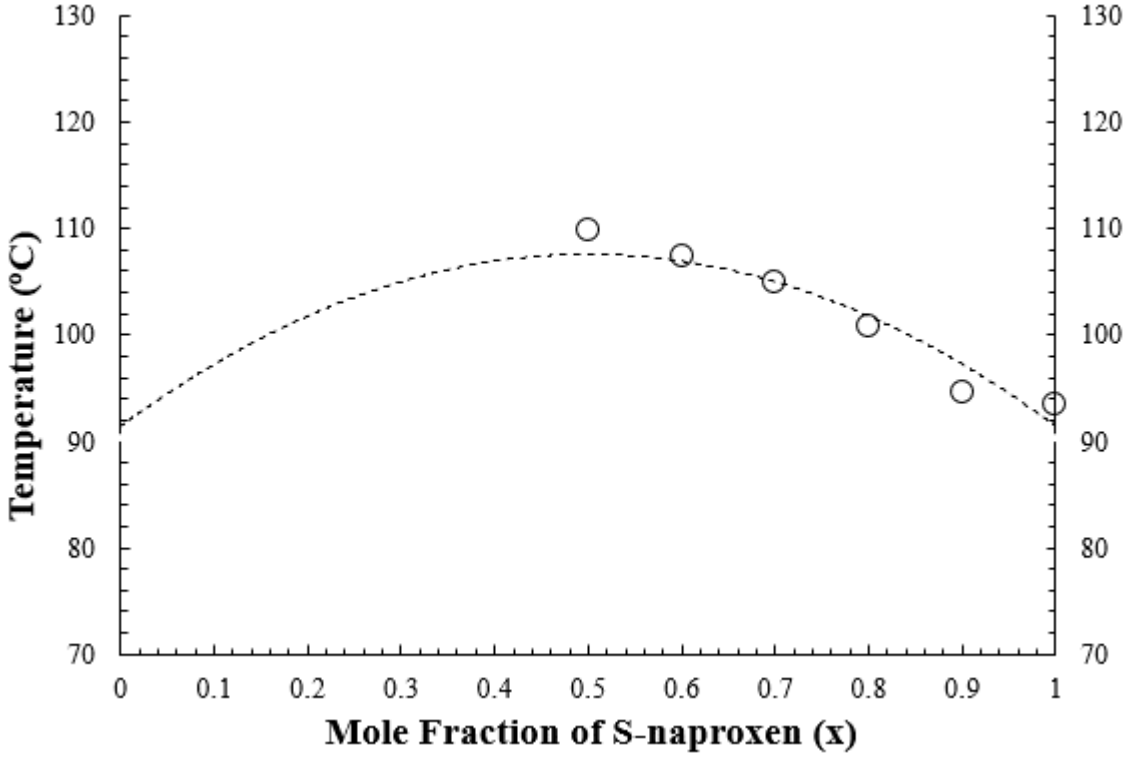

Figure 8. 31 - Binary (melting) point phase diagram, with changing enantiomeric composition of *rNPX* and *sNPX*, for the 1:1 co-crystals incorporating the co-former, *A*, highlighting the liquidus (○) point

8.3.2.3 Crystallography – Crystal structure analysis

The crystal structures for each of the discovered co-crystalline forms of *NPX* with A were determined using SCXRD. For all relevant crystallographic data, including hydrogen bond lengths and angles, as well as the relative occupancies for any disordered atoms, see Appendix A8.3. The corresponding CIF files (19-22) can be found on the accompanying CD-ROM. The unit cell parameters and details of the crystallographic refinement of both the (1:1) homochiral, Form I, and racemic phases can be found in Table 8.5. The arrangement of molecules and the relevant hydrogen bonding motifs for these materials are depicted in Figures 8.32 and 8.33, respectively.

Upon assessing the crystals grown from the 1:1 enantiopure solution of ethanol, seeded with material prepared via mechanochemistry, it was shown that the API and the co-former molecules crystallised in an orthorhombic $P2_12_12_1$ space group, a non-centrosymmetric space group. As such, the asymmetric unit was shown to consist of two sets of stoichiometrically related constituent starting materials, used to construct the whole unit cell ($Z = 8$, $Z' = 2$). No proton transfer was evident, confirming the formation of a S-naproxen:acridine (1:1) co-crystal, Form I.

The key interaction unit formed through a $D_1^1(3)$ hydrogen bond, acting through the O-H donor group of *sNPX* and the aromatic nitrogen atom of the A molecule (O-H···N), connecting the respective molecular entities. These moieties were then paired up with a corresponding interaction unit, with the co-former molecules parallel and slightly off-set, creating a zig-zag packing motif. Using these, as described by the symmetry operations, the whole crystal structure can be constructed, generating channels, the core of which was made up from a herring-bone spine of paired *A* molecules. Running in opposite directions either side of this central spine were the API molecules, with the relative positioning of each molecular entity alternating, so that the methyl group was pointing towards or away from the co-former. This co-crystal also demonstrated disorder about its carboxylic acid functionality, reflecting

the flexibility of the structure and the variability of the molecular positioning. This correlates with the findings from IR spectroscopy.

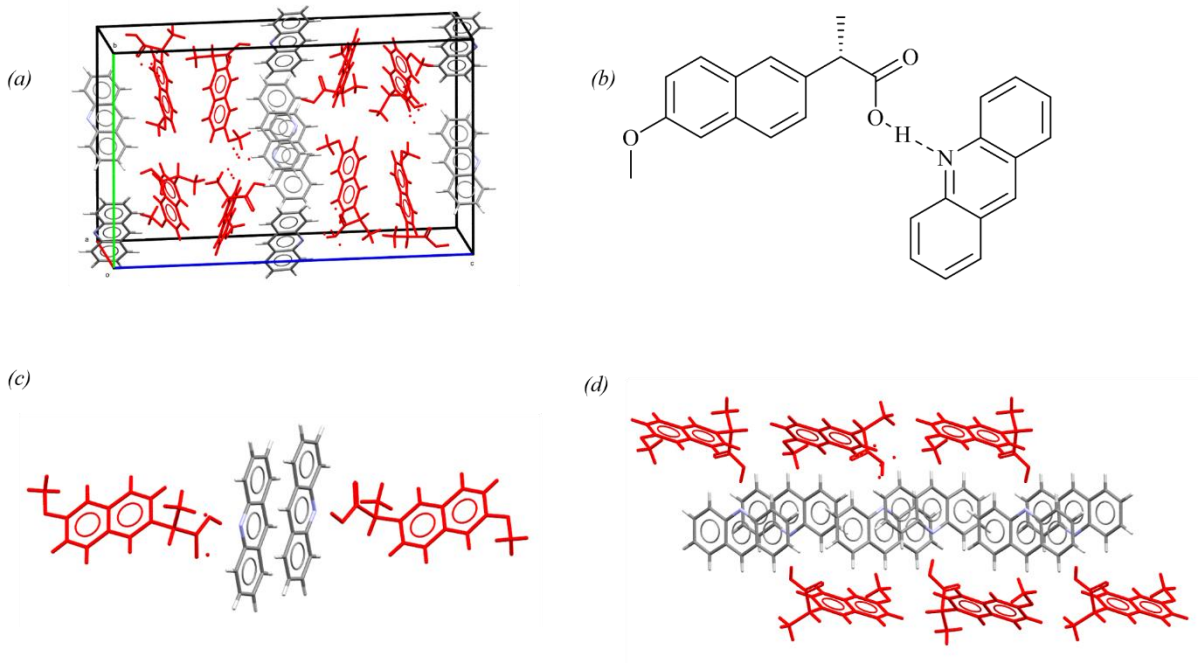

Figure 8. 32 - Crystal structure of the S-naproxen:acridine (1:1) co-crystal, Form I, highlighting (a) the unit cell, (b) hydrogen bonding synthon, (c) packing unit and (d) overall packing arrangement (*sNPX* in red)

Table 8. 5 - Unit cell and crystallographic parameters for the S-naproxen:acridine (1:1) co-crystal, Form I and the RS-naproxen:acridine (1:1) co-crystal

Material	**S-naproxen:acridine (1:1) co-crystal, Form I**	**RS-naproxen:acridine (1:1) co-crystal**
Empirical formula	$C_{27}H_{23}NO_3$	$C_{27}H_{23}NO_3$
Formula weight	409.46	409.46
Temperature (K)	150.00(10)	150.03(10)
Crystal system	orthorhombic	orthorhombic
Space group	$P2_12_12_1$	*P*bca
***a* (Å)**	8.58630(10)	7.8445(2)
***b* (Å)**	17.3784(2)	18.8698(5)
***c* (Å)**	28.5664(3)	28.2197(7)
***α* (°)**	90	90
***β* (°)**	90	90
***γ* (°)**	90	90
Volume (Å^3)	4262.57(8)	4177.19(19)
Z*, *Z'	8, 2	8, 1
ρ_{calc} (g/cm^3)	1.276	1.302
μ (mm^{-1})	0.662	0.676
F(000)	1728.0	1728.0
Crystal size (mm^3)	0.446 × 0.194 × 0.129	0.212 × 0.095 × 0.049
Radiation	CuKα (λ = 1.54184)	CuKα (λ = 1.54184)
2Θ range for data collection (°)	5.952 to 140.136	6.264 to 136.496
Index ranges	$-8 \le h \le 10$, $-17 \le k \le 21$, $-34 \le l \le 34$	$-8 \le h \le 9$, $-22 \le k \le 22$, $-33 \le l \le 33$
Reflections collected	24472	42938
Independent reflections	8102 [R_{int} = 0.0175, R_{sigma} = 0.0153]	3831 [R_{int} = 0.0479, R_{sigma} = 0.0172]
Data/restraints/parameters	8102/509/576	3831/0/282
Goodness-of-fit on F^2	1.026	1.050
Final R indexes [I>=2σ (I)]	R_1 = 0.0484, wR_2 = 0.1361	R_1 = 0.0502, wR_2 = 0.1358
Final R indexes [all data]	R_1 = 0.0502, wR_2 = 0.1384	R_1 = 0.0579, wR_2 = 0.1430
Largest diff. peak/hole (e Å^{-3})	0.76/-0.36	0.23/-0.34
Flack parameter	-0.04(6)	N/A

Crystals obtained from the racemic solution again demonstrated the 1:1 stoichiometric relationship between *NPX* and *A*, with molecules crystallising in the centrosymmetric orthorhombic *P*bca space group. Each unit cell was made up from eight asymmetric units, consisting of an API and co-former molecules, with both enantiomers being accounted for (Z = 8, Z' = 1). As with the homochiral co-crystal, no proton transfer was observed, allowing for this material to be described as a RS-naproxen:acridine (1:1) co-crystal. The only hydrogen bonding interaction present within this structure was that of the $D_1^1(3)$ interaction, common to all the structures exploiting *NPX* and *A*. Upon building up the crystalline assembly, similarities were observed between this racemic species and that of the homochiral. The main body of each *NPX* molecule was noted to be directed in the same orientations in both cases, with the only difference arising from the relative positioning of the combined carboxylic acid and methyl functionalities. For the racemic co-crystal, both enantiomers were accounted for, with the channels either side of the co-former spine alternating between the enantiomers. Furthermore, these channels ran in a non-concurrent manner to each other.

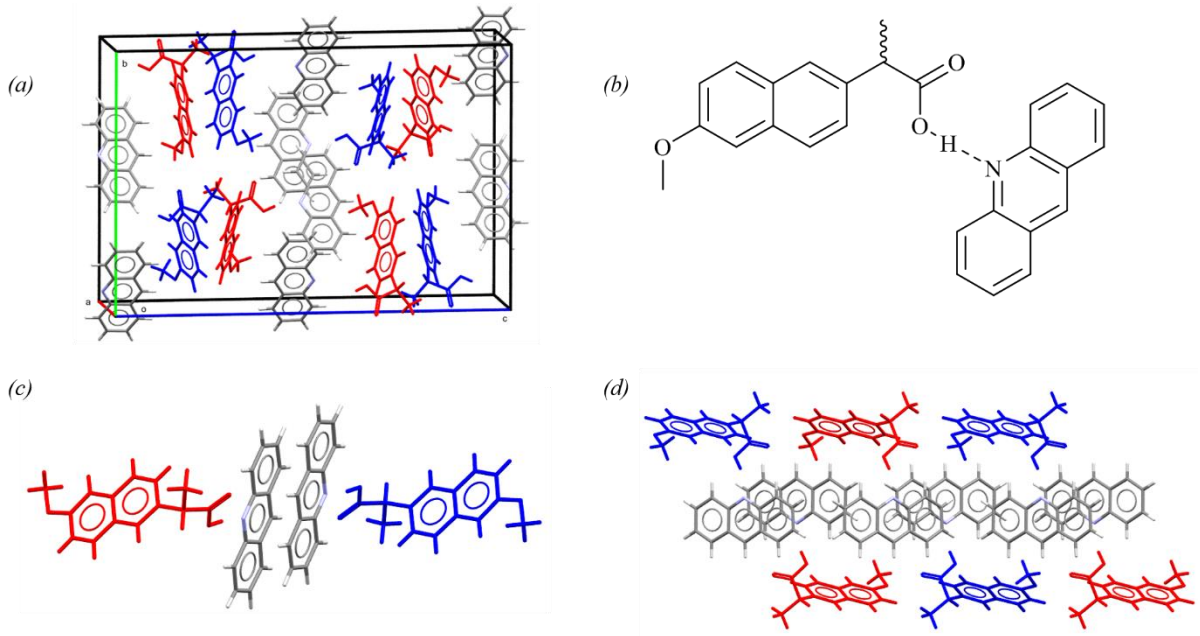

Figure 8. 33 - Crystal structure of the RS-naproxen:acridine (1:1) co-crystal, highlighting (a) the unit cell, (b) hydrogen bonding synthon, (c) packing unit and (d) overall packing arrangement (*sNPX* in red, *rNPX* in blue)

Given the structural similarities between the enantiopure and racemic co-crystals, with both expressing similar structures, this combination of co-former and API was shown to generate a material that could allow for the composition of enantiomers to be continuous. However, given that the racemic form expressed a higher melting point and a calculated packing density (1.302 g/cm^3 and 1.276 g/cm^3 for racemic and homochiral, respectively), the packing efficiency was shown to be greater towards equal quantities of enantiomer. Hence, this system can be described as a Type II, racemic solid solution.

The crystal structures for the (1:1) polymorphic and (2:3) stoichiometric co-crystal variants of *sNPX* with *A* are shown in Figures 8.34 and 35, with their unit cell parameters being shown in Tables 8.6 and 7, respectively. In the polymorphic case, the molecules crystallised together in a 1:1 ratio in an orthorhombic $P2_12_12_1$ space group, with the asymmetric units comprising of the API and co-former in a 1:1 molar ratio (Z = 4, Z' = 1). Here, the same hydrogen bonding motif was used as before, but in this case, rather than forming pairs of these interaction units, individual units were stacked together, interlocking with neighbouring units, forming distinct channels of *sNPX* and A, with the each like molecule in these channels alternating in orientation, as described through the crystal symmetry. The

packing density of this polymorphic form was greater than that of Form I (1.324 g/cm^3), highlighting greater packing efficiency and rationalising its higher melting point.

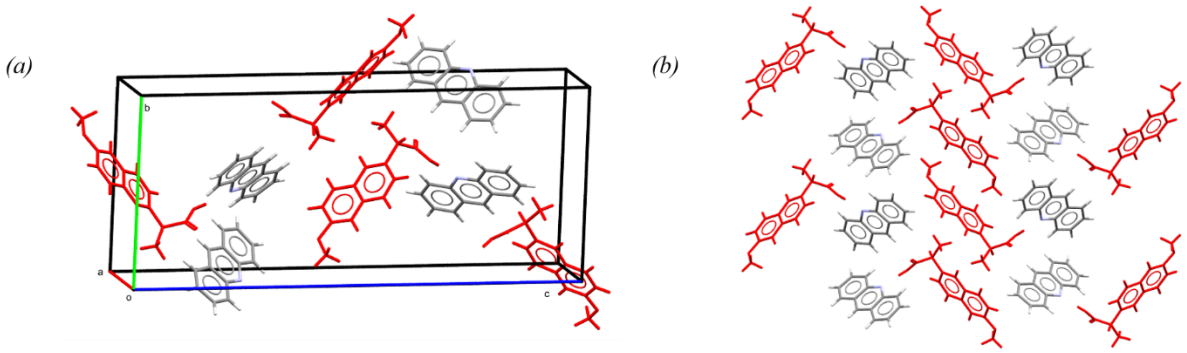

Figure 8. 34 - Crystal structure of the S-naproxen:acridine (1:1) co-crystal, Form II, highlighting (a) the unit cell and (b) packing arrangement (*sNPX* in red)

For the final form, the asymmetric unit consisted of two molecules of *sNPX* to three of *A*, a stoichiometric variant on that observed previous. With two of these making up the unit cell (Z = 2, Z' = 1), these molecules were shown crystallise in the non-centrosymmetric monoclinic space group, $P2_1$, with the same hydrogen bonding motif being used as before. However, this interaction was not utilised by every co-former. For every two co-former molecules that formed hydrogen bonding interactions with two API molecules, a third non-bonding species of *A* was shown to be present. The hydrogen bonded entities were shown to pack in such a way so as produce rings, within which pores of sufficient size were generated, capable of accommodating two channels of co-formers.

Table 8. 6 - Unit cell and crystallographic parameters for the S-naproxen:acridine (1:1) co-crystal, Form II

Material	**S-naproxen:acridine (1:1) co-crystal, Form II**
Empirical formula	$C_{27}H_{23}NO_3$
Formula weight	409.46
Temperature (K)	150.00(10)
Crystal system	orthorhombic
Space group	$P2_12_12_1$
***a* (Å)**	5.54150(10)
***b* (Å)**	12.5633(2)
***c* (Å)**	29.5070(4)
***α* (°)**	90
***β* (°)**	90
***γ* (°)**	90
Volume (Å^3)	2054.26(6)
Z*, *Z'	4, 1
ρ_{calc} (g/cm^3)	1.324
μ (mm^{-1})	0.687
F(000)	864.0
Crystal size (mm^3)	0.05 × 0.05 × 0.05
Radiation	CuKα (λ = 1.54184)
2Θ range for data collection (°)	5.99 to 146.24
Index ranges	$-4 \leq h \leq 6$, $-15 \leq k \leq 15$, $-35 \leq l \leq 36$
Reflections collected	23848
Independent reflections	4070 [R_{int} = 0.0314, R_{sigma} = 0.0193]
Data/restraints/parameters	4070/0/283
Goodness-of-fit on F^2	1.057
Final R indexes [I>=2σ (I)]	R_1 = 0.0386, wR_2 = 0.1049
Final R indexes [all data]	R_1 = 0.0416, wR_2 = 0.1081
Largest diff. peak/hole (e Å^{-3})	0.23/-0.26
Flack parameter	0.01(9)

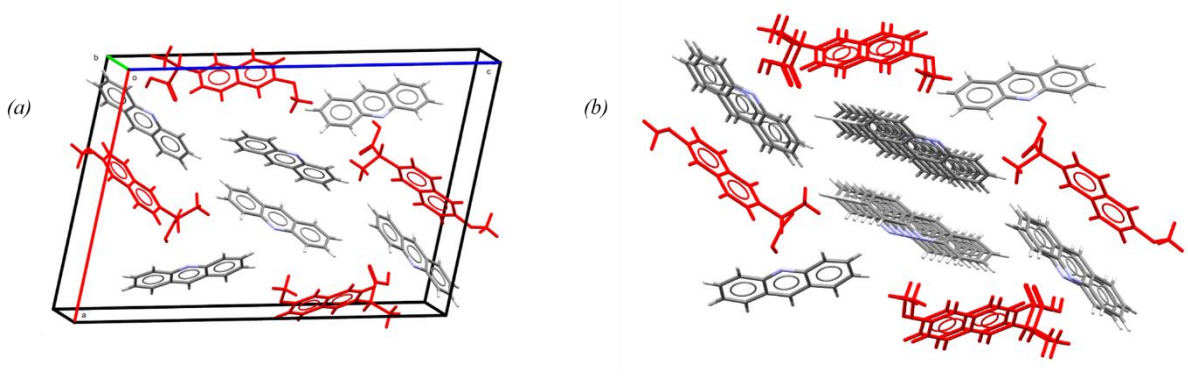

Figure 8. 35 - Crystal structure of the S-naproxen:acridine (2:3) co-crystal, highlighting (a) the unit cell and (b) packing arrangement (*sNPX* in red)

Table 8. 7 - Unit cell and crystallographic parameters for the S-naproxen:acridine (2:3) co-crystal

Material	**S-naproxen:acridine (2:3) co-crystal**
Empirical formula	$C_{67}H_{55}N_3O_6$
Formula weight	998.14
Temperature (K)	150.00(10)
Crystal system	monoclinic
Space group	$P2_1$
***a* (Å)**	17.2022(8)
***b* (Å)**	5.9240(2)
***c* (Å)**	25.3678(11)
***α* (°)**	90
***β* (°)**	101.465(5)
***γ* (°)**	90
Volume (Å^3)	2533.54(19)
Z*, *Z'	2, 1
ρ_{calc} (g/cm^3)	1.308
μ (mm^{-1})	0.084
F(000)	1052.0
Crystal size (mm^3)	0.32 × 0.126 × 0.124
Radiation	MoKα (λ = 0.71073)
2Θ range for data collection (°)	5.272 to 51.362
Index ranges	$-20 \leq h \leq 20$, $-7 \leq k \leq 7$, $-30 \leq l \leq 30$
Reflections collected	18594
Independent reflections	9606 [R_{int} = 0.0281, R_{sigma} = 0.0488]
Data/restraints/parameters	9606/1/691
Goodness-of-fit on F^2	1.078
Final R indexes [I>=2σ (I)]	R_1 = 0.0433, wR_2 = 0.0878
Final R indexes [all data]	R_1 = 0.0529, wR_2 = 0.0935
Largest diff. peak/hole (e Å^{-3})	0.15/-0.19
Flack parameter	-0.4(5)

8.4 Summary, conclusions and future work

Following on from the previous work conducted with the *NPX* and the *2AP* derivatives, further screening was carried out using co-formers exhibiting a different set of hydrogen bonding interactions. These included imidazole (*I*) and its derivative, benzimidazole (*BI*), as well as that of acridine (*A*). Whilst the first two species both exhibited the same hydrogen bond acceptor and donor functionalities, with the capability to facilitate proton transfer with *NPX*, the third co-former contained only one group that could form a contact with the API. Each of these co-formers, as single-component entities, were known to crystallise as a variety of forms, presenting the possibility of forming structurally varying multi-component forms.

As with the *2AP* derivatives, mechanochemistry was utilised as a first reference point and was shown to be capable of precipitating at least one novel crystalline multi-component phase for each of the co-formers used. Whilst translation to solution crystallisation was not always directly possible, the solid prepared via grinding provided material that could be used as a seed into the necessary crystallisation media, allowing for the growth of the necessary crystals and hence, structural characterisation. As such, the combination of mechanochemical and crash cooling crystallisations allowed for the effective screening of the API with these co-formers, allowing for the discovery of eight novel multi-component complexes of varying enantiomeric and stoichiometric composition, with a several polymorphs being found.

In the case of *NPX* with *I*, different salt forms were shown to precipitate at racemic and homochiral compositions, each expressing a (2:1) stoichiometry. For the enantiopure complex, a hydrogen bonded chain, alternating from *NPX* to *I*, formed the basis of the structure, with proton transfer occurring between the two molecular entities. An additional neutral API molecule was shown to interact with the chained *NPX* species, culminating in a branches protruding from the chain. In contrast, the racemic multi-component material demonstrated a zig-zagged chained structure, with the co-former molecule forming contacts, bridging between the protonated and deprotonated *NPX* molecules, each representing a different enantiomer. These in turn were shown to interact. Whilst the initial evidence suggested the crystallisation of a racemic compound system, the melting point of the homochiral salt was shown to be higher (124-127^{o}C) than that of the heterochiral (113-117^{o}C), highlighting similar characteristics to that of the *NPX-2AP* complex. Therefore, this system was deemed to have the properties of a metastable conglomerate and applications for chiral resolution methods, subject to further investigation. These would consist of probing the ability of the homochiral phase to crystallise at compositions towards that of racemic, hence, assessing its kinetic stability.

Upon manipulating the structure of the first co-former with the introduction of a benzene functionality, *BI* was shown to generate a different set of crystalline materials at racemic and enantiopure contributions than that observed for *I*. Having been prepared reliably via mechanochemical means, both complexes were shown to not only possess the same diffraction patterns, but also broadly the same thermal phenomena from 128^{o}C to 131^{o}C. By assessing the crystal structures of the two materials, it was shown that both possessed the same arrangement of molecular entities, with the key interaction unit consisting of a ring of two co-former and two API molecules, all hydrogen bonded together. It was further shown that by changing the enantiomeric composition, the packing density did not vary, highlighting that the positioning of the *NPX* molecules within the structure did not depend upon its chirality. Hence, this system was defined as an ideal racemic solid solution and had no application towards a preferential crystallisation process.

For the final system discussed in this chapter, the co-former *A* was selected owing to its lone functionality capable of forming a strong hydrogen bonding interaction, allowing for a greater number of molecular conformations and hence, polymorphic forms. The aim, alongside discovering structures

that are applicable to chiral resolution processes, was to explore the polymorphic landscape of multi-component materials made in combination with *NPX*. As such, three different structural variations of the homochiral form of the API with the co-former were prepared; two polymorphic (1:1) and one (2:3) stoichiometric co-crystalline phases. In comparison, only one form was found, to date, with racemic compositions, that of a (1:1) co-crystal. The different materials were prepared either by mechanochemistry, through the direct crystallisation from ethanol or acetonitrile solutions or upon seeding said solutions. Upon comparing and contrasting the (1:1) structures of *NPX* and *A*, it was shown that both a conventional racemic compound and a racemic solid solution were possible, which showed little use for chiral resolution via crystallisation.

With particular emphasis on the system incorporating the co-former *A* and whilst each of the multi-component structures presented the same hydrogen bonding interaction, the polymorphic nature of this system could be attributed to different orientations the various molecular species could take about this contact. An interesting feature was that only the enantiopure preparations demonstrated polymorphism, whilst the racemic did not. It is plausible that the number of degrees of freedom exhibited by a racemic system would be less than that for the homochiral, owing to the need to find structures within which the three molecular components, i.e. the two enantiomers and the co-former, could interact and pack efficiently.

Further to the work completed here, the polymorphic landscape of each case can still be explored to a greater extent. By using the crash cooling method, further solvent environments should be assessed, maintaining the different stoichiometric combinations of API to co-former and applying seeding where necessary. In addition, the potential of the *NPX-I* system should be explored further, confirming the metastability of the enantiomerically pure complex towards racemic compositions and designing cooling crystallisations accordingly that could have implications for a preferential process.

9 Selective preparation and crystallisation of stoichiometric co-crystals of oxalic acid and urea, driving towards continuous crystallisation

As shown from previous studies, upon combining of oxalic acid (*OA*) and urea (*U*), two stoichiometric co-crystals were able to form, that of the oxalic acid:urea (1:2[188, 189, 191, 193]) and (1:1[188, 191, 192]) co-crystals (*OAU*-1:1 & *OAU*-1:2). These materials show different crystalline structures, highlighted in Chapter 3, each with their own stabilities. These are reflected by the thermal phenomena exhibited in Figure 9.1, details of which can be found in Appendix A9.

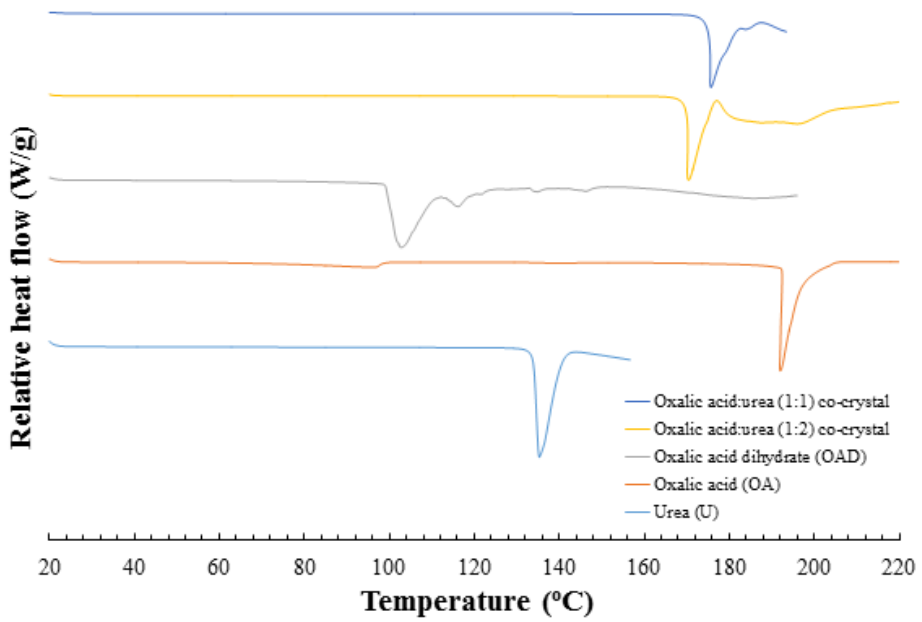

Figure 9. 1 - DSC traces highlighting the thermal phenomena associated with urea (*U*), oxalic acid (*OA*) and oxalic acid dihydrate (*OAD*) starting materials, as well as that of the oxalic acid-urea (1:1) & (1:2) co-crystals

These crystalline phases were produced *via* various and contrasting preparation methods, discussed in detail in the material literature review. These include mechanochemical[192] methods, slurrying[188, 191] and evaporation[189, 190, 193] from solution. Each preparation method operates in a different area of the ternary phase diagram for a given system of components and solvent, as indicated in Figure 9.2 (a) and (b). For ground samples, a given stoichiometry of the starting components is selected and the materials are placed under mechanical stress. In certain cases, minimal solvent is added to facilitate the process of co-crystallisation. The role of the solvent is still debated, postulated to be either acting to facilitate the movement of molecules or aiding through the introduction of minor dissolution effects.

Upon increasing the contribution of solvent and avoiding complete dissolution, slurrying can also be utilised as an effective multi-component material preparation method. Here, the starting components are mixed together in a given amount of solvent, whereby the molecules are constantly transitioning between the solid and solution states, thus aiding in the complexation of different crystalline forms. The phases yielded are dependent upon a variety of factors, each reliant on the location of the operation within the phase diagram at a given temperature. These include the degree of solid loading and the initial stoichiometry of starting materials used.

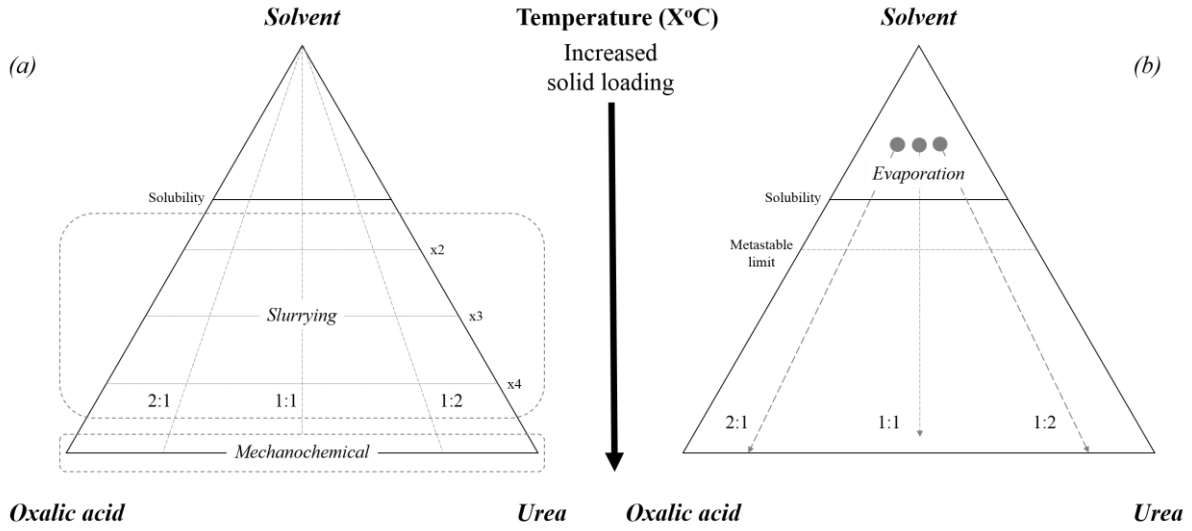

Figure 9. 2 - Simplified ternary phase diagrams, highlighting the areas utilised by different isothermal methods for co-crystal preparation, including (a) mechanochemical, slurrying and (b) evaporative techniques

For both mechanochemical and slurrying methods, a given concentration or solid loading of the individual starting materials to solvent is selected and maintained through the time period of the experiment. In contrast, by evaporating off solvent at a specified temperature, the concentration constantly changes, moving from an undersaturated to a saturated to a supersaturated state. Once the supersaturation has been reached, nucleation and growth is then able to occur. As with grinding and slurrying, the initial stoichiometry plays a key role in determining which combination of phases are generated.

These preparation methods, whilst operating in various areas of the ternary phase landscape, are each carried out under a single temperature environment. In cooling crystallisations, the inherent property that the solubility of the system changes with temperature, at a given composition, is utilised and upon altering the thermal conditions used, the system can transition to the supersaturated state necessary for crystallisation to occur. This is shown in the example ternary phase diagrams in Figure 9.3. To date, this method has not be used for the system of *OA* and *U*.

Each of the methods discussed above can allow for the preparation of both the thermodynamically and kinetically stable phase, depending upon the conditions used. For the two methods reliant on excessive mixing and grinding, i.e. mechanochemistry and slurrying, the intensity of the processing and the time utilised can both play a key role for the nature of the end phases generated. In evaporative and cooling environments, the rate at which supersaturation is achieved is of great significance in this respect, with different temperatures and cooling rates influencing both these processes, respectively.

Within this chapter, the system of *OA* and *U* will be examined, reassessing the initial crystallisation techniques used, exploring the important parameters of each method for the preparation of the individual co-crystals. Routes will be examined for the reproducible preparation of both these multi-component phases, with a particular emphasis on their preparation in water. This focus on crystallisation from water will form the foundation for subsequent cooling crystallisation experiments, looking towards the preparation of the co-crystals in the batch environment. This will lead towards the specific preparation of the *OAU*-1:2 form through the continuous crystallisation rigs in operation at the University of Bath, assessing their capabilities and limitations. Where possible, material preparation was conducted towards room temperature conditions. For the cooling crystallisations, the predominant

aim was to attempt material precipitation between 20-30ºC; such conditions would be ideal, for example, in an industrial crystallisation environment.

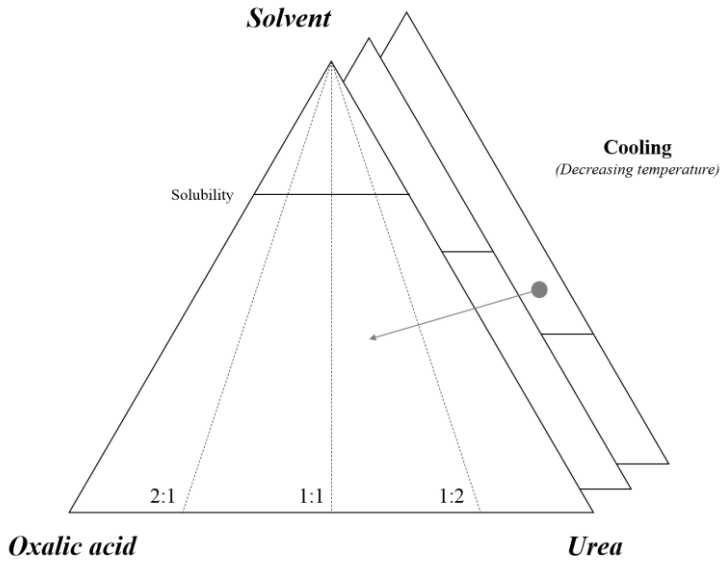

Figure 9. 3 - Simplified ternary phase diagrams, highlighting cooling crystallisation, the variability of solubility with temperature and some of the different solution stoichiometries to be probed

9.1 Mechanochemical preparation

Based upon the work conducted by Onija *et al.*[192], mechanochemical methods were utilised for the generation of the *OAU*-1:1 co-crystal, whereby 1:1 combinations of *OA* and *U* were combined and ground with the aid of minimal quantities of water. To date, grinding has not be used to prepare the *OAU-1:2* stoichiometric form. In the work outlined in this section, mechanochemical preparations utilising different solvents will be assessed for their ability to yield the different co-crystalline forms. With a focus on liquid-assisted grinding with water, further preparations will be explored for the effect of starting materials used, grinding time and water quantity on complexation. Finally, mechanochemistry will be used to determine the ability of the two co-crystals to interconvert, providing an indication as to their relative stabilities.

9.1.1 Variation in solvent

Initial preparations were conducted whereby different stoichiometric amounts of *OA* and *U* (2:1, 1:1 and 1:2) were ground together for 10 minutes, either neat or with the assistance of few drops of water, methanol, ethanol or isopropanol. Figures 9.4 and 9.5 outline the PXRD patterns for the 1:1 and 1:2 preparations, with those of the 2:1 samples located in Appendix A9.1.

For the equimolar preparation, both the neat and aqueous grindings demonstrated the formation of a mixture of the (1:2) co-crystal with *OAD*. It should be noted that under the atmospheric conditions used, the *OA* starting material, stored in a desiccated oven, readily took on water, forming the dihydrate. However, when utilising the alcohols, the (1:1) form could be obtained consistently, without excess starting material. These observations, particularly for the samples prepared from water, were in contrast to those made from the literature, where the (1:1) co-crystal could be accessed at the corresponding stoichiometry through liquid assisted grinding.

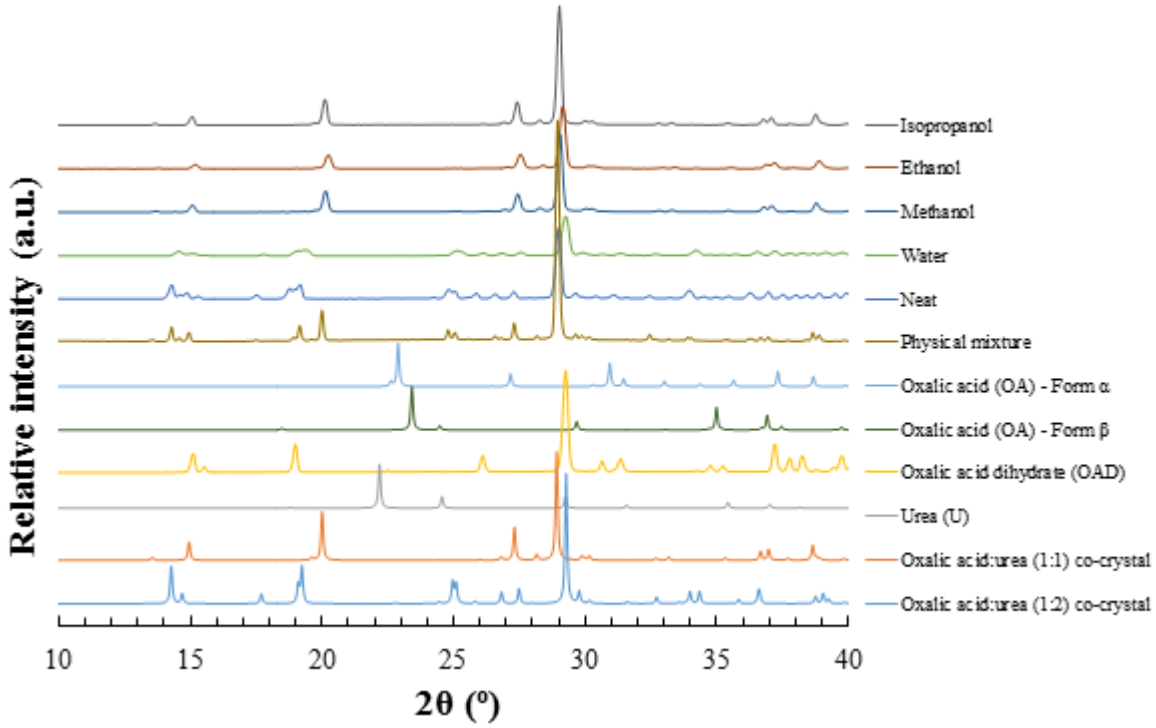

Figure 9. 4 - PXRD patterns highlighting the mechanochemical 1:1 combinations of *OA* and *U*, either neat or with minimum quantities of water, methanol, ethanol or isopropanol (top six patterns)

When the grinding stoichiometry was changed to reflect the 1:2 molar ratio, it was shown (Figure 9.5) that the *OAU*-1:2 co-crystal could be generated across all preparations, with or without solvent. By considering the phases prepared across the three stoichiometries, where the 2:1 preparations demonstrated the formation of the (1:2) phase and excess *OAD* for the neat and water-based grindings, with the alcohols each showing that the (1:1) co-crystal could also be prepared with *OAD*, it was summarised that solvent environment and molar ratio of components each played an important role. Both co-crystals could be selectively accessed at their corresponding stoichiometries for the alcohol environments, whilst the only the (1:2) co-crystal could be obtained from the aqueous preparations. This provided an initial indication that the (1:1) multi-component form had limited stability in aqueous environments.

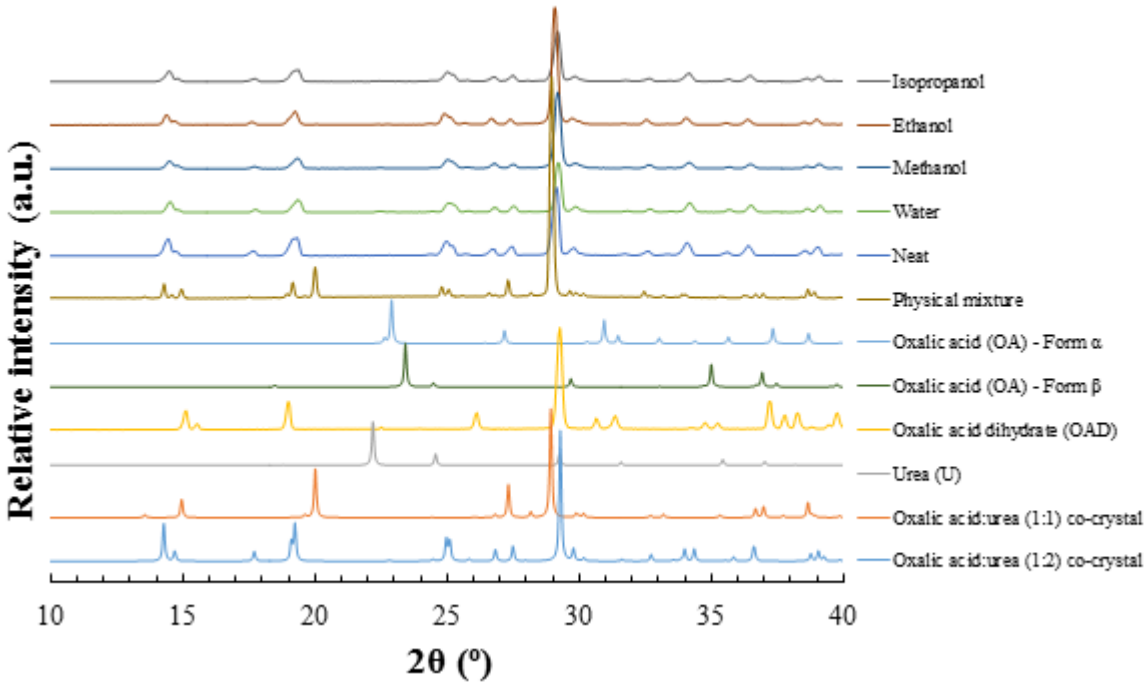

Figure 9. 5 - PXRD patterns highlighting the mechanochemical 1:2 combinations of *OA* and *U*, either neat or with minimum quantities of water, methanol, ethanol or isopropanol (top six patterns)

9.1.2 Variation in the starting components (OA and OAD) and grinding times

In order to determine a method for obtaining the *OAU*-1:1 phase, variations in the mechanochemical parameters were explored, each investigating the role of water. Firstly, neat grindings were conducted, whereby subtle changes in the starting material were examined alongside different grinding times. This change in the starting material was done by comparing grindings with anhydrous *OA* against those incorporating water already complexed within the structure, i.e. *OAD*. The PXRD patterns for the respective 2:1, 1:1 and 1:2 combinations can be found in Appendix A9.1.

With an initial focus on the 1:2 mechanochemical samples, the *OAU*-1:2 co-crystal was shown to form rapidly, within two minutes, upon *OAD* and *U* being ground together neat in the corresponding stoichiometry. In contrast, upon using the dehydrated starting material, the same co-crystalline phase was shown to evolve slowly over time (greater than 20 minutes), with excess raw components being consumed or converted to the dihydrate before being used to generate the co-crystal. An initial suggestion would be that the water present as part of the complexed *OA* form was able to catalyse the co-crystallisation process, benefiting the interactions and structure of the (1:2) form.

Continuing the study using a 1:1 ratio of starting materials, be it *OAD* or *OA*, both preparation types demonstrated the initial formation of the (1:2) multi-component phase along with excess *OAD*, *OA* (α), *U* or combinations thereof. As time progressed, it was shown that the contribution of the individual starting materials diminished, along with that of *OAU*-1:2. Through this, the relative proportions of the (1:1) co-crystal increased. Similar observations were made for the 2:1 samples, where the *OAU*-1:1 complex was shown to develop over time, along with the presence of excess *OA* starting material, always developing into the dihydrate form. Owing to the similarity in observations for the anhydrous and hydrated preparations, the presence of water was not deemed the defining factor for the development of the (1:1) co-crystal.

9.1.3 Variation in water quantity

To further explore the role of water in the formation of the two respective co-crystals, further preparations were made, exploiting the same stoichiometries as before, but here utilising different aliquots of water (0 μL to 140 μL). Each sample was ground until all the solvent was deemed to have evaporated. The diffraction patterns for each preparation are outlined in the Appendix A9.1.

As before, the *OAU*-1:2 co-crystal was shown to precipitate directly from its corresponding molar ratio with only a small quantity of water being added. In contrast, for the two ground sets of samples incorporating a greater molar contribution of *OA*, the *OAU*-1:2 co-crystal was again shown to be consistently produced, alongside excess *OAD*. The supported the findings from the previous experiments, suggesting that water was able to facilitate the formation of (1:2) form, whilst hindering that of the (1:1) at its related stoichiometric preparations. These collective observations raised questions as to the results previously reported[192] for the selective preparation of the *OAU*-1:1 co-crystalline phase *via* mechanochemical means.

9.1.4 Mechanochemical interconversion

In addition to being utilised for the direct selective complexation of the different co-crystalline phases, mechanochemistry can also be used to probe the ability of these multi-component forms to interconvert. This, as a result, provides an indication as to the relative stability of the two materials under different grinding conditions. Hence, using the same preparation method used, initial 1:1 and 1:2 molar ratios of *OA* to *U* were combined together either neat or using water, methanol, ethanol or isopropanol, and ground for 10 minutes, or until sufficiently dry. From here, additional starting material was introduced so as to change the stoichiometries from 1:2 to 1:1 or 1:1 to 1:2, respectively. The samples were ground further, either neat or with solvent, and analysed using PXRD, the patterns of which are highlighted in Figures 9.6 and 9.7.

Upon introducing excess *U* after the original complexation, the *OAU*-1:2 co-crystal was shown to form consistently from the 1:1 preparations across all solvent environments, along with additional *U* starting material. Likewise, with the addition of further *OA* to the 1:2 preparations, the (1:1) multi-component form was shown to precipitate dependably across all mechanochemical preparations. However, particularly in the alcohol samples, the (1:1) co-crystal was shown to be present in combination with the (1:2) phase. Whilst it was demonstrated that both co-crystalline forms could be accessed from their opposing stoichiometric variant, the PXRD patterns indicated that there was a greater barrier to conversion with that from the 1:2 to 1:1 phase. Together, the initial results taken from these mechanochemical experiments suggested that the *OAU*-1:2 co-crystalline system was marginally more stable than that of the 1:1 variant.

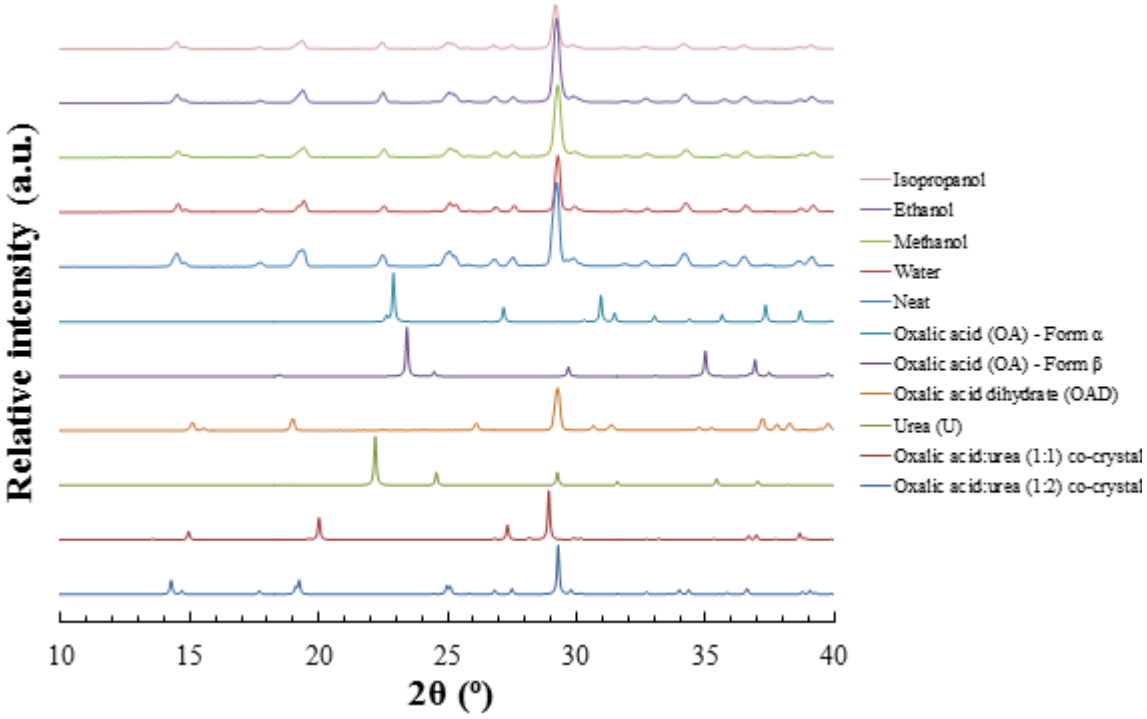

Figure 9. 6 - PXRD patterns highlighting the mechanochemical conversion of the co-crystals of oxalic acid and urea, from a 1:1 composition to a 1:2, in a number of solvent environments (neat, water, methanol, ethanol and isopropanol) (top five patterns)

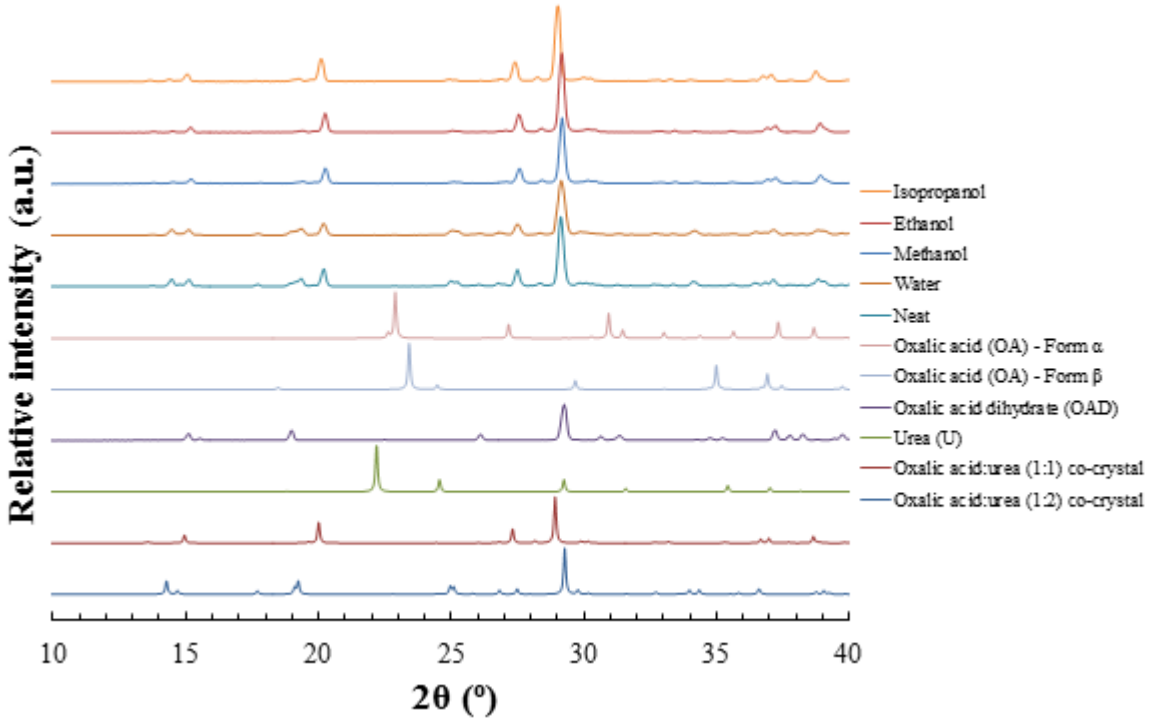

Figure 9. 7 - PXRD patterns highlighting the mechanochemical conversion of the co-crystals of oxalic acid and urea, from a 1:2 composition to a 1:1, in a number of solvent environments (neat, water, methanol, ethanol and isopropanol) (top five patterns)

9.2 Solvent-mediated (slurrying) preparations

Solvent-mediation or slurrying is a popular method for generating different multi-component phases, as highlighted by the work carried out by Dalman *et al.*[188] and Feng *et al.*[191] for the preparation of the (1:1) and (1:2) co-crystalline phase, respectively. In the case of the *OAU*-1:1 phase, *OA* and *U* were combined in a 4.5 to 1 ratio, whilst the *OAU*-1:2 form was prepared from a 1:2 molar ratio, with both systems being suspended in water for 24 hours at 40ºC. In this section, the preparation of the two co-crystals will initially be assessed in different solvent environments, leading to a focus on their preparation exclusively from water at 20ºC. By using various stoichiometries and solid loadings, different areas of the phase diagram were probed. As such, the stability of the different materials can be assessed, providing insights that could be translated towards cooling crystallisation preparations.

9.2.1 Variation in solvent

Using 2:1, 1:1 and 1:2 stoichiometries, *OA* and *U* were mixed for up to 24 hours in a range of solvents (water, methanol, ethanol and isopropanol) at 20ºC. The samples were filtered and analysed for their phase composition using PXRD. Figures 9.8 and 9.9 show the patterns for the materials yielded from the 2:1 and 1:2 preparations, with that of the 1:1 samples in Appendix A9.2.

For the preparations utilising the 2:1 molar ratio of *OA* to *U*, it was shown that the *OAU*-1:1 co-crystal could be accessed from all the solvent environments. However, unlike in the 1:2 samples where the (1:2) multi-component phase was prepared exclusively across all conditions, minimal traces of either the opposing (1:2) co-crystal or starting materials could be found in the 2:1 setups. It was also shown that for the equimolar preparations, the *OAU*-1:2 co-crystal could be consistently obtained from each of the solvent environments used, with the isopropanol case showing minimal amounts of the (1:1) phase in addition.

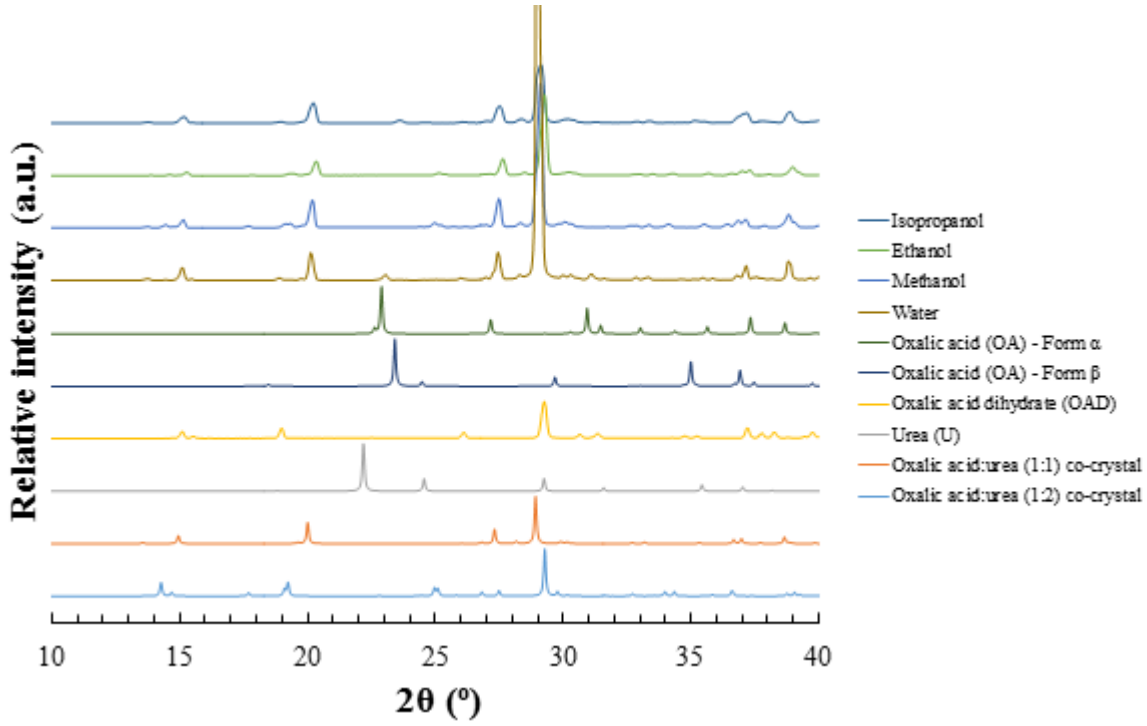

Figure 9. 8 - PXRD patterns highlighting the solid product yielded from initial slurrying experiments of a 2:1 combination of *OA* and *U*, in a variety of solvents; water, methanol, ethanol and isopropanol (top four patterns)

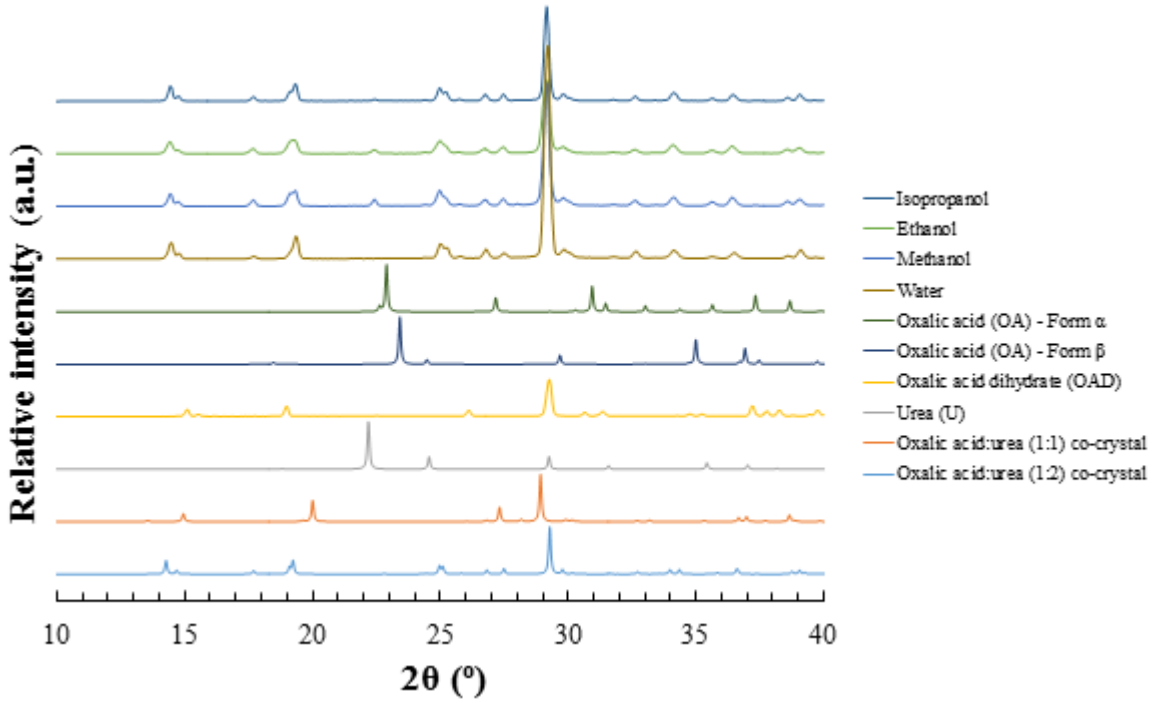

Figure 9. 9 - PXRD patterns highlighting the solid product yielded from initial slurrying experiments of a 1:2 combination of *OA* and *U*, in a variety of solvents; water, methanol, ethanol and isopropanol (top four patterns)

Collectively, these observations emphasised that under the conditions used, the (1:2) co-crystal was broadly the dominant phase at this temperature and in order to establish a route to the pure preparation of the alternative (1:1) form, particularly in water, further probing of the ternary phase diagram should be undertaken.

9.2.2 Bulk preparation and solubility

Due to the reproducible formation of the *OAU*-1:2 co-crystal across a number of solvent and stoichiometric environments, slurrying was used as a means of preparing bulk quantities of the material. Suspensions in water, consisting of a 1:2 combination of *OA* to *U*, were prepared and mixed at 20°C. As previously demonstrated, this particular co-crystalline phase could be yielded reliably and quickly from an aqueous environment. Hence, the slurries were mixed for only one hour. This method was consistently used for the preparation of the (1:2) form, as highlighted from the PXRD patterns shown in Figure 9.10.

Having established a suitable means of preparing this specific multi-component material, its solubility could be determined across a given temperature range. Samples with a predetermined concentration of co-crystal in water were prepared and assessed for their clear points upon heating. These turbidity measurements are shown in comparison to that of *OAD* in Figure 9.11. The key saturations for *OAD* and the *OAU*-1:2 co-crystal at 20°C and 30°C are highlighted in Table 9.1. By considering the proportion of *OA* dissolved in solution as a contribution for the respective dihydrate and co-crystalline phases, dissolution from the hydrated phase was deemed to be four and five times greater than that of the co-crystal at 20°C and 30°C, respectively, emphasising the enhanced stability of the co-crystal when under aqueous conditions.

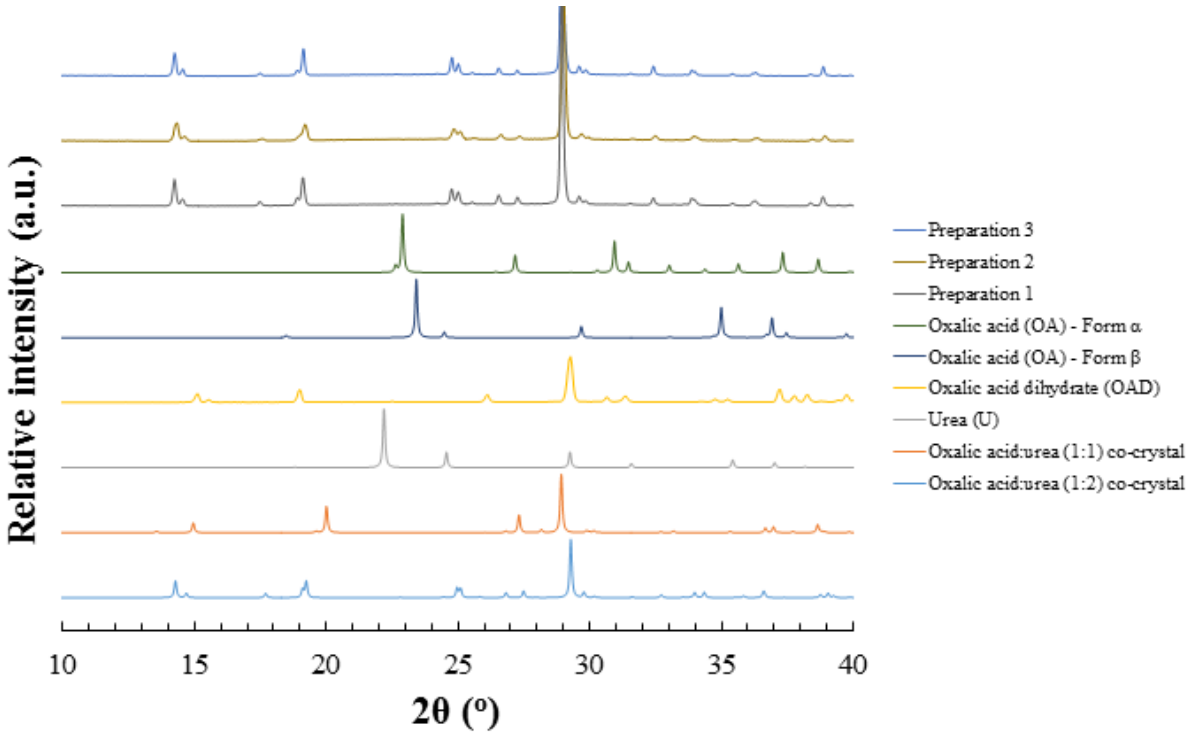

Figure 9. 10 - PXRD patterns highlighting the reproducible preparation of the oxalic acid:urea (1:2) co-crystal from a 1:2 slurry of the starting materials in water (top three patterns)

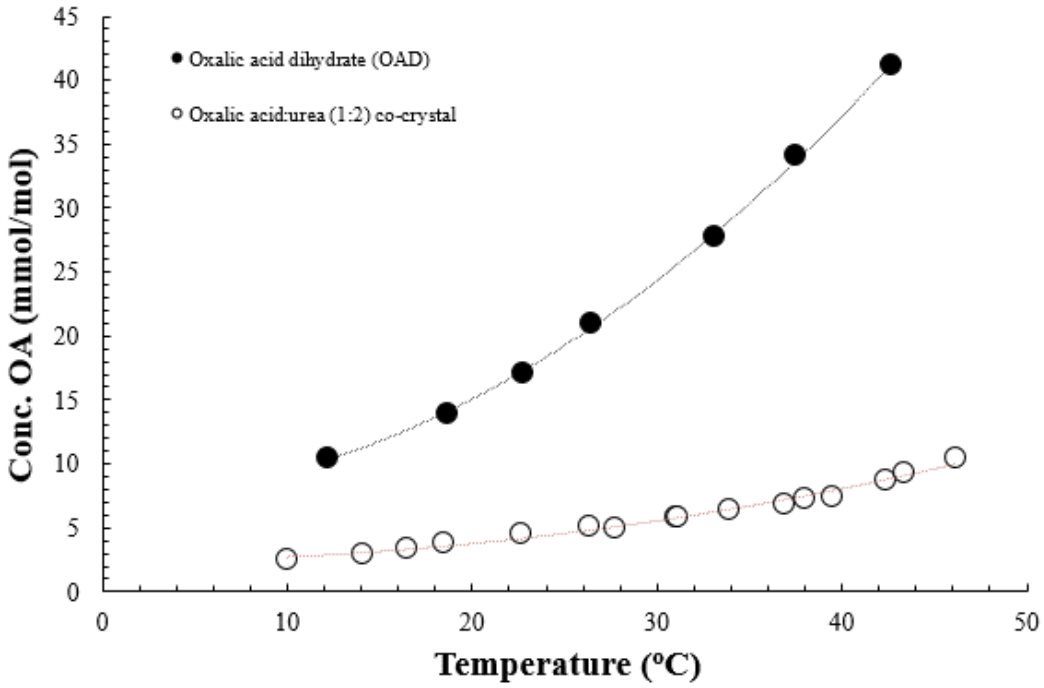

Figure 9. 11 - Solubility curves, as determined from turbidity measurements, of the oxalic acid:urea (1:2) co-crystal and the *OAD* starting material in water, with respect to the relative oxalic acid content (% error is less than 1%)

Table 9. 1 - Saturation points of *OAD* and the oxalic acid:urea (1:2) co-crystal in water, respectively, at 20ºC and 30ºC, with respect to the relative oxalic acid content

Material	Saturation at 20ºC (*OA* mmol/mol)	Saturation at 30ºC (*OA* mmol/mol)
Oxalic acid dihydrate (*OAD*)	15.1	27.4
Oxalic acid:urea (1:2) co-crystal (*OAU*-1:2)	3.8	5.4

9.2.3 Variation in suspension stoichiometry and solid loading

Based upon the solid mass of the *OAU*-1:2 co-crystal required for complete dissolution at 30ºC, various suspensions were prepared so as to assess the ternary phase diagram of *OA* and *U* in water at 20ºC. By maintaining the overall mass of solid used, the stoichiometry of the constituent components was varied, so as to reflect the 5:1, 4:1, 3:1, 2:1, 1:1 and 1:2 ratios. Further to this, to probe different contributions of the solid starting materials with the solvent (water), different solid loadings were prepared, reflecting masses x2, x3, x4 and x5 that of the reference mass. Suspensions were then mixed for either 1, 4, 16 or 64 hours, with the resultant material being analysed by PXRD. A summary of the solid phases yielded are tabulated in Tables 9.2, 9.3, 9.4 and 9.5, with the individual patterns located in Appendix A9.2.

As emphasised below, the *OAU*-1:2 co-crystal could be selectively prepared across a number of degrees of solid loading, over a range of time scales, with particular prominence at its corresponding stoichiometry, 1:2. It was also noted that particularly at the lower loading levels (x2), i.e. closer to the solubility for a given molar ratio, this phase could be routinely accessed without excess starting material or opposing (1:1) co-crystal being present, even at higher suspension stoichiometries with high quantities of *OA*. This was particularly evident upon leaving the system to mix for longer time periods.

In contrast, determining a route for the reproducible preparation of the (1:1) co-crystal *via* slurrying was by no means as straightforward. Though evidence for the formation of this phase was observed, there was limited opportunity for its pure precipitation. For samples made over short time scales and stoichiometries closer to that of 2:1, the *OAU*-1:1 form could be generated, though typically in combination with its related stoichiometric form or excess starting material. It was shown, however, that pure material of this co-crystal could be obtained at the 2:1 composition for the x4 and x5 solid loadings at the one and four hour timescales, respectively.

A general trend was that over extending time periods of slurrying, the (1:2) co-crystal became the dominant phase, with limited opportunities to precipitate its stoichiometric counterpart. For the samples at short suspension times that did yield some of the equimolar co-crystalline phase, as the slurries were allowed to progress further, the system would evolve to reflect a greater contribution of the *OAU*-1:2 form. Collectively, it could be stated that at molar ratios closer to 1:1 or 2:1, upon mixing the starting materials in water, particularly at higher solid loadings, the (1:1) phase could be kinetically stabilised and allowed to form. However, due to its enhanced stability in water, at many stoichiometries and solid loadings, the (1:2) co-crystal reflected the thermodynamically stable form and was able to evolve as the dominant phase with time.

Table 9. 2 - Summary of the solid product, as determined by PXRD, yielded from suspensions of *OA* and *U* in water, at different stoichiometries (5:1, 4:1, 3:1, 2:1, 1:1 and 1:2) and solid loadings (x2, x3, x4 and x5 the solid mass of the oxalic acid and urea (1:2) co-crystal at 30ºC), mixed at 200 rpm for 1 hour, at 20ºC

Suspension stoichiometry	x2	x3	x4	x5
5:1	**OAD, OAU-1:2**	**OAD, OAU-1:2**	**OAU-1:1, OAD** *OA (α)*	**OA (α)** *OAU-1:1, OAD*
4:1	**OAU-1:2** *OAD, OAU-1:1*	**OAD, OAU-1:2** *OAU-1:1*	**OAU-1:1, OAD** *OA (α)*	**OA (α)** *OAU-1:1, OAD*
3:1	**OAU-1:2** *OAU-1:1*	**OAD, OAU-1:2** *OAU-1:1*	**OAU-1:1, OAD** *OA (α)*	**OAU-1:1, OAD** *OA (α)*
2:1	**OAU-1:2** *OAU-1:1*	**OAU-1:2** *OAD, OAU-1:1*	**OAU-1:1**	**OAU-1:1, OAD** *OA (α)*
1:1	**OAU-1:2** *OAU-1:1*	**OAU-1:2**	**OAU-1:2**	**OAU-1:2** *OAU-1:1*
1:2	**OAU-1:2**	**OAU-1:2**	**OAU-1:2**	**OAU-1:2**

Table 9. 3 - Summary of the solid product, as determined by PXRD, yielded from suspensions of *OA* and *U* in water, at different stoichiometries (5:1, 4:1, 3:1, 2:1, 1:1 and 1:2) and solid loadings (x2, x3, x4 and x5 the solid mass of the oxalic acid and urea (1:2) co-crystal at 30ºC), mixed at 200 rpm for 4 hours, at 20ºC

Suspension stoichiometry	x2	x3	x4	x5
5:1	**OAD, OAU-1:2**	**OA (α)** *OAU-1:2, OAD*	**OA (α)** *OAU-1:2, OAD*	**OA (α), OAU-1:1, OAD** *OAU-1:2*
4:1	**OAU-1:2** *OAD*	**OAU-1:2, OAD, OA (α)**	**OAU-1:2, OAD, OA (α)**	**OA (α), OAU-1:1, OAD** *OAU-1:2*
3:1	**OAU-1:2**	**OAU-1:1, OAD, OAU-1:2** *OA (α), U*	**OAU-1:2, OAD, OA (α)**	**OA (α), OAU-1:1, OAD** *OAU-1:2*
2:1	**OAU-1:2**	**OAU-1:1, OAD, OAU-1:2**	**OAU-1:1, OAD, OAU-1:2**	**OAU-1:1**
1:1	**OAU-1:2, OA (α)**	**OAU-1:2**	**OAU-1:2**	**OAU-1:2** *OAU-1:1*
1:2	**OAU-1:2**	**OAU-1:2**	**OAU-1:2**	**OAU-1:2**

Table 9. 4 - Summary of the solid product, as determined by PXRD, yielded from suspensions of *OA* and *U* in water, at different stoichiometries (5:1, 4:1, 3:1, 2:1, 1:1 and 1:2) and solid loadings (x2, x3, x4 and x5 the solid mass of the oxalic acid and urea (1:2) co-crystal at 30ºC), mixed at 200 rpm for 16 hours, at 20ºC

Suspension stoichiometry	x2	x3	x4	x5
5:1	**OAU-1:2, OAD, OA (α)**	**OAU-1:2, OAD, OA (α)**	**OAU-1:2, OAD, OA (α)**	**OA (α), OAD** *OAU-1:2*
4:1	**OAU-1:2**	**OAD, OAU-1:2**	**OAU-1:2, OAD** *OA (α)*	**OA (α), OAD** *OAU-1:2, OAU-1:1*
3:1	**OAU-1:2**	**OAD, OAU-1:2**	**OAU-1:2, OAD** *OA (α)*	**OAU-1:2, OAD** *OA (α)*
2:1	**OAU-1:2**	**OAU-1:2**	**OAU-1:2, OAD** *OA (α)*	**OAU-1:2, OAD** *OAU-1:1*
1:1	**OAU-1:2**	**OAU-1:2**	**OAU-1:2**	**OAU-1:2**
1:2	**OAU-1:2**	**OAU-1:2**	**OAU-1:2**	**OAU-1:2**

Table 9. 5 - Summary of the solid product, as determined by PXRD, yielded from suspensions of *OA* and *U* in water, at different stoichiometries (5:1, 4:1, 3:1, 2:1, 1:1 and 1:2) and solid loadings (x2, x3, x4 and x5 the solid mass of the oxalic acid and urea (1:2) co-crystal at 30ºC), mixed at 200 rpm for 64 hours, at 20ºC

Suspension stoichiometry	x2	x3	x4	x5
5:1	**OAD, OA (α/β)**	**OAD, OA (α/β)** *OAU-1:2*	**OAD, OA (α/β)** *OAU-1:2*	**OAD, OA (α/β)** *OAU-1:2*
4:1	**OAU-1:2, OAD,** *OA (α/β)*	**OAD, OA (α/β)** *OAU-1:2*	**OAD, OA (α/β)** *OAU-1:2*	**OAU-1:2, OAD, OA (α/β)**
3:1	**OAU-1:2**	**OAU-1:2, OAD,** *OA (α)*	**OAU-1:2, OAD,** *OA (α)*	**OAU-1:2, OAD, OA (α/β)**
2:1	**OAU-1:2**	**OAU-1:2, OAD** *OAU-1:1, OA (α)*	**OAU-1:2, OAD** *OAU-1:1, OA (α)*	**OAU-1:2, OAD, OAU-1:1** *OA (α)*
1:1	**OAU-1:2**	**OAU-1:2**	**OAU-1:2**	**OAU-1:2, OA (α)**
1:2	**OAU-1:2**	**OAU-1:2**	**OAU-1:2**	**OAU-1:2**

**Preparations that demonstrated the selective crystallisation of the oxalic acid:urea (1:2) co-crystal are highlighted in green*
*** Preparations that demonstrated the selective crystallisation of the oxalic acid:urea (1:1) co-crystal are highlighted in yellow*

9.3 Evaporative crystallisation

Thus far, both co-crystals of *OA* and *U* have been prepared through either mechanochemical or solvent mediated means, whereby complexation was dependent upon mechanochemical stress, solid-to-solid transitions or the gradual evolution based upon the equilibrium between the solution and solid states. However, despite demonstrating reliability in the selective formation of the respective co-crystals, the techniques discussed thus far present little control over other desirable properties, such as particle size and crystal morphology. As a first point of reference, the direct crystallisation from solution, exploiting spontaneous nucleation and growth, via initial evaporative crystallisations were examined. Both multi-component phases were previous been studied and generated by evaporation, with both Harkema *et al.*[189] and Chithambaram *et al.*[193] crystallising the (1:2) phase from aqueous solutions of the corresponding stoichiometry, with further studies by Harkema *et al.*[190] demonstrating the formation of the (1:1) co-crystal at higher molar ratios with respect to *OA* (5:1).

In this section, the formation of respective co-crystals by evaporation will be explored. Firstly, the dependence on solvent, at given stoichiometries, will be assessed. Then, with a focus on crystallisation from water, further evaporative processes will be examined, evaluating the role of stoichiometry and the rate of nucleation as determined by the evaporation temperature.

9.3.1 Variation in solvent

Evaporative crystallisation experiments were first carried out at either 20ºC or 40ºC, using a range of solvent environments, including water, methanol, ethanol and isopropanol. Molar quantities of *OA* and U were dissolved in the respective solvents in either a 2:1, 1:1 or 1:2 ratio. The samples were then left to evaporate under their specified temperature until complete dryness had been achieved. From here, the resultant crystals grown were photographed under the microscope and analysed in terms of the phases present, using PXRD. Figure 9.12 depicts the individual crystals grown from solution, whilst Table 9.6 summaries the contribution of phases for each sample, the individual patterns of which can be found in Appendix A9.3.

The aim of these experiments was to determine what crystalline materials could be yielded at given compositions, assessing the influence of evaporation temperature of the precipitation of the two co-crystal forms of *OA* and *U*. As shown from the images shown in Figure 9.12, the crystal growth was most prevalent from the samples prepared from water across both temperatures used, where larger and more defined individual crystallites could be generated. In contrast, it was shown for the samples produced from the alcohol environments, that crystallisation was dominated by nucleation, resulting in smaller crystals. These initial observations suggested the favourability of the aqueous environment as a medium from which more sophisticated crystallisation procedures could developed. In addition, it was also emphasised that this solvent was the most appropriate from which single crystals could be selected for SCXRD analysis.

Upon assessment of the diffraction data, particularly from the 1:2 samples from water, it was shown that the corresponding (1:2) co-crystal could be selectively crystallised using either of the two evaporation temperatures. In addition, this particular form could be accessed selectively when evaporating from isopropanol at 40°C, utilising the same stoichiometry. All of the other 1:2 preparations demonstrated the formation of the *OAU*-1:2 co-crystal along with excess starting material. These observations supported the findings from the other crystallisation techniques that at this composition, the (1:2) multi-component phase was the most stable.

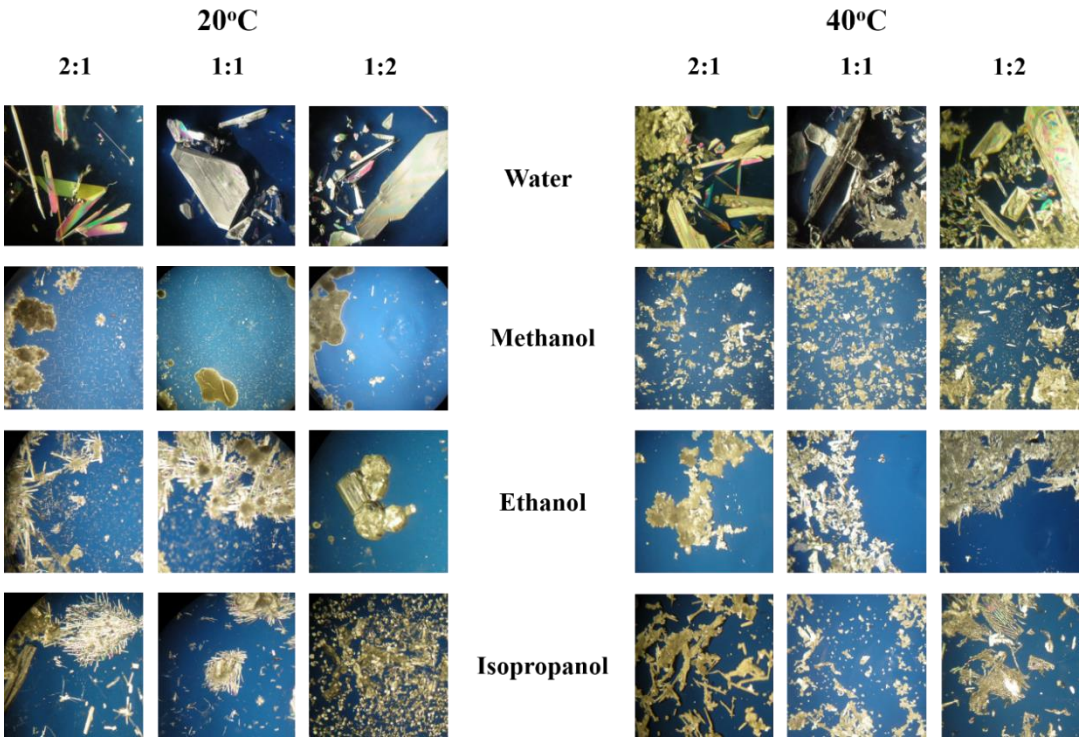

Figure 9. 12 - Images highlighting the crystals formed from the evaporative crystallisation, using 2:1, 1:1 and 1:2 stoichiometries of *OA* and *U*, from water, methanol, ethanol and isopropanol at 20°C and 40°C

Table 9. 6 - Summary of the crystalline phases yielded from evaporative crystallisations of *OA* and *U* in either water, methanol, ethanol or isopropanol, utilising various solution stoichiometries (2:1, 1:1 and 1:2) and evaporation temperatures (20ºC and 40ºC), emphasising the **major** and *minor* products

Solution stoichiometry	Solvent	Evaporation temperatures	
		20ºC	40ºC
2:1	Water	**OAD** *OAU-1:2*	**OAU-1:2, OAD** *OAU-1:1, OA (α/β)*
	Methanol	**OAD** *OAU-1:2*	**OAU-1:1, OAU-1:2** *OAD, other (26.5º)*
	Ethanol	**OAD** *OAU-1:2*	**OAU-1:1, OAU-1:2** *OAD*
	Isopropanol	**OAD** *OAU-1:2*	**OAU-1:1** *OAD, OAU-1:2*
1:1	Water	**OAU-1:2, OAD** *OAU-1:1*	**OAU-1:2, OAD** *OAU-1:1*
	Methanol	**OAU-1:2, OAD**	**OAU-1:2, OAD** *other (26.5º)*
	Ethanol	**OAU-1:2, OAD**	**OAU-1:2, OAD**
	Isopropanol	**OAU-1:2, OAD**	**OAU-1:1** **OAD, OAU-1:2**
1:2	Water	**OAU-1:2**	**OAU-1:2**
	Methanol	**OAU-1:2** *U*	**OAU-1:2** **OA (α/β), U**
	Ethanol	**OAU-1:2** *U*	**OAU-1:2, OAD, U**
	Isopropanol	**OAU-1:2** *U*	**OAU-1:2**

**Preparations that demonstrated the selective crystallisation of the oxalic acid:urea (1:2) co-crystal are highlighted in green*

Despite increasing the molar contribution of *OA*, the exclusive crystallisation of the *OAU*-1:1 co-crystal was found not to be possible under the conditions used. For the 1:1 stoichiometric samples, the (1:1) phase could only be accessed from water or isopropanol at the higher evaporation temperature, but only in combination with that the starting materials and the opposing (1:2) co-crystalline form. Although the proportion of this phase was greater at 40ºC, this specific phase, again, could only be obtained as a mixture with the other solid state materials. It was noted that for all the samples prepared using the 2:1 stoichiometry at 20ºC the (1:2) form was consistently produced along with excess *OAD*.

Collectively, these observations emphasised the stability of the *OAU*-1:2 co-crystal over a large composition range in the solvents used, with particular evidence at 20ºC. Though further experiments would have to be conducted, accessing the (1:1) phase was only deemed possible towards higher molar contributions of *OA* and at higher temperatures, emphasising the existence of a higher temperature co-crystalline form of *OA* and *U*. Further to this, given the observations made for the higher temperature evaporations at the 2:1 stoichiometry, the larger number of nucleation events at these compositions explained why both co-crystalline materials could crystallised, along with the additional starting materials.

9.3.2 Variation in solution stoichiometry and evaporation temperature

Continuing with the study into the preparation of two co-crystalline forms of *OA* and *U via* evaporation, further crystallisation samples were established in aqueous solutions, utilising a range of stoichiometries, ranging from 7:1 to 1:2. Each sample was prepared by dissolving the starting components in a given amount of water, from which the solvent was allowed to evaporate at different

evaporation rates. These rates controlled how quickly supersaturation was achieved and were determined through manipulations in the evaporation temperature. As such, the initial temperatures selected were 4ºC (fridge), 20ºC (room temperature) and 40ºC (hotplate). Images for the resultant crystals are shown in Figure 9.13, with a summary of the phases obtained, as determined by PXRD, highlighted in Table 9.6. The individual diffraction patterns can be found in Appendix A9.3.

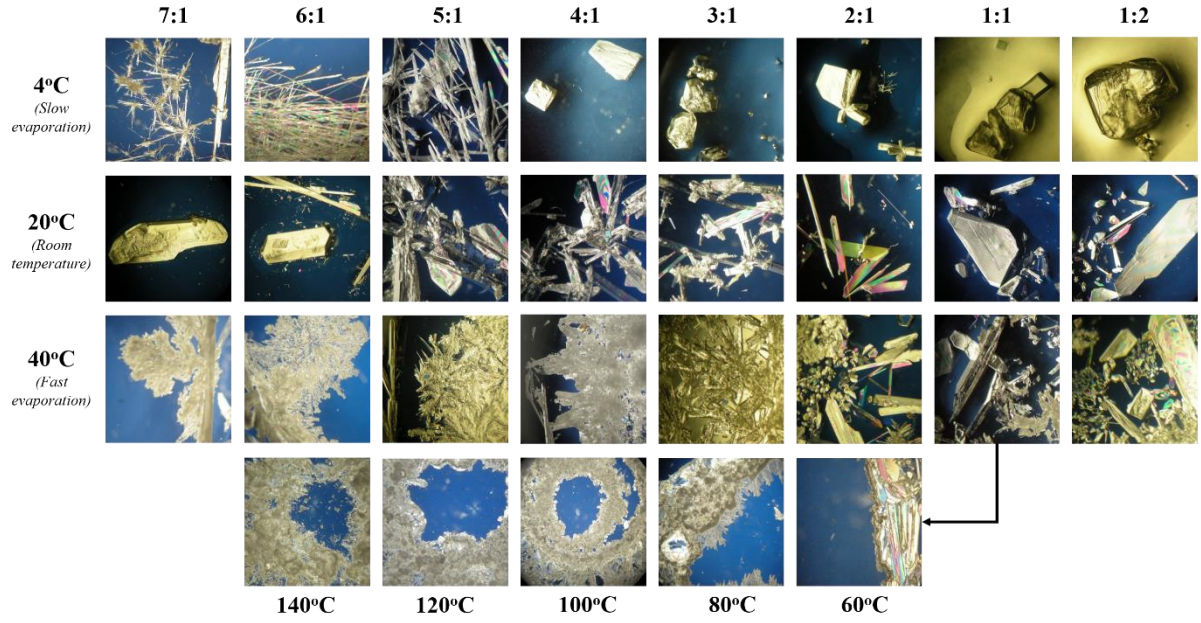

Figure 9. 13 - Images highlighting the crystals formed from the evaporative crystallisation, using 7:1, 6:1, 5:1, 4:1, 3:1, 2:1, 1:1 and 1:2 stoichiometries of *OA* and *U*, from water over a range of evaporation temperatures

Table 9. 7 - Summary of the crystalline phases yielded from evaporative crystallisations of *OA* and *U* in water, utilising various solution stoichiometries (5:1, 4:1, 3:1, 2:1, 1:1 and 1:2) and evaporation temperatures (4ºC, 20ºC and 40ºC), emphasising the **major** and *minor* components

Solution stoichiometry	**Evaporation temperatures** 4ºC	20ºC	40ºC
7:1	**OAD**	**OAD**	**OAD, other (14.5º)**
6:1	**OAD** *OAU-1:2*	**OAD**	**OAD, other (14.5º)**
5:1	**OAD** *OAU-1:2*	**OAD**	**OAU-1:1, OAD** *OA (α/β)*
4:1	**OAD** *OAU-1:2*	**OAD** *OAU-1:2*	**OAU-1:1, OAD**
3:1	**OAD** *OAU-1:2*	**OAD** *OAU-1:2*	**OAU-1:2, OAD** *OAU-1:1, OA (α/β)*
2:1	**OAU-1:2, OAD**	**OAU-1:2, OAD**	**OAU-1:2, OAD** *OAU-1:1, OA (α/β)*
1:1	**OAU-1:2, OAD**	**OAU-1:2, OAD** *OAU-1:1*	**OAU-1:2, OAD** *OAU-1:1*
1:2	**OAU-1:2**	**OAU-1:2**	**OAU-1:2**

**Preparations that demonstrated the selective crystallisation of the oxalic acid:urea (1:2) co-crystal are highlighted in green*
*** Preparations that demonstrated the pseudo-selective crystallisation of the oxalic acid:urea (1:1) co-crystal are highlighted in yellow*

Consistent with the observations made from mechanochemical and slurrying preparations, the *OAU*-1:2 co-crystal, evident by its flat plate morphology, could be reliably prepared from solutions of the same stoichiometry, with no additional crystalline phases present. This observation was made over the three evaporation temperatures used, demonstrating the favourability in the formation of that particular multi-component material. Further to this, with increasing contributions of *OA*, the (1:2) co-crystal continued to crystallise at 4ºC alongside excess *OA* in the form of its dihydrate. Despite the changes in the proportion of *OAD* to co-crystal with increasing quantities of *OA* starting material, the formation of this specific multi-component phase as opposed to the (1:1) form emphasised that with slow evaporation rates, supersaturation was achieved gradually. Hence, the more thermodynamically stable phase was shown to precipitate.

As the temperature was increased, the rate at which supersaturation, and hence nucleation, was achieved increased. In particular at 40ºC, the prevalence of the (1:1) co-crystal improved with the 1:1 preparation and those with greater quantities of *OA*, most notably in the 4:1 and 5:1 samples, where no (1:2) co-crystal was noted within the detection limit of the diffractometer. These observations supported the findings made in the literature and emphasised that with faster nucleation rates and higher *OA* stoichiometries, the *OAU*-1:1 phase could be kinetically stabilised.

It should also be noted that, with specific evidence at the higher evaporation rate and *OA* stoichiometries, the PXRD patterns demonstrated a distinct peak at 14.5º (2θ), with a greater than expected intensity to that otherwise associated with any of the known materials (See Appendix A9.3). As such, this could be associated with either the presence of an additional phase (‘*other*’) or of preferred orientation.

Focusing on the 1:1 evaporative samples across the temperature range, both co-crystalline forms were shown to precipitate, with the (1:2) phase favoured. In order to confirm the metastability and kinetic favourability of the OAU-1:1 co-crystal, further evaporative crystallisations were prepared, utilising the 1:1 stoichiometry and the solvent to dissipate at increasing temperatures from 60ºC to 140ºC. Table 9.7 summaries the resultant crystalline phases, with the PXRD patterns displayed in Appendix A9.3.

Table 9. 8 - Summary of the crystalline phases yielded from evaporative crystallisations of *OA* and *U* in water, utilising the 1:1 solution stoichiometry and various evaporation temperatures (4ºC, 20ºC, 40ºC, 60ºC, 80ºC, 100ºC, 120ºC and 140ºC), emphasising the **major** and *minor* components

Solution stoichiometry	**Evaporation temperatures**							
	4ºC	20ºC	40ºC	60ºC	80ºC	100ºC	120ºC	140ºC
1:1	**OAU-1:2 OAD**	**OAU-1:2 OAD** *OAU-1:1*	**OAU-1:2 OAD** *OAU-1:1*	**OAU-1:2 OAU-1:1**	**OAU-1:2 OAU-1:1**	**OAU-1:1** *OAU-1:2*	**OAU-1:1 U** *OAU-1:2*	**OAU-1:1** *OAU-1:2*

It was shown that as the temperature was raised for each evaporation, the proportion of the two co-crystals precipitated changed in favour of the (1:1) form. This, once again, emphasised the fact that with rapid nucleation rates, both phases could crystallise. However, despite the stoichiometry, the fact that the 1:2 phase was still formed emphasised its thermodynamic stability when crystallising from aqueous conditions. Under the conditions explored here, the selective crystallisation the lone *OAU*-1:1 phase was deemed to not be possible *via* evaporation without the precipitation of a secondary phase. Therefore, prior structural analysis could only have been conducted by fortuitous selection of an individual crystal from a mixture of crystallites of various composition.

Furthermore, it should be noted that whilst changing the rate of nucleation through increases in temperature can allow (limited) access to less stable phases, an obvious consequence is the effect on

crystallite size. With increasing temperatures, a greater degree of nucleation is possible, resulting in smaller crystals, that would impact on further processing steps.

9.4 Batch cooling crystallisation

To date, routes to the preparation of the two co-crystals of *OA* and *U* have been established through mechanochemical, slurrying or evaporative means, demonstrated either in the literature or from the work outlined here. In general, industrial crystallisation procedures do not utilise these methods owing to their limited ability to control the range of particle properties necessary for effective processing, such as particle size and shape. Hence, translating control over particle parameters like size distribution and morphology into a process whereby the phase can be selectively made, is greatly desirable.

Cooling crystallisation, where solutions are able to transition to the supersatured state owing to the change in solubility with decreasing temperature, is a method regularly used within a variety of commercial environments. Through a knowledge of the solubility of a given crystalline system and by controlling factors such as cooling rate, mixing rate, seeding, *etc.*, crystallisations can be designed to regulate an number of key outcomes. With phase selectivity remaining the goal, cooling crystallisation was applied to the system of *OA* and *U*, in a batch context, so as to derive pathways to the selective preparation of the individual co-crystalline forms. Cooling precipitations were carried out initially in isopropanol and subsequently in water.

9.4.1 Cooling crystallisations from isopropanol

Using gravimetric analysis, the solubility of *OA* starting material (taken as the α-polymorph) at 20°C in isopropanol was determined. Three preparations were prepared and assessed, from which an average solubility of 0.22 g/g was taken. The masses used to calculate this value can be found in Appendix A9.4.

Based upon the amount of *OA* capable of dissolving in this given solvent system at 20°C, solutions of *OA* were established, to varying degrees of saturation. Molar quantities of *U* were then added so as to reflect the 4:1, 3:1, 2:1, 1:1 and 1:2 solution stoichiometries. The combinations of solutes and solvent were then heated and allowed to dissolve at 65°C and subsequently cooled to 20°C, at a rate of 0.1°C/minute. The resultant solids were filtered and analysed by PXRD. The diffraction patterns for the individual compositions can be found in Appendix A9.4, with Table 9.8 summarising the findings.

Table 9. 9 - Summary of the solid product, as determined by PXRD, yielded from the cooling crystallisations of solutions of *OA* and *U* in isopropanol, with varying solution stoichiometries (4:1, 3:1, 2:1, 1:1 and 1:2) and saturation levels (based upon x1, x0.5, x0.25, x0.125 & x0.0625 the saturation of the *OA* starting material at 20°C), heated to 65°C and cooled to 20°C at 0.1°C/min, emphasising the **major** and *minor* components

Solution stoichiometry	x1	x0.5	x0.25	x0.125	x0.0625
4:1	**OAU-1:1**	**OAU-1:1**	**U, OAU-1:2** *OAU-1:1*	**OAU-1:2**	**OAU-1:2**
3:1	**OAU-1:1** *U*	**OAU-1:1**	**U, OAU-1:2** *OAU-1:1*	**OAU-1:2**	**OAU-1:2**
2:1	**OAU-1:1** *U*	**OAU-1:1** *U*	**U, OAU-1:2** *OAU-1:1*	**OAU-1:2**	**OAU-1:2**
1:1	**U, OAU-1:1, OAU-1:2**	**U, OAU-1:2** *OAU-1:1*	**OAU-1:2**	**OAU-1:2**	**OAU-1:2**
1:2	**U, OAU-1:2**	**U, OAU-1:2**	**OAU-1:2**	**OAU-1:2**	**OAU-1:2**

**Preparations that demonstrated the selective crystallisation of the oxalic acid:urea (1:2) co-crystal are highlighted in green*
*** Preparations that demonstrated the selective crystallisation of the oxalic acid:urea (1:1) co-crystal are highlighted in yellow*

Isopropanol was selected as a contrasting solvent system to water for cooling crystallisation due to the observations made from the previously used co-crystal preparation methods. With particular reference to the mechanochemical and slurrying techniques, when isopropanol was used as the mediating solvent, it was noted that both the respective multi-component phases of *OA* and *U* could be yielded to a greater degree of purity at the stoichiometries used.

As shown from the diffraction data collected for the various samples prepared from the cooling crystallisations in isopropanol, depending upon the saturation level and solution stoichiometry employed, both co-crystals could accessed. At the higher contributions of *OA*, in terms of both loading and molar ratio with respect to *U*, it was shown that the *OAU*-1:1 phase could be generated, exclusively. Whilst this form could only be obtained purely above a certain saturation threshold (0.5 times saturation), it was demonstrated that the *OAU*-1:2 co-crystal could be crystallised consistently at its corresponding stoichiometry across all the saturations used. Furthermore, it was highlighted that this particular phase could also be generated across all the molar ratios utilised, with particular prevalence towards the lower saturations.

Collectively, these results indicated that by using isopropanol as the crystallisation solvent, both co-crystals could be selectively obtained. It was also made plain that the relative stability difference of the two phases in this given environment was smaller than that observed from aqueous systems, particularly when tending towards 20ºC. However, given the fact that the *OAU*-1:2 co-crystal could be generated over a number of compositions at lower saturations, this provided another indication that, even in this alcohol system, this particular multi-component material was the more stable phase.

9.4.2 Cooling crystallisations of the oxalic acid:urea (1:2) co-crystal from water

Given the reliability of its formation at the corresponding stoichiometry through the other preparation techniques used and having established its solubility in water over a specified temperature range, cooling crystallisations were carried out so as to confirm the preparation of the (1:2) co-crystal. With the solubility of this multi-component form taken as 0.063 g/g (5.4 mmol/mol) at 30ºC, solutions were prepared at the 2 g solvent (water) scale, heated to 45ºC, ensuring complete dissolution, and cooled either 25ºC or 20ºC. The cooling rates used were 0.1ºC/minute and 1ºC/minute, with a constant mixing rate of 200 rpm. The end material in each case was filtered and analysed using PXRD, the patterns of which are shown in Figure 9.14.

For each of the cooling rates used, the *OAU*-1:2 co-crystal was shown to form consistently, with no other phases present. With the saturation level set at 30ºC with respect to this multi-component material, nucleation was shown to occur between 30ºC and 25ºC for each preparation, emphasising the relatively small metastable zone generated under the conditions used.

Selecting the faster cooling rate (1ºC/minute), so as to reflect the more rapid rate of cooling utilised in later continuous crystallisation processes, further crystallisations were conducted at increasing volumes of solvent. Cooling from 45ºC to 20ºC, mixing at 200 rpm, solutions were setup at increasing scales, reflecting that of 10 g, 30 g and 100 g of water with the corresponding quantities of *OA* and *U*. The resultant solid yielded was analysed, the PXRD patterns of which are highlighted in Appendix A9.4. As before, each of the preparations demonstrated the reliable crystallisation of the (1:2) co-crystal, emphasising the use of cooling for multi-component material formation, a process capable of yielding the correct phase over a range of scales.

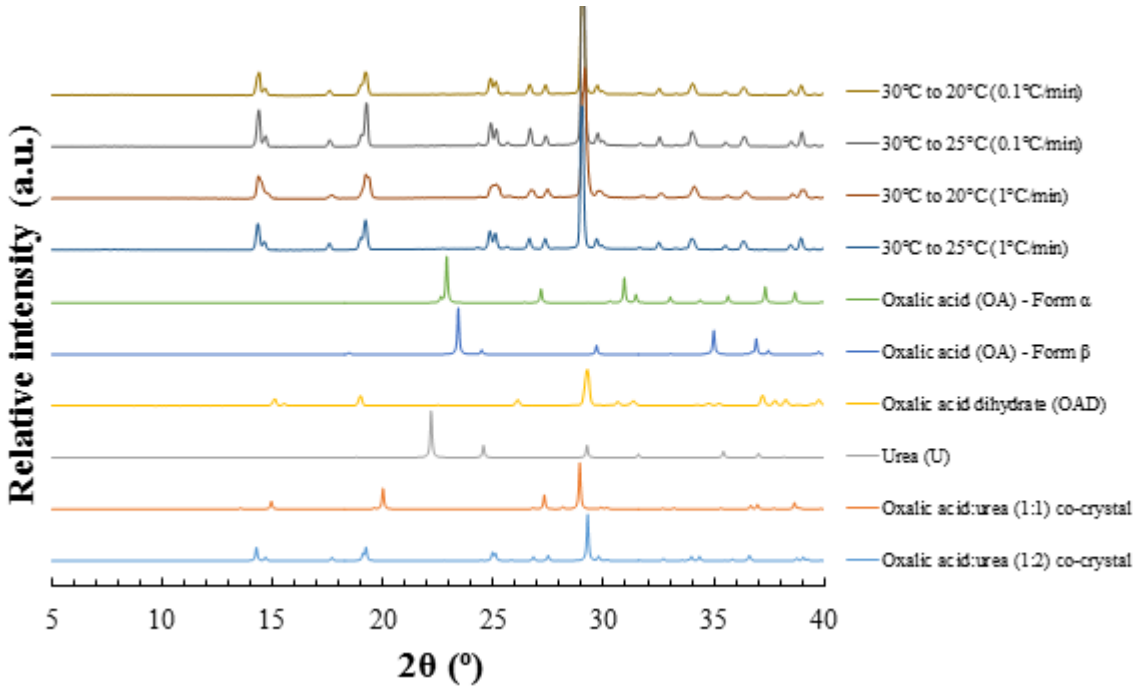

Figure 9. 14 - PXRD patterns highlighting the preparation of the oxalic acid:urea (1:2) co-crystal *via* cooling crystallisation, assessing different cooling rates (0.1°C/min & 1°C/min) and end temperatures (20°C & 25°C) (top four patterns)

9.4.3 Cooling crystallisations of the oxalic acid:urea (1:1) co-crystal from water

Having established from the slurrying experiments in water, both those conducted at 20°C here and those at 30°C (as explored in the literature[188, 191]), that the *OAU*-1:1 co-crystal could be accessed at stoichiometries with higher proportions of *OA* and at higher solid loadings, cooling crystallisation experiments were designed that exploited similar compositions. Once again, the solid mass of the *OAU*-1:2 co-crystal required for complete saturation in water at 30°C was used as a reference mass, from which solutions that reflected the 5:1, 4:1, 3:1 and 2:1 molar ratios of *OA* to *U* were prepared. The relative saturation levels were also changed, constituting x2.5, x3 and x3.5 that of the original, used to achieve higher supersaturations. These samples were heated to 75°C and allowed to completely dissolve. From here, the solutions were cooled to 20°C at 1°C/minute or 0.1°C/minute, with a constant mixing rate of 200 rpm. Once filtered from the mother liquor and dried, the resultant solids were analysed using PXRD. Tables 9.9 and 9.10 summarise the crystalline products yielded for the different cooling rates, with the individual diffraction patterns shown in Appendix A9.4.

From the higher degrees of saturation under the 0.1°C/minute rate of cooling, it was noted that the (1:1) multi-component form was able to precipitate. As the proportion of *OA* was increased, along with the overall saturation level, the proportion of the *OAU*-1:1 form increased, though still in combination with excess starting material. This suggested that upon crystallising material out at these compositions, the conditions were such that this particular phase was able to nucleate pseudo-selectively and be stabilised sufficiently till filtration, without the crystallisation of its stoichiometric relative. Consistent for both cooling rates, the (1:2) co-crystal could be accessed selectively at the stoichiometries using the lowest proportion of *OA* and towards lower solution saturations, with particular evidence at the 2:1 molar combination.

Utilising the same conditions but cooling at the faster cooling rate, it was shown that both multi-component phases could precipitate, along with additional starting materials. This was rationalised based upon how supersaturation was achieved. With increasing rates of cooling, a system can reach

higher proportions of supersaturation more quickly, increasing the likelihood of a greater number of nucleation events. Here, as supersaturation was reached and surpassed, a greater degree of nucleation events were able to occur, a consequence of which was the formation of multiple crystalline phases, including both the stoichiometric co-crystals. Given the previous observations made from slurrying and the inherent thermodynamic stability of the (1:2) phase over a wide composition range, it was therefore expected that, if the resultant solid mixture was left, over time, the *OAU*-1:1 crystal would be suppressed and convert to that of either the starting materials or the (1:2) phase, depending upon the composition.

Table 9. 10 -Summary of the solid product, as determined by PXRD, yielded from the cooling crystallisations of solutions of *OA* and *U* in water, with varying solution stoichiometries (5:1, 4:1, 3:1 and 2:1) and saturation levels (x2.5, x3 & x3.5 the solid mass of the oxalic acid:urea (1:2) co-crystal at 30ºC), heated to 75ºC and cooled to 20ºC at 0.1ºC/min, emphasising the **major** and *minor* components

Solution stoichiometry	x2.5	x3	x3.5
5:1	**OAU-1:1, OAD, OA (α)** *OA (β)*	**OAU-1:1, OAD, OA (α)** *OA (β)*	**OAU-1:1, OAD, OA (α)** *OA (β)*
4:1	**OAU-1:2, OAD, OA (α/β)**	**OAU-1:1, OAD, OA (α)** *OA (β)*	**OAU-1:1, OAD, OA (α)** *OA (β)*
3:1	**OAU-1:2** *OAD, OA (α/β)*	**OAU-1:1, OAD, OAU-1:2** *OA (α/β)*	**OAU-1:1, OAD** *OA (α/β)*
2:1	**OAU-1:2**	**OAU-1:2**	**OAU-1:1, OAD, OAU-1:2** *OA (α/β)*

Table 9. 11 - Summary of the solid product, as determined by PXRD, yielded from the cooling crystallisations of solutions of *OA* and *U* in water, with varying solution stoichiometries (5:1, 4:1, 3:1 and 2:1) and saturation levels (x2.5, x3 & x3.5 the solid mass of the oxalic acid:urea (1:2) co-crystal at 30ºC), heated to 75ºC and cooled to 20ºC at 1ºC/min, emphasising the **major** and *minor* components

Solution stoichiometry	x2.5	x3	x3.5
5:1	**OAD** *OAU-1:2, OA (α/β)*	**OAD** *OAU-1:2, OA (α/β)*	**OAD** *OAU-1:1, OAU-1:2, OA (α)*
4:1	**OAU-1:1, OAU-1:2**	**OAU-1:2, OAD** *OAU-1:1, OA (α/β)*	**OAU-1:1, OAD** *OA (α)*
3:1	**OAU-1:2**	**OAU-1:2, OAD** *OA (α/β)*	**OAU-1:2, OAD, OAU-1:1** *OA (α)*
2:1	**OAU-1:2**	**OAU-1:2**	**OAU-1:2**

**Preparations that demonstrated the selective crystallisation of the oxalic acid:urea (1:2) co-crystal are highlighted in green*
*** Preparations that demonstrated the pseudo-selective crystallisation of the oxalic acid:urea (1:1) co-crystal are highlighted in yellow*

Having shown access to the *OAU*-1:1 co-crystal (with excess starting material) without the precipitation of the (1:2) phase towards higher degrees of saturation and contributions of *OA* (5:1, 4:1 and 3:1) through the slow cooling (0.1ºC/minute) to 20ºC, further crystallisations were prepared utilising the same experimental procedures, but here cooling to 30ºC. Upon immediate filtration, the solid materials yielded were analysed using PXRD, the patterns of which can be found in Appendix A9.4.

As the stoichiometry was altered to reflect decreasing quantities of *OA*, crystallisation was only shown to occur towards the higher saturation levels, with only the x3.5 saturation demonstrating consistent precipitation across the molar ratios used. Whilst preparations at the 5:1 and 3:1 molar ratios for the x3.5 saturation demonstrated the additional formation of either excess *OAD* or the (1:2) phase, it was shown that *OAU*-1:1 co-crystal could be crystallised to high proportions of purity from all the experiments conducted. This was particularly evident for the x3.5 saturated samples at the 5:1 and 4:1 stoichiometries, as well as that at the x3 4:1 preparation, where this specific co-crystal could be accessed with complete selectivity.

To ensure the reproducible crystallisation of the (1:1) multi-component phase, five repeats were carried out, saturating 4:1 solutions to 3.5 times the solid loading of the *OAU*-1:2 co-crystal at 30ºC, heating to 75ºC and cooling to 30ºC, filtering of the solid phase straight after reaching the end temperature. As shown in the PXRD patterns in Figure 9.15, using this method the corresponding *OAU*-1:1 co-crystal could be generated, *via* cooling crystallisation, to high levels of purity, with no evidence of the excess starting material or the opposing co-crystalline form. This reliability in the crystallisation of the (1:1) form at higher temperature supported the findings from other crystallisations from water, demonstrating again the enhanced stability of this particular phase at temperatures greater than that of ambient.

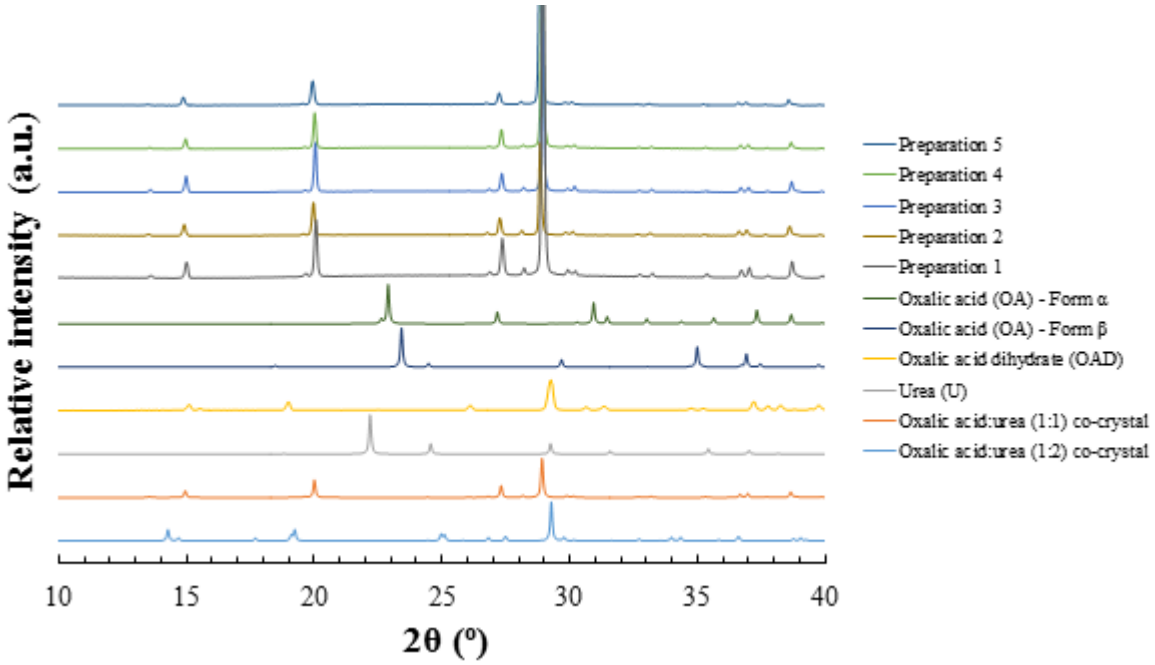

Figure 9. 15 - PXRD patterns highlighting the reproducible preparation of the oxalic acid:urea (1:1) co-crystal *via* cooling crystallisation, cooling from 75ºC to 30ºC at 0.1ºC/min, with a solution concentration and stoichiometry of x3.5 the solid mass of the oxalic acid:urea (1:2) co-crystal at 30ºC and 4:1, respectively (top five patterns)

9.5 Continuous cooling crystallisation

As highlighted in the introduction, despite the general robustness of batch processing, the ability to control a wide spectrum of solid properties via these techniques is limited. In recent years, continuous methods have offered a route to the fine tuning of particle parameters, owing to the heightened control over process environments. The development of continuous crystallisation platforms has been one of the core remits of the Bath Continuous Crystallisation Laboratory, based at the University of Bath. Within this final section, two of the continuous cooling crystallisation setups used within the group, the Continuous Oscillatory Baffled Crystalliser (COBC) and the Kinetically Regulated Automated Input Crystalliser (KRAIC), will be utilised and assessed for the precipitation of the *OAU*-1:2 co-crystal.

As shown from the previous section, both co-crystalline forms of *OA* and *U* could be selectively yielded through batch cooling crystallisation methods. In the case of the *OAU*-1:1 form, crystallisation of the correct phase was shown to occur only from solutions with increased saturations and higher *OA* content. In addition, these systems had to be cooled to temperatures above that of the laboratory norm, i.e. 30°C. Given the issues with filtration at higher temperatures, the continuous platforms were designed to operate primarily so that the end cooling temperature was that of ambient. As such, the selective and pure crystallisation of the (1:1) multi-component phase of *OA* and *U* was deemed an unsuitable target for such setups.

9.5.1 Continuous oscillatory baffled crystalliser (COBC)

Crystallisation of the *OAU*-1:2 co-crystal was first conducted via continuous means using the COBC, the design of which is outlined in Figure 9.16. The general setup consisted of six temperature controlled baffled straights (1-6) into which a high temperature saturated solution could be fed. The solution was flowed through the platform through the action of a peristatic pump, with mixing being enabled by the oscillatory motion of a bellows pump. Moving through the crystalliser, different temperature conditions were experienced by the crystallisation medium, with the temperature dropping from straight to straight, with the final section residing at 20°C. This allowed for stepwise cooling, raising the supersaturation and encouraging nucleation and growth. For each run, the residence time (the theoretical time frame required for a given volume of solution to move through the crystalliser) was taken as approximately 35 minutes. Five continuous crystallisation runs were carried out, each using a different combination of straight temperatures for either a 30°C or 35°C saturated solution with respect to the solubility of the (1:2) co-crystal in water. The parameters used for these runs, as well as the nature of the end solid product, can be found in Table 9.12. The individual PXRD patterns from the resulting products can be found in Appendix A9.5.

Table 9. 12 - Summary of the key parameters and outcomes of the COBC runs, 1-5, conducted with 1:2 solutions of *OA* and *U* in water, highlighting saturation temperatures, straight temperatures and the phase of any resultant solid product

Run	***OAU*-1:2 saturation temperature (°C)**	**Straight Temperature (°C)**						**Solid product**
		1	**2**	**3**	**4**	**5**	**6**	
1	*30*	50	40	40	30	30	20	*No crystallisation**
2	*30*	50	40	40	25	25	20	*No crystallisation**
3	*30*	50	30	30	25	25	20	*No crystallisation**
4	*30*	50	20	20	20	20	20	***OAU 1:2***
5	*35*	50	20	20	20	20	20	***OAU 1:2***

**Crystallisation did not occur in the body of the crystalliser, only at the end piece*

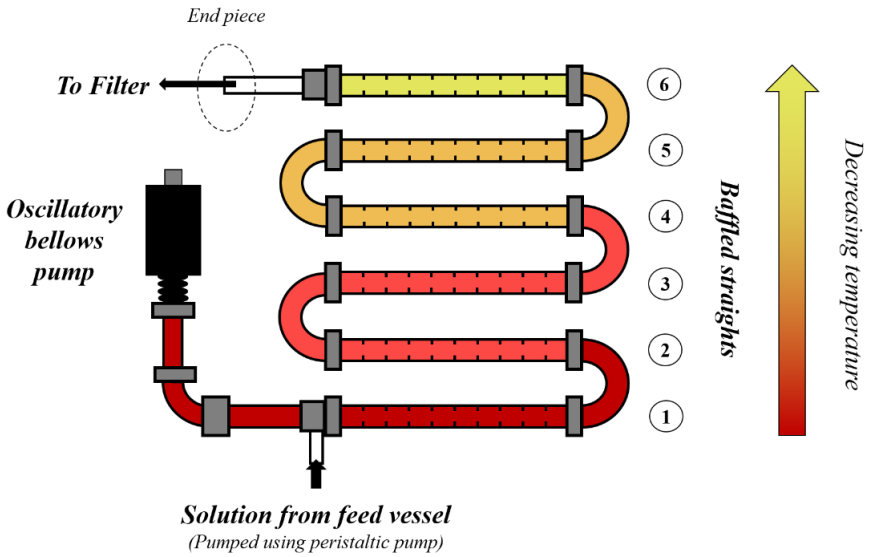

Figure 9. 16 - Schematic diagram of the continuous oscillatory baffled crystalliser (COBC), highlighting the six temperature controlled tubular straights (1-6), solution feed, bellows and filtration point

For the first three continuous runs, the temperature of the straights were set so as to implement a steady decrease in temperature, observing the point of any nucleation within the body of the crystalliser. Run 1 maintained an undersaturated solution until the final straight, whilst runs 2 and 3 exploited a more gradual temperature change, with the latter transitioning from the undersaturated to the supersaturated state via a more severe temperature profile. For each of these procedures, no crystallisation was noted within the straights within the first residence time. Precipitation was noted, however, at the end piece of the platform, once the volume of solution necessary for one residence time had passed through the entire crystalliser, moving from the glass straights through a PTFE tube to the filtration unit. For each of the initial experiments, the precipitation at this point in the crystalliser was taken to have occurred around 48-51 minutes after starting the run, well within the second residence time. Leaving each of these runs to complete a second and third residence time (occurring approximately 35-70 minutes and 70-105 minutes after initiating the crystalliser), crystallisation ensued, propagating from the end piece backwards through straights 6, 5 and 4. The initial crystallisation of material was put down to the interaction of the supersaturated solution with the walls of the PTFE tubing at the end piece, aiding in heterogeneous nucleation. This allowed for nuclei or 'seeds' to facilitate secondary nucleation that propagated back through the straights owing to the oscillatory mixing employed. Phase analysis of the solid product yielded demonstrated the consistent formation of *OAU*-1:2 co-crystal for each of these runs.

To force primary nucleation to occur within the body of the crystalliser, the temperature for straights 2-6 were reduced and set to 20°C, with the first being maintained at 50°C to ensure complete dissolution. This precaution was taken so as to minimise the possibility of crystallisation occurring within the oscillation bellows and thus damaging the pump. Given the unique type of mixing utilised within the COBC, the metastable zone for the crystallisation of the desired co-crystal, when saturated at 30°C, was deemed to be much wider than that observed during batch processing methods. Hence for this experiment, supersaturation was established much earlier stage within the crystalliser, allowing more time for nucleation to occur as the solution flows through the system.

As with the previous runs, no crystallisation was observed until the second residence time, 48 minutes after initiation. However, rather than occurring at the end piece, precipitation was first witnessed midway through straight 4. Again, owing the oscillatory motion inherent to this crystallisation platform, with 10 minutes, further nucleation events were noted in straights 3, 5 and 6. After filtration and

subsequent analysis, the solid product was shown to be that of the (1:2) multi-component material of *OA* and *U*. Figure 9.17a depicts the moment when the first crystals were seen in straight 4, with Figure 9.17b outlining the accumulation of crystals in the same straight after 10 minutes.

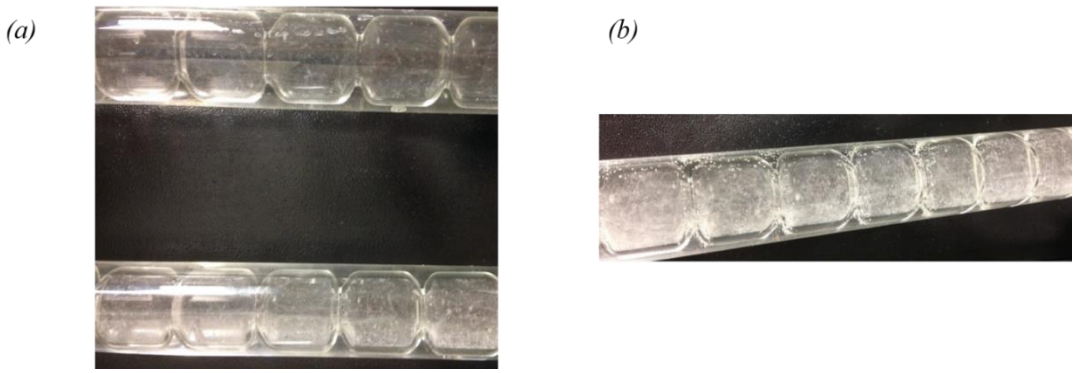

Figure 9. 17 - Images of the COBC straights in run 4, highlighting (a) the initial crystallites observed in straight 4, compared to straight 5, and (b) the growth of the crystals of the oxalic acid-urea (1:2) co-crystal in straight 4

Whilst run 4 exemplified that the desired co-crystal could be formed via an initial primary nucleation process, only a small quantity of material was collected for a given residence time, with the third residency yielding solid with an overall mass of 2.55g. In an effort to improve the amount of solid obtained for a given residence time, a further continuous run was carried out at a higher saturation level, with solutions prepared to an *OAU*-1:2 co-crystal 35ºC saturation. Exploiting the same temperature profile as in run 4 and upon commencing the run, crystallisation was originally shown to occur within the first residence time in straight 4 after 30 minutes. After a further 23 minutes, additional nucleation events had proliferated to straights 3, 5 and 6. The process was continued till the end of the second residence time, with the solid collected demonstrating a total mass of 8.26g, a substantially greater quantity than taken from previous runs. Figures 9.18a, b and c demonstrate the initial crystallites and propagation of crystallisation throughout the crystalliser for run 5.

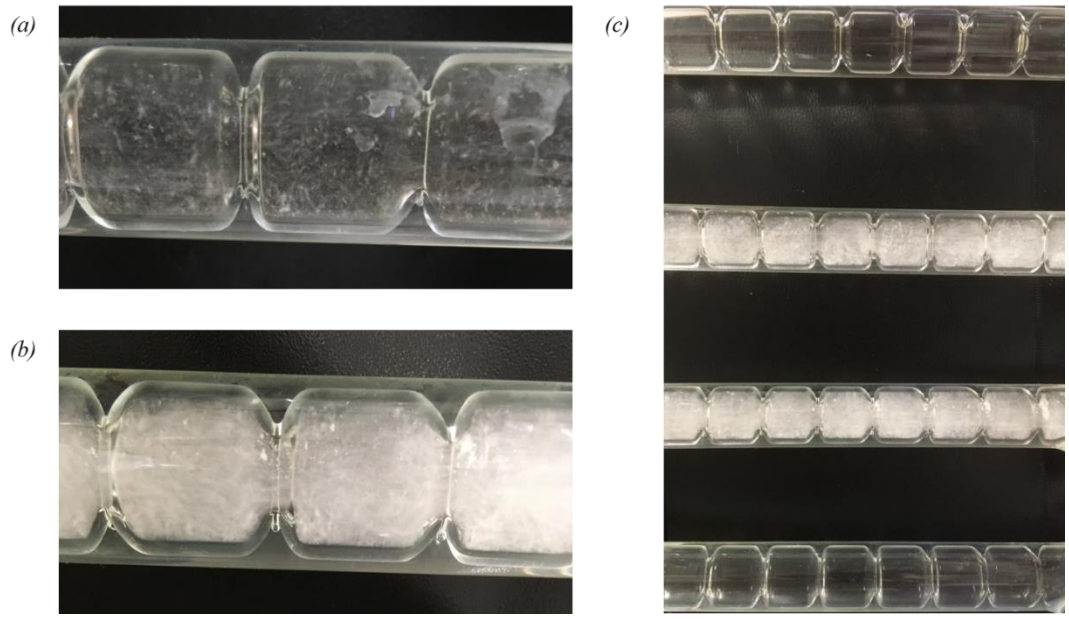

Figure 9. 18 - Images for COBC run 5 highlighting (a) the initial crystallites observed in straight 4, (b) the accumulation and growth of crystals in straight 4 and (c) the propagation of crystallisation for the oxalic acid-urea (1:2) co-crystal from straight 4 to 5

Although solid product could be generated in a larger yield with the same co-crystalline consistency, it was deemed not possible to produce material beyond a second residence time under the conditions used for run 5. This was as a result of the uncontrolled build-up of crystals at various points within the crystalliser. As demonstrated in Figure 9.19a, as well as primary homogenous nucleation occurring within the body of the platform, further nucleation phenomena were shown to ensue on the inner surface of the baffled straights. This encrustation developed over time, impacting on the flow dynamics inside the platform, as well as having implications towards the possible phases present in the end solid product. Furthermore, due to the vertical orientation of this particular setup, crystals were shown to accumulate at the bends connecting consecutive straights. Given the set flow and oscillation rates, the solid product could not overcome these connections and move up through the crystalliser, presenting issues in terms of obtaining material at the end of the process for filtration and that of blockages. The latter consideration presented problems upon transitioning from the second to the third residence time, with the blockages causing increases in pressure, presenting a safety hazard. An example of this build up is shown in Figure 9.19b.

The final issue concerned preventing crystallisation occurring within the bellows utilised for the oscillatory motion exploited within the platform (Figure 9.19c). The bellows themselves were connected to the main straights via an L-unit of unjacketed, unbaffled glass piping which was filled with water and in contact with the solution medium. Despite the higher temperature of the first straight and given the back mixing generated upon oscillation, solution was able to enter the connecting piece and become supersaturated upon cooling to room temperature. Hence, crystallisation was able to occur, with the possibility of precipitation occurring within the bellows themselves. As such, upon noticing the initial crystal formation within this component, the crystalliser was stopped so as to avoid damage. Despite these issues, the COBC was shown to allow for the selective continuous crystallisation of the desired (1:2) co-crystalline phase of *OA* and *U*.

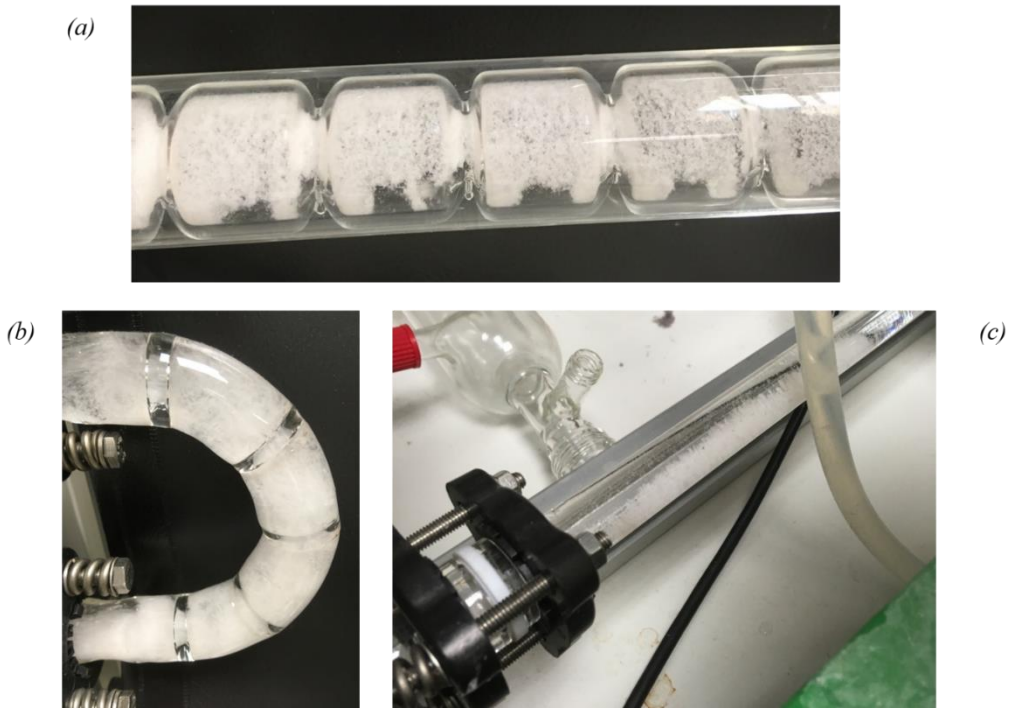

Figure 9. 19 - Images from COBC run 5, highlighting (a) encrustation in straight 4, (b) crystal build up in the bend between straight 3 & 4 and (c) crystallisation in the back piece connecting the oscillatory baffles to straight 1

9.5.2 Kinetically regulated automated input crystalliser (KRAIC)

Further continuous crystallisations were carried out using the KRAIC platform, whereby a solution of *OA* and *U* was progressively cooled through a mesotubular segmented flow reactor to room temperature, with solution within the slugs created by phase segmentation and mixed by bolus flow action. The starting components were combined in a 1:2 stoichiometry and saturated with respect to the corresponding co-crystal at 35ºC, heated to 40ºC to ensure complete dissolution. The degree of saturation was selected based upon the observations made from the previous COBC runs. Given the inherently gentle type of mixing exploited within this crystalliser, the metastable zone was expected to be larger than that generated under oscillatory homogenisation, justifying the heightened saturation level. The heated feed solution was then fed to the mixing piece and upon contact with the carrier fluid and air, segmentation was generated. The resultant solution slugs, coated with the immiscible fluid (minimise heterogeneous nucleation with the tube walls) and supported against the air segment (maximising efficient flow through the system), were able to move through the consecutive coils, gradually being cooled. The slugs were analogous to micro-batch units, with the solution being mixed by the generation of internal vortices. Upon reaching the end of the cooling tubing, the phases were separated and the solid filtered off. Figure 9.20 outlines the general setup for the KRAIC platform, highlighting the segmentation cross piece and the cooling coils.

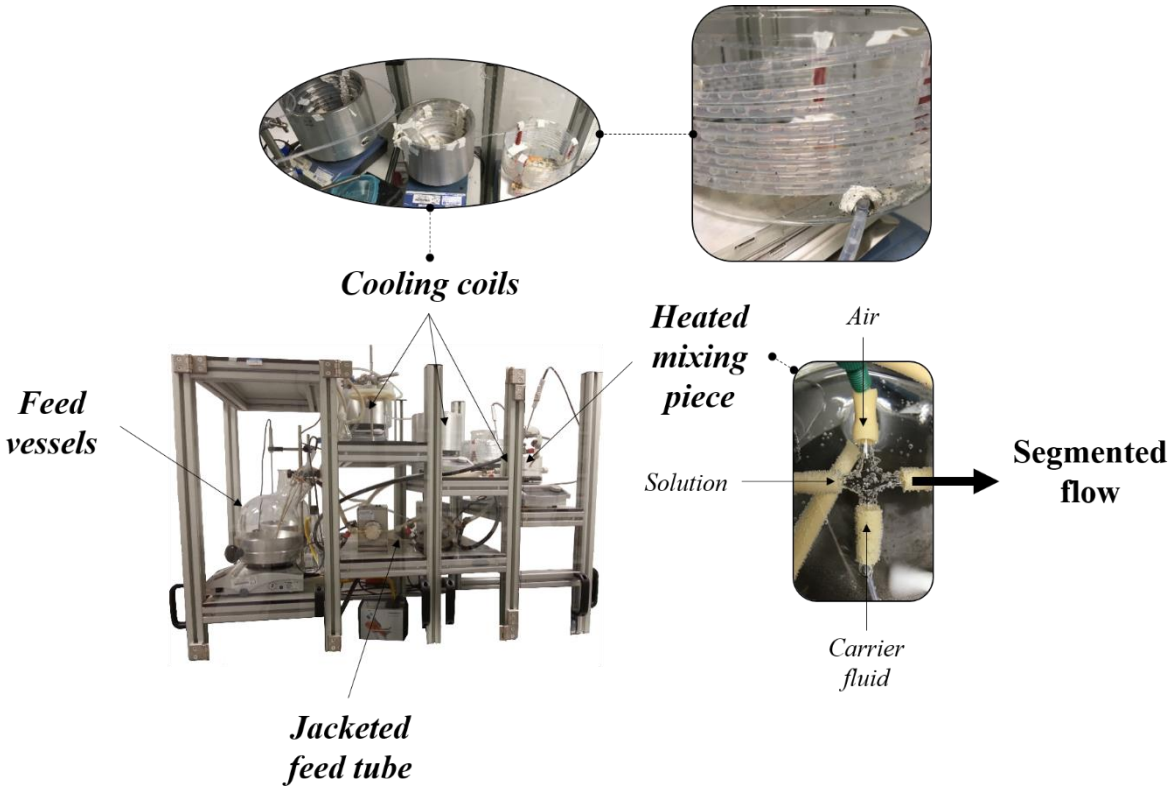

Figure 9. 20 - Schematic diagram of the Kinetically Regulated Automated Input Crystalliser (KRAIC), highlighting cooling coils, the heated mixing piece and segmented flow in operation

For the flow rates used, the residence time was estimated to be 17 minutes from the mixing piece to the filtration unit. Crystallisation was first noted towards the end of the third coil, 16 minutes after starting the run. Individual crystals were shown to have grown within specific slugs, though precipitation was observed only in a few of the segments initially. Continuing into the second residence time, crystallisation was shown to occur earlier in the process, with crystallites found in the midst of the

second cooling coil. Towards the end of this period (38 minutes), crystals were present in nearly every solution segment, with solid precipitating from the early stage of the second coil.

Whilst this platform showed consistent crystallisation within the body of the tubing for a whole residence time, issues manifested themselves increasingly as time progressed. Entering into the third time period (40 minutes), a blockage was noted at the end piece to the filtration unit. Subsequently, further obstructions were observed within the body of the crystalliser, in the first coil. This caused a slowing of the flow rate, affecting the time over which crystallisation could occur. For each such issue found, the process had to be stopped.

Figure 9.21 shows the crystals obtained from the first three residences, demonstrating the particular success of residence time two. As shown, the KRAIC was used to generate individual crystals in individual solution slugs, with crystals growing beyond 1 mm in length. Phase analysis of the solid obtained (PXRD patterns shown in Appendix A9.5) showed, once again, the successful and consistent preparation of the (1:2) co-crystalline phase of *OA* and *U* at this given solution composition. Furthermore, this setup also demonstrated the potential for segmented flow crystallisers to allow for single crystal growth, sufficient for SCXRD analysis.

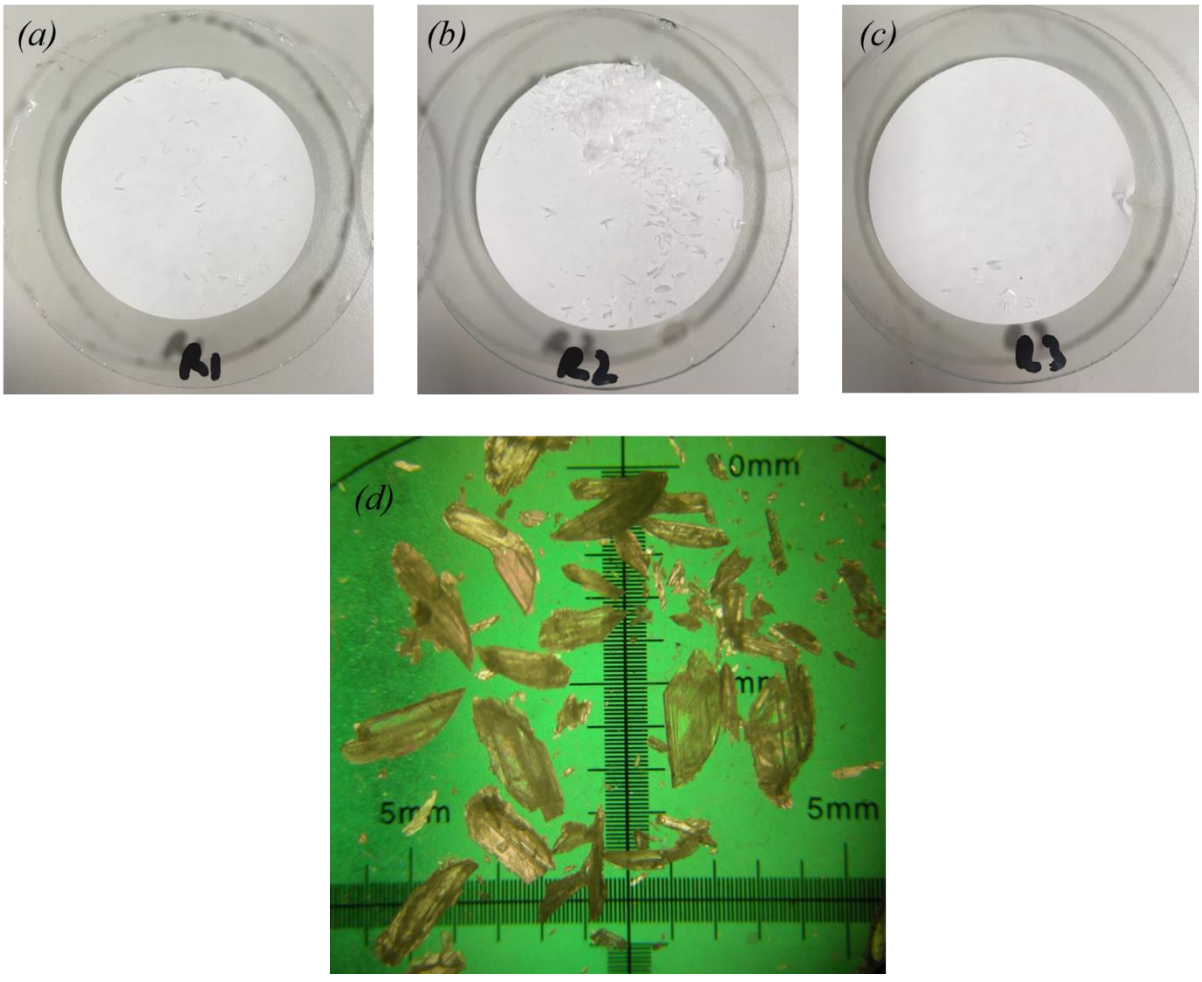

Figure 9. 21 - Images of the crystals yielded from residence times 1-3 (a-c), with a close up view of those obtained for the second residence time (d)

9.6 Summary, conclusions and future work

Within this chapter, a variety of preparation methods were examined, assessing their ability to allow for the selective crystallisation of the stoichiometrically diverse *OAU*-1:1 and *OAU*-1:2 co-crystals, respectively. By using different quantities of solvent, ranging from the minimal, via mechanochemical or solvent-mediated means, to those reliant on complete dissolution, i.e. evaporative or cooling crystallisation, routes were devised for discerning between the two co-crystalline forms. For each preparatory method used, key parameters were explored, with particular emphasis on solvent environment, sample stoichiometry and solid loading.

In terms of the (1:1) form, this phase could be accessed across the different preparation methods utilised, either in pure form or in combination with excess starting material. By using non-aqueous solvent environments, in particular that of isopropanol, this co-crystal could be prepared selectively at 20ºC when utilising larger molar proportions of *OA*. This suggested an enhanced stabilisation effect with respect to this solvent when compared to the equivalent preparations from water. As such, the formation of this multi-component material via these methods in water was shown to be hindered across a number of stoichiometries at lower solid loadings at 20ºC. However, by maintaining higher solid to solvent ratios and larger molar ratios of *OA*, this co-crystal could be kinetically stabilised under ambient conditions. Given this metastability towards room temperatures, cooling crystallisations were developed, again using higher quantities of *OA* (4:1) and saturation levels, with the temperature being held at 30ºC. As suggested by these initial results, the *OAU*-1:1 form represented a less stable material at room temperature with respect to the (1:2) co-crystal, though it could be kinetically stabilised and accessed under given conditions. The stability of this phase was shown to increase with temperature, highlighting the existence of a co-crystalline material with a relatively reduced stability difference with respect to that of the opposing multi-component phase at higher temperatures.

In contrast, the *OAU*-1:2 form represented the formation of the more thermodynamically stable multi-component phase under laboratory conditions, demonstrating consistent selectivity over a range of stoichiometries, with particular emphasis on the 1:2 combination of starting materials. In aqueous conditions, this specific phase could be stabilised with respect to its stoichiometric counterpart, with mechanochemical, slurrying, evaporative and cooling methods all exhibiting pathways to its reproducible preparation. Due to its reliable formation at 20ºC, this co-crystal embodied the necessary characteristics for trials through the continuous cooling crystallisation platforms available at the University of Bath; the COBC and KRAIC. Both setups could be used successfully to prepare the (1:2) form, though further optimisation, in terms of the crystallisation parameters used and the design of the crystallisers, was necessary, with the aim of enhancing the yield of the *OAU*-1:2 phase in these runs.

Drawing on the work outlined here, the system of *OA* and *U* can be explored further, with particular emphasis on continuing to design cooling crystallisations where the (1:1) co-crystal could potentially be accessed at room temperature. Using the appropriate techniques, complete ternary phase diagrams can be developed for the temperatures ranges of interest, focussing on that of 20ºC and 30ºC. Given the metastability in the aqueous environment of this phase, the kinetic parameters for its generation should be explored further. This could be conducted through the manipulation of the cooling profile used or through the introduction of the necessary seed. Building upon this, methods could be established for the continuous crystallisation of this phase, reconfiguring the platforms available so as to access materials with a reduced metastability at higher temperatures. For crystallisation experiments carried out using the COBC, the orientation of the platform could be altered, laying it flat, minimising the obstructions caused by the build-up of solid at the bend units. Furthermore, future designs of this particular rig should explore the possibility of using different materials for the construction of the individual baffled straights. At present, the glass surface utilised presents an opportunity for uncontrolled heterogeneous nucleation to occur. By coating this surface with a compatible substance to reduce this effect, more

efficient processes can be designed. As for the KRAIC, the main issues arise from blockages manifesting at the end piece as well as in the body of the crystalliser. Again, these issues can be overcome through the careful consideration of the material used for the coil tubing, as well as the design of the end piece that couples the segmented phase separation with the liquid-solid filtration.

10 Conclusions

When developing species such as salts and co-crystals, initial screening ought to be conducted, outlining early routes for the reproducible preparation of material, allowing for characterisation to take place. Depending upon the method used, various properties can be assessed, defining the phase behaviour, melting phenomena and crystal structure for a particular form. In addition, the potential for polymorphic and stoichiometric variations can be explored. To this end, comparisons can be made with the starting materials so as to determine whether the novel entity demonstrates any particular advantages. Upon the discovery of such a system, processes can be designed for the efficient crystallisation for the preferred multi-component phase, taking advantage of more robust methods, such as cooling crystallisation. In the research outlined in this thesis, two projects relating to the preparation, characterisation and application of multi-component materials is discussed. The first was centred on the API, naproxen (*NPX*), exploring the potential of salt or co-crystal formation in the alteration of the chiral crystalline class yielded, with uses towards preferential crystallisation processes. In the second, various crystallisation methods were considered for the selective preparation of the stoichiometric co-crystals of oxalic acid (*OA*) and urea (*U*), driving towards the design of cooling crystallisation pathways, in either a batch or continuous setup.

NPX at racemic compositions forms a racemic compound, where opposing enantiomers crystallise preferentially within the same crystalline lattice. By introducing the complementary molecule, 2-aminopyridine (*2AP*), novel salts can be generated at both racemic and homochiral compositions, where the enantiopure phase demonstrated metastability under certain conditions. This material was defined as a metastable conglomerate. By characterising this system using binary and ternary phase diagrams, crystallisations were developed that showed that complexes of homogeneous chirality could be obtained at compositions that tended towards the formation of the racemic multi-component phase. These crystallisations utilised faster cooling rates that allowed for the kinetic stabilisation of the enantiomerically pure phase. This emphasised that through the introduction of an appropriate secondary molecular entity, systems could be obtained that allow for the preferential precipitation of a desired enantiomer near racemic contributions.

Based upon these findings, further multi-component material screening was conducted for *NPX* with a range of co-formers, using a combined approach of mechanochemical and crash cooling crystallisation techniques. The molecules selected were based on derivatives of *2AP*, as well as those utilising different functional groups, and were combined with the API at both racemic and enantiopure combinations. By using grinding, either with or without solvent, it was shown that an efficient initial assessment could be made as to whether or no co-crystal or salt formation was possible. In addition, this preparative method also lent itself to the development of binary (melting point) phase diagrams, aiding in the characterisation of the chiral crystalline material present. Moreover, by using mechanochemistry, seed could be readily made for input into solution crystallisations, allowing for consistency in the crystalline product made across the different methods.

For all the molecules used, a range of co-crystals and salts were found at racemic or homochiral compositions. In the majority of cases, no change was noted when compared to that of single-component component *NPX* in terms of the chiral crystalline material developed. Upon combination with the *2AP* derivatives 2-aminopyrimidine (*2APM*), 2-amino-3-chloropyridine (*2A3CP*), 2-amino-4-chloropyridine (*2A3CP*) and 2-amino-5-chloropyridine (*2A5CP*), as well as the co-former acridine (*A*), distinct crystalline phases were shown to precipitate at both enantiopure and racemic contributions, with evidence to suggest the formation of stable racemic compounds. Further to this, with particular emphasis on the preparations with A, additional polymorphic or stoichiometric forms were also discovered, whereby the chiral composition within the racemic co-crystal was shown to be continuous.

This demonstrated the formation of a racemic solid solution. Likewise, this was also shown to occur upon multi-component material formation with 2-amino-4,6-dimethylpyrimidine (*2ADMP*) and benzimidazole (*BI*). Whilst each of the solid solutions displayed different packing efficiencies at the two key enantiomeric compositions, like with the racemic compound forming systems, these types of material were deemed to not be suitable for future preferential crystallisation processes.

Two other systems of interest were those incorporating imidazole (*I*) and 2-amino-6-chloropyridine (*2A6CP*). As observed with *2AP*, upon combining *NPX* with *I*, discrete salt forms were shown to crystallise at racemic and enantiopure compositions, with the racemic phase exhibiting a lower melting point than that of its homochiral counterpart. This demonstrated a degree of stability in the solid state for the enantiomerically pure form, again providing an initial indication of a metastable conglomerate, with applicability towards a preferential crystallisation process. In the case of the *2A6CP*, whereas the homochiral co-crystal could be freely made at the corresponding API compositions, to date no evidence has been found from early screening that any novel material, let alone a racemic phase, could be prepared at the 50:50 molar ratio of API enantiomers. By considering the location of the halogen substituent about the aromatic ring of the co-former, it could be suggested that no efficient packing was possible to accommodate both chiral forms of *NPX* within the same multi-component crystalline structure. As such, this system was deemed to have potential in the design of processes for the separation of enantiomers.

Collectively, it was shown that by combining secondary components with a target API, novel co-crystals or salts could be accessed with the potential of changing the chiral crystalline nature with respect to the starting components. By first considering what interactions were likely and selecting the appropriate co-former, new materials could be screened for with ease, through mechanochemical and solution-based means.

Multi-component systems can show a variety of structural variations, be they polymorphic or stoichiometric. Depending upon the method of preparation used and the conditions thereof, different phases can be obtained. By exploiting diverse compositions of the two starting components at varying solvent contributions, the pathways to the selective preparation of the two respective co-crystals of *OA* and *U* (*OAU*-1:1 and *OAU*-1:2) were examined. The methods used included mechanochemical, slurrying, evaporative and cooling crystallisation techniques.

With emphasis on grinding and slurrying, it was shown that both co-crystalline forms could be accessed from different alcohol environments (methanol, ethanol and isopropanol), although the (1:1) phase could only be prepared at higher molar quantities of *OA*, especially in samples utilising isopropanol. Likewise, when using solution crystallisation methods, such as cooling and evaporation, the *OAU*-1:1 co-crystal was only shown to form when *OA* was in a greater proportion or when the degree of saturation was higher. This, again, was particularly prevalent for experiments conducted from isopropanol. Across all the preparation methods and solvents used, the *OAU*-1:2 co-crystal could be reliably made at its corresponding stoichiometry.

When water was applied as the crystallisation medium of choice, over all the preparations used, the (1:2) phase demonstrated the greatest degree of stability at room temperature (20^{o}C). The opposing equimolar co-crystal could only be generated by using larger molar contributions of *OA*, increasing the over saturation level and by crystallising this given form at higher temperatures. By considering all the observations made, it was suggested that under ambient conditions the *OAU*-1:2 phase had the greater thermodynamic stability over the composition range, with the only opportunity to crystallise the *OAU*-1:1 co-crystal coming from an exploitation of the crystallisation kinetics.

Given the comparative stability and ease of crystallisation of the (1:2) form, this system was applied to the continuous crystallisation rigs based at the University of Bath; the COBC and KRAIC. As such, the *OAU*-1:2 co-crystal was shown to crystallise consistently within both platforms. As both of these methods utilise a gentler type of mixing than used in batch processing, the metastable zone was observed to be much wider, with spontaneous nucleation only occurring after a lengthy induction period. Furthermore, whilst methods demonstrated the consistent preparation of the correct co-crystalline phase, additional platform optimisation needs to be conducted so as to achieve the production of the necessary material beyond a few residence times. In the case of the COBC, this requires re-evaluating the inner surface of the crystalliser, to minimise the possibility of undesired heterogeneous nucleation that could cause encrustation, as well as changing the orientation of the crystalliser to the horizontal geometry. The aim of this being to stop blockages at the bend units between the straights. For the KRAIC, further development needs to be conducted to reduce the likelihood of blockages at the end piece, with additional investigations into the homogeneity of the crystallisation coil tubing, again to minimise the possibility of heterogeneous primary nucleation.

10.1 Future work

The specific aspects of future work to be carried out are outlined in detail at the end of each research chapter (Chapters 6-9). Broadly, all research to be conducted focusses on two main areas; further material screening and crystallisation development.

In terms of material screening with *NPX*, co-formers should be selected based on functionalities that are deemed likely to interact with the API. Consideration should also be given to other groups that may influence these intermolecular interactions, with the eventual aim of generating multi-component materials that are able to preferentially form the enantiopure phase towards racemic compositions, i.e. a racemic conglomerate. Supposing that a conglomerate was found, further work should be conducted into the development of processes that can apply these materials in the resolution of the different chiral forms. In order for a robust preferential crystallisation to be developed, additional work should be done to explore methods for the in-line assessment of solution enantiomeric composition. Circular dichroism offers a unique opportunity to achieve this, given its ability to monitor solution concentration, as well as chiral compositions. These ideas form the basis of the on-going collaboration between the Wilson (University of Bath) and ter Horst (University of Strathclyde) groups, as part of the EPSRC Future Manufacturing Hub, aiming to develop methods for the complete resolution of enantiomers *via* crystallisation.

Furthermore, additional work should be carried out into the optimisation of the continuous crystallisation platforms based at the University of Bath; the COBC and the KRAIC. By changing the setup orientation of the COBC and improving the filtration unit within the KRAIC, these systems can be vastly improved. Through the implementation of enhanced temperature control, particularly for the segmented flow crystalliser, crystallisations can be developed that could allow for the selective preparation of the less stable co-crystalline form of *OA* and *U*, that of the (1:1) phase. Collectively, the observations made from the study with *OA* and *U* could benefit other systems in terms of developing methods for the selective preparation of structurally variant (polymorphic or stoichiometric) multi-component materials. This could be either for small-scale screening techniques or larger scale industrial methods.

References

1. A. Newman, *Org. Process Res. Dev.*, 2012, **17**, 457-471.
2. J. Chen, B. Sarma, J. M. B. Evans and A. S. Myerson, *Cryst. Growth Des.*, 2011, **11**, 887-895.
3. N. Qiao, M. Li, W. Schlindwein, N. Malek, A. Davies and G. Trappitt, *Int. J. Pharm.*, 2011, **419**, 1-11.
4. G. R. Desiraju, *J. Am. Chem. Soc.*, 2013, **135**, 9952-9967.
5. G. He, P. S. Chow and R. B. H. Tan, *Cryst. Growth Des.*, 2010, **10**, 3763-3769.
6. D. J. Berry and J. W. Steed, *Adv. Drug Deliv. Rev.*, 2017, **117**, 3-24.
7. A. M. Healy, Z. A. Worku, D. Kumar and A. M. Madi, *Adv. Drug Deliv. Rev.*, 2017, **117**, 25-46.
8. S. T. Taylor and S. L. Shamblin, in *Polymorphism in Pharmaceutical Solids*, ed. H. G. Brittain, Informa Healthcare USA, Inc., New York, 2nd edn., 2009, ch. 16, pp. 587-629.
9. S. Petit and G. Coquerel, in *Polymorphism in the pharmaceutical industry*, ed. R. Hilfiker, Wiley-VCH Verlang GmbH & Co., Weinhiem, Germany, 2006, ch. 10.
10. L. E. Smart and E. A. Moore, *Solid-state chemistry: an introduction*, CRC Press, Taylor & Francis Group, 3rd edn., 2005.
11. W. Beckmann, in *Crystallization: Basic concepts and industrial applications*, ed. W. Beckmann, Wiley-VCH Verlang GmbH & Co., Weinheim, Germany, 1st edn., 2013, ch. 2.
12. X. Lin, Y. Hu, L. Liu, L. Su, N. Li, J. Yu, B. Tang and Z. Yang, *Pharm. Res.*, 2018, **35**, 125-143.
13. N. Schultheiss and A. Newman, *Cryst. Growth Des.*, 2009, **9**, 2950-2967.
14. R. Hilfiker, F. Blatter and M. von Raumer, in *Polymorphism in the pharmaceutical industry*, ed. R. Hilfiker, Wiley-VCH Verlang GmbH & Co., Weinhiem, Germany, 2006, ch. 1.
15. N. Shan and M. J. Zaworotko, *Drug Discovery Today*, 2008, **13**, 440-446.
16. S. Jin, H. Zhang, H. Liu, X. Wen, M. Li and D. Wang, *J. Mol. Struct.*, 2015, **1096**, 157-170.
17. D. P. Elder, R. Holm and H. L. Diego, *Int. J. Pharm.*, 2013, **453**, 88-100.
18. N. Blagden, S. J. Coles and D. J. Berry, *CrystEngComm*, 2014, **16**, 5753-5761.
19. K. K. Arora and M. J. Zaworotko, in *Polymorphism in Pharmaceutical Solids*, ed. H. G. Brittain, Informa Healthcare USA, Inc., New York, 2nd edn., 2009, ch. 8, pp. 282-317.
20. U. J. Griesser, in *Polymorphism in the pharmaceutical industry*, ed. R. Hilfiker, Wiley-VCH Verlang GmbH & Co., Weinhiem, Germany, 2006.
21. K. E. Wittering, L. R. Agnew, A. R. Klapwijk, K. Robertson, A. J. P. Cousen, D. L. Cruickshank and C. C. Wilson, *CrystEngComm*, 2015, **17**, 3610-3618.
22. L. H. Thomas, A. R. Klapwijk, C. Wales and C. C. Wilson, *CrystEngComm*, 2014, **16**, 5924.
23. A. V. Trask, *Mol. Pharm.*, 2007, **4**, 301-309.
24. S. Lohani and D. J. W. Grant, in *Polymorphism in the pharmaceutical industry*, ed. R. Hilfiker, Wiley-VCH Verlang GmbH & Co., Weinhiem, Germany, 2006, ch. 2.
25. H. G. Brittain, in *Polymorphism in Pharmaceutical Solids*, ed. H. G. Brittain, Informa Healthcare USA, Inc., New York, 2nd edn., 2009, ch. 1, pp. 1-23.
26. R. J. Davey and J. Garside, *From molecules to crystallizers: An introduction to crystallization*, Oxford University Press, Oxford, 2000.
27. J. W. Mullin, *Crystallization*, Butterworth-Heinemann, Oxford, 4th edn., 2001.
28. S. Aitipamula, P. S. Chow and R. B. H. Tan, *CrystEngComm*, 2014, **16**, 3451.
29. A. O. Surov, K. A. Solanko, A. D. Bond, A. Bauer-Brandl and G. L. Perlovich, *CrystEngComm*, 2014, **16**, 6603-6611.
30. R. Prohens, R. Barbas, A. Portell, M. Font-Bardia, X. Alcobé and C. Puigjaner, *Cryst. Growth Des.*, 2016, **16**, 1063-1070.
31. Z. Zhou, H. M. Chan, H. H. Sung, H. H. Tong and Y. Zheng, *Pharm. Res.*, 2016.
32. G. Kaupp, *CrystEngComm*, 2009, **11**, 388-403.
33. A. Burrows, J. Holman, A. Parsons, G. Pilling and G. Price, *Chemistry*^{3}, Oxford University Press, Oxford, 1st edn., 2009.
34. J. McMurry, *Organic Chemistry*, Brooks/Cole Publishing Company, Belmont, California, 3rd edn., 1992.

35. S. Srisanga and J. H. ter Horst, *Cryst. Growth Des.*, 2010, **10**, 1808-1812.
36. H. Lorenz, A. Perlberg, D. Sapoundjiev, M. P. Elsner and A. Seidel-Morgenstern, *Chem. Eng. Process.*, 2006, **45**, 863-873.
37. G. Levilain and G. Coquerel, *CrystEngComm*, 2010, **12**, 1983-1992.
38. K. Petruševska-Seebach, A. Seidel-Morgenstern and M. P. Elsner, *Cryst. Growth Des.*, 2011, **11**, 2149-2163.
39. W. H. Lam and K. M. Ng, *AIChE J.*, 2007, **53**, 429-437.
40. H. Wu, A. R. West, M. Vickers, D. C. Apperley and A. G. Jones, *Chem. Eng. Sci.*, 2012, **77**, 47-56.
41. S. Chen, H. Xi, R. F. Henry, I. Marsden and G. G. Z. Zhang, *CrystEngComm*, 2010, **12**, 1485.
42. L. C. Sogutoglu, R. R. Steendam, H. Meekes, E. Vlieg and F. P. Rutjes, *Chem. Soc. Rev.*, 2015, **44**, 6723-6732.
43. T. Lee, Y. H. Chen and Y. W. Wang, *Cryst. Growth Des.*, 2008, **8**, 415-426.
44. J. Mahieux, S. Gonella, M. Sanselme and G. Coquerel, *CrystEngComm*, 2012, **14**, 103-111.
45. D. A. Bock and C. W. Lehmann, *CrystEngComm*, 2012, **14**, 1534-1537.
46. E. Arunan, G. R. Desiraju, R. A. Klein, J. Sadlej, S. Scheiner, I. Alkorta, D. C. Clary, R. H. Crabtree, J. J. Dannenberg, P. Hobza, H. G. Kjaergaard, A. C. Legon, B. Mennucci and D. J. Nesbitt, *Pur. Appl. Chem.*, 2011, **83**, 1619-1636.
47. C. B. Aakeröy and N. Schultheiss, in *Making crystals by design: methods, techniques and applications*, eds. D. Braga and F. Grepioni, Wiley-VCH Verlang GmbH & Co., Weinhiem, Germany, 2007, ch. 2.5.
48. J. J. Novoa, E. D'Oria and M. A. Carvajal, in *Making crystals by design: methods, techniques and applications*, eds. D. Braga and F. Grepioni, Wiley-VCH Verlang GmbH & Co., Weinhiem, Germany, 2007, ch. 1.2.
49. P. Atkins, T. Overton, J. Rourke, M. T. Weller and F. Armstrong, *Inorganic Chemistry*, Oxford University Press, Oxford, 5th edn., 2010.
50. O. Almarsson and M. J. Zaworotko, *Chem. Commun.* , 2004, 1889-1896.
51. G. R. Desiraju, *Nature*, 2001, **412**, 397-400.
52. G. A. Jeffery, *An Introduction to Hydrogen Bonding*, Oxford University Press, New York, 1st edn., 1997.
53. R. Paulini, K. Muller and F. Diederich, *Angewandte Chemie International Edition*, 2005, **44**, 1788-1805.
54. P. Metrangolo, H. Neukirch, T. Pillati and G. Resnati, *Acc. Chem. Res.*, 2005, **38**, 386-395.
55. C. B. Aakeröy and D. J. Salmon, *CrystEngComm*, 2005, **7**, 439-448.
56. M. C. Etter, *Acc. Chem. Res.*, 1990, **23**, 120-126.
57. P. H. Stahl and B. Sutter, in *Polymorphism in the pharmaceutical industry*, ed. R. Hilfiker, Wiley-VCH Verlang GmbH & Co., Weinhiem, Germany, 2006, ch. 12.
58. L. Fabian, *Cryst. Growth Des.*, 2009, **9**, 1436-1443.
59. C. R. Groom, I. J. Bruno, M. P. Lightfoot and S. C. Ward, *Acta Cryst., Sect. B: Struct. Sci.* , 2016, **72**, 171-179.
60. P. A. Wood, N. Feeder, M. Furlow, P. T. A. Galek, C. R. Groom and E. Pidcock, *CrystEngComm*, 2014, **16**, 5839-5848.
61. R. Hilfiker and S. M. De Paul, in *Polymorphism in the pharmaceutical industry*, ed. R. Hilfiker, Wiley-VCH Verlang GmbH & Co., Weinhiem, Germany, 2006, ch. 11.
62. D. Braga and J. Bernstein, in *Making crystals by design: methods, techniques and applications*, eds. D. Braga and F. Grepioni, Wiley-VCH Verlang GmbH & Co., Weinhiem, Germany, 2007.
63. J. Bauer, S. Spanton, R. Henry, J. Quick, W. Dziki, W. Porter and J. Morris, *Pharm. Res.*, 2001, **18**, 859-866.
64. P. W. Cains, in *Polymorphism in Pharmaceutical Solids*, ed. H. G. Brittain, Informa Healthcare USA, Inc., New York, 2009.
65. D. Q. M. Craig, in *Polymorphism in the pharmaceutical industry*, ed. R. Hilfiker, Wiley-VCH Verlang GmbH & Co., Weinhiem, Germany, 2006, ch. 3.
66. J. M. Chalmers and G. Dent, in *Polymorphism in the pharmaceutical industry*, ed. R. Hilfiker, Wiley-VCH Verlang GmbH & Co., Weinhiem, Germany, 2006, ch. 5.

67. P. Ochsenbein and K. J. Schenk, in *Polymorphism in the pharmaceutical industry*, ed. R. Hilfiker, Wiley-VCH Verlang GmbH & Co., Weinhiem, Germany, 2006.
68. S. Bhattacharya, H. G. Brittain and R. Suryanarayanan, in *Polymorphism in Pharmaceutical Solids*, ed. H. G. Brittain, Informa Healthcare USA, Inc., New York, 2nd edn., 2009, ch. 9, pp. 318-346.
69. A. T. M. Serajuddin and M. Pudipeddi, in *Handbook of pharmaceutical salts: properties, selection and use*, eds. P. H. Stahl and C. G. Wermuth, Wiley-VCH Verlang GmbH & Co., Weinhiem, Germany, 2008, ch. 6.
70. M. Malamatari, S. A. Ross, D. Douroumis and S. P. Velaga, *Adv. Drug Deliv. Rev.*, 2017, **117**, 162-177.
71. M. J. Bowker, in *Handbook of pharmaceutical salts: properties, selection and use*, eds. P. H. Stahl and C. G. Wermuth, Wiley-VCH Verlang GmbH & Co., Weinhiem, Germany, 2008, ch. 7.
72. P. Desrosiers, E. Carlson, W. Chandler, H. Chau, P. Cong, R. Doolen, C. Freitag, S. Lin, C. Masui, E. Wu, T. Crevier, D. Mullins, L. Song, R. Lou, J. Zhan, A. Tangkilisan, Q. Ung and K. Phan, *Acta Cryst., Sect. A: Found. Crystallogr.*, 2002, **58**, 10-15.
73. N. Blagden, D. J. Berry, A. Parkin, H. Javed, A. Ibrahim, P. T. Gavan, L. L. De Matos and C. C. Seaton, *New J. Chem.*, 2008, **32**, 1659-1672.
74. H. G. Brittain, in *Polymorphism in Pharmaceutical Solids*, ed. H. G. Brittain, Informa Healthcare USA, Inc., New York, 2nd edn., 2009, ch. 2, pp. 24-51.
75. H. Lorenz, in *Crystallization: Basic concepts and industrial applications*, ed. W. Beckmann, Wiley-VCH Verlang GmbH & Co., Weinhiem, Germany, 2013, ch. 3.
76. P. Atkins and J. de Paula, *Physical Chemistry*, Oxford University Press, Oxford, 2010.
77. G. Coquerel, *Chem. Soc. Rev.*, 2014, **43**, 2286-2300.
78. Y. Yan, J.-M. Chen and T.-B. Lu, *CrystEngComm*, 2015, **17**, 612-620.
79. F. C. Wang, F. Peyronel and A. G. Marangoni, *Cryst. Growth Des.*, 2016, **16**, 297-306.
80. X. Sun, Q. Yin, S. Ding, Z. Shen, Y. Bao, J. Gong, B. Hou, H. Hao, Y. Wang, J. Wang and C. Xie, *J. Chem. Eng. Data*, 2015, **60**, 1166-1172.
81. H.-H. Tung, E. L. Paul, M. Midler and J. A. McCauley, *Crystallization of organic compounds: An industrial perspective*, John Wiley & Sons, Inc., New Jersey, 2009.
82. S. Boyd, K. Back, K. Chadwick, R. J. Davey and C. C. Seaton, *J. Pharm. Sci.*, 2010, **99**, 3779-3786.
83. C. Guo, J. Wang, J. Li, Z. Wang and S. Tang, *J. Phys. Chem. Lett.*, 2016, **7**, 5008-5014.
84. D. Erdemir, A. Y. Lee and A. S. Myerson, *Acc. Chem. Res.*, 2009, **42**, 621-629.
85. L. Tan, R. M. Davis, A. S. Myerson and B. L. Trout, *Cryst. Growth Des.*, 2015, **15**, 2176-2186.
86. P. L. D. Wildfong, in *Polymorphism in Pharmaceutical Solids*, ed. H. G. Brittain, Informa Healthcare USA, Inc., New York, 2009, pp. 510-559.
87. J. F. B. Black, P. T. Cardew, A. J. Cruz-Cabeza, R. J. Davey, S. E. Gilks and R. A. Sullivan, *CrystEngComm*, 2018, **20**, 768-776.
88. A. R. Klapwijk, E. Simone, Z. K. Nagy and C. C. Wilson, *Cryst. Growth Des.*, 2016, **16**, 4349-4359.
89. D. J. Weyna, T. Shattock, P. Wishweshwar and M. J. Zaworotko, *Cryst. Growth Des.*, 2009, **9**, 1106-1123.
90. K. E. Wittering, J. King, L. H. Thomas and C. C. Wilson, *Crystals*, 2014, **4**, 123-140.
91. S. Jiang, P. J. Jansens and J. H. ter Horst, *Cryst. Growth Des.*, 2010, **10**, 2541-2547.
92. W. Beckmann, in *Crystallization: Basic concepts and industrial applications*, ed. W. Beckmann, Wiley-VCH Verlang GmbH & Co., Weinhiem, Germany, 1st edn., 2013, ch. 9.
93. E. Aamir, Z. K. Nagy and C. D. Rielly, *Chem. Eng. Sci.*, 2010, **65**, 3602-3614.
94. N. Sanzida and Z. K. Nagy, *Comput. Chem. Eng.*, 2013, **59**, 111-121.
95. T. Rager and R. Hilfiker, *Cryst. Growth Des.*, 2010, **10**, 3237-3241.
96. H. Abourahma, D. D. Shah, J. Melendez, E. J. Johnson and K. T. Holman, *Cryst. Growth Des.*, 2015, **15**, 3101-3104.
97. A. Delori, T. Friščić and W. Jones, *CrystEngComm*, 2012, **14**, 2350-2362.

98. S. L. James, C. J. Adams, C. Bolm, D. Braga, P. Collier, T. Friscic, F. Grepioni, K. D. Harris, G. Hyett, W. Jones, A. Krebs, J. Mack, L. Maini, A. G. Orpen, I. P. Parkin, W. C. Shearouse, J. W. Steed and D. C. Waddell, *Chem. Soc. Rev.*, 2012, **41**, 413-447.
99. A. V. Trask, N. Shan, W. D. Motherwell, W. Jones, S. Feng, R. B. Tan and K. J. Carpenter, *Chem. Commun.*, 2005, 880-882.
100. J. A. Fernandes, M. Sardo, L. Mafra, D. Choquesillo-Lazarte and N. Masciocchi, *Cryst. Growth Des.*, 2015, **15**, 3674-3683.
101. D. Hasa, E. Miniussi and W. Jones, *Cryst. Growth Des.*, 2016, **16**, 4582-4588.
102. T. Friscic and W. Jones, *Cryst. Growth Des.*, 2009, **9**, 1621-1637.
103. A. M. Belenguer, G. I. Lampronti, A. J. Cruz-Cabeza, C. A. Hunter and J. K. M. Sanders, *Chem. Sci.*, 2016, **7**, 6617-6627.
104. R. P. Rastogi and N. B. Singh, *J. Phys. Chem.* , 1968, **72**, 4446-4449.
105. K. Chadwick and R. J. Davey, *CrystEngComm*, 2007, **9**, 732-734.
106. A. Jayasankar, Z. J. Somwangthanaroj and N. Rodrigues-Hornedo, *Pharm. Res.*, 2006, **23**.
107. E. Sangtani, S. K. Sahu, S. H. Thorat, R. L. Gawade, K. K. Jha, P. Munshi and R. G. Gonnade, *Cryst. Growth Des.*, 2015, **15**, 5858-5872.
108. D. Braga, L. Maini and F. Grepioni, *Chem. Soc. Rev.*, 2013, **42**, 7638-7648.
109. D. Wieckhusen, in *Crystallization: Basic concepts and industrial applications*, ed. W. Beckmann, Wiley-VCH Verlag GmbH &Co., Weinhiem, Germany, 1st edn., 2013, ch. 10.
110. T. McGlone, N. E. B. Briggs, C. A. Clark, C. J. Brown, J. Sefcik and A. J. Florence, *Org. Process Res. Dev.*, 2015, **19**, 1186-1202.
111. S. Lawton, G. Steele and P. Shering, *Org. Process Res. Dev.*, 2009, **13**, 1357-1363.
112. K. Plumb, *Chemical Engineering Research and Design*, 2005, **83**, 730-738.
113. J. C. Pastre, D. L. Browne and S. V. Ley, *Chem. Soc. Rev.*, 2013, **42**, 8849-8869.
114. A. M. Sahlodin and P. I. Barton, *Ind. Eng. Chem. Res.*, 2015, **54**, 11344-11359.
115. G. Hofmann and C. Meiches, in *Crystallization: Basic concepts and industrial applications*, ed. W. Beckmann, Wiley-VCH Verlag GmbH & Co., Weinhiem, Germany, 1st edn., 2013, ch. 11.
116. J. Li, B. L. Trout and A. S. Myerson, *Org. Process Res. Dev.*, 2016, **20**, 510-516.
117. K. A. Powell, G. Bartolini, K. E. Wittering, A. N. Saleemi, C. C. Wilson, C. D. Rielly and Z. K. Nagy, *Cryst. Growth Des.*, 2015, **15**, 4821-4836.
118. S. Diab and D. I. Gerogiorgis, *Ind. Eng. Chem. Res.*, 2018, **57**, 9489-9499.
119. A. J. Alvarez and A. S. Myerson, *Cryst. Growth Des.*, 2010, **10**, 2219-2228.
120. L. R. Agnew, T. McGlone, H. P. Wheatcroft, A. Robertson, A. R. Parsons and C. C. Wilson, *Cryst. Growth Des.*, 2017, **17**, 2418-2427.
121. L. Zhao, V. Raval, N. E. B. Briggs, R. M. Bhardwaj, T. McGlone, I. D. H. Oswald and A. J. Florence, *CrystEngComm*, 2014, **16**, 5769-5780.
122. B. Ahmed, D. Barrow and T. Wirth, *Advanced Synthesis & Catalysis*, 2006, **348**, 1043-1048.
123. M. Su and Y. Gao, *Ind. Eng. Chem. Res.*, 2018, **57**, 3781-3791.
124. K. Robertson, P.-B. Flandrin, A. R. Klapwijk and C. C. Wilson, *Cryst. Growth Des.*, 2016, **16**, 4759-4764.
125. K. Robertson, P.-B. Flandrin, H. J. Shepherd and C. C. Wilson, *Chim. Oggi*, 2017, **35**, 19-22.
126. G. Nichols, in *Polymorphism in the pharmaceutical industry*, ed. R. Hilfiker, Wiley-VCH Verlang GmbH & Co., Weinhiem, Germany, 2006, ch. 7.
127. R. Hilfiker, in *Crystallization: Basic concepts and industrial applications*, ed. W. Beckmann, Wiley-VCH Verlang GmbH & Co., Weinhiem, Germany, 2013, ch. 8.
128. A. R. West, *Basic Solid State Chemistry*, John Wiley & Sons Ltd., Chichester, 3rd edn., 1996.
129. W. Clegg, *Crystal Structure Determination*, Oxford University Press, Oxford, 1998.
130. J. P. Eberhart, *Structural and chemical analysis of materials: X-ray, electron and neutron diffraction, X-ray, electron and ion spectrometry, electron microscopy*, John Wiley & Sons Ltd., Chichester, 1991.
131. M. Ermrich and D. Opper, *XRD for the analyst: getting acquainted with the principles*, PANalytical B.V., Almelo, The Netherlands, 2013.

132. G. M. Espallargas and L. Brammer, in *Making crystals by design: methods, techniques and applications*, eds. D. Braga and F. Grepioni, Wiley-VCH Verlang GmbH & Co., Weinhiem, Germany, 2007, ch. 3.1.
133. W. Clegg, in *X-ray Structure Analysis*, The 16th BCA/CCG Intensive Teaching School in X-ray Structure Analysis, Durham, UK, 2017.
134. H. G. Brittain, S. R. Byrn and E. Lee, in *Polymorphism in Pharmaceutical Solids*, ed. H. G. Brittain, Informa Healthcare USA, Inc., New York, 2nd edn., 2009, ch. 6, pp. 185-232.
135. R. Copley and H. J. Shepherd, in *X-ray Structure Analysis*, The 16th BCA/CCG Intensive Teaching School in X-ray Structure Analysis, Durham, UK, 2017.
136. W. Clegg, in *X-ray Structure Analysis*, The 16th BCA/CCG Intensive Teaching School in X-ray Structure Analysis, Durham, UK, 2017.
137. L. Palatinus, in *X-ray Structure Analysis*, The 16th BCA/CCG Intensive Teaching School in X-ray Structure Analysis, Durham, UK, 2017.
138. G. M. Sheldrick, *Acta Crystallogr., Sect. A: Found. Crystallogr.*, 2015, **71**, 3-8.
139. L. Palatinus, in *X-ray Structure Analysis*, The 16th BCA/CCG Intensive Teaching School in X-ray Structure Analysis, Durham, UK, 2017.
140. R. Cooper and S. Parsons, in *X-ray Structure Analysis*, The 16th BCA/CCG Intensive Teaching School in X-ray Structure Analysis, Durham, UK, 2017.
141. S. Parsons, in *X-ray Structure Analysis*, The 16th BCA/CCG Intensive Teaching School in X-ray Structure Analysis, Durham, UK, 2017.
142. R. Cooper, in *X-ray Structure Analysis*, The 16th BCA/CCG Intensive Teaching School in X-ray Structure Analysis, Durham, UK, 2017.
143. S. Parsons and W. Clegg, in *X-ray Structure Analysis*, The 16th BCA/CCG Intensive Teaching School in X-ray Structure Analysis, Durham, UK, 2017.
144. R. Copley and H. J. Shepherd, in *X-ray Structure Analysis*, The 16th BCA/CCG Intensive Teaching School in X-ray Structure Analysis, Durham, UK, 2017.
145. H. D. Flack and G. Bernardinelli, *Acta Cryst., Sect. A: Found. Crystallogr.*, 1999, **A55**, 908-915.
146. S. Parsons, in *X-ray Structure Analysis*, The 16th BCA/CCG Intensive Teaching School in X-ray Structure Analysis, Durham, UK, 2017.
147. D. L. Cruickshank, Y. Younis, N. M. Njuguna, D. S. B. Ongarora, K. Chibale and M. R. Caira, *CrystEngComm*, 2014, **16**, 5781-5792.
148. M. A. Elbagerma, H. G. M. Edwards, T. Munshi, M. D. Hargreaves, P. Matousek and I. J. Scowen, *Cryst. Growth Des.*, 2010, **10**, 2360-2371.
149. V. Nemec, N. Škvorc and D. Cinčić, *CrystEngComm*, 2015, **17**, 6274-6277.
150. D. E. Braun, M. Ardid-Candel, E. D'Oria, P. G. Karamertzanis, J.-B. Arlin, A. J. Florence, A. G. Jones and S. L. Price, *Cryst. Growth Des.*, 2011, **11**, 5659-5669.
151. H. Yamashita, Y. Hirakura, M. Yuda and K. Terada, *Pharm. Res.*, 2014, **31**, 1946-1957.
152. H. Yamashita, Y. Hirakura, M. Yuda, T. Teramura and K. Terada, *Pharm. Res.*, 2013, **30**, 70-80.
153. R. A. Castro, J. D. B. Ribeiro, T. M. R. Maria, M. R. Silva, C. Yuste-Vivas, J. Canotilho and M. E. S. Eusébio, *Cryst. Growth Des.*, 2011, **11**, 5396-5404.
154. D. J. Berry, C. C. Seaton, W. Clegg, R. W. Harrington, S. J. Coles, P. N. Horton, M. B. Hursthouse, R. Storey, W. Jones, T. Friscic and N. Blagden, *Cryst. Growth Des.*, 2008, **8**, 1697-1712.
155. L. M. Harwood and T. D. W. Claridge, *Introduction to Organic Spectroscopy*, Oxford Univeristy Press, Oxford, 1997.
156. B. Norden, A. Rodger and T. Daffron, *Linear Dichroism and Circular Dichroism*, RSC Publishing, 2010.
157. J. T. Vázquez, *Tetrahedron: Asymmetry*, 2017, **28**, 1199-1211.
158. M. Tao, Z. Wang, J. Gong, H. Hao and J. Wang, *Ind. Eng. Chem. Res.*, 2013, **52**, 3036-3041.
159. M. A. Reus, A. E. D. M. van der Heijden and J. H. ter Horst, *Org. Process Res. Dev.*, 2015, **19**, 1004-1011.
160. G. D. Maia and M. Giulietti, *J. Chem. Eng. Data*, 2008, **53**, 256-258.
161. J. H. ter Horst, M. A. Deij and P. W. Cains, *Cryst. Growth Des.*, 2009, **9**, 1531-1537.

162. E. Beetage, J. du Plessis, D. G. Muller, C. Googen and F. J. van Rensburg, *Int. J. Pharm.*, 2000, **193**, 261-264.
163. B. Hachula, *Spectrochim. Acta, Part A*, 2018, **188**, 189-196.
164. S. M. Sondhi, S. Rajuanshi, N. Singh, S. Jain and A. M. Lahsti, *Cent. Eur. J. Chem.*, 2004, **2**, 141-187.
165. N. U. Y. Okur, A.; Karasulu, H. Y., *Chem. Pharm. Bull.*, 2014, **62**, 135–143.
166. D. Bolten, R. Lietzow and M. Türk, *Chem. Eng. Tech.*, 2013, **36**, 426-434.
167. L. Liu and H. Gao, *Spectrochim. Acta, Part B.*, 2012, **86**, 131-138.
168. L. Dupont, B. Pirotte, P. De Tullio and J. Delarge, *Acta Cryst.*, 1996, **C52**, 393-395.
169. M. D. King, W. D. Buchanan and T. M. Korter, *Phys. Chem. Chem. Phys.*, 2011, **13**, 4250-4259.
170. K. Ravikumar, S. S. Rajan and V. Pattabhi, *Acta. Cryst.*, 1985, **C41**, 280-282.
171. G.-M. Tang, J.-H. Wang, C. Zhao, Y.-T. Wang, Y.-Z. Cui, F.-Y. Cheng and S. W. Ng, *CrystEngComm*, 2015, **17**, 7258-7261.
172. W. L. Noorduin, B. Kaptein, H. Meekes, W. J. P. van Enchevort, R. M. Kellogg and E. Vlieg, *Angew. Chem. Int. Ed.*, 2009, **48**, 4581-4583.
173. S. Ando, J. Kikuchi, Y. Fujimura, Y. Ida, K. Higashi, K. Moribe and K. Yamamoto, *J. Pharm. Sci.*, 2012, **101**, 3214-3221.
174. Y. Kobayashi, K. Kinbara, M. Sato and K. Saigo, *Chirality*, 2005, **17**, 108-112.
175. C. Neurohr, M. Marchivie, S. Lecomte, Y. Cartigny, N. Couvrat, M. Sanselme and P. Subra-Paternault, *Cryst. Growth Des.*, 2015, **15**, 4616-4626.
176. K. Manoj, R. Tamura, H. Takahashi and H. Tsue, *CrystEngComm*, 2014, **16**, 5811-5819.
177. S. W. Zhang and Å. C. Rasmuson, *CrystEngComm*, 2012, **14**, 4644-4655.
178. F. Fischer, G. Scholz, L. Batzdorf, M. Wilke and F. Emmerling, *CrystEngComm*, 2015, **17**, 824-829.
179. M. Schmidtmann, D. S. Middlemiss and C. C. Wilson, *CrystEngComm*, 2015, **17**, 5273-5279.
180. Y. Zhou, F. Guo, C. E. Hughes, D. L. Browne, T. R. Peskett and K. D. M. Harris, *Crystal Growth & Design*, 2015, **15**, 2901-2907.
181. J. L. Derissen and P. H. Smit, *Acta Cryst.*, 1974, **B30**, 2240-2242.
182. N. Okazaki and E. Takemura, *Bull. Chem. Soc. Jpn.*, 1961, **34**, 977-982.
183. H. Tanaka, *J. Therm. Anal.*, 1984, **29**, 1115-1122.
184. L. A. Pinck and M. A. Kelly, *J. Am. Chem. Soc.*, 1925, **47**, 2170-2172.
185. M. K. Singh, *CrystEngComm*, 2015, **17**, 7731-7744.
186. M. K. Singh and V. S. Tiwari, *Cryst. Growth Des.*, 2015, **15**, 3220-3234.
187. K. Roszak and A. Katrusiak, *J. Phys. Chem. C*, 2017, **121**, 778-784.
188. L. H. Dalman, *J. Am. Chem. Soc.*, 1934, **56**, 549-553.
189. S. Harkema, J. W. Bats, A. M. Weyenberg and D. Feil, *Acta Cryst., Sect. B: Struct. Sci.* , 1972, **B28**, 1646-1648.
190. S. Harkema and J. H. M. ter Brake, *Acta Cryst., Sect. B: Struct. Sci.* , 1979, **B35**, 1011-1013.
191. Y. Feng, L. Dang and H. Wei, *Cryst. Growth Des.*, 2012, **12**, 2068-2078.
192. O. Onija, G. Borodi, I. Kacso, M. N. Pop, D. Dadarlat, I. Bratu, N. Jumate and M. D. Lazar, *AIP Conf. Proc.*, 2012, **1425**, 35-38.
193. V. Chithambaram, S. Jerome Das, S. Krishnan, M. Basheer Ahamed and R. Arivudai Nambi, *Eur. Phys. J. Appl. Phys.*, 2013, **64**, 20201.
194. I. J. Bruno, J. C. Cole, P. R. Edgington, M. Kessler, C. F. Macrae, P. McCabe, J. Pearson and R. Taylor, *Acta Cryst.*, 2002, **B58**, 389-397.
195. O. V. Dolomanov, L. J. Bourhis, R. J. Gildea, J. A. K. Howard and H. Puschmann, *J. Appl. Crystallogr.*, 2009, **42**, 339-341.
196. G. M. Sheldrick, *Acta Cryst., Sect. A: Found. Crystallogr.*, 2008, **64**, 112-122.
197. G. M. Sheldrick, *Acta Crystallogr., Sect. C: Cryst. Struct. Commun.*, 2015, **71**, 3-8.
198. S. K. Nechipadappu and D. R. Trivedi, *J. Mol. Struct.*, 2017, **1141**, 64-74.
199. M. Chao, E. Schempp and R. D. Rosenstein, *Acta Cryst.*, 1975, **B31**, 2922-2294.
200. J. Scheinbeim and E. Schempp, *Acta Cryst.*, 1976, **B32**, 607-609.
201. C. Zhou, Y. Jin, J. R. Kenseth, M. Stella, K. R. Wehmeyer and W. R. Heineman, *J. Pharm. Sci.*, 2005, **94**, 576-589.

202. W. W. Fu, Y. Liu, G. Huang and X. M. Zhu, *Acta Crystallogr., Sect. E: Struct. Rep. Online*, 2013, **69**, o32.
203. D. A. Adsmond, A. t. S. Sinha, U. B. R. Khandavilli, A. R. Maguire and S. E. Lawrence, *Cryst. Growth Des.*, 2016, **16**, 59-69.
204. Z.-N. Hu, H.-B. Yang, H. Luo and B. Li, *Acta Crystallogr., Sect. E: Struct. Rep. Online*, 2011, **67**, 1138-1142.
205. D. Rasala, *Bull. Soc. Chim. Fr.*, 1992, **5**.
206. M. Pourayoubi, S. Ghadimi and A. A. Ebrahimi Valmoozi, *Acta Crystallogr., Sect. E: Struct. Rep. Online*, 2007, **63**, 4631-4637.
207. M. Hemamalini, W.-S. Loh, C. K. Quah and H.-K. Fun, *Chem. Cen. J.*, 2014, **8**, 1-9.
208. D. Paliwoda, K. F. Dziubek and A. Katrusiak, *Cryst. Growth Des.*, 2012, **12**, 4302-4305.
209. H. Walba and R. W. Isensee, *J. Org. Chem.*, 1961, **26**, 2789-2791.
210. W. Zieliński and A. Katrusiak, *Cryst. Growth Des.*, 2012, **13**, 696-700.
211. E. Schur, J. Bernstein, A. Lemmerer and R. Vainer, *Acta Crystallogr., Sect. E: Struct. Rep. Online*, 2011, **67**, o2761.
212. X. Mei and C. Wolf, *Cryst. Growth Des.*, 2004, **4**, 1099-1103.
213. F. H. Herbstein and G. M. J. Schmidt, *Acta Cryst.*, 1955, **8**, 399-405.

List of Appendices Figures

List of Appendices Tables

Appendix (A3) Chapter 3

Table A3. 1 - CSD search for single and multi-component materials of *NPX*, highlighting crystallographic parameters

	Comments (and related structures)	CSD reference code	a (Å)	b (Å)	c (Å)	α (º)	β (º)	γ (º)	Space group	Collection temperature (K)	Formula	Secondary species name
1	L-co-former + *rsNPX* monohydrate (BEYTUW)	BEXGUI	13.122	5.898	24.075	90	95.56	90	$P2_1$	293	C14 H14 O3 C5 H9 N1 O2 H2 O1	**Pyrrolidinium-2-carboxylate monohydrate**
2	DL-co-former + *rsNPX* monhydrate (BEXGUI)	BEYTUW	6.1054	12.475	49.1664	90	90	90	*P*bca	293	C14 H14 O3 C5 H9 N1 O2 H2 O1	**Pyrrolidinium-2-carboxylate monohydrate**
3		COYRUD	13.315	5.7765	7.8732	90	93.88	90	$P2_1$	295	C14 H14 O3	
4		COYRUD01	7.855	5.783	13.349	90	93.9	90	$P2_1$	295	C14 H14 O3	
5	*sNPX*	COYRUD11	13.375	5.793	7.914	90	93.91	90	$P2_1$	295	C14 H14 O3	**N/A**
6		COYRUD12	7.7354	5.7181	13.3641	90	93.737	90	$P2_1$	102	C14 H14 O3	
7		COYRUD13	7.8759	5.7834	13.323	90	93.877	90	$P2_1$	298	C14 H14 O3	
8		COYRUD14	7.7162	5.7022	13.371	90	93.73	90	$P2_1$	100	C14 H14 O3	
9	Co-former + *sNPX* (1:2)	COZYAS	5.7645	7.607	19.109	84.851	83.797	89.241	*P*1	100	2(C14 H14 O3) C12 H10 N2	**trans-1,2-bis(4-pyridyl)ethene**
10	R-co-former + *sNPX*	DEQYIH	11.1692	6.3276	12.898	90	93.33	90	$P2_1$	295	C14 H13 O3 1- C5 H14 N1 1+	**R-3-Methyl-2-butylammonium**
11	Co-former + *sNPX* monohydrate	EZEKUP	12.568	11.93	16.956	90	102.4	90	$P2_1$	295	C23 H32 N4 O1 2(C14 H14 O3) C3 H8 O1 H2 O1	**Allyl-terguride 2-propanol solvate monohydrate**
12	R-co-former + *sNPX* (FEVZUD)	FEVZOX	5.7713	6.252	23.8346	90	92.047	90	$P2_1$	293	C14 H14 O3 C5 H9 N1 O2	**(R)-pyrrolidinium-2-carboxylate**
13	S-co-former + *sNPX* (FEVZOX)	FEVZUD	5.6999	6.5428	23.1874	90	94.835	90	$P2_1$	293	C14 H14 O3 C5 H9 N1 O2	**(S)-pyrrolidinium-2-carboxylate**

14	Co-former + *sNPX*	FIWYUH	15.9309	6.3941	18.8138	90	107.606	90	$P2_1$	296	C14 H13 O3 1- C6 H14 N1 1+	**Cyclohexanaminium**
15	Co-former + *sNPX*	FIWZOC	11.632	5.9372	13.377	90	90.327	90	$P2_1$	296	C7 H10 N1 1+ C14 H13 O3 1-	**Benzylammonium**
16	Co-former + *sNPX*	FIWZUI	5.7688	8.478	48.065	90	90	90	$P2_12_12_1$	296	C14 H16 N1 1+ C14 H13 O3 1-	**Dibenzylammonium**
17	Co-former + *sNPX*	GIPTIJ	9.5594	5.8786	29.704	90	96.345	90	$P2_1$	293	C5 H6 N1 1+ C14 H13 O3 1-	**Pyridinium**
18	Co-former + *sNPX* (JULEH) 1:2	HEGGAD	5.96338	15.1283	32.5411	90	90	90	$P2_12_12_1$	223	2(C14 H14 O3) C6 H6 N2 O1	**Nicotinamide**
19		HEGGAD01	5.96338	15.1283	32.5411	90	90	90	$P2_12_12_1$	223	2(C14 H14 O3) C6 H6 N2 O1	
20	R-co-former + *sNPX*	HIFRIX	11.6395	5.9814	13.6907	90	94.462	90	$P2_1$	295	C8 H12 N1 1+ C14 H13 O3 1-	**(R)-1-Phenylethylammonium**
21	S-co-former + *sNPX* (QANPEB)	JASHOB	14.662	9.225	17.129	90	113.865	90	*C*2	295	C6 H15 N4 O2 1+ C14 H13 O3 1-	**(S)-Arginine**
22	Co-former + *rsNPX* (HEGGAD) 1:2	JULJEH	16.0822	5.7965	32.892	90	99.314	90	$P2_1/c$	293	2(C14 H14 O3) C6 H6 N2 O1	**Nicotinamide**
23	D-co-former + *sNPX*	MICFEJ	6.1246	8.7821	27.1377	92.707	95.925	90.101	*P*1	295	C14 H14 O3 C14 H31 N1 O5	**N-octyl-D-(-)-glucamine**
24	Co-former + *sNPX* hemihydrate (PAMPIF polymorph)	NABMAH	26.87	5.4794	15.955	90	102.335	90	*C*2	200	C13 H14 N1 O1 1+ C14 H13 O3 1- 0.5(H2 O1)	**(2-hydroxyphenyl)(phenyl) hemihydrate**
25	S,S-co-former + *sNPX*	OKIQAA	12.32	5.854	13.929	90	97.971	90	$P2_1$	293	C9 H12 N1 O1 1+ C14 H13 O3 1-	**(1S,2S) -trans-1-Aminoindan-2-ol**
26	Co-former + *sNPX* hemihydrate (NABMAH polymorph)	PAMPIF	23.818	5.5862	15.671	90	113.803	90	*C*2	150	C8 H12 N1 O1 1+ C14 H13 O3 1- 0.5(H2 O1)	**(S)-1-(2-hydroxyphenyl) ethanaminium hemihydrate**
27	Co-former + *sNPX*	PAMQAX	5.8146	6.2269	49.37	90	90.531	90	$P2_1$	293	C14 H14 O3 C6 H6 N2 O1	**Isonicotinamide**
28	*rsNPX*	PAPTUX	25.8301	15.4939	5.9465	90	90	90	*P*bca	298	C14 H14 O3	**N/A**
29	Co-former + *sNPX*	POPVAR	5.8526	16.166	26.694	90	90	90	$P2_12_12_1$	295	C14 H19 N2 O2 S1 1+ C14 H13 O3 1-	**6-Phenylsulfonyl-10-aza-2-azoniabicyclo(4.4.0)dec-1-ene**

30	S-co-former + *sNPX* (JASHOB)	QANPEB	9.145	9.145	43.307	90	90	120	$P3_221$	295	C6 H15 N4 O2 1+ C14 H13 O3 1-	**(S)-Arginine**
31	S-co-former + *sNPX* (RODSIO)	RODSEK	5.05836	7.1121	45.2723	90	90	90	$P2_12_12_1$	100	C14 H14 O3 C3 H7 N1 O2	**(S)-2-Aminopropionic acid**
32	R-co-former + *sNPX* (RODSEK)	RODSIO	5.3366	6.9013	44.227	90	90	90	$P2_12_12_1$	150	C14 H14 O3 C3 H7 N1 O2	**(R)-2-Aminopropionic acid**
33	R-co-former + *sNPX* monohydrate	RODSOU	5.88418	11.3844	34.6863	90	90	90	$P2_12_12_1$	150	C14 H14 O3 C11 H12 N2 O2 H2 O1	**(2R)-2-amino-3-(1H-indol-3-yl)propanoic acid monohydrate**
34	R-co-former + *sNPX*	RODSUA	9.4508	5.9725	18.9525	90	103.814	90	$P2_1$	295	C14 H14 O3, C9 H11 N1 O3	**(R)-2-Amino-3-(4-hydroxyphenyl)propanoic acid**
35	Co-former + *sNPX*	SAJCOY	5.3048	31.891	10.508	90	98.184	90	$P2_1$	120	C14 H14 O3 C6 H6 N2 O1	**Pyridine-2-carboxamide**
36	Co-former + *sNPX* monohydrate	TAMDAP	10.0057	5.9515	15.3212	90	99.389	90	$P2_1$	296	C14 H13 O3 1- C5 H7 N2 1+ H2 O1	**4-aminopyridinium monohydrate**
37	Co-former + *sNPX*	TAMDET	9.7396	6.11	14.6168	90	95.383	90	$P2_1$	296	C5 H7 N2 1+ C14 H13 O3 1-	**2-aminopyridinium**
38	R,S-co-former + *sNPX* monohydrate IPA	TERYEU	12.688	11.894	16.876	90	101.78	90	$P2_1$	295	C23 H31 N4 O1 1+ C14 H13 O3 1- C14 H14 O3 C3 H8 O1 H2 O1	**(+)-(5R,8S)-1-Allyl-9,10-didehydro-8-(N',N'-diethylureido)-6-methylergolin-6-ium isopropanol solvate monohydrate**
39	Co-former + *rsNPX* (TOBMAA) (1:2)	TOBLUT	7.624	5.8	36.02	90	90.017	90	$P2_1/c$	173	2(C14 H14 O3) C10 H8 N2	**4,4'-bipyridine**
40	Co-former + *sNPX* (TOBLUT) (1:2)	TOBMAA	15.206	5.766	19.37	90	111.189	90	$P2_1$	173	2(C14 H14 O3) C10 H8 N2	
41	Co-former + *sNPX* (TOBMII) (1:2)	TOBMEE	7.966	6.012	28.985	90	91.739	90	$P2_1/c$	173	2(C14 H14 O3) C4 H10 N2	**Piperazine**
42	Co-former + *sNPX* (TOBMEE) (1:2)	TOBMII	8.029	6.118	28.045	90	93.99	90	$P2_1$	173	2(C14 H14 O3) C4 H10 N2	
43	S,S-co-former + *sNPX*	YALWEO	5.301	15.006	28.421	90	90	90	$P2_12_12_1$	298	C13 H14 N1 O1 1+ C14 H13 O3 1-	**(1S,2S)-trans-1-Aminobenz[f]indan-2-ol**
44	Co-former + *sNPX*	YOCZUL	8.538	10.596	6.815	106.84	108.6	99.84	$P1$	295	C14 H14 O3 C10 H2 N4	**1,2,4,5-tetracyanobenzene**
45	Co-former + *sNPX*	ZIFQOU	15.179	21.407	27.67	90	90	90	$P2_12_12_1$	258	C63 H112 O35 C14 H14 O3	**heptakis(2,3,6-Tri-O-methyl)-beta-cyclodextrin**

46	Co-former + *sNPX*	TEQCAW	6.312	8.531	33.196	90	90	90	$P2_12_12_1$	296	C14 H13 O3 1- C4 H12 N1 O3 1+	**1,3-dihydroxy-2-(hydroxymethyl)propan-2-aminium**
47	Co-former + *rNPX*	TEQDIF	9.239	6.523	14.92	90	101.94	90	$P2_1$	120	C14 H13 O3 1- C4 H12 N1 1+	**2-methylpropan-2-aminium**
48	R-co-former + *sNPX*	NIFGOB	9.978	6.0394	16.685	90	101.711	90	$P2_1$	90	C14 H13 O3 1- C9 H14 N1 1+	**1-(4-methylphenyl)ethan-1-aminium**

Table A3. 2 - Unit cell parameters of the *OAD* and the polymorphs of *OA* (α and β) and *U* (I, III and IV)

Material	**CSD reference code**	**a (Å)**	**b (Å)**	**c (Å)**	**α (º)**	**β (º)**	**γ (º)**	**Volume (Å^3)**	**Space group**
Oxalic acid (*OA*-α)	OXALAC03	6.548(5)	7.844(5)	6.086(5)	90	90	90	312.592	*P*bca
Oxalic acid (*OA*-β)	OXALAC04	5.330(4)	6.015(5)	5.436(4)	90	115.83(3)	90	156.866	$P2_1$/c
Oxalic acid dihydrate (*OAD*)	OXACDH01	6.102(<1)	3.497(<1)	11.959(<1)	90	105.77(<1)	90	245.612	$P2_1$/n
Urea (*U*-I)	UREAXX30	5.638(4)	5.638(4)	4.714(3)	90	90	90	149.844	*P*–4 2_1 m
Urea (*U*-III)	UREAXX37	3.420(1)	8.145(3)	8.758(4)	90	90	90	243.969	$P2_12_12_1$
Urea (*U*-IV)	UREAXX38	3.408(<1)	7.363(<1)	4.648(1)	90	90	90	116.633	$P2_12_12$

Appendix (A5) Chapter 5

Table A5. 1 – The CIF files corresponding to the multi-component materials prepared during this research, found on the accompanying CD-ROM

File number	File name	Multi-component material
1	1_*sNPX_2AP*_11.cif	S-naproxen:2-aminopyridine (1:1) salt
2	2_*rsNPX_2AP*_11.cif	RS-naproxen:2-aminopyridine (1:1) salt
3	3_*sNPX_2APM*_21.cif	S-naproxen:2-aminopyrimidine (2:1) co-crystal
4	4_*sNPX_2APM*_11.cif	S-naproxen:2-aminopyrimidine (1:1) co-crystal
5	5_*rsNPX_2APM*_11.cif	RS-naproxen:2-aminopyrimidine (1:1) co-crystal
6	6_*sNPX_2ADMP*_11.cif	S-naproxen:2-amino-4,6-dimethylpyrimidine (1:1) co-crystal
7	7_*rsNPX_2ADMP*_11.cif	RS-naproxen:2-amino-4,6-dimethylpyrimidine (1:1) co-crystal
8	8_*sNPX_2A3CP*_11.cif	S-naproxen:2-amino-3-chloropyridine (1:1) co-crystal
9	9_*rsNPX_2A3CP*_11.cif	RS-naproxen:2-amino-3-chloropyridine (1:1) co-crystal
10	10_*sNPX_2A4CP*_21.cif	S-naproxen:2-amino-4-chloropyridine (2:1) salt
11	11_*rsNPX_2A4CP*_11.cif	RS-naproxen:2-amino-4-chloropyridine (1:1) co-crystal
12	12_*sNPX_2A5CP*_11.cif	S-naproxen:2-amino-5-chloropyridine (1:1) co-crystal
13	13_*rsNPX_2A5CP*_11.cif	RS-naproxen:2-amino-5-chloropyridine (1:1) co-crystal
14	14_*sNPX_2A6CP*_11.cif	S-naproxen:2-amino-6-chloropyridine (1:1) co-crystal
15	15_*sNPX*_I_21.cif	S-naproxen:imidazole (2:1) salt
16	16_*rsNPX*_I_21.cif	RS-naproxen:imidazole (2:1) salt
17	17_*sNPX*_BI_11.cif	S-naproxen:benzimidazole (1:1) co-crystal
18	18_*rsNPX*_BI_11.cif	RS-naproxen:benzimidazole (1:1) co-crystal
19	19_*sNPX*_A_11_FormI.cif	S-naproxen:acridine (1:1) co-crystal Form I
20	20_*sNPX*_A_11_FormII.cif	S-naproxen:acridine (1:1) co-crystal Form II
21	21_*sNPX*_A_23.cif	S-naproxen:acridine (2:3) co-crystal
22	22_*rsNPX*_A_11.cif	RS-naproxen:acridine (1:1) co-crystal

Appendix (A6) Chapter 6

A6.1 Characterisation of racemic and enantiopure naproxen

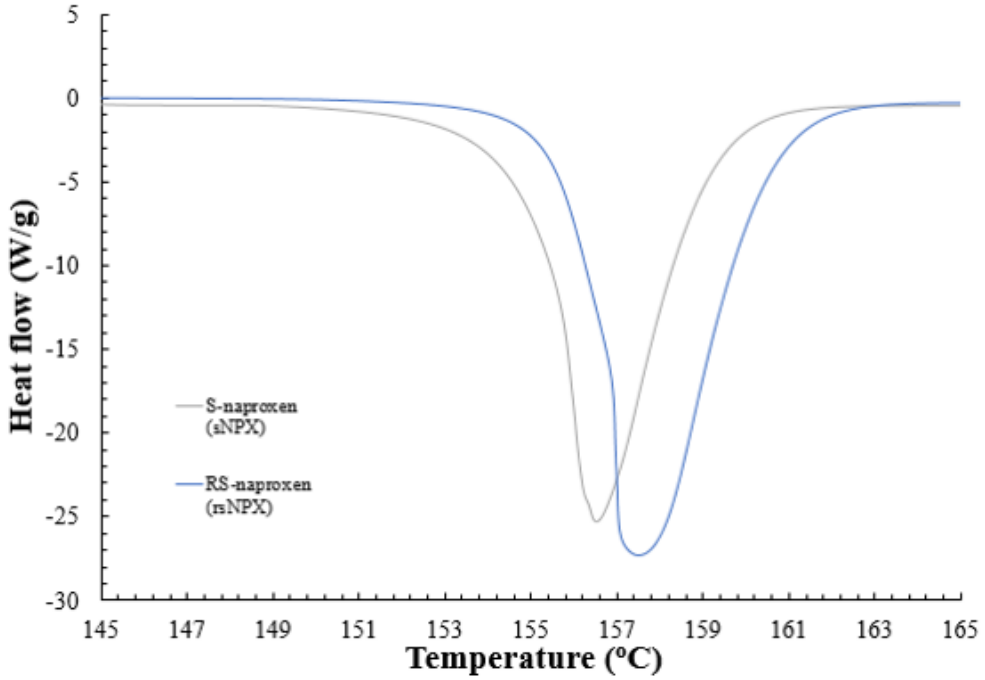

Figure A6. 1 - DSC traces for *sNPX* and *rsNPX*, highlighting the individual melting points for each composition

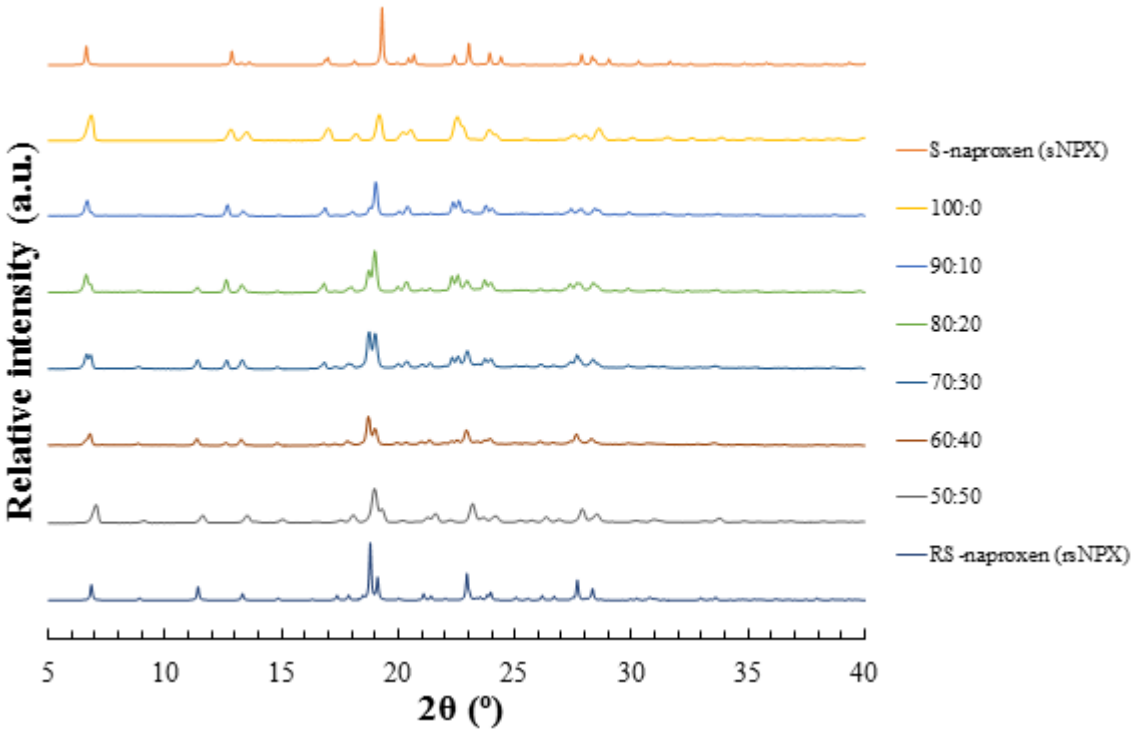

Figure A6. 2 - PXRD patterns, highlighting the change in phase from the racemic to the enantiopure *NPX*, with increasing molar contributions of *sNPX* (100:0, 90:10, 80:20, 70:30, 60:40, 50:50)

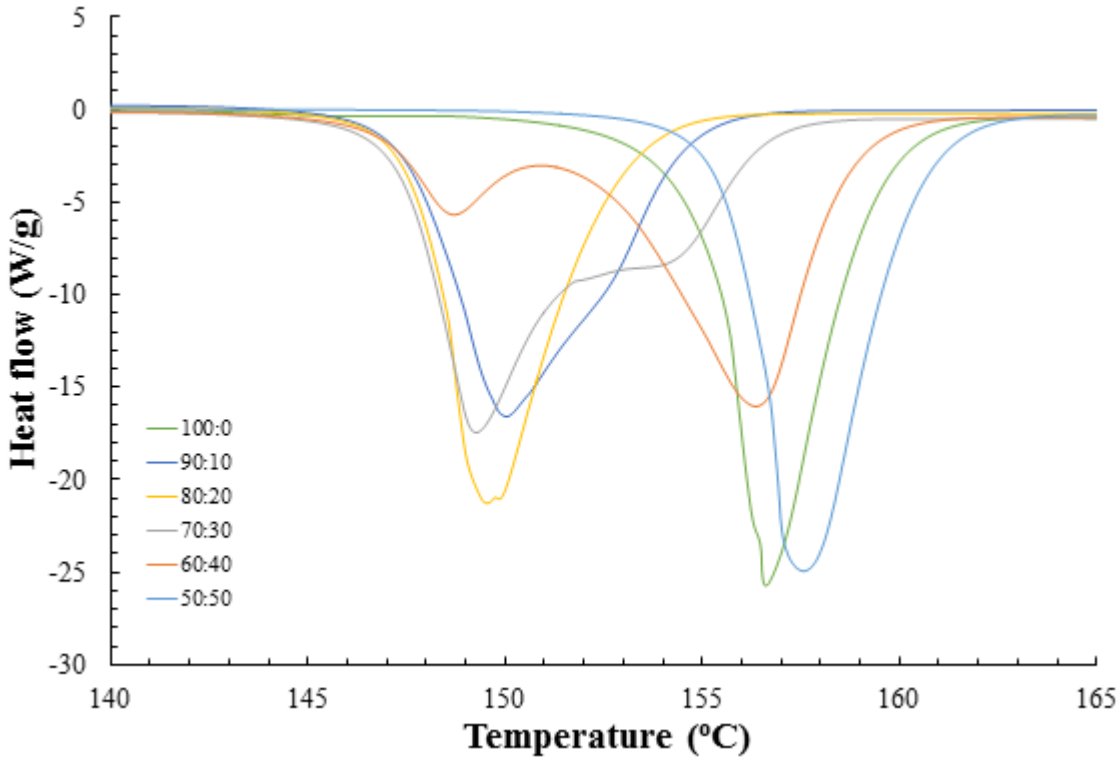

Figure A6. 3 - DSC traces, highlighting the change in phase from the racemic to the enantiopure *NPX*, with increasing molar contributions of *sNPX*

Table A6. 1 - Saturation of ethanol solutions with varying compositions of *sNPX* and *rNPX* (excess *sNPX*) at 20°C and 30°C, respectively, utilised for the construction of a ternary phase diagram

Mole fraction of *sNPX*	**Saturation of *NPX* at 20°C (mmol/mol)**	**Saturation of *NPX* at 30°C (mmol/mol)**
0.5	7.7	11.5
0.6	8.4	12.2
0.7	10.1	13.8
0.75	11.4	15.8
0.8	13.1	16.7
0.85	13.4	17.5
0.9	13.6	18.4
0.95	13.1	18.5
1.0	12.0	17.6

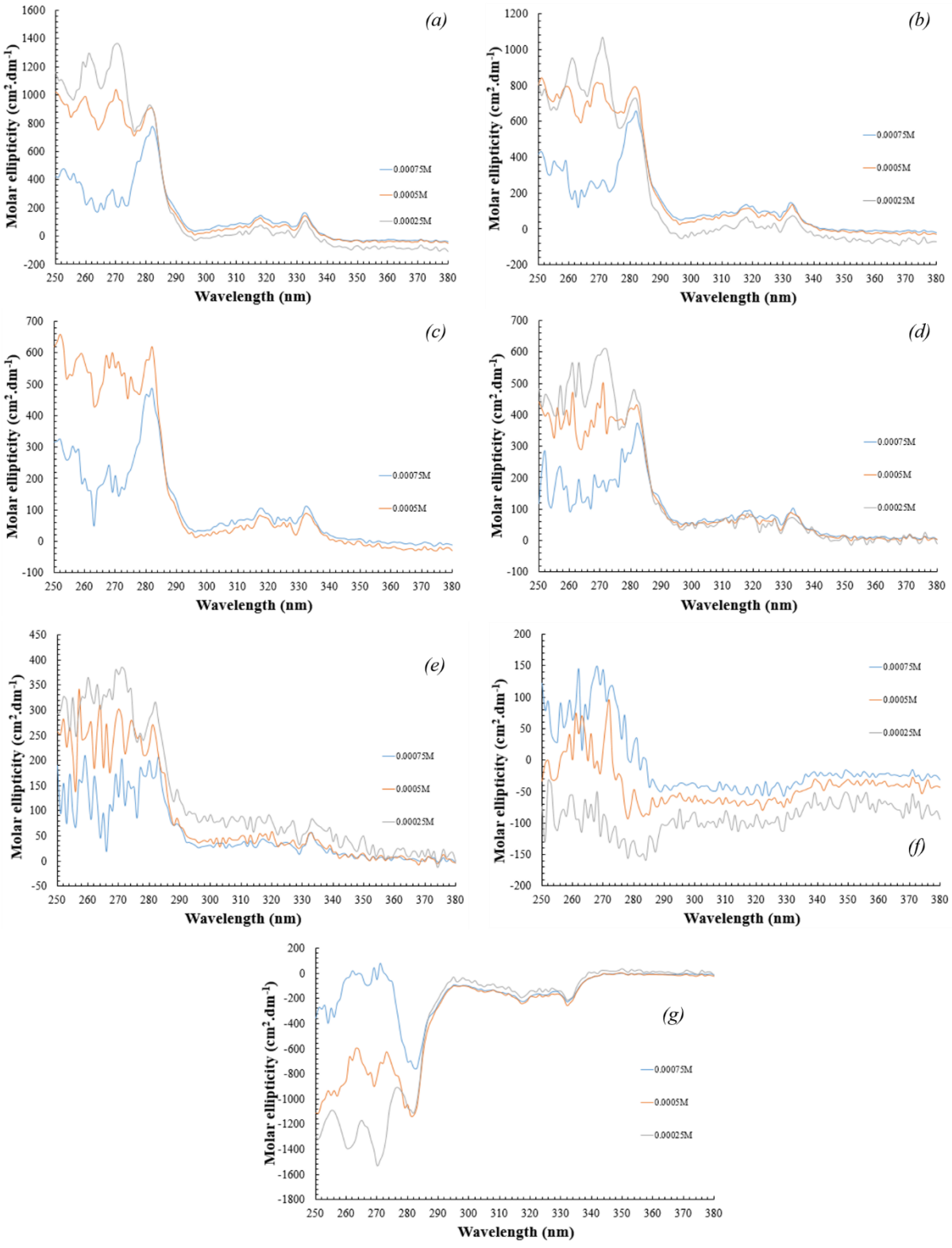

Figure A6. 4 - Molar ellipticity, taken over a range of wavelengths, for 0.75mM, 0.5mM and 0.25mM ethanol solutions of *NPX*, for different variations in the enantiomeric composition; (a) 1.0, (b) 0.9, (c) 0.8, (d) 0.7, (e) 0.6, (f) 0.5 and (g) 0.0

A6.2 Materials of racemic and enantiopure naproxen with 2-aminopyridine (*2AP*)

Table A6. 2 - Crystallographic data for the co-formers 2-aminopyridine (*2AP*), as found from the CSD

Co-former	CSD reference code	a (Å)	b (Å)	c (Å)	α (º)	β (º)	γ (º)	Volume (Å^3)	Space group	Collection temperature (K)	Formula
2-aminopyridine (*2AP*)	AMPYRD	11.709 (4)	5.673 (6)	7.594 (6)	90	95.55(4)	90	502.068	$P2_1/c$	283-303	$C_5H_6N_2$

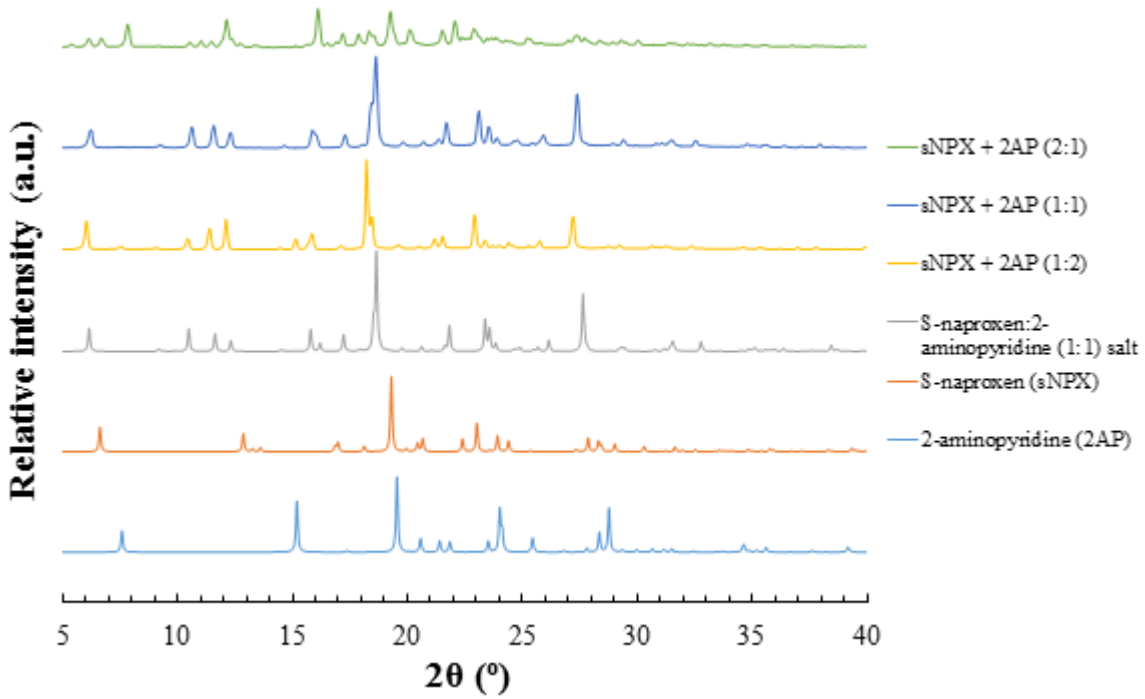

Figure A6. 5 - PXRD patterns from mechanochemically prepared samples of *sNPX* and *2AP*, ground with minimum ethanol in either 2:1, 1:1 or 1:2 molar ratios (top three patterns)

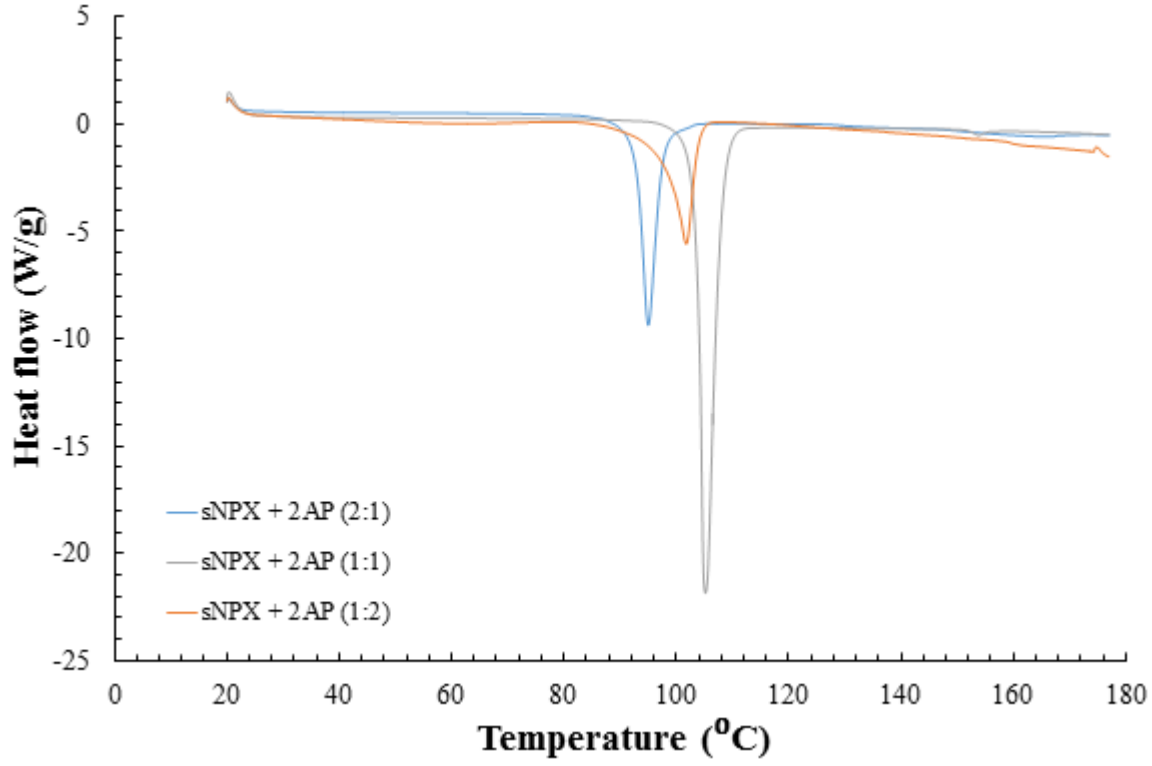

Figure A6. 6 - DSC traces from mechanochemically prepared samples of *sNPX* and *2AP*, ground with minimum ethanol in either 2:1, 1:1 or 1:2 molar ratios

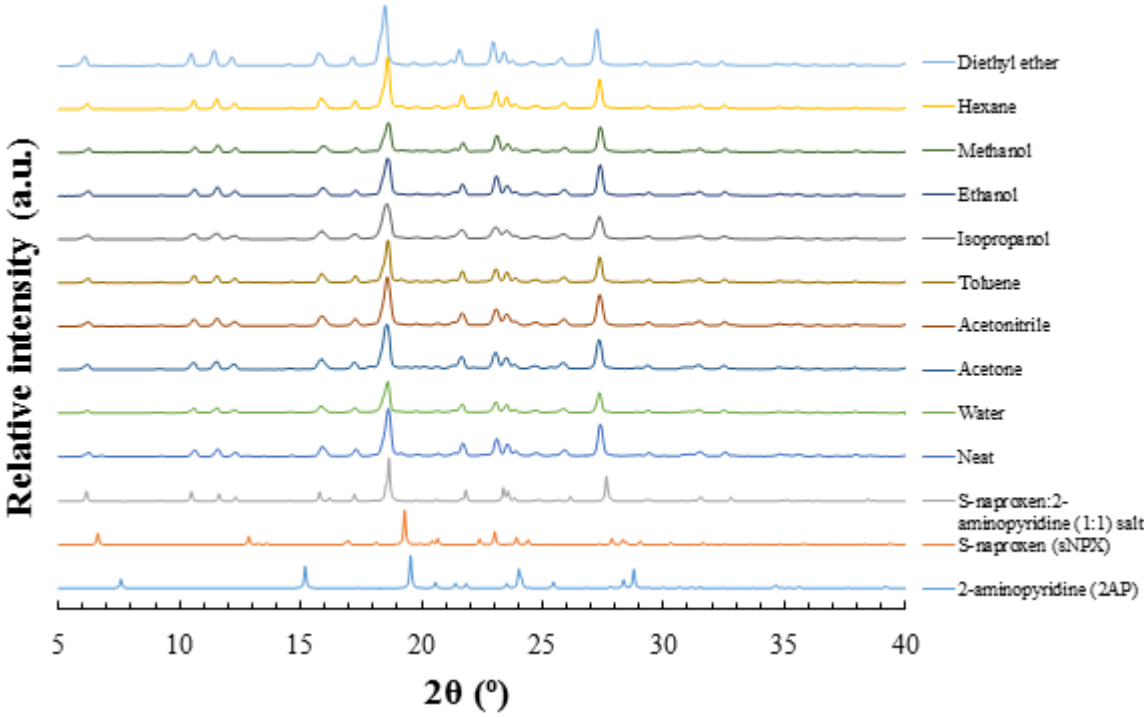

Figure A6. 7 - PXRD patterns from mechanochemically prepared samples of *sNPX* and *2AP*, ground in a 1:1 molar ratio either neat or with minimum water, acetone, acetonitrile, toluene, isopropanol, ethanol, methanol, hexane or diethyl ether

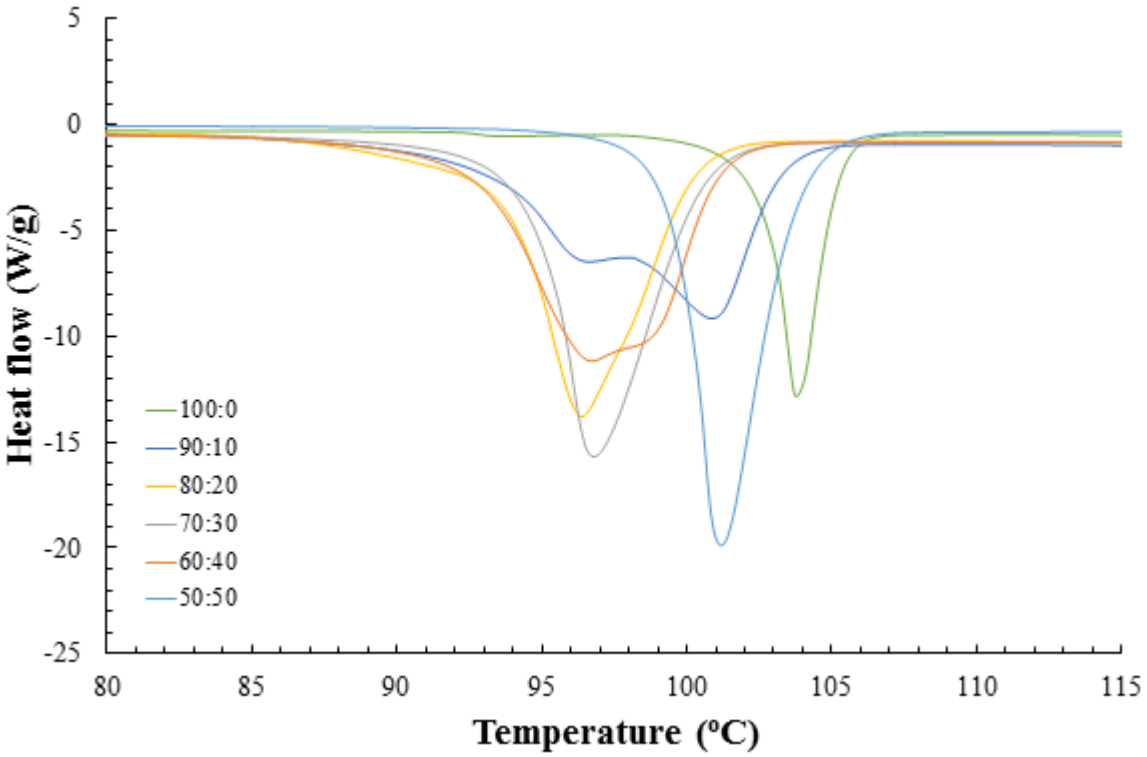

Figure A6. 8 - DSC traces corresponding to the mechanochemical combination of *rsNPX* and *sNPX*, in different enantiomeric compositions (excess *sNPX*), in a constant 1:1 stoichiometry with *2AP*

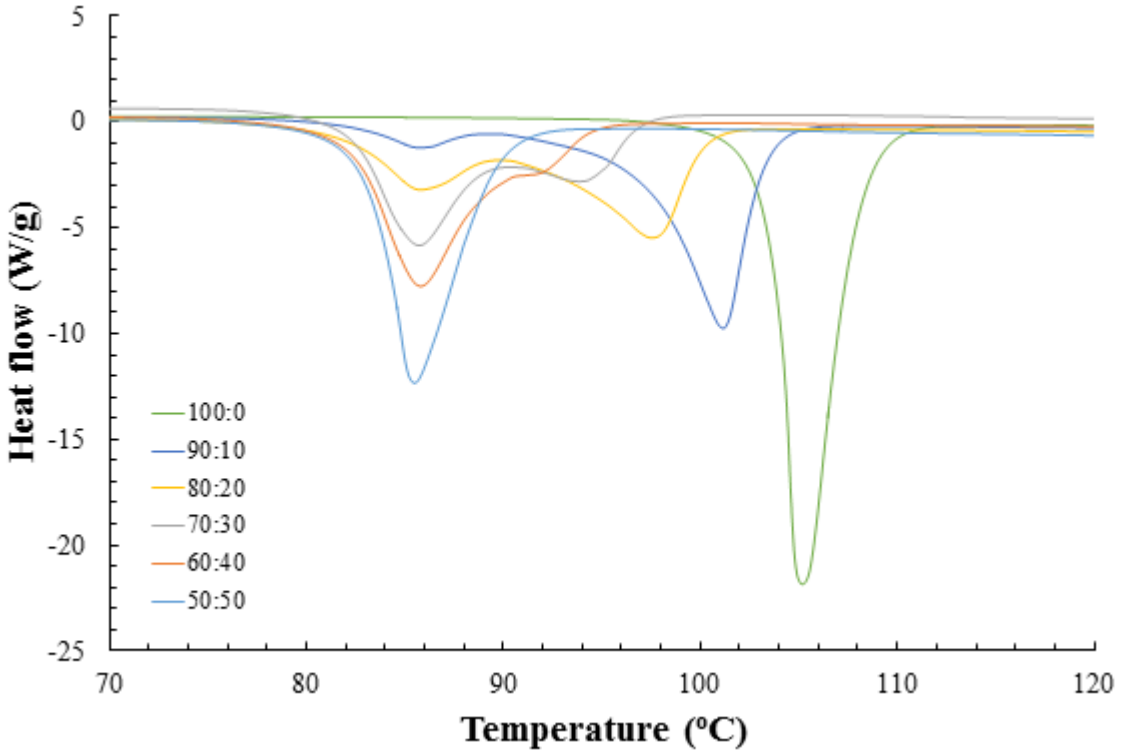

Figure A6. 9 - DSC traces corresponding to the mechanochemical combination of *rNPX* and *sNPX*, in different enantiomeric compositions (excess *sNPX*), in a constant 1:1 stoichiometry with *2AP*

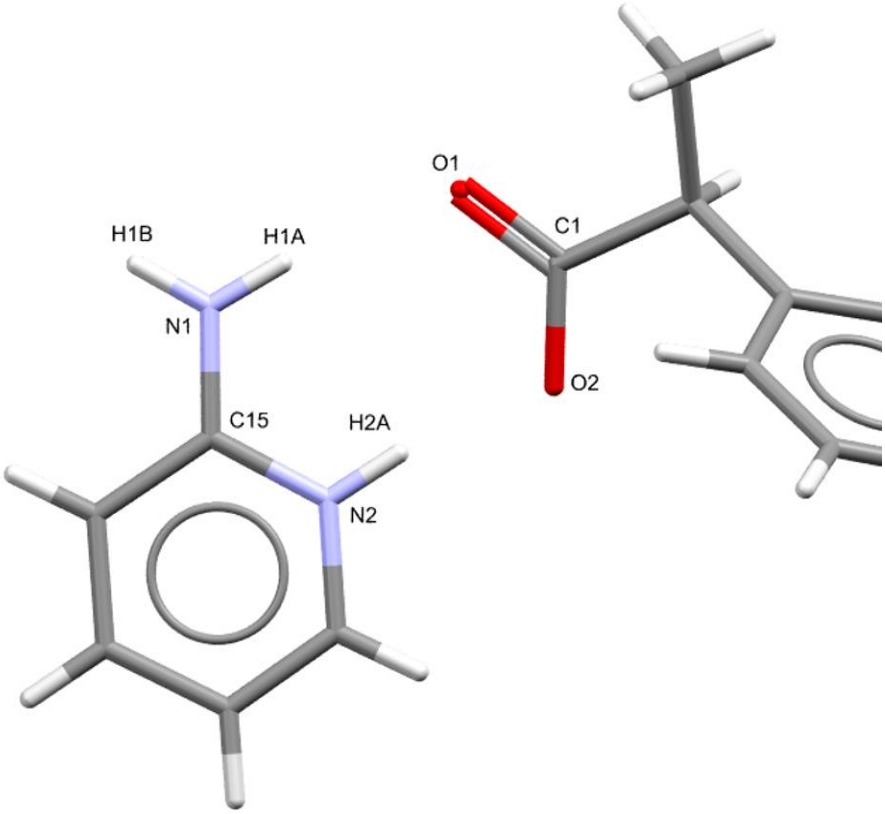

Figure A6. 10 - Key functional groups of the S-naproxen:2-aminopyridine (1:1) salt, with the atoms associated with hydrogen bonding and proton transfer highlighted

Table A6. 3 - Hydrogen bonding interactions with the S-naproxen:2-aminopyridine (1:1) salt, highlighting the key interaction lengths and angles

D	**H**	**A**	**d(D-H) (Å)**	**d(H-A) (Å)**	**d(D-A) (Å)**	**D-H-A (º)**
N2	*H2A*	*O2*	0.86	1.73	2.583(3)	169.1
N1	*H1A*	*O1*	0.86	2.01	2.850(4)	166.3
N1	*H1B*	*O1*[1]	0.86	2.12	2.848(4)	141.9

[1]2-X,-1/2+Y,-Z

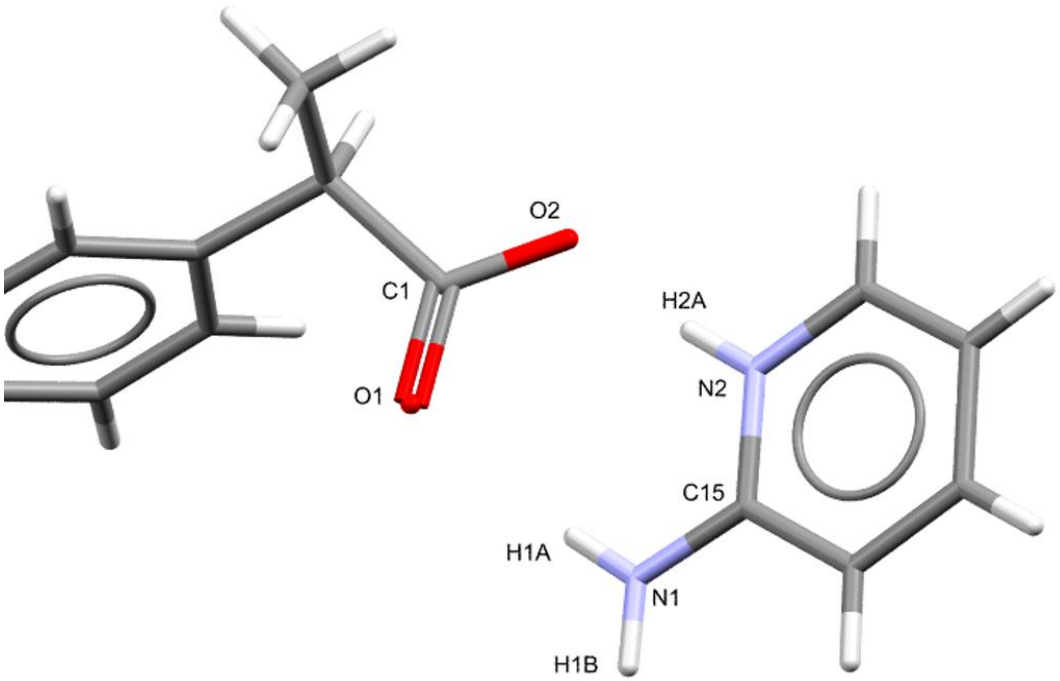

Figure A6. 11 - Key functional groups of the RS-naproxen:2-aminopyridine (1:1) salt, with the atoms associated with hydrogen bonding and proton transfer highlighted

Table A6. 4 - Hydrogen bonding interactions with the RS-naproxen:2-aminopyridine (1:1) salt, highlighting the key interaction lengths and angles

D	**H**	**A**	**d(D-H) (Å)**	**d(H-A) (Å)**	**d(D-A) (Å)**	**D-H-A (º)**
N2	*H2A*	*O2*	0.86	1.76	2.6130(17)	174.3
N1	*H1A*	*O1*	0.86	2.04	2.8452(17)	155.5
N1	*H1B*	*O1*[1]	0.86	2.02	2.8345(17)	157.0

[1] 1-X,1-Y,1-Z

A6.3 Multi-component material cooling crystallisation

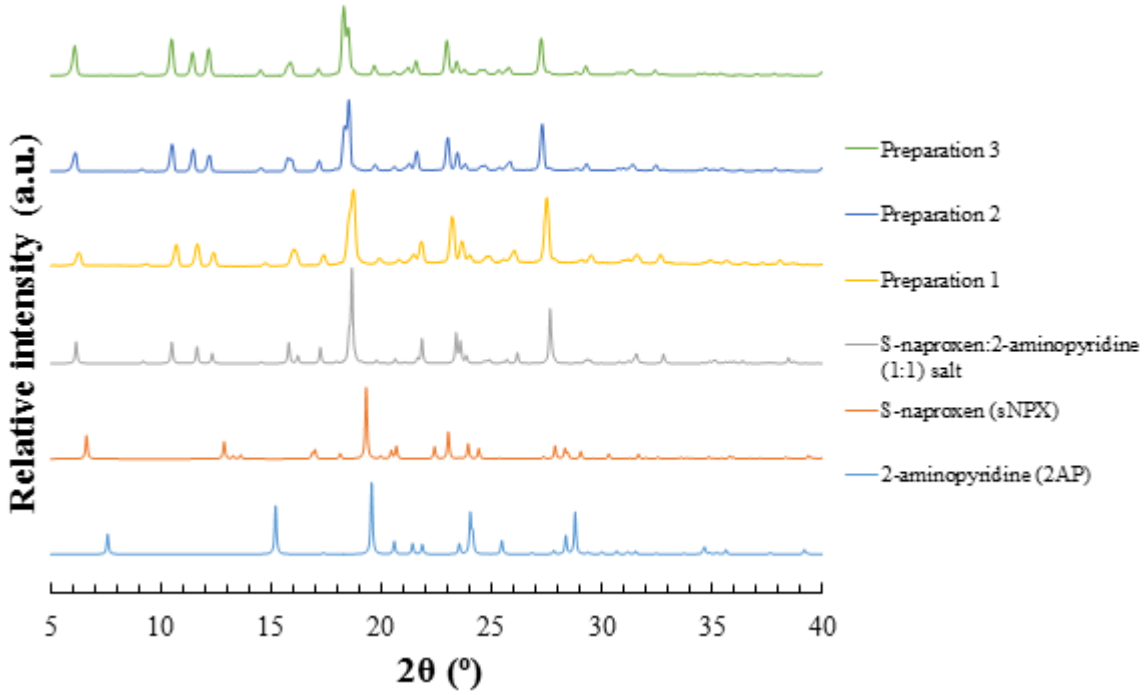

Figure A6. 12 - PXRD patterns of three iterations of solid material produced via the 1:1 slurrying of *sNPX* and *2AP* at 20ºC, 200 rpm for 1 hour in hexane (top three patterns)

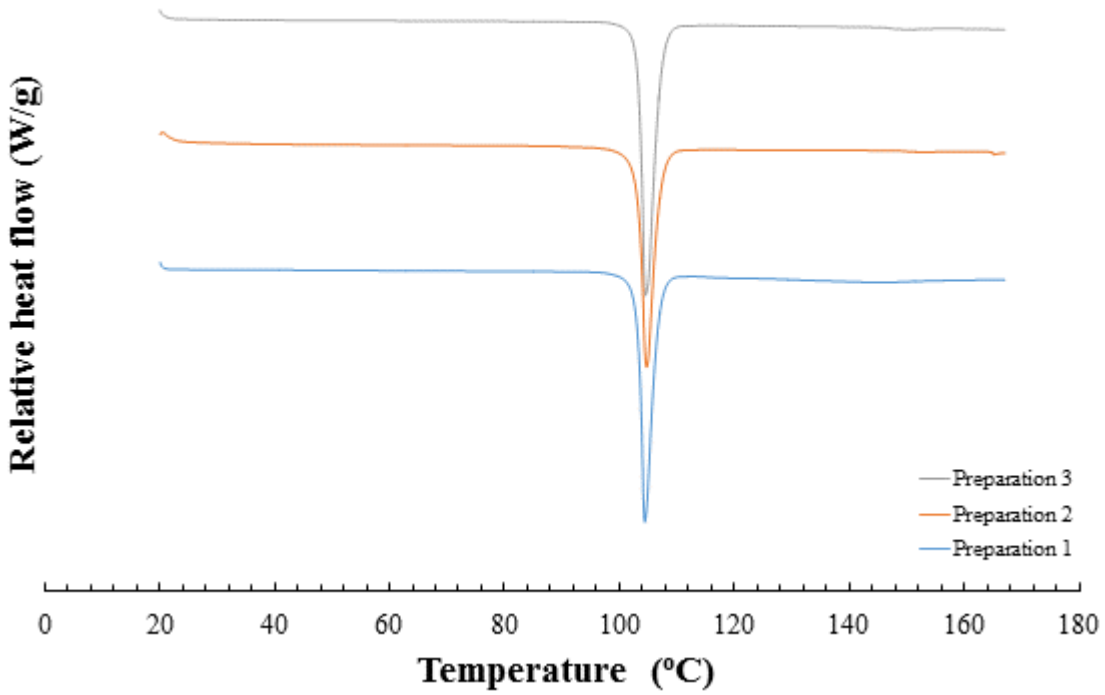

Figure A6. 13 - DSC traces of three iterations of solid material produced via the 1:1 slurrying of *sNPX* and *2AP* at 20ºC, 200 rpm for 1 hour in hexane

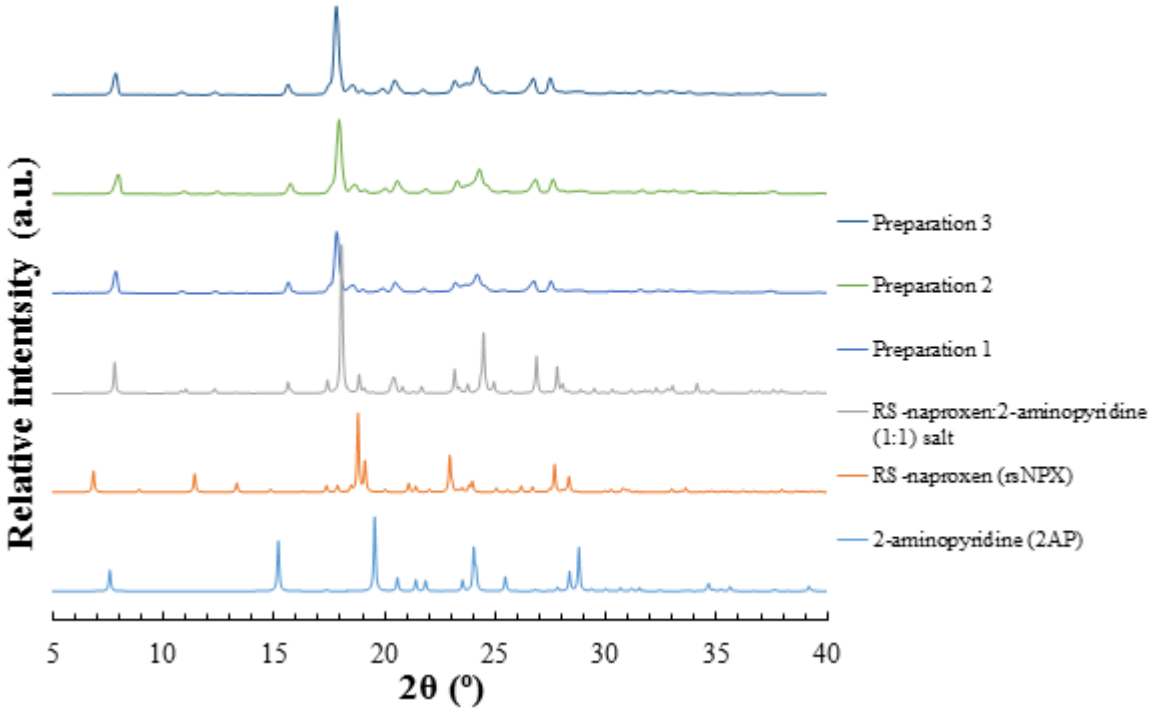

Figure A6. 14 - PXRD patterns of three iterations of solid material produced via the 1:1 slurrying of *rsNPX* and *2AP* at 20ºC, 200 rpm for 1 hour in hexane (top three patterns)

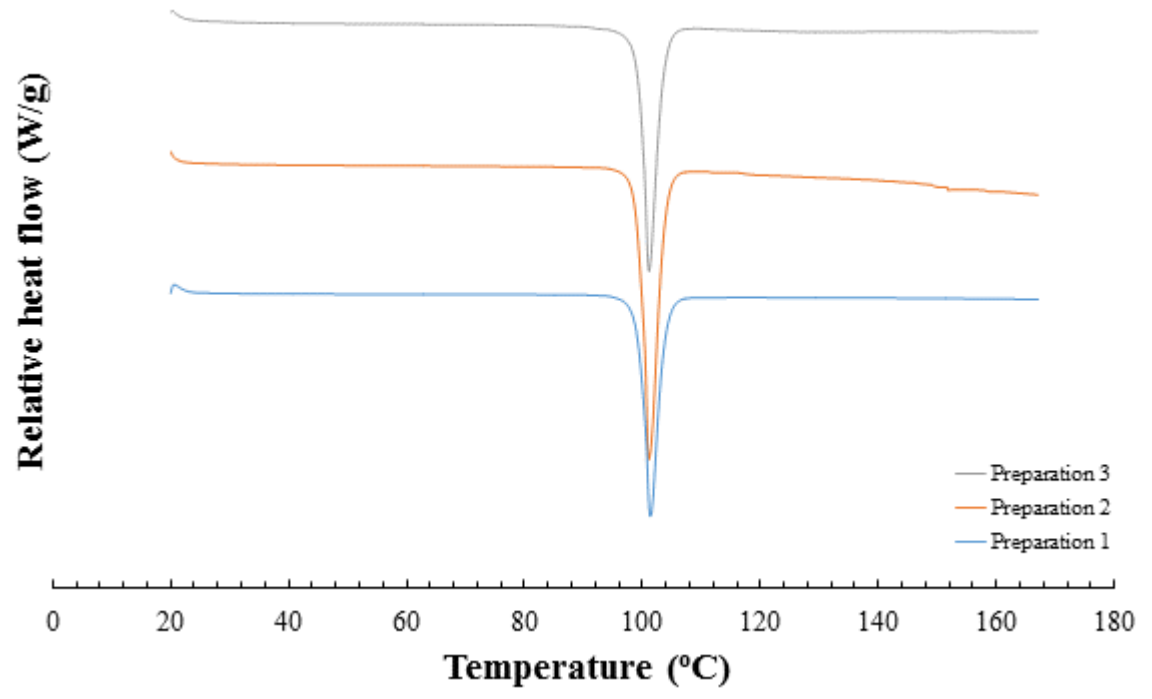

Figure A6. 15 - DSC traces of three iterations of solid material produced via the 1:1 slurrying of *rsNPX* and *2AP* at 20ºC, 200 rpm for 1 hour in hexane

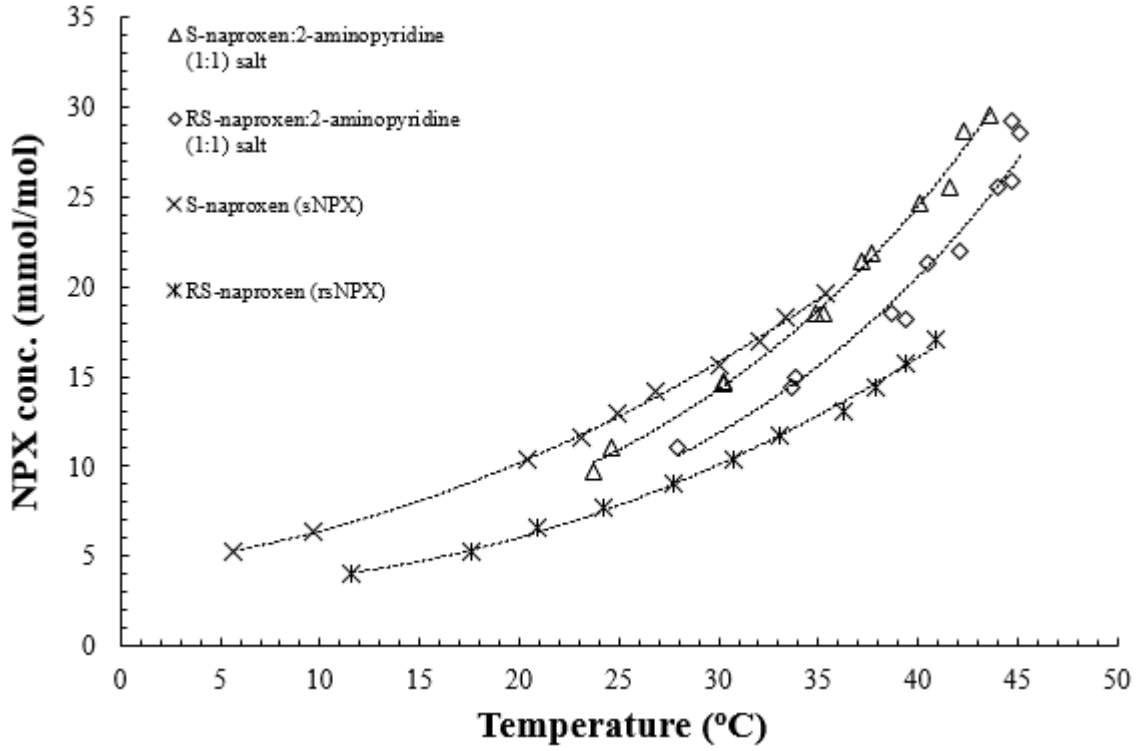

Figure A6. 16 - Solubility data of the S-naproxen:2-aminopyridine (1:1) and RS-naproxen:2-aminopyridine (1:1) salts in isopropanol, as determined from turbidity measurements (concentration taken with respect to *NPX*) (% error less than 1%)

Table A6. 5 - Clear points of the S-naproxen:2-aminopyridine (1:1) and RS-naproxen:2-aminopyridine (1:1) salts in isopropanol, at 20ºC and 30ºC (concentration taken with respect to *NPX*)

Material	Solvent	Clear point at 20ºC (*NPX* mmol/mol)	Clear point at 30ºC (*NPX* mmol/mol)
S-naproxen:2-aminopyridine (1:1) salt	Isopropanol	8.4	14.3
RS-naproxen:2-aminopyridine (1:1) salt		6.8	11.9

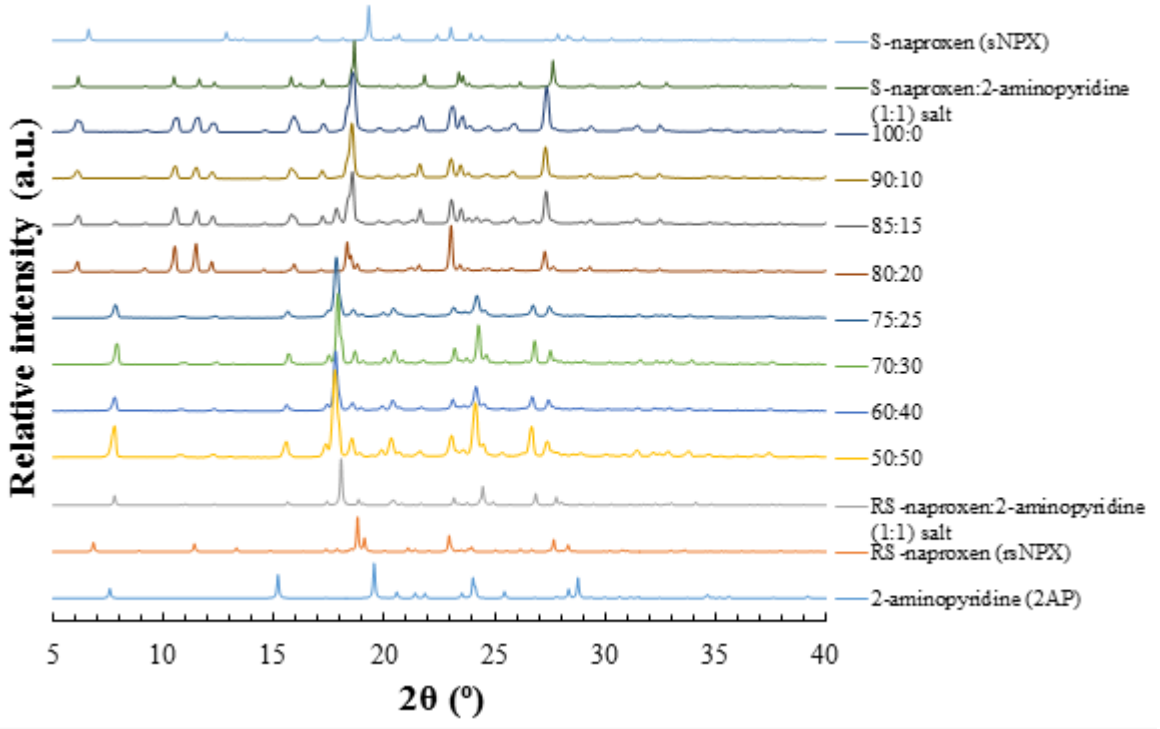

Figure A6. 17 - PXRD patterns of the solid yielded from the slurrying of varying enantiomeric compositions of *sNPX* and *rNPX* in ethanol at 20ºC, from which ternary phase diagrams could be derived (100:0, 90:10, 80:20, 70:30, 60:40, 50:50)

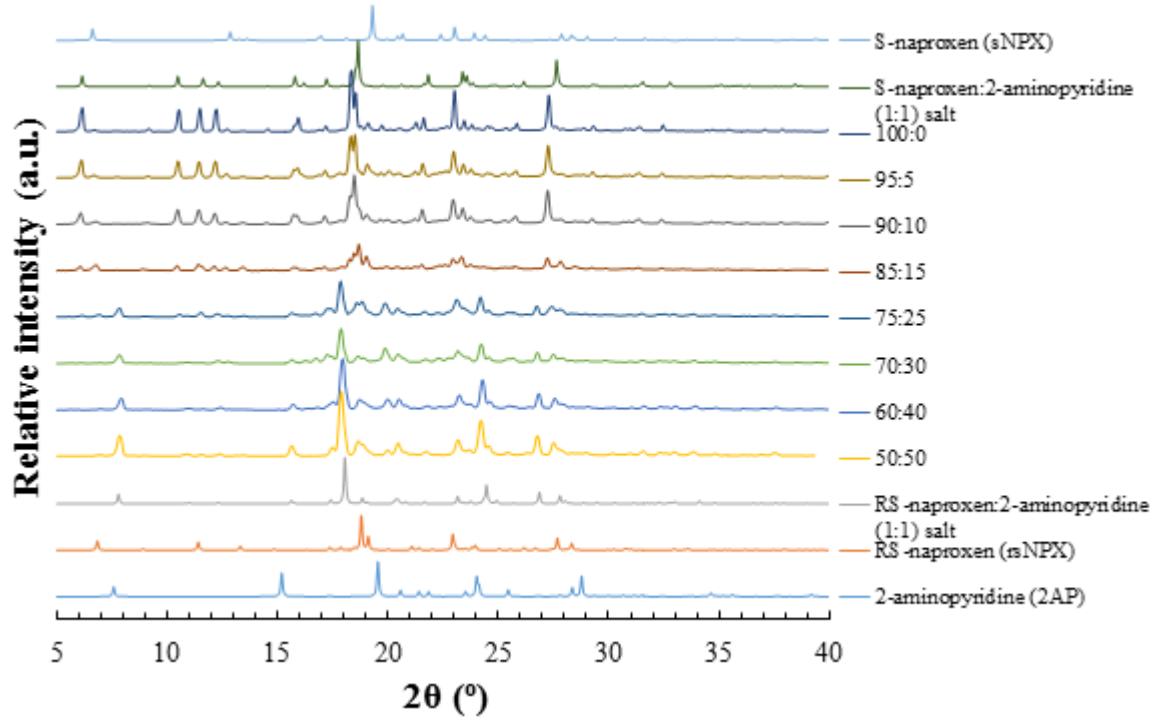

Figure A6. 18 - PXRD patterns of the solid yielded from the slurrying of varying enantiomeric compositions of *sNPX* and *rNPX* in ethanol at 30ºC, from which ternary phase diagrams could be derived (100:0, 90:10, 80:20, 70:30, 60:40, 50:50)

Table A6. 6 - Saturation of ethanol solutions with varying compositions of *sNPX* and *rNPX* (excess *sNPX*), in a 1:1 combination with *2AP*, at 20ºC and 30ºC, respectively, utilised for the construction of a ternary phase diagram

Mole fraction of *sNPX*	**Saturation of *NPX-2AP* (1:1) at 20ºC (*NPX* mmol/mol)**	**Saturation of *NPX-2AP* (1:1) at 30ºC (*NPX* mmol/mol)**
0.5	13.3	30.7
0.6	13.3	23.1
0.7	14.2	26.7
0.75	15.5	29.3
0.8	16.9	32.4
0.85	18.3	33.7
0.9	18.1	31.7
0.95	-	28.4
1.0	15.5	26.1

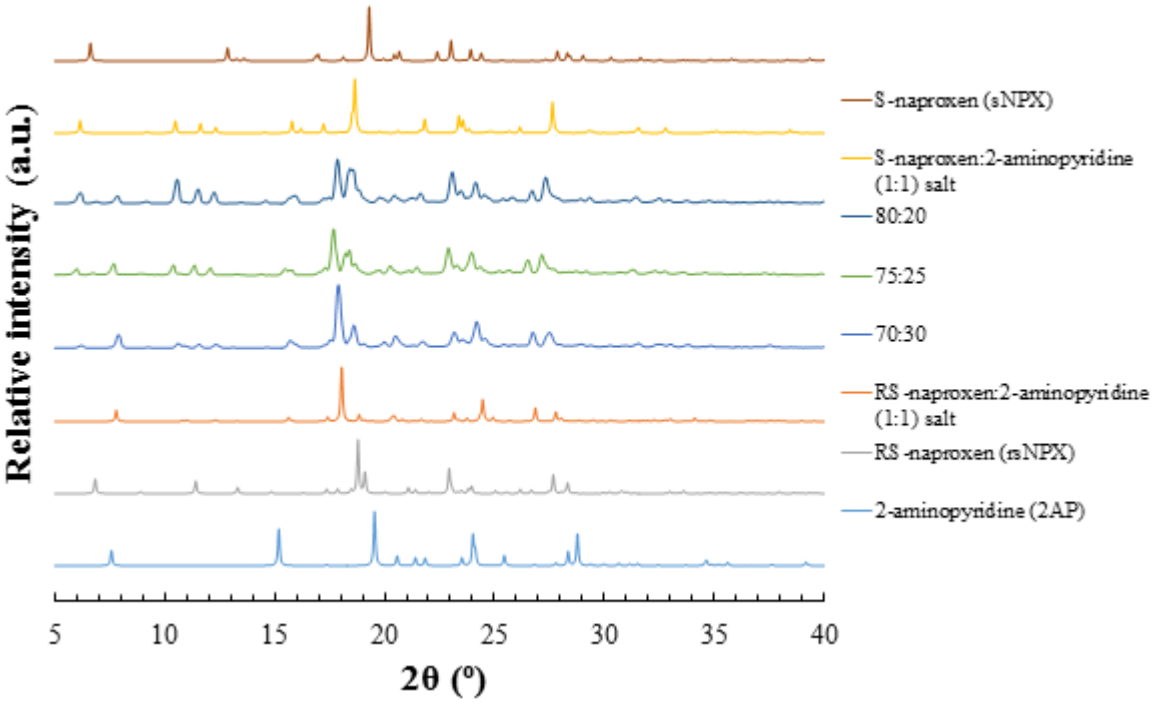

Figure A6. 19 - PXRD patterns of the solid yielded from cooling crystallisations, utilising 1:1 ethanol solutions of *NPX* to *2AP*, with varying enantiomeric compositions (80:20, 75:25 and 70:30, excess *sNPX*), cooled at 0.1ºC/min from 45ºC to 10ºC, mixing at 150 rpm

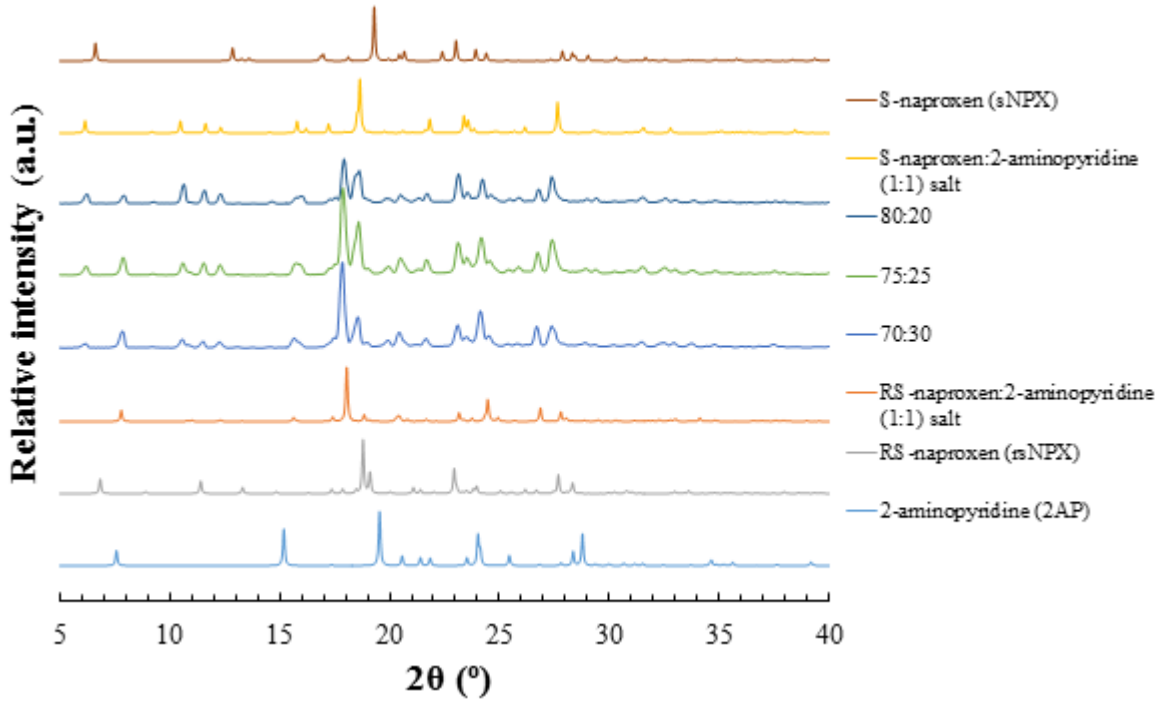

Figure A6. 20 - PXRD patterns of the solid yielded from cooling crystallisations, utilising 1:1 ethanol solutions of *NPX* to *2AP*, with varying enantiomeric compositions (80:20, 75:25 and 70:30, excess *sNPX*), cooled at 0.1ºC/min from 45ºC to 5ºC, mixing at 150 rpm

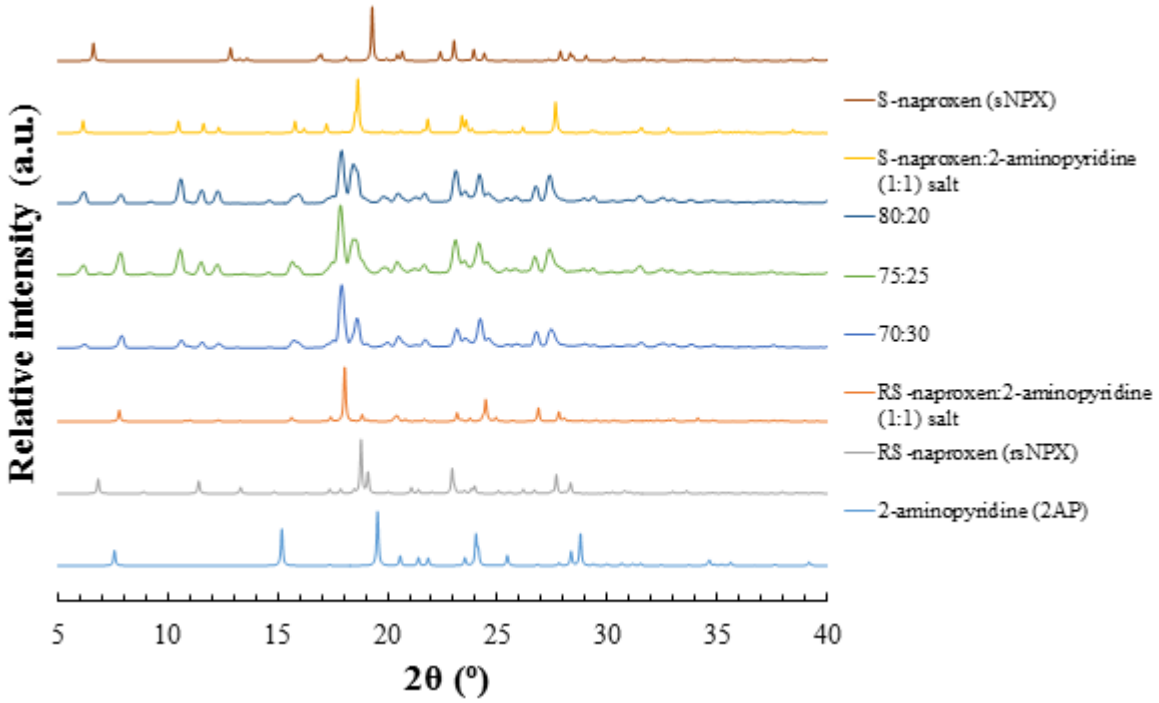

Figure A6. 21 - PXRD patterns of the solid yielded from cooling crystallisations, utilising 1:1 ethanol solutions of *NPX* to *2AP*, with varying enantiomeric compositions (80:20, 75:25 and 70:30, excess *sNPX*), cooled at 0.1ºC/min from 45ºC to 0ºC, mixing at 150 rpm

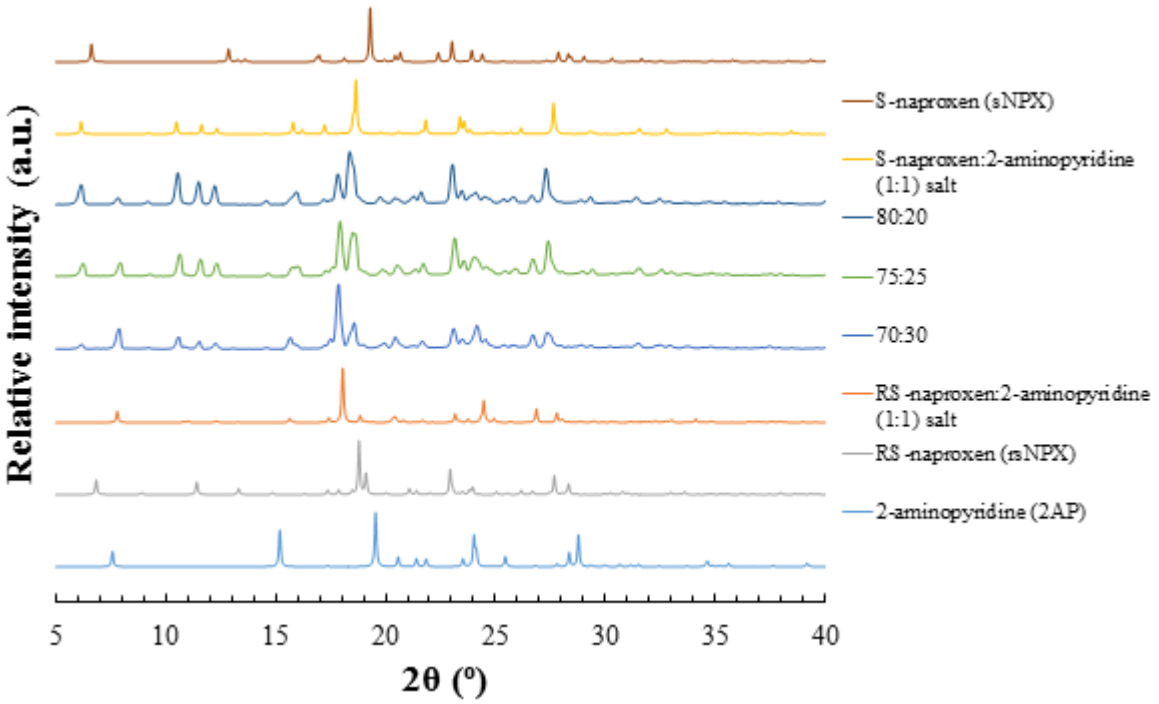

Figure A6. 22 - PXRD patterns of the solid yielded from cooling crystallisations, utilising 1:1 ethanol solutions of *NPX* to *2AP*, with varying enantiomeric compositions (80:20, 75:25 and 70:30, excess *sNPX*), cooled at 0.1ºC/min from 45ºC to 5ºC, mixing at 600 rpm

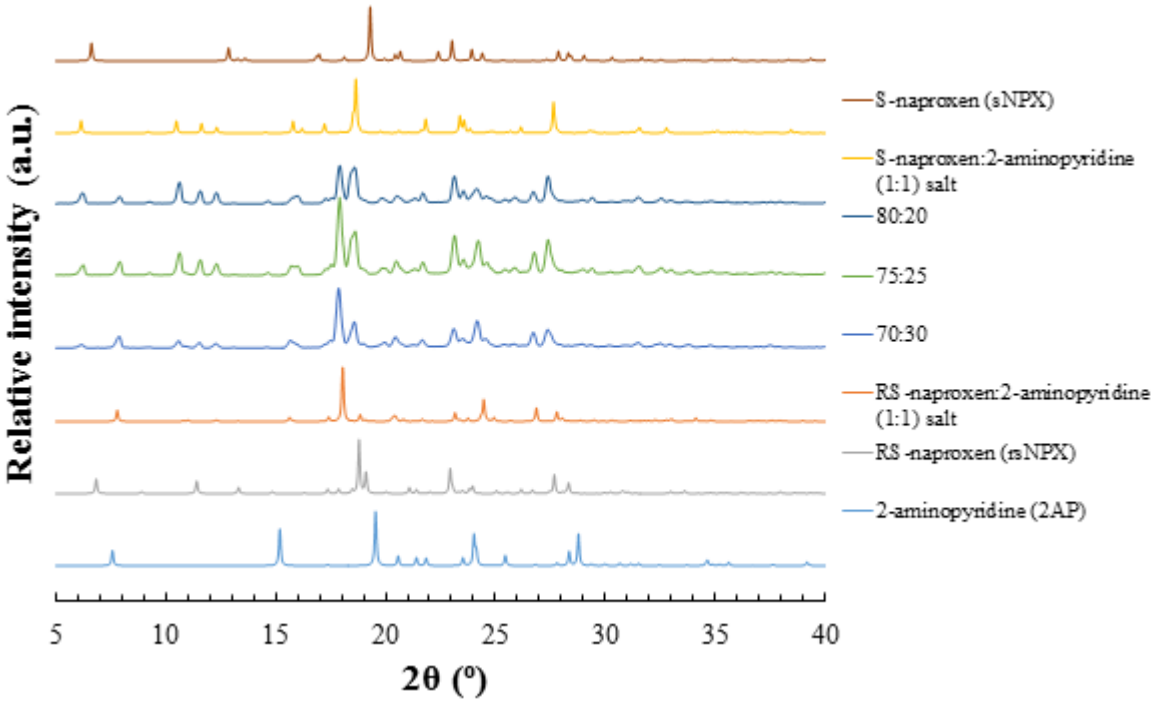

Figure A6. 23 - PXRD patterns of the solid yielded from cooling crystallisations, utilising 1:1 ethanol solutions of *NPX* to *2AP*, with varying enantiomeric compositions (80:20, 75:25 and 70:30, excess *sNPX*), cooled at 0.1ºC/min from 45ºC to 0ºC, mixing at 600 rpm

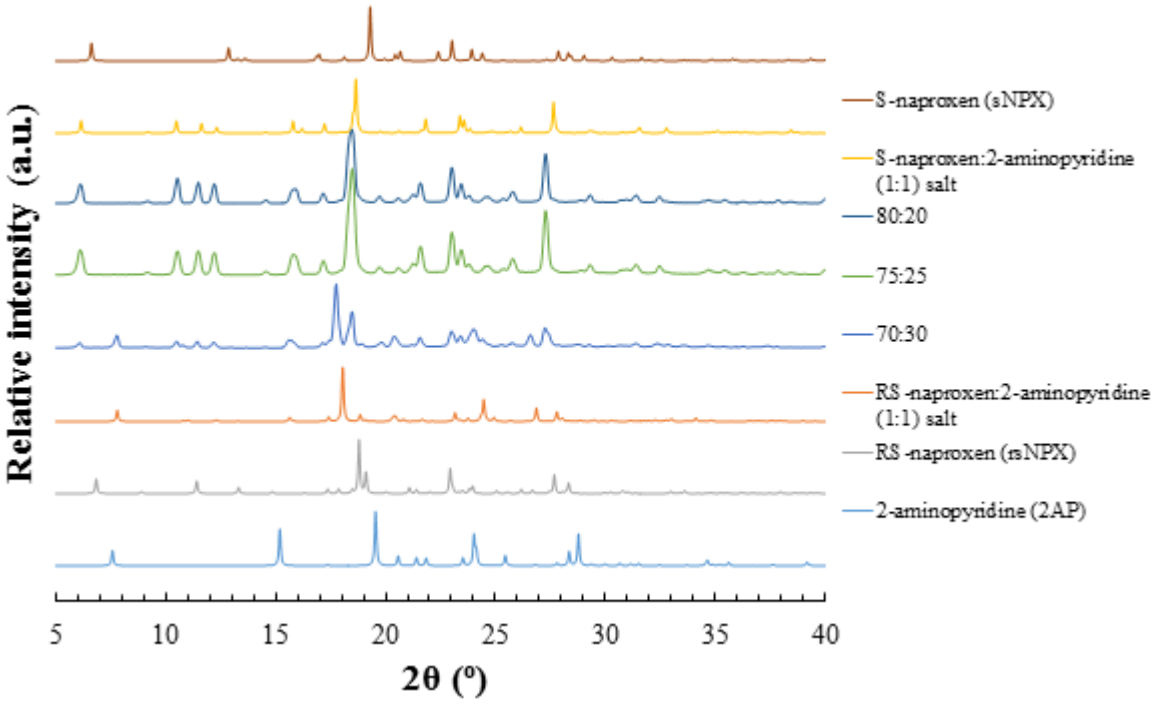

Figure A6. 24 - PXRD patterns of the solid yielded from cooling crystallisations, utilising 1:1 ethanol solutions of *NPX* to *2AP*, with varying enantiomeric compositions (80:20, 75:25 and 70:30, excess *sNPX*), cooled at 1ºC/min from 45ºC to 5ºC, mixing at 150 rpm

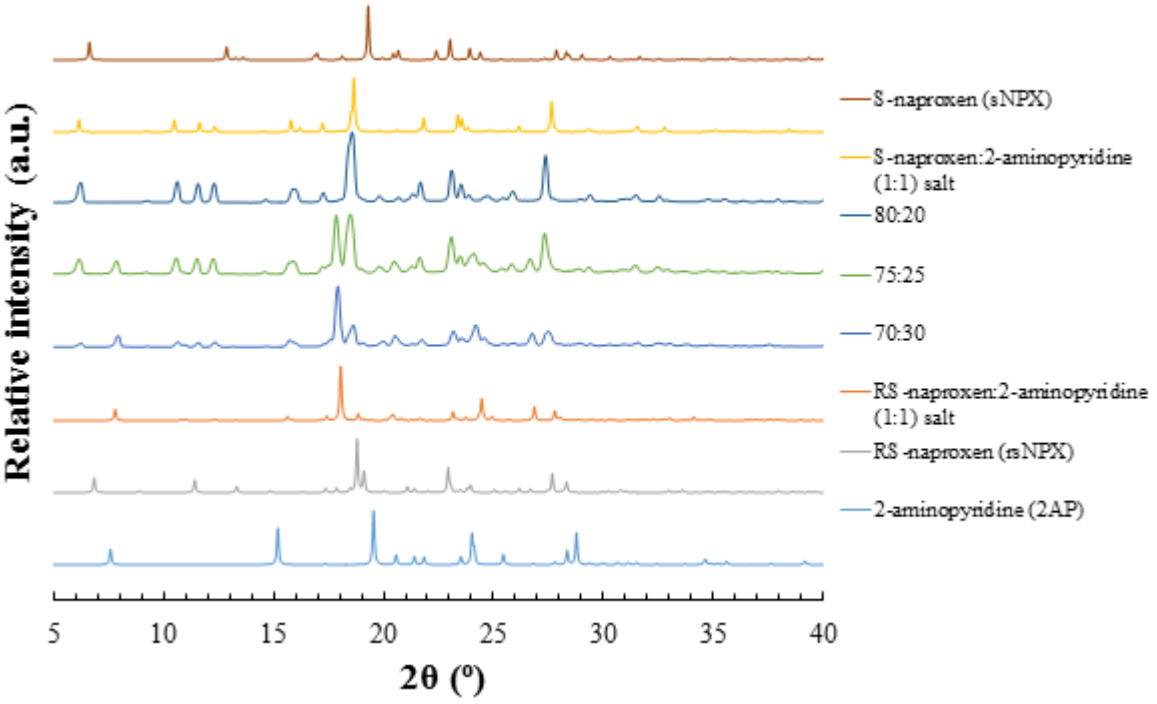

Figure A6. 25 - PXRD patterns of the solid yielded from cooling crystallisations, utilising 1:1 ethanol solutions of *NPX* to *2AP*, with varying enantiomeric compositions (80:20, 75:25 and 70:30, excess *sNPX*), cooled at 1ºC/min from 45ºC to 0ºC, mixing at 150 rpm

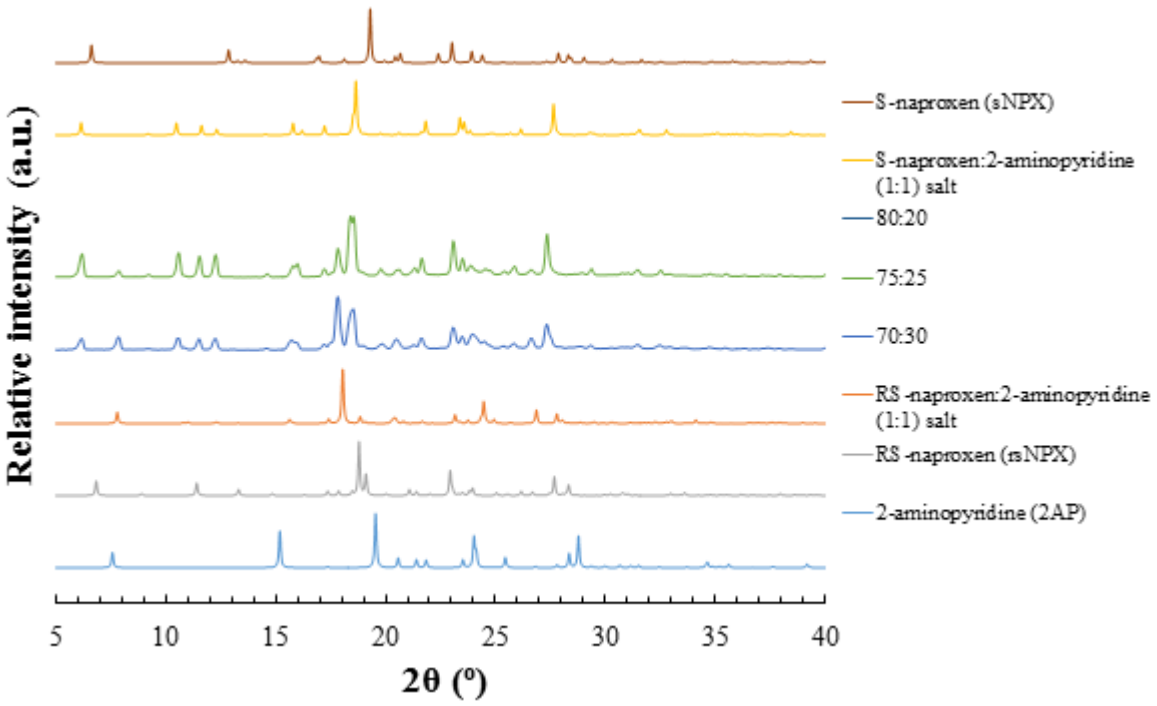

Figure A6. 26 - PXRD patterns of the solid yielded from cooling crystallisations, utilising 1:1 ethanol solutions of *NPX* to *2AP*, with varying enantiomeric compositions (80:20, 75:25 and 70:30, excess *sNPX*), cooled at 1ºC/min from 45ºC to 10ºC, mixing at 600 rpm

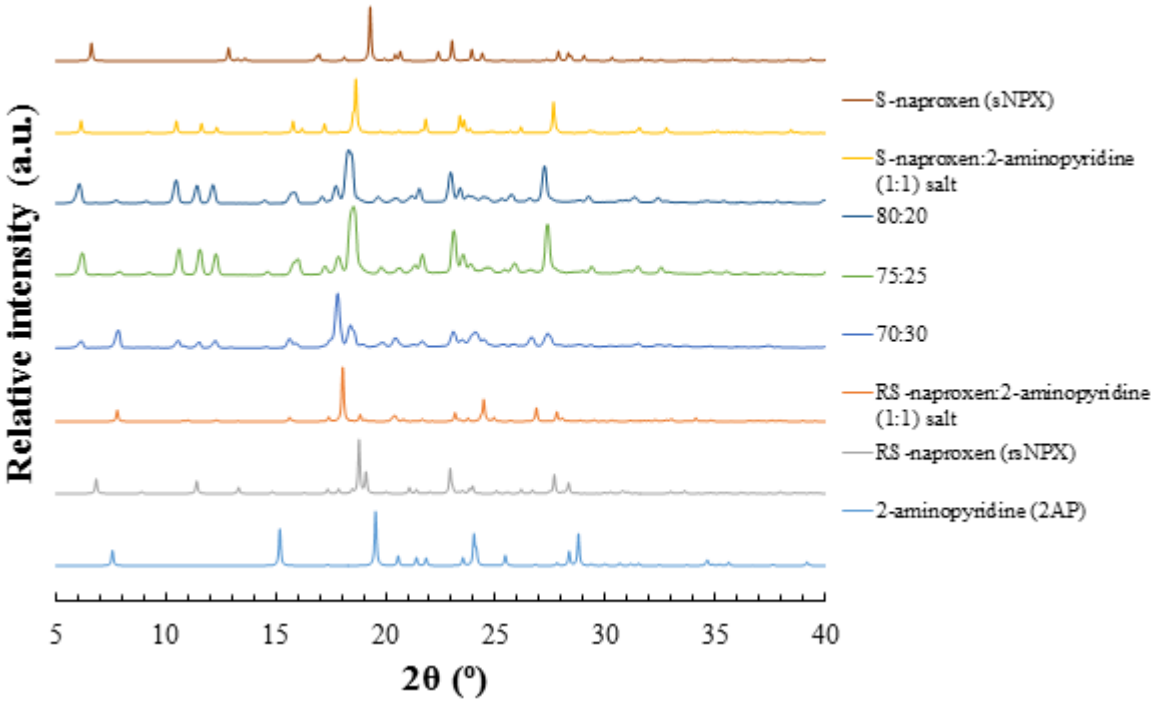

Figure A6. 27 - PXRD patterns of the solid yielded from cooling crystallisations, utilising 1:1 ethanol solutions of *NPX* to *2AP*, with varying enantiomeric compositions (80:20, 75:25 and 70:30, excess *sNPX*), cooled at 1ºC/min from 45ºC to 5ºC, mixing at 600 rpm

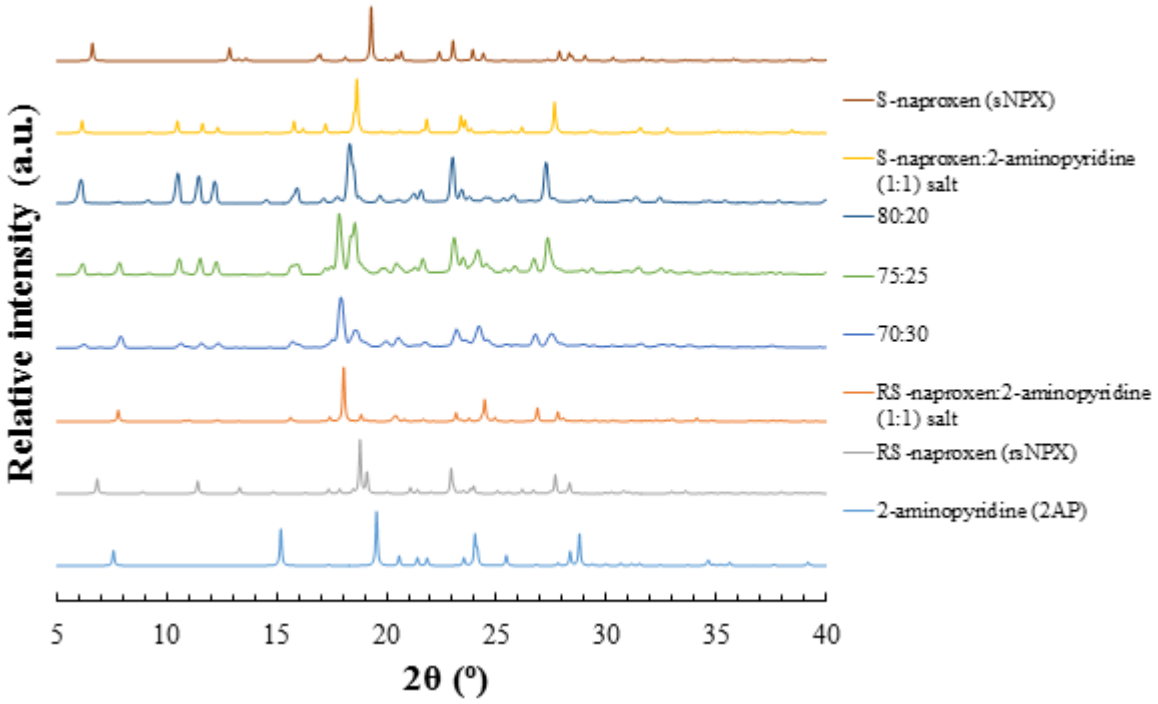

Figure A6. 28 - PXRD patterns of the solid yielded from cooling crystallisations, utilising 1:1 ethanol solutions of *NPX* to *2AP*, with varying enantiomeric compositions (80:20, 75:25 and 70:30, excess *sNPX*), cooled at 1ºC/min from 45ºC to 0ºC, mixing at 600 rpm

Appendix (A7) Chapter 7

Table A7. 1 - Crystallographic data for the co-formers 2-aminopyrimidine (*2APM*), 2-amino-4,6-dimethylpyrimdine (*2ADMP*), 2-amino-3-chloropyridine (*2A3CP*), 2-amino-4-chloropyridine (*2A4CP*), 2-amino-5-chloropyridine (*2A5CP*) and 2-amino-6-chloropyridine (*2A6CP*), as found from the CSD

Co-former	CSD reference code	a (Å)	b (Å)	c (Å)	α (º)	β (º)	γ (º)	Volume (Å^3)	Space group	Collection temperature (K)	Formula
2-aminopyrimidine (*2APM*)	AMPYRM10	5.709(2)	10.917(2)	15.103(2)	90	90	90	941.297	*P*bca	283-303	$C_4H_5N_3$
2-amino-4,6-dimethylpyrimidine (*2ADMP*)	NEQLOM	11.519(7)	11.021(6)	32.386(18)	90	91.11(1)	90	4110.658	*C*2/c	283-303	$C_6H_9N_3$
2-amino-3-chloropyridine (*2A3CP*)	URAXER	11.149(8)	5.453(4)	9.848(7)	90	90	90	598.440	$P2_1/c$	283-303	$C_5H_5ClN_2$
2-amino-4-chloropyridine (*2A4CP*)*	-	-	-	-	-	-	-	-	-	-	$C_5H_5ClN_2$
2-amino-5-chloropyridine (*2A5CP*)	AMCLPY12	13.352(4)	5.758(1)	7.266(2)	90	104.79(<1)	90	540.078	$P2_1/c$	100	$C_5H_5ClN_2$
2-amino-6-chloropyridine (*2A6CP*)	XONQAU	11.934(1)	4.699(<1)	11.225(1)	90	112.60(<1)	90	581.178	$P2_1$ /c	100	$C_5H_5ClN_2$

*No previously published structures of 2-amino-4-chloropyridine (*2A4CP*) could be found in the CSD as of July 2018

A7.1 Materials of racemic and enantiopure naproxen with 2-aminopyrimidine (*2APM*)

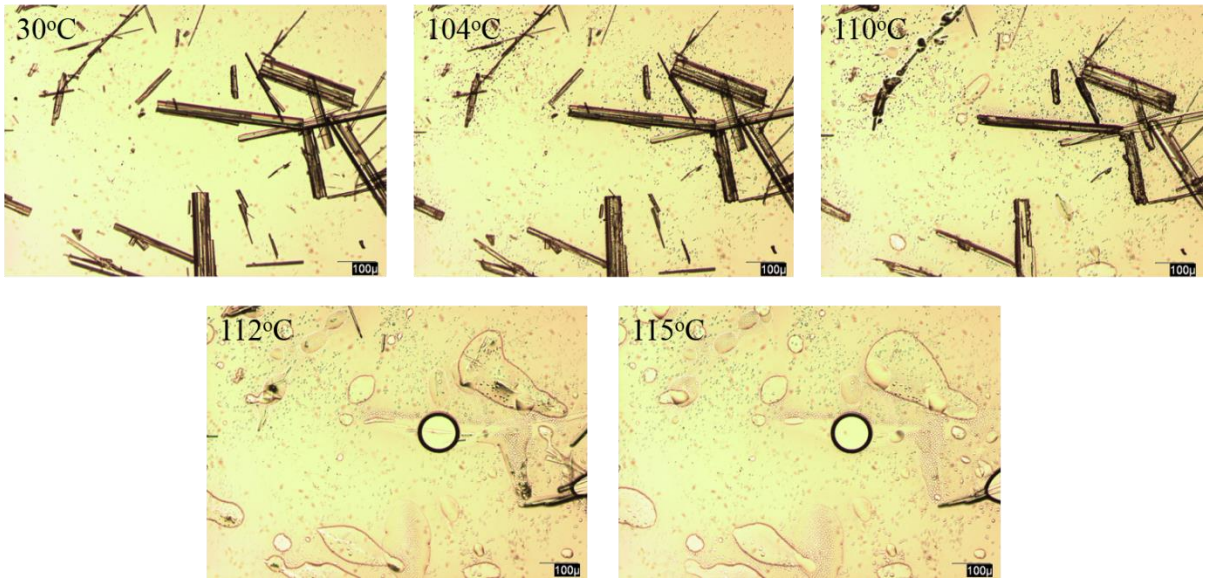

Figure A7. 1 - HSM images of the S-naproxen:2-aminopyrimidine (1:1) co-crystal, prepared via seeded crash cooling crystallisation from ethanol (100µm scale)

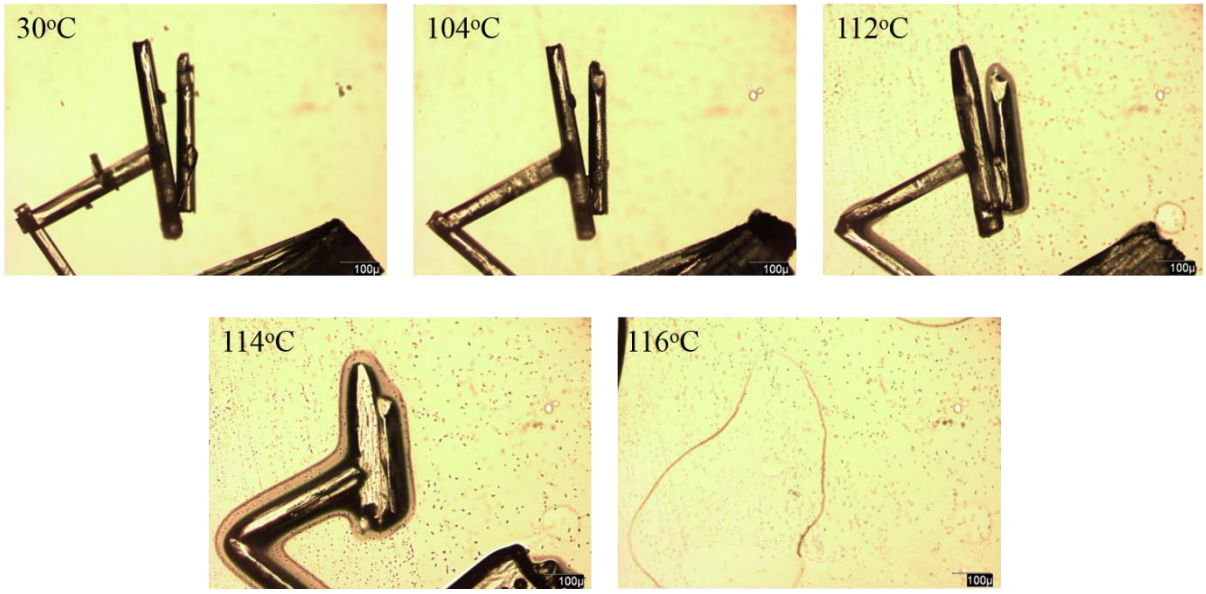

Figure A7. 2 - HSM images of the RS-naproxen:2-aminopyrimidine (1:1) co-crystal, prepared via crash cooling crystallisation from ethanol (100µm scale)

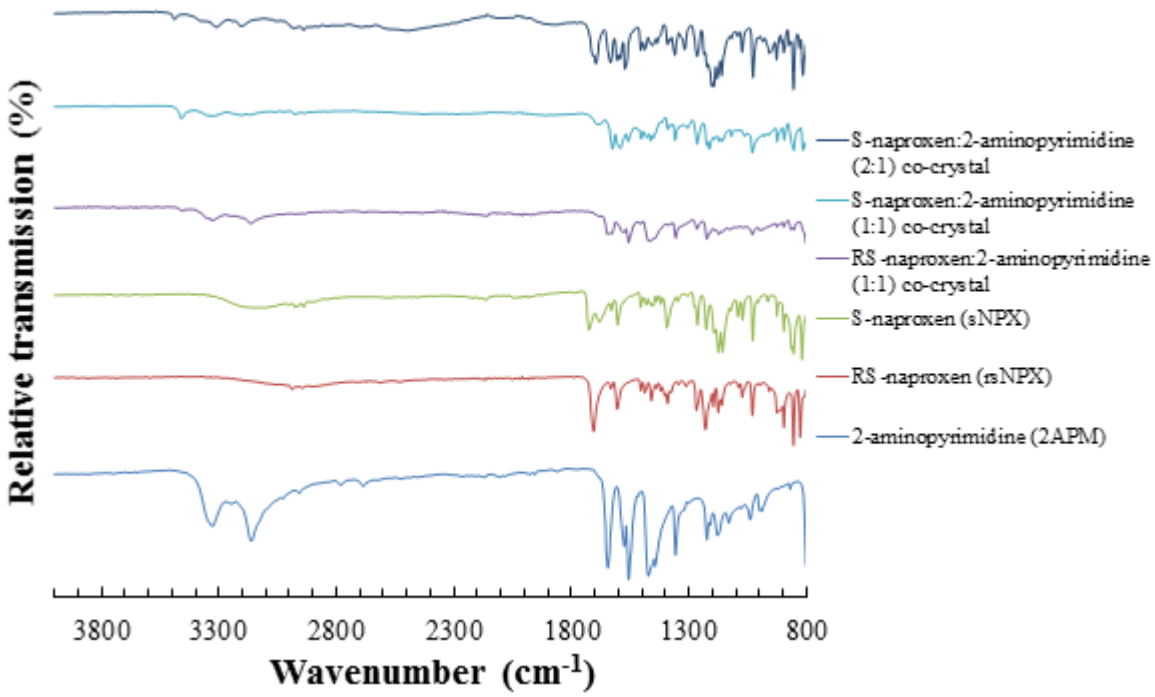

Figure A7. 3 - IR spectra of the S-naproxen:2-aminopyrimidine (2:1) & (1:1) co-crystals, the RS-naproxen:2-aminopyrimidine (1:1) co-crystal and that of the starting materials

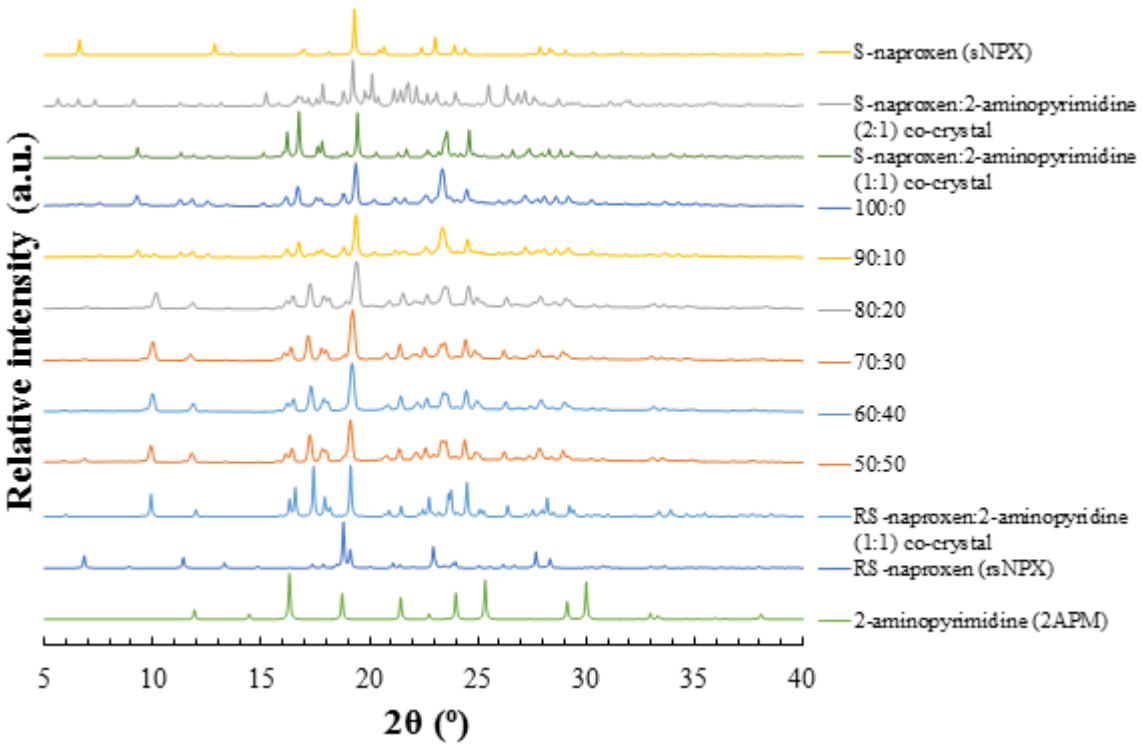

Figure A7. 4 - PXRD patterns, highlighting the change in phase from the racemic to the enantiopure (1:1) co-crystal of *NPX* and *2APM*, with increasing molar contributions of *sNPX* (100:0, 90:10, 80:20, 70:30, 60:40, 50:50)

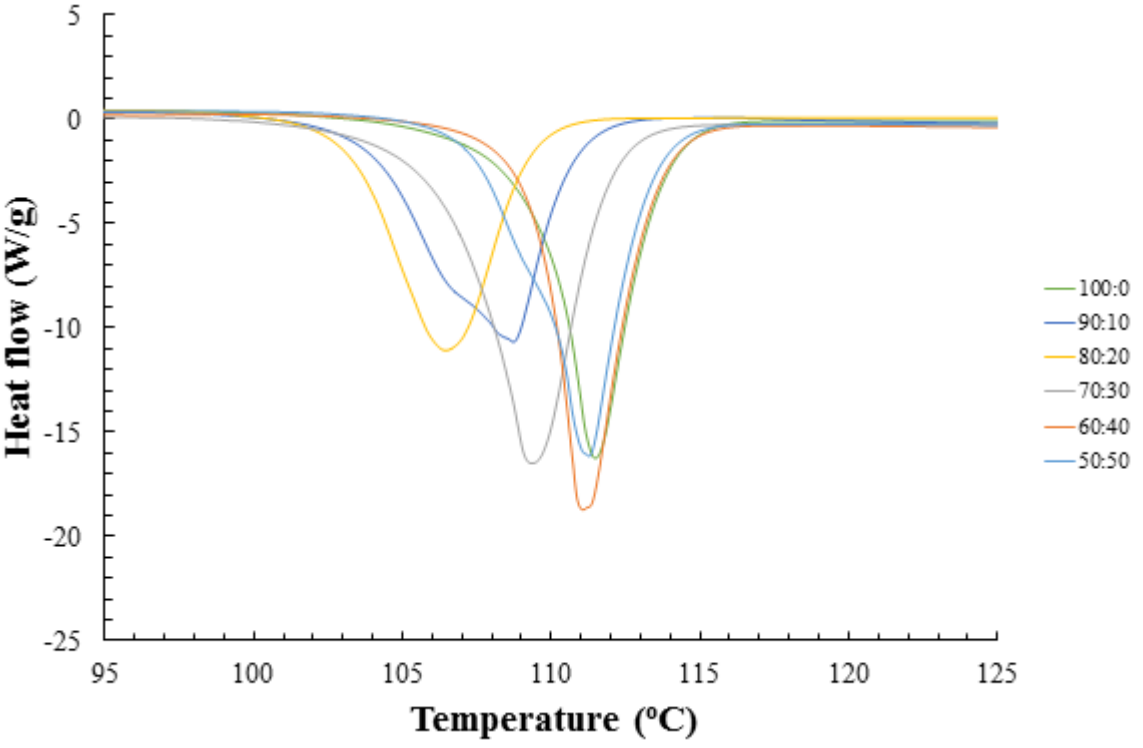

Figure A7. 5 - DSC traces, highlighting the change in phase from the racemic to the enantiopure (1:1) co-crystal of *NPX* and *2APM*, with increasing molar contributions of *sNPX*

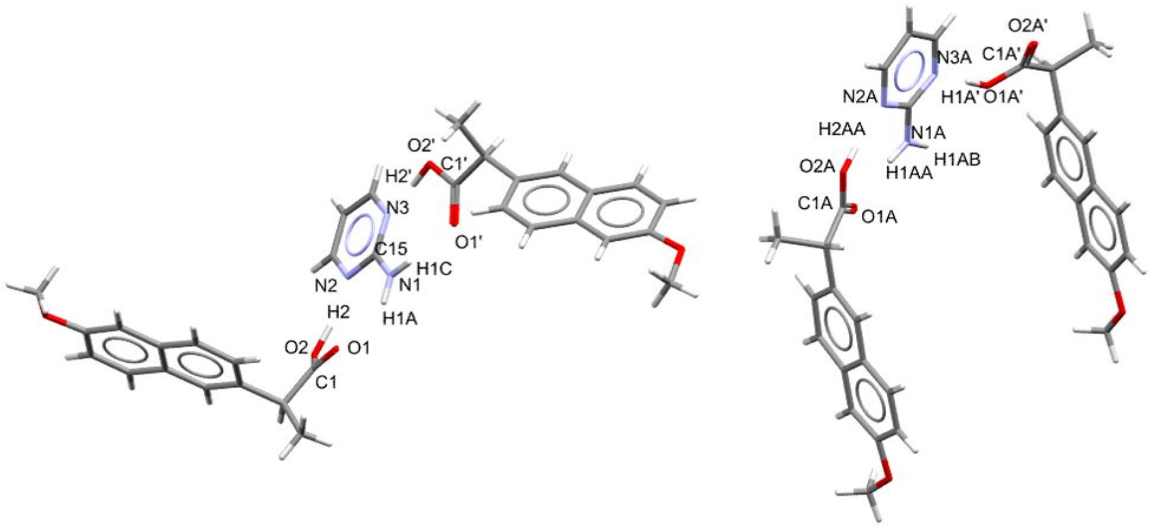

Figure A7. 6 - Asymmetric unit of S-naproxen:2-aminopyrimidine (2:1) co-crystal, highlighting labelling of atoms involved in key intermolecular interactions

Table A7. 2 - Hydrogen bonding interactions with the S-naproxen:2-aminopyrimidine (2:1) co-crystal, highlighting the key interaction lengths and angles

D	**H**	**A**	**d(D-H) (Å)**	**d(H-A) (Å)**	**d(D-A) (Å)**	**D-H-A (º)**
N1	*H1A*	*O1*	0.86	2.16	2.941(4)	150.9
N1	*H1C*	*O1'*	0.86	2.08	2.921(4)	167.3
N1A	*H1AA*	*O1A*	0.86	2.02	2.879(4)	173.3
O2'	*H2'*	*N3*	1.006(14)	1.698(15)	2.701(4)	174(5)
O2	*H2*	*N2*	1.003(14)	1.696(16)	2.691(4)	171(4)
O2A	*H2AA*	*N2A*	1.001(14)	1.75(3)	2.725(4)	163(7)
O1A'	*H1A'*	*N3A*	1.004(14)	1.721(15)	2.725(4)	178(5)

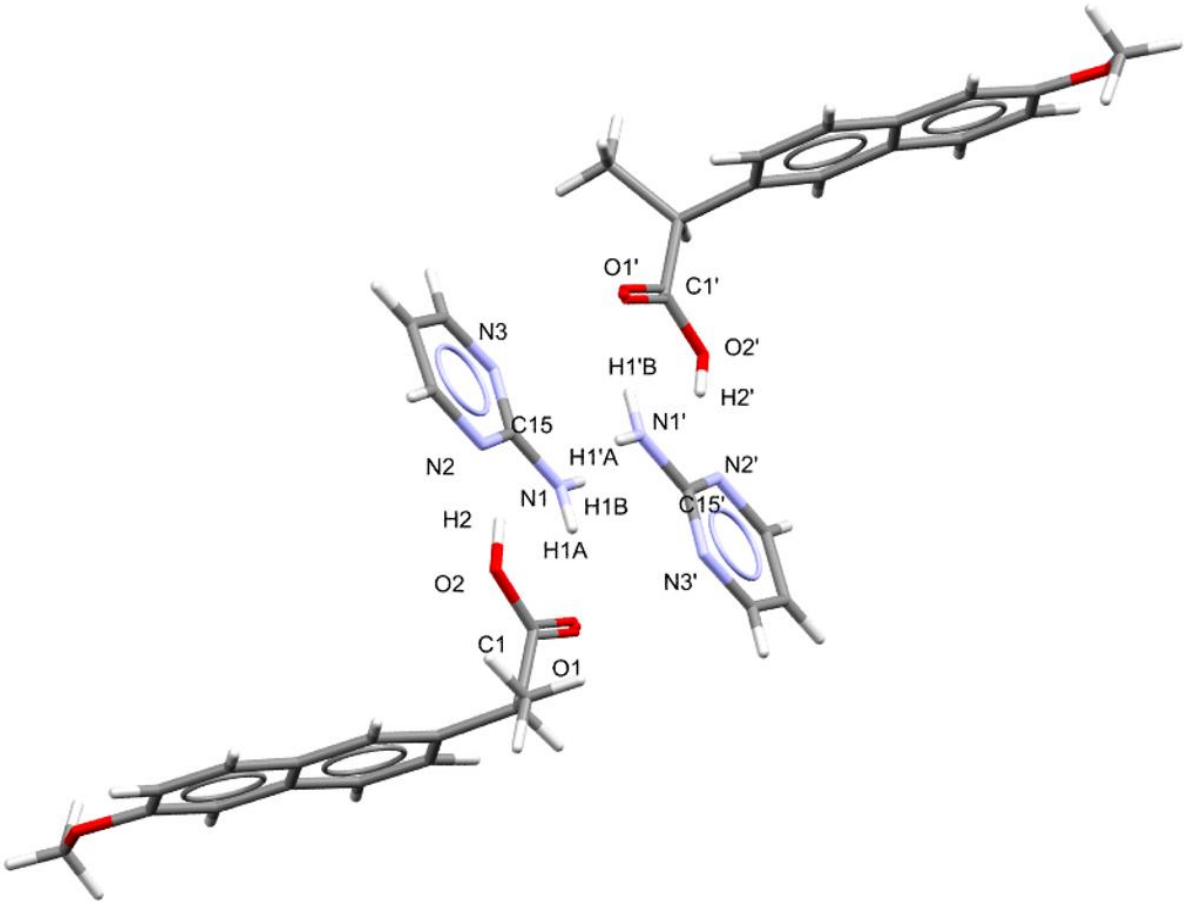

Figure A7. 7 - Asymmetric unit of S-naproxen:2-aminopyrimidine (1:1) co-crystal, highlighting labelling of atoms involved in key intermolecular interactions

Table A7. 3 - Hydrogen bonding interactions with the S-naproxen:2-aminopyrimidine (1:1) co-crystal, highlighting the key interaction lengths and angles

D	H	A	d(D-H) (Å)	d(H-A) (Å)	d(D-A) (Å)	D-H-A (º)
O2'	*H2'*	*N2'*	0.82	1.80	2.602(3)	164.8
N1	*H1A*	*O1*	0.86	2.07	2.919(3)	167.7
N1	*H1B*	*O1'*[1]	0.86	2.28	3.001(4)	142.0
N1'	*H1'A*	*O1*[2]	0.86	2.22	2.930(4)	140.0
N1'	*H1'B*	*O1'*	0.86	2.16	3.007(3)	169.0
O2	*H2*	*N2*	1.000(13)	1.606(18)	2.588(3)	166(5)

[1] 1+X,+Y,+Z; [2] -1+X,+Y,+Z

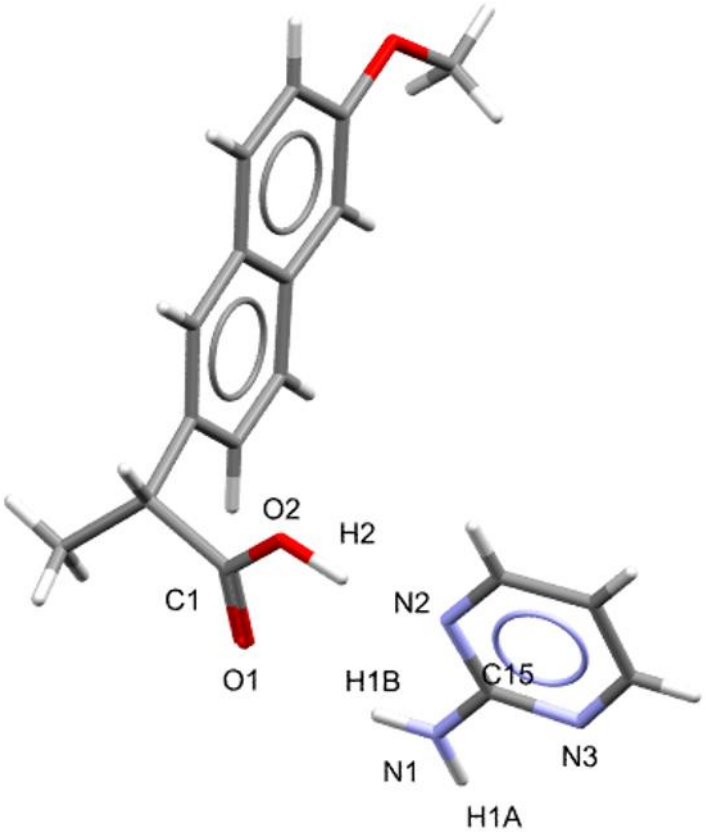

Figure A7. 8 - Asymmetric unit of RS-naproxen:2-aminopyrimidine (1:1) co-crystal, highlighting labelling of atoms involved in key intermolecular interactions

Table A7. 4 - Hydrogen bonding interactions with the RS-naproxen:2-aminopyrimidine (1:1) co-crystal, highlighting the key interaction lengths and angles

D	**H**	**A**	**d(D-H) (Å)**	**d(H-A) (Å)**	**d(D-A) (Å)**	**D-H-A (º)**
N1	*H1A*	*O1*[1]	0.86	2.23	2.9967(17)	148.2
N1	*H1B*	*O1*	0.86	2.13	2.9748(17)	168.3
O2	*H2*	*N2*	0.997(10)	1.601(10)	2.5867(16)	169(2)

[1]2-X,1-Y,1-Z

A7.2 Materials of racemic and enantiopure naproxen with 2-amino-4,6-dimethylpyrimidine (*2ADMP*)

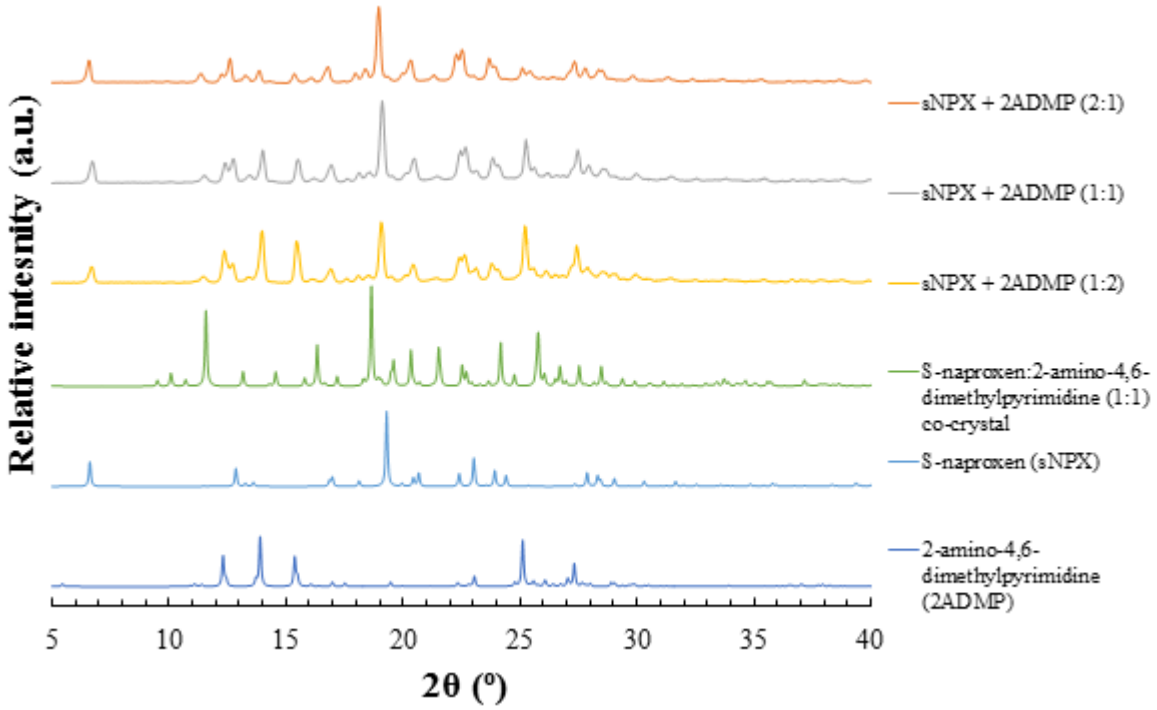

Figure A7. 9 - PXRD patterns from mechanochemically prepared samples of *sNPX* and *2ADMP*, ground neat in either 2:1, 1:1 or 1:2 molar ratios (top three patterns)

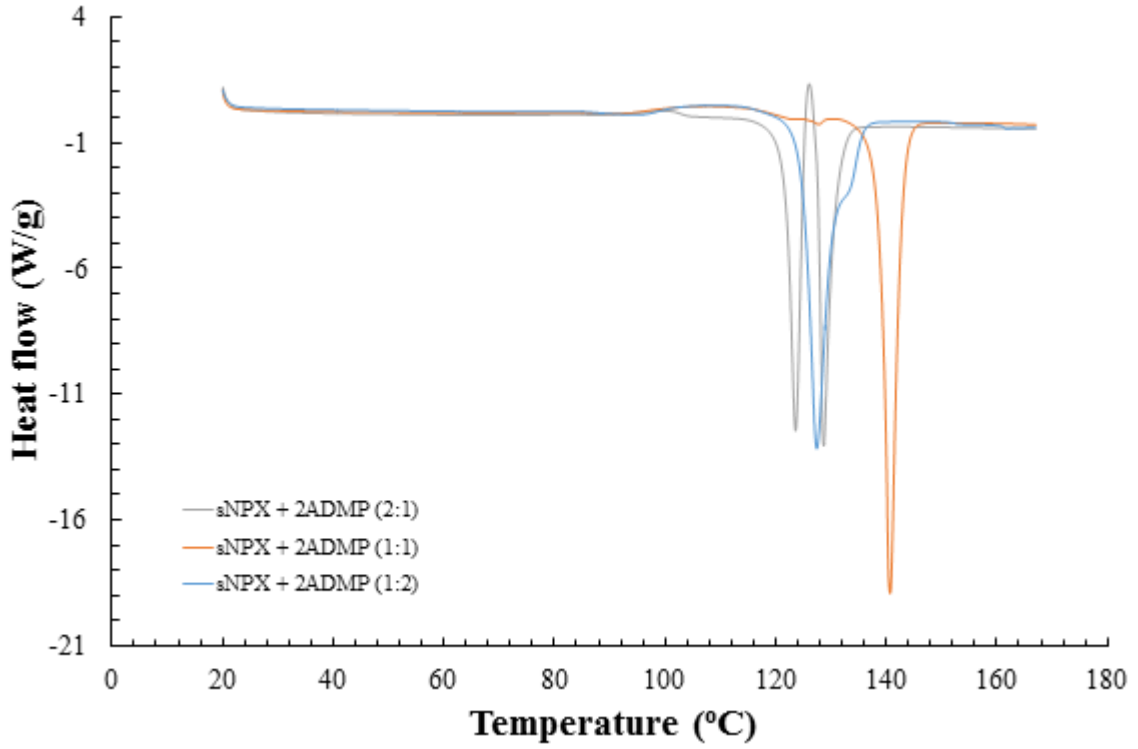

Figure A7. 10 - DSC traces from mechanochemically prepared samples of *sNPX* and *2ADMP*, ground neat in either 2:1, 1:1 or 1:2 molar ratios

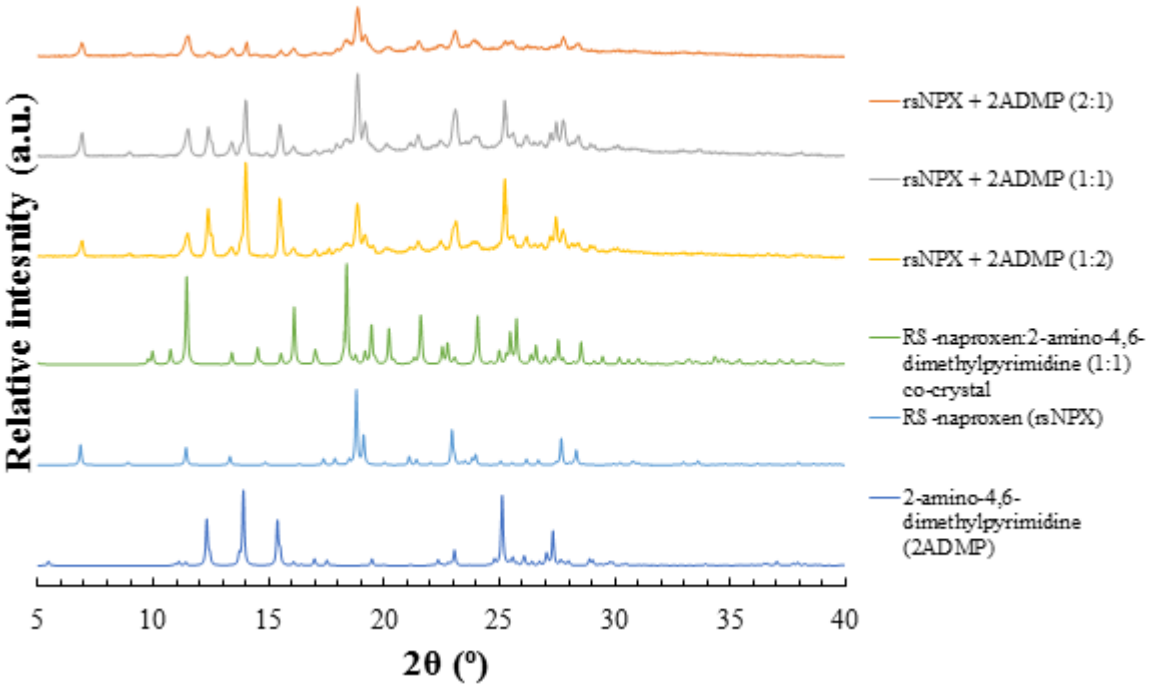

Figure A7. 11 - PXRD patterns from mechanochemically prepared samples of *rsNPX* and *2ADMP*, ground neat in either 2:1, 1:1 or 1:2 molar ratios (top three patterns)

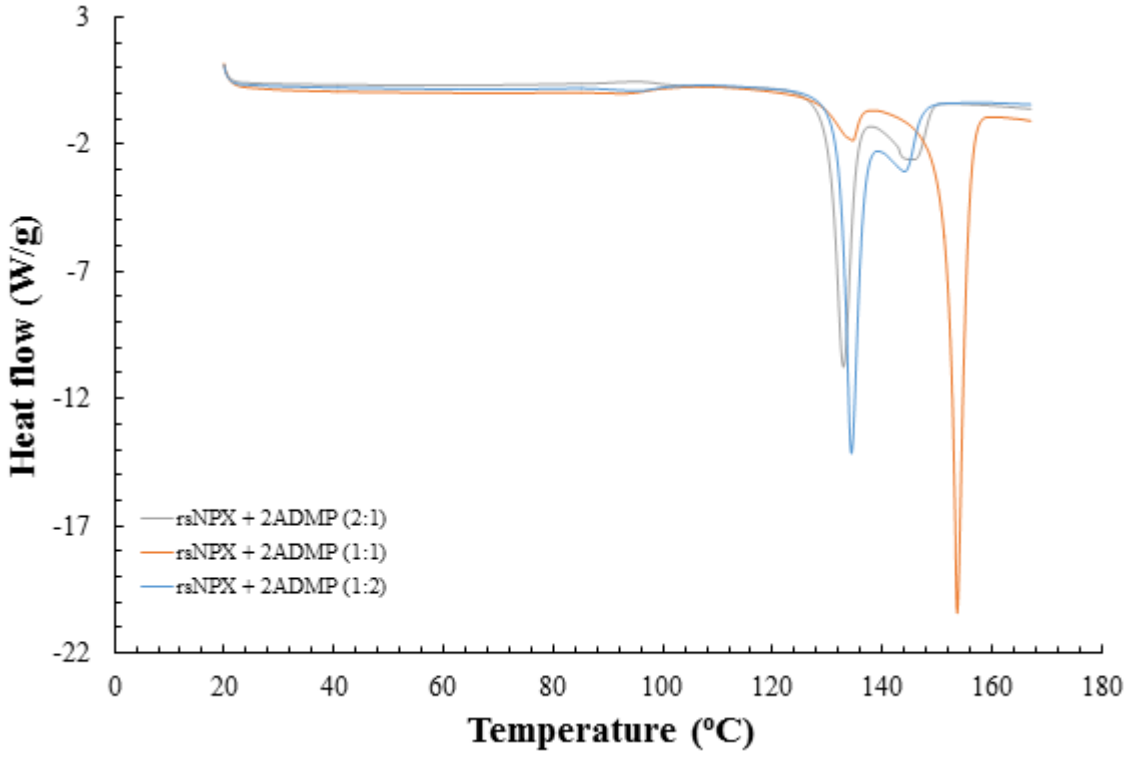

Figure A7. 12 - DSC traces from mechanochemically prepared samples of *rsNPX* and *2ADMP*, ground neat in either 2:1, 1:1 or 1:2 molar ratios

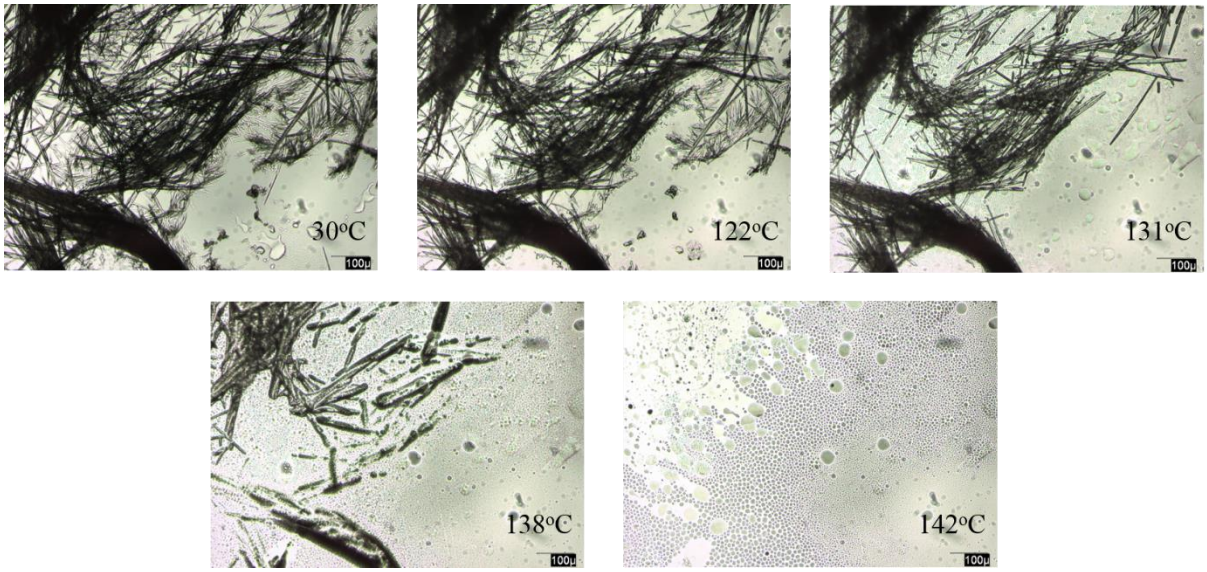

Figure A7. 13 - HSM images of the S-naproxen:2-amino-4,6-dimethylpyrimidine (1:1) co-crystal, prepared via crash cooling crystallisation from ethanol (100µm scale)

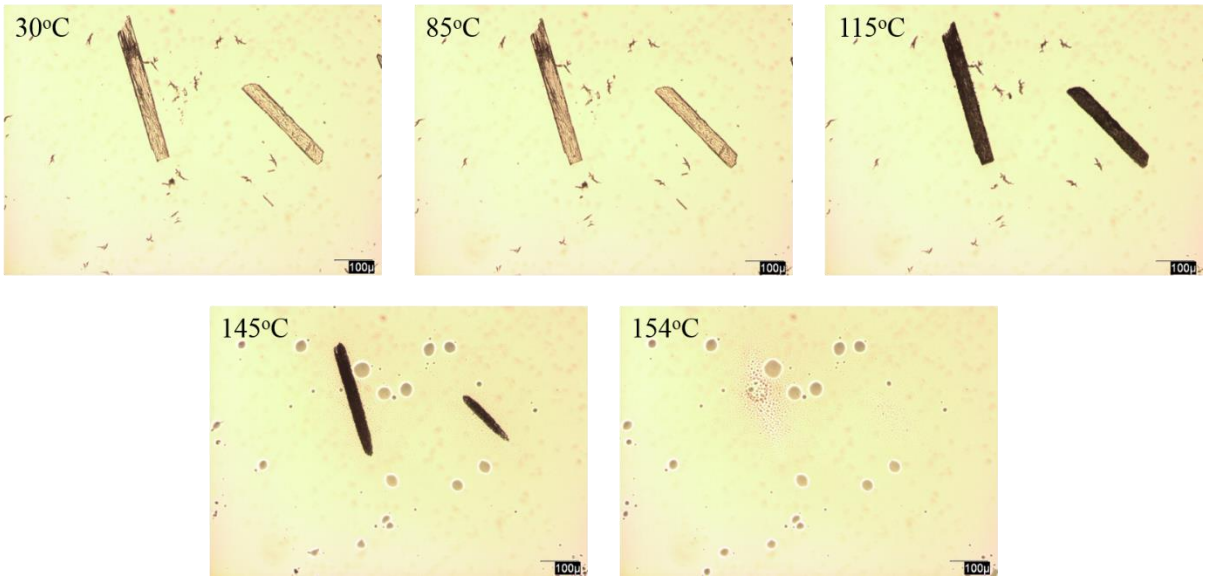

Figure A7. 14 - HSM images of the RS-naproxen:2-amino-4,6-dimethylpyrimidine (1:1) co-crystal, prepared via crash cooling crystallisation from ethanol (100µm scale)

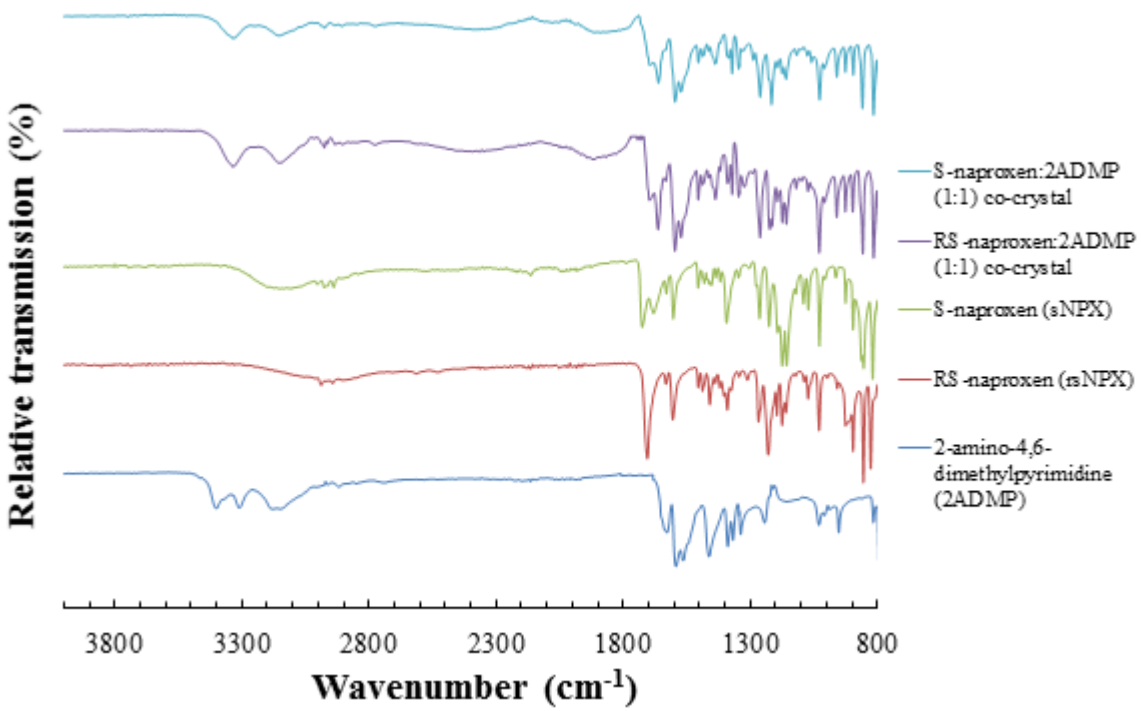

Figure A7. 15 - IR spectra of the S-naproxen:2-amino-4,6-dimethylpyrimidine (1:1) and RS-naproxen:2-amino-4,6-dimethylpyrimidine (1:1) co-crystals, compared to that of the starting materials

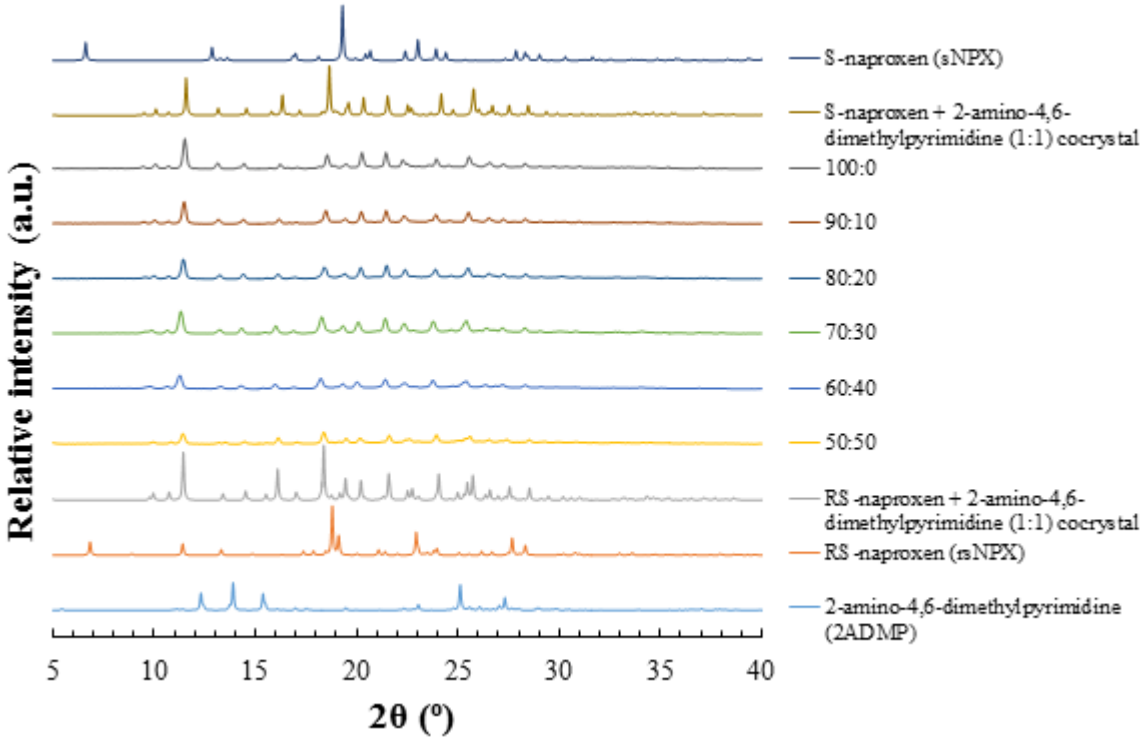

Figure A7. 16 - PXRD patterns, highlighting the change in phase from the racemic to the enantiopure (1:1) co-crystal of *NPX* and *2ADMP*, with increasing molar contributions of *sNPX* (100:0, 90:10, 80:20, 70:30, 60:40, 50:50)

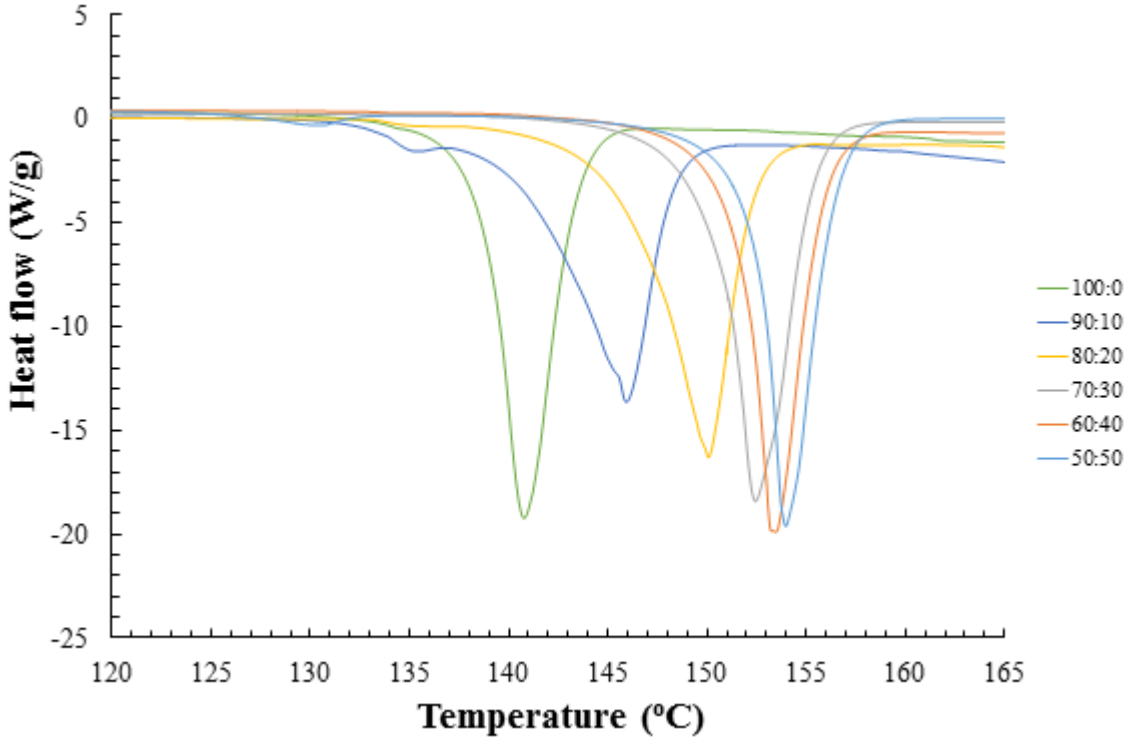

Figure A7. 17 - DSC traces, highlighting the change in phase from the racemic to the enantiopure (1:1) co-crystal of *NPX* and *2ADMP*, with increasing molar contributions of *sNPX*

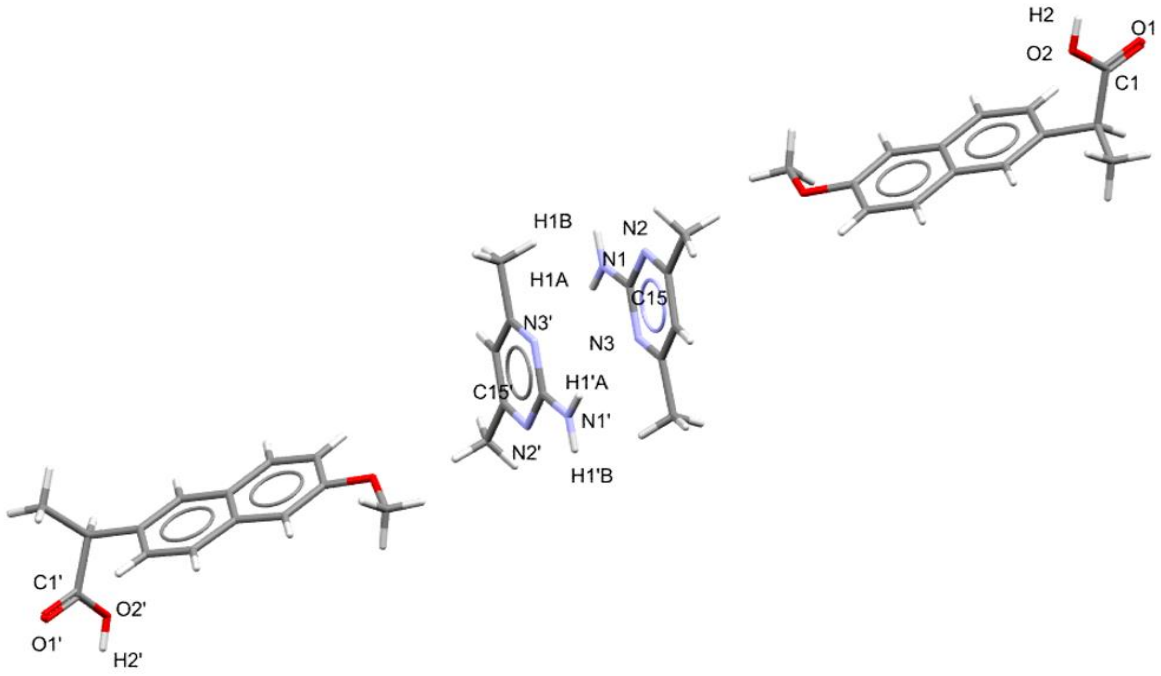

Figure A7. 18 - Asymmetric unit of S-naproxen:2-amino-4,6-dimethylpyrimidine (1:1) co-crystal, highlighting labelling of atoms involved in key intermolecular interactions

Table A7. 5 - Hydrogen bonding interactions with the S-naproxen:2-amino-4,6-dimethylpyrimidine (1:1) co-crystal, highlighting the key interaction lengths and angles

D	H	A	d(D-H) (Å)	d(H-A) (Å)	d(D-A) (Å)	D-H-A (º)
O2'	*H2'*	*N2'*[1]	0.82	1.82	2.629(4)	168.7
N1'	*H1'A*	*N3*[2]	0.86	2.18	3.040(4)	178.9
N1'	*H1'B*	*O1'*[3]	0.86	2.14	2.976(4)	163.5
O2	*H2*	*N2*[4]	0.82	1.88	2.683(4)	165.8
N1	*H1A*	*N3'*[5]	0.86	2.10	2.962(4)	177.3
N1	*H1B*	*O1*[6]	0.86	2.07	2.913(4)	165.5

[1]1-X,1/2+Y,-Z; [2]+X,-1+Y,+Z; [3]1-X,-1/2+Y,-Z; [4]1-X,-1/2+Y,1-Z; [5]+X,1+Y,+Z; [6]1-X,1/2+Y,1-Z

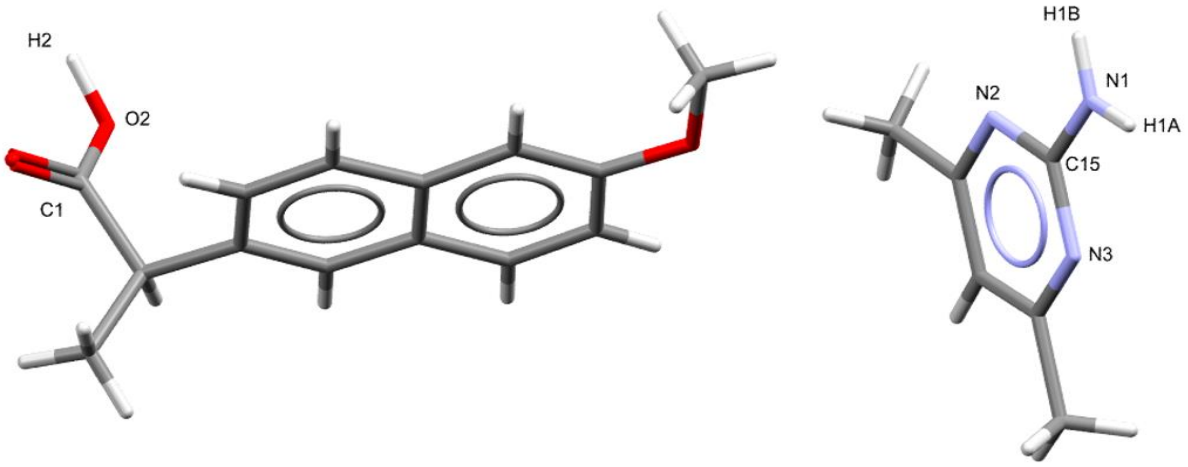

Figure A7. 19 - Asymmetric unit of RS-naproxen:2-amino-4,6-dimethylpyrimidine (1:1) co-crystal, highlighting labelling of atoms involved in key intermolecular interactions

Table A7. 6 - Hydrogen bonding interactions with the RS-naproxen:2-amino-4,6-dimethylpyrimidine (1:1) co-crystal, highlighting the key interaction lengths and angles

D	H	A	d(D-H) (Å)	d(H-A) (Å)	d(D-A) (Å)	D-H-A (º)
N1	*H1A*	*N3*[1]	0.86	2.14	3.002(3)	178.4
N1	*H1B*	*O1*[2]	0.86	2.12	2.957(3)	163.7
O2	*H2*	*N2*[3]	1.003(10)	1.645(15)	2.631(3)	167(5)

[1]-X,2-Y,-Z; [2]-X,1/2+Y,1/2-Z; [3]-X,-1/2+Y,1/2-Z

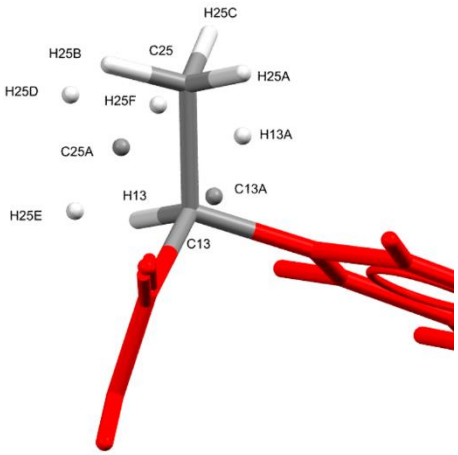

Figure A7. 20 - Labelled atoms, highlighting disorder in the RS-naproxen:2-amino-4,6-dimethylpyrimidine (1:1) co-crystal

Table A7. 7 - Atomic occupancy of disordered atoms in the RS-naproxen:2-amino-4,6-dimethylpyrimidine (1:1) co-crystal

Atom	Occupancy	Atom	Occupancy	Atom	Occupancy
C13	0.913(5)	*H13*	0.913(5)	*C25*	0.913(5)
H25A	0.913(5)	*H25B*	0.913(5)	*H25C*	0.913(5)
C13A	0.087(5)	*H13A*	0.087(5)	*C25A*	0.087(5)
H25D	0.087(5)	*H25E*	0.087(5)	*H25F*	0.087(5)

A7.3 Materials of racemic and enantiopure naproxen with 2-amino-3-chloropyridine (*2A3CP*)

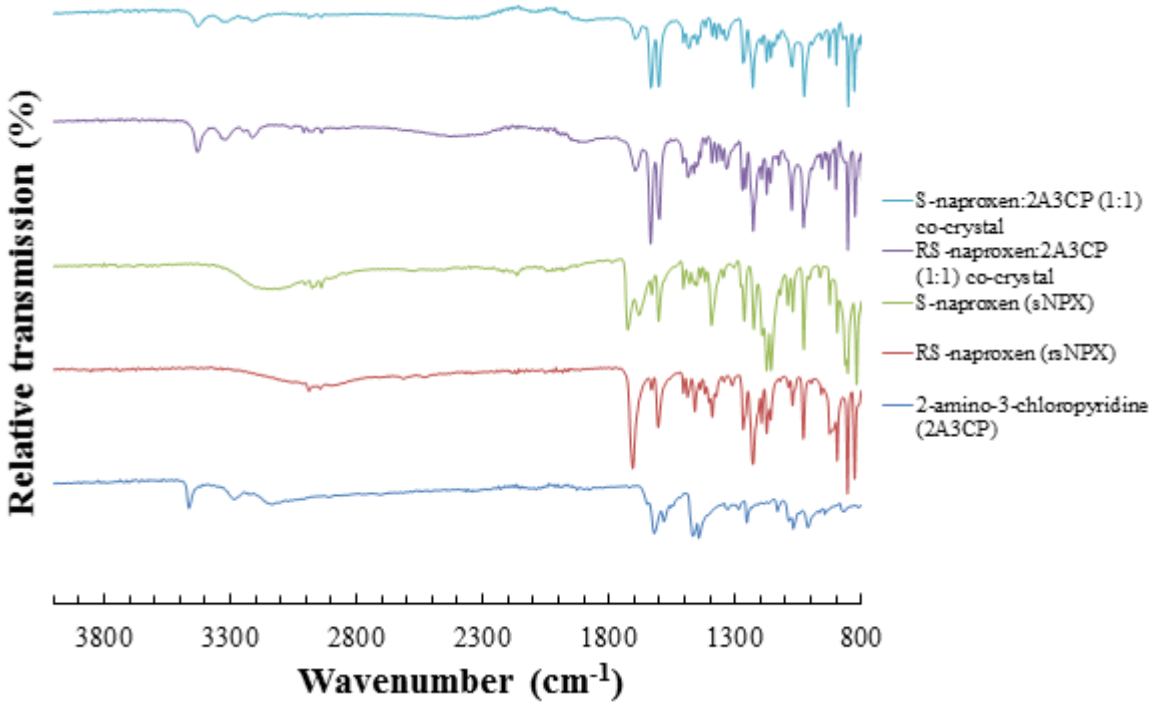

Figure A7. 21 - IR spectra of the S-naproxen:2-amino-3-chloropyridine (1:1) and RS-naproxen:2-amino-3-chloropyridine (1:1) co-crystals, compared to that of the starting materials

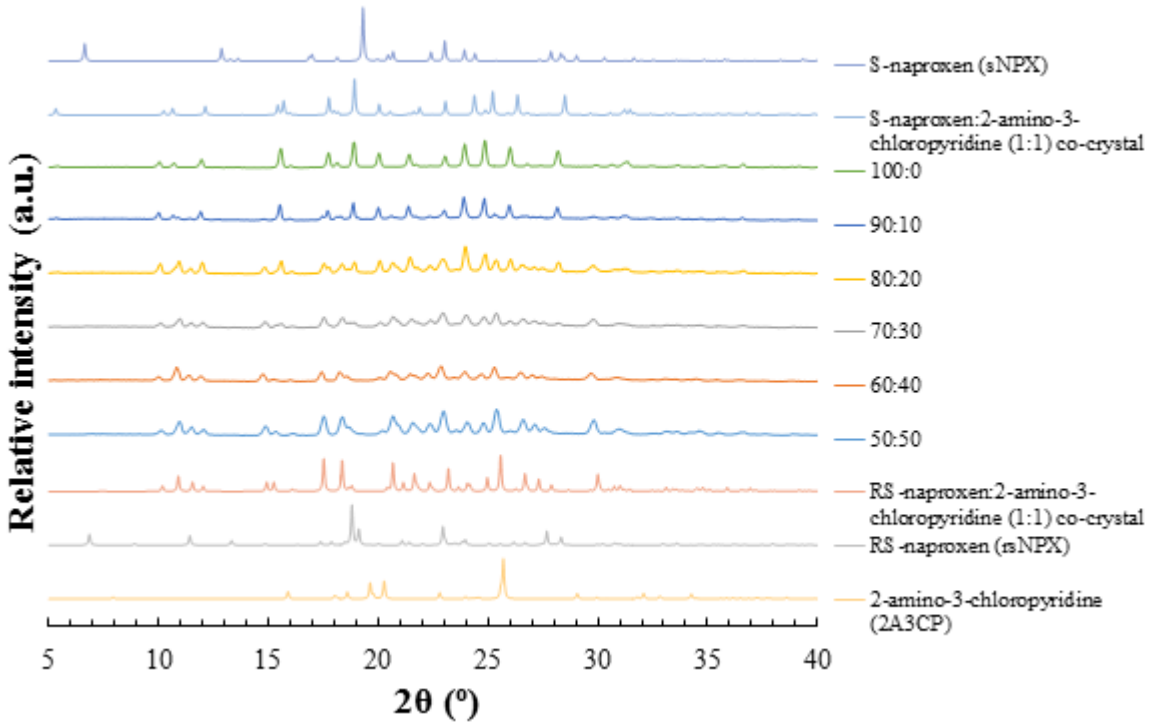

Figure A7. 22 - PXRD patterns, highlighting the change in phase from the racemic to the enantiopure (1:1) co-crystal of *NPX* and *2A3CP*, with increasing molar contributions of *sNPX* (100:0, 90:10, 80:20, 70:30, 60:40, 50:50)

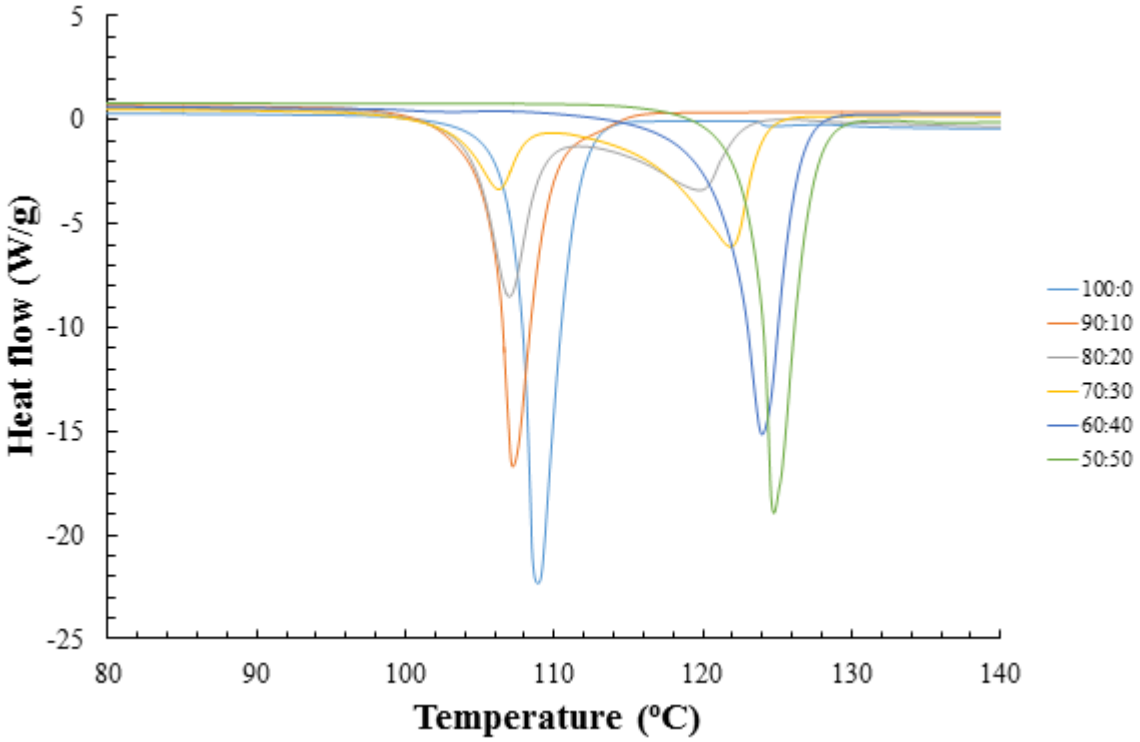

Figure A7. 23 - DSC traces, highlighting the change in phase from the racemic to the enantiopure (1:1) co-crystal of *NPX* and *2A3CP*, with increasing molar contributions of *sNPX*

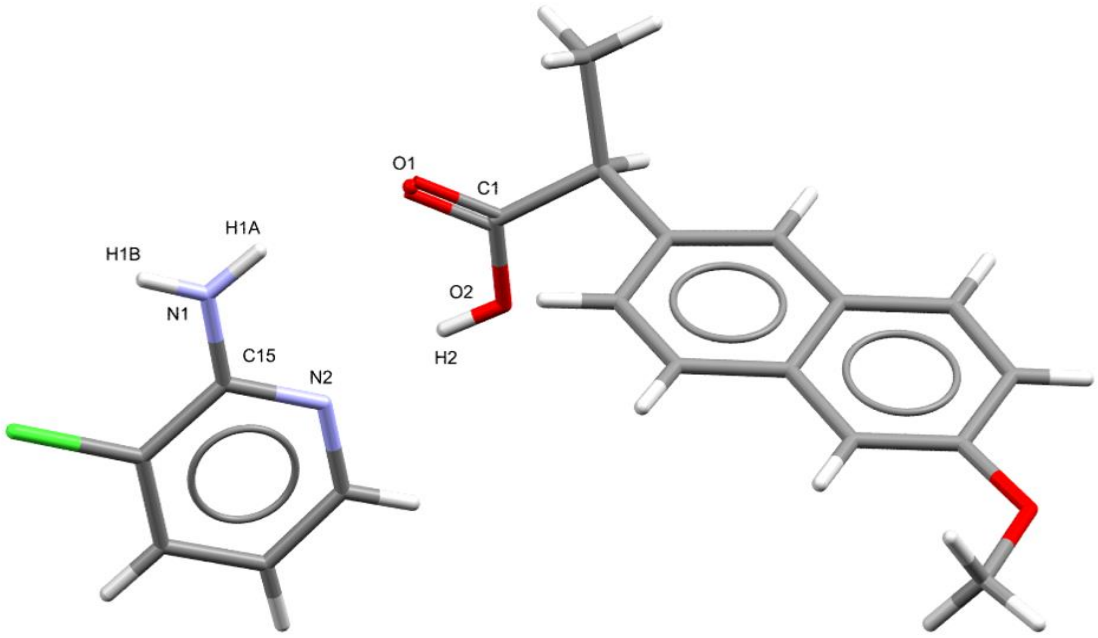

Figure A7. 24 - Asymmetric unit of S-naproxen:2-amino-3-chloropyridine (1:1) co-crystal, highlighting labelling of atoms involved in key intermolecular interactions

Table A7. 8 - Hydrogen bonding interactions with the RS-naproxen:2-amino-3-chloropyridine (1:1) co-crystal, highlighting the key interaction lengths and angles

D	H	A	d(D-H) (Å)	d(H-A) (Å)	d(D-A) (Å)	D-H-A (º)
O2	H2	N2	0.82	1.82	2.636(2)	170.5
N1	H1A	O1	0.86	2.11	2.948(2)	163.9
N1	H1B	O1[1]	0.86	2.25	2.992(2)	145.0

[1]1-X,-1/2+Y,2-Z

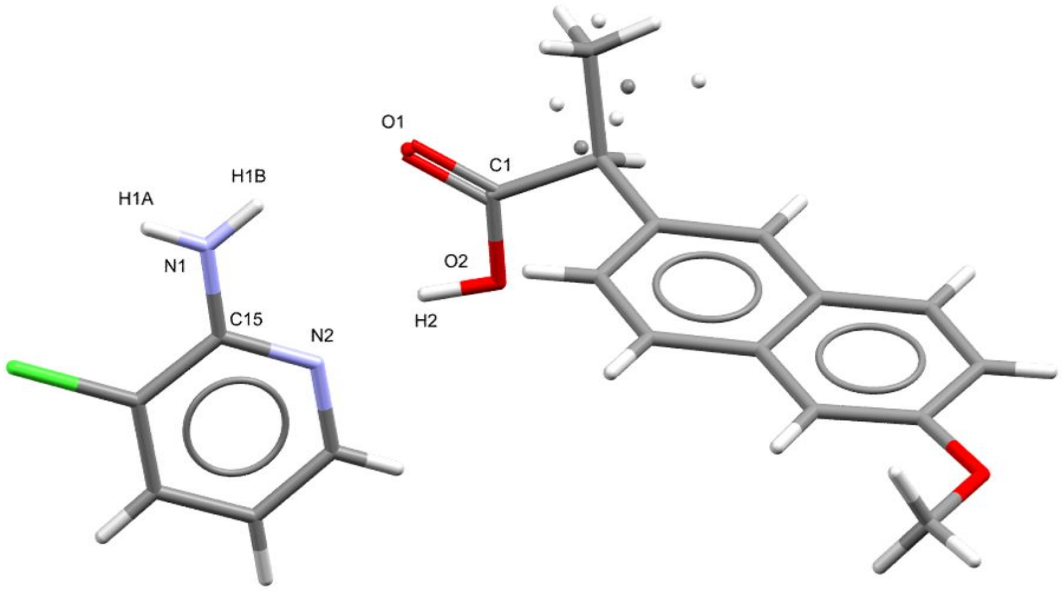

Figure A7. 25 - Asymmetric unit of RS-naproxen:2-amino-3-chloropyridine (1:1) co-crystal, highlighting labelling of atoms involved in key intermolecular interactions

Table A7. 9 - Hydrogen bonding interactions with the RS-naproxen:2-amino-3-chloropyridine (1:1) co-crystal, highlighting the key interaction lengths and angles

D	**H**	**A**	**d(D-H) (Å)**	**d(H-A) (Å)**	**d(D-A) (Å)**	**D-H-A (º)**
N1	H1A	O1[1]	0.86	2.22	3.016(6)	154.5
N1	H1B	O1	0.86	2.16	2.991(7)	161.3
O2	H2	N2	1.003(13)	1.74(3)	2.694(6)	157(6)

[1]1-X,2-Y,-1/2+Z

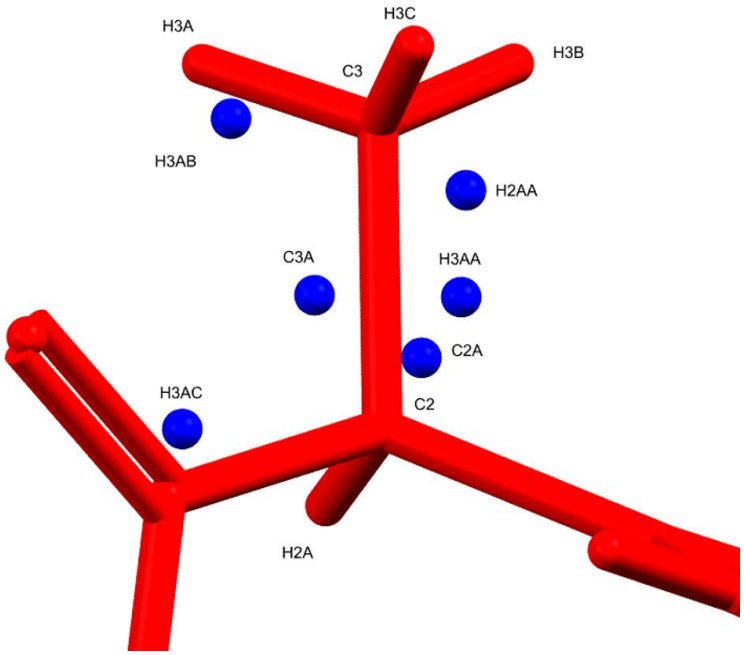

Figure A7. 26 - Labelled atoms, highlighting disorder in the RS-naproxen:2-amino-3-chloropyridine (1:1) co-crystal (*sNPX* in red, *rNPX* in blue)

Table A7. 10 - Atomic occupancy of disordered atoms in the RS-naproxen:2-amino-3-chloropyridine (1:1) co-crystal

Atom	***Occupancy***	**Atom**	***Occupancy***	**Atom**	***Occupancy***
C2	0.813(10)	H2A	0.813(10)	C3	0.813(10)
H3A	0.813(10)	H3B	0.813(10)	H3C	0.813(10)
C2A	0.187(10)	H2AA	0.187(10)	C3A	0.187(10)
H3AA	0.187(10)	H3AB	0.187(10)	H3AC	0.187(10)

A7.4 Materials of racemic and enantiopure naproxen with 2-amino-4-chloropyridine (*2A4CP*)

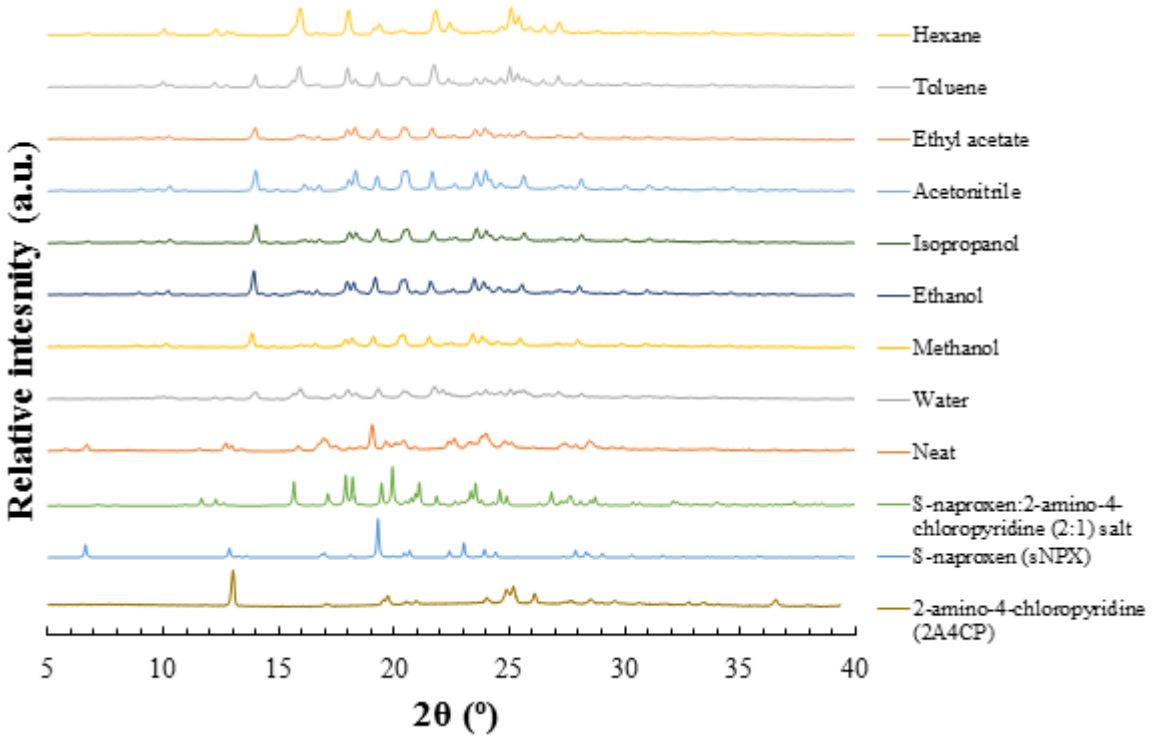

Figure A7. 27 - PXRD patterns of mechanochemical preparations of *sNPX* with *2A4CP* in a 1:1 molar ratio, ground either neat, or with minimum quantities of water, methanol, ethanol, isopropanol, acetonitrile, ethyl acetate, toluene or hexane, respectively

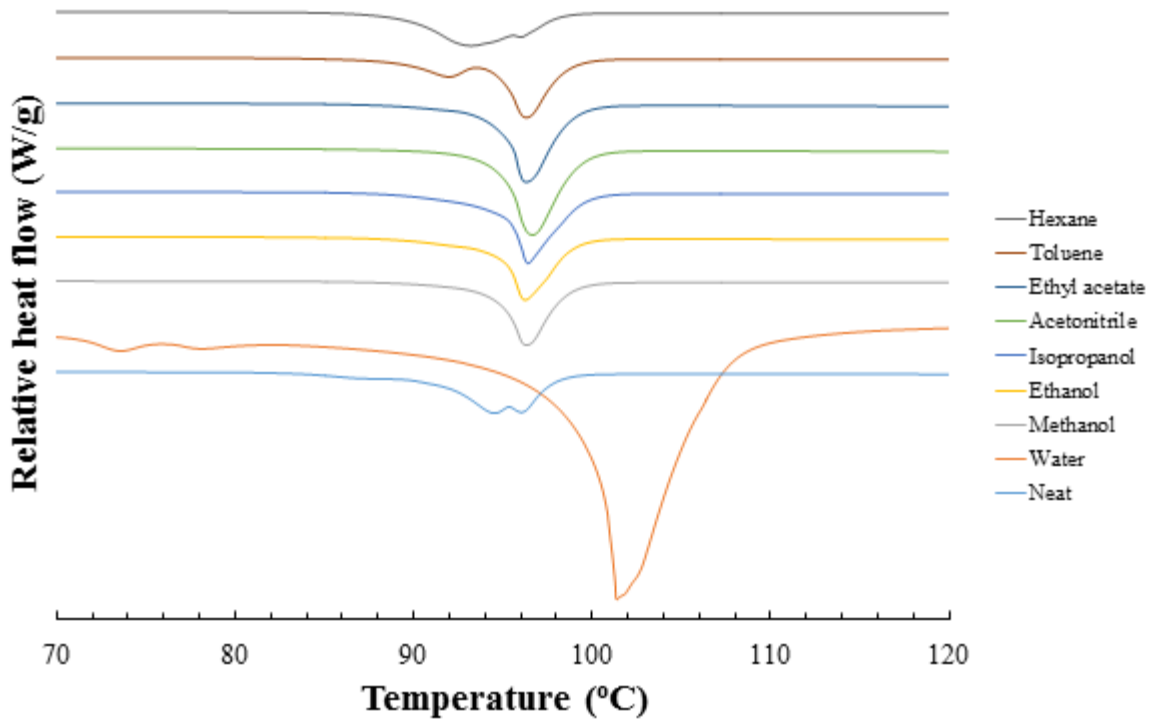

Figure A7. 28 - DSC traces of mechanochemical preparations of *sNPX* with *2A4CP* in a 1:1 molar ratio, ground either neat, or with minimum quantities of water, methanol, ethanol, isopropanol, acetonitrile, ethyl acetate, toluene or hexane, respectively

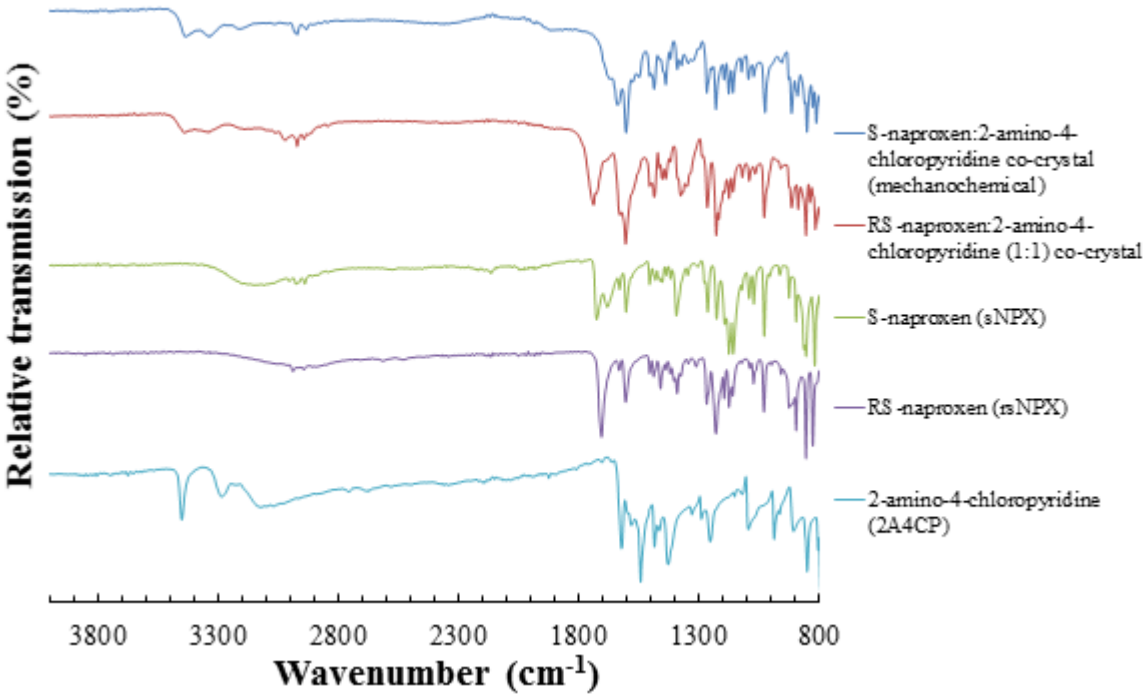

Figure A7. 29 - IR spectra of the S-naproxen:2-amino-4-chloropyridine co-crystal (mechanochemically prepared) and RS-naproxen:2-amino-4-chloropyridine (1:1) co-crystals, compared to that of the starting materials

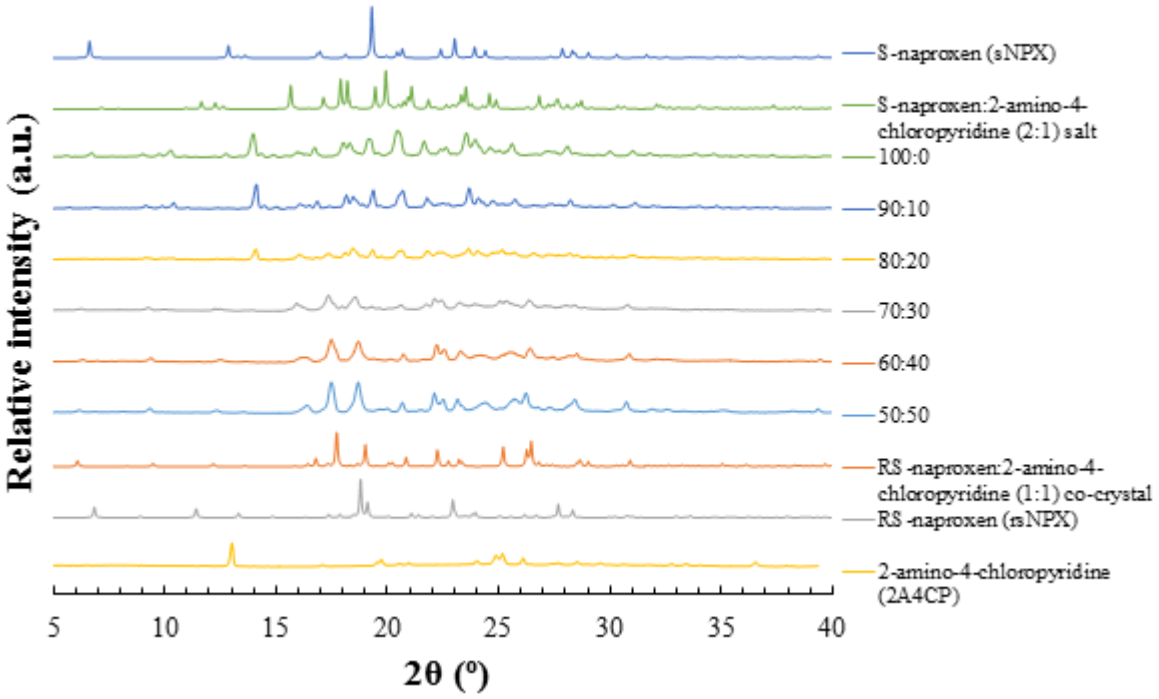

Figure A7. 30 - PXRD patterns, highlighting the change in phase from the racemic to the enantiopure (1:1) co-crystal of *NPX* and *2A4CP*, with increasing molar contributions of *sNPX*, prepared mechanochemically with ethanol (100:0, 90:10, 80:20, 70:30, 60:40, 50:50)

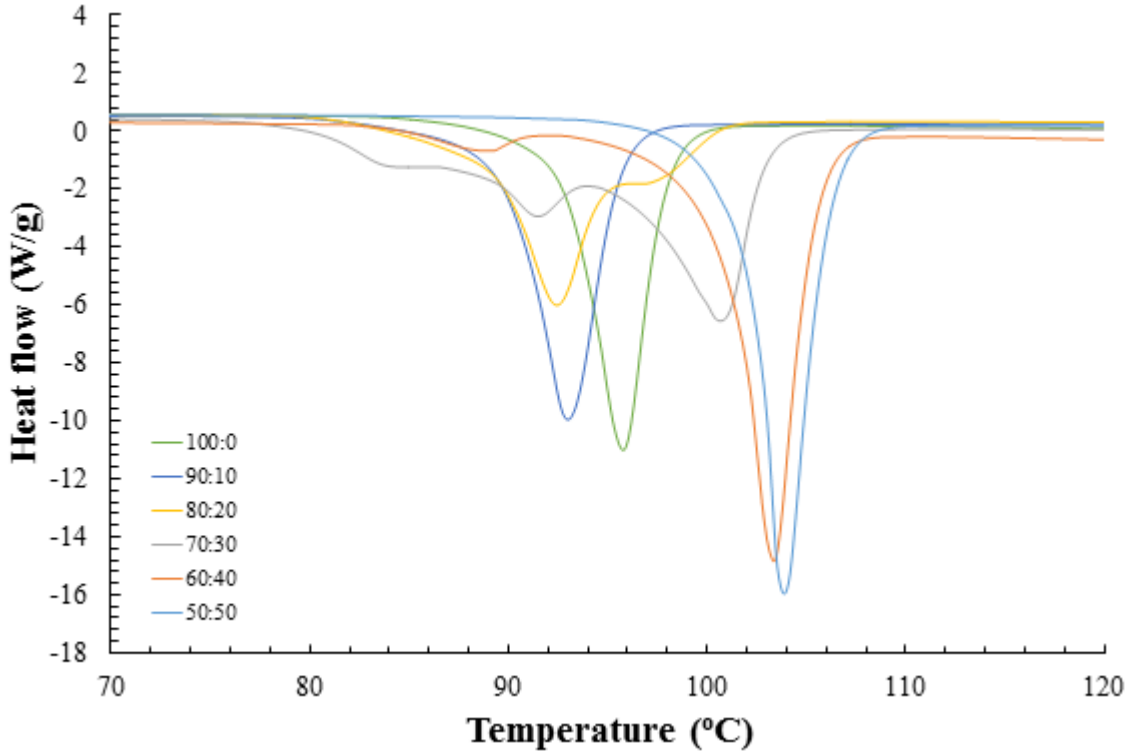

Figure A7. 31 - DSC traces, highlighting the change in phase from the racemic to the enantiopure (1:1) co-crystal of *NPX* and *2A4CP*, with increasing molar contributions of *sNPX*, prepared mechanochemically with ethanol

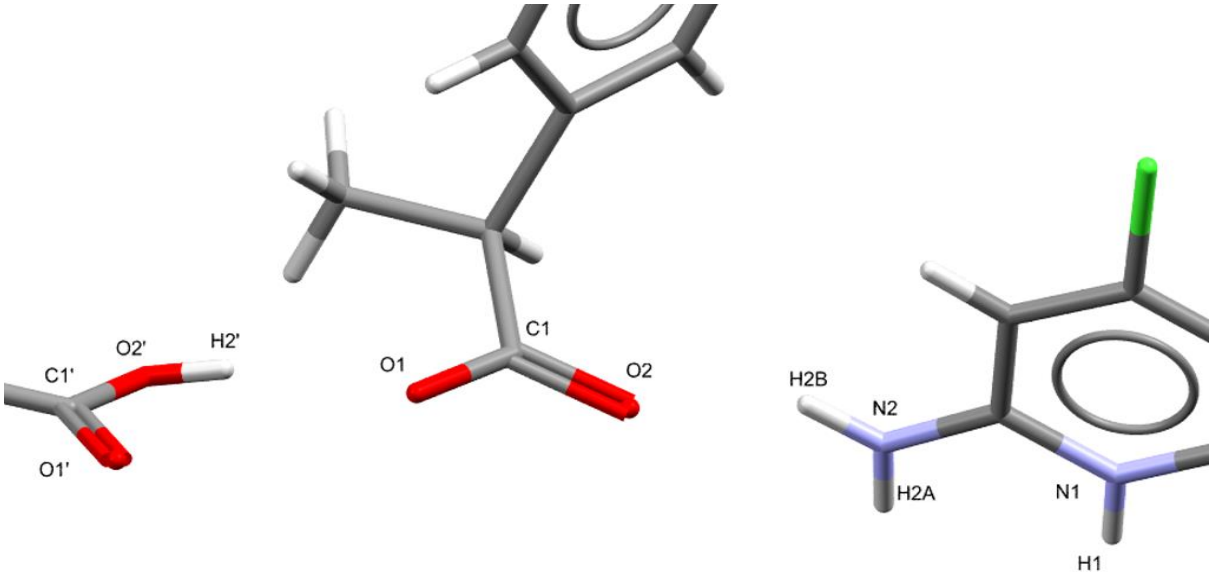

Figure A7. 32 - Asymmetric unit of S-naproxen:2-amino-4-chloropyridine (2:1) salt, highlighting labelling of atoms involved in key intermolecular interactions

Table A7. 11 - Hydrogen bonding interactions with the S-naproxen:2-amino-4-chloropyridine (2:1) salt, highlighting the key interaction lengths and angles

D	H	A	d(D-H) (Å)	d(H-A) (Å)	d(D-A) (Å)	D-H-A (º)
N1	H1	O1[1]	0.86	1.86	2.717(7)	172.1
N2	H2A	O2[1]	0.86	1.89	2.741(8)	173.3
N2	H2B	O2	0.86	1.99	2.773(8)	150.9
O2'	H2'	O1	0.800(14)	1.89(4)	2.643(6)	157(10)

[1]1-X,-1/2+Y,1-Z

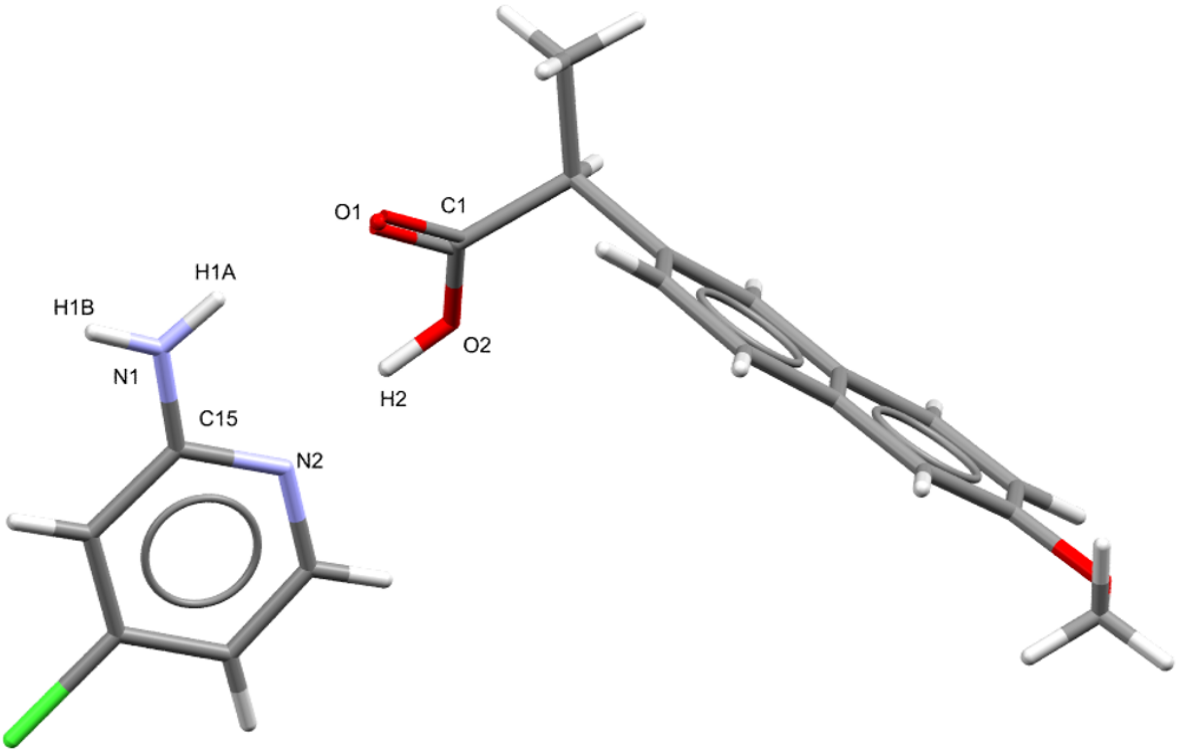

Figure A7. 33 - Asymmetric unit of RS-naproxen:2-amino-4-chloropyridine (1:1) co-crystal, highlighting labelling of atoms involved in key intermolecular interactions

Table A7. 12 - Hydrogen bonding interactions with the RS-naproxen:2-amino-4-chloropyridine (1:1) co-crystal, highlighting the key interaction lengths and angles

D	H	A	d(D-H) (Å)	d(H-A) (Å)	d(D-A) (Å)	D-H-A (º)
N1	H1A	O1	0.86	2.11	2.946(3)	163.8
N1	H1B	O1[1]	0.86	2.23	2.866(3)	131.1
O2	H2	N2	0.916(10)	1.635(12)	2.544(3)	171(3)

[1]-X,-Y,2-Z

A7.5 Materials of racemic and enantiopure naproxen with 2-amino-5-chloropyridine (*2A5CP*)

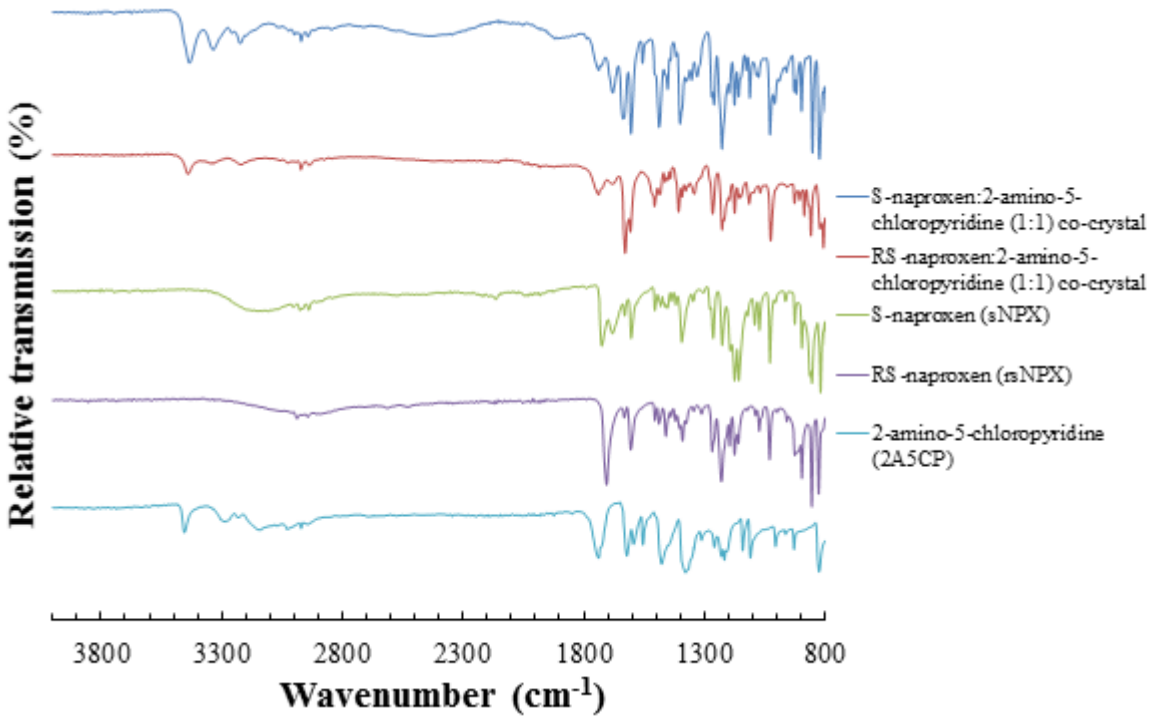

Figure A7. 34 - IR spectra of the S-naproxen:2-amino-5-chloropyridine (1:1) and RS-naproxen:2-amino-5-chloropyridine (1:1) co-crystals, compared to that of the starting materials

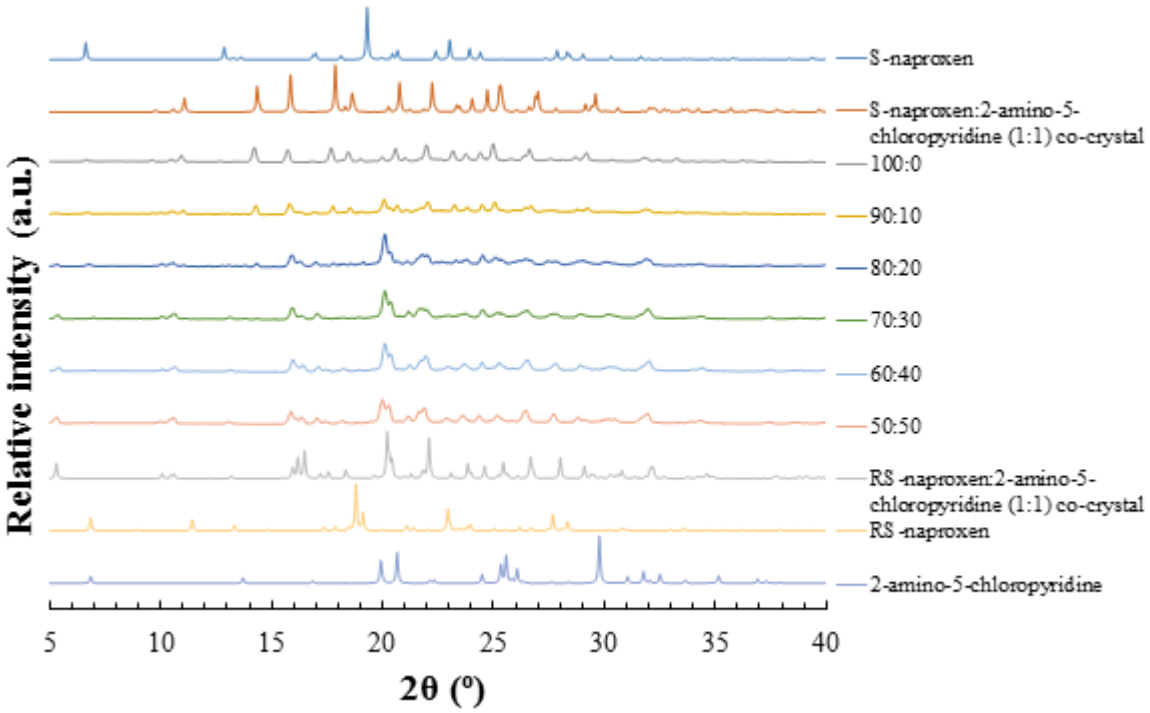

Figure A7. 35 - PXRD patterns, highlighting the change in phase from the racemic to the enantiopure (1:1) co-crystal of *NPX* and *2A5CP*, with increasing molar contributions of *sNPX*, prepared mechanochemically with ethanol (100:0, 90:10, 80:20, 70:30, 60:40, 50:50)

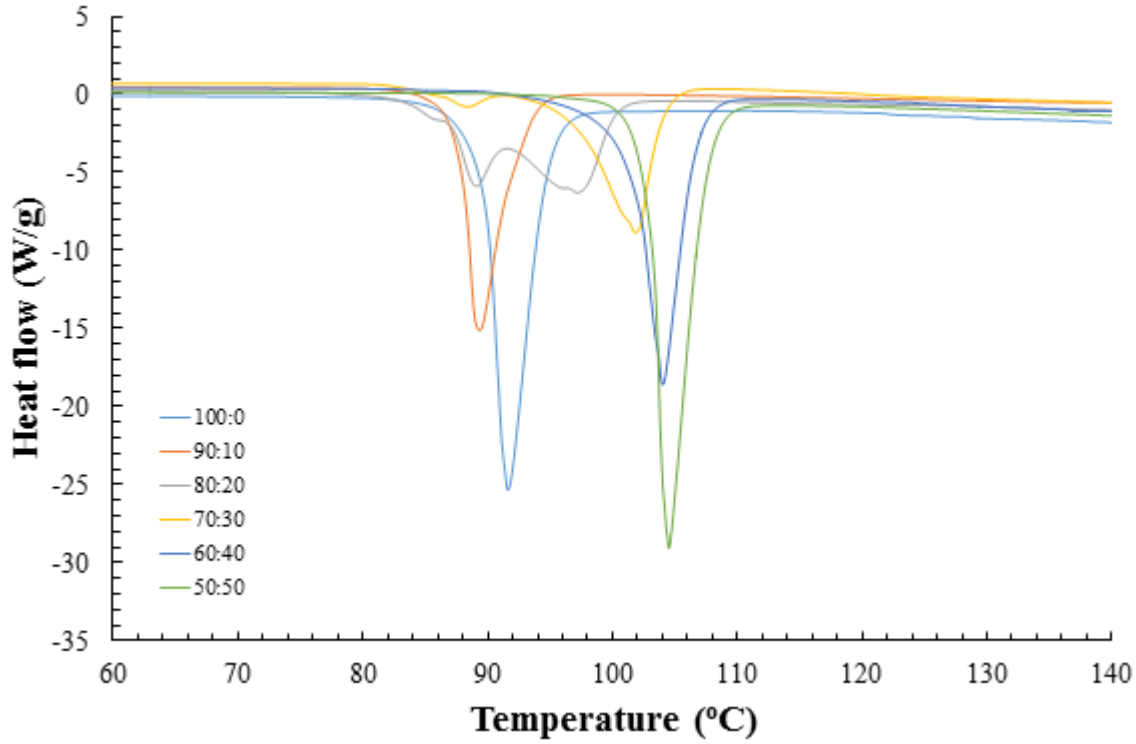

Figure A7. 36 - DSC traces, highlighting the change in phase from the racemic to the enantiopure (1:1) co-crystal of *NPX* and *2A5CP*, with increasing molar contributions of *sNPX*, prepared mechanochemically with ethanol

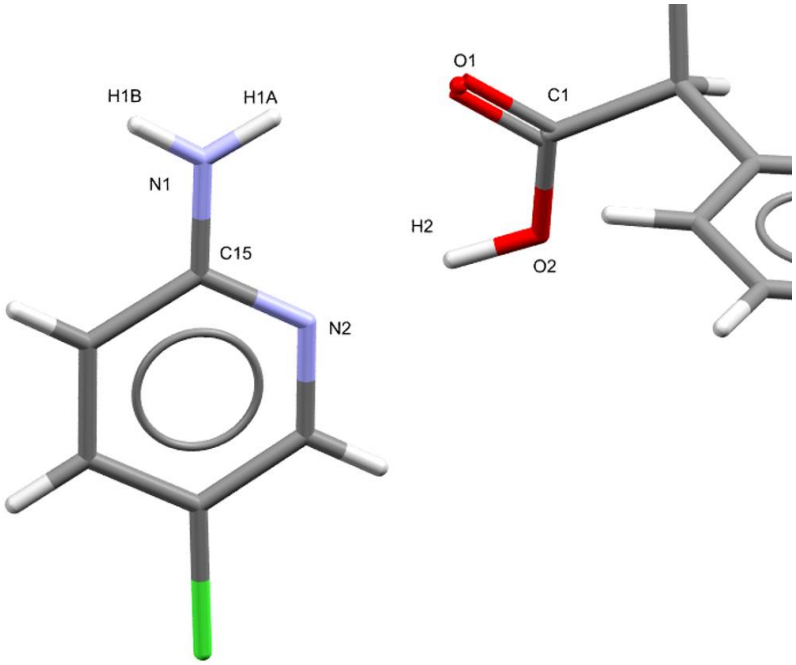

Figure A7. 37 - Asymmetric unit of S-naproxen:2-amino-5-chloropyridine (1:1) co-crystal, highlighting labelling of atoms involved in key intermolecular interactions

Table A7. 13 - Hydrogen bonding interactions with the S-naproxen:2-amino-5-chloropyridine (1:1) co-crystal, highlighting the key interaction lengths and angles

D	H	A	d(D-H) (Å)	d(H-A) (Å)	d(D-A) (Å)	D-H-A (º)
N1	H1A	O1	0.86	2.13	2.928(2)	154.8
N1	H1B	O1[1]	0.86	2.13	2.944(2)	158.5
O2	H2	N2	0.991(13)	1.718(14)	2.704(2)	173(3)

[1]1-X,1/2+Y,-Z

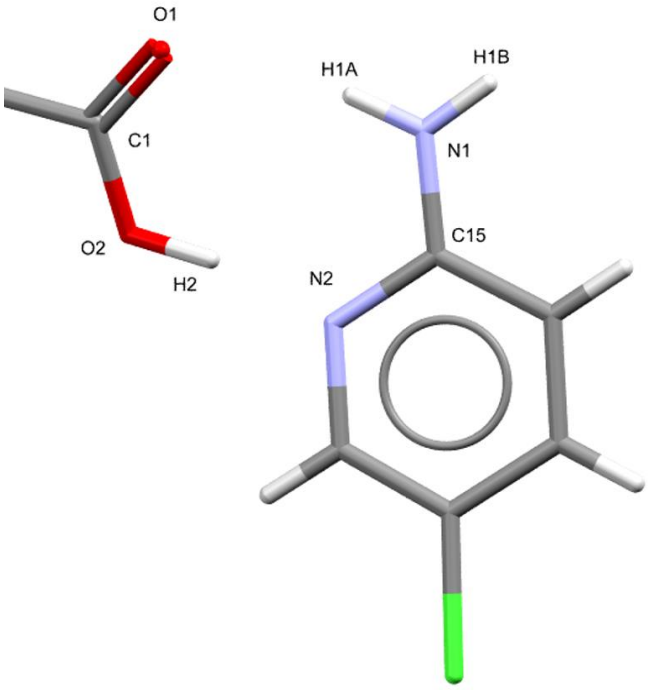

Figure A7. 38 - Asymmetric unit of RS-naproxen:2-amino-5-chloropyridine (1:1) co-crystal, highlighting labelling of atoms involved in key intermolecular interactions

Table A7. 14 - Hydrogen bonding interactions with the RS-naproxen:2-amino-5-chloropyridine (1:1) co-crystal, highlighting the key interaction lengths and angles

D	**H**	**A**	**d(D-H) (Å)**	**d(H-A) (Å)**	**d(D-A) (Å)**	**D-H-A (º)**
N1	H1A	O1	0.86	2.10	2.948(3)	167.7
N1	H1B	O1[1]	0.86	2.15	2.942(3)	152.9
O2	H2	N2	1.02(4)	1.57(4)	2.574(3)	169(4)

[1]-X,-Y,1-Z

A7.6 Materials of racemic and enantiopure naproxen with 2-amino-6-chloropyridine (*2A6CP*)

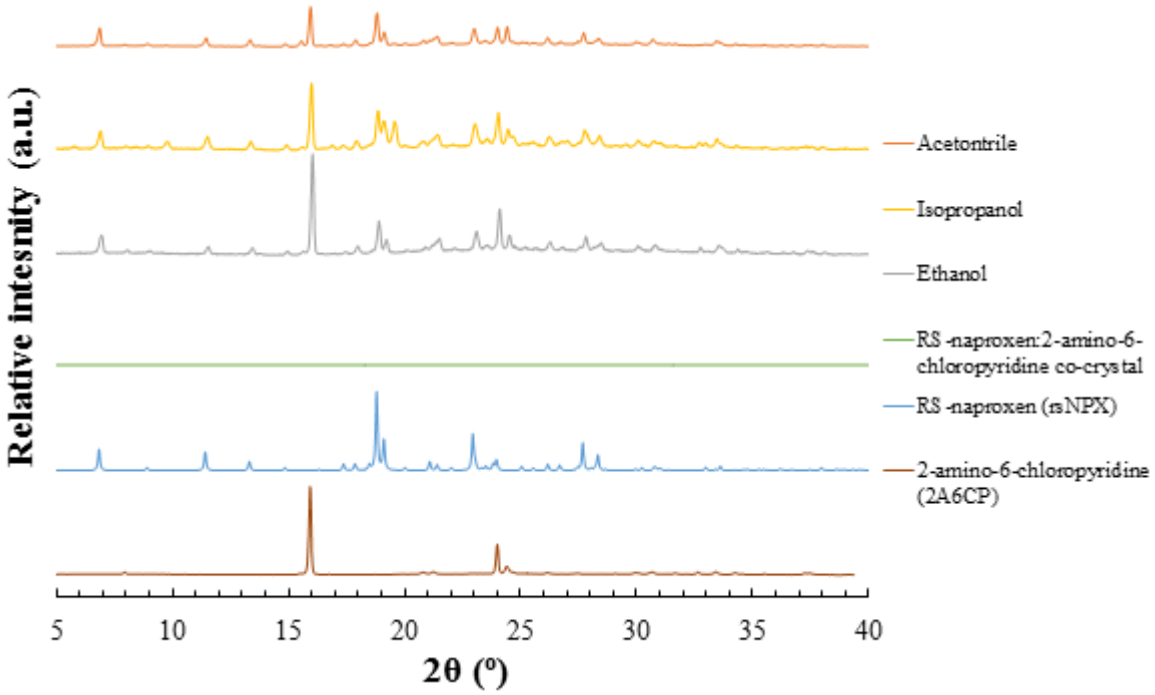

Figure A7. 39 - PXRD patterns of mechanochemical preparations of *sNPX* with *2A6CP* in a 1:1 molar ratio, ground with minimum quantities of ethanol, isopropanol and acetonitrile, respectively

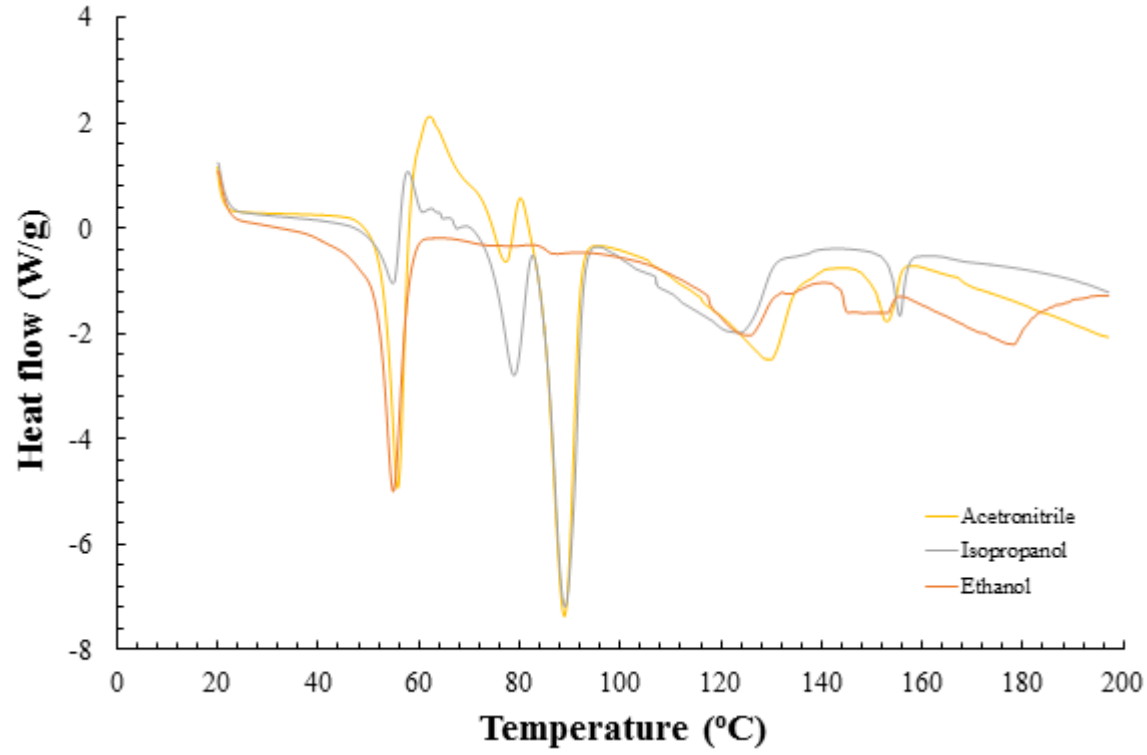

Figure A7. 40 - DSC traces of mechanochemical preparations of *sNPX* with *2A6CP* in a 1:1 molar ratio, ground with minimum quantities of ethanol, isopropanol and acetonitrile, respectively

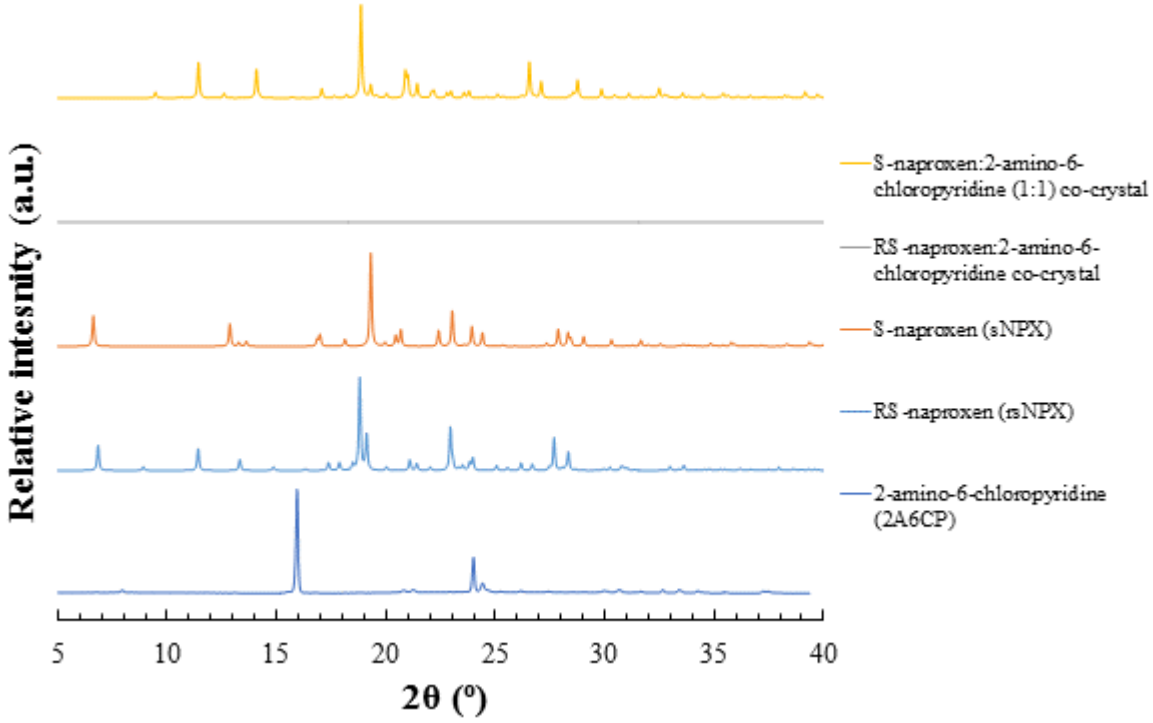

Figure A7. 41 - PXRD patterns of the S-naproxen:2-amino-6-chloropyridine (1:1) co-crystal, as derived from SCXRD, compared to that of the starting materials

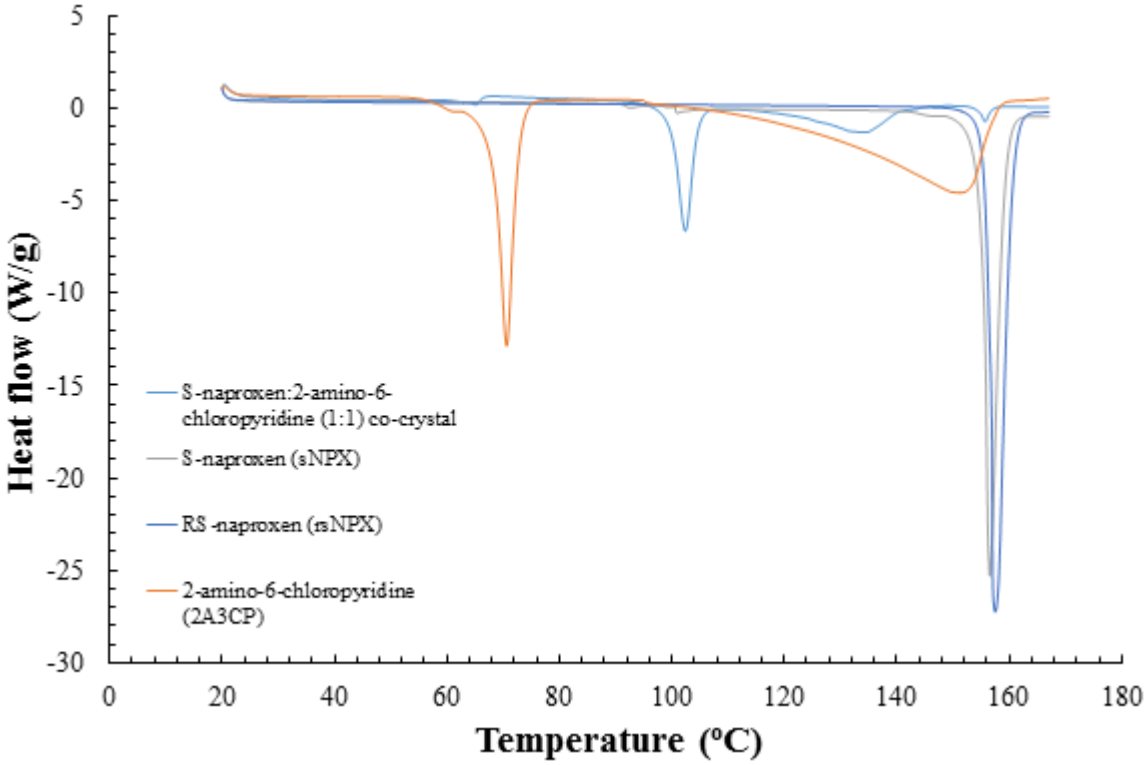

Figure A7. 42 - DSC traces of the S-naproxen:2-amino-6-chloropyridine (1:1) co-crystal, compared to that of the starting materials

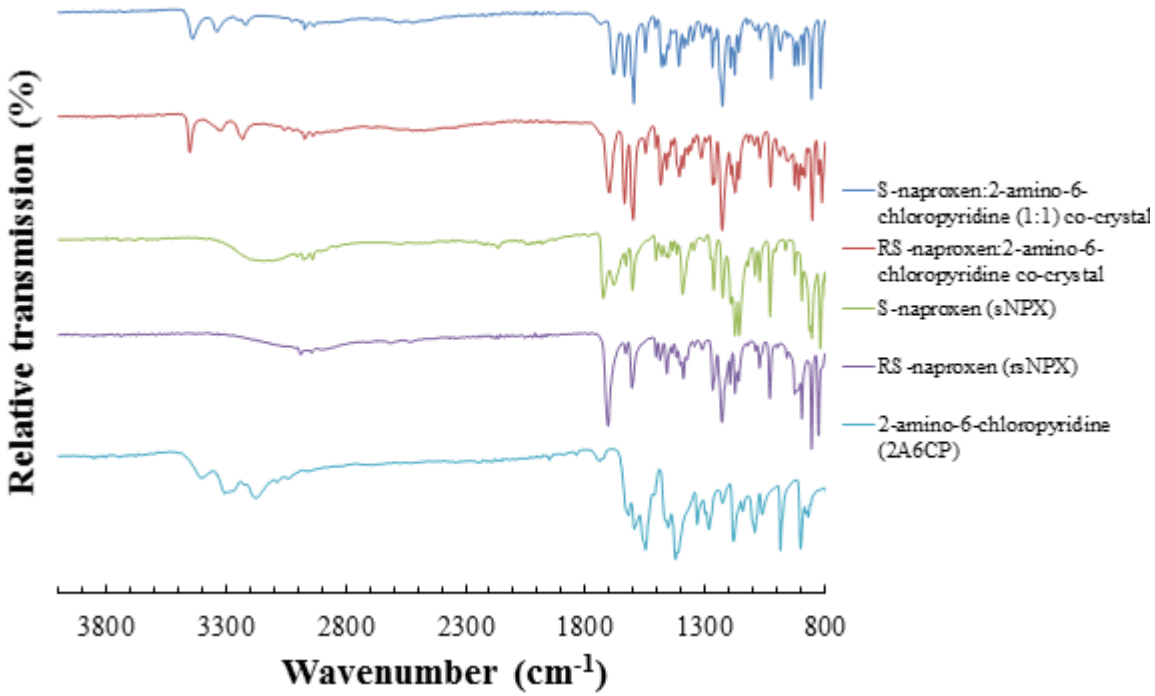

Figure A7. 43 - IR spectra of 1:1 mechanochemically prepared samples of either *sNPX* or *rsNPX* with *2A6CP*, compared to that of the starting materials

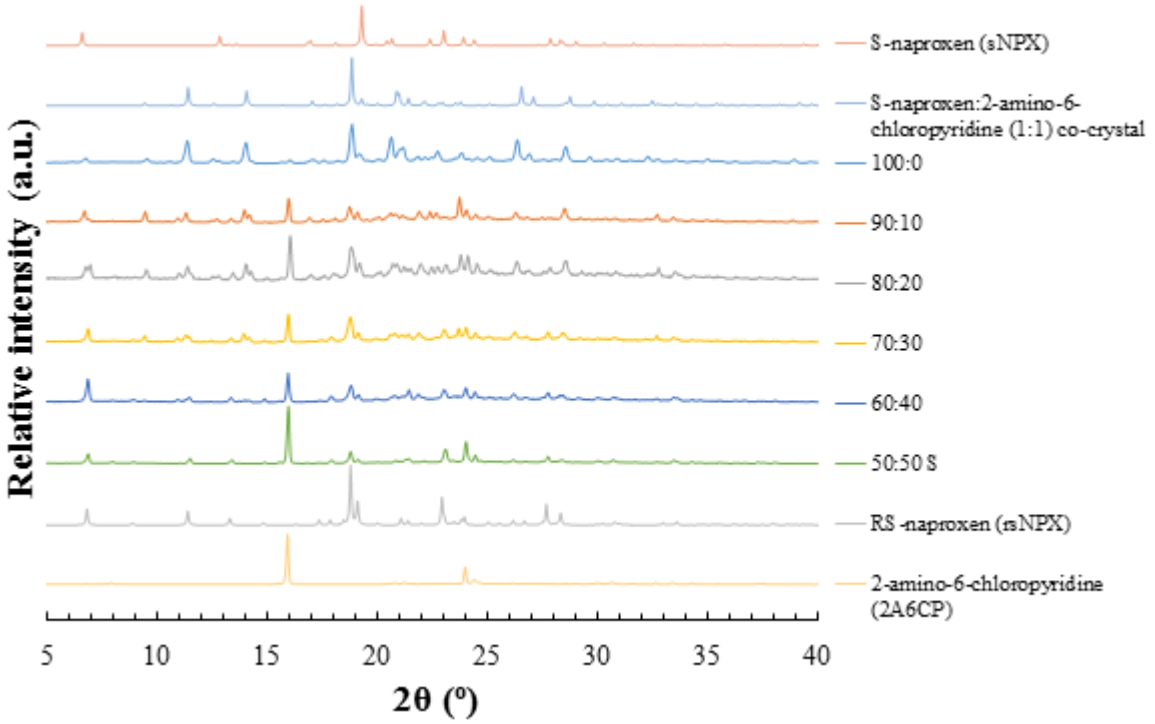

Figure A7. 44 - PXRD patterns, highlighting the change in phase from the racemic to the enantiopure (1:1) co-crystal of *NPX* and *2A6CP*, with increasing molar contributions of *sNPX*, prepared mechanochemically with ethanol (100:0, 90:10, 80:20, 70:30, 60:40, 50:50)

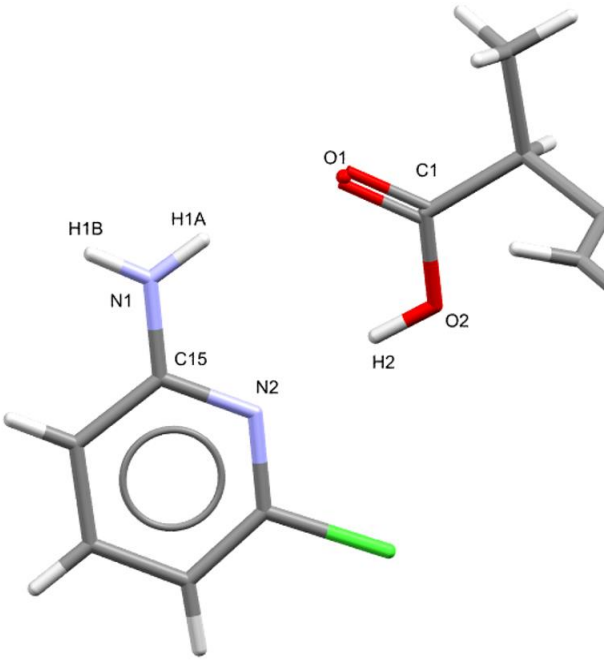

Figure A7. 45 - Asymmetric unit of S-naproxen:2-amino-6-chloropyridine (1:1) co-crystal, highlighting labelling of atoms involved in key intermolecular interactions

Table A7. 15 - Hydrogen bonding interactions with the S-naproxen:2-amino-6-chloropyridine (1:1) co-crystal, highlighting the key interaction lengths and angles

D	H	A	d(D-H) (Å)	d(H-A) (Å)	d(D-A) (Å)	D-H-A (º)
N1	H1A	O1	0.86	2.11	2.936(4)	160.7
N1	H1B	O1[1]	0.86	2.09	2.917(3)	161.4
O2	H2	N2	0.89(4)	1.89(4)	2.779(4)	174(4)

[1] 1/2+X,1/2-Y,1-Z

Appendix (A8) Chapter 8

Table A8. 1 - Crystallographic data for the polymorphic forms of the co-formers imidazole (*I*), benzimidazole (*BI*) and acridine (*A*)

Co-former *Polymorph*	**CSD reference code**	**a (Å)**	**b (Å)**	**c (Å)**	**α (º)**	**β (º)**	**γ (º)**	**Volume (Å^3)**	**Space group**	**Collection temperature (K)**	**Formula**
Imidazole (I) *Form α*	IMAZOL21	7.326(7)	4.997(4)	9.556(9)	90	122.68(7)	90	294.449	$P2_1/c$	283-303	$C_3H_4N_2$
Imidazole (I) *Form β*	IMAZOL22	14.250(8)	8.623(4)	5.399(4)	90	90	90	663.417	Aba2	283-303	$C_3H_4N_2$
Benzimidazole (BI) *Form α*	BZDMAZ02	13.492(3)	6.805(1)	6.939(1)	90	90	90	637.101	$Pna2_1$	283-303	$C_7H_6N_2$
Benzimidazole (BI) *Form β*	BZDMAZ03	9.726(1)	16.688(1)	7.606(1)	90	90	90	1234.400	Pccn	283-303	$C_7H_6N_2$
Benzimidazole (BI) *Form γ*	BZDMAZ05	9.782(6)	7.859(4)	12.967(8)	90	90	90	996.861	Pbca	283-303	$C_7H_6N_2$
Acridine (A) hydrate *Form I*	ZZZRLO01	26.400(5)	8.893(5)	17.492(5)	90	90	90	4106.69	Pbcn	197	$C_{13}H_9N$ $0.75(H_2O)$
Acridine (A) *Form II*	ACRDIN01	11.375(3)	5.988(3)	13.647(3)	90	98.97	90	918.177	$P2_1/n$	283-303	$C_{13}H_9N$
Acridine (A) *Form III*	ACRDIN	16.292	18.831	6.072	90	95.07	90	1855.569	$P2_1/a$	283-303	$C_{13}H_9N$
Acridine (A) *Form IV*	ACRDIN03	15.610	29.340	6.220	90	90	90	2848.744	$P2_12_12_1$	283-303	$C_{13}H_9N$
Acridine (A) *Form V**	ACRDIN02	20.040	5.950	16.370	90	110.63	90	1826.759	Aa	283-303	$C_{13}H_9N$
Acridine (A) *Form VI*	ACRDIN05	6.174(2)	23.497(8)	12.868(4)	90	96.48(<1)	90	1854.830	Cc	187	$C_{13}H_9N$
Acridine (A) *Form VII*	ACRDIN06	6.057(1)	22.813(4)	13.204(2)	90	95.94(<1)	90	1814.687	$P2_1/n$	185	$C_{13}H_9N$

*Only unit cell parameters have been determined, no atomic coordinates available

A8.1 Materials of racemic and enantiopure naproxen with imidazole (*I*)

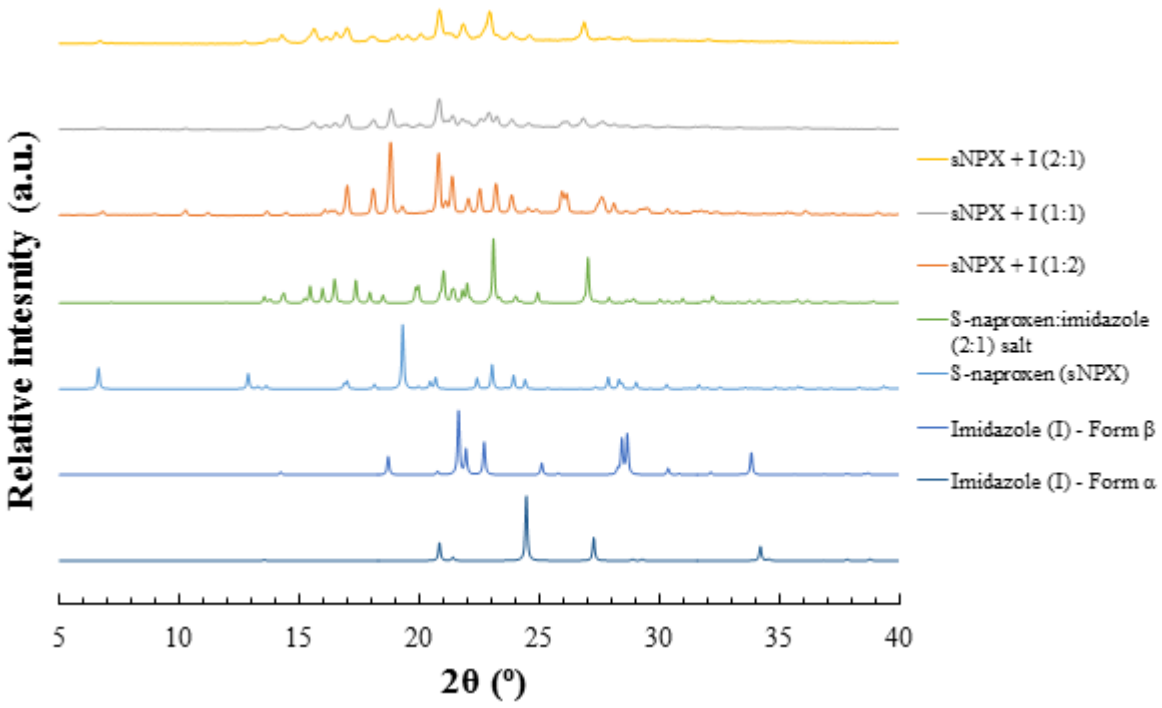

Figure A8. 1 - PXRD patterns from mechanochemically prepared samples of *sNPX* and *I*, ground neat in either 2:1, 1:1 or 1:2 molar ratios (top three patterns)

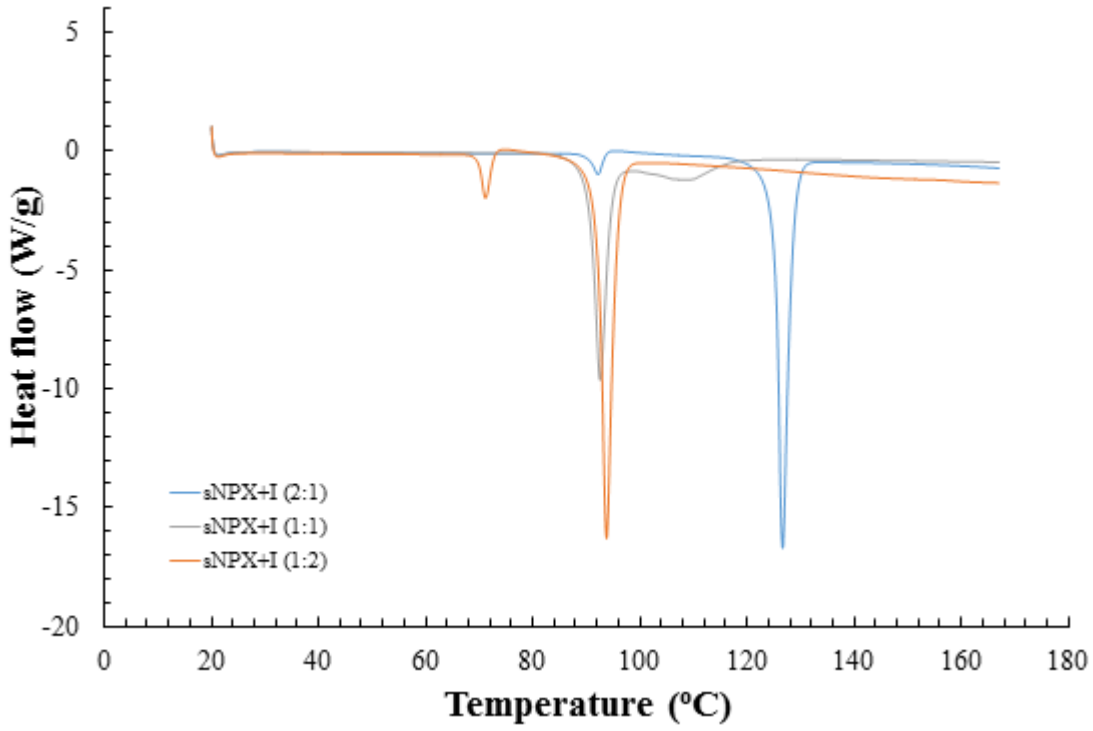

Figure A8. 2 - DSC traces from mechanochemically prepared samples of *sNPX* and *I*, ground neat in either 2:1, 1:1 or 1:2 molar ratios

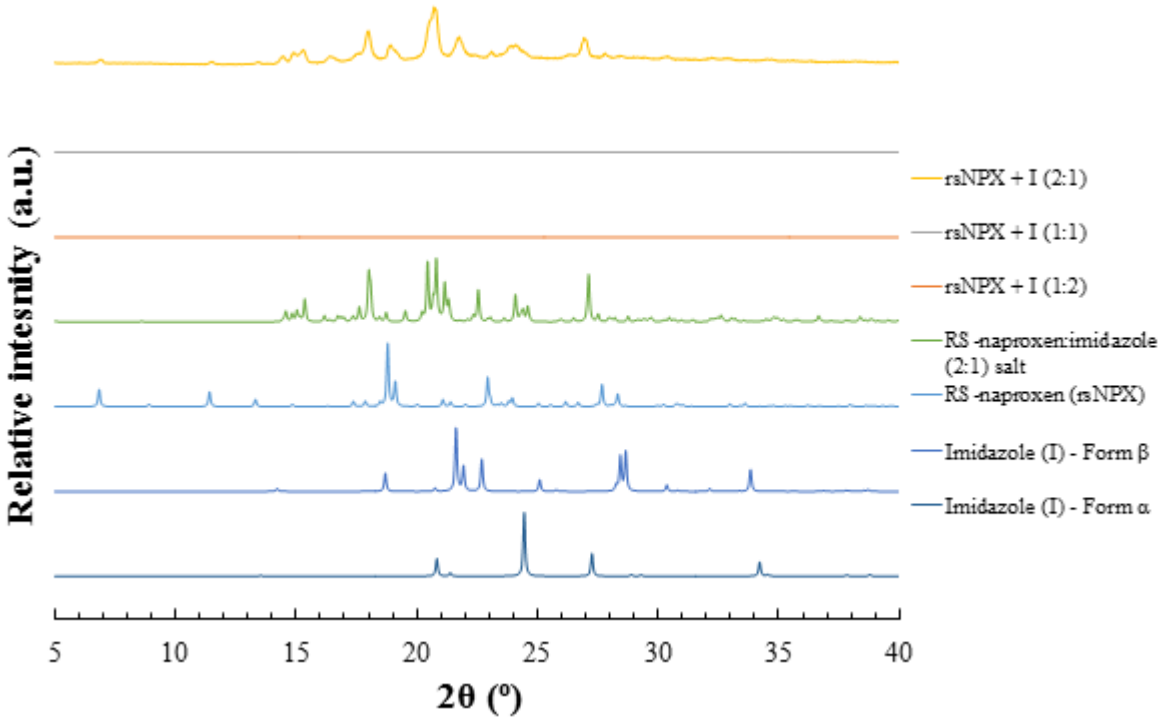

Figure A8. 3 - PXRD patterns from mechanochemically prepared samples of *rsNPX* and *I*, ground neat in either 2:1, 1:1 or 1:2 molar ratios (top three patterns)

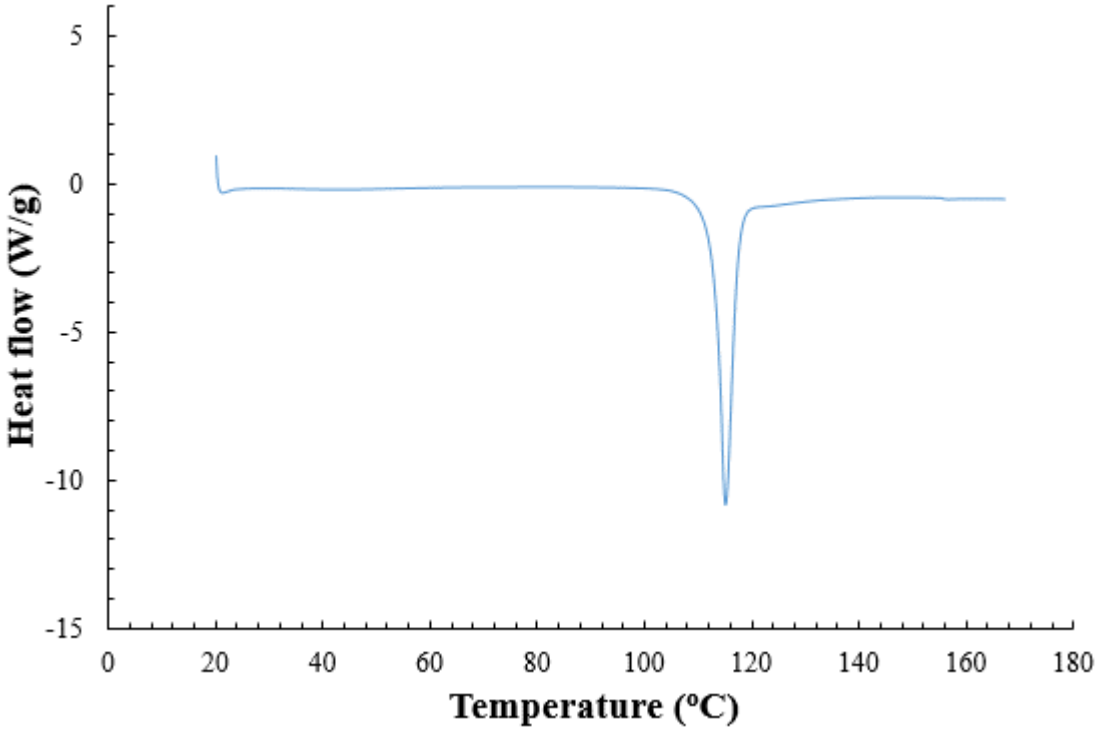

Figure A8. 4 - DSC traces from mechanochemically prepared samples of *rsNPX* and *I*, ground neat in either 2:1, 1:1 or 1:2 molar ratios

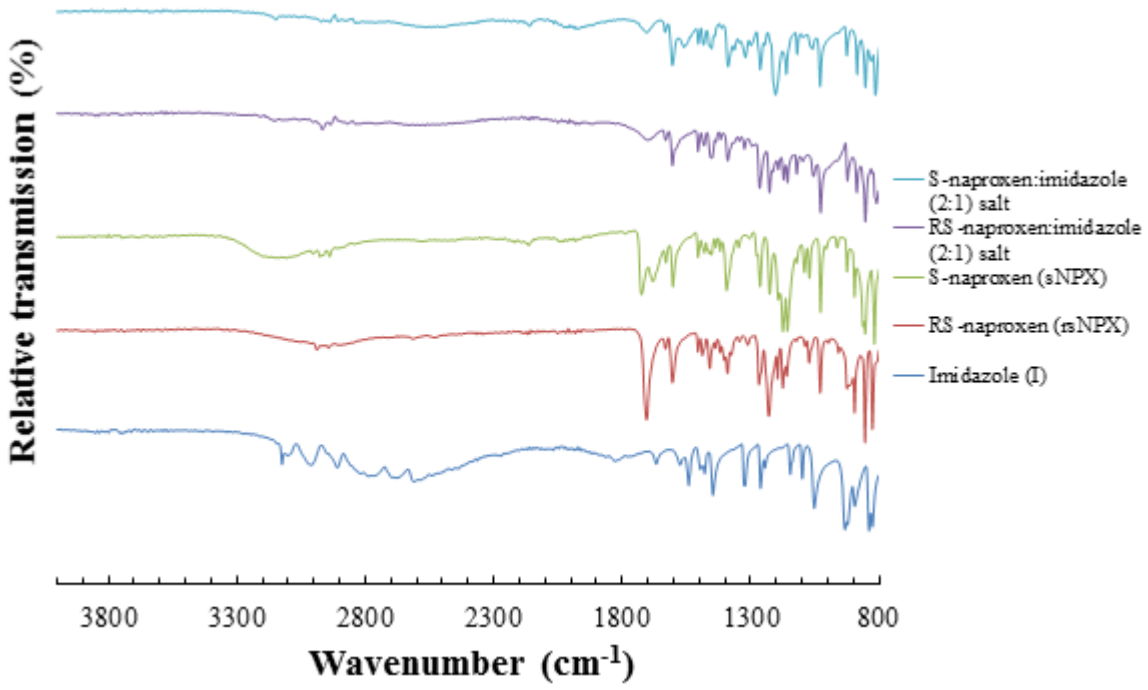

Figure A8. 5 - IR spectra of the S-naproxen:imidazole & RS-naproxen:imidazole (2:1) salts, prepared mechanochemically, compared to that of the starting materials

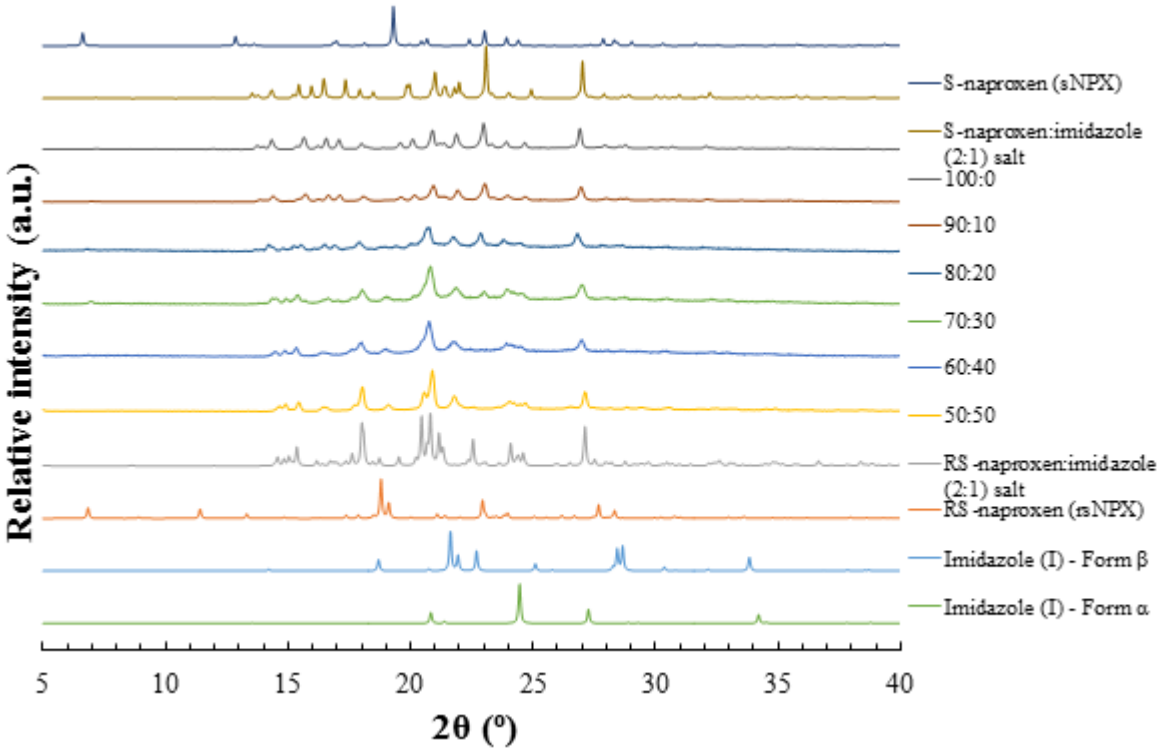

Figure A8. 6 - PXRD patterns, highlighting the change in phase from the racemic to the enantiopure (2:1) salts of *NPX* and *I*, with increasing molar contributions of *sNPX* (100:0, 90:10, 80:20, 70:30, 60:40, 50:50)

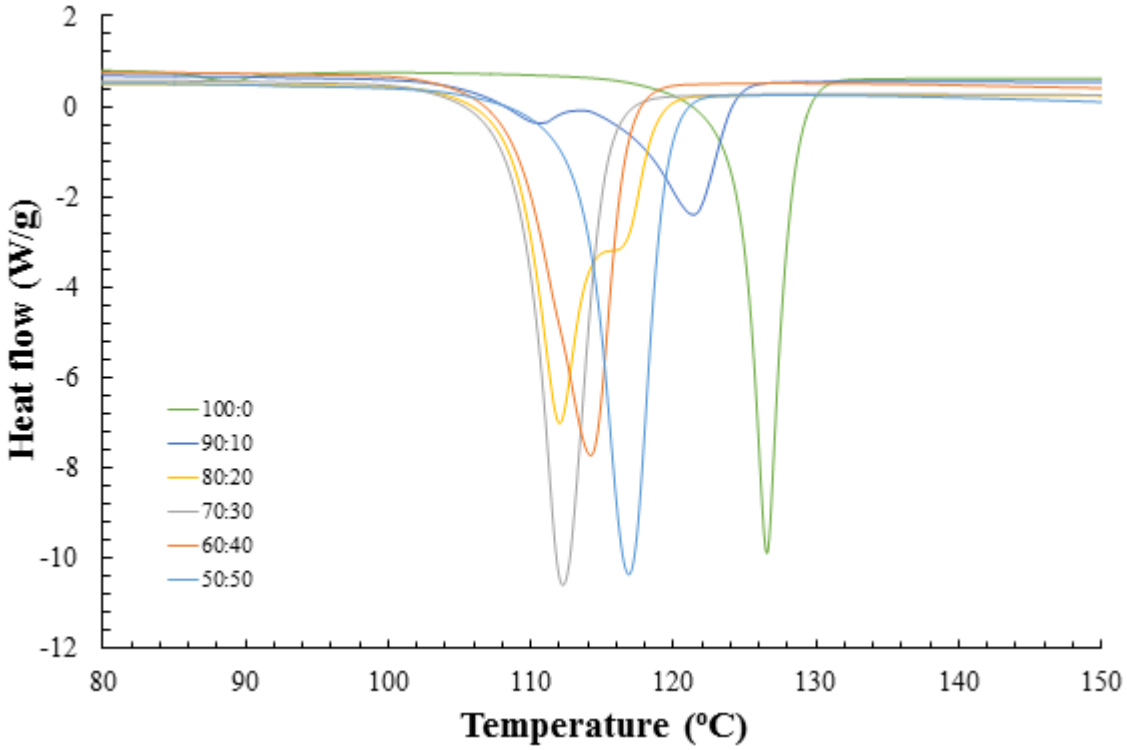

Figure A8. 7 - DSC traces, highlighting the change in phase from the racemic to the enantiopure (2:1) salts of *NPX* and *I*, with increasing molar contributions of *sNPX*

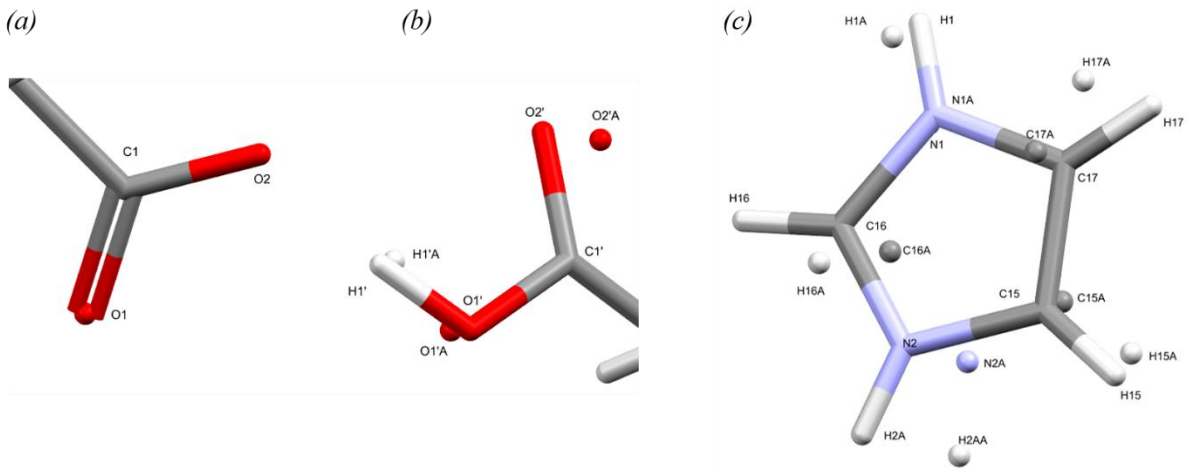

Figure A8. 8 - Key functional groups and disordered atoms of the S-naproxen:imidazole (2:1) salt, highlighting labelled atoms of the (a) carboxylate and (b) carboxylic acid groups of *sNPX*, as well as that for (c) the co-former, *I*

Table A8. 2 - Hydrogen bonding interactions with the S-naproxen:imidazole (2:1) salt, highlighting the key interaction lengths and angles

D	H	A	d(D-H) (Å)	d(H-A) (Å)	d(D-A) (Å)	D-H-A (º)
N1	*H1*	*O1*	0.86	1.85	2.662(9)	156.8
N2	*H2A*	*O2*[1]	0.86	1.87	2.710(5)	165.3
N1A	*H1A*	*O1*	0.86	1.83	2.68(2)	174.2
O1'	*H1'*	*O2*	1.002(14)	1.513(16)	2.509(6)	172(2)
O1'A	*H1'A*	*O2*	1.001(14)	1.64(3)	2.612(12)	161(6)
N1	*H1*	*O1*	0.86	1.85	2.662(9)	156.8

[1] 1+X,-1+Y,+Z

Table A8. 3 - Atomic occupancy of disordered atoms in the S-naproxen:imidazole (2:1) salt

Atom	*Occupancy*	Atom	*Occupancy*	Atom	*Occupancy*
C15	0.705(5)	*H15*	0.705(5)	*C16*	0.705(5)
H16	0.705(5)	*C17*	0.705(5)	*H17*	0.705(5)
N1	0.705(5)	*H1*	0.705(5)	*N2*	0.705(5)
H2A	0.705(5)	*C15A*	0.295(5)	*H15A*	0.295(5)
C16A	0.295(5)	*H16A*	0.295(5)	*C17A*	0.295(5)
H17A	0.295(5)	*N1A*	0.295(5)	*H1A*	0.295(5)
N2A	0.295(5)	*H2AA*	0.295(5)	*O1'*	0.624(5)
O2'	0.624(5)	*O1'A*	0.376(5)	*O2'A*	0.376(5)
H1'	0.624(5)	*H1'A*	0.376(5)		

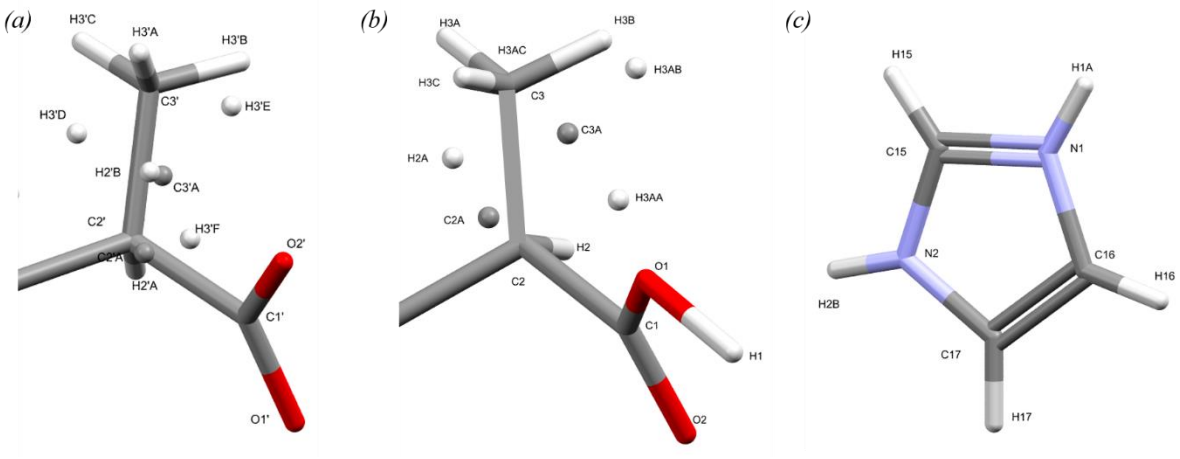

Figure A8. 9 - Key functional groups and disordered atoms of the RS-naproxen:imidazole (2:1) salt, highlighting labelled atoms of the (a) carboxylate and (b) carboxylic acid groups of *NPX*, as well as that for (c) the co-former, I

Table A8. 4 - Hydrogen bonding interactions with the RS-naproxen:imidazole (2:1) salt, highlighting the key interaction lengths and angles

D	H	A	d(D-H) (Å)	d(H-A) (Å)	d(D-A) (Å)	D-H-A (º)
N2	*H2B*	*O2*[1]	0.848(10)	1.834(11)	2.677(3)	173(3)
N1	*H1A*	*O1'*[2]	0.851(10)	1.854(13)	2.696(3)	170(4)
O2'	*H2'*	*O2'*[3]	1.2387(14)	1.2387(14)	2.477(3)	180.00(15)

[1]1+X,+Y,+Z; [2]2-X,1-Y,-Z; [3]2-X,2-Y,-Z

Table A8. 5 - Atomic occupancy of disordered atoms in the RS-naproxen:imidazole (2:1) salt

Atom	*Occupancy*	Atom	*Occupancy*	Atom	*Occupancy*
C2'	0.910(3)	*H2'A*	0.910(3)	*C3'*	0.910(3)
H3'A	0.910(3)	*H3'B*	0.910(3)	*H3'C*	0.910(3)
C2	0.910(3)	*H2*	0.910(3)	*C3*	0.910(3)
H3A	0.910(3)	*H3B*	0.910(3)	*H3C*	0.910(3)
C3'A	0.090(3)	*H3'D*	0.090(3)	*H3'E*	0.090(3)
H3'F	0.090(3)	*C2'A*	0.090(3)	*H2'B*	0.090(3)
C2A	0.090(3)	*H2A*	0.090(3)	*C3A*	0.090(3)
H3AA	0.090(3)	*H3AB*	0.090(3)	*H3AC*	0.090(3)

A8.2 Materials of racemic and enantiopure naproxen with benzimidazole (*BI*)

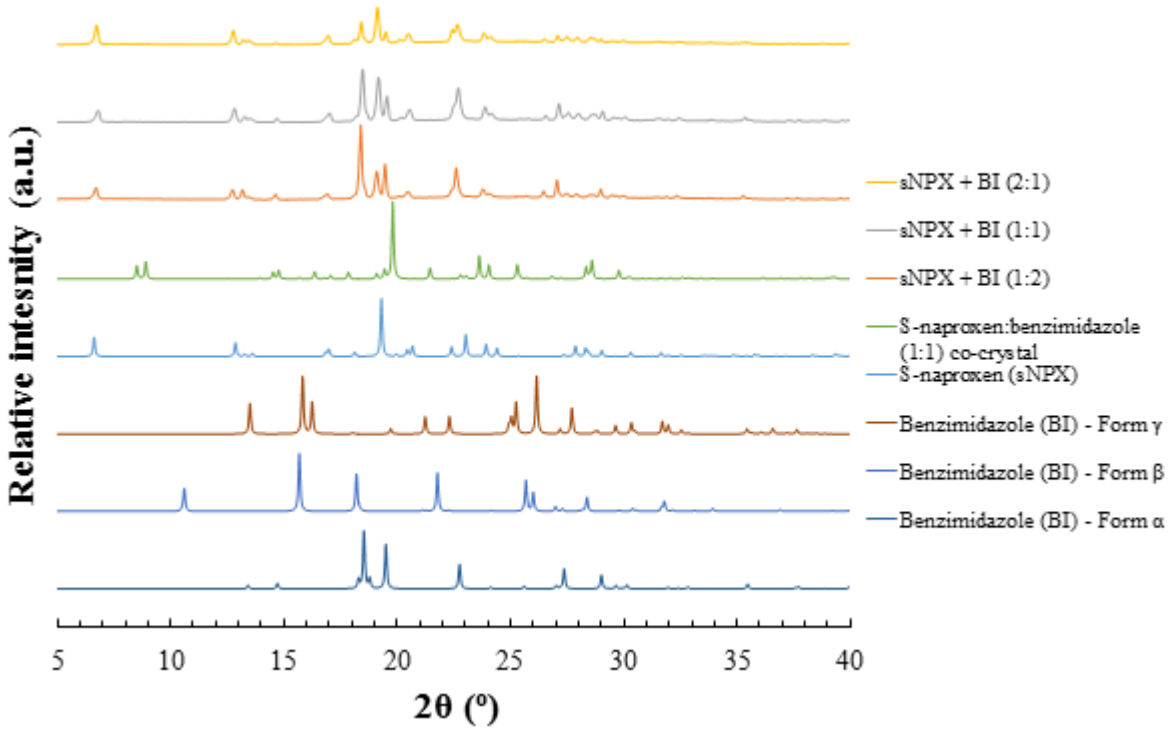

Figure A8. 10 - PXRD patterns from mechanochemically prepared samples of *sNPX* and *BI*, ground neat in either 2:1, 1:1 or 1:2 molar ratios (top three patterns)

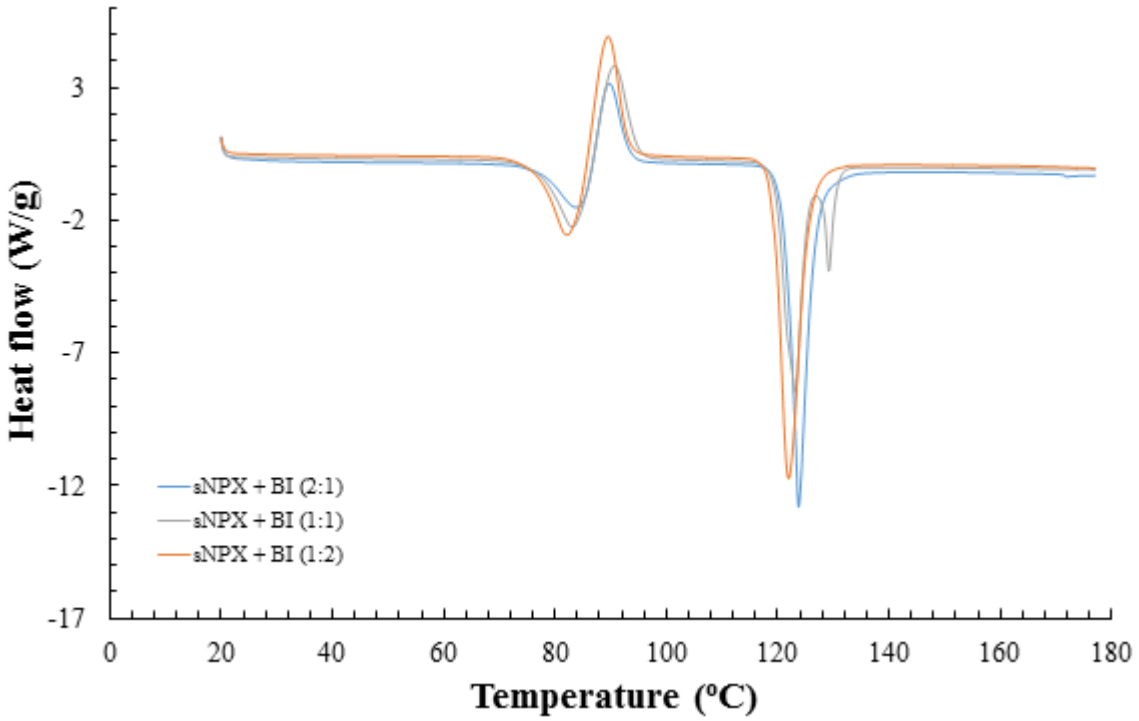

Figure A8. 11 - DSC traces from mechanochemically prepared samples of *sNPX* and *BI*, ground neat in either 2:1, 1:1 or 1:2 molar ratios

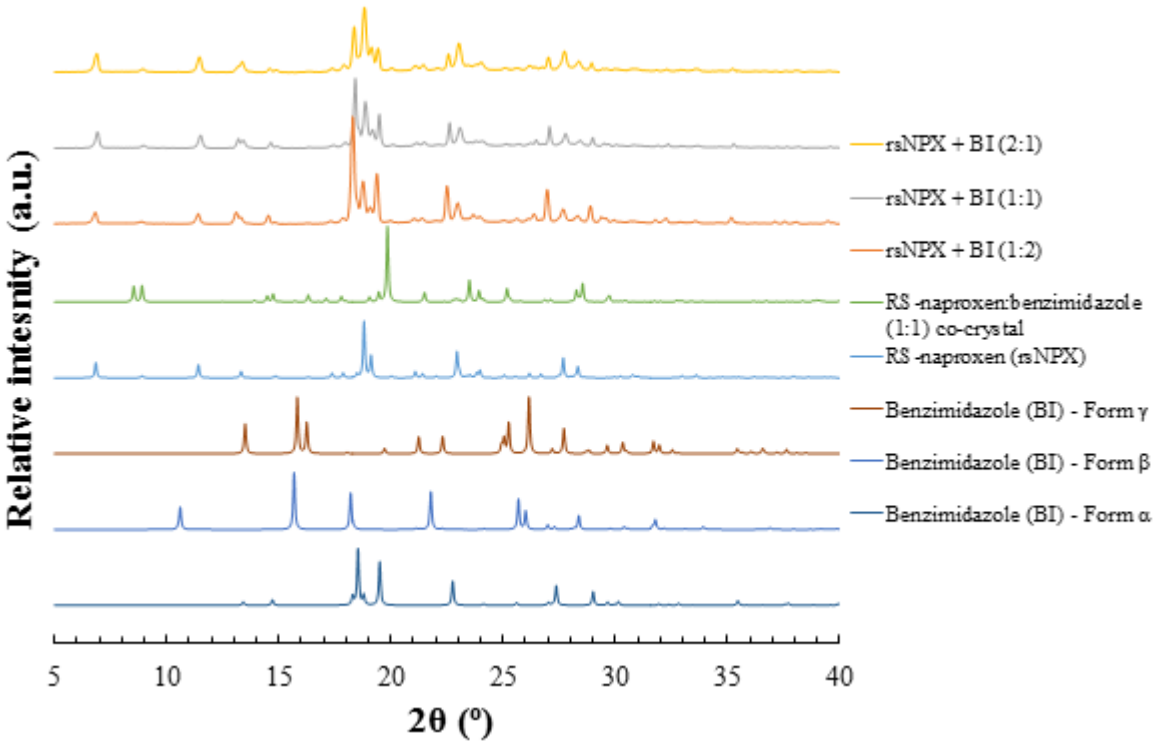

Figure A8. 12 - PXRD patterns from mechanochemically prepared samples of *rsNPX* and *BI*, ground neat in either 2:1, 1:1 or 1:2 molar ratios

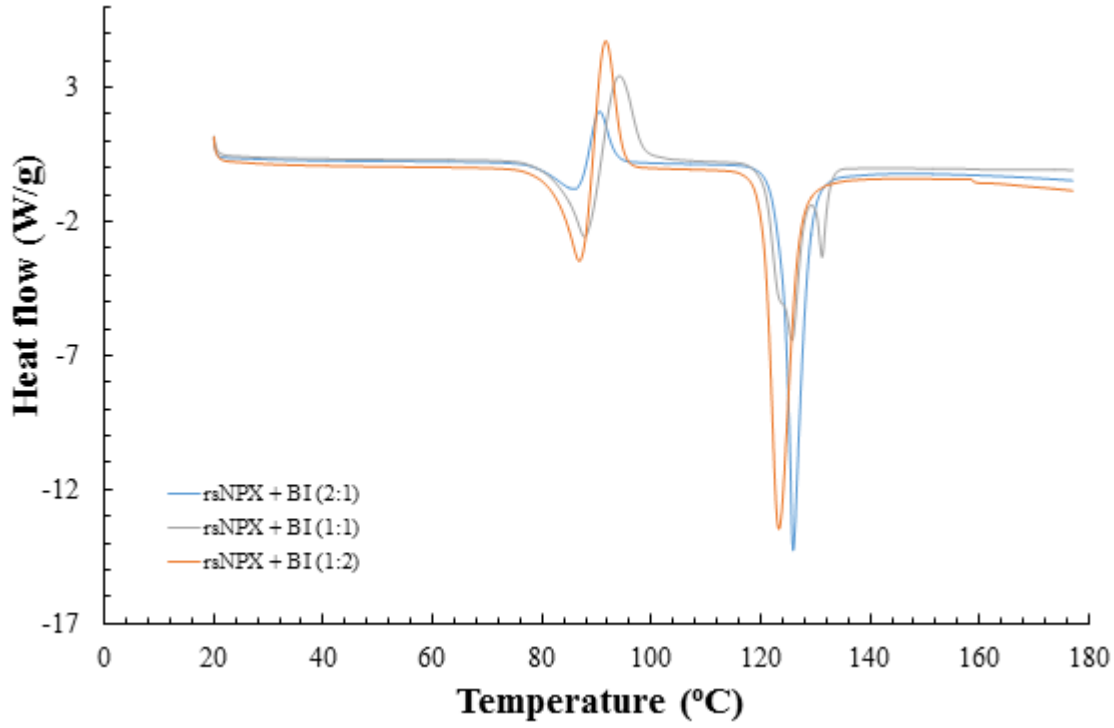

Figure A8. 13 - DSC traces from mechanochemically prepared samples of *rsNPX* and *BI*, ground neat in either 2:1, 1:1 or 1:2 molar ratios

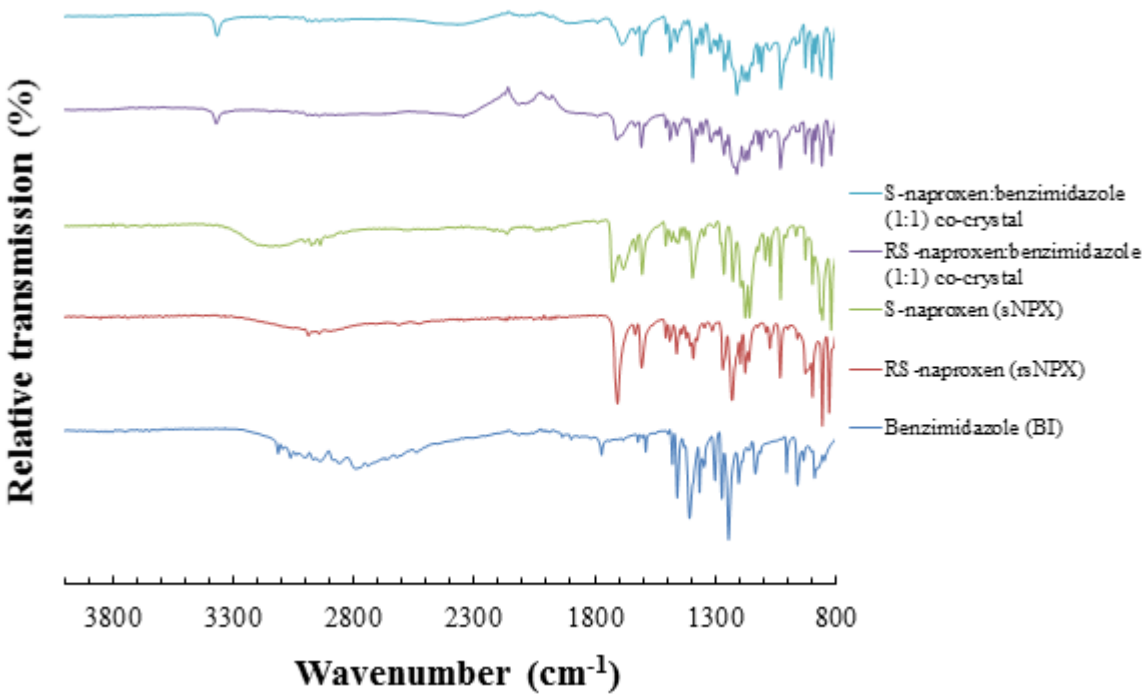

Figure A8. 14 - IR spectra of the S-naproxen:benzimidazole & RS-naproxen:benzimidazole (1:1) co-crystals, prepared mechanochemically, compared to that of the starting materials

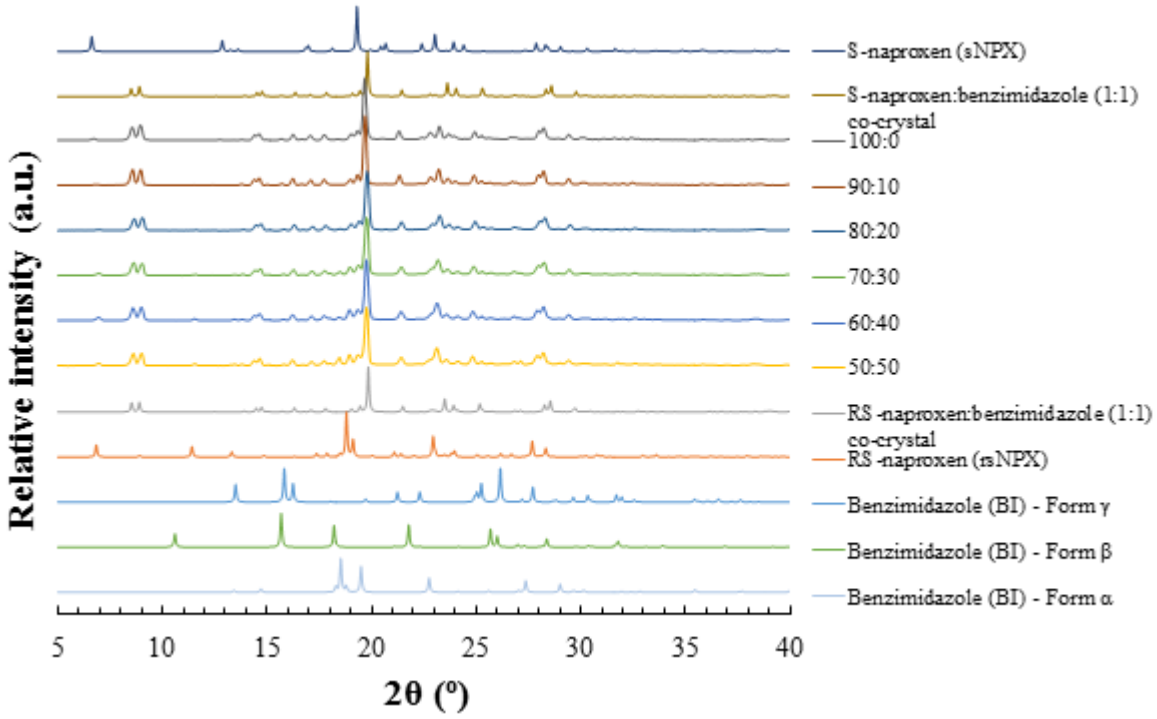

Figure A8. 15 - PXRD patterns, highlighting the change in phase from the racemic to the enantiopure (1:1) co-crystals of *NPX* and *BI*, with increasing molar contributions of *sNPX*, prepared in a 1:1 API to co-former stoichiometry (100:0, 90:10, 80:20, 70:30, 60:40, 50:50)

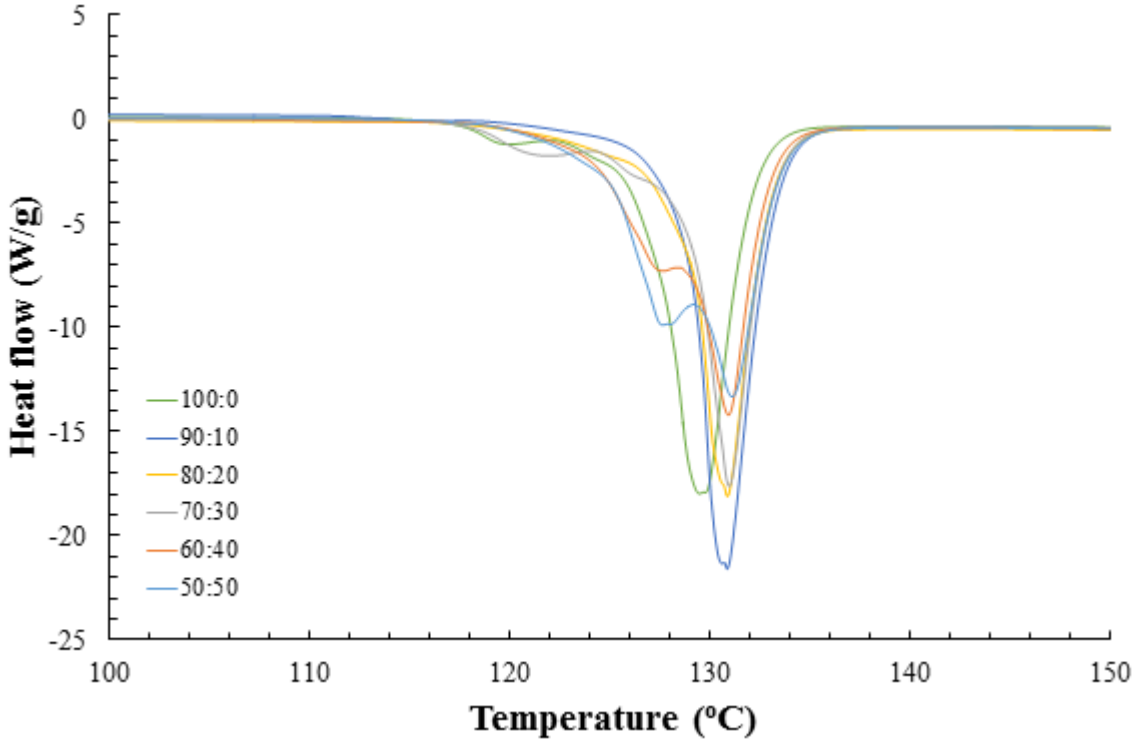

Figure A8. 16 - DSC traces, highlighting the change in phase from the racemic to the enantiopure (1:1) co-crystals of *NPX* and *BI*, with increasing molar contributions of *sNPX*, prepared in a 1:1 API to co-former stoichiometry

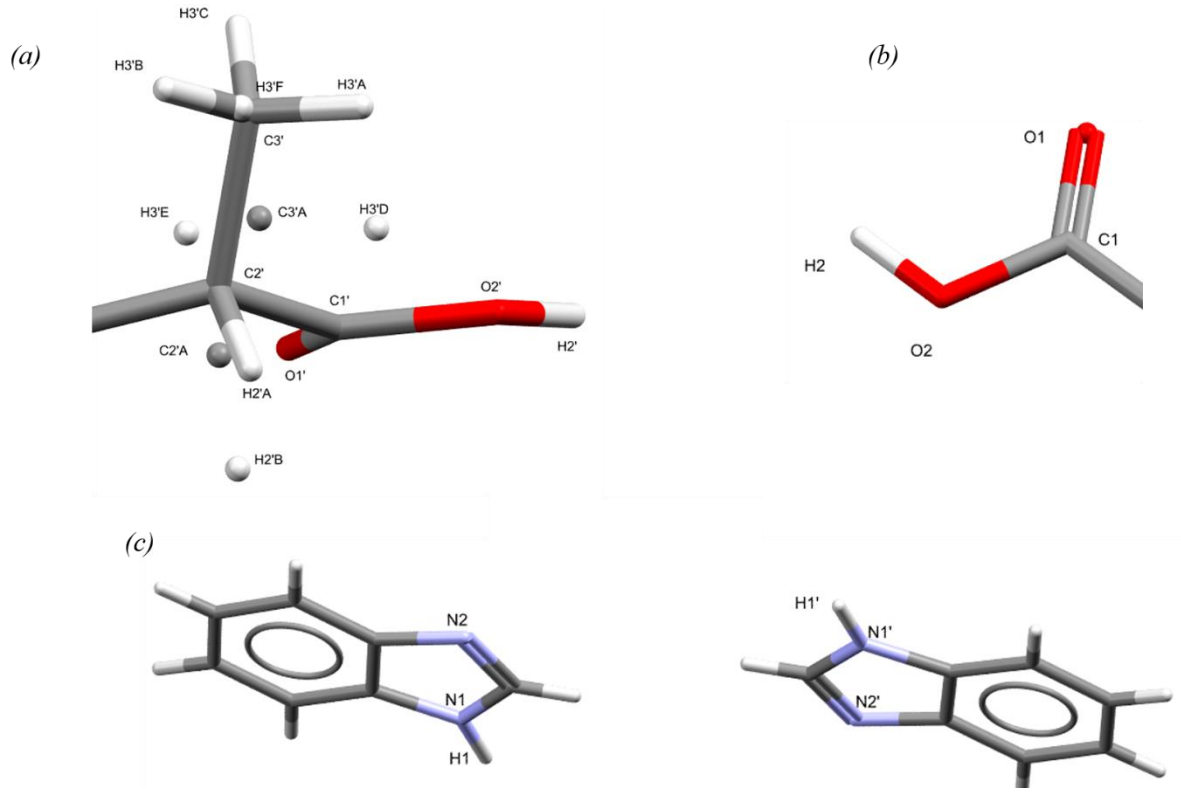

Figure A8. 17 - Key functional groups and disordered atoms of the S-naproxen:benzimidazole (1:1) co-crystal, highlighting labelled atoms of the carboxylic acid functions that make up the key interaction unit, (a) and (b), as well as that for (c) the co-former, *BI*

Table A8. 6 - Hydrogen bonding interactions with the S-naproxen:benzimidazole (1:1) co-crystal, highlighting the key interaction lengths and angles

D	H	A	d(D-H) (Å)	d(H-A) (Å)	d(D-A) (Å)	D-H-A (º)
N1	*H1*	*O1'*[1]	0.963(13)	2.33(3)	2.934(3)	120(2)
N1'	*H1'*	*O1*	0.965(14)	2.37(3)	2.973(3)	120(2)
O2'	*H2'*	*N2'*[2]	1.001(14)	1.631(15)	2.623(3)	171(4)
O2	*H2*	*N2*	0.998(14)	1.642(15)	2.633(3)	172(4)

[1]+X,1+Y,+Z; [2]+X,-1+Y,+Z

Table A8. 7 - Atomic occupancy of disordered atoms in the S-naproxen:benzimidazole (1:1) co-crystal

Atom	Occupancy	Atom	Occupancy	Atom	Occupancy
C2'	0.599(6)	*H2'A*	0.599(6)	*C3'*	0.599(6)
H3'A	0.599(6)	*H3'B*	0.599(6)	*H3'C*	0.599(6)
C2'A	0.401(6)	*H2'B*	0.401(6)	*C3'A*	0.401(6)
H3'D	0.401(6)	*H3'E*	0.401(6)	*H3'F*	0.401(6)

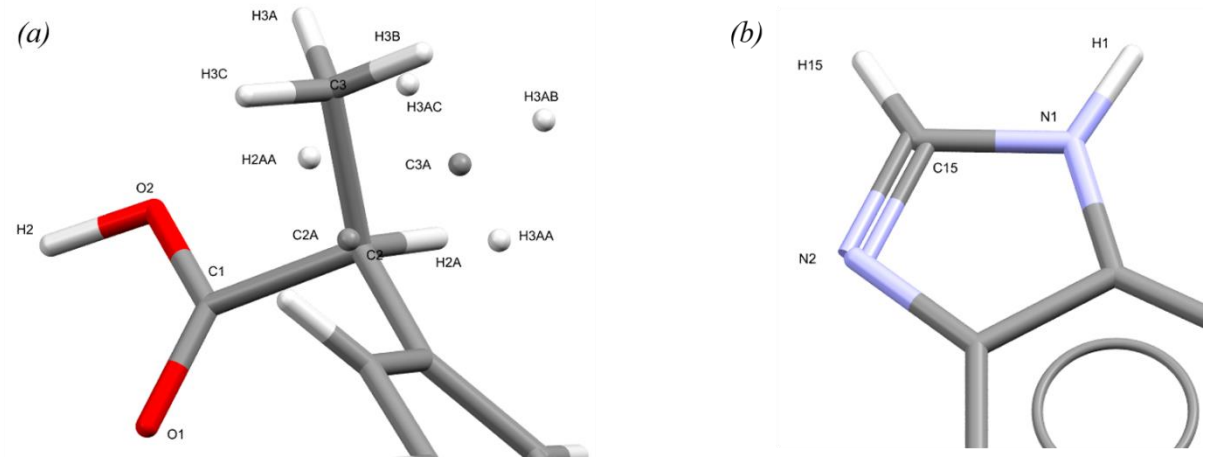

Figure A8. 18 - Key functional groups and disordered atoms of the RS-naproxen:benzimidazole (1:1) co-crystal, highlighting labelled atoms of the carboxylic acid functions that make up the key interaction unit, (a), as well as that for (b) the co-former, *BI*

Table A8. 8 - Hydrogen bonding interactions with the RS-naproxen:benzimidazole (1:1) co-crystal, highlighting the key interaction lengths and angles

D	H	A	d(D-H) (Å)	d(H-A) (Å)	d(D-A) (Å)	D-H-A (º)
O2	*H2*	*N2*[1]	0.998(10)	1.635(11)	2.6279(18)	173(3)
N1	*H1*	*O1*	0.980(9)	2.308(18)	2.9555(17)	122.7(16)

[1]-X,-Y,-Z

Table A8. 9 - Atomic occupancy of disordered atoms in the RS-naproxen:benzimidazole (1:1) co-crystal

Atom	Occupancy	Atom	Occupancy	Atom	Occupancy
C2	0.583(4)	*H2A*	0.583(4)	*C3*	0.583(4)
H3A	0.583(4)	*H3B*	0.583(4)	*H3C*	0.583(4)
C2A	0.417(4)	*H2AA*	0.417(4)	*C3A*	0.417(4)
H3AA	0.417(4)	*H3AB*	0.417(4)	*H3AC*	0.417(4)

A8.3 Materials of racemic and enantiopure naproxen with acridine (*A*)

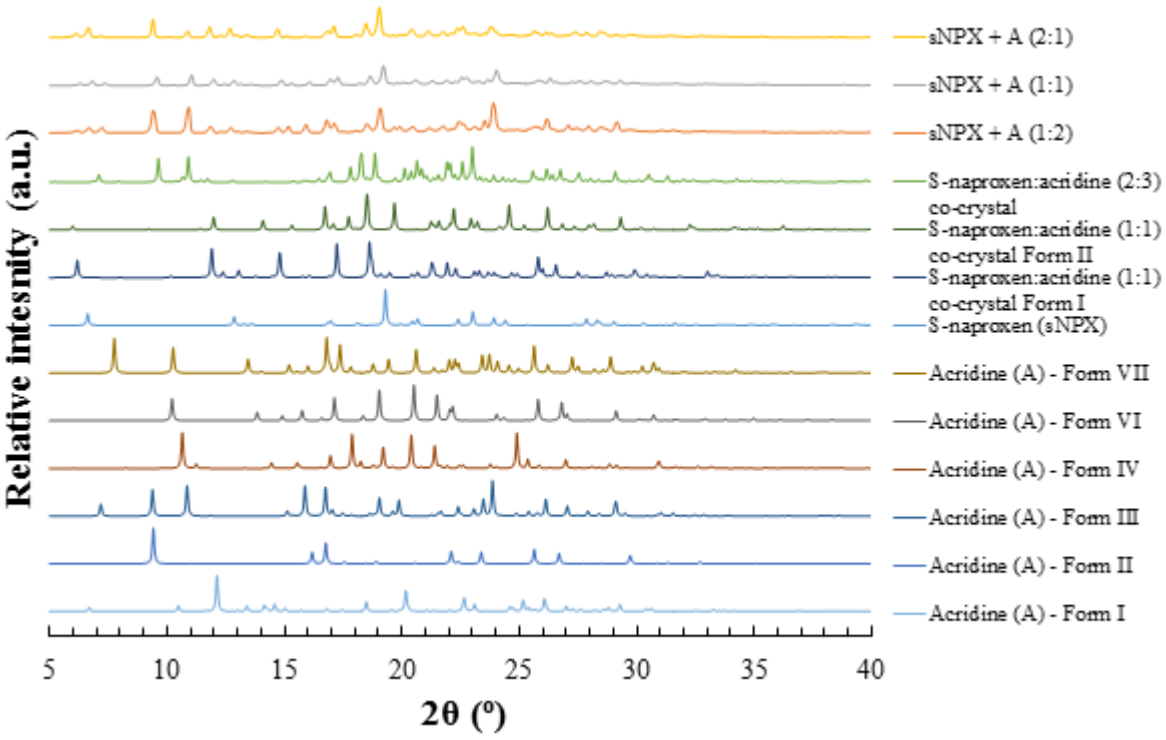

Figure A8. 19 - PXRD patterns from mechanochemically prepared samples of *sNPX* and *A*, ground neat in either 2:1, 1:1 or 1:2 molar ratios (top three patterns)

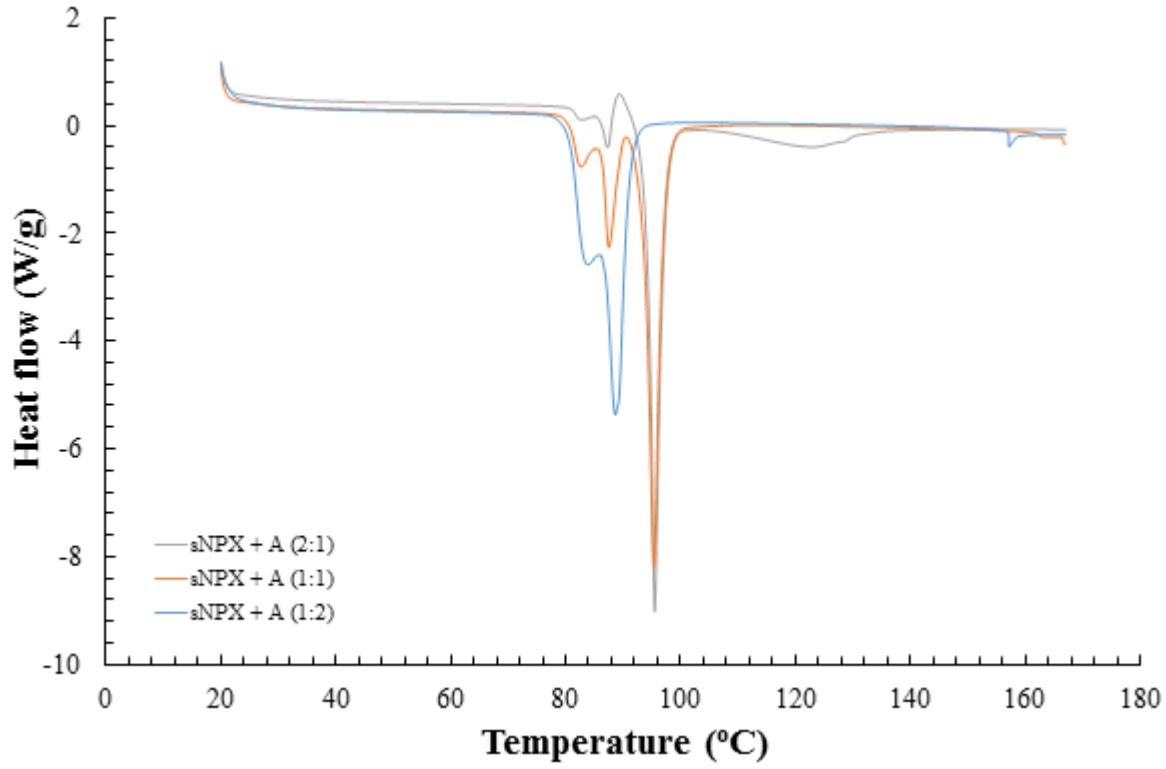

Figure A8. 20 - DSC traces from mechanochemically prepared samples of *sNPX* and *A*, ground neat in either 2:1, 1:1 or 1:2 molar ratios

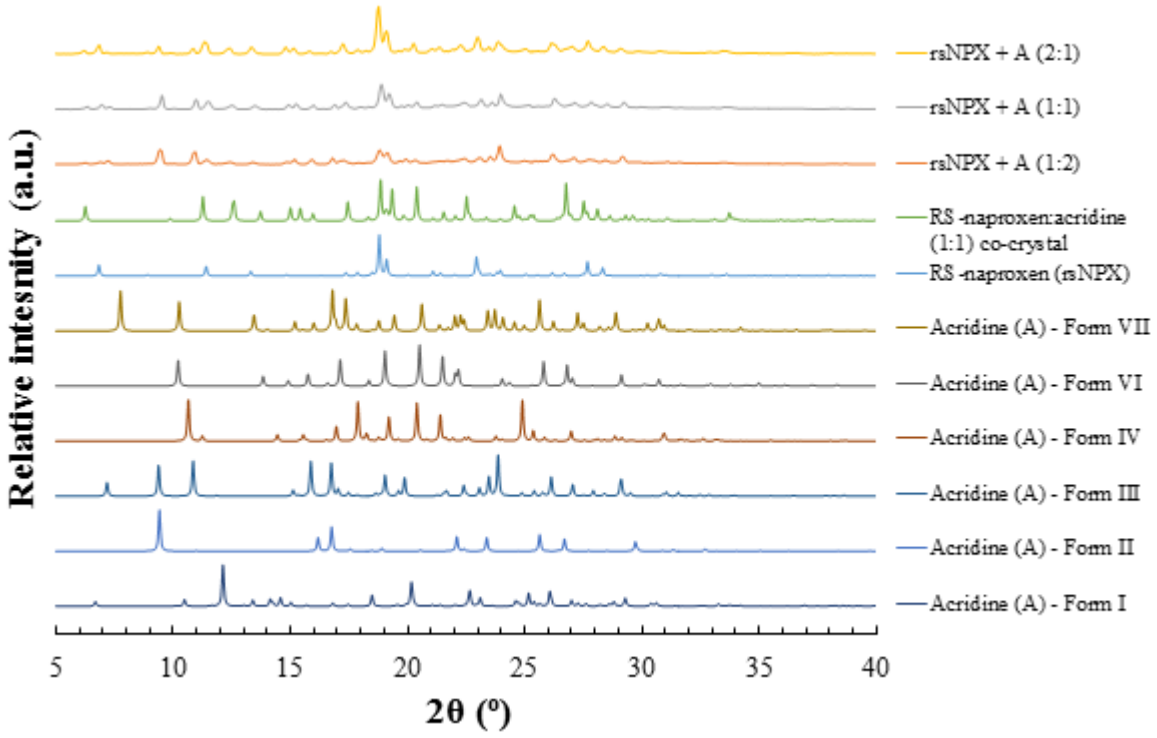

Figure A8. 21 - PXRD patterns from mechanochemically prepared samples of *rsNPX* and *A*, ground neat in either 2:1, 1:1 or 1:2 molar ratios (top three patterns)

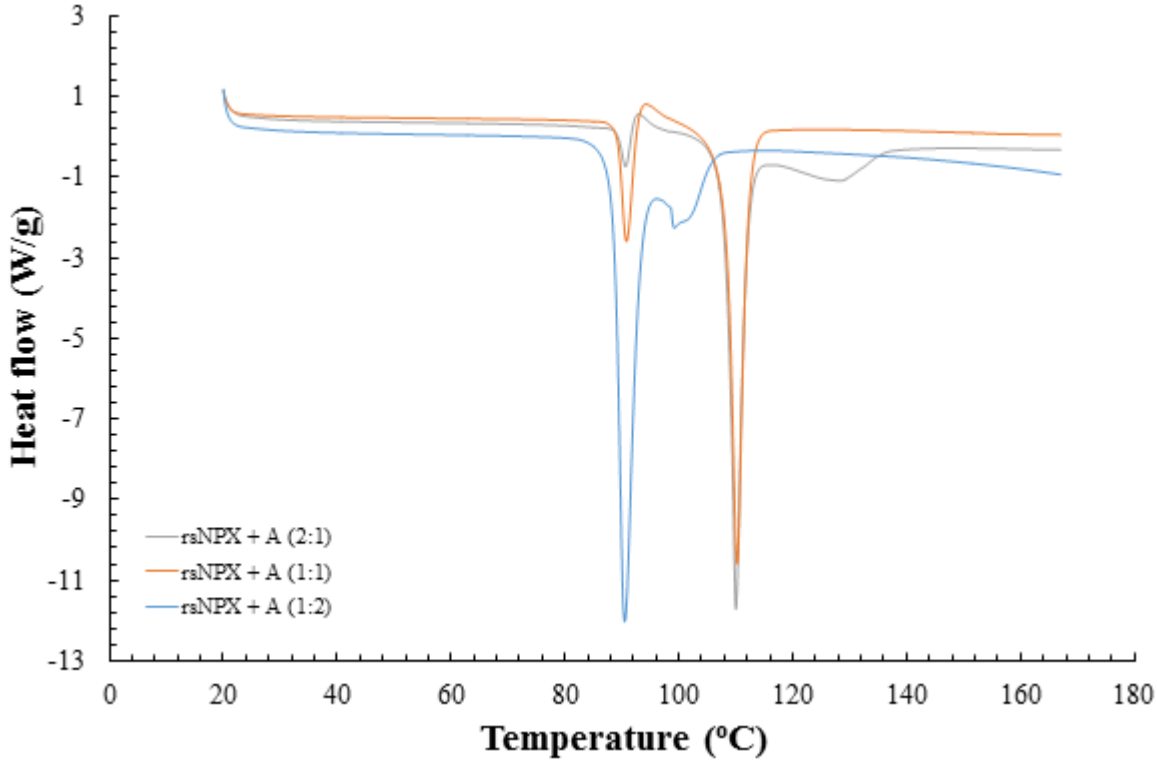

Figure A8. 22 - DSC traces from mechanochemically prepared samples of *rsNPX* and *A*, ground neat in either 2:1, 1:1 or 1:2 molar ratios

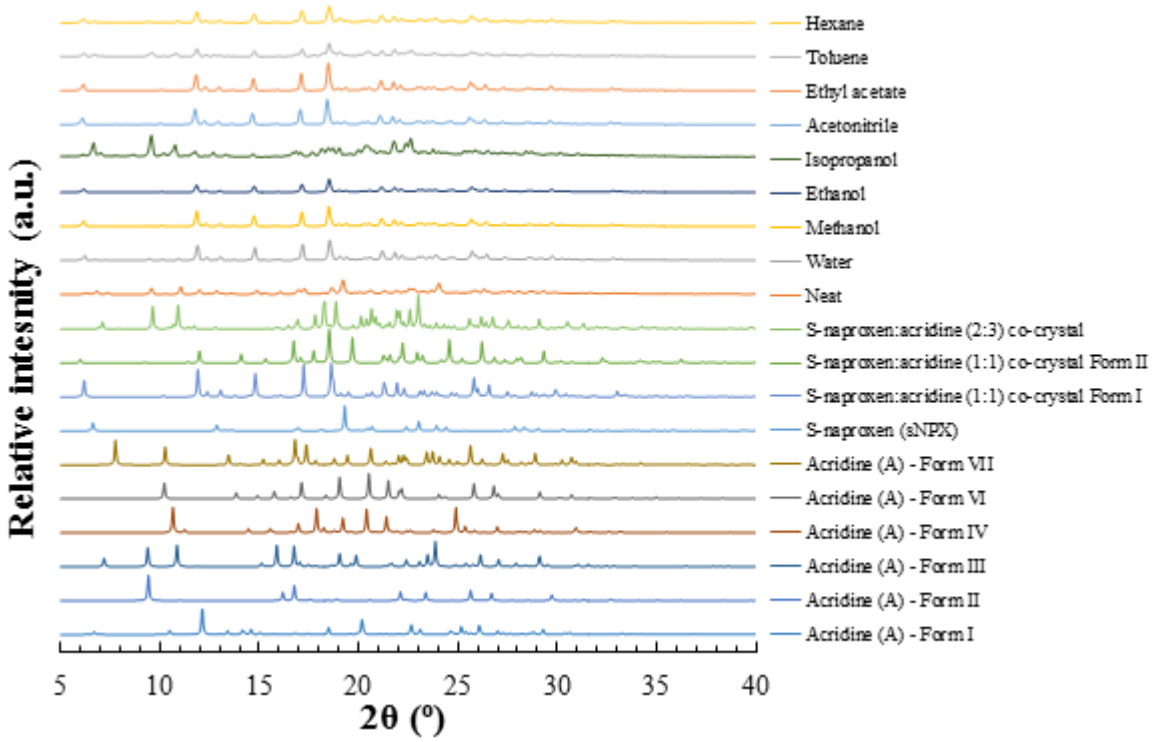

Figure A8. 23 - PXRD patterns from mechanochemically prepared samples of *sNPX* and *A*, ground a 1:1 molar ratio, either neat or with minimum quantities of water, methanol, ethanol, isopropanol, acetonitrile, ethyl acetate, toluene or hexane

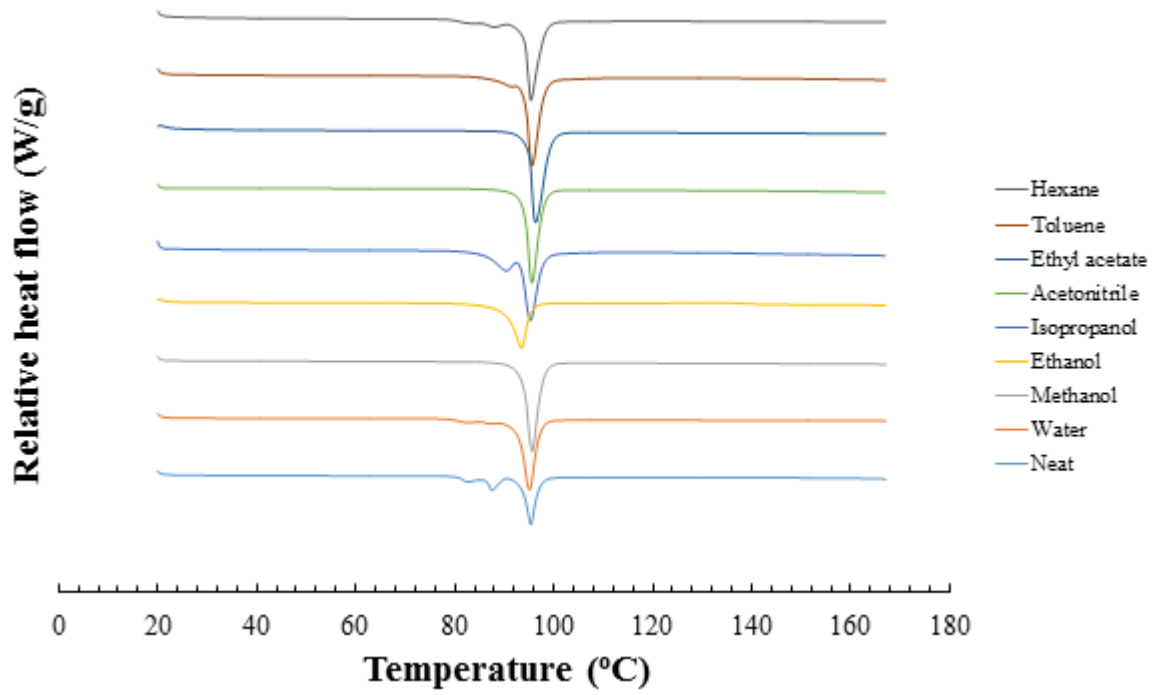

Figure A8. 24 - DSC traces from mechanochemically prepared samples of *sNPX* and *A*, ground a 1:1 molar ratio, either neat or with minimum quantities of water, methanol, ethanol, isopropanol, acetonitrile, ethyl acetate, toluene or hexane

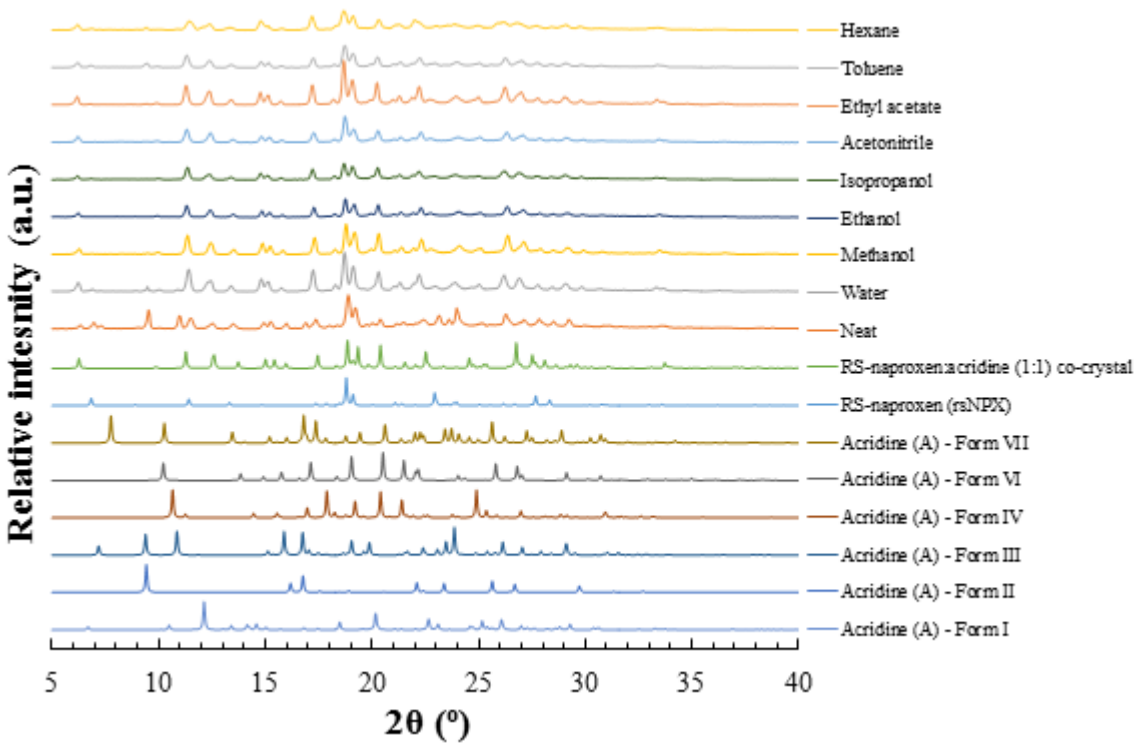

Figure A8. 25 - PXRD patterns from mechanochemically prepared samples of *rsNPX* and *A*, ground a 1:1 molar ratio, either neat or with minimum quantities of water, methanol, ethanol, isopropanol, acetonitrile, ethyl acetate, toluene or hexane

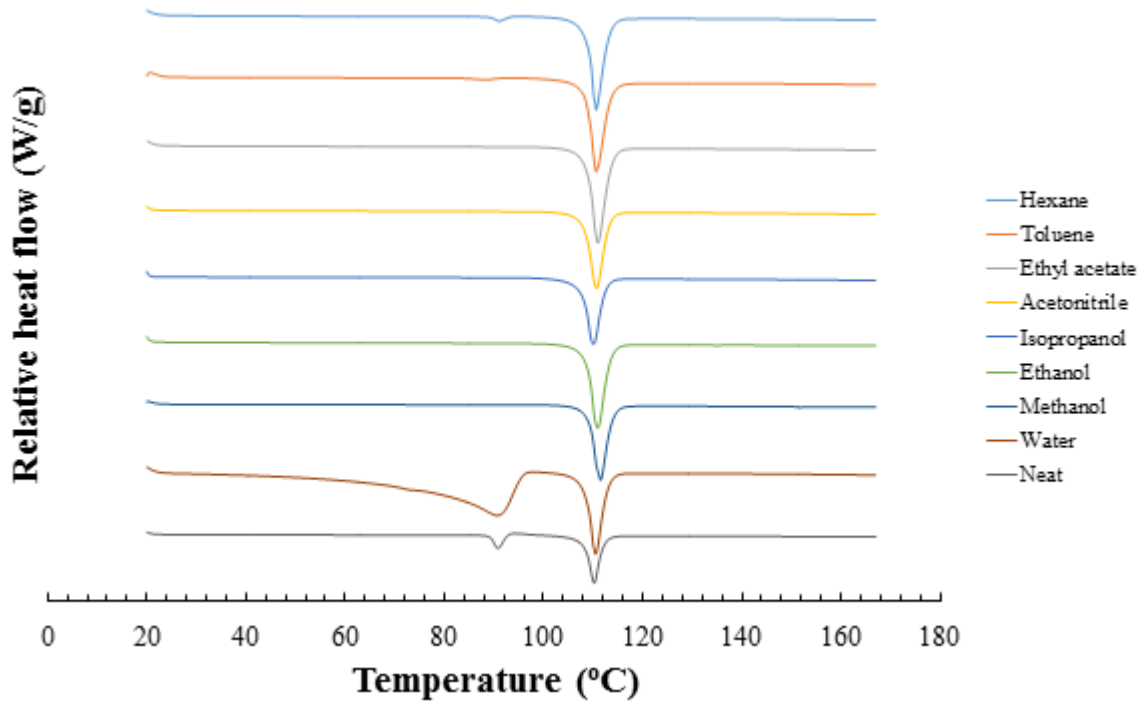

Figure A8. 26 - DSC traces from mechanochemically prepared samples of *rsNPX* and *A*, ground a 1:1 molar ratio, either neat or with minimum quantities of water, methanol, ethanol, isopropanol, acetonitrile, ethyl acetate, toluene or hexane

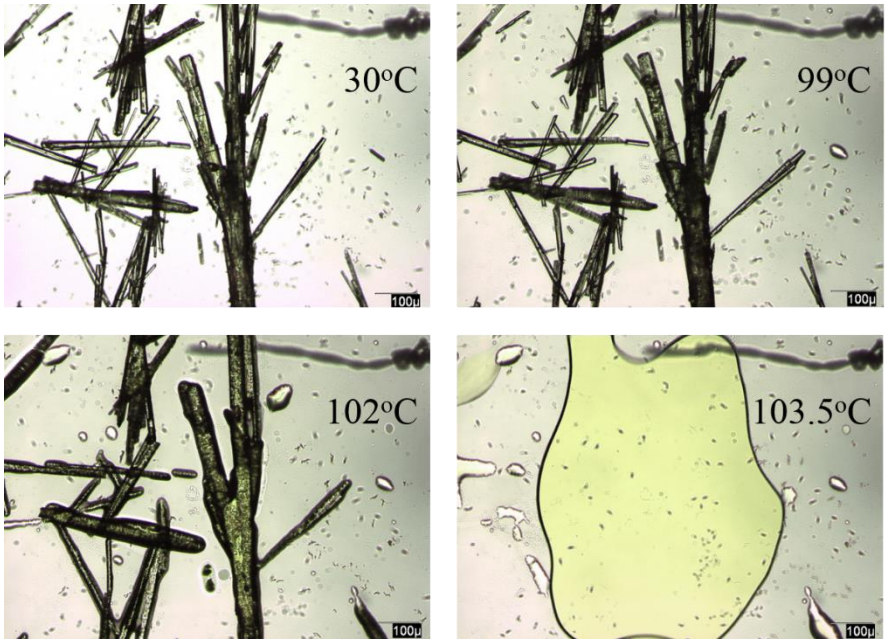

Figure A8. 27 - HSM images of individual crystals obtained from homochiral ethanol solutions, with 1:1 molar ratio of *NPX* to *A*, taken at a variety of temperatures (100µm scale)

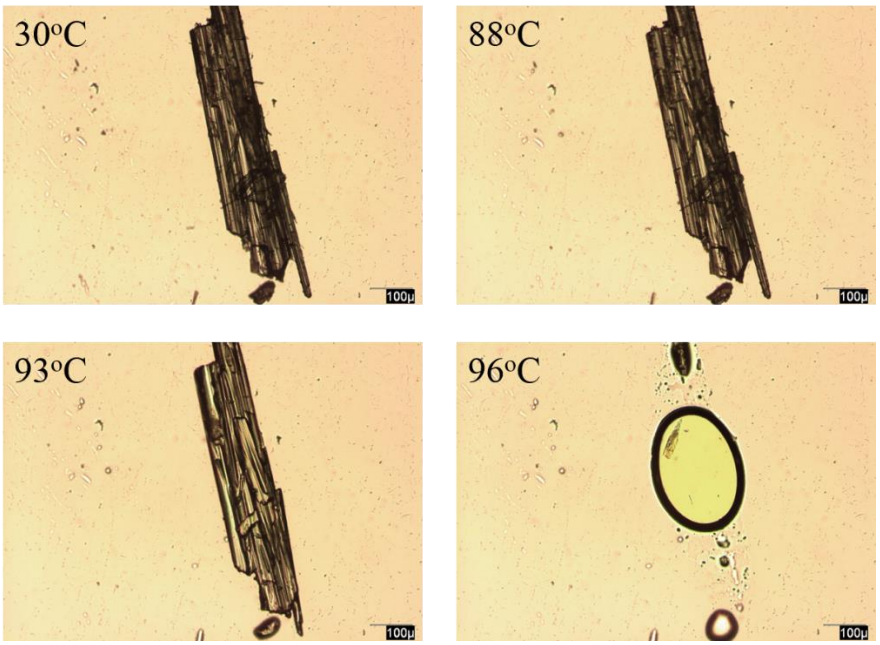

Figure A8. 28 - HSM images of individual crystals obtained from homochiral acetonitrile solutions, with 1:1 molar ratio of *NPX* to *A*, taken at a variety of temperatures (100µm scale)

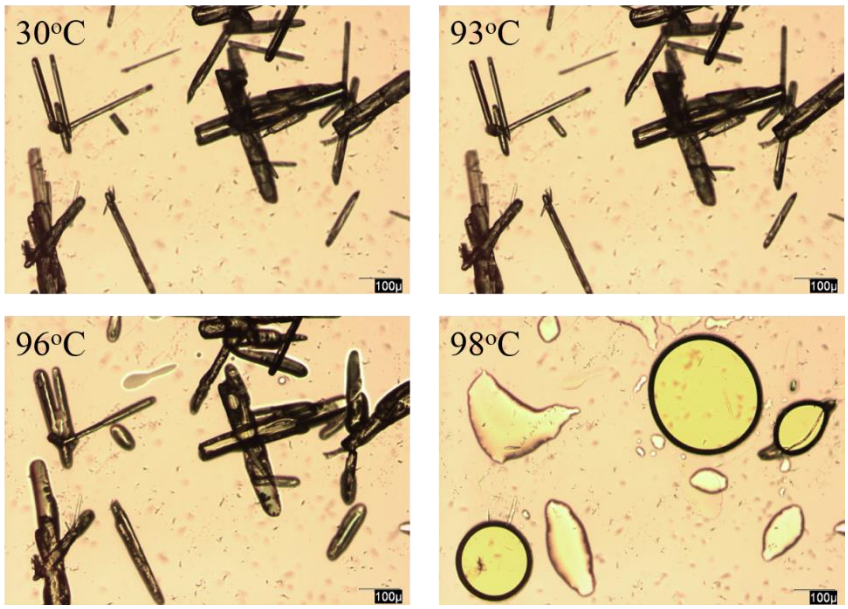

Figure A8. 29 - HSM images of individual crystals obtained from seeded homochiral ethanol solutions, with 1:1 molar ratio of *NPX* to *A*, taken at a variety of temperatures (100µm scale)

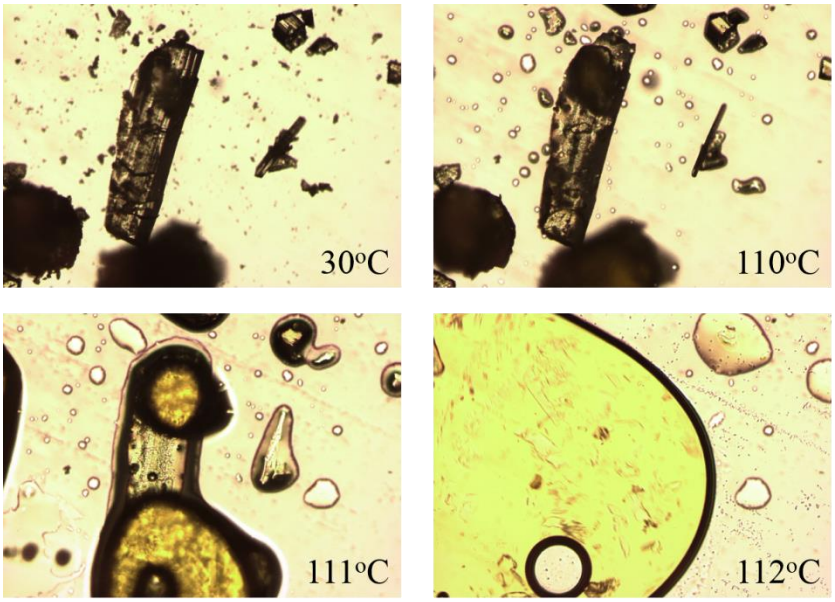

Figure A8. 30 - HSM images of individual crystals obtained from racemic ethanol solutions, with 1:1 molar ratio of *NPX* to *A*, taken at a variety of temperatures (100µm scale)

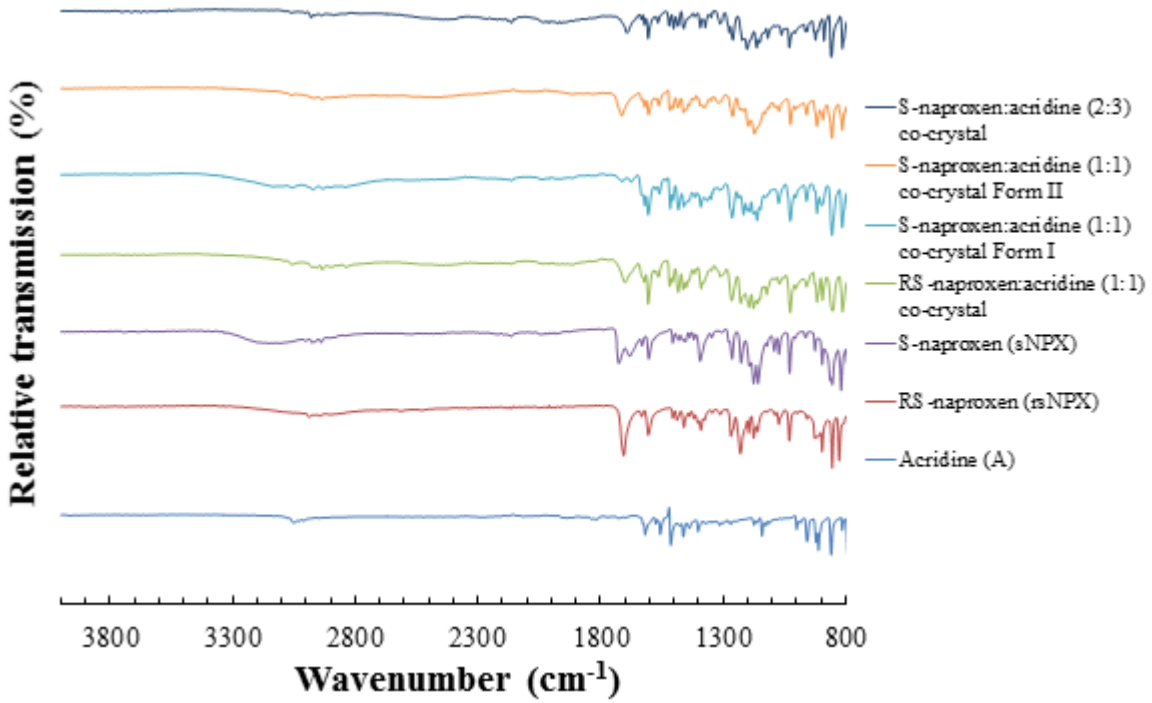

Figure A8. 31 - IR spectra of the S-naproxen:acridine (1:1), Forms I & II, and (2:3) co-crystals, as well as the RS-naproxen:acridine (1:1) co-crystal, prepared either from solution or mechanochemically, compared to that of the starting materials

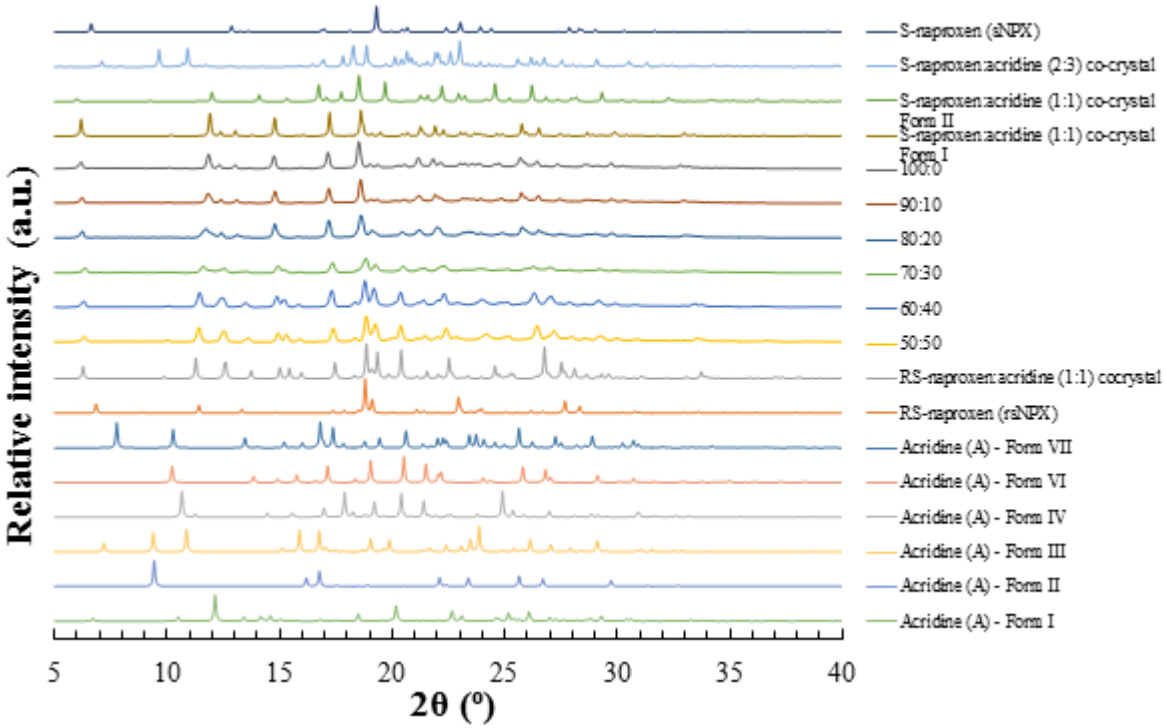

Figure A8. 32 - PXRD patterns, highlighting the change in phase from the racemic to the enantiopure (1:1) co-crystals of *NPX* and *A*, with increasing molar contributions of *sNPX* (100:0, 90:10, 80:20, 70:30, 60:40, 50:50)

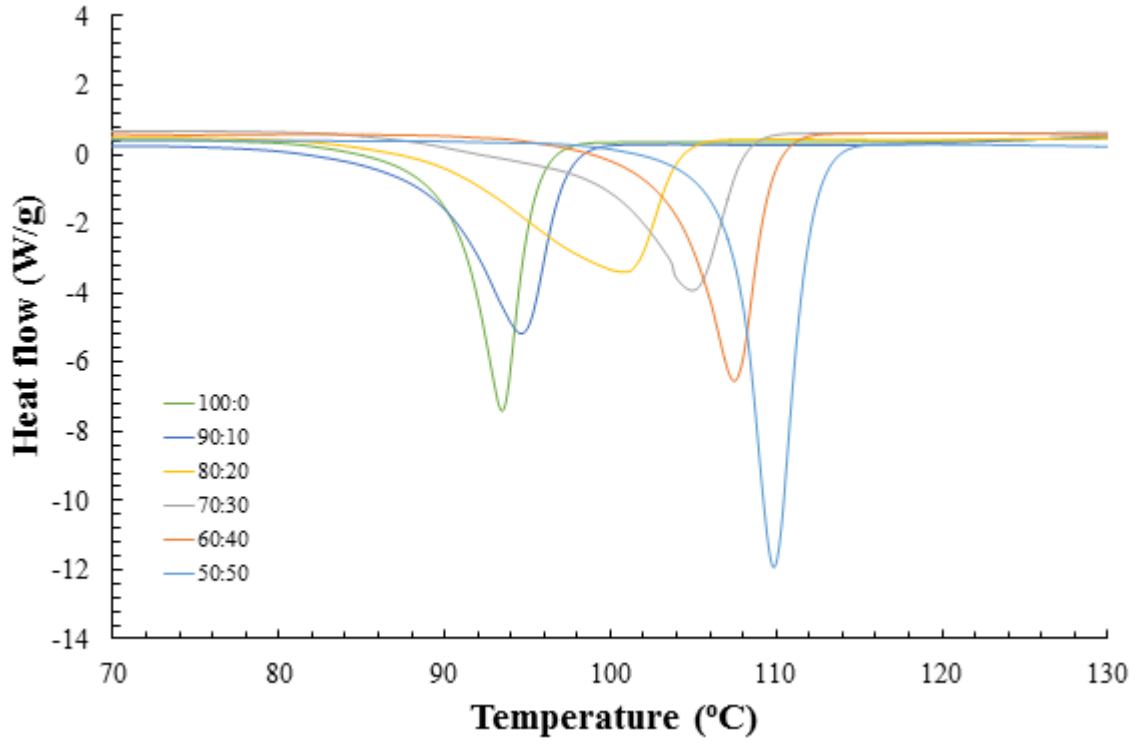

Figure A8. 33 - DSC traces, highlighting the change in phase from the racemic to the enantiopure (1:1) co-crystals of *NPX* and *A*, with increasing molar contributions of *sNPX*

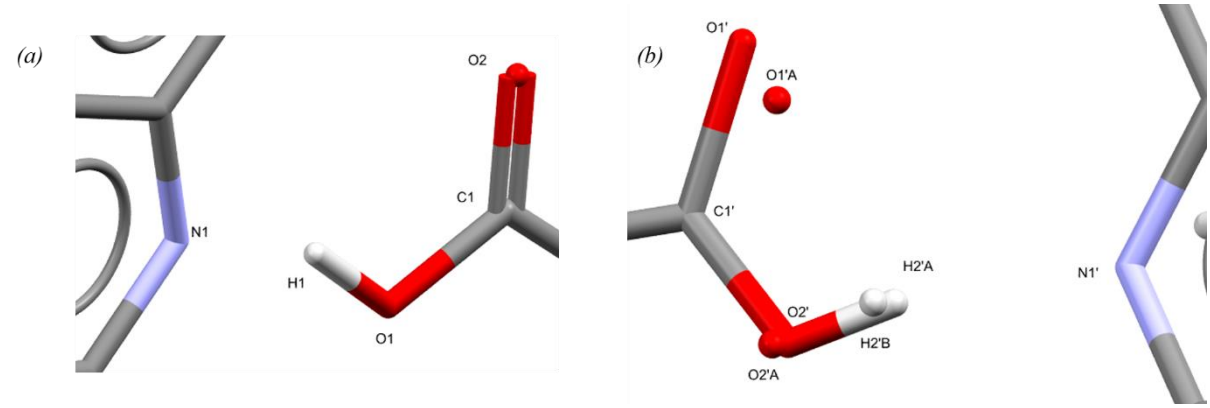

Figure A8. 34 - Key functional groups and disordered atoms of the S-naproxen:acridine (1:1) co-crystal, Form I, highlighting the atoms involved in the two hydrogen bonding interactions, (a) and (b)

Table A8. 10 - Hydrogen bonding interactions with the S-naproxen:acridine (1:1) co-crystal, Form I, highlighting the key interaction lengths and angles

D	H	A	d(D-H) (Å)	d(H-A) (Å)	d(D-A) (Å)	D-H-A (º)
O2'	*H2'A*	*N1'*	0.82	2.00	2.77(2)	155.3
O1	*H1*	*N1*	0.996(14)	1.73(2)	2.677(3)	158(4)
O2'A	*H2'B*	*N1'*	0.82	1.94	2.74(2)	166.1
O2'	*H2'A*	*N1'*	0.82	2.00	2.77(2)	155.3

Table A8. 11 - Atomic occupancy of disordered atoms in the S-naproxen:acridine (1:1) co-crystal, Form I

Atom	Occupancy	Atom	Occupancy	Atom	Occupancy
O2'	0.504(8)	*H2'A*	0.504(8)	*O1'*	0.504(8)
O1'A	0.496(8)	*O2'A*	0.496(8)	*H2'B*	0.496(8)

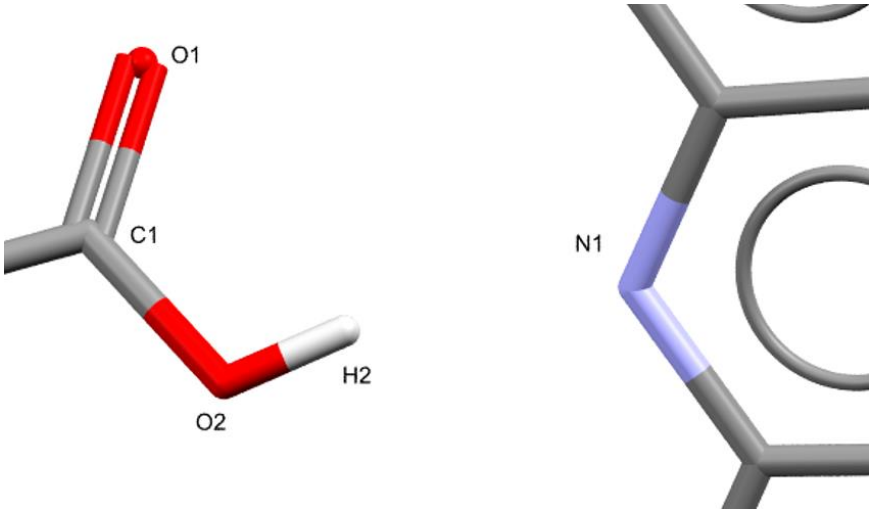

Figure A8. 35 - Key functional groups of the RS-naproxen:acridine (1:1) co-crystal, highlighting the atoms involved in hydrogen bonding

Table A8. 12 - Hydrogen bonding interactions with the RS-naproxen:acridine (1:1) co-crystal, highlighting the key interaction lengths and angles

D	**H**	**A**	**d(D-H) (Å)**	**d(H-A) (Å)**	**d(D-A) (Å)**	**D-H-A (º)**
O2	*H2*	*N1*[1]	0.82	1.88	2.6748(18)	162.9

[1] 5/2-X,-1/2+Y,+Z

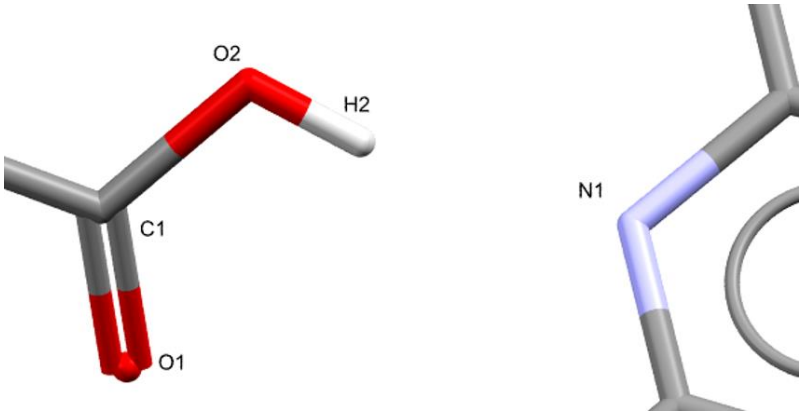

Figure A8. 36 - Key functional groups of the S-naproxen:acridine (1:1) co-crystal, Form II, highlighting atoms involved in hydrogen bonding

Table A8. 13 - Hydrogen bonding interactions with the S-naproxen:acridine (1:1) co-crystal, Form II, highlighting the key interaction lengths and angles

D	**H**	**A**	**d(D-H) (Å)**	**d(H-A) (Å)**	**d(D-A) (Å)**	**D-H-A (º)**
O2	*H2*	*N1*	0.82	1.85	2.662(2)	168.6

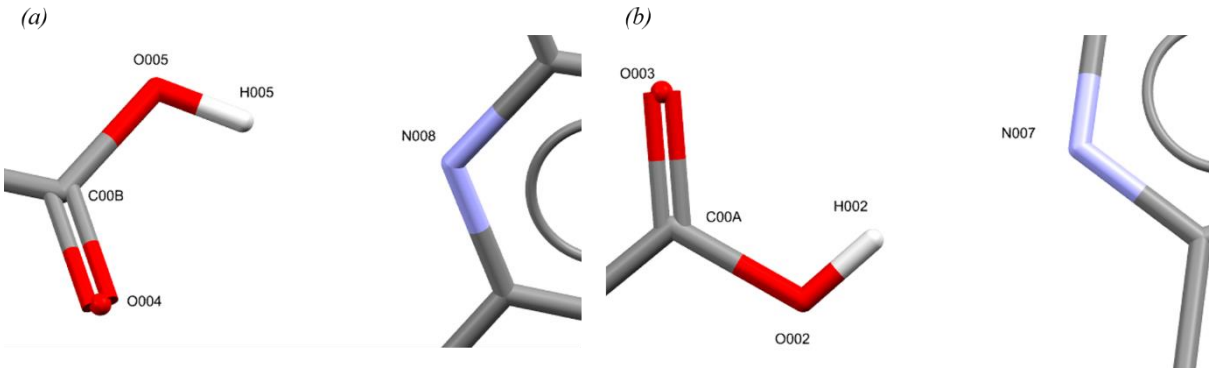

Figure A8. 37 - Key functional groups of the S-naproxen:acridine (2:3) co-crystal, highlighting the atoms involved in hydrogen bonding, (a) and (b)

Table A8. 14 - Hydrogen bonding interactions with the S-naproxen:acridine (2:3) co-crystal, highlighting the key interaction lengths and angles

D	**H**	**A**	**d(D-H) (Å)**	**d(H-A) (Å)**	**d(D-A) (Å)**	**D-H-A (º)**
O002	*H002*	*N007*	0.82	2.02	2.809(3)	161.5
O005	*H005*	*N008*	0.82	1.90	2.714(3)	168.8

Appendix (A9) Chapter 9

Table A9. 1 - Major endothermic thermal events (melting points) exhibited by the prepared and starting materials of *OA* and *U*, as determined by DSC

Material	Major thermal event (ºC)
Urea *(U)*	133.9 – 135.3
Oxalic acid *(OA)*	190.8 – 192.0
Oxalic acid dihydrate *(OAD)*	99.4 – 102.6
Oxalic acid:urea (1:1) co-crystal *(OAU-1:1)*	175.4 – 175.7
Oxalic acid:urea (1:2) co-crystal *(OAU-1:2)*	170.1 – 170.4

A9.1 Mechanochemical preparation

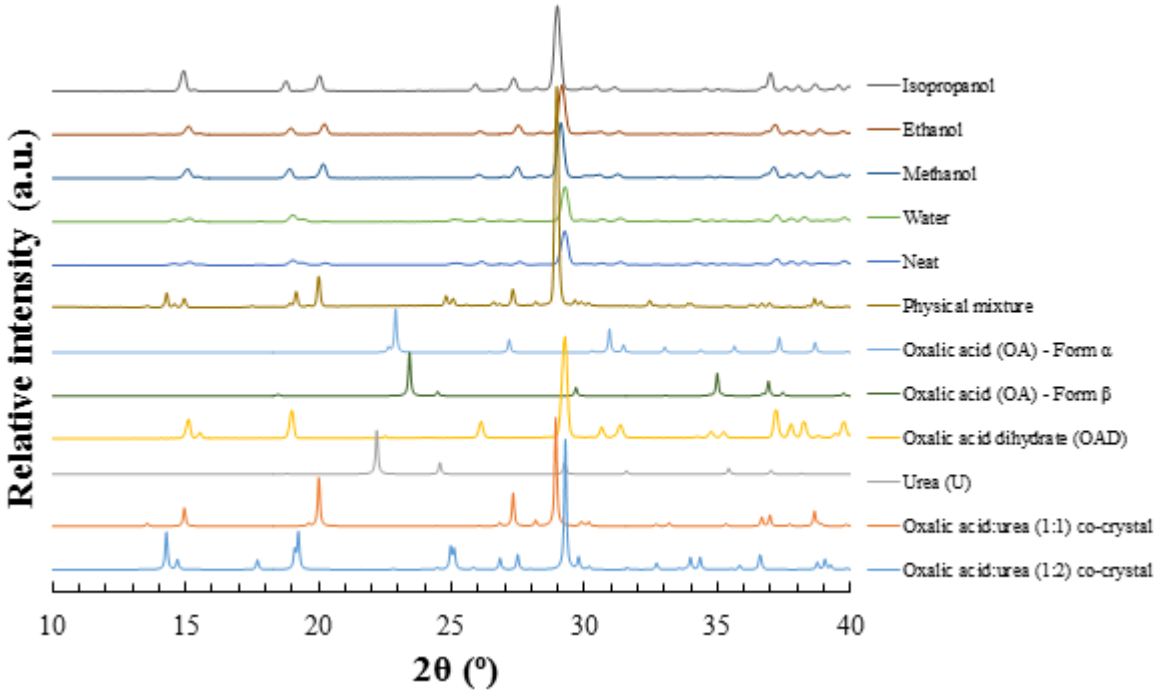

Figure A9. 1 - PXRD patterns highlighting the mechanochemical 2:1 combinations of OA and U, either neat or with minimum quantities of water, methanol, ethanol or isopropanol

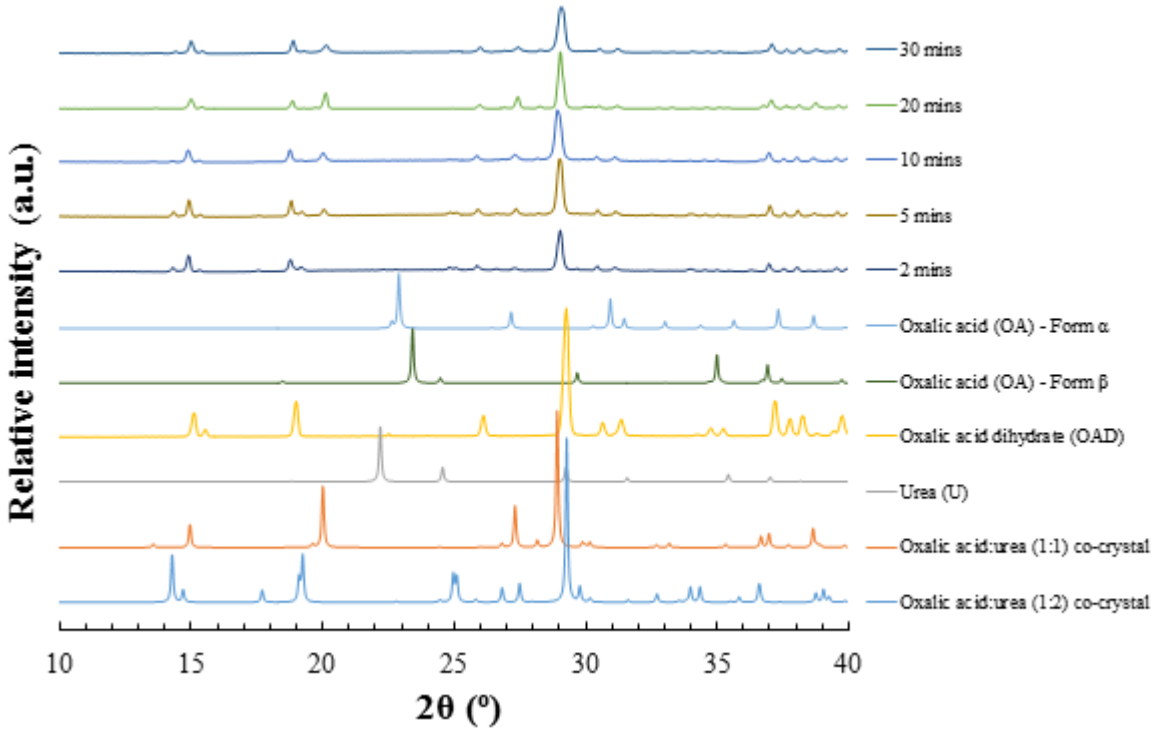

Figure A9. 2 - PXRD patterns highlighting the neat mechanochemical 2:1 combinations of OAD and U, ground for different time periods (top five patterns)

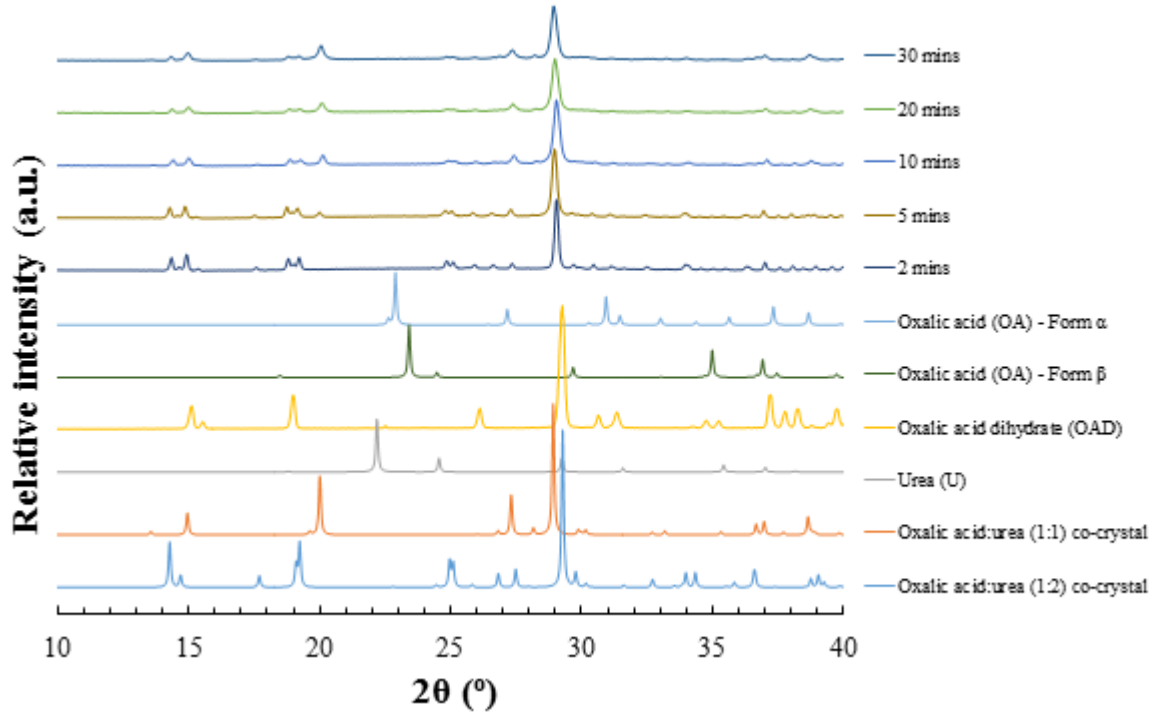

Figure A9. 3 - PXRD patterns highlighting the neat mechanochemical 1:1 combinations of OAD and U, ground for different time periods (top five patterns)

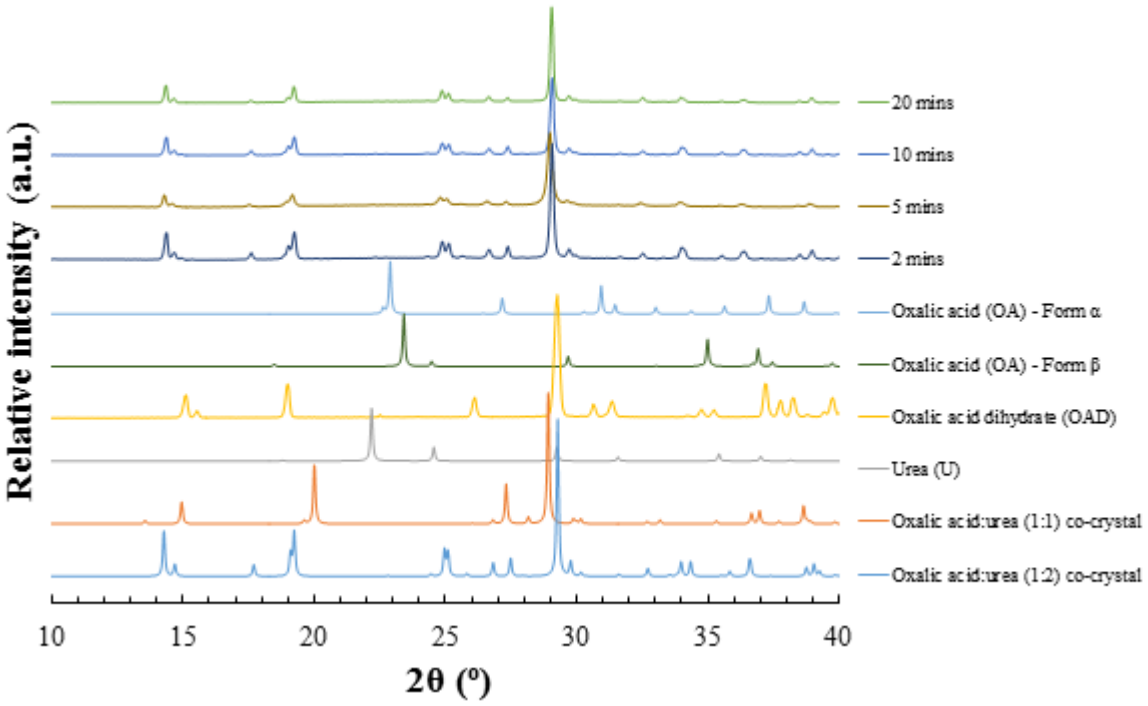

Figure A9. 4 - PXRD patterns highlighting the neat mechanochemical 1:2 combinations of OAD and U, ground for different time periods (top four patterns)

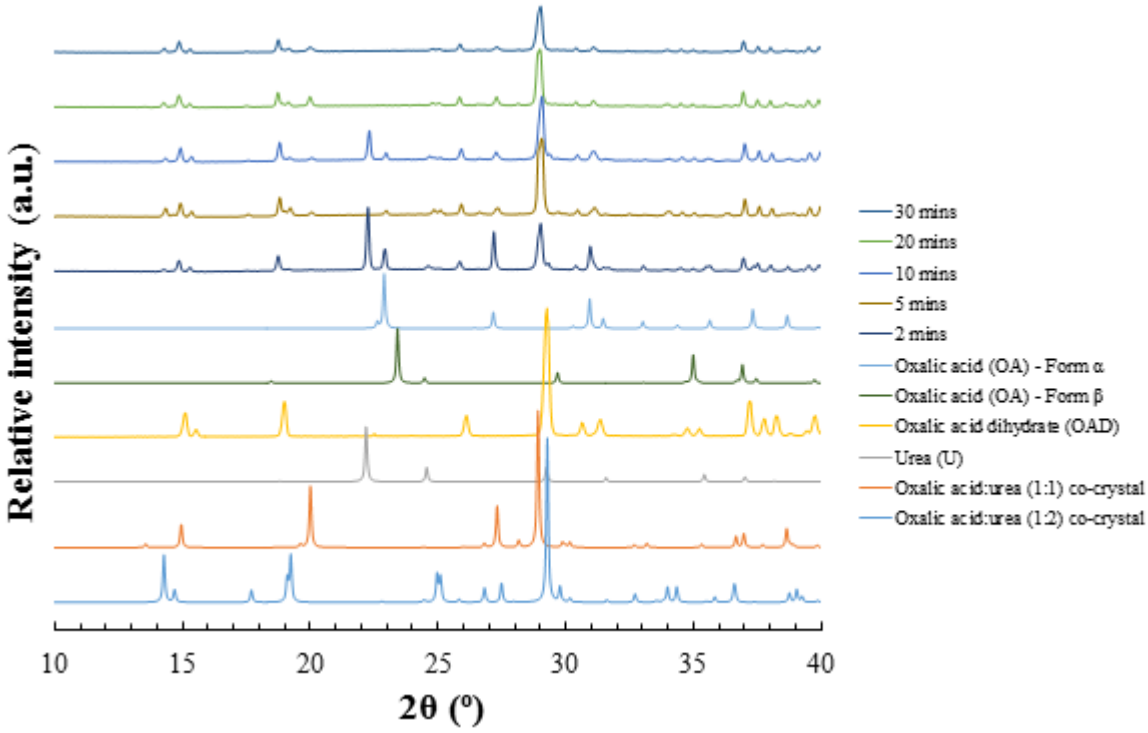

Figure A9. 5 - PXRD patterns highlighting the neat mechanochemical 2:1 combinations of OA and U, ground for different time periods (top five patterns)

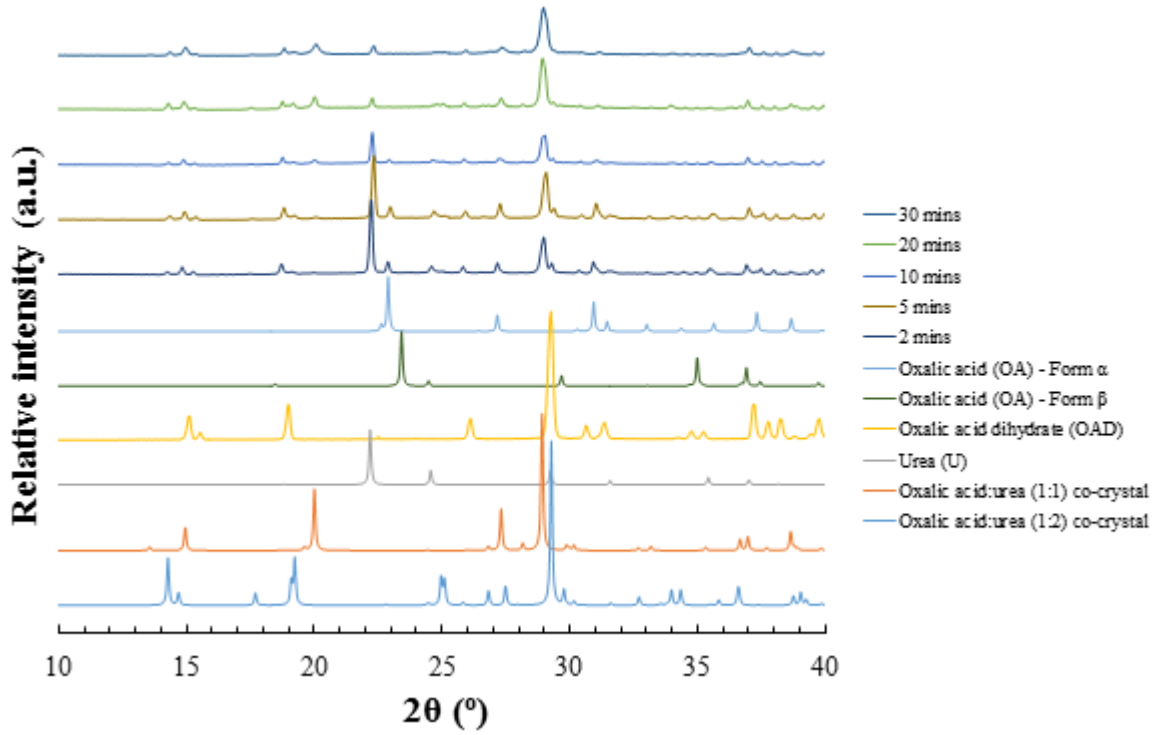

Figure A9. 6 - PXRD patterns highlighting the neat mechanochemical 1:1 combinations of OA and U, ground for different time periods (top five patterns)

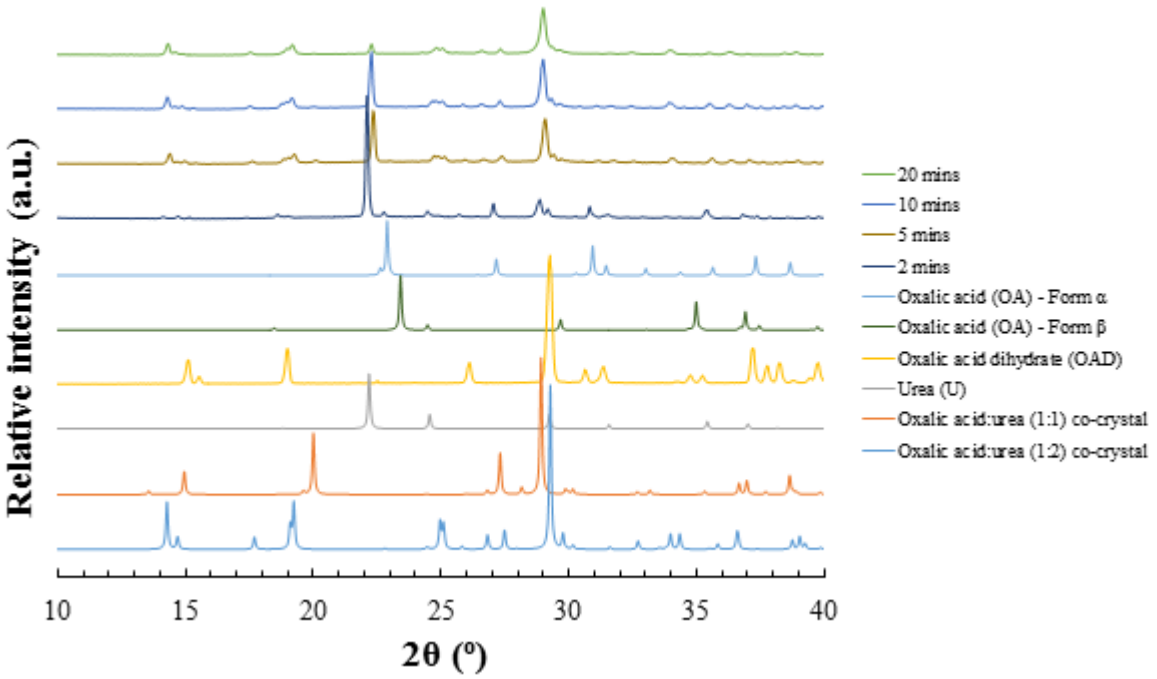

Figure A9. 7 - PXRD patterns highlighting the neat mechanochemical 1:2 combinations of OA and U, ground for different time periods (top four patterns)

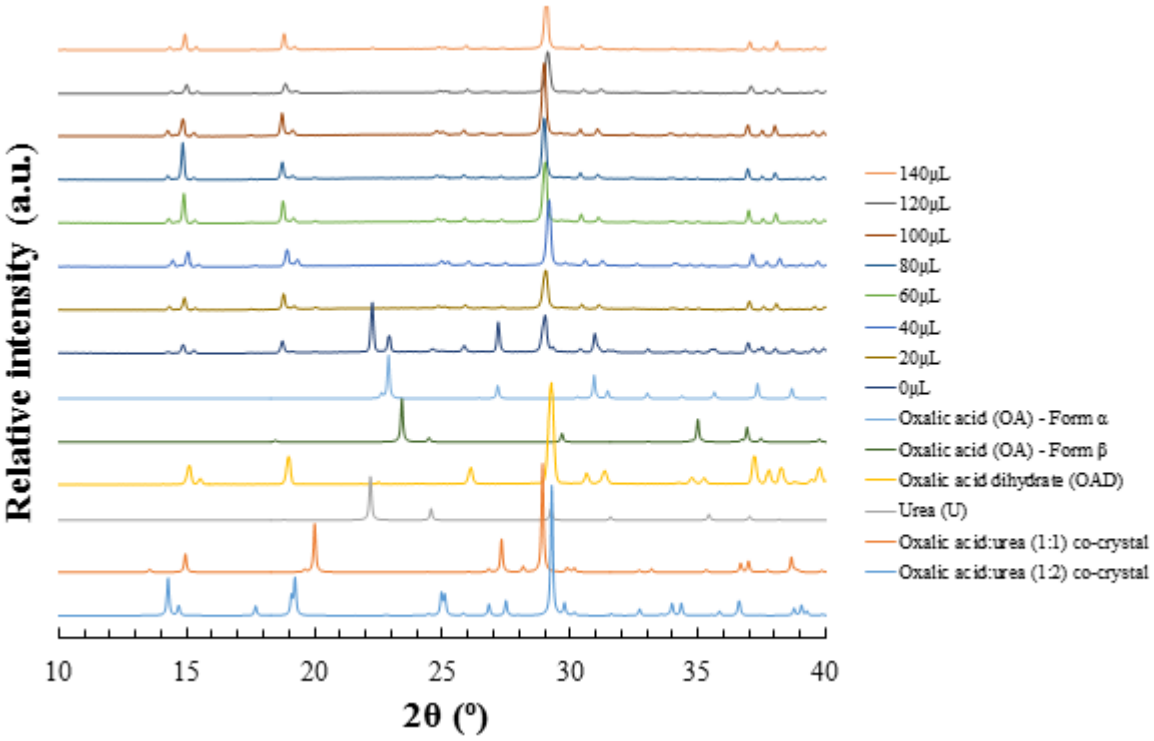

Figure A9. 8 - PXRD patterns highlighting the mechanochemical 2:1 combinations of OA and U, ground with different volumes of water (top eight patterns)

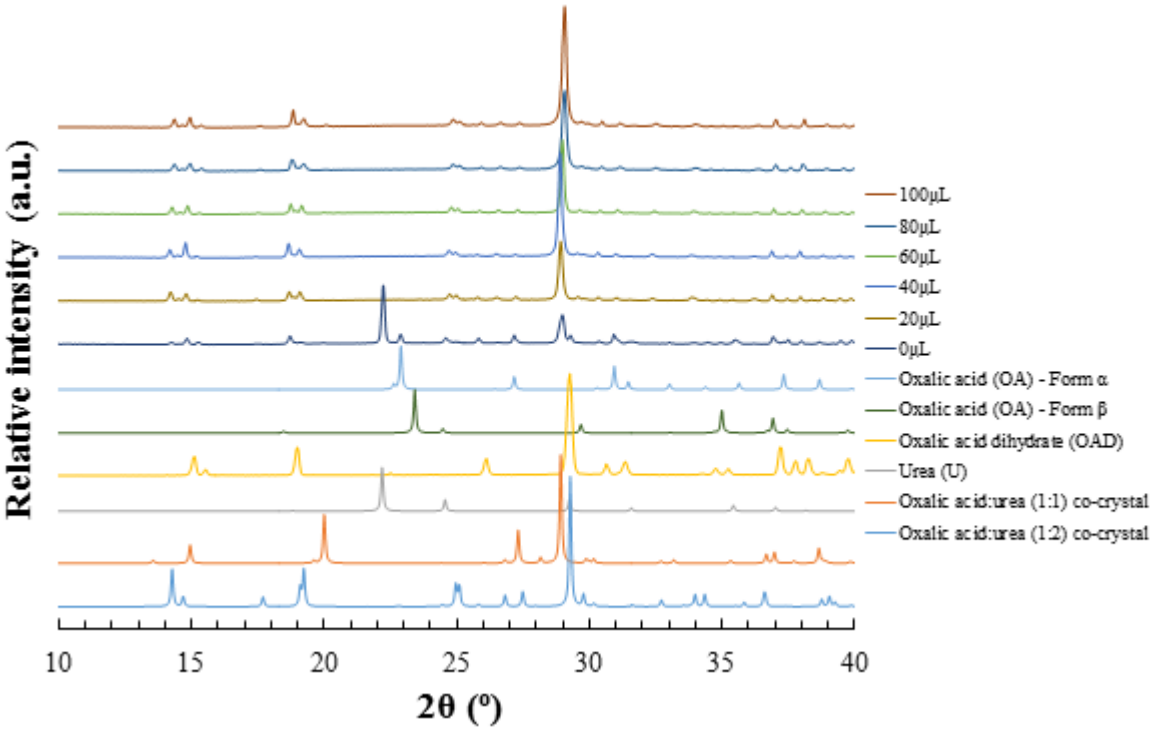

Figure A9. 9 - PXRD patterns highlighting the mechanochemical 1:1 combinations of OA and U, ground with different volumes of water (top six patterns)

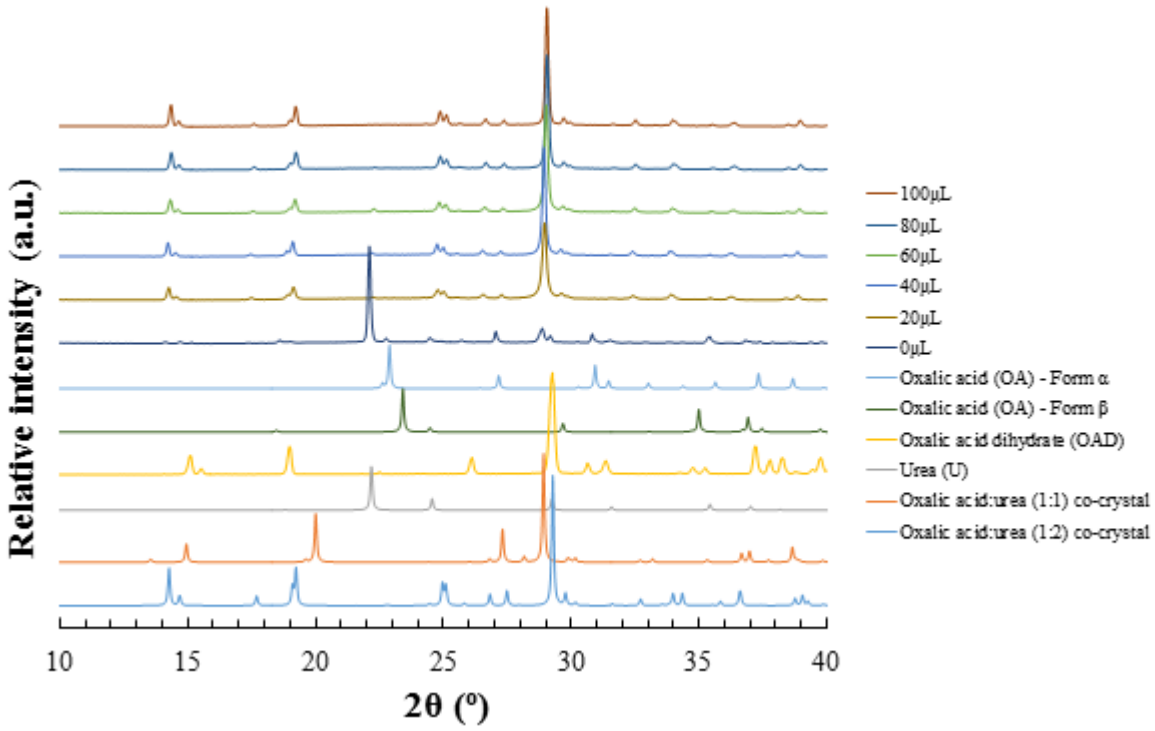

Figure A9. 10 - PXRD patterns highlighting the mechanochemical 1:2 combinations of OA and U, ground with different volumes of water (top six patterns)

A9.2 Solvent-mediated (slurrying) preparations

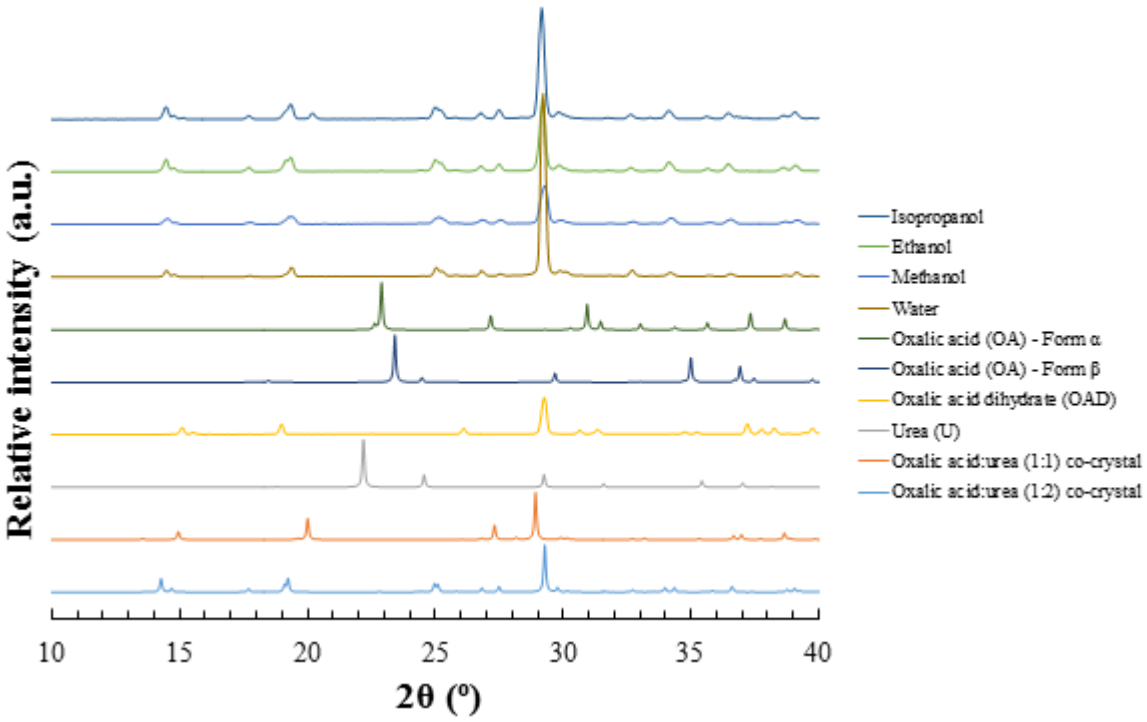

Figure A9. 11 - PXRD patterns highlighting the solid product yielded from initial slurrying experiments of a 1:1 combination of oxalic and urea, in a variety of solvents; water, methanol, ethanol and isopropanol

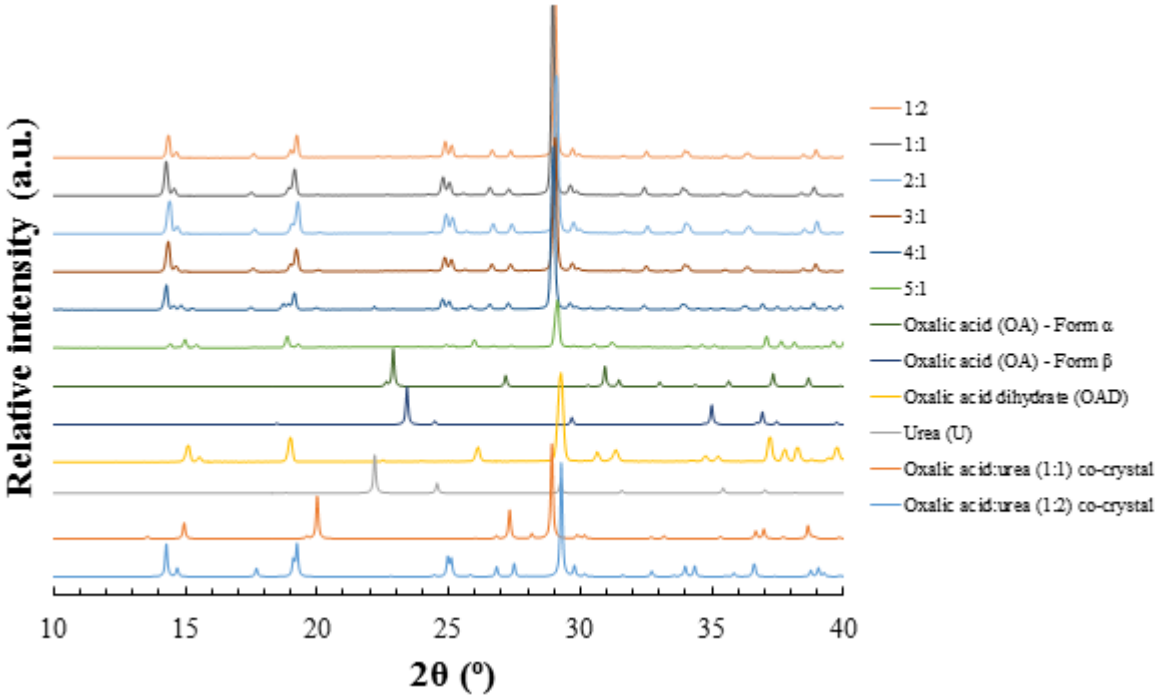

Figure A9. 12 - PXRD patterns highlighting the solid product yielded from slurrying experiments in water, with a solid loading of x2 that of the solid mass of the oxalic acid:urea (1:2) co-crystal at 30ºC, mixed for 1 hour, utilising a range of suspension stoichiometries (top six patterns)

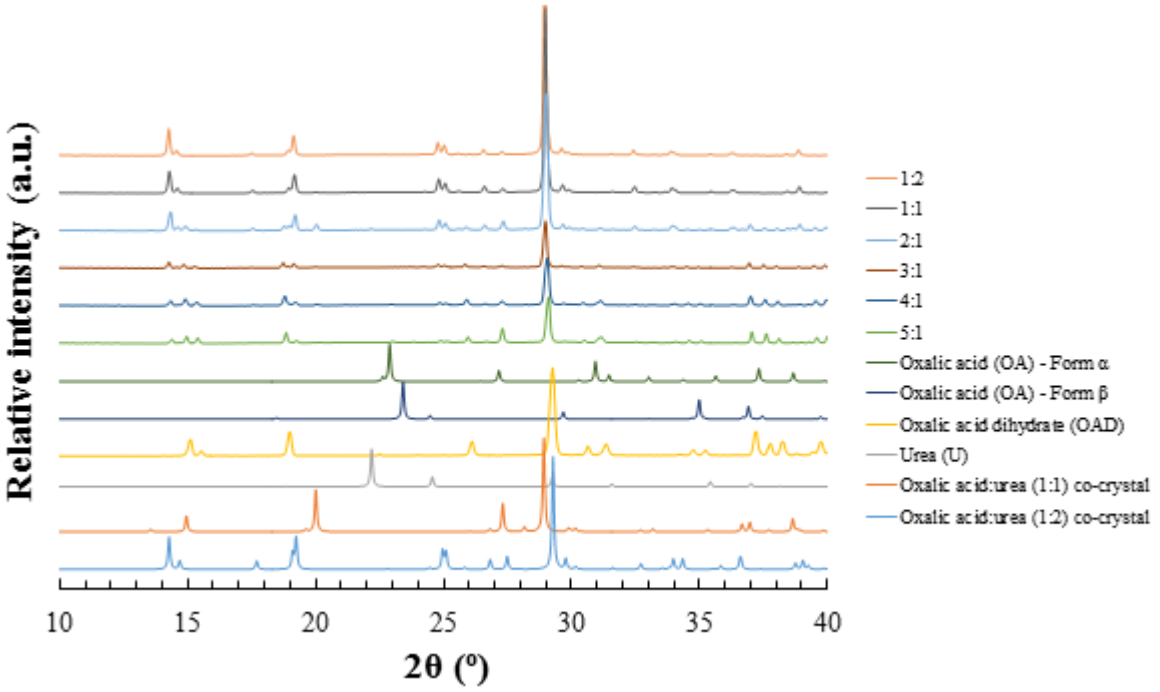

Figure A9. 13 -PXRD patterns highlighting the solid product yielded from slurrying experiments in water, with a solid loading of x3 that of the solid mass of the oxalic acid:urea (1:2) co-crystal at 30ºC, mixed for 1 hour, utilising a range of suspension stoichiometries (top six patterns)

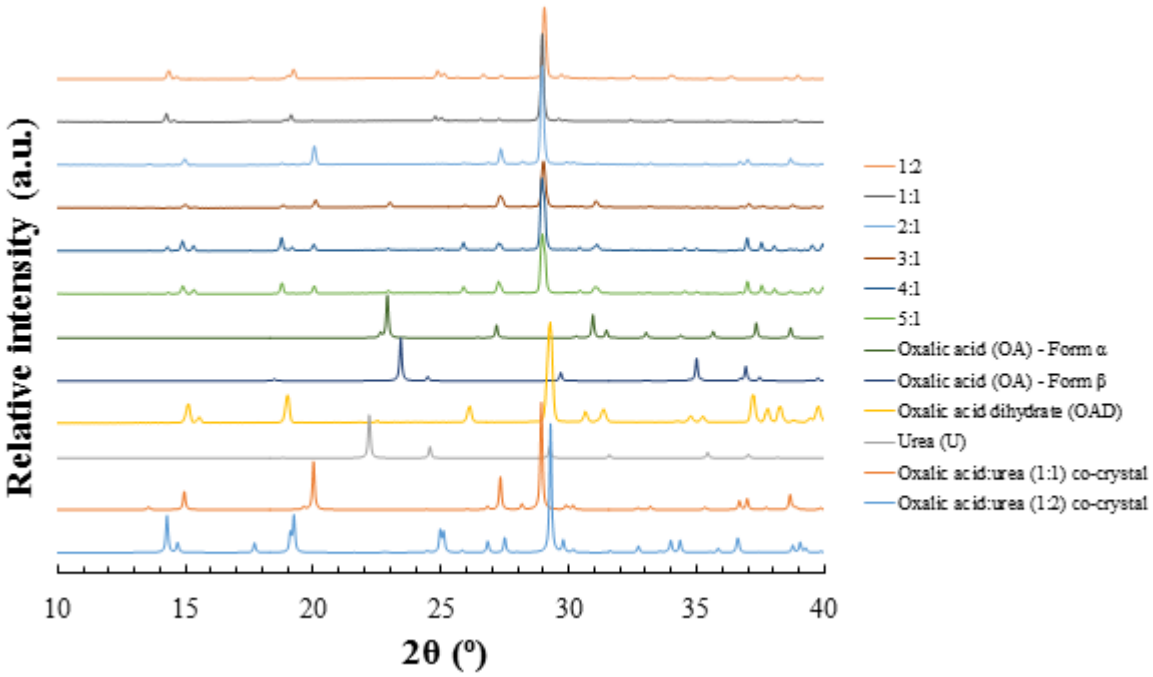

Figure A9. 14 - PXRD patterns highlighting the solid product yielded from slurrying experiments in water, with a solid loading of x4 that of the solid mass of the oxalic acid:urea (1:2) co-crystal at 30ºC, mixed for 1 hour, utilising a range of suspension stoichiometries (top six patterns)

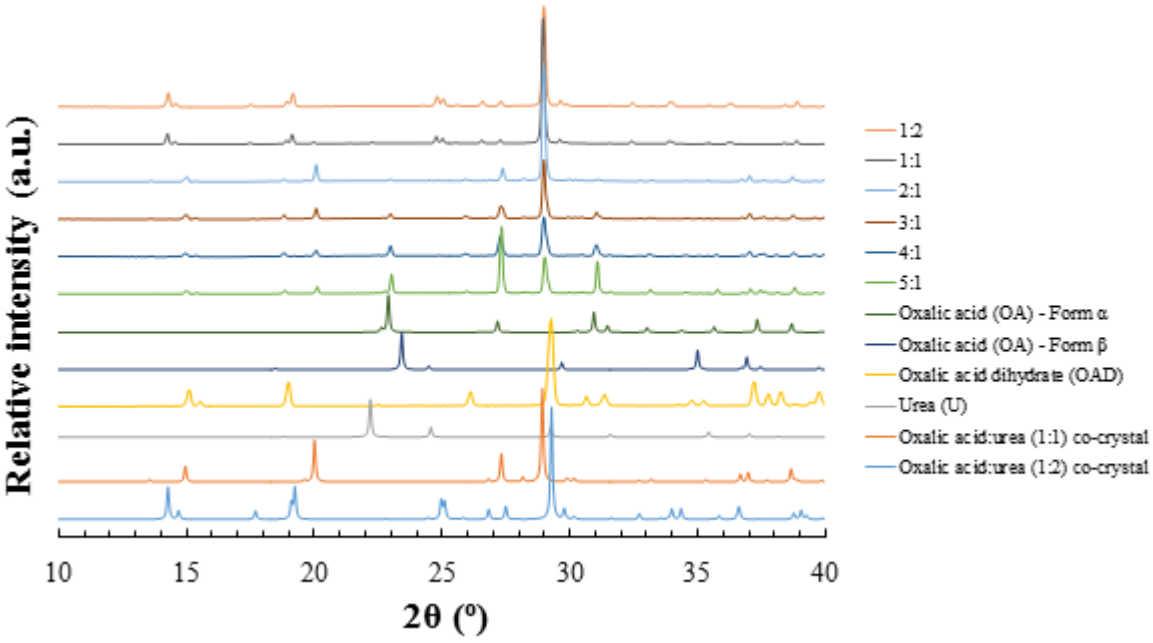

Figure A9. 15 - PXRD patterns highlighting the solid product yielded from slurrying experiments in water, with a solid loading of x5 that of the solid mass of the oxalic acid:urea (1:2) co-crystal at 30ºC, mixed for 1 hour, utilising a range of suspension stoichiometries (top six patterns)

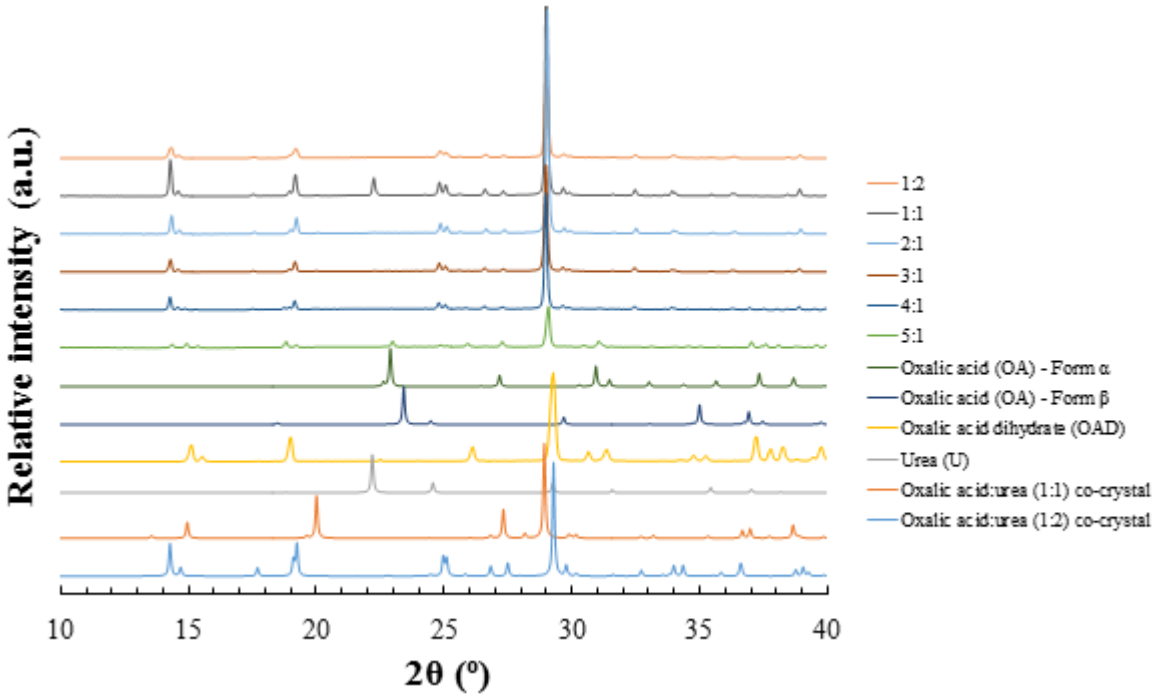

Figure A9. 16 - PXRD patterns highlighting the solid product yielded from slurrying experiments in water, with a solid loading of x2 that of the solid mass of the oxalic acid:urea (1:2) co-crystal at 30ºC, mixed for 4 hours, utilising a range of suspension stoichiometries (top six patterns)

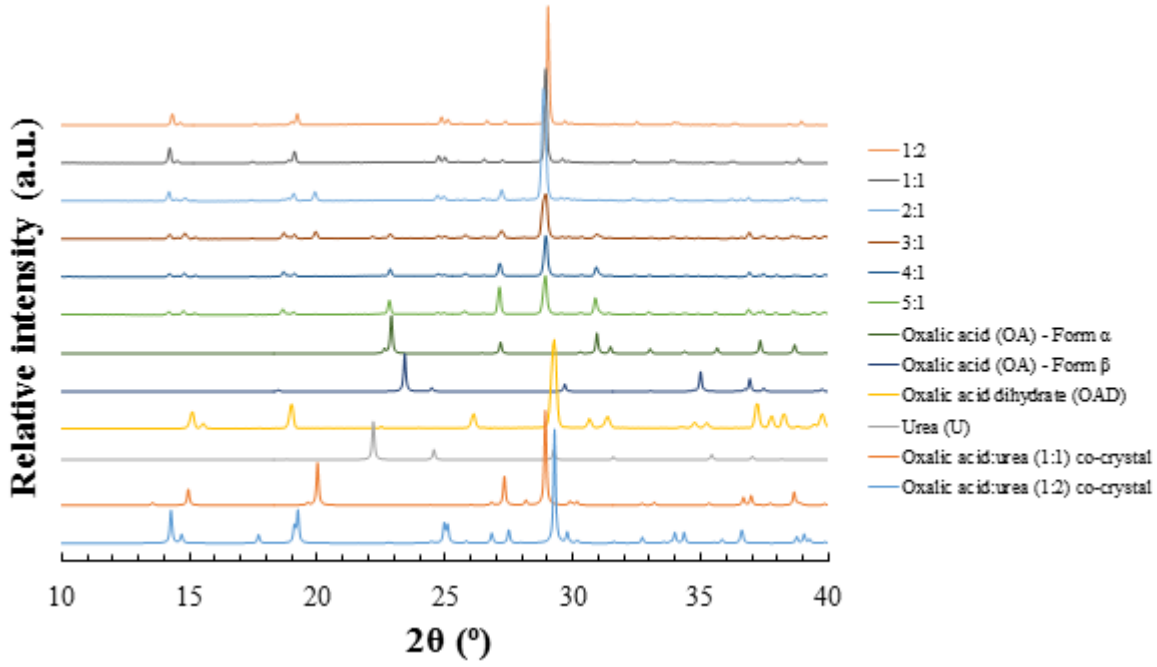

Figure A9. 17 -PXRD patterns highlighting the solid product yielded from slurrying experiments in water, with a solid loading of x3 that of the solid mass of the oxalic acid:urea (1:2) co-crystal at 30ºC, mixed for 4 hours, utilising a range of suspension stoichiometries (top six patterns)

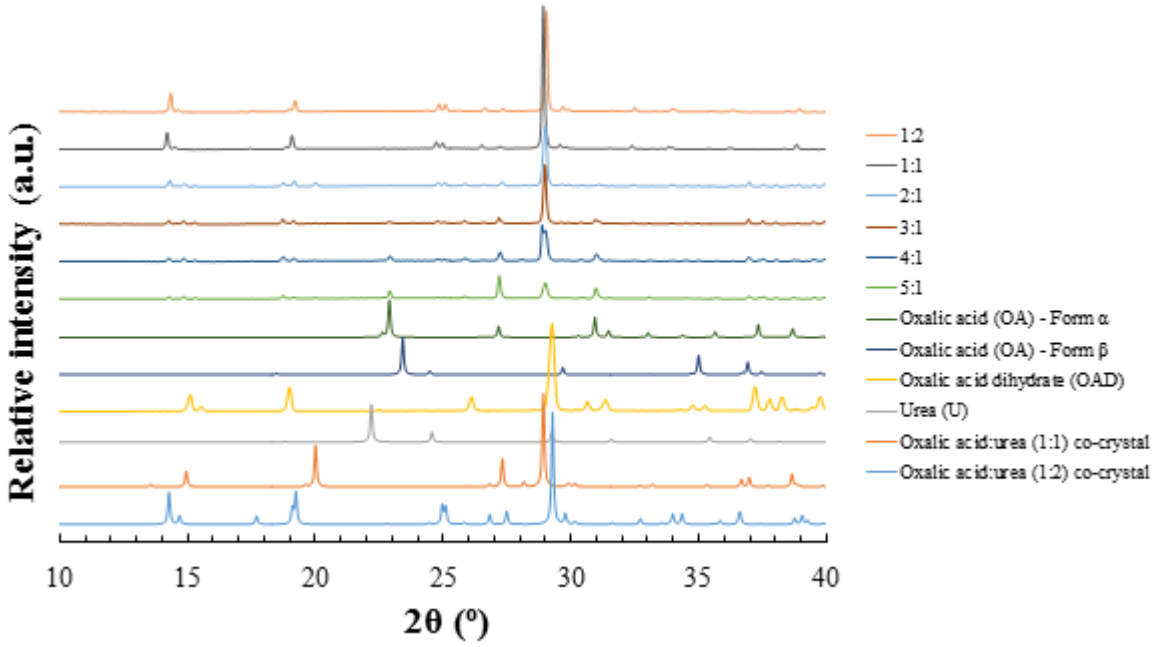

Figure A9. 18 - PXRD patterns highlighting the solid product yielded from slurrying experiments in water, with a solid loading of x4 that of the solid mass of the oxalic acid:urea (1:2) co-crystal at 30ºC, mixed for 4 hours, utilising a range of suspension stoichiometries (top six patterns)

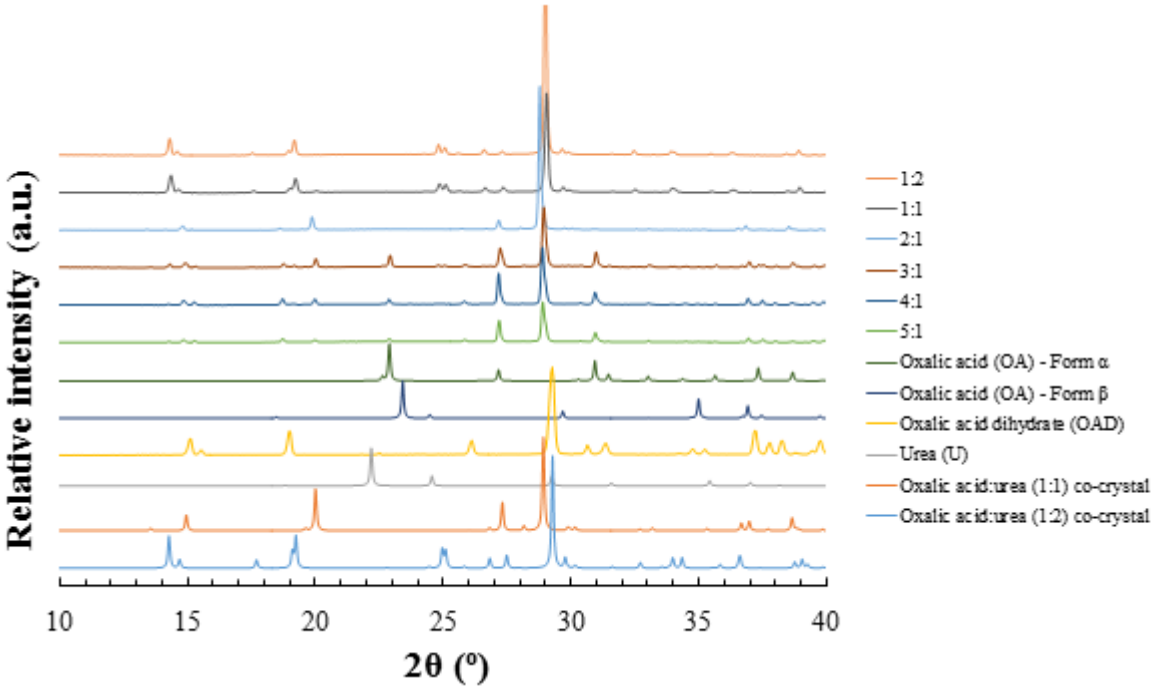

Figure A9. 19 - PXRD patterns highlighting the solid product yielded from slurrying experiments in water, with a solid loading of x5 that of the solid mass of the oxalic acid:urea (1:2) co-crystal at 30ºC, mixed for 4 hours, utilising a range of suspension stoichiometries (top six patterns)

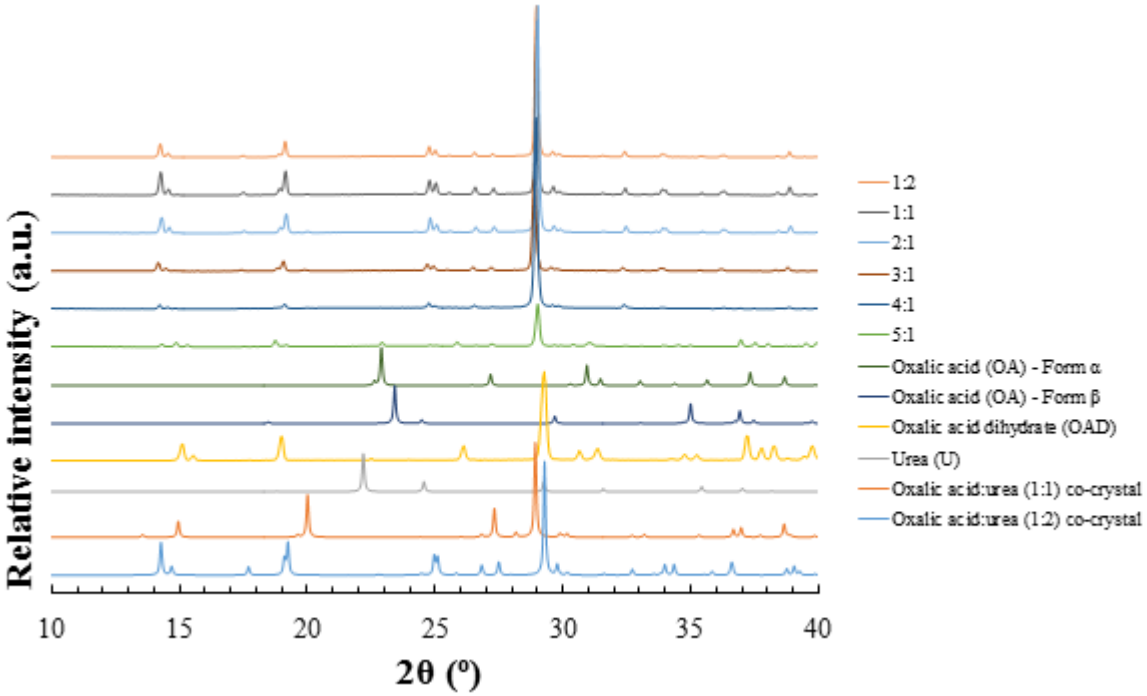

Figure A9. 20 - PXRD patterns highlighting the solid product yielded from slurrying experiments in water, with a solid loading of x2 that of the solid mass of the oxalic acid:urea (1:2) co-crystal at 30ºC, mixed for 16 hours, utilising a range of suspension stoichiometries (top six patterns)

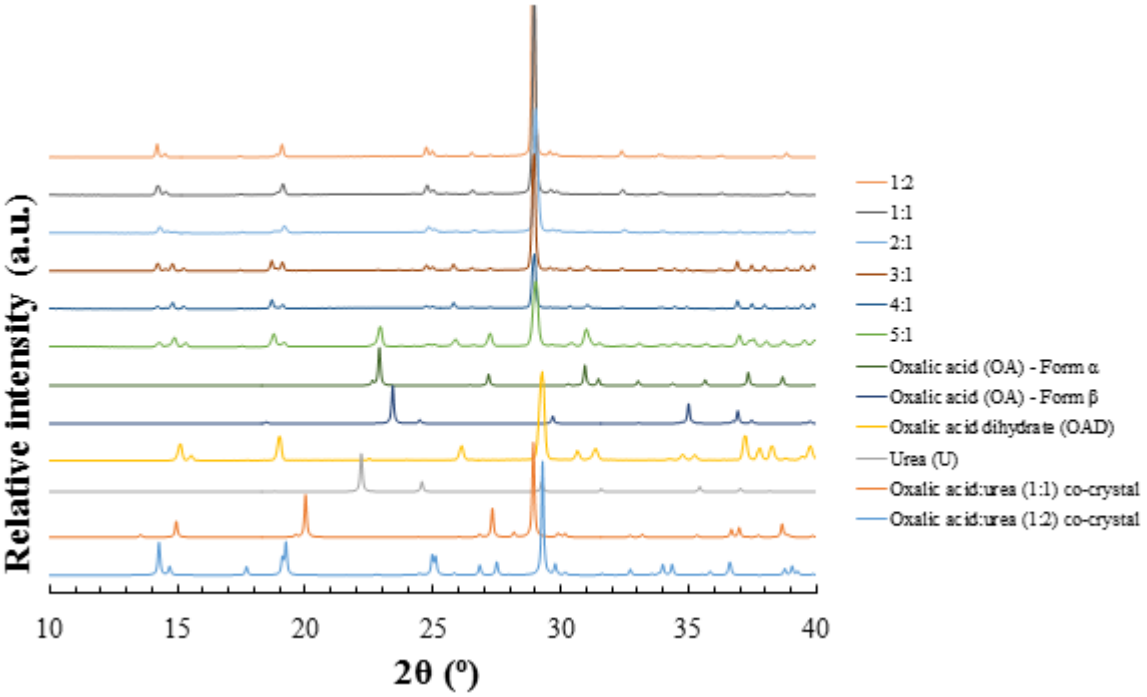

Figure A9. 21 - PXRD patterns highlighting the solid product yielded from slurrying experiments in water, with a solid loading of x3 that of the solid mass of the oxalic acid:urea (1:2) co-crystal at 30ºC, mixed for 16 hours, utilising a range of suspension stoichiometries (top six patterns)

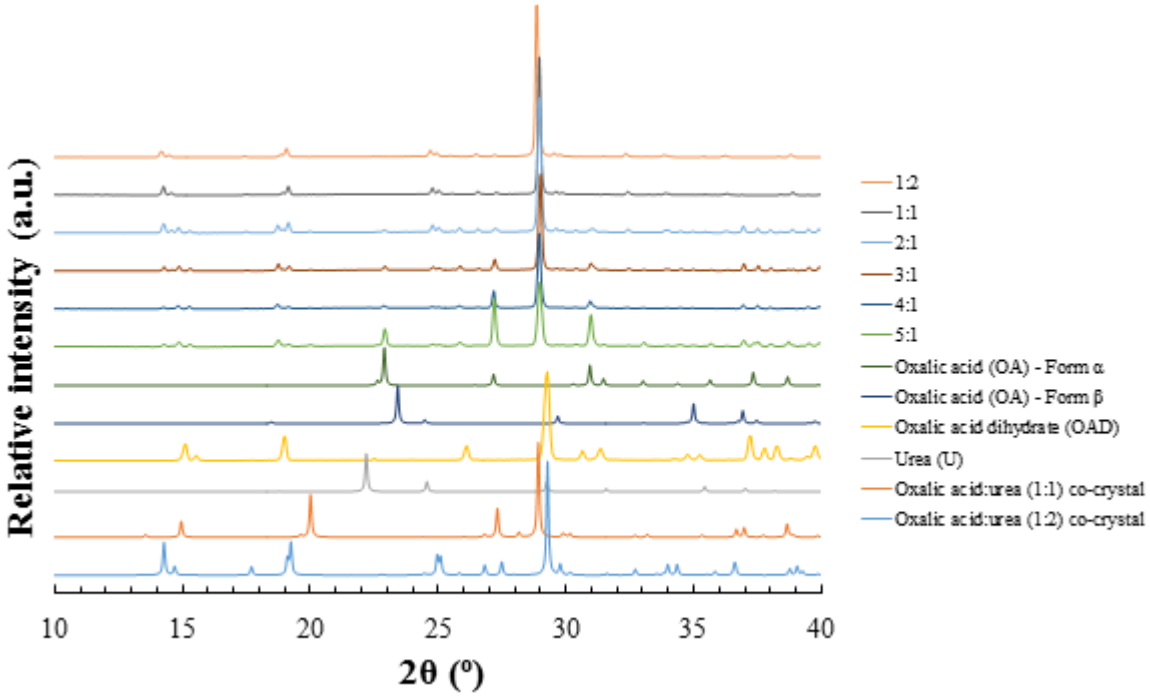

Figure A9. 22 - PXRD patterns highlighting the solid product yielded from slurrying experiments in water, with a solid loading of x4 that of the solid mass of the oxalic acid:urea (1:2) co-crystal at 30ºC, mixed for 16 hours, utilising a range of suspension stoichiometries (top six patterns)

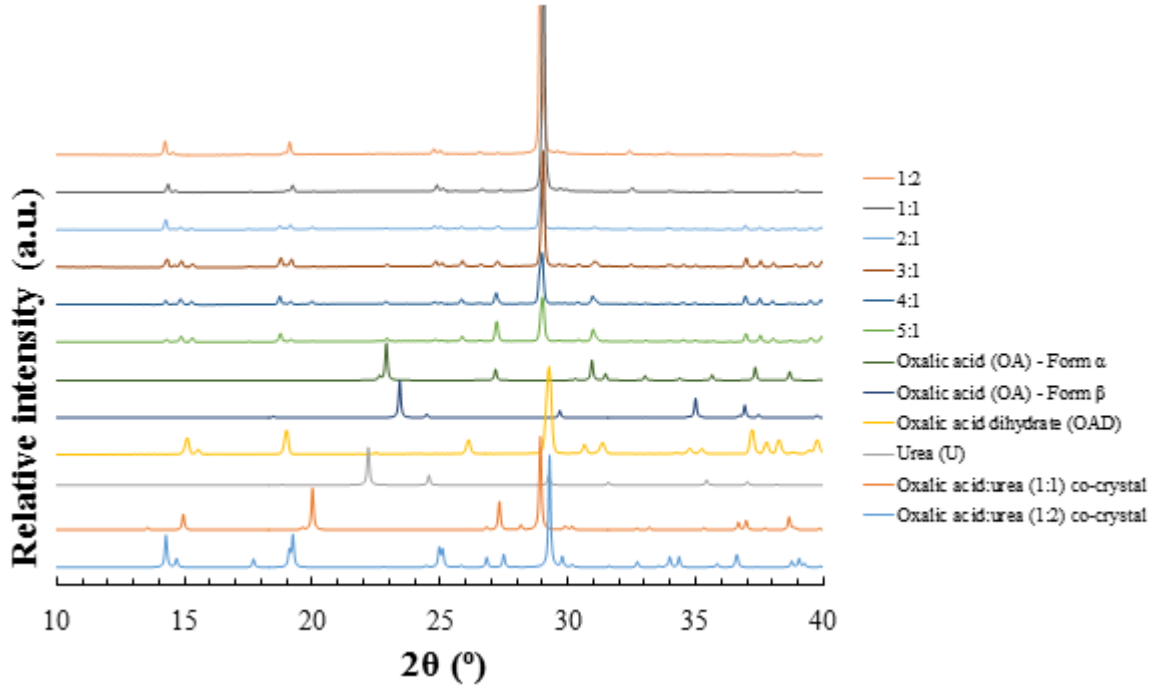

Figure A9. 23 - PXRD patterns highlighting the solid product yielded from slurrying experiments in water, with a solid loading of x5 that of the solid mass of the oxalic acid:urea (1:2) co-crystal at 30ºC, mixed for 16 hours, utilising a range of suspension stoichiometries (top six patterns)

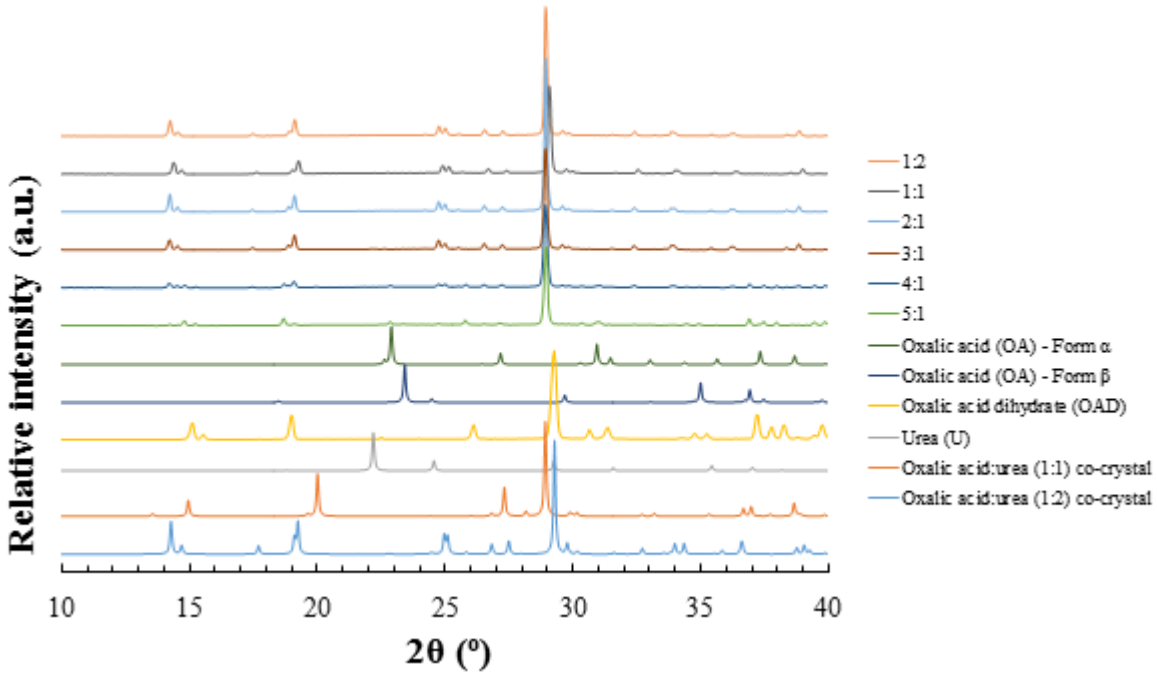

Figure A9. 24 - PXRD patterns highlighting the solid product yielded from slurrying experiments in water, with a solid loading of x2 that of the solid mass of the oxalic acid:urea (1:2) co-crystal at 30ºC, mixed for 64 hours, utilising a range of suspension stoichiometries (top six patterns)

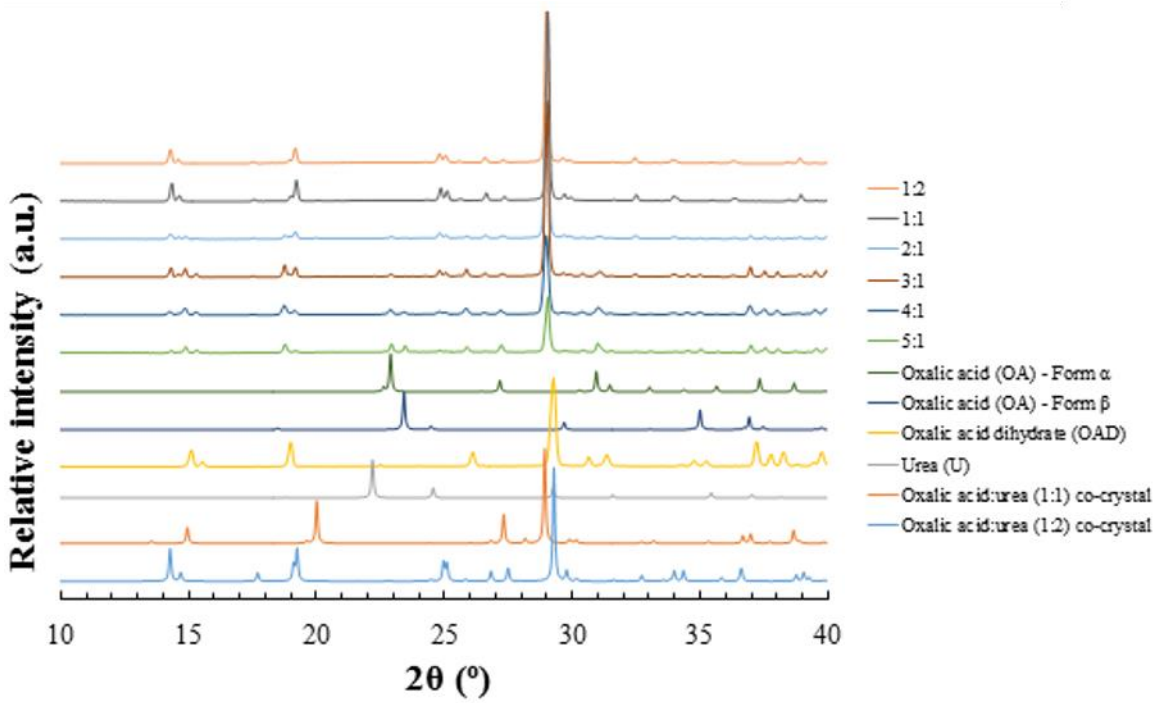

Figure A9. 25 - PXRD patterns highlighting the solid product yielded from slurrying experiments in water, with a solid loading of x3 that of the solid mass of the oxalic acid:urea (1:2) co-crystal at 30ºC, mixed for 64 hours, utilising a range of suspension stoichiometries (top six patterns)

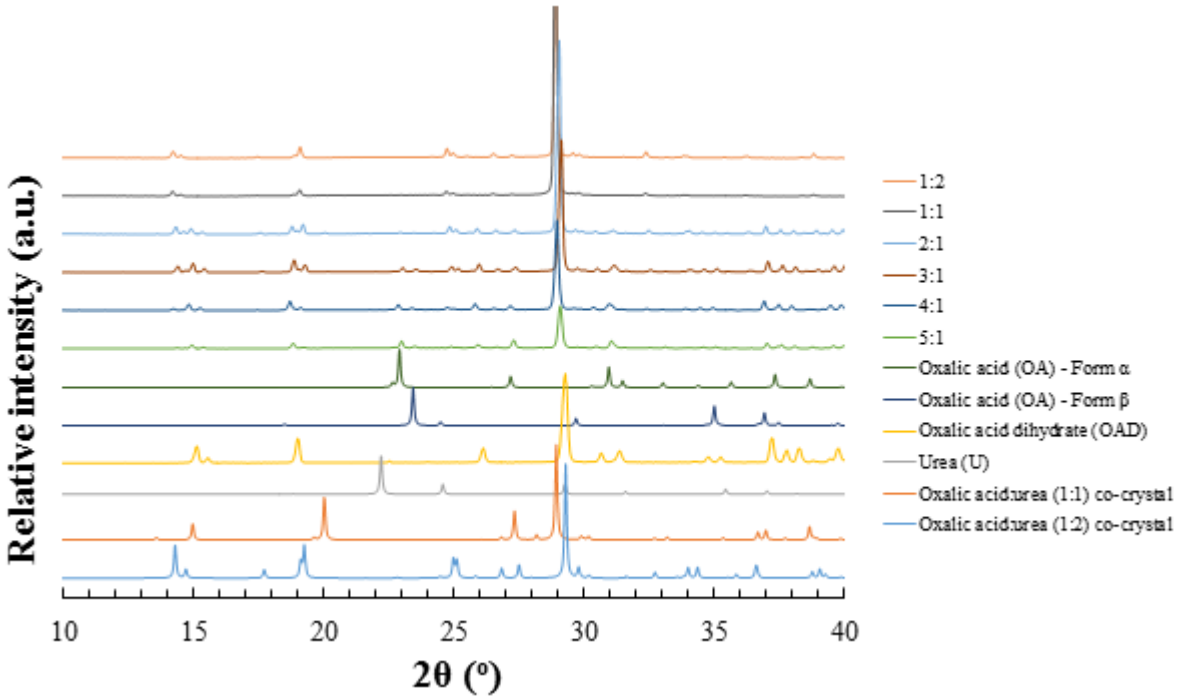

Figure A9. 26 - PXRD patterns highlighting the solid product yielded from slurrying experiments in water, with a solid loading of x4 that of the solid mass of the oxalic acid:urea (1:2) co-crystal at 30ºC, mixed for 64 hours, utilising a range of suspension stoichiometries (top six patterns)

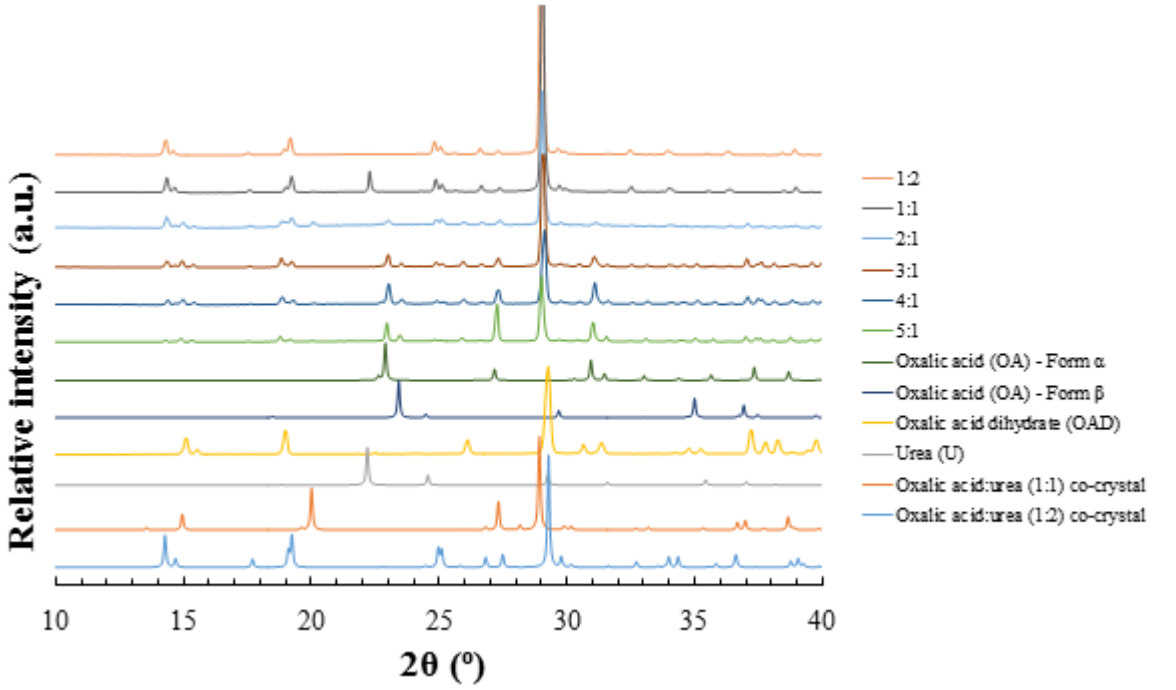

Figure A9. 27 - PXRD patterns highlighting the solid product yielded from slurrying experiments in water, with a solid loading of x5 that of the solid mass of the oxalic acid:urea (1:2) co-crystal at 30ºC, mixed for 64 hours, utilising a range of suspension stoichiometries (top six patterns)

A9.3 Evaporative crystallisation

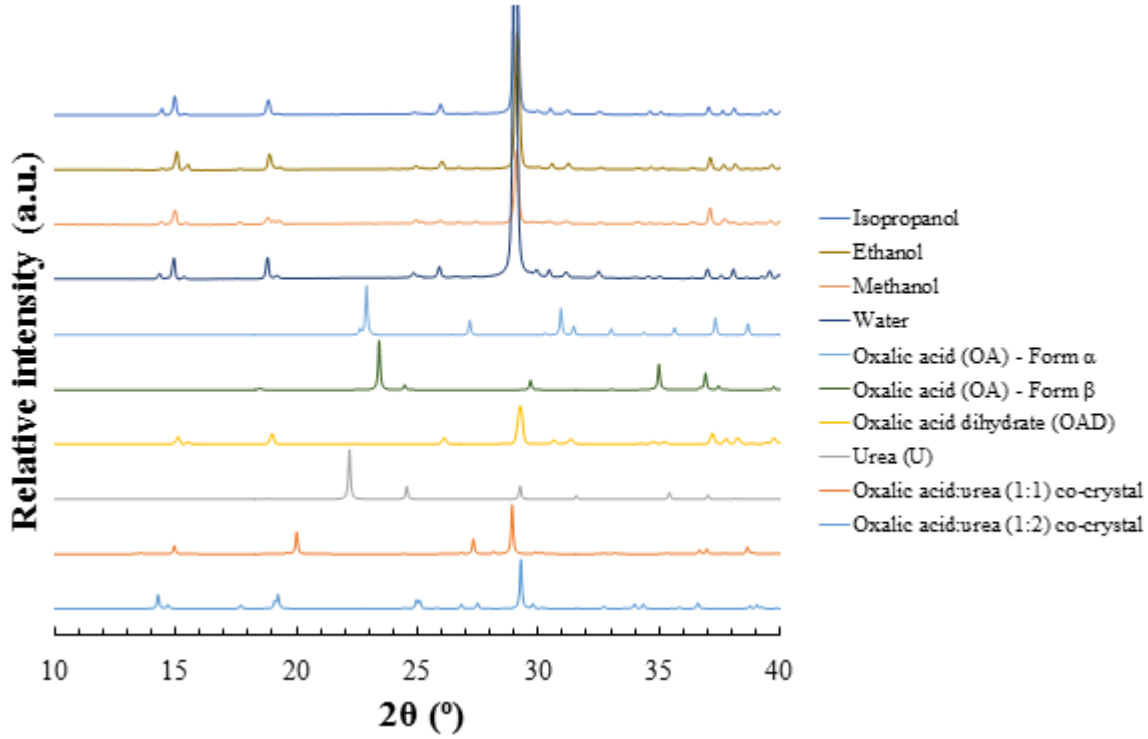

Figure A9. 28 - PXRD patterns highlighting the crystalline phases yielded from evaporative crystallisations at 20ºC, from water, methanol, ethanol and isopropanol, with oxalic acid and urea in a 2:1 stoichiometry

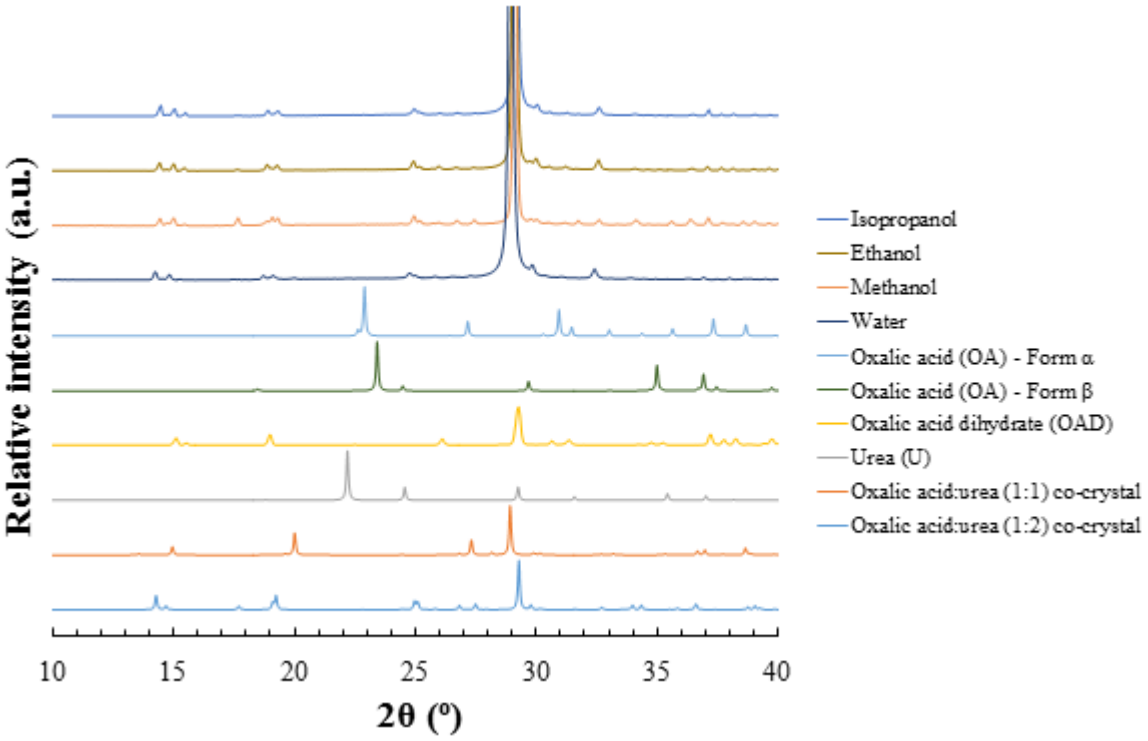

Figure A9. 29 - PXRD patterns highlighting the crystalline phases yielded from evaporative crystallisations at 20ºC, from water, methanol, ethanol and isopropanol, with oxalic acid and urea in a 1:1 stoichiometry

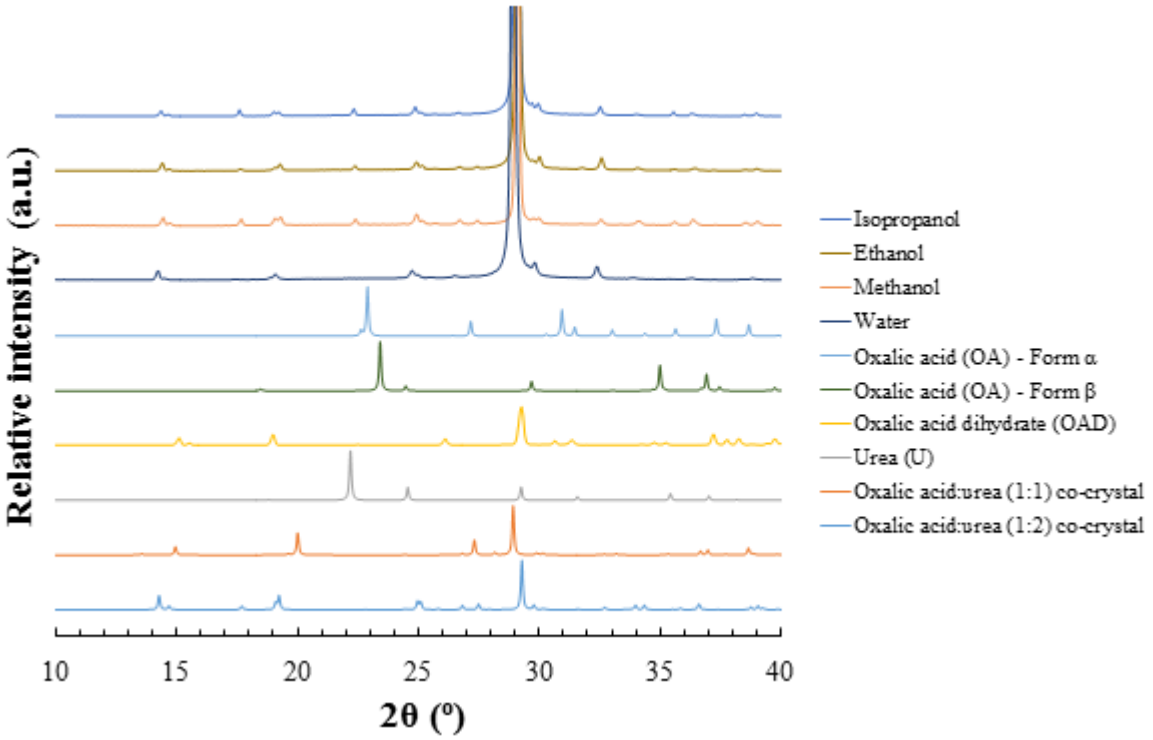

Figure A9. 30 - PXRD patterns highlighting the crystalline phases yielded from evaporative crystallisations at 20ºC, from water, methanol, ethanol and isopropanol, with oxalic acid and urea in a 1:2 stoichiometry

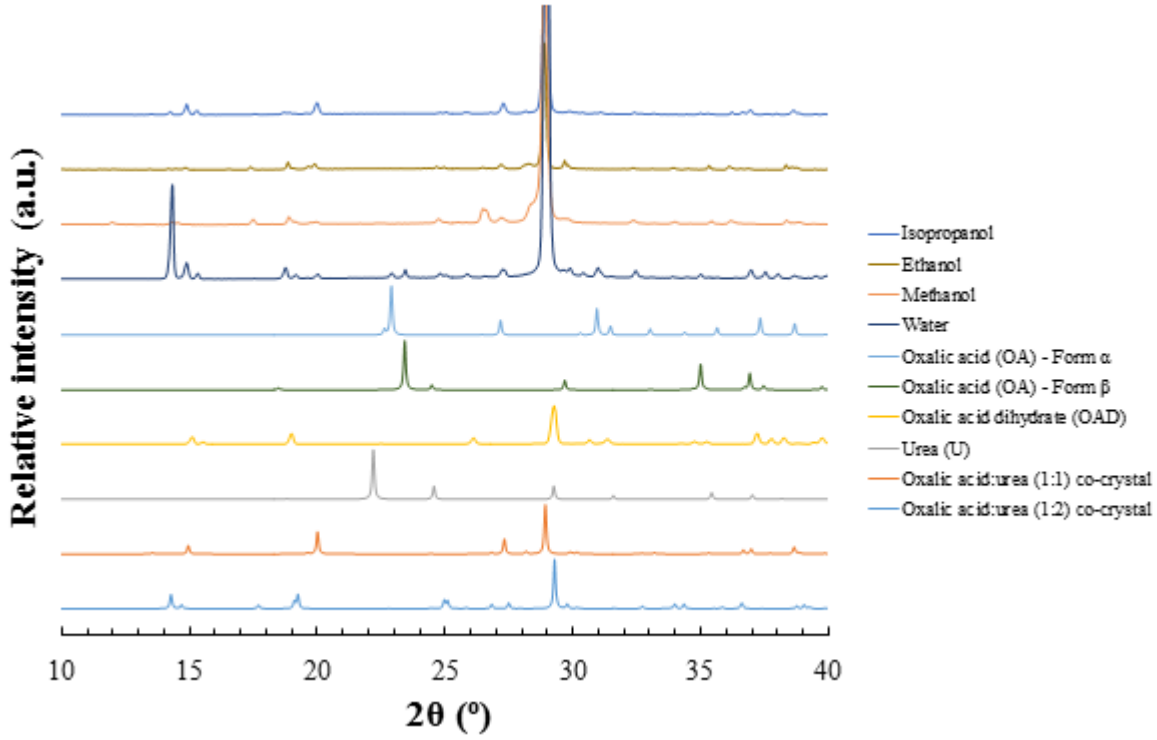

Figure A9. 31 - PXRD patterns highlighting the crystalline phases yielded from evaporative crystallisations at 40ºC, from water, methanol, ethanol and isopropanol, with oxalic acid and urea in a 2:1 stoichiometry

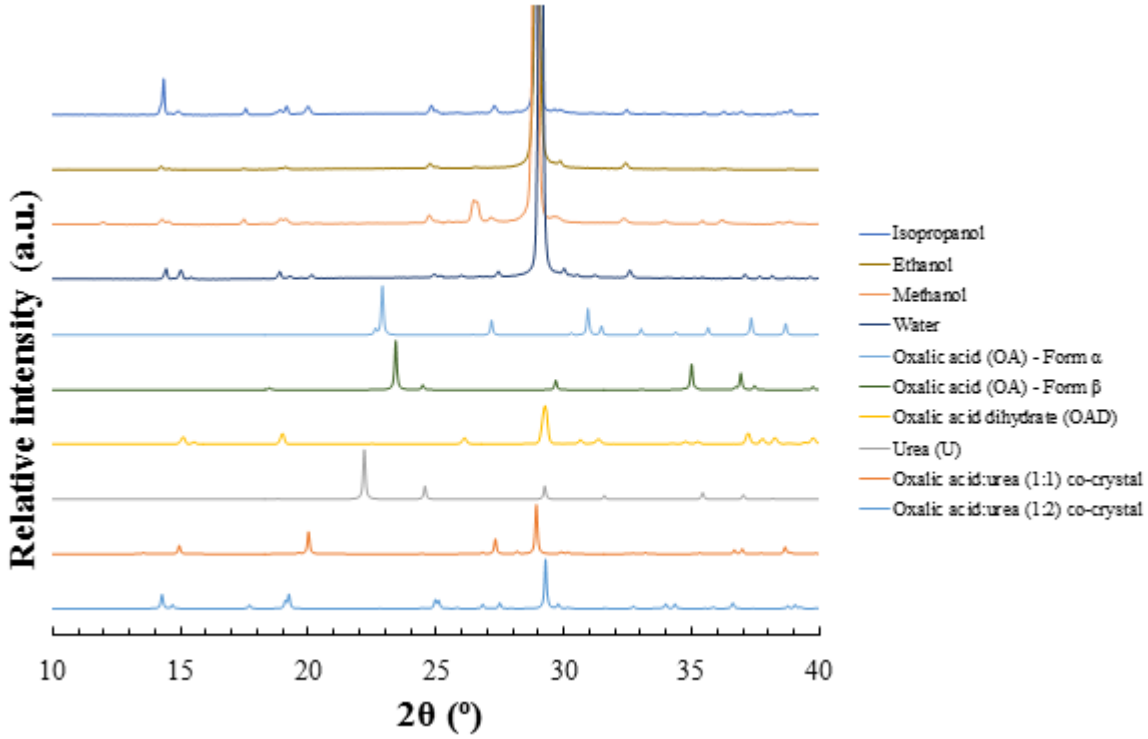

Figure A9. 32 - PXRD patterns highlighting the crystalline phases yielded from evaporative crystallisations at 40ºC, from water, methanol, ethanol and isopropanol, with oxalic acid and urea in a 1:1 stoichiometry

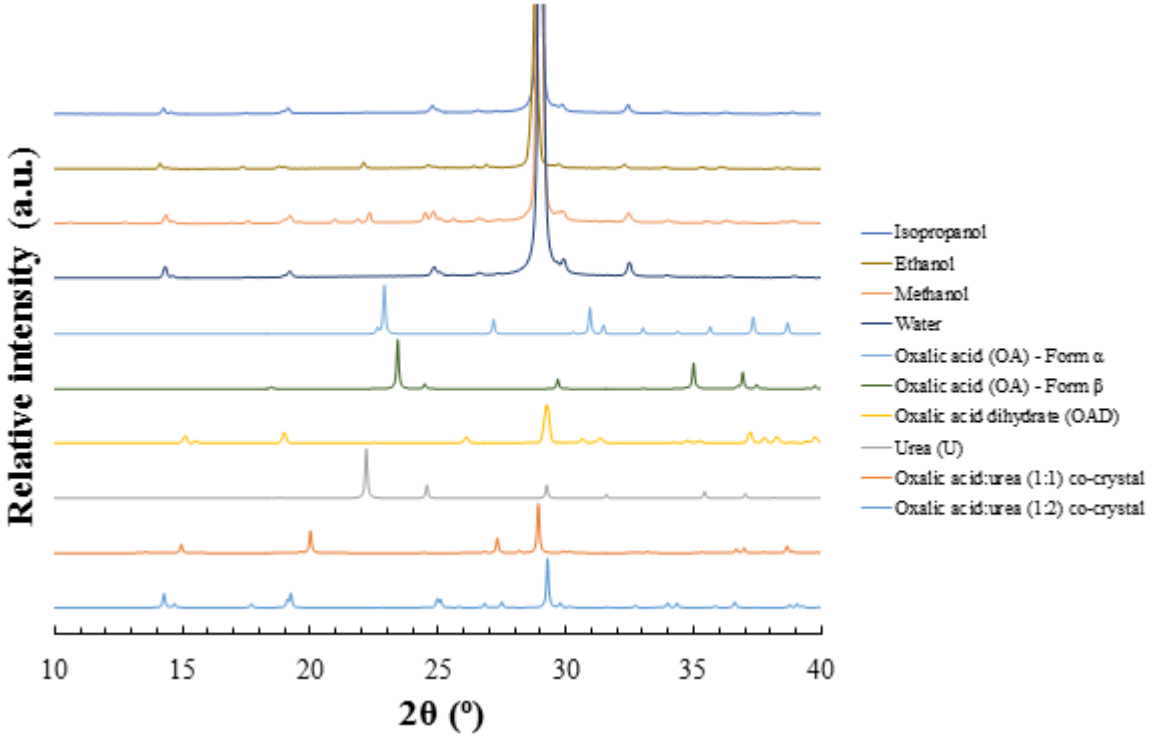

Figure A9. 33 - PXRD patterns highlighting the crystalline phases yielded from evaporative crystallisations at 40ºC, from water, methanol, ethanol and isopropanol, with oxalic acid and urea in a 1:2 stoichiometry

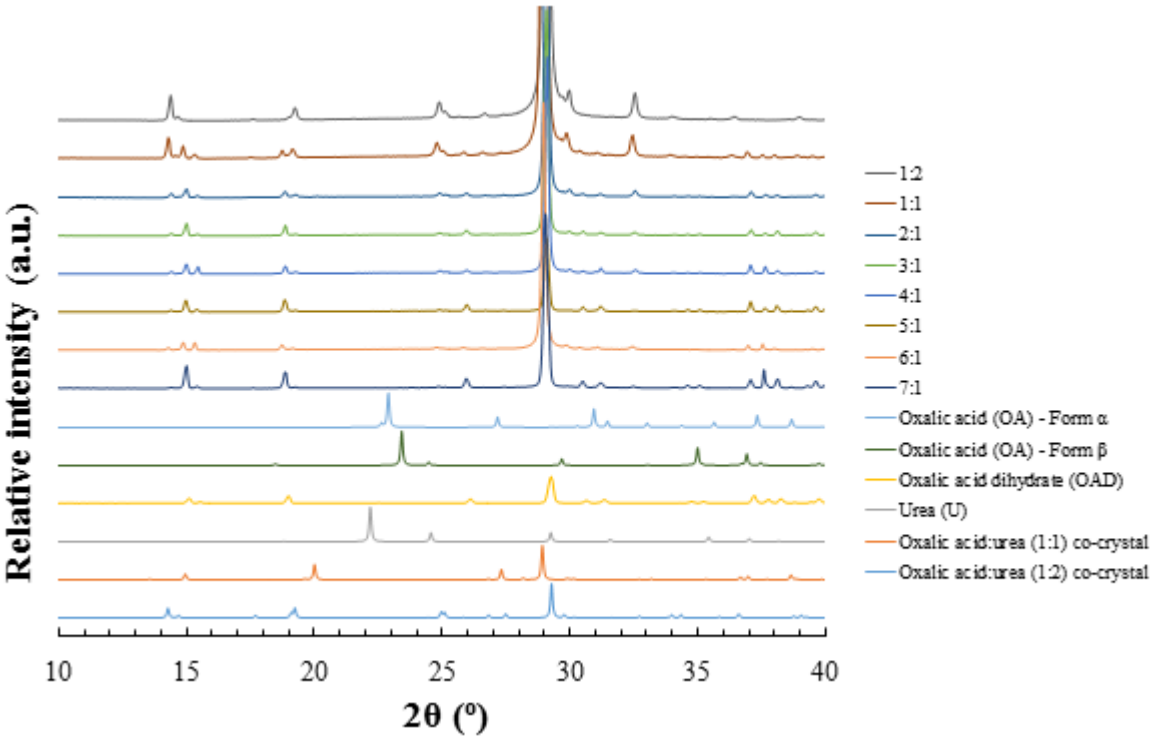

Figure A9. 34 - PXRD patterns highlighting the crystalline phases yielded from evaporative crystallisations at 4ºC, from water, with oxalic acid and urea in a range of stoichiometries (top eight patterns)

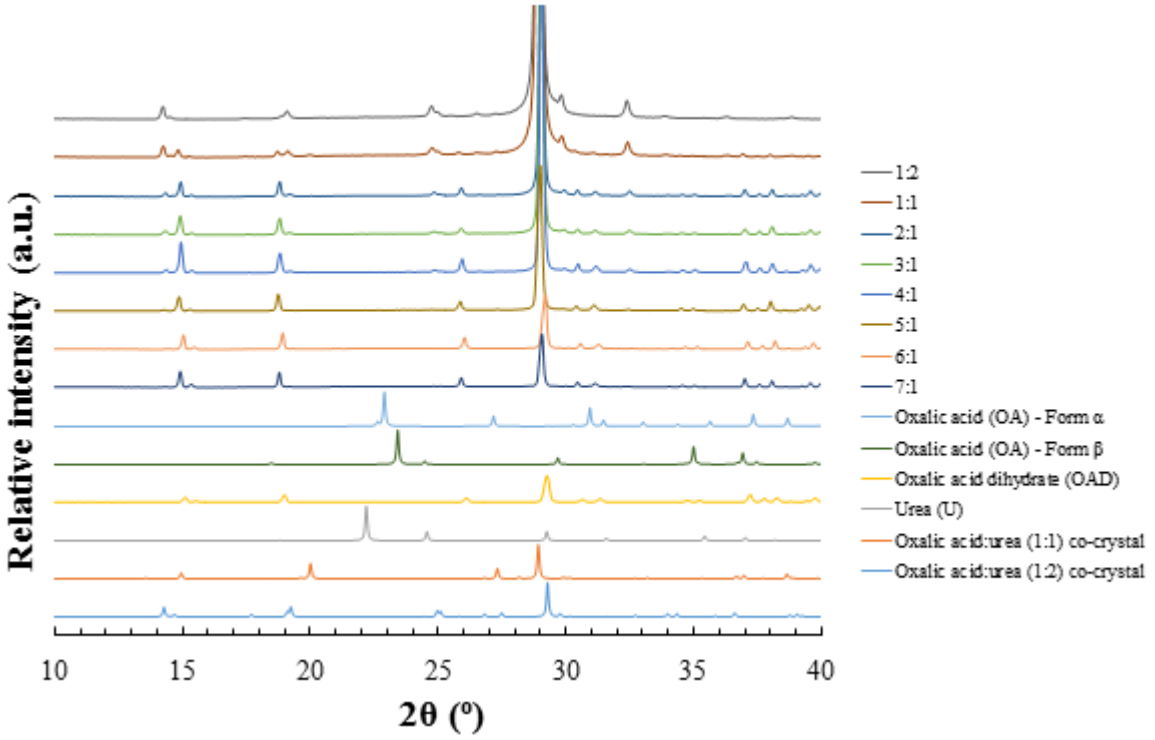

Figure A9. 35 - PXRD patterns highlighting the crystalline phases yielded from evaporative crystallisations at 20ºC, from water, with oxalic acid and urea in a range of stoichiometries (top eight patterns)

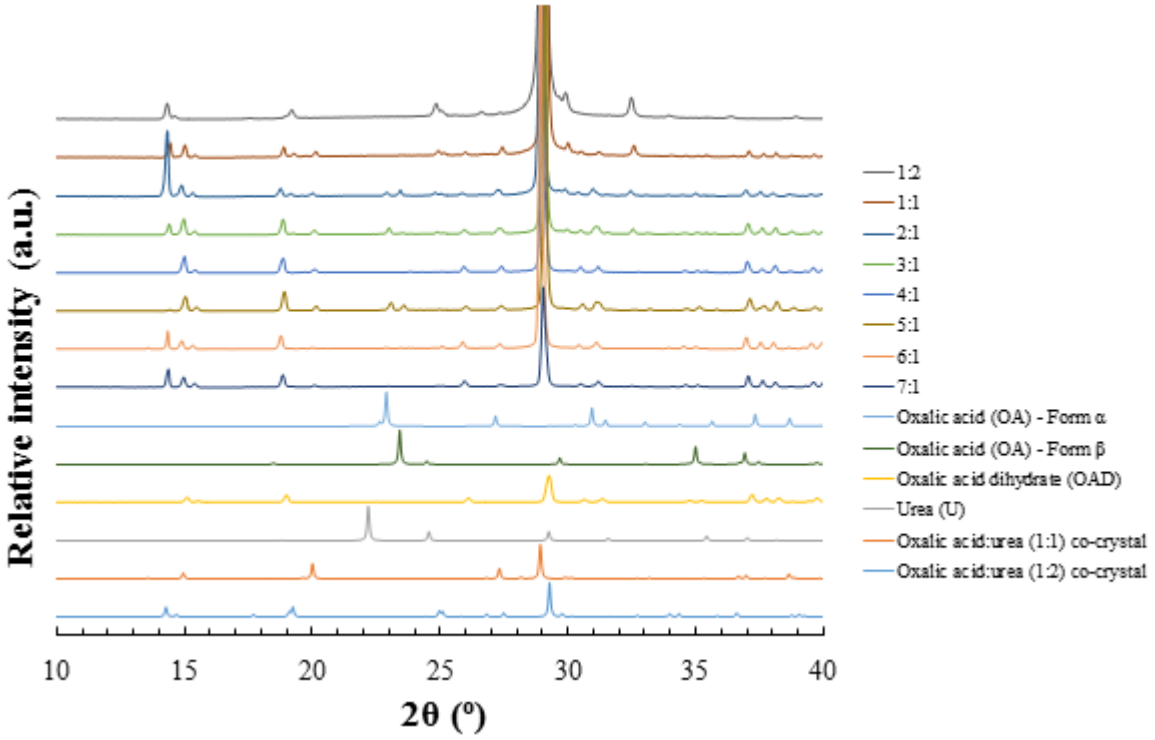

Figure A9. 36 - PXRD patterns highlighting the crystalline phases yielded from evaporative crystallisations at 40ºC, from water, with oxalic acid and urea in a range of stoichiometries (top eight patterns)

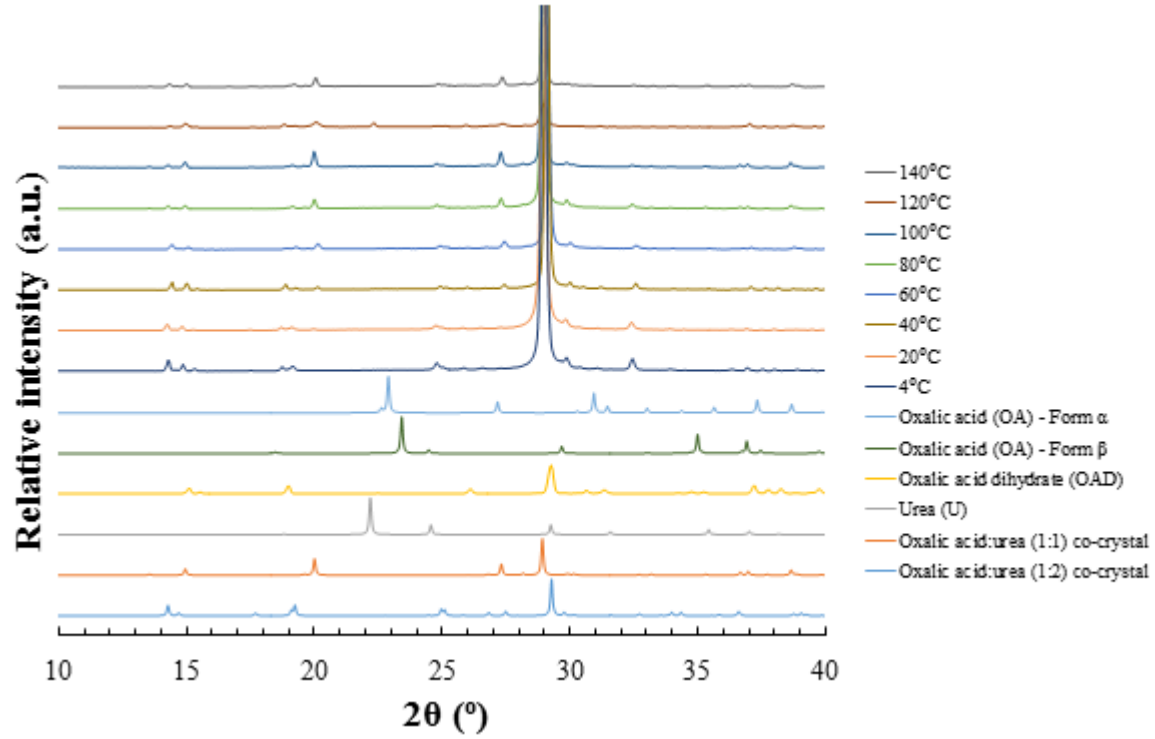

Figure A9. 37 - PXRD patterns highlighting the crystalline phases yielded from evaporative crystallisations over a range of temperatures, from water, with oxalic acid and urea in a 1:1 stoichiometry (top eight patterns)

A9.4 Batch cooling crystallisation

Table A9. 2 - Summary of the gravimetric analysis of the *OA* starting material in isopropanol, highlighting its solubility at 20ºC

Preparation	Vial (g)	Vial & Solution (g)	Vial & Solid (g)	Solution (g)	Solid (g)	Solvent (g)	Conc. (g/g)
1	6.6172	7.565	6.7794	0.9478	0.1622	0.7856	0.2064
2	6.6505	7.7001	6.8471	1.0496	0.1966	0.853	0.2304
3	6.5888	7.6885	6.7921	1.0997	0.2033	0.8964	0.2267
						Average (g/g)	0.2212

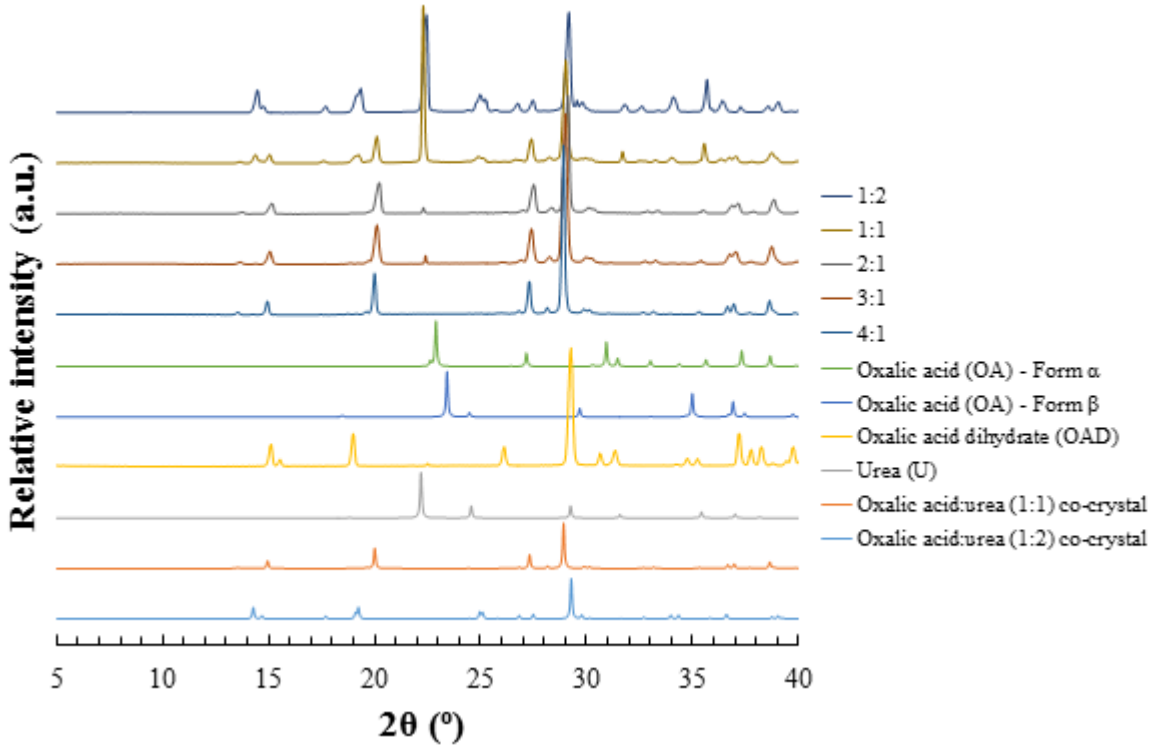

Figure A9. 38 - PXRD patterns highlighting the solid product yielded from cooling crystallisations from isopropanol over a number of *OA* to *U* stoichiometries (4:1, 3:1, 2:1, 1:1 and 1:2), with a solid loading of x1 that of the saturation of the *OA* starting material at 20ºC, cooled from 45ºC to 20ºC, mixed at 200 rpm (top five patterns)

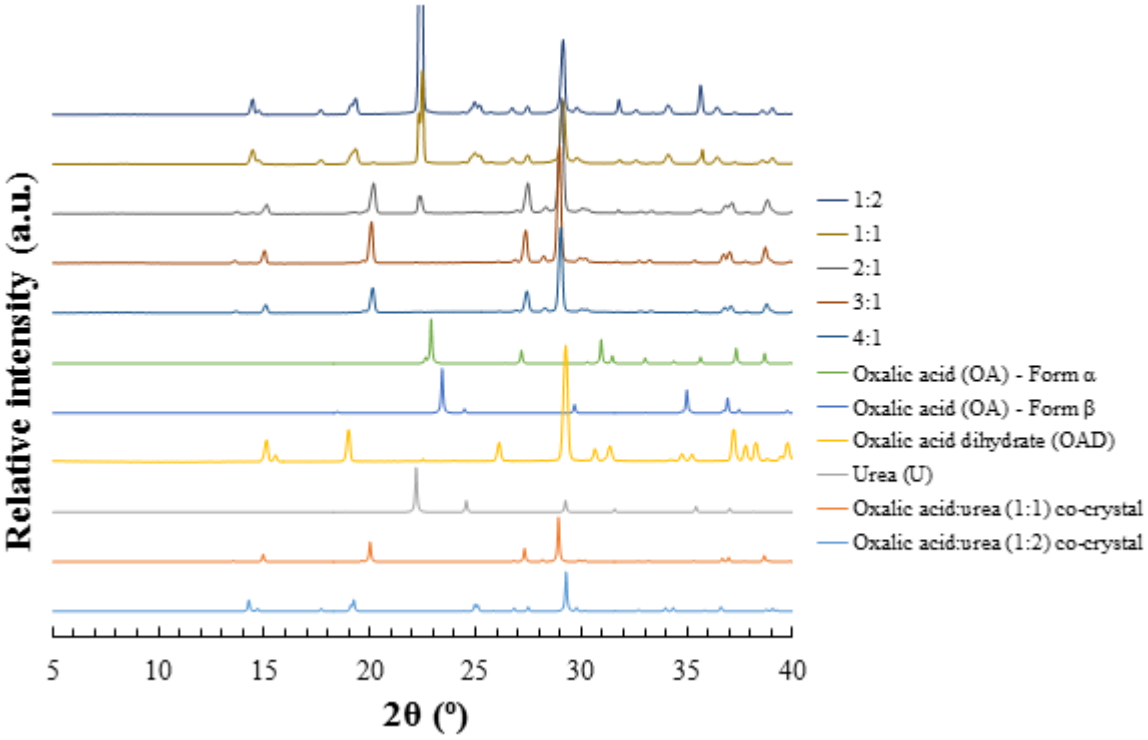

Figure A9. 39 - PXRD patterns highlighting the solid product yielded from cooling crystallisations from isopropanol over a number of *OA* to *U* stoichiometries (4:1, 3:1, 2:1, 1:1 and 1:2), with a solid loading of x0.5 that of the saturation of the *OA* starting material at 20ºC, cooled from 45ºC to 20ºC, mixed at 200 rpm (top five patterns)

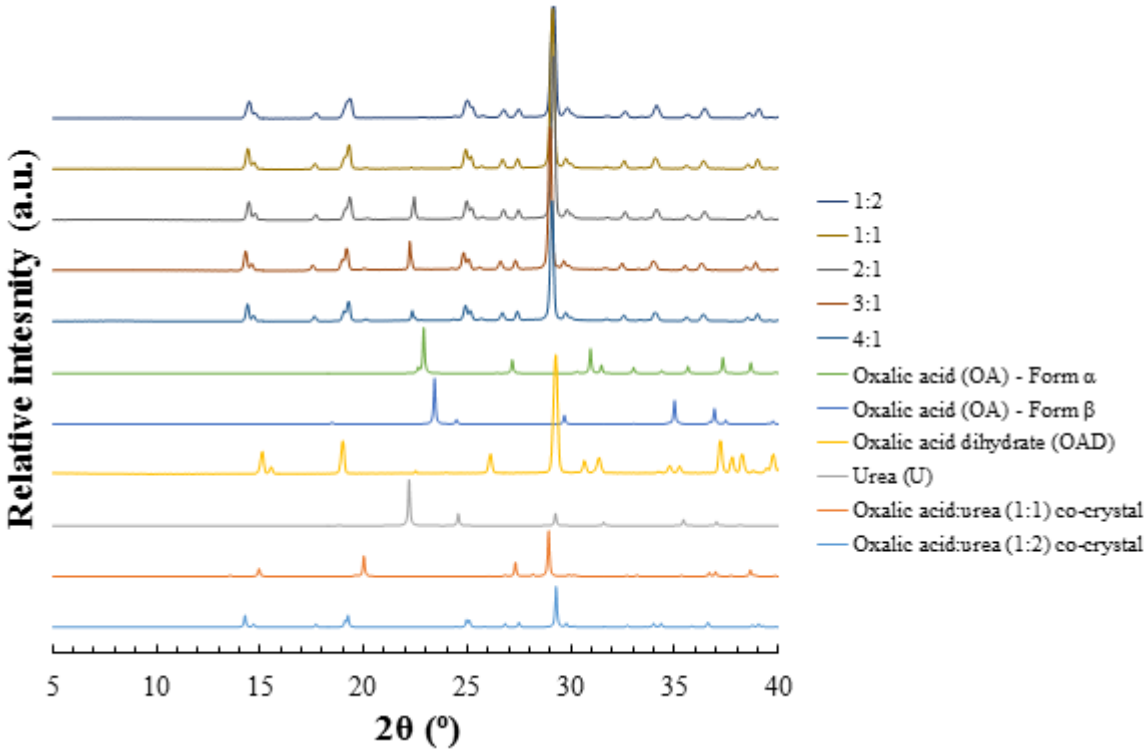

Figure A9. 40 - PXRD patterns highlighting the solid product yielded from cooling crystallisations from isopropanol over a number of *OA* to *U* stoichiometries (4:1, 3:1, 2:1, 1:1 and 1:2), with a solid loading of x0.25 that of the saturation of the *OA* starting material at 20ºC, cooled from 45ºC to 20ºC, mixed at 200 rpm (top five patterns)

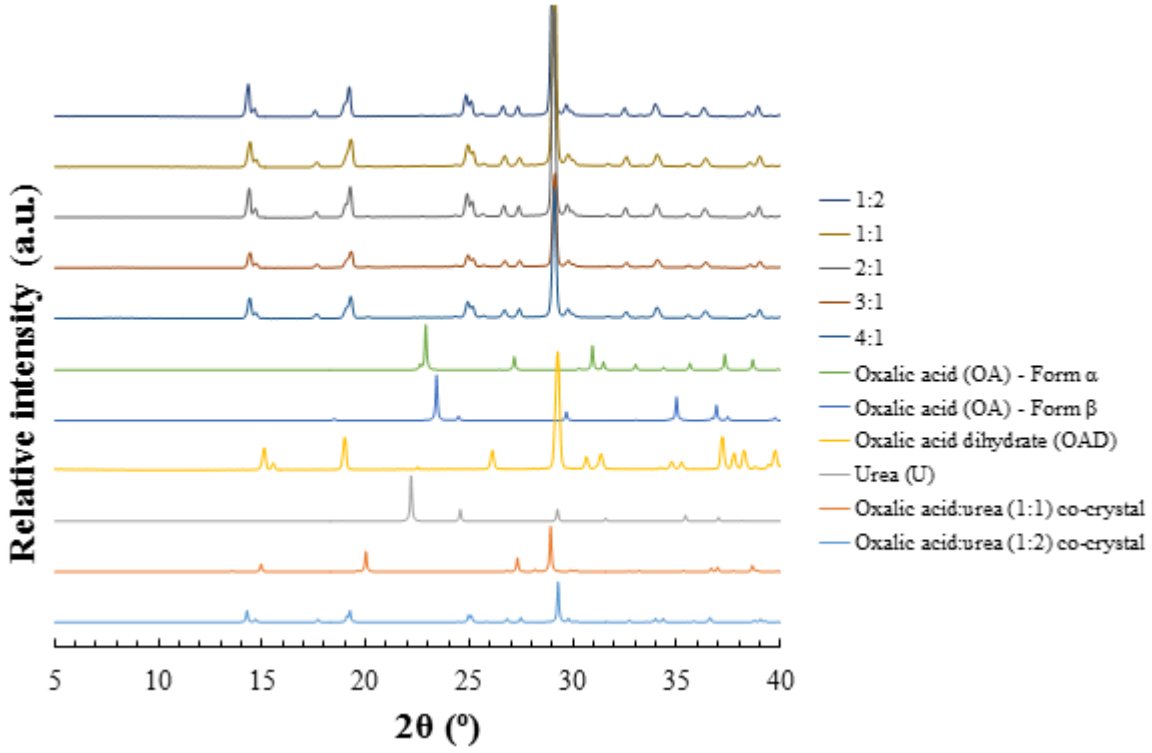

Figure A9. 41 - PXRD patterns highlighting the solid product yielded from cooling crystallisations from isopropanol over a number of *OA* to *U* stoichiometries (4:1, 3:1, 2:1, 1:1 and 1:2), with a solid loading of x0.125 that of the saturation of the *OA* starting material at 20ºC, cooled from 45ºC to 20ºC, mixed at 200 rpm (top five patterns)

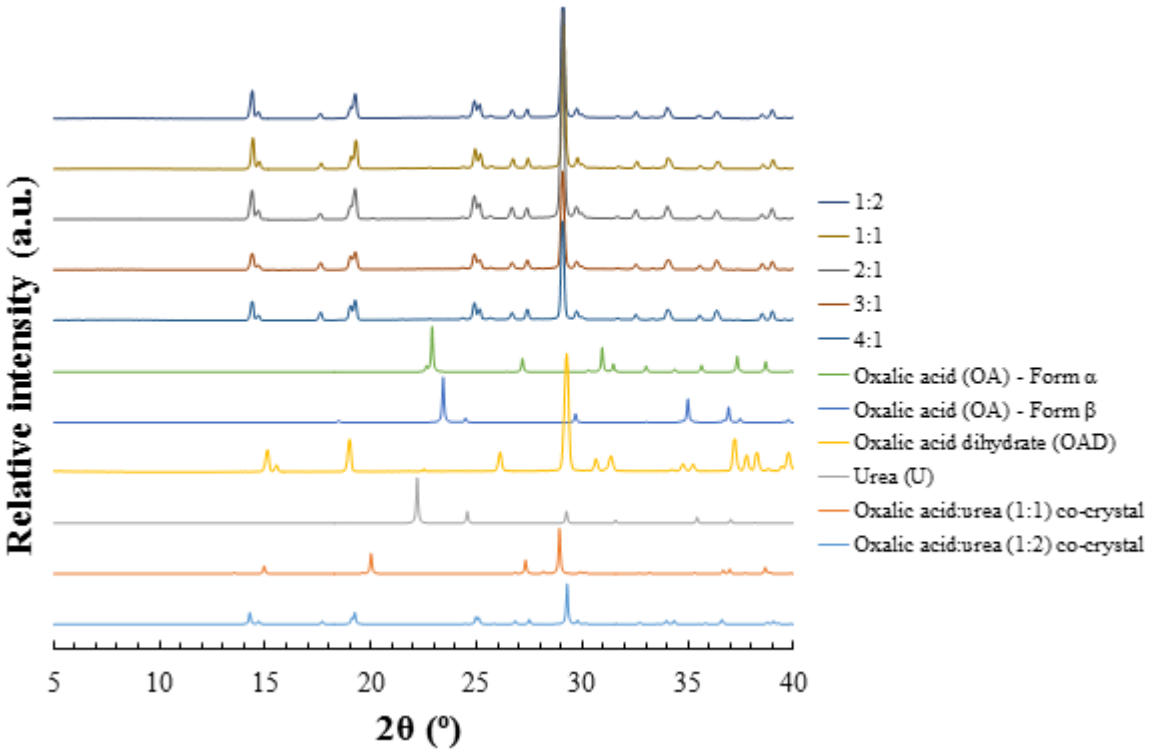

Figure A9. 42 - PXRD patterns highlighting the solid product yielded from cooling crystallisations from isopropanol over a number of *OA* to *U* stoichiometries (4:1, 3:1, 2:1, 1:1 and 1:2), with a solid loading of x0.0625 that of the saturation of the *OA* starting material at 20ºC, cooled from 45ºC to 20ºC, mixed at 200 rpm (top five patterns)

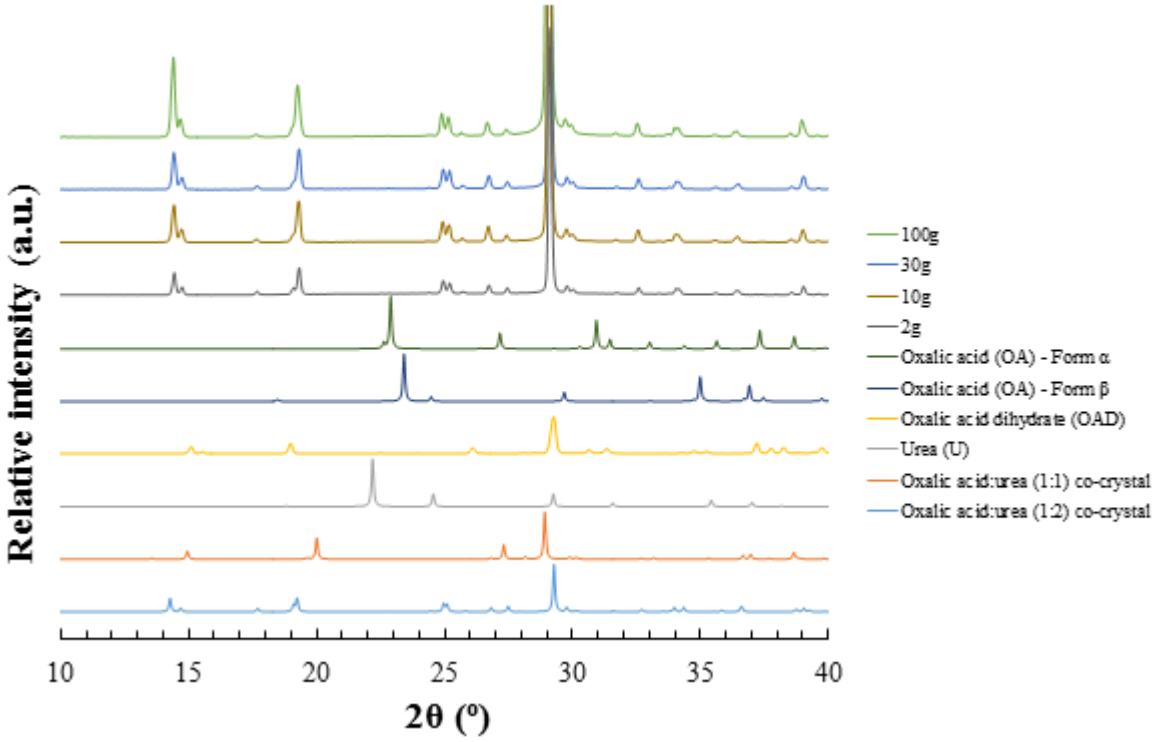

Figure A9. 43 - PXRD patterns highlighting the preparation of the oxalic acid:urea (1:2) co-crystal via cooling crystallisation at a variety of scales of water content (2g, 10g, 30g and 100g), saturated with respect to the co-crystal at 30ºC, heated to 45ºC and cooled to 20ºC at 1ºC/min

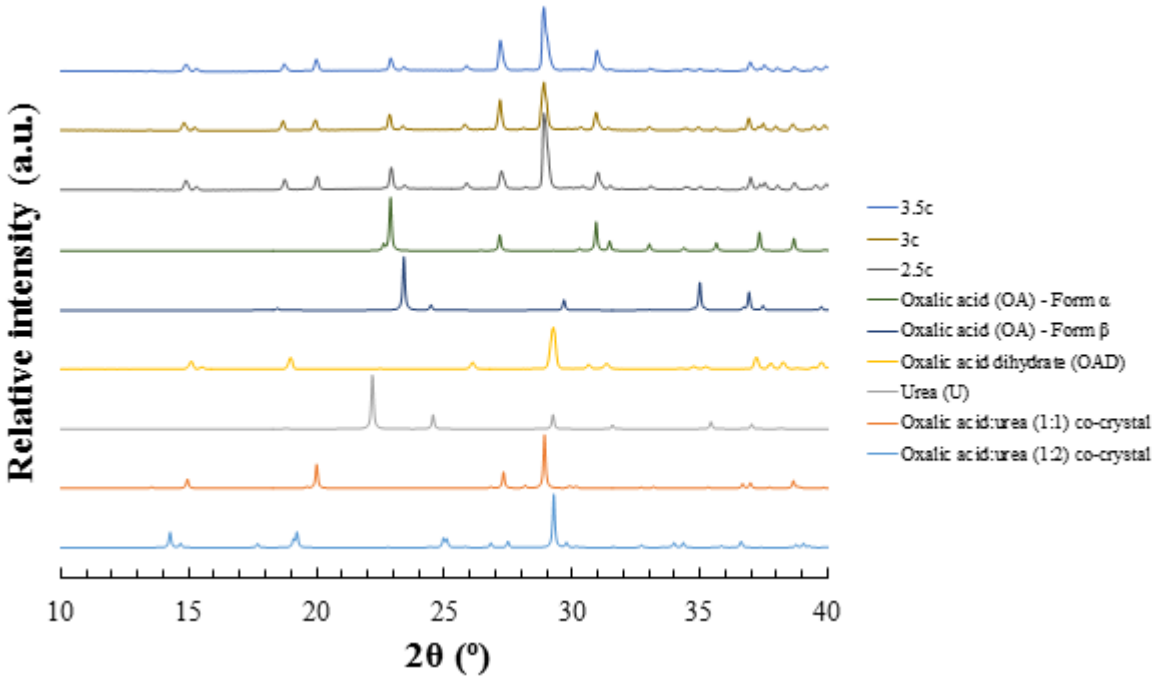

Figure A9. 44 - PXRD patterns highlighting the solid product yielded from 5:1 preparations of the oxalic acid and urea cooling crystallisation, at three saturation levels (x2.5, x3 & x3.5 the solid mass of the oxalic acid:urea (1:2) co-crystal at 30ºC), heated to 75ºC and cooled to 20ºC at 0.1ºC/min

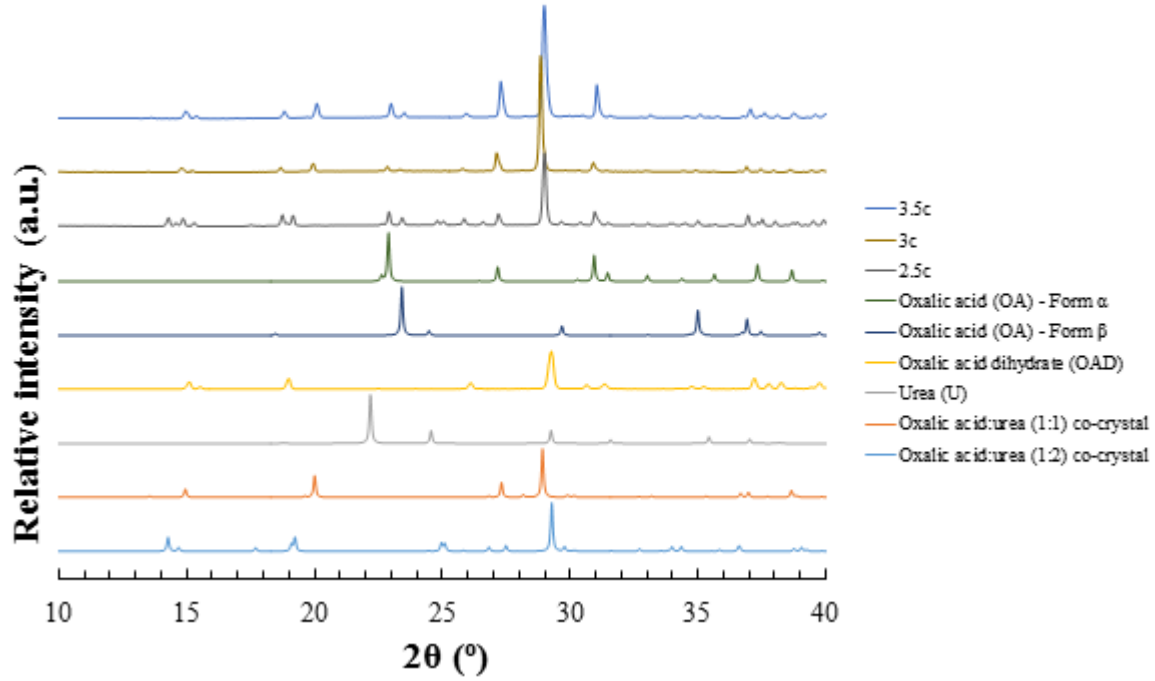

Figure A9. 45 - PXRD patterns highlighting the solid product yielded from 4:1 preparations of the oxalic acid and urea cooling crystallisation, at three saturation levels (x2.5, x3 & x3.5 the solid mass of the oxalic acid:urea (1:2) co-crystal at 30ºC), heated to 75ºC and cooled to 20ºC at 0.1ºC/min

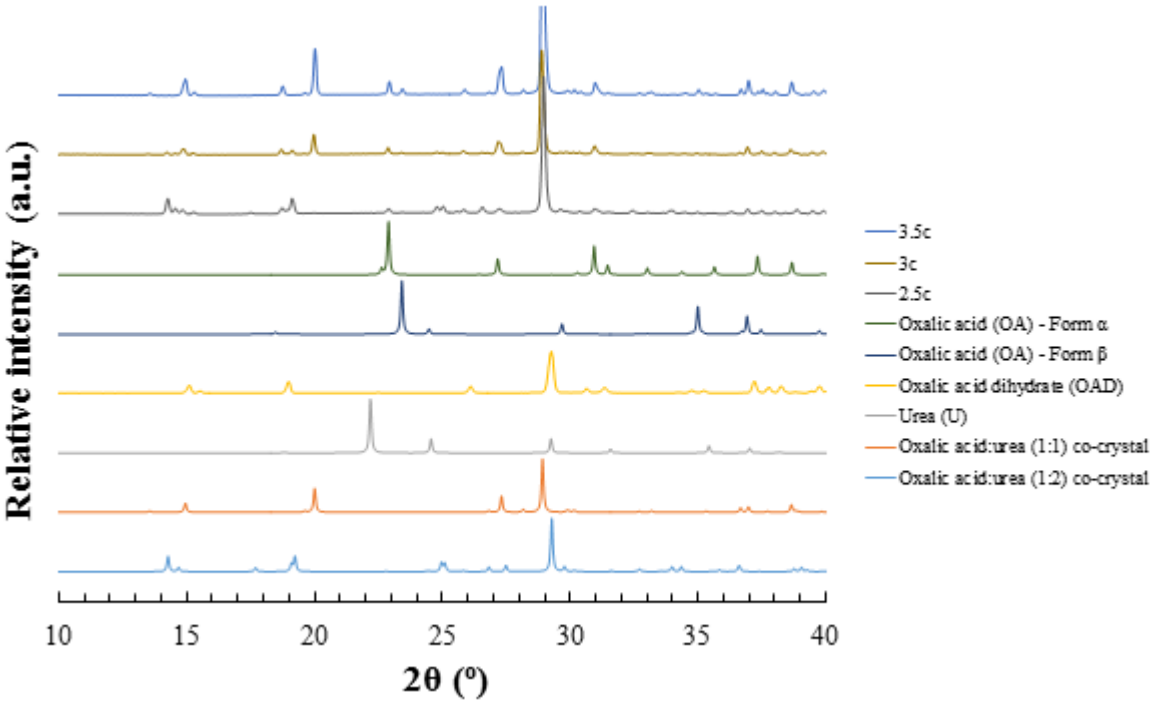

Figure A9. 46 - PXRD patterns highlighting the solid product yielded from 3:1 preparations of the oxalic acid and urea cooling crystallisation, at three saturation levels (x2.5, x3 & x3.5 the solid mass of the oxalic acid:urea (1:2) co-crystal at 30ºC), heated to 75ºC and cooled to 20ºC at 0.1ºC/min

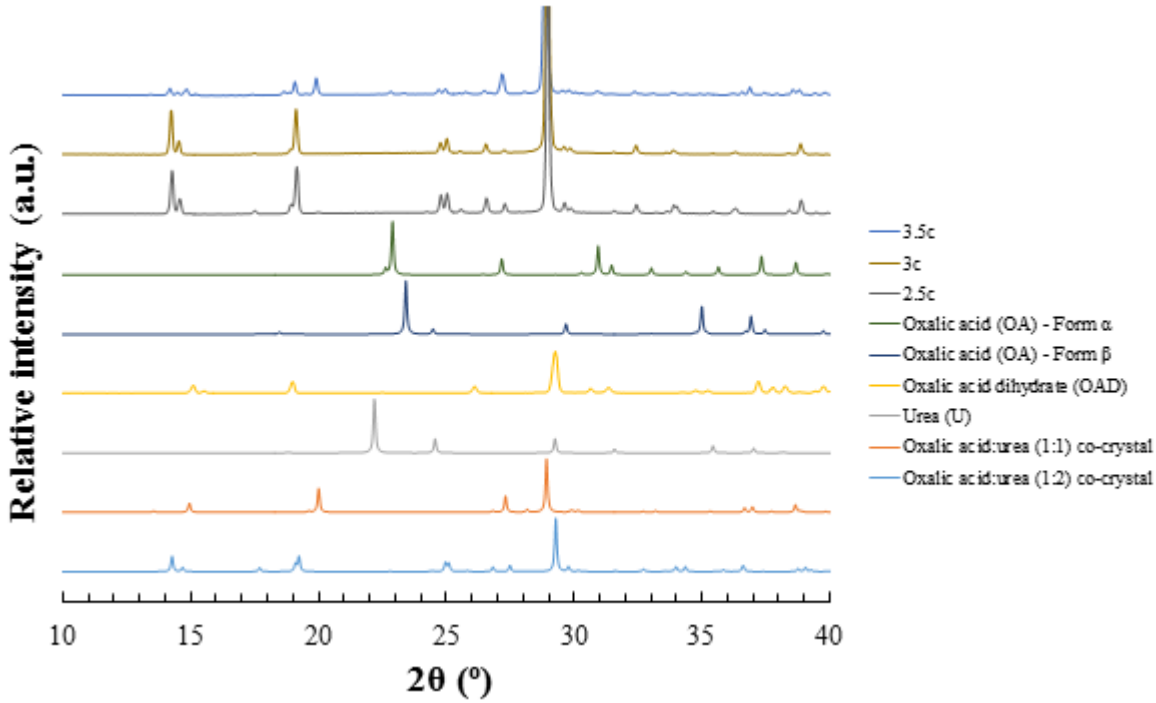

Figure A9. 47 - PXRD patterns highlighting the solid product yielded from 2:1 preparations of the oxalic acid and urea cooling crystallisation, at three saturation levels (x2.5, x3 & x3.5 the solid mass of the oxalic acid:urea (1:2) co-crystal at 30ºC), heated to 75ºC and cooled to 20ºC at 0.1ºC/min

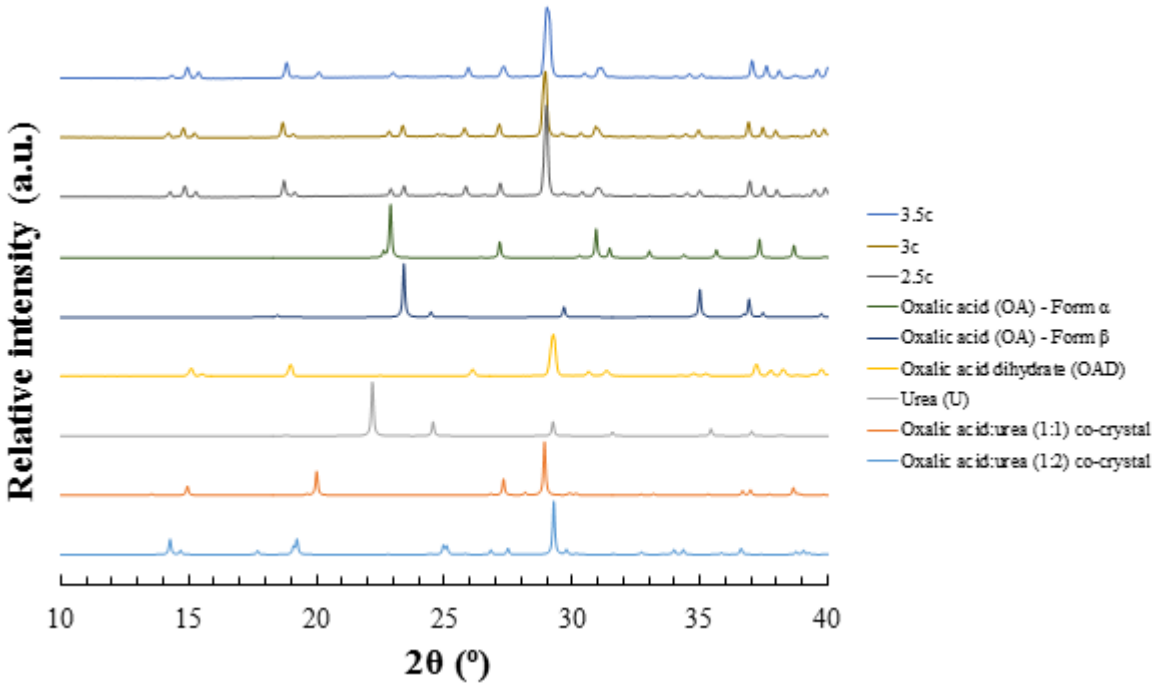

Figure A9. 48 - PXRD patterns highlighting the solid product yielded from 5:1 preparations of the oxalic acid and urea cooling crystallisation, at three saturation levels (x2.5, x3 & x3.5 the solid mass of the oxalic acid:urea (1:2) co-crystal at 30ºC), heated to 75ºC and cooled to 20ºC at 1ºC/min

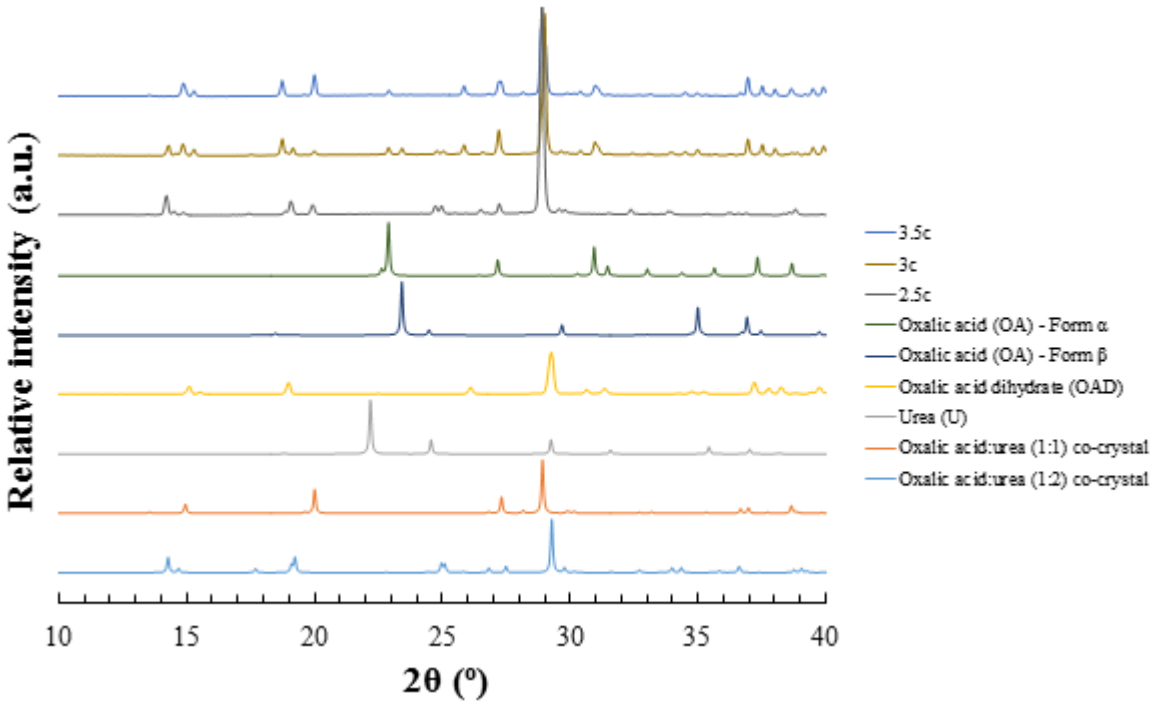

Figure A9. 49 -PXRD patterns highlighting the solid product yielded from 4:1 preparations of the oxalic acid and urea cooling crystallisation, at three saturation levels (x2.5, x3 & x3.5 the sold mass of the oxalic acid:urea (1:2) co-crystal at 30ºC), heated to 75ºC and cooled to 20ºC at 1ºC/min

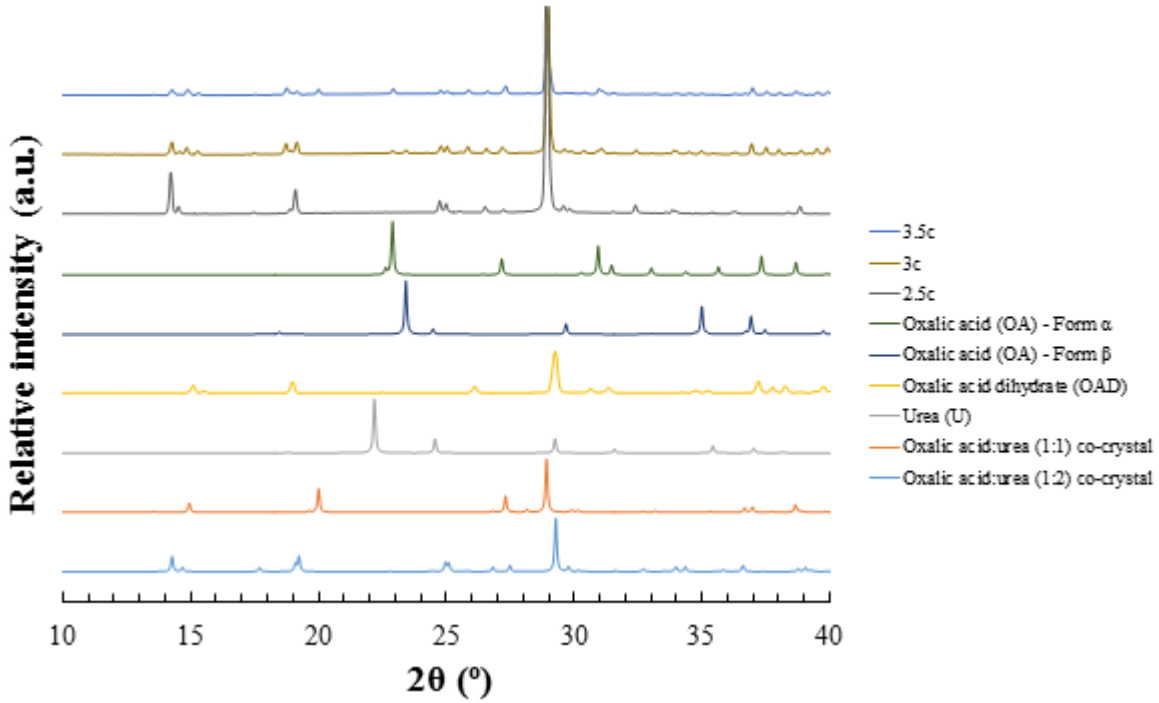

Figure A9. 50 - PXRD patterns highlighting the solid product yielded from 3:1 preparations of the oxalic acid and urea cooling crystallisation, at three saturation levels (x2.5, x3 & x3.5 the solid mass of the oxalic acid:urea (1:2) co-crystal at 30ºC), heated to 75ºC and cooled to 20ºC at 1ºC/min

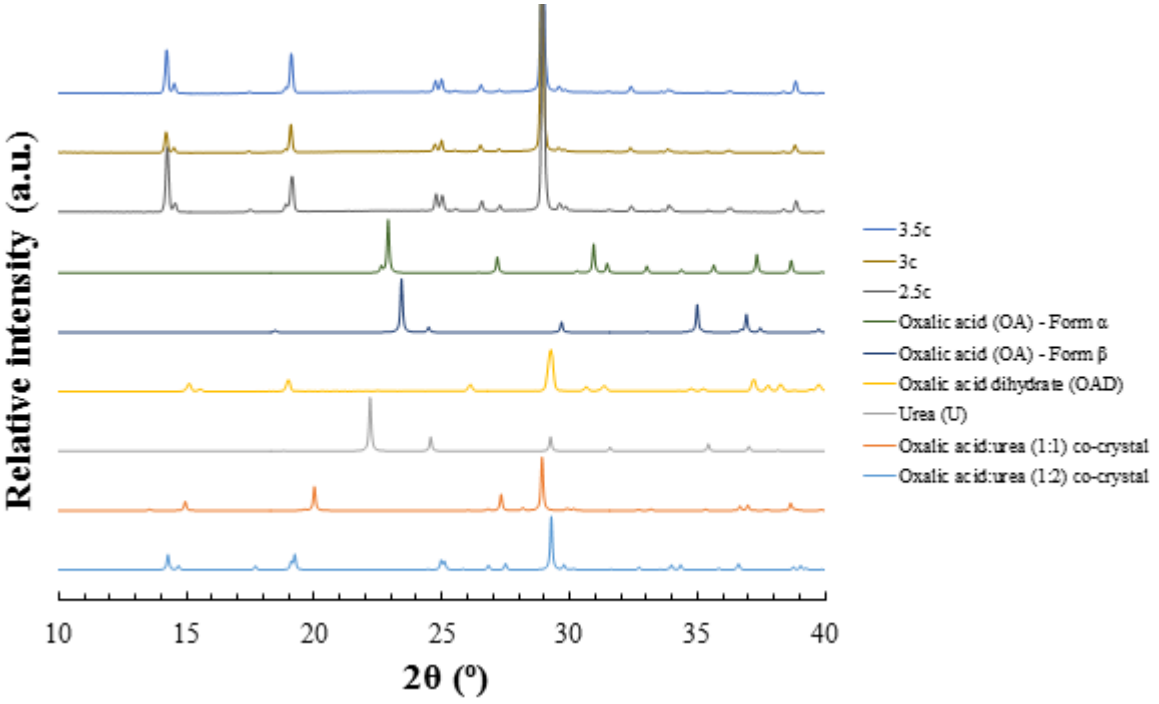

Figure A9. 51 - PXRD patterns highlighting the solid product yielded from 2:1 preparations of the oxalic acid and urea cooling crystallisation, at three saturation levels (x2.5, x3 & x3.5 the solid mass of the oxalic acid:urea (1:2) co-crystal at 30ºC), heated to 75ºC and cooled to 20ºC at 1ºC/min

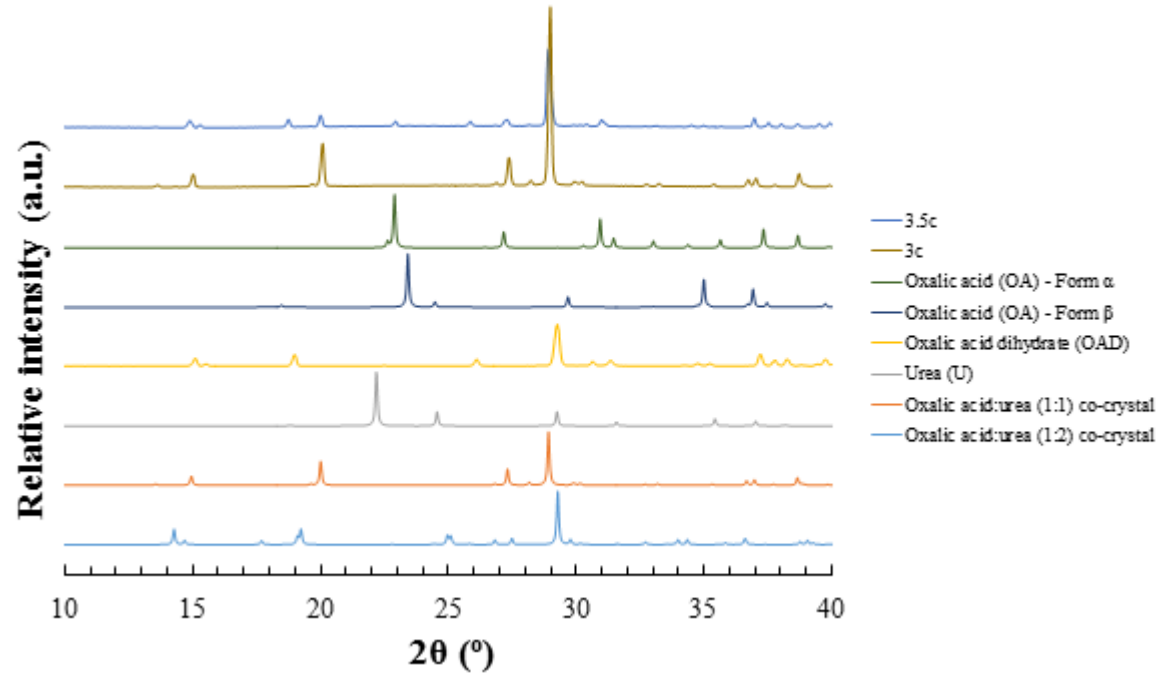

Figure A9. 52 - PXRD patterns highlighting the solid product yielded from 5:1 preparations of the oxalic acid and urea cooling crystallisation, at three saturation levels (x3 & x3.5 the solid mass of the oxalic acid:urea (1:2) co-crystal at 30ºC), heated to 75ºC and cooled to 30ºC at 0.1ºC/min

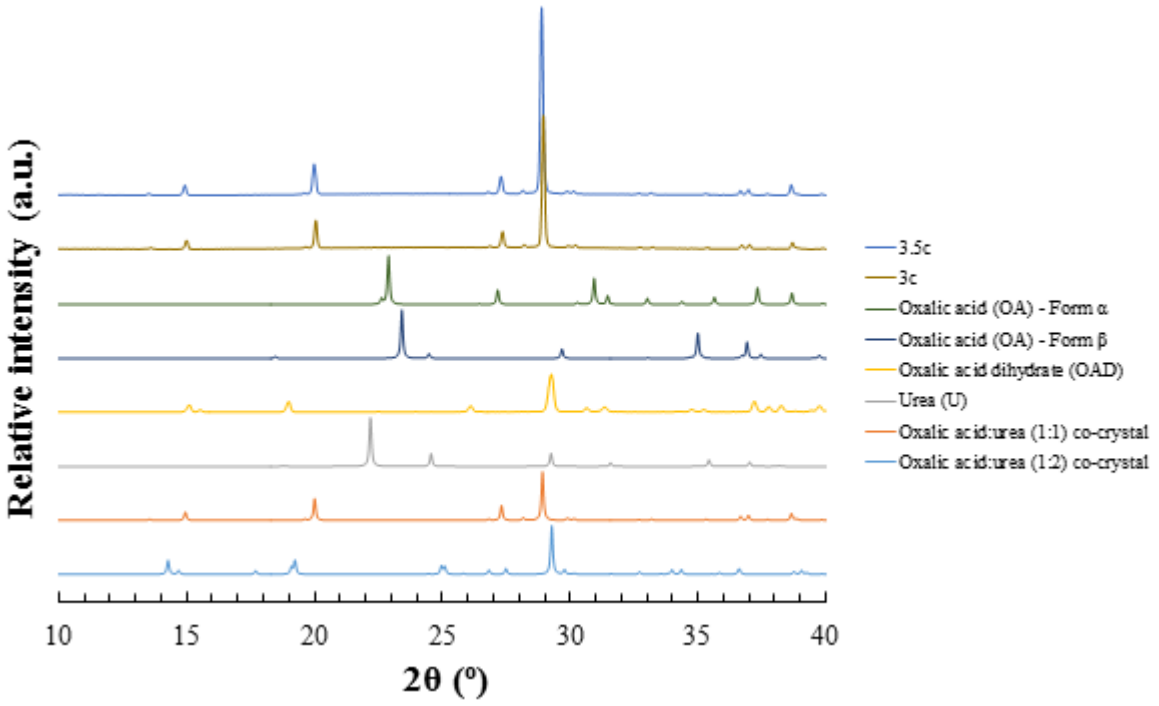

Figure A9. 53 - PXRD patterns highlighting the solid product yielded from 4:1 preparations of the oxalic acid and urea cooling crystallisation, at three saturation levels (x3 & x3.5 the solid mass of the oxalic acid:urea (1:2) co-crystal at 30ºC), heated to 75ºC and cooled to 30ºC at 0.1ºC/min

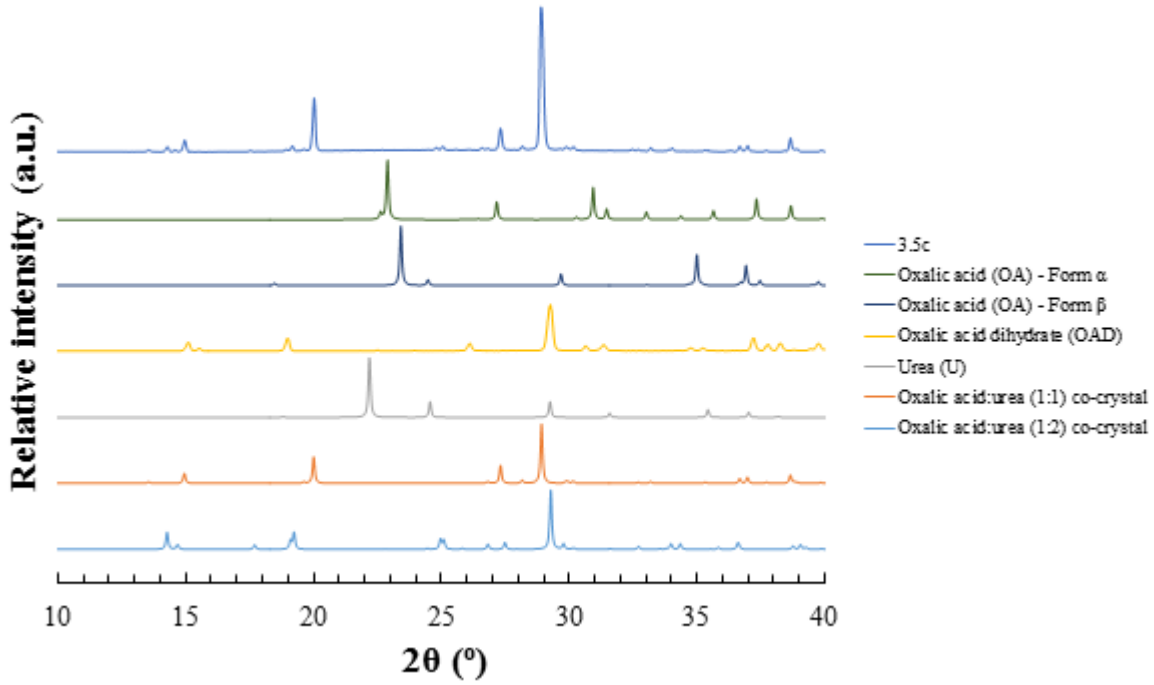

Figure A9. 54 - PXRD patterns highlighting the solid product yielded from 3:1 preparations of the oxalic acid and urea cooling crystallisation, at three saturation levels (x3.5 the solid mass of the oxalic acid:urea (1:2) co-crystal at 30ºC), heated to 75ºC and cooled to 30ºC at 0.1ºC/min

A9.5 Continuous cooling crystallisation

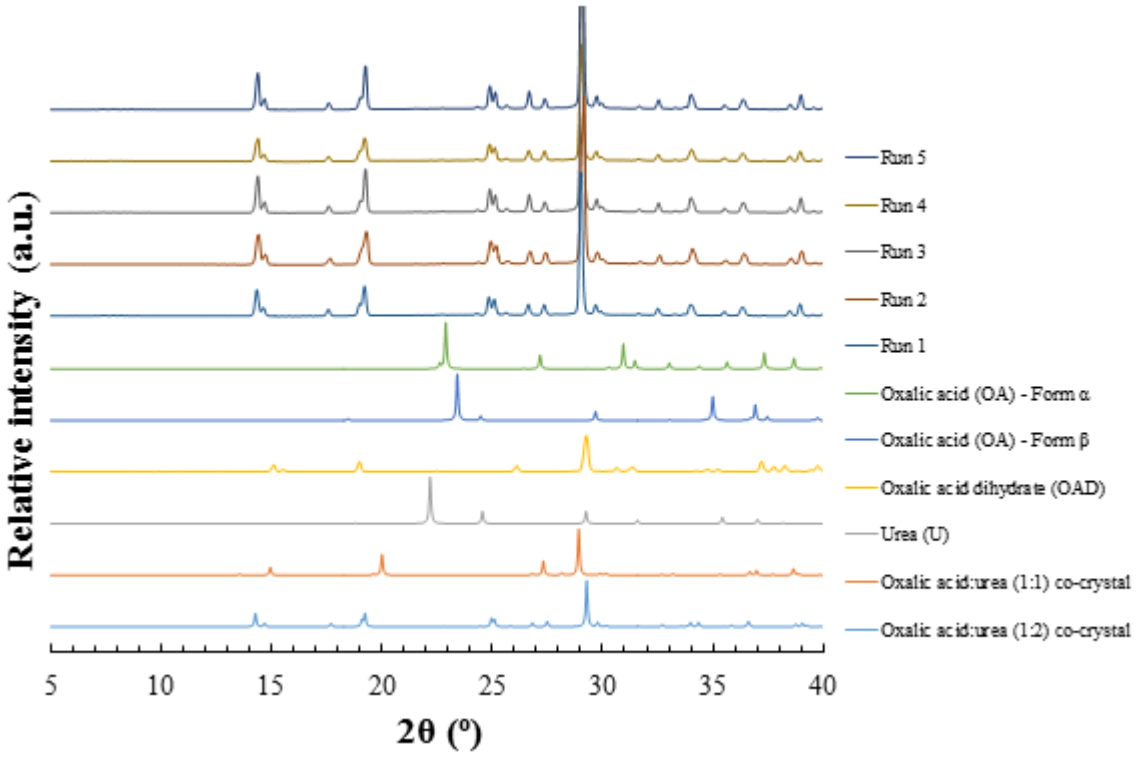

Figure A9. 55 - PXRD patterns highlighting the solid material obtained from COBC runs 1-5, collected either as precipitate from the end piece or as product from the body of the crystalliser

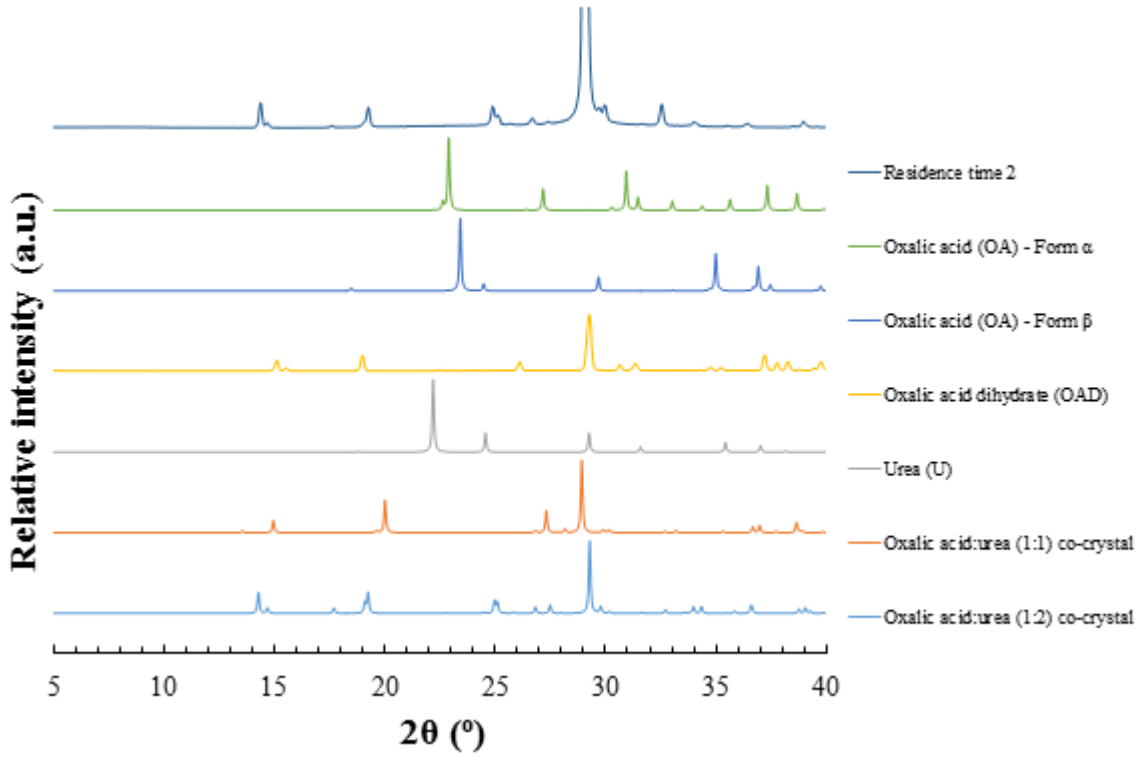

Figure A9. 56 - PXRD patterns, highlighting the phase of the solid product yielded from the second residence time as collected from the KRAIC